Transactions of the ASME®

Transactions of the ASME, Journal of Turbomachinery (ISSN 0889-504X) is published quarterly (Jan., Apr., July, Oct.) by The American Society of Mechanical Engineers, Three Park Avenue, New York, NY 10016. Periodicals postage paid at New York, NY and additional mailing offices. POSTMASTER: Send address changes to Transactions of the ASME, Journal of Turbomachinery, c/o THE AMERICAN SOCIETY OF MECHANICAL ENGINEERS, 22 Law Drive, Box 2300, Fairfield, NJ 07007-2300.
CHANGES OF ADDRESS must be received at Society headquarters seven weeks before they are to be effective. Please send old label and new address.
STATEMENT from By-Laws. The Society shall not be responsible for statements or opinions advanced in papers or ... printed in its publications (B7.1, Par. 3).

INDEXED by Applied Mechanics Reviews and Engineering Information, Inc. Canadian Goods & Services Tax Registration #126148048

Journal of Turbomachinery

Published Quarterly by The American Society of Mechanical Engineers

VOLUME 122 • NUMBER 4 • OCTOBER 2000

TECHNICAL PAPERS

(**Contents continued on inside back cover**)

This journal is printed on acid-free paper, which exceeds the ANSI Z39.48-1992 specification for permanence of paper and library materials. ♾™
♻ 85% recycled content, including 10% post-consumer fibers.

Journal of Turbomachinery **Volume 122, Number 4** **OCTOBER 2000**

ANNOUNCEMENT

A Transport Model for the Deterministic Stresses Associated With Turbomachinery Blade Row Interactions

Allan G. van de Wall[1]

Jaikrishnan R. Kadambi

Department of Mechanical and Aerospace Engineering, Case Western Reserve University, Cleveland, OH 44106

John J. Adamczyk

NASA Glenn Research Center, Cleveland, OH 44135

The unsteady process resulting from the interaction of upstream vortical structures with a downstream blade row in turbomachines can have a significant impact on the machine efficiency. The upstream vortical structures or disturbances are transported by the mean flow of the downstream blade row, redistributing the time-average unsteady kinetic energy (K) associated with the incoming disturbance. A transport model was developed to take this process into account in the computation of time-averaged multistage turbomachinery flows. The model was applied to compressor and turbine geometry. For compressors, the K associated with upstream two-dimensional wakes and three-dimensional tip clearance flows is reduced as a result of their interaction with a downstream blade row. This reduction results from inviscid effects as well as viscous effects and reduces the loss associated with the upstream disturbance. Any disturbance passing through a compressor blade row results in a smaller loss than if the disturbance was mixed-out prior to entering the blade row. For turbines, the K associated with upstream two-dimensional wakes and three-dimensional tip clearance flows are significantly amplified by inviscid effects as a result of the interaction with a downstream turbine blade row. Viscous effects act to reduce the amplification of the K by inviscid effects but result in a substantial loss. Two-dimensional wakes and three-dimensional tip clearance flows passing through a turbine blade row result in a larger loss than if these disturbances were mixed-out prior to entering the blade row. [S0889-504X(00)01804-3]

Introduction

A series of experiments on a four-stage low-speed research compressor reported on by Smith [1] was conducted in the late 1960's. He observed that the four-stage average total pressure efficiency increased when the axial gap between the rotors and stators was decreased. The results, shown in Fig. 1, show the efficiency as a function of the flow coefficient at a reduced gap case (7 percent axial chord) and a wide gap case (37 percent axial chord). The efficiency of the reduced gap case is approximately one point higher than the wide gap case. Observations by Mikolajczak [2] for a compressor were similar. For a turbine, the efficiency is also a function of axial spacing; however, the opposite effect appears to be true. As the axial gap is increased, the efficiency of the turbine increases. Figure 2 shows the results for a series of experiments on a reaction turbine [3]. The results show an increase in peak overall efficiency as the stator–rotor gap is increased from 0.10 to 0.60 in. Note that the efficiency increases rapidly to a value above which any increase in stator–rotor gap results in no increase in efficiency. Similar observations for a 1.5 stage low-speed turbine were reported by Sharma et al. [4].

Using these examples, one can ask the following two questions: ''What process is causing this change in the efficiency with a change in axial gap?'' and ''Is this change the result of steady or unsteady flow processes?'' These examples do not explicitly show that the changes in performance are the result of unsteady flows. However, one possible explanation for the effect relating to unsteady flow is that a change in the mixing losses of wakes of each blade row is occurring. The loss associated with a wake is not fully realized until the wake under goes a viscous mixing process. If some process exists that can reduce the wake mixing loss, the total loss could be reduced. Consider a rotor followed by a stator. The wake of a rotor operating in isolation will convect downstream and eventually decay by viscous means and incur a loss in efficiency. However, if the rotor is followed by a stator, the rotor wakes are then chopped up by the stator into segments and transported through the stator by the time-average or mean flow. The transported wake segments are reoriented (i.e., the wake segments are tilted and stretched). As the wake segments are tilted and stretched, vorticity kinematics begins to play a role changing the decay of the rotor wake. The rotor wake decay in the stage now involves two mechanisms, viscosity as well as the kinematics of wake stretching and tilting resulting from the stator row. Vorticity kinematics can act to reduce (or increase) the velocity deficit associated with a wake by a process that is reversible, therefore reducing (or increasing) the mixing loss associated with the wake. This was first postulated by Smith [5] and was referred to as recovery.

This recovery process can have a significant impact on turbomachine performance. Adamczyk [6] stated that the mixing loss of a compressor blade in a well-designed machine is approximately 15 percent of the total loss of the blade. If 70 percent of the wake mixing loss could be reduced by recovery of the wake [7], the total loss of the compressor blade could be reduced by 10.5 percent. Smith [8] estimated that at design condition, the recovery process can yield a half-point increase in adiabatic efficiency.

The conclusions from this literature review provide evidence that the effect on turbomachine performance of recovery is of significant magnitude to justify further investigation. Since time-averaged codes used in turbomachinery analysis currently do not explicitly include the effects of recovery, the objective of this paper is to develop a model for this recovery process. The poten-

[1]Present address: General Electric Aircraft Engines, Cincinnati, OH.

Contributed by the International Gas Turbine Institute and presented at the 45th International Gas Turbine and Aeroengine Congress and Exhibition, Munich, Germany, May 8–11, 2000. Manuscript received by the International Gas Turbine Institute February 2000. Paper No. 2000-GT-430. Review Chair: D. Ballal.

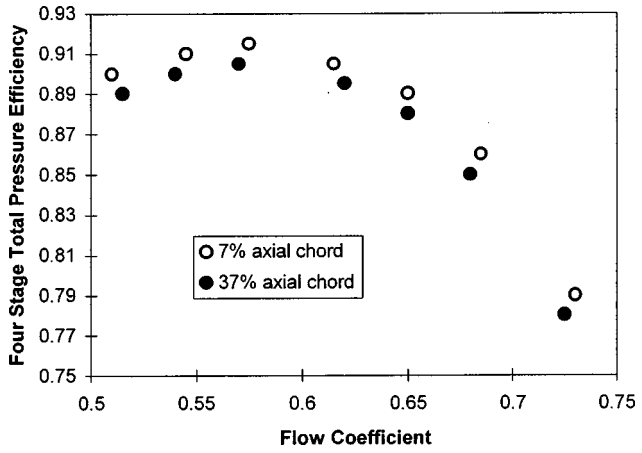

Fig. 1 Change in efficiency for a four stage axial compressor operating at two axial gaps [1]

tial payoff of this research is that the insight gained into the flow process associated with recovery will provide direction for improving turbomachine performance.

This paper is divided up into five further sections. In the next section, recovery is formally defined and methods for computing it are described. This is followed by a description of the development of a transport model to calculate recovery that can be used in the time-averaged calculation of turbomachinery flows. A validation study of the model is described next using the results of previous work as well as analytical models. The model is then applied to both compressor and turbine geometry of current interest. Finally, conclusions and recommendations for future work are described.

Recovery

To illustrate the physics behind recovery as postulated by Smith [5], two examples are given, one relating to a compressor and one relating to a turbine. Imagine an unsteady process in which a velocity disturbance in the z direction is oriented perpendicular to the centerline of a diffusing duct, and is convected by the mean flow (Fig. 3). Assuming the flow is two-dimensional, incompressible, and inviscid, and using Kelvin's theorem, the circulation around a loop of fluid that consists of the disturbance edge and centerline (contour C) is constant throughout the duct and is given by,

$$\Gamma = v_d l = \text{const}, \tag{1}$$

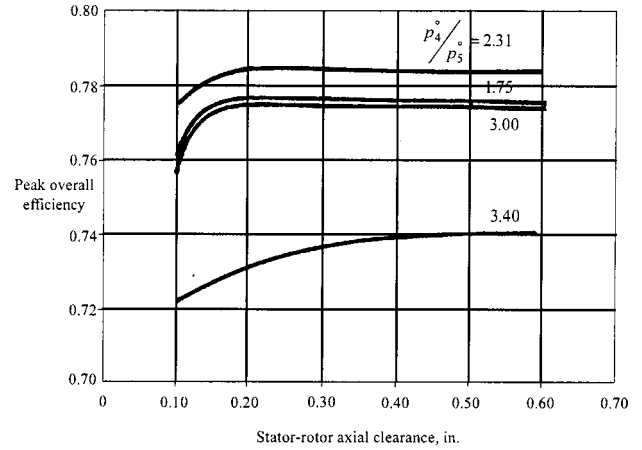

Fig. 2 Change in peak overall efficiency for a reaction turbine from data of WRIGHT AERONAUTICAL CORP [3]

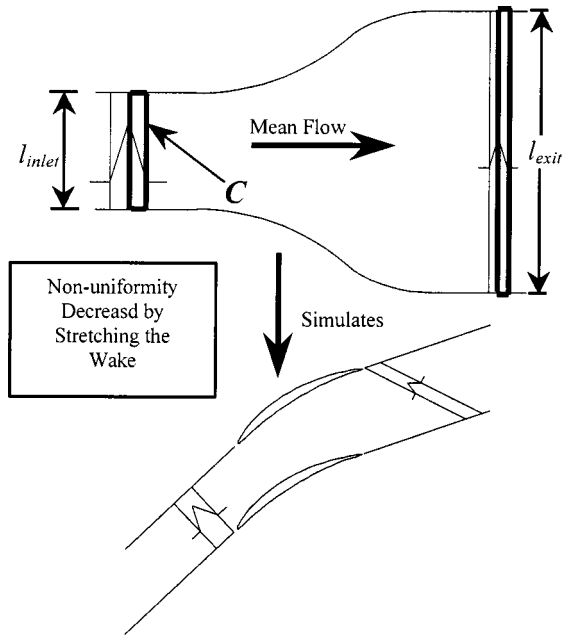

Fig. 3 Illustration of how a wake stretching in a diffusing duct simulates compressor flows

where v_d is the disturbance depth, and l is the length of the disturbance segment. If the exit disturbance segment length is increased, the magnitude of the disturbance depth is reduced by a reversible flow process. If the disturbance is now mixed-out by viscosity, it will incur a smaller loss than if the disturbance was mixed-out prior to entering the duct. This situation simulates that of a compressor, where the disturbance is a wake from the upstream blade row and the wake segments are stretched as they are convected through the downstream blade row.

Now consider a situation in which a velocity disturbance is oriented perpendicular to the centerline of an accelerating duct and is convected by the mean flow (Fig. 4). The exit disturbance

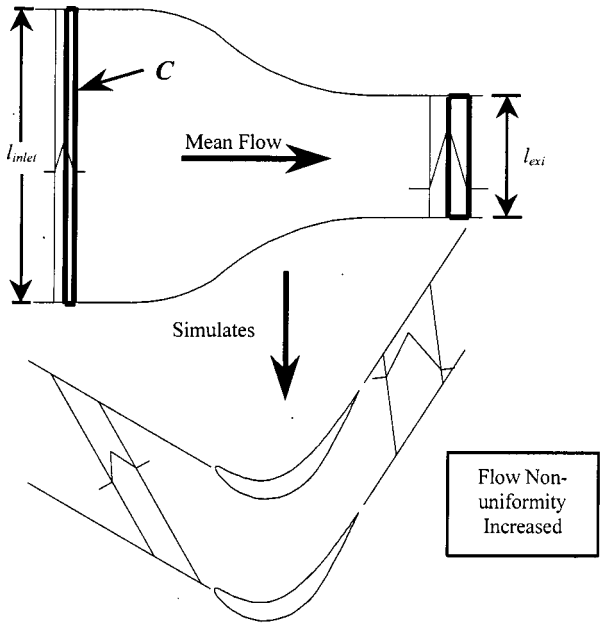

Fig. 4 Illustration of how a wake compressing in an accelerating duct simulates turbine flows

length is reduced and therefore the depth is increased by a reversible flow process. If the disturbance is now mixed-out by viscosity, it will incur a larger loss than if the disturbance was mixed-out prior to entering the duct. This situation simulates that of a wake generated by an upstream blade row in a turbine, where the wake segments are compressed as they are convected through the downstream blade row.

Neither case incurs any loss until the wake nonuniformity is mixed-out by viscosity. However, the magnitude of the wake depth is decreased in the compressor case and increased in the turbine case by inviscid means, this is the key to recovery. Therefore, one would expect the mixing loss to decrease in the case of the compressor and increase in the case of the turbine. However, in both of these cases, viscosity is acting concurrently with the inviscid mechanism to reduce the magnitude of the disturbance. This process is not reversible and will incur a loss. The relative magnitudes of the inviscid and viscous mechanisms involved is important to determining the potential benefit from recovery. Finally, in both of these examples, the upstream disturbance was a wake caused by an upstream blade row. However, the same principles apply to any upstream vortical disturbance such as tip vortices, streamwise vorticies, and wakes caused by struts or other obstructions in the primary flowpath.

In order to understand and calculate the recovery process, we first need to examine the mixing process of a flow nonuniformity such as a wake created by an upstream blade row for an unsteady subsonic flow and determine how it relates to mixing loss. This is the mixing loss that would occur if the wake were allowed to mix-out in isolation by viscosity alone. Adamczyk [7] showed that for an incompressible flow, the mixing loss could be evaluated using linear theory, but can also apply to higher order disturbances. Later, van de Wall [9] came to the same conclusion for a subsonic flow. In addition, van de Wall [9] showed that in a subsonic flow, the mixing loss could be estimated to good accuracy by assuming that the flow is incompressible. If we only consider upstream vortical flow disturbances, the total pressure mixing loss coefficient can be written as [9],

$$\chi = \left(\frac{\overline{u_1^2} + \overline{v_1^2} + \overline{w_1^2}}{u_0^2} \right), \tag{2}$$

where u, v, and w are the unsteady velocity components; the overbar denotes time average. The subscript 0 represents the mean flow, which is equivalent to the time-averaged flow, and the subscript 1 represents a linear unsteady disturbance to the mean flow.

Calculation of the Recovery Process. Having described and given an expression for the mixing loss, a method of obtaining the unsteady velocity components are required. To evaluate the magnitude of the recovery process, it is first necessary to define some terms. Assume that mixing planes are located at the inlet of and at the exit of a blade row. If a disturbance is mixed-out at the inlet to the blade row, it is equivalent to the disturbance mixing-out in isolation. This is the potential mixing loss. Now, if the disturbance is passed through the blade row, neglecting viscous decay of the disturbance, and mixed-out at the exit of the blade row, the difference in mixing loss is a *mixing loss benefit*. In other words, the change in the mixing loss by inviscid means is the recovery. If viscosity is considered throughout the passage, it contributes to an additional loss and is termed *passage loss*.

Solving the unsteady Navier–Stokes equations will capture the effects of the recovery process without modeling. However, it is difficult to isolate the effects of recovery from other unsteady effects. In addition, the computational time required of three-dimensional unsteady solutions is still quite large.

Another way to capture the effects of recovery is to use a time-averaged code and model the recovery process through the use of the deterministic stress [10]. The deterministic stress is defined as velocity correlations arising from time and passage-to-passage averaging of the ensemble-averaged Navier–Stokes equations. Adamczyk [7] linked the recovery process to a component of the deterministic stress through the use of the unsteady kinetic energy as follows:

$$K_{\text{inlet}} - K_{\text{exit}} = \frac{1}{u_0 L} \int_{\text{vol}} (\overline{u_i u_j}) \frac{\partial U_i}{\partial x_j} \delta \,\text{vol}, \tag{3}$$

where K_{inlet} and K_{exit} is the unsteady kinetic energy at the inlet and the exit to a blade row respectively, and L is the pitch of the blade row. The factor in the parentheses is the deterministic stress [10] and the derivatives are the gradient of the mean flow. The integral is taken over the volume consisting of periodic boundaries and mixing planes upstream and downstream of the blade row. The unsteady kinetic energy can be related to the mixing loss coefficient (Eq. (2)) by

$$\frac{1}{2} u_0^2 (\chi_{\text{inlet}} - \chi_{\text{exit}}) = K_{\text{inlet}} - K_{\text{exit}}, \tag{4}$$

u_0 is the axial mean flow.

In this work, the approach taken to calculate the effect of the recovery process is to develop a deterministic stress transport model, which consists of calculating the values in parenthesis in Eq. (3) throughout the geometry where the disturbance–blade row encounter is occurring. There are two advantages of this approach. First, it provides a simplified model that designers can use. Second, it can provide insight into the mechanisms involved in recovery and thus give directions for improving turbomachine performance.

Model Development

Assumptions Used in Transport Model. Two sets of assumptions were used in the development of the transport model. The first set is obtained from the results of the mixing study [9] referred to in the previous section. They are that incompressible flow and the use of linear theory are adequate to characterize the recovery process. The second set is obtained by the work of Adamczyk [7], where he showed that the mixing loss is essentially independent of the reduced frequency of the upstream disturbance. The implications of this are that the frequency dependence of the transport model can be omitted. This also means that the higher harmonics needed to characterize the wake shape can also be neglected. A transport model for the deterministic stresses was developed such that the stresses are transported by the mean flow.

Derivation of the Transport Model. The equations governing the transport of the deterministic stresses were derived in van de Wall [9] and are presented here. Its three-dimensional Cartesian form (with the coordinates x, y, and z as the axial, spanwise, and pitchwise coordinates, respectively) is presented here as:

$$\underset{I}{U_k \frac{\partial \overline{u_i u_k}}{\partial x_k}} + \underset{II}{\overline{u_k u_j} \frac{\partial U_i}{\partial x_k}} + \underset{III}{\overline{u_k u_i} \frac{\partial U_j}{\partial x_\kappa}} = \underset{IV}{-\frac{1}{\rho} \overline{u_j \frac{\partial p}{\partial x_i}}} \underset{V}{- \frac{1}{\rho} \overline{u_i \frac{\partial p}{\partial x_j}}} \underset{IV}{+ v_t \overline{u_i \frac{\partial^2 u_j}{\partial x_k^2}}} \underset{VII}{+ v_t \overline{u_j \frac{\partial^2 u_i}{\partial x_k^2}}} \tag{5}$$

The upper case letters denote mean flow velocities, and the lower case letters denote an unsteady perturbation from the mean. The p is the unsteady pressure and v_t is the turbulent viscosity. The i and j are free indices and represent the x, y, and z components, and the k is a dummy index.

Term *I* in Eq. (5) is a spatial gradient of a time-averaged term and is thus a transport term. It represents the transport of the deterministic stress. Terms *II* and *III* are inviscid terms, labeled the mean flow gradient terms. It is through these terms that the coupling of the transport equation to the mean flow exists. These terms can be either positive or negative. In other words, through the mechanism of the mean flow gradients, energy from the un-

Table 1 Comparison methods

Comparison Method	Applicability
(1) Smith's Model [5]	Two Dimensional, steady, inviscid, avg K_{exit} only (analytical)
(2) UVF Model [9]	Two Dimensional, unsteady, linear, inviscid, (analytical)
(3) LINFLO code [14]	Two Dimensional, unsteady, linear, inviscid (computational)
(4) Navier-Stokes results [18]	Three Dimensional, unsteady, nonlinear, viscous (computational)-GE_LSRC
(5) Experimental [21]	Two Dimensional measurement of a Three Dimensional flow (exerpimental)-NASA Stator37

steady flow (deterministic stresses) can be either added or removed from the mean flow. This is contrary to turbulence theory, where the mean flow adds energy to the random unsteady flow, where the energy is ultimately dissipated, but the random unsteady flow in general does not add useful energy to the mean flow. On the right-hand side of Eq. (5) are the source/sink terms. Terms *IV* and *V* are the pressure velocity correlation terms with its trace representing the work done by unsteady pressure fluctuations. The last two terms (Terms *VI* and *VII*) are the viscous terms. Note that the deterministic stress transport equation is similar to the transport equation for the Reynolds stress with the triple correlation term omitted. The dropping of the triple correlation term is based on the linearization procedure used in the construction of Eq. (5) [9].

The transport equations (Eq. (5)) are written in a convenient form such that the various terms can be turned on and off to determine their effect. For example, the inviscid form of the transport equation would omit terms *VI* and *VII*. The effect of the pressure–velocity terms will be shown to be significant.

Equation (5) represents a coupled set of three equations in two dimensions, and six equations in three dimensions. The mean flow quantities as described are known. For three-dimensions, this leaves six deterministic stress components, the unsteady pressure–velocity terms, and the viscous terms as unknowns. With only six equations and eight unknowns, the transport model is underspecified and requires that a model be developed for the pressure–velocity correlation terms and the viscous terms.

The pressure–velocity terms were developed based on the high-frequency limit of the theory of rapid distortion as described in van de Wall [9]. The terms are presented in Appendix A.

The viscous terms were developed based on the similarity between the transport equations (Eq. 5) and the work of Hill et al. [11]. Hill et al. [11] developed a model for a wake decaying on the centerline of a duct with a non-zero pressure gradient, where both inviscid and viscous mechanisms act on the wake. The wake is stretched or compressed depending on whether the pressure gradient in the duct is favorable or adverse respectively. This situation simulates both compressor and turbine cases where the wake is stretched or compressed. The equations are presented in Appendix A.

Solution Procedure for the Transport Equations. The solution of the transport equations requires that the mean flow be known. For this work, the mean flows were inviscid and two-dimensional and were generated by PCPANEL developed by McFarland [12] and SFLOW developed by Hoyniak [13]. The streamfunction (i.e., see Appendix A) associated with the mean flow was obtained by the code LINFLO developed by Verdon et al. [14]. The mesh as well as the corresponding mean flow velocities were used as input to the transport code. The inviscid forms of the transport equations are independent of the reduced frequency of the upstream disturbance as well as independent of the length scale of the disturbance. However, when considering the viscous form of the model, the length scale must be included. This requires specifying the initial disturbance half width, b (i.e., the width from the centerline to the edge), and the initial disturbance depth, v_d.

The inlet deterministic stresses, $\overline{u_1u_1}$, $\overline{u_1v_1}$, $\overline{v_1v_1}$, $\overline{u_1w_1}$, $\overline{v_1w_1}$, and $\overline{w_1w_1}$, were specified depending on the upstream disturbance modeled and are given in Appendix B. All deterministic stresses are normalized by the inlet unsteady kinetic energy, K_{inlet} (i.e., $1/2\overline{u_1u_1}+1/2\overline{v_1v_1}+1/2\overline{w_1w_1}$). The procedure used to solve the equations employs a finite volume technique with a Runge–Kutta integration as described by Celestina et al. [15] and Adamczyk et al. [16].

A typical run for a two-dimensional calculation requires approximately 1 minute using an R10000 Silicon Graphics workstation on a 90×31 mesh. The same geometry utilizing a three-dimensional mesh with 31 spanwise mesh points requires approximately 30 minutes to complete. These run times assume that the mean flow is known and is input to the code.

Validation Study

For validation, the transport model was compared against analytical methods, established computational methods, and in one case experimental data. These comparison methods are described in detail in van de Wall [9] and are listed in Table 1 along with their applicability. Smith's model (1) is valid at inlet and exit of a blade row only and is based on the velocity triangles of the mean flow. It assumes that the wake segment remains straight as they convect through the blade row. Comparison method 2, the UVF (unsteady vortical field) model [9] is an analytical model for the far downstream unsteady velocity field. It is based on linear theory and does not include the effect of shed vorticity caused by the time-varying loading on the blades caused by the incoming wakes. The LINFLO code is unsteady and includes the effect of shed vorticity. It is valid throughout the blade row.

For all of the comparisons in this section, the inlet boundary conditions used consist of two-dimensional blade wakes and three-dimensional tip clearance flow structures described in Appendix B.

Compressor Comparisons

Two-Dimensional Wake Comparisons—Turning Duct. The first validation case consists of a turning duct with incident two-dimensional wakes. This case validates the inviscid form of the transport model for a compressor. Imagine a set of infinitely thin compressor stators, where the inlet rotor wake angle, θ_w, can be varied. The insert in Fig. 5 shows the compressor duct, where the infinitely thin wall was chosen so that the effect of blade thickness is neglected. In addition, the duct includes inlet and exit extensions so that the effect of wake impingement on the leading edge is neglected. The stators turn the mean flow through an angle of 45 deg, where the exit flow is axial.

Figure 5 shows a comparison of the pitchwise average K^*_{exit}, as a function of θ_w for the transport model, Smith's model, the UVF model, and the LINFLO code. Both the UVF model and the LINFLO code are at a reduced frequency of fifteen. The agreement between all the model is very good for $-70<\theta_w<-10$ deg, which covers the range of wake angles for axial flow compressors. The results from the LINFLO code start diverging from the others at $\theta_w>-10$ deg. The UVF model has some oscillation from $10<\theta_w<45$ deg.

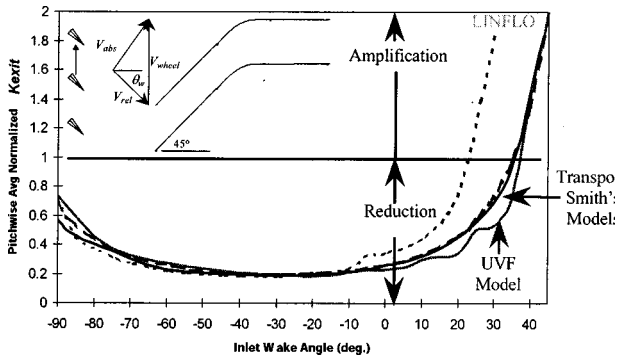

Fig. 5 Pitchwise average normalized K_{exit} for the 45 deg turning duct (no viscosity)

Two-Dimensional Wake Comparisons—GE-LSRC. The next test geometry is of a low-speed model of stage 7 stator taken from a 10-stage compressor [17] with incident two-dimensional blade wakes. This test case was chosen to compare the inviscid form of the transport model to unsteady Navier–Stokes results from Valkov [18]. The blade section used is at 70 percent of stator span. It is characterized by an inlet flow angle of 46.4 deg, exit flow angle of 19.1 deg, and a solidity of 1.67. Figure 6 shows the *mixing loss benefit*, $(\chi_{\text{inlet}}-\chi_{\text{exit}})$, in units of total pressure loss coefficient (Eq. (2)) as a function of the inlet wake velocity defect in the rotor relative reference frame. The inlet rotor wake is oriented at $\theta_w=-49.7$ deg, which places the wake disturbance approximately perpendicular to the stator inlet mean flow. Over this range of wake deficits, χ_{inlet} varies from 0.0028 to 0.0247. The results from the transport model compare very well with the Navier–Stokes results for inlet wake defects less than 50 percent. However, for wake defects in excess of 50 percent the transport model over predicts the *mixing loss benefits*. This could be caused by two reasons. First, more viscous diffusion exists at larger wake defects, which is not captured by the inviscid form of the transport model. Second, it could be caused by nonlinear effects, which the transport model neglects.

Three points can be made regarding the results presented in Fig. 6 in terms of the assumptions used in the derivation of the transport model. First, the work of Valkov [18] included a viscous mean flow, while the mean flow used in the transport model was inviscid. This implies that the boundary layer flow does not significantly affect the wake recovery. Second, since Valkov's [18] results are nonlinear, the good agreement with the transport model justifies the use of linear unsteady flow models in the transport equations. Finally, since the work of Valkov [18] was unsteady, while the transport model neglects the effects of reduced frequency, the good comparison justifies neglecting the frequency effects in the transport model.

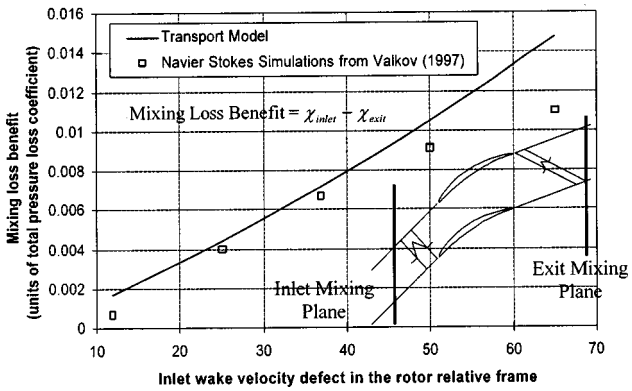

Fig. 6 Mixing loss benefit for several inlet wake defects

Table 2 Mixing loss benefit for tip flow

Mixing Loss Benefit (Total Pressure Loss Coefficient)	Area Average Loss Transport Model	Area Average Loss [18]
χ_{inlet}-χ_{inlet} (Inviscid)	0.0027	0.0033
χ_{inlet}-χ_{exit} (Viscous)	0.0041	0.0043
Passage	0.0014	0.0010

Three-Dimensional Tip Vortex Comparisons—GE-LSRC. For this case, the mean flow remains two dimensional; however, the upstream disturbance is three dimensional. The upstream disturbance is that of a tip clearance flow and resembles an axisymmetric wake and is essentially a defect in total pressure. It can be described as a velocity deficit region, however, unlike a two-dimensional wake, the vorticity is no longer purely spanwise. No velocity disturbance exists in the spanwise direction.

A comparison is made between the transport model and a computation conducted by Valkov [18] using an unsteady three-dimensional Navier–Stokes code. Table 2 gives a comparison of the change in the area-averaged loss across the stator for the transport model and the results of Valkov [18] in terms of the total pressure loss coefficient. The first line shows the *mixing loss benefit* due to recovery (inviscid estimate). Note that the transport model gives this value directly by turning off the viscous terms. The second line shows the *mixing loss benefit* when considering both the inviscid and viscous effects. The final line shows the *passage loss* that is caused by viscous mixing of the tip clearance flow within the passage. This is not beneficial because the reduction in K is caused by viscous mixing. The net benefit to the mixing loss is simply the difference between lines 2 and 1. The transport model agrees quite well against the unsteady nonlinear Navier–Stokes results of Valkov [18].

Turbine Comparisons

Two-Dimensional Wake Comparisons. The next validation case consists of a turning duct designed to accelerate the mean flow. The incident wakes are two dimensional. The geometry consists of a NACA0012 airfoil with no camber at a stagger angle of −40 deg, and a solidity of one. It has an axial inlet flow, and a −40 deg exit flow.

Figure 7 shows the effect on recovery of varying the inlet wake angle. The wake angle is varied from 0 deg, which is the limit of

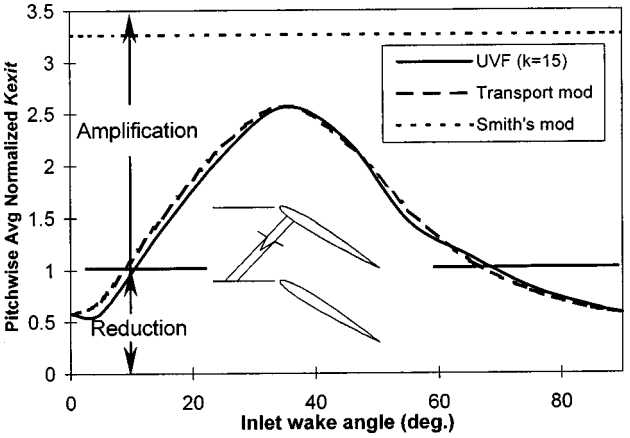

Fig. 7 Pitchwise average K_{exit} versus inlet wake angle for the 40 deg turbine, no viscosity

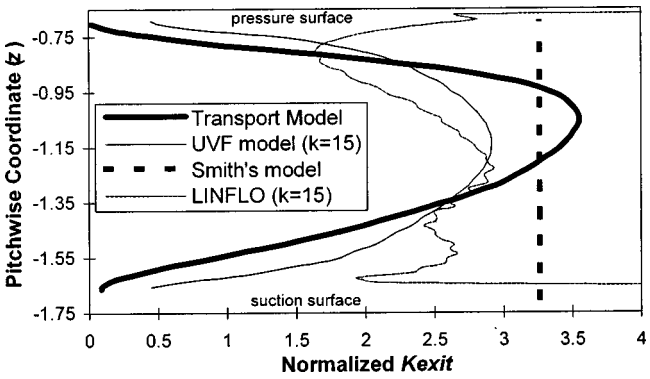

Fig. 8 Distribution of normalized K_{exit} for the 40 deg turbine (no viscosity)

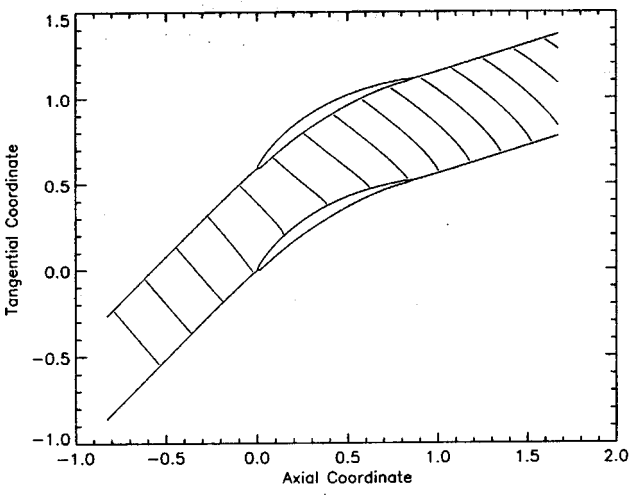

Fig. 9 Transport of disturbances through GE-LSRC with $\theta_w = -49.7$ deg

zero wheel speed of the blade row generating the wake, to 90 deg, the infinite wheel speed limit. Figure 7 shows a comparison of the pitchwise average of K^*_{exit} as a function of the inlet wake angle, θ_w, for the transport model, Smith's model, and the UVF model. The transport and UVF model compare very well. Smith's model overpredicts the results of the other two models significantly. This can be explained by the fact that Smith's model assumes that the wakes remain straight as they transport through the blade row. This does not occur in the case of a turbine and is explained further in the Results section.

The last comparison is for a fixed inlet wake angle, $\theta_w = 45$ deg. Figure 8 shows the distribution of K^*_{exit} across the passage. The comparison of the distribution of K^*_{exit} between the transport and UVF models is good with the transport model giving a larger amplification near midpitch. The LINFLO results are in reasonable agreement with the transport model over most of the pitch. The divergence in the inner and outer pitch regions is caused by a lack of grid points in LINFLO to resolve the fine spatial details near the blade and wake surfaces.

Results

The previous section illustrated the validity of the transport model and gave confidence in applying the model to a compressor and turbine geometry of current interest. In the results that are to follow, only the exit unsteady kinetic energy as well as half of each of the unsteady kinetic energy components of the deterministic stresses are shown (i.e., $1/2\overline{u_1u_1}$, $1/2\overline{v_1v_1}$, and $1/2\overline{w_1w_1}$). For the cases shown, the exit is at one chord downstream of the blade trailing edge. All unsteady kinetic energy components are normalized by K_{inlet}. As in the validation cases, the mean flow is two dimensional and inviscid. However, both two and three-dimensional disturbances representing two-dimensional blade wakes and three-dimensional clearance vortices (wakes), respectively, are used. This allows the direct investigation of the three-dimensional nature of the disturbance flow. Details about the distribution of all the deterministic stress components within the blade passage as well as the application of the model to other geometry are given in van de Wall [9].

Compressor Recovery Predictions

Effect of Inlet Wake Angle on Recovery. Consider again the results of the turning duct case shown in Fig. 5, where the effects of viscosity are neglected. An inlet wake angle of 45 deg represents the limit of zero wheel speed, and an inlet wake angle of -90 deg represents the limit of infinite wheel speed. The pitchwise average K^*_{exit} associated with the wake is less than one for most of the inlet wake angles. This means that the wake mixing loss is reduced as a result of the encounter with the blade row, resulting in a *mixing loss benefit*. However, near $\theta_w = 45$ deg, the steady flow limit, K, is being amplified. This can be explained as follows. The wake is traveling downstream and is being compressed by the slowing of the mean flow. This results in an increase in the wake depth and therefore an increase in the wake mixing loss. A typical compressor design point velocity triangle will put $\theta_w \cong -45$ deg, the wake being perpendicular to the inlet mean flow. At this point, the mixing loss of the wake is reduced nearly 80 percent, which is a substantial amount. In addition, notice that K^*_{exit} is insensitive to the wake angle near the design point. This implies that severe off design operation can still result in a substantial *mixing loss benefit*.

Recovery Within a Compressor Stator. The geometry is of a low speed model of stage 7 stator taken from a 10-stage compressor [17] as discussed in the Validation section. The geometry is shown in Fig. 9.

Figure 9 shows the transport of the wakes through the compressor stator by the mean flow in the blade-to-blade plane. The wakes are shown as lines whose spacing is equal to the distance between the wakes. The inlet wake angle, θ_w, is -49.7 deg, resulting in values for the inlet deterministic stresses for $\overline{u_1u_1}$, $\overline{u_1w_1}$, and $\overline{w_1w_1}$ of 0.418, -0.493, and 0.582, respectively. Any deterministic stresses involving the spanwise component of the unsteady velocity is zero. The wakes essentially remain straight as they are transported through the stator passage. Near the exit of the blade row, the wakes bow slightly. Recalling that Smith's model assumes that the disturbances remain straight, it appears that this is a good approximation for compressors. However, Smith's model only gives the average value of K^*_{exit}, where the transport model gives the distribution of all the deterministic stresses throughout the passage. Figure 10 shows the unsteady kinetic energy components of the deterministic stress as well as K^*_{exit}, as a function of pitch for both two-dimensional and three-dimensional wakes. This calculation is from the inviscid form of the transport model. The exit pitch coordinate is normalized by the exit pitch, where values of zero and one represent the suction and pressure surfaces of the blade, respectively. The value of K^*_{exit} is less than one for both the two-dimensional and three-dimensional wakes across the entire pitch, indicating that a wake *mixing loss benefit* is occurring. K^*_{exit} for the three-dimensional wake is greater than the two-dimensional wake. This is primarily the result of the increase in the value of the $\overline{v_1v_1}$ component of the deterministic stress. At the inlet, the $\overline{v_1v_1}$ stress component is zero, since there is no spanwise velocity component of the disturbance. Near the suction surface, K^*_{exit} is essentially identical for both two-dimensional and three-dimensional disturbances. The smaller value of K^*_{exit} near the pres-

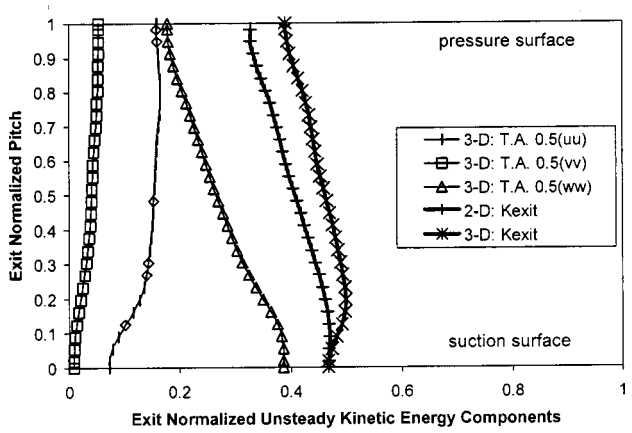

Fig. 10 Deterministic stresses versus pitch for GE-LSRC, no viscosity

sure side indicates that the wake is being stretched more locally than near the suction side of the passage. In addition, the larger value of $\overline{w_1 w_1}$ near the suction side indicates a more pitchwise orientation of the disturbance. This can be seen in Fig. 9.

In order to determine the effects causing the change in K from inlet to exit, the transport equation can be written as

$$\text{Transport of } K = (\Delta K \text{ by mean flow gradients}) + (\Delta K \text{ by unsteady pressure}) + (\Delta K \text{ by viscosity}).$$

To determine the various effects on K, the appropriate terms in the transport model are turned off. For example, to determine the mean flow gradient effect on K, the unsteady pressure and viscous terms are turned off. Figure 11 shows the various effects causing the decay of K for both two-dimensional and three-dimensional wakes. The line on the far right is the inviscid decay in K caused by mean flow gradients alone, reducing K to approximately 60 percent of its inlet value. Notice that the decay is identical for both two-dimensional and three-dimensional wakes. This is because the mean flow is two dimensional, and no velocity disturbance exists upstream in the spanwise direction, resulting in no mechanism to increase the value of $\overline{v_1 v_1}$. When the unsteady pressure effects are considered, K is decayed even further; however, with the unsteady pressure term modeled, there is a difference in K for the two-dimensional and three-dimensional wakes. As described above, this is primarily caused by the increase in the $\overline{v_1 v_1}$ component of the deterministic stress caused by the coupling

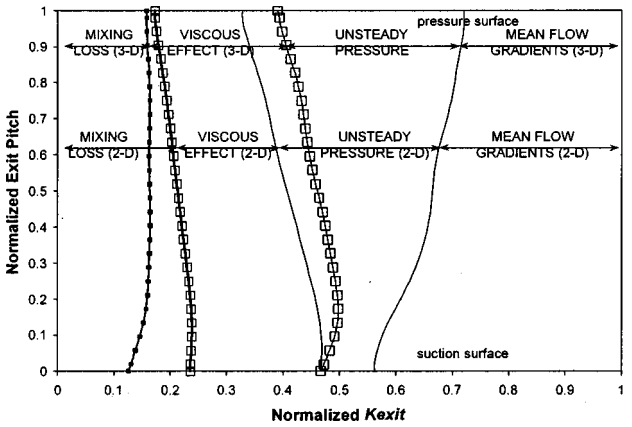

Fig. 11 Audit of normalized K_{exit} versus pitch for GE-LSRC

of the transport equations through the unsteady pressure term. Finally, when viscous effects are considered, K is decayed even further. For a three-dimensional wake, the viscous mixing has a larger effect than for the two-dimensional wake. The resulting K^*_{exit} is ultimately the mixing loss associated with the upstream disturbance, which is approximately 20 percent of the inlet value. The inviscid effects reduced the mixing loss by approximately 60 percent. However, the viscous mixing within the passage must be taken as a loss. Both the inviscid effects and viscous effects are comparable in terms of the decay in K; therefore, both effects must be considered when modeling the recovery process. One final note on recovery in compressors is that the upstream disturbance is almost completely attenuated by its interaction with a downstream blade row.

Turbine Recovery Predictions

Effect of Inlet Wake Angle on Recovery. Consider again the results of the 40 deg turbine cascade case shown in Fig. 7, where the effects of viscosity are neglected. An inlet wake angle of 0 deg represents the limit of zero wheel speed, and an inlet wake angle of 90 deg represents the limit of infinite wheel speed. The pitchwise-averaged K associated with the wake is greater than one for most of the inlet wake angles. This means that the wake mixing loss is increased as a result of the encounter with the blade row resulting in a mixing loss increase. Near 0 deg, the steady flow limit, K, is being reduced. This can be explained as follows. The wake is traveling downstream and is being stretched by the acceleration of the mean flow, resulting in a decrease in the wake depth and therefore a decrease in the wake mixing loss. Turbines typically have inlet wake angles in the neighborhood of 45 deg. At this point, the mixing loss of the wake is increased by a factor greater than 2. Notice, that the mixing loss is sensitive to inlet wake angle, which is not the case for the compressor (Fig. 5).

Recovery Within a Turbine Rotor. The geometry is of a low-speed turbine rotor designed by Pratt & Whitney [19]. The turbine rotor is characterized by an inlet flow angle of -35 deg, and exit flow angle of 57 deg, and a solidity of 1.13. The geometry is shown in Fig. 12. The inlet wakes are identical to the compressor blade of the previous section for comparative purposes.

Figure 12 shows the transport of the wakes through the turbine rotor by the mean flow in the blade-to-blade plane. The inlet disturbance angle is -60 deg, resulting in values for the inlet deterministic stresses for $\overline{u_1 u_1}$, $\overline{u_1 w_1}$, and $\overline{w_1 w_1}$ of 0.250, 0.433, and 0.750, respectively. Any deterministic stress involving the spanwise component of the unsteady velocity is zero. It is obvious that this picture of the wakes transporting through the turbine is quite different from that of the compressor (Fig. 9). As the wakes approach the leading edge plane of the blade, they begin to bow near midpitch due to the acceleration of the flow. As they convect downstream, they become significantly distorted. The wake is being stretched near the blade surfaces, but it is not clear over how much of the passage the stretching occurs, and where if any compression of the disturbance is taking place. In the compressor case, it was clear that the wake segments were being stretched. This significant distortion calls into question the validity of Smith's model, which assumes that the wakes remain straight as they are transported through the passage. This also helps explain why Smith's model overpredicts the mixing loss as shown in Fig. 7. Some recovery must be occurring near the blade surfaces by the stretching of the wake segments, which Smith's model does not take into account.

Figure 13 shows the unsteady kinetic energy components of the deterministic stress as well as K^*_{exit} as a function of pitch for both two-dimensional and three-dimensional wakes. This calculation is from the inviscid form of the transport model. Over most of the passage, the value of K^*_{exit} is greater than one indicating an amplification of K is occurring. As in the case of the compressor, K^*_{exit} for the three-dimensional disturbance is greater than the two-

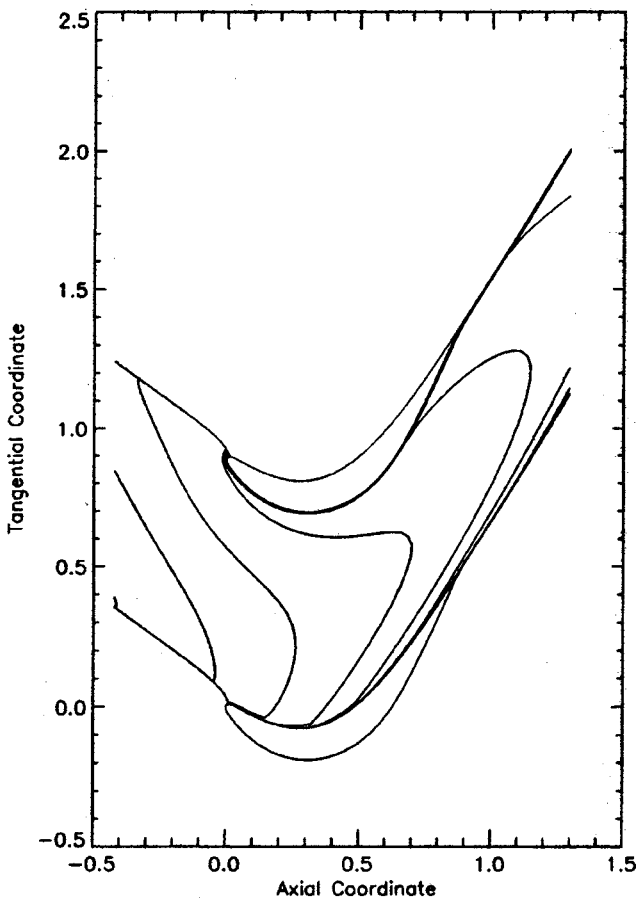

Fig. 12 Transport of disturbances through PW-LPT with $\theta_w = 60$ deg

dimensional disturbance. This is caused by the increase in the value of the $\overline{v_1 v_1}$ component of the deterministic stress. The $\overline{v_1 v_1}$ component is the only component which is amplified near the pressure surface. As seen in the compressor case, near the suction surface, the value of K^*_{exit} is identical for both two-dimensional and three-dimensional wakes. Both $\overline{u_1 u_1}$ and $\overline{w_1 w_1}$ components are comparable in magnitude and are attenuated near the blade surfaces. For a two-dimensional wake, over 40 percent of the pitch near both the pressure and suction surfaces, K^*_{exit} is less than one, indicating that the wake is being stretched. In fact, K^*_{exit} is

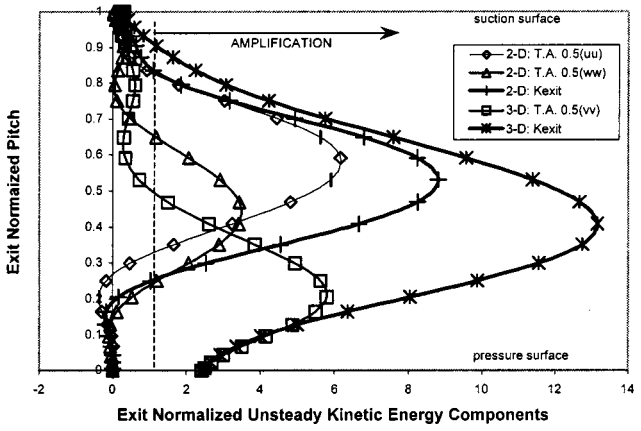

Fig. 13 Deterministic stresses versus pitch for PW-LPT, no viscosity

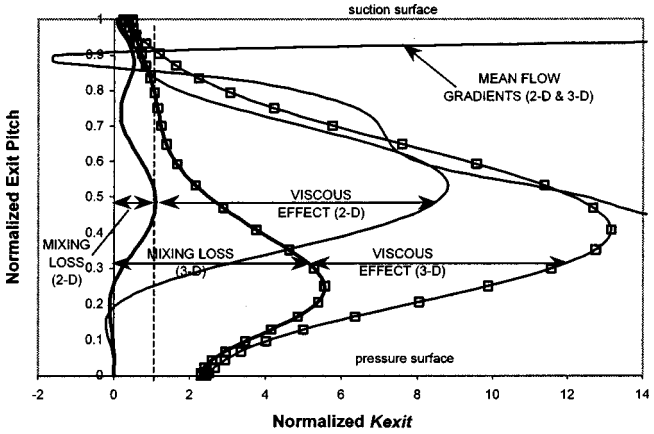

Fig. 14 Audit of normalized K_{exit} versus pitch for PW-LPT.

near zero, indicating that the wake is being stretched significantly. The negative values are the result of numerical errors and are not physical.

Figure 14 shows the various effects causing the change in K from inlet to exit for both two-dimensional and three-dimensional wakes. The line on the far right of Fig. 14 is the inviscid effect on K caused by the mean flow gradient alone, and is the same for both two-dimensional and three-dimensional wakes as discussed above. Near the suction surface and from approximately midpitch to the pressure surface, the value of K^*_{exit} is very large. When the unsteady pressure effects are considered, K^*_{exit} is reduced significantly, but it is still greater than one. The pressure–velocity term does not have a large effect from the suction surface to near midpitch. However, from midpitch to the pressure surface, the effect is large. This further justifies the inclusion of a model for the pressure–velocity term in the transport model. Finally, when viscous effects are considered, K^*_{exit} is reduced significantly across the entire passage. For a two-dimensional wake, K^*_{exit} is less than one, indicating that a *mixing loss benefit* is occurring, with the pitchwise area average being approximately 0.39. For a three-dimensional disturbance, K^*_{exit} is greater than one, with the pitchwise area average being approximately 2.55. The difference is caused primarily by the increase in the $\overline{v_1 v_1}$ component of the stress. The limitation of the viscous model on spanwise velocity disturbances prevents the decay of the $\overline{v_1 v_1}$ component of the stress. The remaining K^*_{exit} is ultimately the mixing loss associated with the upstream disturbance. The inviscid effects increase the pitchwise area average exit K to 3.30 and 6.89 times the inlet value for two-dimensional and three-dimensional wakes, respectively. This large increase is reduced by viscosity. The *passage loss* is significant when compared to the *mixing loss benefit*, and thus must be accounted for to establish the net benefit of mixing.

Two points can be made with regard to disturbances interacting with a downstream turbine blade row. First, a significant *passage loss* is taken when a disturbance interacts with a downstream turbine blade row. Second, the wakes persist after passing through the blade row, which is contrary to what happens in compressors.

Summary and Conclusions

A model was developed for the transport of upstream vortical disturbances through a blade row. These disturbances are represented by the deterministic stresses described by Adamczyk [10]. The transport model is based on incompressible, linear unsteady flow theory, and is independent of the frequency of the disturbance. The models account for the unsteady pressure field and

viscosity. The model was tested against analytical, numerical, and experimental results with good agreement. The model is fast, allowing turbomachinery designers to determine quickly how the recovery process impacts a given design.

This research has answered the two questions posed in the Introduction by showing that the recovery process is causing a change in the efficiency with a change in axial gap, and that the flow physics is the result of unsteady flows. The model developed adequately captures this process and can be used in the time-averaged calculation of turbomachinery flows.

The conclusions for compressors are as follows:

1 K of the upstream disturbance is significantly reduced by inviscid means for both the two-dimensional and three-dimensional wakes considered, with more decay occurring in the two-dimensional case. This is called recovery and leads to a significant reduction in the wake mixing loss.

2 Viscosity acts to decay the disturbance further reducing K and thus reducing the wake mixing loss. However, the decay of the disturbance within the passage contributes to a *passage loss*. Both viscous and inviscid effects act to reduce K and are comparable in magnitude.

3 For a subsonic compressor blade row, the two-dimensional and three-dimensional wakes considered are almost completely attenuated as they exit the blade row. Therefore, the closer the spacing between blade rows, the larger the efficiency, which agrees with experimental observations [1,2]. In addition, clocking or indexing of rotor or stator blade rows will have a minimal impact on subsonic compressor performance, as demonstrated by Barankiewicz and Hathaway [20].

The conclusions for turbines are as follows:

1 K of the upstream disturbance is significantly reduced by inviscid means for both the two-dimensional and three-dimensional wakes considered, with more decay occurring in the two-dimensional case. This recovery is negative because it leads to a significant increase in the wake mixing loss.

2 Viscosity acts to decay the disturbance to approximately the inlet value of K. However, this decay is by viscous means and contributes to a substantial *passage loss*. Both viscous and inviscid effects are comparable in magnitude.

3 For a subsonic turbine blade row, the two-dimensional and three-dimensional wakes considered persist after passing through the blade row. Therefore, the wider the spacing between blade rows, the larger the efficiency, which agrees with experimental observations [3,4]. In addition, because wakes persist through subsonic turbine blade rows, stage-to-stage interactions (clocking effects) impact subsonic turbine performance. This is consistent with the finding of Sharma et al. [4].

Acknowledgments

The authors would like to thank Dr. Eric McFarland for his help on the PCPANEL code as well as many helpful suggestions and Dr. Dale Var Zante for his help on the topic of wake recovery. In addition, the authors also wish to thank the Compressor Branch and the Average Passage development team at the NASA Glenn Research Center for their help. Finally, the sponsorship of this research by the NASA Glenn Research Center (Grant No. NCC3-263) is gratefully acknowledged.

Nomenclature

C = contour for circulation calculation
C_v = constant for viscous calculation
GE-LSRC = General Electric Low Speed Research Comp.
K = time-averaged unsteady kinetic energy
L = pitch of blade row
PW-LPT = Pratt & Whitney Low-Pressure Turbine Rotor
S = Lagrangian coordinate (follows a fluid particle)
$U_{i,j,k}$ = mean flow velocities
b = width of the upstream disturbance
$h_{-\infty}$ = pitch of the upstream disturbance
k = reduced frequency
l = length of a disturbance segment
p = unsteady pressure
$q_{-\infty}$ = inlet mean flow speed
$u_{i,j,k,l}$ = unsteady flow velocities
u_0 = axial component of mean flow
u_1 = axial component linear disturbance
v_1 = spanwise component of linear disturbance
v_d = disturbance depth
w_1 = pitchwise component of linear disturbance
$x_{i,j,k,}$ = coordinate
x = axial coordinate
y = spanwise coordinate
z = pitchwise coordinate
Γ = circulation
Δ = drift function
Ψ = streamfunction
θ = momentum thickness
θ_0 = initial momentum thickness
θ_w = inlet disturbance angle (relative to axial dir)
$\theta_{-\infty}$ = inlet mean flow angle (relative to axial dir)
λ_B = disturbance wavelength in blade-to-blade plane
λ_s = disturbance wavelength in the spanwise direction
ν_t = turbulent viscosity
ρ = density
χ = total pressure mixing loss coefficient

Subscripts

exit = @ exit to blade row
inlet = @ inlet to blade row
i = free index
j = free index
k = dummy index
l = dummy index

Superscripts

* = normalized with respect to inlet kinetic energy

Appendix A

Unsteady Pressure Terms. The derivation of the pressure-velocity correlation is lengthy and is given in van de Wall [9]. It involves the use of linear theory and a perturbation expansion using $1/k$ as the expansion parameter, where k is the wave number of the incoming disturbance. The resulting expressions to lowest order of $1/k$ are

$$\frac{1}{\rho}\overline{u_i\frac{\partial p}{\partial x_j}} \approx -2\frac{\partial S}{\partial x_j}\frac{\partial S}{\partial x_k}\frac{\partial U_k}{\partial x_l}\frac{\overline{u_i u_l}}{\left[\left(\frac{\partial S}{\partial x}\right)^2+\left(\frac{\partial S}{\partial y}\right)^2+\left(\frac{\partial S}{\partial z}\right)^2\right]}, \quad (A1)$$

and similarly,

$$\frac{1}{\rho}\overline{u_j\frac{\partial p}{\partial x_i}} \approx -2\frac{\partial S}{\partial x_i}\frac{\partial S}{\partial x_k}\frac{\partial U_k}{\partial x_l}\frac{\overline{u_j u_l}}{\left[\left(\frac{\partial S}{\partial x}\right)^2+\left(\frac{\partial S}{\partial y}\right)^2+\left(\frac{\partial S}{\partial z}\right)^2\right]}. \quad (A2)$$

The subscripts i and j are free indices, while k and l are dummy indices. To lowest order, the correlation is independent of the reduced frequency and involves a linear relationship in the deterministic stress. It introduces the Lagrangian Coordinate, S, which is simply a coordinate that follows a collection of fluid particles as they are transported downstream by the mean flow. It is given as

$$S \equiv q_{-\infty}\Delta \sin(-\theta_w + \theta_{-\infty}) + Y\frac{\lambda_B}{\lambda_y} + \Psi \cos(-\theta_w + \theta_{-\infty}), \tag{A3}$$

where $q_{-\infty}$ is the far upstream time-averaged flow speed, Y is the spanwise coordinate, and Ψ is the stream function. The angle $\theta_{-\infty}$ is the inlet flow angle of the mean flow relative to the axial direction and θ_w is the inlet disturbance angle relative to the axial direction. The inlet disturbance angle is the exit flow angle of the preceding blade row. The λ_B and λ_y are the wavelengths of the incoming disturbance in the blade-to-blade plane and in the spanwise direction, respectively. With λ_y nonzero, the three-dimensional nature of the disturbance is taken into account. Finally, the drift function, Δ, is simply the time it takes a fluid particle to travel a certain distance along a streamline (Ψ = const) and is defined as

$$\Delta = \int_{\psi} \frac{ds}{q}, \tag{A4}$$

where ds is an infinitesimal distance along a streamline and q is the local time-averaged local flow speed.

Viscous Terms. The viscous terms are modeled using the similarity between the model of Hill et al. [11] for the decay of the wake and the transport model. Their equations were rewritten in the form of the transport equations in the present analysis. The viscous contribution for the model was simply the viscous term obtained from the equation in [11]. The resulting equations are

$$2v_t\overline{u\frac{\partial^2 u}{\partial x_k \partial x_k}} = -C_v\frac{16}{3}\pi\left(\frac{v_t}{U_s\theta}\right)\frac{h_{-\infty}}{bU_x\theta_0}(\overline{u_1 u_1})^2, \tag{A5}$$

$$2v_t\overline{u\frac{\partial^2 \nu}{\partial x_k \partial x_k}} = 0, \tag{A6}$$

$$2v_t\overline{v\frac{\partial^2 u}{\partial x_k \partial x_k}} = 0, \tag{A7}$$

$$v_t\overline{u\frac{\partial^2 w}{\partial x_k \partial x_k}} + v_t\overline{w\frac{\partial^2 u}{\partial x_k \partial x_k}} = -C_v\frac{16}{3}\pi\left(\frac{v_t}{U_s\theta}\right)\frac{h_{-\infty}}{bU_x\theta_0}\frac{1}{\tan\theta_w}(\overline{u_1 w_1})^2, \tag{A8}$$

$$2v_t\overline{v\frac{\partial^2 w}{\partial x_k \partial x_k}} = 0, \tag{A9}$$

and

$$2v_t\overline{w\frac{\partial^2 w}{\partial x_k \partial x_k}} = -C_v\frac{16}{3}\pi\left(\frac{v_t}{U_s\theta}\right)\frac{h_{-\infty}}{bU_x\theta_0}\frac{1}{\tan^2\theta_w}(\overline{w_1 w_1})^2. \tag{A10}$$

In these equations, the $h_{-\infty}$ is the pitch of the upstream disturbance and b is the local disturbance half width. The θ_0 is the initial momentum thickness and the C_v is a constant whose value is obtained by comparing the transport model to the model of Hill et al. [11] for a constant area duct [9] and is set to 0.3. The quantity $(v_t/U_s\theta)$ is set to 0.044 as in [11] analysis, where they assumed that the eddy viscosity is constant across the wake. Notice that viscous terms are zero for any of the correlations involving the spanwise unsteady velocity component, v. This is a limitation of the model. Note that the viscous terms are the only terms in the transport model that involve a length scale of the disturbance. A comparison between the transport model and experimental data for NASA Stator37 [21] is given in van de Wall [9] and shows good agreement.

Appendix B

Inlet Disturbances. The two-dimensional blade wakes and three-dimensional tip clearance flows from a preceding blade row are used as inlet boundary conditions. The three-dimensional tip clearance flows resemble an axisymmetric wake (three-dimensional wake) and is essentially a defect in total pressure. It can be described as a velocity deficit region; however, unlike a two-dimensional wake, the vorticity is no longer purely spanwise. No velocity disturbance exists in the spanwise direction. The resulting inlet deterministic stresses are

$$\overline{u_1 u_1} = \frac{0.75}{\cos\theta_w}\frac{b(y)}{h_{-\infty}}\nu_d^2(y)\cos^2\theta_w, \tag{B1}$$

$$\overline{u_1 w_1} = \frac{0.75}{\cos\theta_w}\frac{b(y)}{h_{-\infty}}\nu_d^2(y)\cos\theta_w \sin\theta_w, \tag{B2}$$

and

$$\overline{w_1 w_1} = \frac{0.75}{\cos\theta_w}\frac{b(y)}{h_{-\infty}}\nu_d^2(y)\sin^2\theta_w, \tag{B3}$$

with the remaining stresses set to zero.

For all the two-dimensional wake disturbances, $\nu_d = 0.225$ and $b = 0.1$. The three-dimensional disturbance was obtained from the work of Valkov [18] for comparative purposes. It consisted of a total pressure deficit region that extends over 60 percent of the pitch and over 15 percent of the span centered at 90 percent span. The maximum velocity defect at the center of the tip clearance flow is 46 percent of the upstream exit rotor mean flow.

References

[1] Smith, L. H., Jr., 1970, ''Casing Boundary Layers in Multistage Axial-Flow Compressors,'' *Flow Research in Blading*, L. S. Dzung, ed., Elsevier Publishing Company, Amsterdam.

[2] Mikolajczak, A. A., 1977, ''The Practical Importance of Unsteady Flow'' in: *Unsteady Phenomena in Turbomach.* AGARD CP-144, North Atlantic Treaty Organization.

[3] Wu, C. H., 1952, ''A General Theory of Three-Dimensional Flow in Subsonic and Supersonic Turbomachines of Axial-, Radial-, and Mixed-Flow Types,'' NACA TN 2604.

[4] Sharma, O. P., Stetson, G. M., Daniels, W. A., Greitzer, E. M., Blair, M. F., and Dring, R. P., 1996, ''Impact of Periodic Unsteadiness and Heat Load in Axial Flow Turbomachines,'' Final report from United Technologies Corporation, Pratt & Whitney for NASA Lewis Research Center.

[5] Smith, L. H., Jr. 1966, ''Wake Dispersion in Turbomachines,'' ASME J. Basic Eng., **88**, pp. 688–690.

[6] Adamczyk, J. J., 2000, ''Aerodynamic Analysis of Multistage Turbomachinery Flows in Support of Aerodynamic Design,'' ASME J. Turbomach., **122**, pp. 189–217.

[7] Adamczyk, J. J., 1996, ''Wake Mixing in Axial Flow Compressors,'' ASME Paper No. 96-GT-29.

[8] Smith, L. H., Jr., 1996, ''Discussion of ASME Paper No. 96-GT-029: Wake Mixing in Axial Flow Compressors,'' ASME Turbo Expo, Birmingham, England, June 10–13.

[9] van de Wall, A. G., 1999, ''A Transport Model for the Deterministic Stresses Associated With Turbomachinery Blade Row Interactions,'' Ph.D. Thesis, Department of Mechanical and Aerospace Engineering, Case Western Reserve University.

[10] Adamczyk, J. J., 1985, ''Model Equation for Simulating Flows in Multistage Turbomachinery,'' ASME Paper No. 85-GT-226.

[11] Hill, P. G., Schaub, U. W., and Senoo, Y., 1963, ''Turbulent Wakes in Pressure Gradients,'' ASME J. Appl. Mech., **30**, pp. 518–524.

[12] McFarland, E. R., 1984, ''A Rapid Blade-to-Blade Solution for Use in Turbomachinery Design,'' ASME J. Eng. Gas Turbines Power, **106**, pp. 376–382.

[13] Hoyniak, D., and Verdon, J. M., 1994, ''Steady and Linearized Unsteady Transonic Analyses of Turbomachinery Blade Rows,'' presented at the Seventh International Symposium on Unsteady Aerodynamics and Aeroelasticity of Turbomachines, Fukuoka, Japan, Sept. 25–29.

[14] Verdon, J. M., Barnett, M., Hall, K. C., and Ayer, T. C., 1991, ''Development of Unsteady Aerodynamic Analyses for Turbomachinery Aeroelastic and Aeroacoustic Applications,'' NASA CR 4405.

[15] Celestina, M. L., Mulac, R. A., and Adamczyk, J. J., 1986, ''A Numerical Simulation of the Inviscid Flow Through a Counterrotating Propeller,'' ASME J. Eng. Gas Turbines Power, **108**, pp. 187–193.

[16] Adamczyk, J. J., Celestina, M. L., Beach, T. A., and Barnett, M., 1990, ''Simulation of Three-Dimensional Viscous Flow Within a Multistage Turbine,'' ASME J. Biomech. Eng., **112**, pp. 370–376.

[17] Wisler, D. C., 1977, ''Core Compressor Exit Stage Study, Vol. I—Blading Design,'' NASA CR-135391.
[18] Valkov, T., 1997, ''The Effect of Upstream Rotor Vortical Disturbances on the Time-Average Performance of Axial Compressor Stators,'' Gas Turbine Laboratory Report No. 227, MIT.
[19] Sharma, O. P., 1997, personal communications.
[20] Barankiewicz, W. S., and Hathaway, M. D., 1997, ''Effects of Stator Indexing on Performance in a Low Speed Multistage Axial Compressor,'' ASME Paper No. 97-GT-496.
[21] Van Zante, D. E., Adamczyk, J. J., Strazisar, A. J., Okiishi, T. H., 1997, ''Wake Recovery Performance Benefit in a High-Speed Axial Compressor,'' ASME Paper No. 97-GT-535.

Unsteady Transport Mechanisms in an Axial Turbine

Claudia Casciaro
Martin Treiber
Michael Sell

Turbomachinery Laboratory,
Institute of Energy Technology,
Swiss Federal Institute of Technology,
8092 Zurich, Switzerland

A numerical analysis using a commercial unsteady Navier–Stokes solver has been performed on a pin/blade configuration, in order to assess the efficacy of a commercial code in calculating time-periodic interactions and to gain a better understanding of the unsteady flow physics in axial turbines. Two cases have been investigated, with the pin positioned at 25 and 50 percent of true chord ahead of the leading edge. Both configurations have been computed both two and three dimensionally. The two-dimensional case was used to examine the influence of numerical parameters, such as mesh, time, and space discretization. The three-dimensional case allowed insight into the complete flow field including the wake influence on the secondary flow and mixing processes of the blade row. The basic mechanisms of the wake–blade interaction proved, as expected, to be the same for both pin positions. Yet, as the closest pin wake interaction with the blade field was much stronger, its features have helped to identify the respective roles of wake fluid transport and blade potential field for both cases. The latter effect, noticeably strong with the thick leading edge blade form presented in this study, has often been neglected, and this study helps shed new light on this phenomenon. The code used had been validated in previous work for pin-free steady flow within the same blade row and the new time-dependent case has served to confirm the code range and limitations.
[S0889-504X(00)02104-8]

I Introduction and Aims

Turbomachines must be inherently unsteady (at least in the absolute frame of reference) in order to produce work. In fact, the stagnation enthalpy of a particle can change only if the pressure varies in time (see, for example, [1]), which is a direct consequence of the energy balance of the Navier–Stokes equations. However, if the rotor row is considered isolated, the very same flow will appear steady in the rotor fixed frame of reference.

Yet, turbomachines are formed by multiple rows, each of which creates a disturbed, ''unclean'' environment for the preceding and following rows. Only the analysis of the flow in this context can give an insight into design failures. The interaction between blade rows occurs in various manners: The one through the wake and the potential field are considered in this paper.

The disturbances are generally convected downstream, because the distance between blade rows is too small to allow them to mix out. The *potential field* is felt both up- and downstream at about one chord of distance, its strength depending on the Mach number.

In general, the interpretation of the unsteady effects in turbines is still a controversial subject. The common opinion says that unsteadiness always brings a decrease in efficiency [2–5], although this has been also questioned at least for the adiabatic efficiency [6], because of the isentropic rearrangement of temperature and pressure, known as energy separation.

I.1 Unsteady Transport Theories. Before entering into the details of wake/blade-row interaction, a discussion of wake definition is appropriate. The question is not trivial as the next paragraphs demonstrate that the modes of interaction change according to what it is meant by wake.

If one considers a body in a fluid stream (for example the cylinder in Fig. 1), the interference between the two results in a decrease of velocity behind the body. Due to viscous effects, the local velocities become uniform at a certain distance behind the body, when the wake can be considered mixed out. Thus, it was decided to define a wake as *any velocity deficit in the body-relative frame of reference occurring in a space much smaller than the one analyzed*. This is the classical definition used by most of the scientists, whose findings are briefly described hereafter.

This means that, if the instantaneous velocity field is decreased of the undisturbed value, a wake looks like a backward-facing jet, that is the so-called ''negative jet'' (Fig. 1). Meyer [7] was one of the first to use the negative jet theory to explain the unsteady behavior in compressor stages. Some years later, Kerrebrock and Mikolajczak [8] observed that in a compressor the pressure side presence hinders the wake transport and consequently the stator wake fluid accumulates on the rotor pressure side. Thus, the wake convected downstream by the free-stream velocity appears as a jet to an observer placed on the hit-blade pressure side (suction side if the blade belongs to a turbine), where the velocity component normal to the blade acts, changing both incidence and lift, tending to decrease the load on a compressor blade (and analogously increase it on a turbine blade). The authors also stated that there is a tendency for the wake fluid to be separated from the inviscid flow rather than mix. This phenomenon persists in the blade row.

Since then many authors have confirmed the negative jet theory in axial turbine as being the main unsteady transport mechanism or regarded it as of secondary importance: No agreement on the role of the unsteady fluid physics has yet been reached.

Recently, Hodson and Dawes [9] found that the wake transport could be explained through convective mechanisms of fluid mechanics of a wake being chopped by the following row, bowed, and sheared by the pressure/velocity fields. Entropy contours showed uniformity outside the wakes, according to the authors, due to the Eulerian energy separation, varying total temperature and pressure isentropically. The velocity field created by the blade row distorted the wake as the particles near the suction side were accelerated more than those near the pressure side, but less than those in the midpassage: the wake bows and shears. Bowing and shearing are then a direct consequence of the blade loading: The higher this is, the stronger the deformation of the wake.

As far as the *secondary flow* distortion due to the interaction with an incoming wake is concerned, there are few data. Gallus et al. [10] found that although a steady-stage computation with mixing plane would compute the time-averaged flow field quite accurately, the secondary flow distribution would be totally

Contributed by the International Gas Turbine Institute and presented at the 45th International Gas Turbine and Aeroengine Congress and Exhibition, Munich, Germany, May 8–11, 2000. Manuscript received by the International Gas Turbine Institute February 2000. Paper No. 2000-GT-440. Review Chair: D. Ballal.

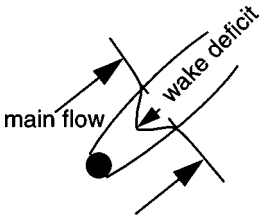

Fig. 1 Negative jet in relative frame of reference

wrong, especially in terms of flow angles. In fact, the interaction with the wakes of the preceding stage would drag the near-hub vortex away from the endwall, modifying the entire flow distribution. A similar result was also found by McFarland et al. [11] in a linear turbine cascade, who found that the wake passing enhanced the transport of endwall fluid toward the midspan, as also reported by Boletis et al. [2].

I.2 Contribution. This work aims at contributing to the understanding of wake fluid transport and its effect on the secondary flow formation. The loss production mechanism as specific to unsteady environment is also discussed.

This aim is achieved through the numerical analysis of an annular turbine cascade, where the rotor wakes are generated by a pin wheel, which can be mounted in two locations at different axial distances from the stator. This configuration has been chosen because it corresponds to the experimental facility of the Laboratory of Turbomachinery of the ETH, Zurich.

The unsteady flow field is analyzed both in its two- and three-dimensional characteristics, using several parameters such as the wake velocity deficit, the flow angles, the absolute total and static pressure coefficients, and the absolute total temperature.

Unsteady transport mechanisms are difficult to show on paper. Please consider visiting our homepage at http://www.lsm.ethz.ch/activities/RGP/first.htm.

The wake is identified through the velocity field, which basically means through the negative jet, without examining the merits of whether this may represent the major unsteady transport mechanism. Thus, in the absolute frame of reference: $c_{\text{negative-jet}} = c(t) - \overline{c}$. It can be easily seen from Fig. 2 that this way an error is introduced. In fact, all the idealized theories considered a field where an undisturbed velocity can be always recognized, because of massive geometric simplifications. This ideal velocity is impossible to identify, and it would also be conceptually wrong to define one, in the highly three-dimensional field of a turbine stage. By choosing a time-averaged velocity as reference an error is introduced, where the effects of the negative jet are decreased and the free-stream unsteadiness enhanced.

Other quantities cannot be used to identify a wake, especially in a CFD environment. One problem is represented by the phenomenon of energy separation, which is an isentropic rearrangement of total enthalpy and pressure, which occurs in unsteady flows. Eckert [12] reports that whenever vortex shedding behind a blunt body occurs, it results in energy separation, which is transported downstream by the Karman vortex street. The Karman vortex street can be neither measured nor computed properly. Thus, both total enthalpy and total pressure cannot be used as a precise mean of wake recognition.

Other quantities, such as entropy, are difficult to use in an unsteady environment. The limitations, described in Baehr [13] and Callen [14] concern the choice of a proper entropy formulation in unsteady environment and as a local value in the case of highly unsteady and strong accelerating flows, where, to the authors' knowledge, equilibrium has not yet been proven.

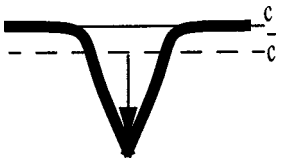

Fig. 2 Error made by considering average velocity instead of undisturbed velocity

II Cases and Tools

II.1 Test Case. The research blade is prismatic with the leading edge mounted radially and a stagger angle of 54.5 deg from tangential direction, of a type typically used in reaction-type turbines. The operating point is at a nominal midspan exit Mach number of 0.5.

A pin wheel is placed at two distances (Fig. 3) upstream of the leading edge plane equivalent to 10 and 20 pin diameters. Some geometric features of the cascade are described in Table 1.

II.2 CFD. The numerical analysis has been performed with CFX-Tascflow, V2.8, by AEA Technology Ltd. This is a finite volume three-dimensional Navier–Stokes solver, with a second-order accurate upwind differencing scheme. Reynolds-stress averaging is applied to the governing equations in strong conservation form and the closure is implemented through the standard $k-\varepsilon$ turbulence model. The near-wall region is resolved with the logarithmic velocity profile. The flow is viscous and compressible, computed in fully turbulent regime. This code has been applied several times within the group in Zurich for steady-state computations [15–17].

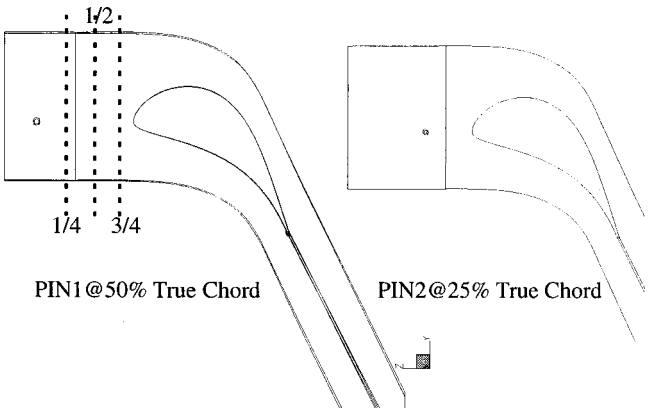

Fig. 3 Configurations and block topologies

Table 1 Test case geometric parameters

Tip Radius [mm]	400
Blade Height [mm]	90
Blade and Pin Number [-]	48
True Chord Length [mm]	60
Casing-Hub Ratio [-]	1.29
Pin Diameter [mm]	1.5
Pin Frequency [Hz]	50

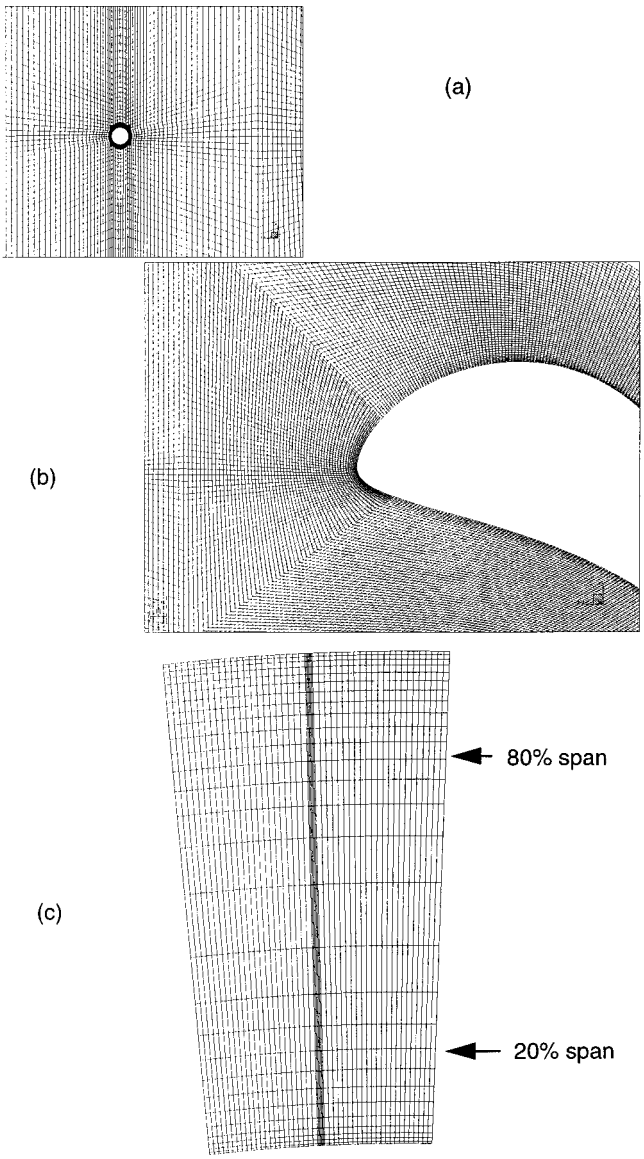

Fig. 4 Details of pin (*a*) and leading edge (*b*) grids or two-dimensional computations (from topology in Fig. 3). Outlet grid (*c*) for three-dimensional cases (same topology). Figures not to same scale.

The grid, generated with ICEM CFD/CAE 3.3, is block-structured and has three blocks, as in Fig. 3: The pin has been blocked off within the inlet block; the blade is obtained by a combination of *H* and *C*-type grids. This allows an improvement of cell orthogonality at the leading and trailing edges, as well as a better control on node density and distribution in these areas. An example of these grids is shown in Fig. 4 for the two-dimensional computations, where 40K nodes were used. For the three-dimensional computations (Fig. 4), a three times coarser grid on a two-dimensional plane was employed with 29 planes in the radial direction. Yet, the computations on the two-dimensional basis were in good agreement, where the wake velocity deficit mixed out faster on the coarser grid. The three-dimensional mesh resolution allowed the computation of all the fluid dynamic structures (proven in previous publications and in particular in Casciaro [16]).

For the three-dimensional computations, the first near-wall node has been positioned so that $y^+ > 30$, even if it is well known that the logarithmic velocity profile does not apply at all to unsteady flow fields.

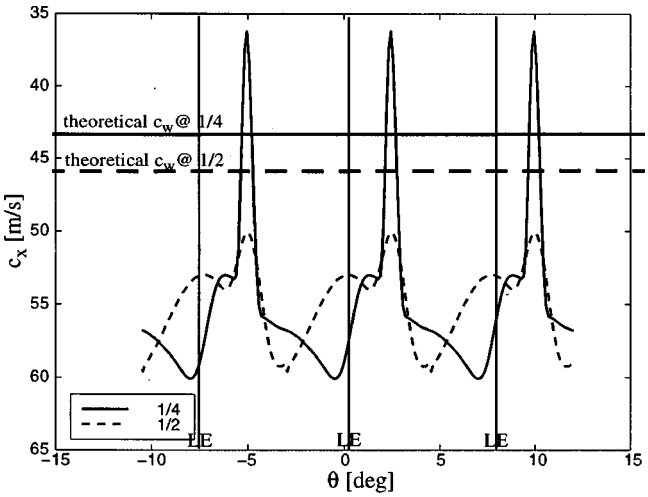

Fig. 5 Axial velocity: comparison of computed and theoretical values, expected with Dullenkopf's model, for PIN1

Numerical Boundary Conditions. At the inlet (ahead of the pin, Fig. 3), the absolute total pressure profile, constant absolute total temperature, 2 percent turbulence intensity, and 5 mm eddy length scale are imposed. Ahead of the pin, the absolute direction is axial and therefore no extra swirl is introduced in the domain. The inlet boundary layer thickness is 10 percent of span.

At the outlet, a time-constant static pressure profile, obtained by a linear fitting of the hub and tip experimental values (without the pin), is imposed. It was assumed that one chord downstream of the trailing edge, the static pressure had leveled out, as shown by the steady-state measurements.

The Rotor/Stator Interface. The interface between the two grids (the grid with the rotating pin and the one with the stator), where the reference system changes, should be ''transparent'' to the computations. Instead, a second-order interpolation error occurs. In order to quantify it consider Fig. 5, where the axial velocity of PIN1 computed at two stations: 1/4 (upstream of the interface) and 1/2 (downstream of the interface; visual help from Fig. 3) at one time step (irrelevant for the specific considerations) is compared and contrasted to the minimum wake velocity expected by applying Dullenkopf's model of wake deficit [18]. It can be noticed that at 1/4 (upstream of the interface), the wake deficit appears much deeper than theoretically expected (about 23 percent). Yet, at 1/2 the wake deficit has become weaker (about 13 percent) compared to the theoretical value. If the theoretical wake is compared at both stations to the computed one, it is clear that the effects are devastating on the wake: While theoretically the axial velocity should decrease only a few percentage points, computationally it loses 2/3 of its deficit. However, the strong mixing cannot be attributed only to the interface, but also to the turbulence model and to mesh effects. Considering the velocity deficit in Fig. 5 and Dullenkopf's correlation, it can be computed that the wake at 3/4 corresponds in terms of thickness and deficit to a ''fictitious'' wake generated by a pin of diameter 1.9 mm and positioned nearly one true chord upstream of the leading edge. Similar effects are to be observed on all computed quantities.

III Velocity Field

Subtracting the time-averaged field from the time-dependent one, the disturbance field, or unsteady velocity field, is obtained. Figure 6 shows this unsteady velocity field at midspan for PIN2, where PIN1 presents the same physical mechanisms, yet quantitatively weaker. The wake appears strongly sheared for two opposite reasons: the blade potential field locally creating an adverse pressure gradient and the downstream accelerating blade environ-

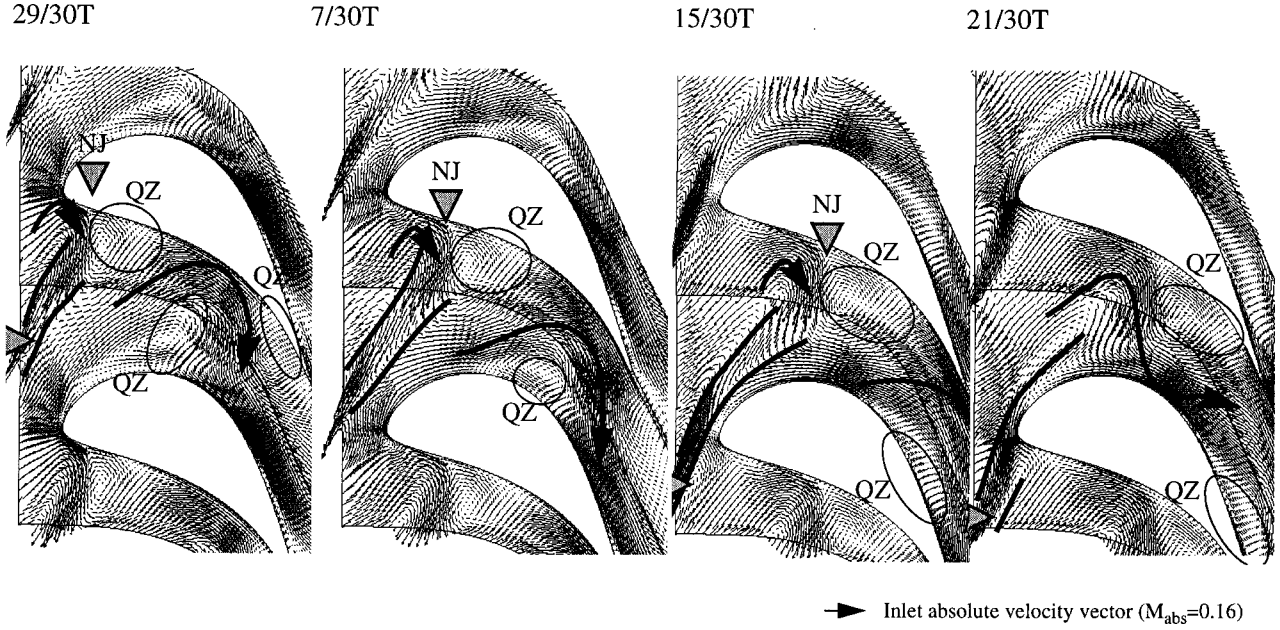

Fig. 6 Negative jet at midspan for PIN2

ment. The wake is observed spending 20 percent of a period interacting with the leading edge, without anchoring,[1] because of the downstream convection. It can be noted that once the wake has hit the leading edge, two regions form, the first on the pressure side and then, at the wake chopping, on the suction side, with very low unsteadiness. These regions can be called **quiescent**, because, considering the way the unsteady velocity field has been defined, they represent areas where the flow does not deviate much from the time-averaged value and thus can be considered as areas where the unsteadiness is damped. The birth of the quiescent zones can be associated with the feeding mechanisms of the negative jet. In fact, as the negative jet course is interrupted by the wall, feeding and discharge action starts for continuity reasons (Fig. 7 gives a schematic of this mechanisms). Yet, most of the feeding and discharge comes with the main flow direction (downstream), while little happens ahead of the wake for the feeding and behind it for the discharge. This means that convection is regulating the negative jet structure.

The quiescent regions are different from each other: On the pressure side this is quite extended, to a maximum of half a channel; on the suction side this thins out quickly, but residence time is longer before fading out at the trailing edge. For PIN2 these zones are more extended than for PIN1 and they do not fade out at the trailing edge, where they are evident on both suction and pressure sides. It would be reasonable to hypothesize that these zones travel downstream at the local time-averaged velocity, according to a convective mechanism. Instead, they travel somewhat faster and nearly at the same average rate (e.g., for PIN1 about $2.2\,c_{x\_\mathrm{inlet}}$ on the pressure side and $2.4\,c_{x\_\mathrm{inlet}}$ on the suction side at midspan). Their speed could be associated with a balance of various phenomena, such as: the pin tangential speed (of about $2\,c_{x\_\mathrm{inlet}}$ at midspan) and the convective speed, which is higher on the suction side than on the pressure side. These quiescent regions appear to play a central role in the unsteady transport of wake fluid. In fact, from Fig. 6, it can be observed that the unsteady transport assumes an *S* shape, transporting low momentum fluid from suction to pressure side, or vice versa, according to the quiescent zone's position. Finally, it is stressed that because the mechanism observed in Fig. 7 is the same for both pin configurations, it is believed to be independent of wake decay.

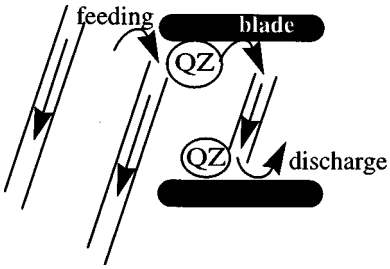

Fig. 7 Schematics of negative jet feeding mechanisms

[1]It seems necessary to define the meaning of anchoring. Considering a deficit of thickness *d* normal to the flow direction and moving downstream, the deficit is considered ''anchoring'' on the leading edge when its residence time on the leading edge is bigger than the time needed for the disturbance thickness to flow downstream.

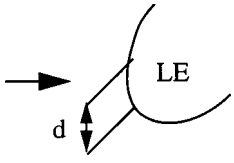

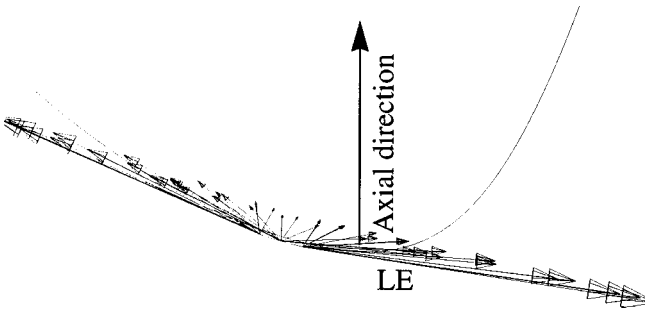

Fig. 8 Absolute vectors near leading edge over one period for PIN2

As far as the leading edge area is concerned, the changes in direction of unsteady transport near the stagnation point regard nearly a 180 deg turn on one period, as shown by means of absolute-velocity vectors in Fig. 8. If leading edge cooling were necessary, the coolant flow will go either on the pressure or on the suction side during a wake-passing period. Yet, this does not relevantly change the blade loading.

IV Potential Field

The type of blade under investigation presents a thick leading edge and thus a strong potential field extending upstream.

$\partial p/\partial \tau$ has been observed to be at the lowest in the quiescent regions and maximum near the location where the unsteady transport changes directions (compare Fig. 7). The leading edge also appears to be quite unsteady, showing high gradients of time-dependent pressure from the moment the wake hits it and for more than half a period. The trailing edge, on the contrary, is observed to be highly unsteady only for a shorter time. Most of the time the unsteady pressure field extends across the channel instead of being near the blade walls.

This unsteady behavior of the pressure field is also reflected on the blade loading. The unsteady field loading is less than the steady one (equals to a maximum difference in approach Mach number of 0.035) probably due to the velocity deficit introduced by the pin wake. Furthermore, on a time-averaged basis, the blade appears to be even more back-loaded, which could be explained reconsidering the unsteady transport mechanism (Fig. 7). However, the blade loading for PIN2 does not seem more disturbed than the loading for PIN1. The maximum load variation is only negligibly bigger than the one of PIN1. This is probably due to the particular blade geometry, which has been shown to be insensitive to inlet angle variations [16], where the leading edge is particularly loaded but the blade geometry damps the unsteadiness. It can be concluded that blade leading edges designed to be less sensitive to inlet angle variations [19] will be also more efficient in time-periodic flow fields, because they are less reactive to these and thus operate closer to the design point.

The difference of Cp at discrete locations on the blade (monitor points) is enhanced in Fig. 9. It can be noticed first that the PIN2 loading change is stronger in comparison to PIN1. A strikingly different behavior is to be observed near the leading edge.

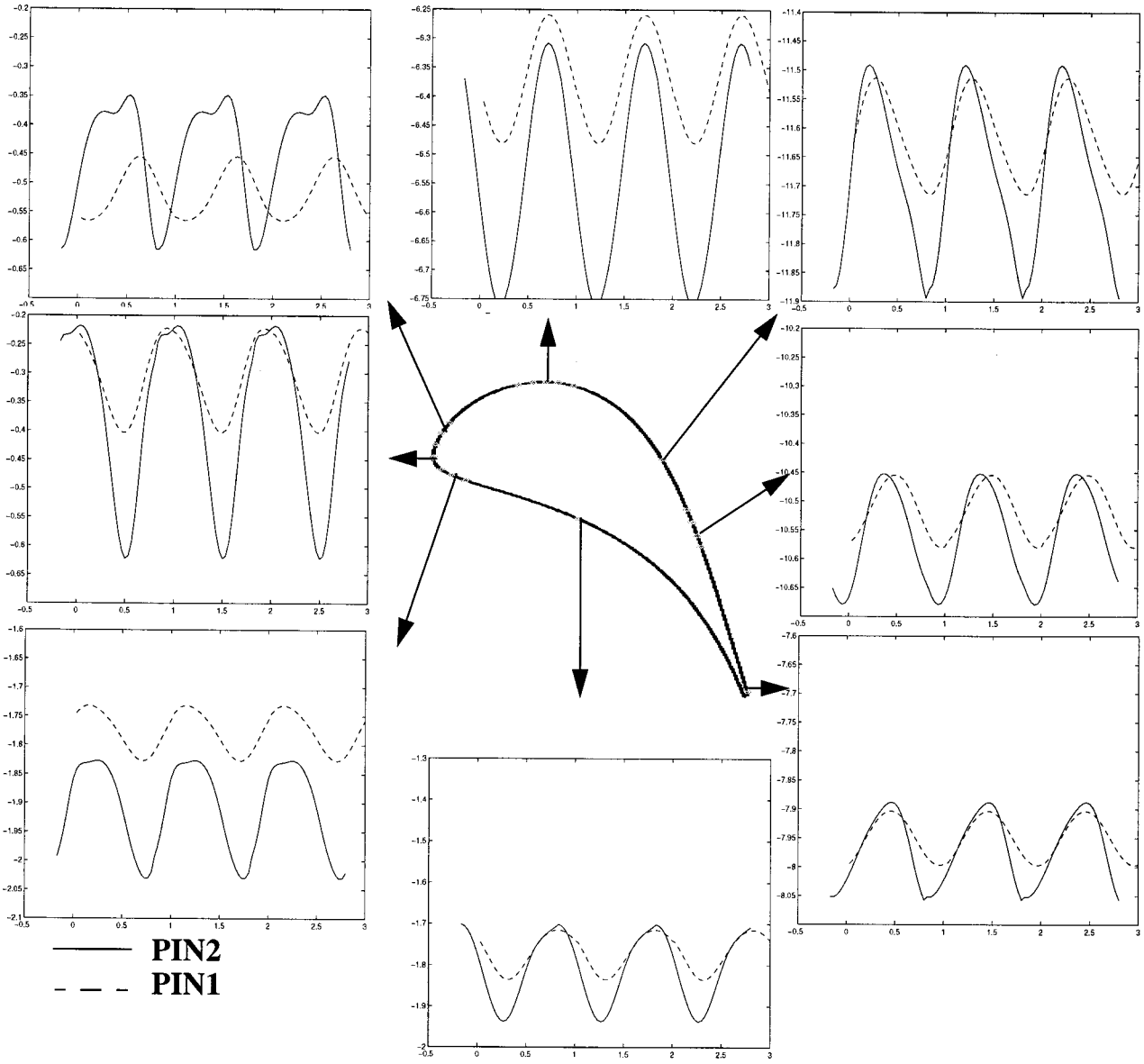

Fig. 9 Static pressure coefficient versus nondimensionalized time at midspan (three periods are represented)

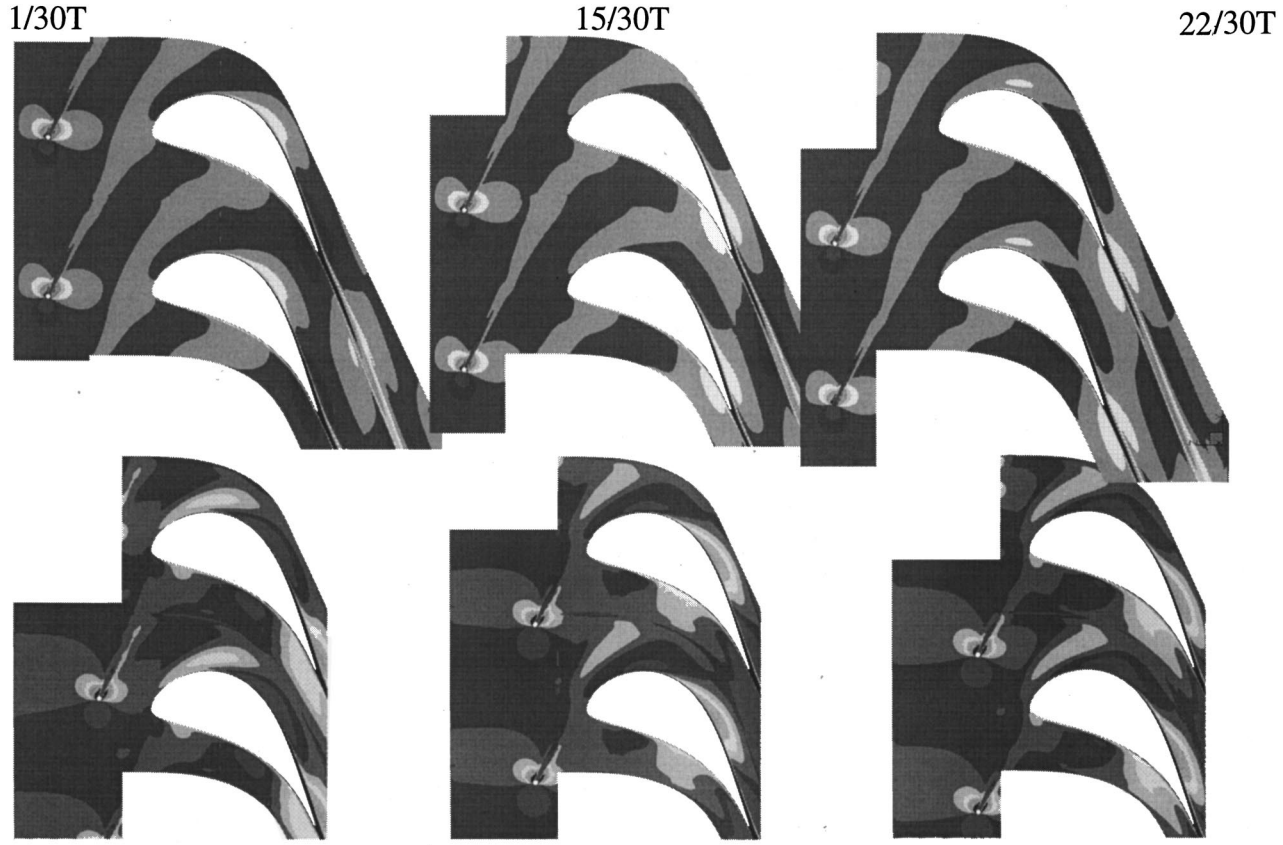

Fig. 10 Absolute total pressure contours for PIN1 (above) and PIN2 (below)

V Absolute Total Pressure Field

Figure 10 shows the absolute total pressure field for the two-dimensional computations of PIN1 at midspan. It can be seen that the wake centerline undergoes a direction and width transformation due to the interaction with the blade field and the wake appears much more influenced by the shear action of the accelerating flow. Comparing time steps 15/30*T* and 22/30*T* in Fig. 10, the wake is seen first deviating against the flow direction and then drawn into the blade row, its width increasing. As far as PIN1 is concerned, the absolute total-pressure wake anchors on the leading edge starting at 7/30*T*, although the interaction with the leading edge appears earlier than that, already at 28/30*T* (compare 1/30*T*). This early interaction appears to establish a bubble of sound flow on the suction side, which affects the anchoring process. In fact, while on the pressure side the wake moves downstream, it appears to be blocked for a while on the suction side. The wake spends half of a period on the leading edge. It is important to stress that although the suction side presents a faster fluid, the total-pressure ''wake'' on this side starts moving only after having been chopped (occurring at 11/30*T* for PIN1). Thus, as seen at 15/30*T*, the wake segment reaches the trailing edge first on the pressure side than on the suction side. For PIN2 (Fig. 10) on the other hand, an interaction pin/blade can always be observed. The absolute total pressure wake is estimated hitting the leading edge at about 15/30*T* and being chopped at 24/30*T*. Yet, it can be seen that the residence time on the suction side is long enough to bring an interaction with the following pin wake.

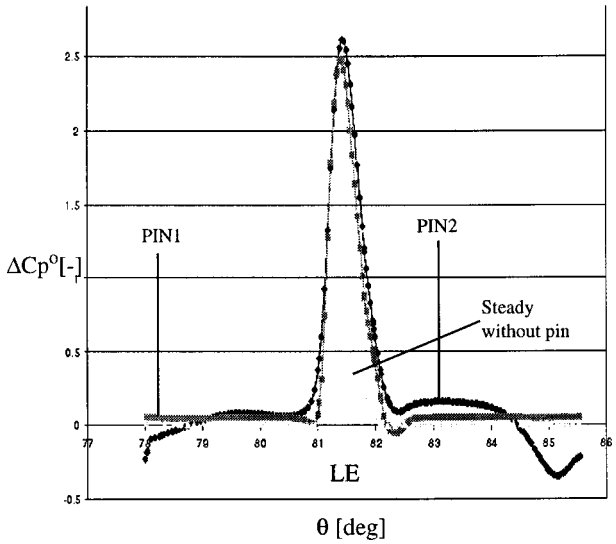

Fig. 11 Absolute total pressure coefficient at midspan 1/6th axial chord downstream of trailing edge

From Fig. 10 it can be also seen that the blade field drives the total pressure difference[2] from the pressure to the suction side showing an accumulation of this onto the suction side. Observing these results, in the optic of the wake-fluid unsteady transport mechanism of Fig. 6, it can be concluded that the final balance is determined not only by the wake characteristics, but also by the blade loading and, thus geometry.

Figure 11 shows the time-averaged total pressure coefficient. It can be seen that besides grid effects modifying the wake thickness, the deviation from the steady state flow increases when the pin is positioned closer to the leading edge.

[2]This term is preferred to loss, because the total pressure changes do not represent a loss in an unsteady flow field, due to energy separation effects.

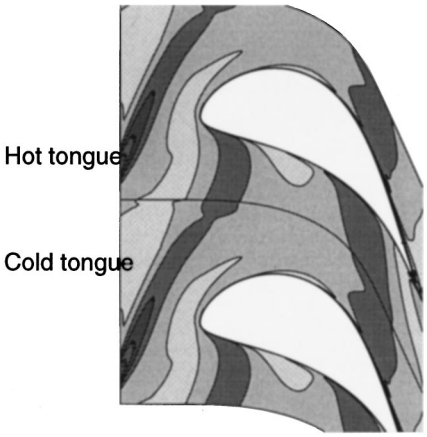

Fig. 12 Total temperature for PIN1 at midspan at 23/30*T*

VI Temperature (and Equivalently Enthalpy) Field

The wake presents the highest static temperature and in the absolute frame of reference the highest total temperature. This can create a phenomenon similar to hot streaks and has brought to the idea of trailing edge cooling through cold flow injection [20].

The temperature changes are more gradual in comparison to the changes of other flow quantities, i.e., they never have strong and sudden gradient and also oppose more inertia.

The static temperature is, as expected, at the highest near the leading edge with about 305 K. An area of high static temperature is always present near the leading edge.

In terms of total temperature, two ''tongues'' have been observed (Fig. 12): the wake and the sound flow. The latter presents a lower total temperature, but the gradient to the wake is smooth. Both the ''tongues'' anchor, although the chopping appears to occur before the anchoring, probably because of the acceleration in the middle of the channel favoring the temperature mixing. Considering for example PIN1, the wake is chopped at 26/30*T* and two segments proceed downstream: one from the pin with a free end and one from the free end to the suction side. The phase of their evolution is a little postponed in respect to the other flow quantities. In fact the wake is observed to be clearly anchored between 13/30*T* and 24/30*T*. Afterward, the wake moves on the pressure side, leaving a little bubble of high total pressure on the suction side, which is transported downstream and grows until 13/30*T*. At this point, this bubble merges again with the wake segment and a new blade-to-blade segment is formed.

As far as PIN2 is concerned, the temperature field is analogous in all respects to the one described for PIN1.

VII Secondary Flow and Other Aspects of Three-Dimensional Field

Considering the three-dimensional velocity field, the obvious must be stated: This is influenced by the wake being skewed, because of the boundary layer velocity profile and the radial growing tangential velocity. This is quite relevant in this configuration, because of the thick incoming boundary layers influencing the secondary flow formation.

The shape of the incoming wake can be seen in Fig. 13, where the quiescent zones at two representative time steps are represented. The physics of the development and downstream transport is analogous to the two-dimensional behavior described in the preceding paragraphs. Yet, unlike the steady-state computations, the flow is nowhere two-dimensional (not even at midspan) and a radial component from casing to hub always exists. It can be observed that, on the suction side, the quiescent zones affect only the center part of the blade, while on the pressure side these extend over the entire span. The behavior on the suction side can

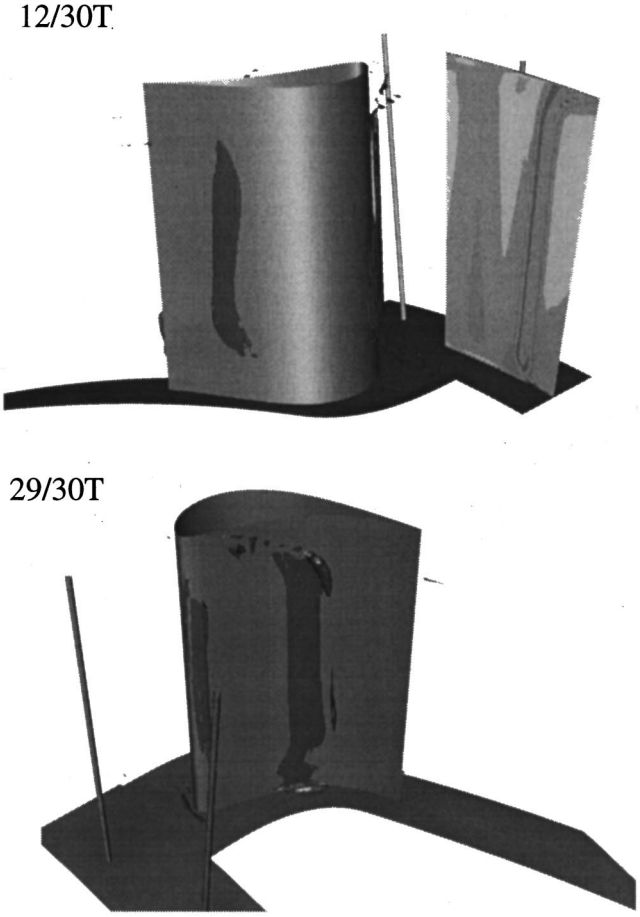

Fig. 13 Quiescent zones (as isosurfaces for 1 percent of averaged unsteady velocity field) near wall on suction side at 12/30*T* and pressure side 29/20*T* for PIN1. In the top picture a cut at 1/4 can also be seen, with unsteady velocity field, showing incoming wake shape.

actually be given two meanings. First, it could be a representation of higher unsteadiness; second, it could also indicate the presence of a strong quasi-steady secondary vortex, whose position changes little in time (but enough because of the vector-angle change in a swirling structure). On the pressure side, the deformation of the quiescent zones can also be seen, occurring because near the endwalls the wake hits the leading edge afterward, due to the velocity triangle.

As far as the secondary flow structures are concerned, a relevant radial migration has been observed (Fig. 14, top part). At the trailing edge the loss core has been detected at 6.5 percent of span (hub structure) and 86.3 percent of span (tip structure), where the latter has doubled its radial distance from the endwall in comparison to the steady case. As the wall suction side static pressure can be used to detect the horseshoe vortex suction side leg movement, this is shown in Fig. 14 (bottom part), where the steady-state static pressure coefficient is compared to the time-averaged one.

This radial migration continues also downstream for the near-tip vortical structures and reaches 81.6 percent of span at 1/6th of axial chord downstream of the trailing edge. Yet, it is practically unchanged in time. This could be a relevant observation for design purposes, showing that the secondary flow vortical structure present an inertia stronger than the time-dependent flow variations, probably due to the vorticity being higher than the unsteady forces. The migration of the secondary flow toward the inner parts of the channel has been observed by other authors [21], yet it

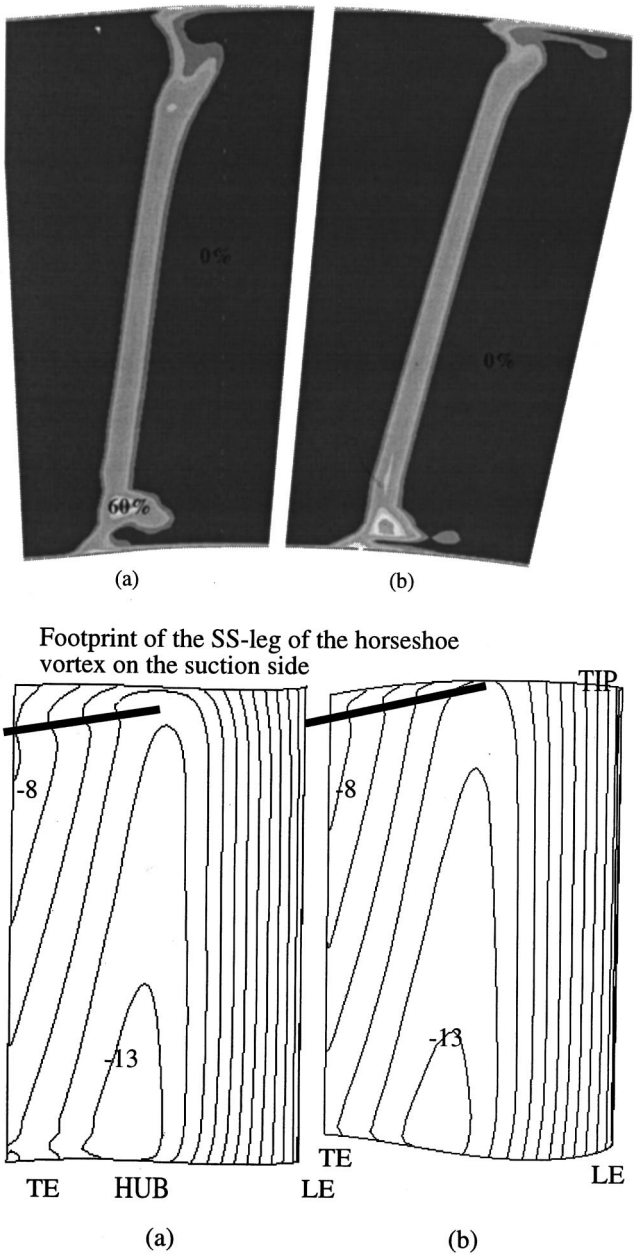

Fig. 14 Time-averaged absolute total pressure coefficient at 1/6th axial chord downstream of trailing edge (top) and static pressure coefficient on suction side (bottom) for PIN1 (*a*) and steady-state computation (*b*)

cannot be demonstrated by means of CFD results only that it depends exclusively on the physics. In fact, for steady flow fields it has been shown that $k-\varepsilon$ type turbulence models tend to move vortical structures away from the walls. Thus, as the turbulence model used for the computations has been calibrated on steady flows, the same effect could be expected. The grid effects are believed to be of secondary importance because of the appropriate node distribution shown in Fig. 3.

Three-dimensionally, the wake represents always a way for low-momentum fluid to be transported radially inward. This is true both in steady and unsteady state and thus it represents more or less a ''wall,'' which other transport mechanisms have to cope with. For all the analyzed quantities, it has been noticed that there is little mixing between the disturbance field created by the incoming wakes and the blade wake. Thus the disturbances seem to stand on the wake.

VIII Summary and Conclusions

The interaction between the wake created by a pin wheel and a turbine stator has been analyzed using CFD. The pin has been positioned at two axial locations upstream of the leading edge plane in order to investigate the effects of row spacing.

It has been observed that the wake is best defined through the velocity field. The following conclusions can be drawn:

- The wake does not anchor at the leading edge. The absolute total temperature and total pressure fields associated with it do;
- When the wake hits the leading edge, two zones are created with low unsteadiness. These have been called quiescent;
- The unsteady transport mechanisms seems guided by the creation and downstream movement of these quiescent zones;
- The quiescent zones have been shown to be dependent upon the feeding and discharging mechanisms of the negative jet;
- A coupling of the two pressure fields (pin and blade) exists. It would be interesting to investigate a blade/blade coupling;
- The secondary flow structure moves radially inward, but it is very stable in time (as far as total pressure loss values and core position).

As the physics observed in this research is the same for both pin configurations, it is believed to be independent of wake decay.

Acknowledgments

The authors are grateful to the Emeritus Prof. Dr. George Gyarmathy, who has supervised the research of the Annular Cascade Group until his retirement.

The first author acknowledges the financial support of the Swiss ERCOFTAC Pilot Centre. Parts of the project were sponsored by ABB Power Generation Ltd., NEFF (Swiss National Energy Research Foundation).

Nomenclature

CFD = computational fluid-dynamic
LE = leading edge
PS = pressure side
SS = suction side
TE = trailing edge
ε = turbulent dissipation rate
κ = turbulent kinetic energy
θ = tangential location, deg
C_p = static pressure coefficient $=-(\overline{p_1^0}-p)/(\overline{p_1^0}-\overline{p_1})$
ΔC_p^0 = total pressure coefficient $=(\overline{p_1^0}-p^0)/(\overline{p_1^0}-\overline{p_1})$
c_x = absolute axial velocity, m/s
c_w = minimum wake velocity, m/s
p = static pressure, Pa
p^0 = total pressure, Pa

Subscripts and Superscripts

1 = inlet (one axial chord ahead of the LE)
- = time-averaged

References

[1] Dean, R. C., 1959, ''On the Necessity of Unsteady Flow in Fluid Machines,'' ASME J. Basic Eng., **82**, pp. 24–28.
[2] Boletis, E., and Sieverding, C. H., 1991, ''Experimental Study of the Three-Dimensional Flow Field in a Turbine Stator Preceded by a Full Stage,'' ASME J. Turbomach., **113**, pp. 1–8.
[3] Funazaki, K., Tetsuka, N., and Tanuma, T., 1997, ''Experimental Studies on Unsteady Aerodynamic Loss of a High-Pressure Turbine Cascade,'' ASME Paper No. 97-GT-52.

[4] Schulte, V., and Hodson, H. P., 1998, ''Unsteady Wake-Induced Boundary Layer Transition in High Lift LP Turbines,'' ASME J. Turbomach., **120**, pp. 28–35.
[5] Sharma, O. P., Picket, G. F., and Ni, R. H., 1992, ''Assessment of Unsteady Flows in Turbines,'' ASME J. Turbomach., **114**, pp. 79–90.
[6] Epstein, A. H., Giles, M. B., Shang, T., and Sehra, A. K., 1989, ''Blade Row Interaction Effects on Compressor Measurements,'' *Unsteady Aerodynamic Phenomena in Turbomachines*, AGARD-CP-468, pp. 14.1–14.11.
[7] Meyer, R. X., 1958, ''The Effect of Wakes on the Transient Pressure and Velocity Distributions in Turbomachines,'' ASME J. Basic Eng., **80**, pp 1544–1552.
[8] Kerrebrock, J. L., and Mikolajczak, A. A., 1970, ''Intra-Stator Transport of Rotor Wakes and Its Effect on Compressor Performance,'' ASME J. Eng. Power, **92**, pp. 359–370.
[9] Hodson, H. P., and Dawes, W. N., 1998, ''On the Interpretation of Measured Profile Losses in Unsteady Wake-Turbine Blade Interaction Studies,'' ASME J. Turbomach., **120**, pp. 276–284.
[10] Gallus, H. E., Zeschky, J., and Hah, C., 1994, ''Endwall and Unsteady Flow Phenomena in an Axial Turbine Stage,'' ASME Paper No. 94-GT-143.
[11] McFarland, V. E., and Tiederman, W. G., 1992, ''Viscous Interaction Upstream and Downstream of a Turbine Stator Cascade with a Periodic Wake Field,'' ASME Paper No. 92-GT-162.
[12] Eckert, E. R. G., 1986, ''Energy Separation in Fluid Stream,'' Int. Commun. Heat Mass Transfer, **13**, pp. 127–143.
[13] Baehr, H. D., 1989, *Thermodynamik*, Springer-Verlag, Berlin.
[14] Callen, H. B., 1960, *Thermodynamics*, Wiley, New York.
[15] Casciaro, C., Sell, M., and Gyarmathy, G., 1998, ''Towards Reliable Computations for a Subsonic Turbine,'' *Proc. Symposium on Verification of Design Methods by Test and Analysis*, London, UK, Paper No. 15.
[16] Casciaro, C., 1999, ''A Numerical Analysis of Viscous Blade/Row Interactions in Axial-flow Turbines,'' Ph.D. thesis No. 13478, ETH, Zurich, Switzerland.
[17] Casciaro, C., Sell, M., Treiber, M., and Gyarmathy, G., 1999, ''Vortex Interaction and Breakdown Phenomena in an Axial Turbine,'' *Computational Technologies for Fluid/Thermal/Chemical Systems With Industrial Applications*, Vol. II, ASME PVP-Vol. 28, p. 155.
[18] Dullenkopf, K., 1992, ''Untersuchungen zum Einfluβ periodisch instationärer Nachlauf-strömungen auf den Wärmeübergang konvektiv gekühlter Gasturbinenschaufeln,'' Ph.D. thesis, Universität Karlsruhe, Germany.
[19] Casartelli, E., 1999, ''Dreidimensionale Diffusorströmung im Radialverdichter, numerisch untersuch,'' Ph.D. thesis No. 13056, ETH, Zurich, Switzerland.
[20] Rose, M. G., and Harvey, N. W., 2000, ''Turbomachinery Wakes: Differential Work and Mixing Losses,'' ASME J. Turbomach., **122**, pp. 68–77.
[21] VKI Lecture Series 1998-08, 1998, ''Blade Row Interference Effects in Axial Turbomachinery Stages,'' Von Karman Institute for Fluid Dynamics.

Effects of Tip Clearance on Hot Streak Migration in a High-Subsonic Single-Stage Turbine

Daniel J. Dorney
Virginia Commonwealth University,
Department of Mechanical Engineering,
Richmond, VA 23113

Douglas L. Sondak
Boston University,
Office of Information Technology,
Boston, MA 02215

Experimental data have shown that combustor temperature nonuniformities can lead to the excessive heating of first-stage rotor blades in turbines. This heating of the rotor blades can lead to thermal fatigue and degrade turbine performance. The results of recent studies have shown that variations in the circumferential location, or clocking, of the first-stage vane airfoils can be used to minimize the adverse effects of the hot streaks due to the hot fluid mixing with the cooler fluid contained in the vane wake. In addition, the effects of the hot streak/airfoil count ratio on the heating patterns of turbine airfoils have been quantified. In the present investigation, three-dimensional unsteady Navier–Stokes simulations have been performed for a single-stage high-pressure turbine geometry operating in high subsonic flow to study the effects of tip clearance on hot streak migration. Baseline simulations were initially performed without hot streaks to compare with the experimental data. Two simulations were then performed with a superimposed combustor hot streak; in the first the tip clearance was set at the experimental value, while in the second the rotor was allowed to scrape along the outer case (i.e., the limit as the tip clearance goes to zero). The predicted results for the baseline simulations show good agreement with the available experimental data. The simulations with the hot streak indicate that the tip clearance increases the radial spreading of the hot fluid, and increases the integrated rotor surface temperature compared to the case without tip clearance. [S0889-504X(00)02204-2]

Introduction

Hot streaks are known to have a significant impact on the wall temperature distributions of first-stage turbine rotors. The migration of hot streaks through turbines has been simulated by many researchers including Krouthen and Giles [1], Rai and Dring [2], Takahashi and Ni [3,4], Dorney et al. [5–7], Gundy and Dorney [8], and Shang et al. [9]. While these numerical simulations have produced significant insights into the mechanisms controlling hot streak migration, there is still a significant amount of research needed to formulate design criteria for minimizing the adverse effects of hot streaks. Most simulations have been performed at low-speed conditions, but additional physics can come into play at actual operating conditions.

Some of the earliest experimental investigations of hot streaks were performed on a high-speed turbine by researchers at NASA Lewis Research Center (Whitney et al. [10], Schwab et al. [11], Stabe et al. [12]). The goal of these experiments was to study the effects of typical nonuniform inlet radial temperature profiles on the performance of axial turbines. The inlet radial temperature profile in the experiment was produced using a Combustor Exit Radial Temperature Simulator (CERTS) inlet, which injected cool air through circumferential slots in the hub and tip endwalls upstream of the vane. In addition to a total temperature profile, a total pressure profile was generated using the CERTS inlet (see Figs. 1 and 2).

The focus of the present effort has been to study the effects of tip clearance on the migration of combustor hot streaks. The goal is to quantify the modification to rotor heating patterns caused by variations in tip clearance. Therefore, the focus will be on the overall effects of tip clearance, not the details of the flow in the tip gap. The NASA CERTS geometry was chosen as the test article for the current simulations because the flow conditions are representative of an actual engine environment. Simulations have been performed with the original CERTS profile, as well as with a discrete hot streak superimposed on the CERTS profile. Time-averaged and unsteady temperature data have been analyzed, as well as comparisons with available experimental data.

Numerical Method

The governing equations considered in this study are the time-dependent, three-dimensional Reynolds-averaged Navier–Stokes equations. The viscous fluxes are simplified by incorporating the thin layer assumption [13]. In the current study, viscous terms are

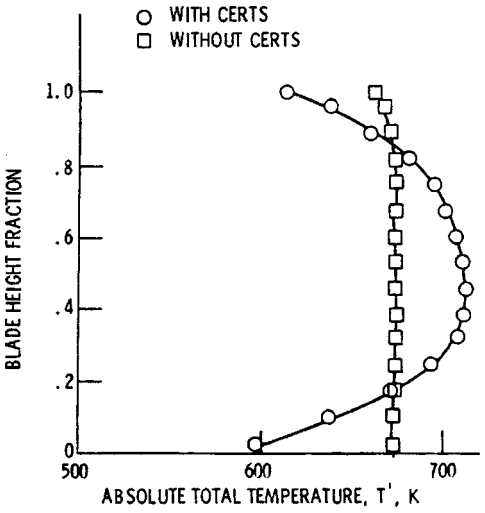

Fig. 1 CERTS total temperature profile

Contributed by the International Gas Turbine Institute and presented at the 45th International Gas Turbine and Aeroengine Congress and Exhibition, Munich, Germany, May 8–11, 2000. Manuscript recieved by the International Gas Turbine Institute February 2000. Paper No. 2000-GT-441. Review Chair: D. Ballal.

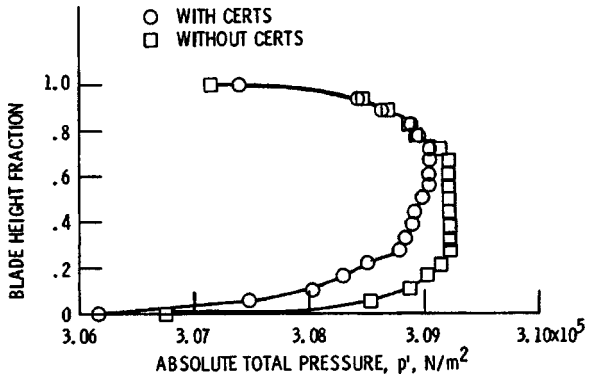

Fig. 2 CERTS total pressure profile

retained in the direction normal to the hub and shroud surfaces, and in the direction normal to the blade surfaces. To extend the equations of motion to turbulent flows, an eddy viscosity formulation is used. The turbulent viscosity is calculated using the two-layer Baldwin–Lomax [13] algebraic turbulence model.

The numerical algorithm used in the three-dimensional computational procedure consists of a time-marching, implicit, finite-difference scheme. The procedure is third-order spatially accurate and second-order temporally accurate. The inviscid fluxes are discretized according to the scheme developed by Roe [14]. The viscous fluxes are calculated using standard central differences. An approximate-factorization technique is used to compute the time rate changes in the primary variables. In addition, Newton subiterations are used at each global time step to increase stability and reduce linearization errors. For all cases investigated in this study, one Newton subiteration was performed at each time step. Further details on the numerical procedure can be found in Dorney et al. [5,6,15].

The Navier–Stokes analysis uses O- and H-type zonal grids to discretize the flow field and facilitate relative motion of the airfoils. The O-grids are body-fitted to the surfaces of the airfoils and generated using an elliptic equation solution procedure. They are used to resolve the viscous flow in the blade passages properly and to apply the algebraic turbulence model easily. Algebraically generated H-grids are used to discretize the remainder of the flow field.

The code has been parallelized using the Message Passing Interface (MPI) library. In the current implementation, the solution is decomposed by blade row, blade passage, or individual grid depending on the number of processors available.

Boundary Conditions

The theory of characteristics is used to determine the boundary conditions at the inlet and exit of the computational domain. At the inlet, the total pressure, total temperature, and the circumferential and radial flow angles are specified as a function of radius. The upstream running Riemann invariant is extrapolated from the interior of the computational domain.

For simulations containing inlet hot streaks, the flow variables within the hot streak must be modified. Within the hot streak, the inlet flow variables used to define the specified boundary conditions can be written as

$$u_{hs}=u_\infty\sqrt{T_{hs}/T_\infty} \quad v_{hs}=v_\infty\sqrt{T_{hs}/T_\infty}$$
$$w_{hs}=w_\infty\sqrt{T_{hs}/T_\infty} \quad P_{hs}=P_\infty \tag{1}$$
$$a_{hs}=a_\infty\sqrt{T_{hs}/T_\infty} \quad \rho_{hs}=\rho_\infty/(T_{hs}/T_\infty)$$

where T_{hs} is the temperature within the hot streak and T_∞ is the temperature of the undisturbed inlet flow. The static and total pressures within the hot streak are assumed to be equal to those of the undisturbed inlet flow [16]. In the current investigation two different hot streak configurations have been implemented. The first configuration used the original CERTS profiles to allow comparisons with experimental data, while in a second set of simulations a discrete hot streak was superimposed on the CERTS profiles to model engine conditions more realistically.

The superimposed hot streak is circular in shape with a diameter equal to 50 percent of the span. The temperature profile within the hot streak is based on a hyperbolic tangent distribution with the center located at 40 percent of span. This distribution is consistent with the one described by Butler et al. [16], although actual temperature profiles are dependent on the design of the combustor. The hot streak was aligned circumferentially with the leading edge of a vane.

At the exit the circumferential and radial velocity components, entropy, and the downstream running Riemann invariant are extrapolated from the interior of the computational domain. The pressure ratio, P_4/P_{t1}, is specified at midspan of the computational exit, and the pressure values at all other radial locations are obtained by integrating the equation for radial equilibrium. Periodicity is enforced along the outer boundaries of the H-grids in the circumferential direction.

No-slip boundary conditions are enforced at the hub and tip end walls, and along airfoil surfaces. It is assumed that the normal derivative of the pressure is zero at solid wall surfaces, and that the walls are adiabatic.

The flow variables at zonal boundaries are explicitly updated after each time step by interpolating values from the adjacent grid.

Geometry and Grid

The CERTS test turbine was a 0.767 scale rig modeling the first stage of a two-stage core turbine designed for a modern high bypass ratio engine. The design criteria for the model were to accommodate the high-work, low-flow characteristics for this type of turbine and achieve a subsonic design with reasonable blade height. The vane has a constant section (untwisted), and was designed for a constant exit flow angle of 75 deg from axial. The rotor leading edge was designed to accept the vane exit flow with either zero or small negative incidence. The rotor exit was designed for free vortex flow. The design conditions for the turbine are shown in Table 1.

The inlet radial temperature profile in the experiments was produced using the CERTS inlet, which injected cool air through circumferential slots in the hub and tip endwalls upstream of the vane (see Fig. 1). In addition to a total temperature profile, a total pressure profile was generated using the CERTS inlet (see Fig. 2). The ratio of the maximum total temperature to the average total temperature was approximately 1.05, and the ratio of maximum-to-minimum total temperature was approximately 1.20. The peak Mach number in the turbine was in the high subsonic range, approximately 0.92.

A total of four computations were performed. In the first two simulations the baseline CERTS flow conditions were run with: (1) the actual tip clearance, and (2) the rotor scraping the outer casing (the limit as the tip clearance approaches zero). In the third and fourth simulations a discrete hot streak was added to the simulations and computations were again performed with the actual tip clearance and the rotor scraping the outer casing (see Fig. 3).

Table 1 CERTS flow conditions

Inlet total temperature	672.2 k
Inlet total pressure	3.103×10^5 Pa
Mass flow	6.130 kg/s
Specific work	1.229×10^5 J/kg
Rotational speed	11,373 rpm
Total pressure ratio	2.360

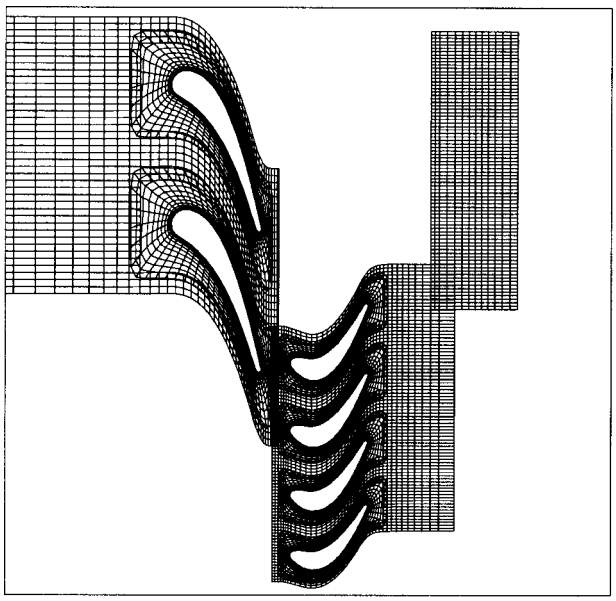

Fig. 4 Computational grid: spanwise view

The experimental configuration has 26 vane airfoils and 48 rotor airfoils. A three-dimensional computation of the flow through the complete turbine configuration would be prohibitively expensive. To reduce the cost of the computation, the number of vanes in the first row was decreased to 24 and the size of the vane was increased by a factor of 26/24 to maintain the same blockage. In the simulations with only the CERTS profile, a one-vane/two-rotor airfoil count ratio was used, while in the simulations with the superimposed hot streak a two-vane/four-rotor ratio was used to allow a more realistic configuration of one hot streak for every other vane passage.

Two views of the grids used to discretize the hot streak flow field are shown in Figs. 4 and 5 (every other grid point has been removed for clarity). The O-grids each contain 121 points in the wrap-around direction, 31 points in the surface-normal direction, and 51 points in the radial direction. The H-grids for the vane and rotor regions each contain 86 points in the axial direction, 51 points in the circumferential direction, and 51 points in the radial direction. The H-grid used to discretize the outlet region of the turbine stage contains 14 points in the axial direction, 41 points in the circumferential direction, and 51 points in the radial direction. In the simulations in which the tip clearance region was discretized, the clearance O-grid contained 121 points in the wrap-around direction, 17 points normal to the collapsed centerline, and 7 points in the radial direction (see Fig. 6). The axial and circumferential grid dimensions necessary to resolve convected wakes and hot streaks were determined using a two-dimensional analysis. The average value of y^+, the nondimensional distance of the first grid point above a surface, was approximately 1.5 for the airfoil surfaces and 3.0 for the endwall surfaces. The total number

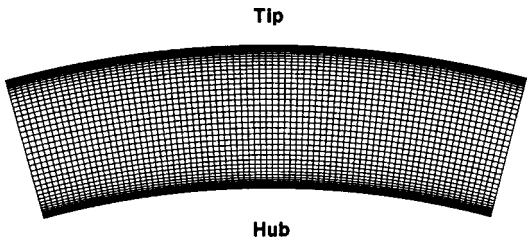

Fig. 5 Computational grid: axial view

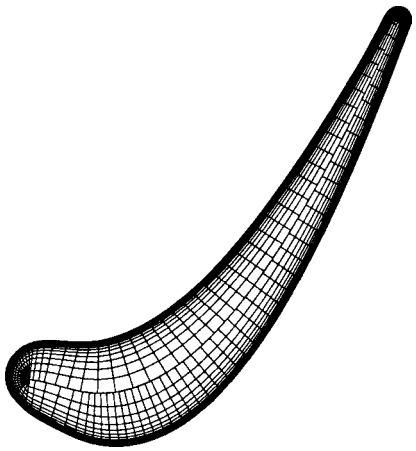

Fig. 6 Computational grid in tip clearance region

of grid points used to discretize the turbine flow field for the cases with the CERTS profile alone was approximately 1.27 million, while the simulations with a superimposed hot streak utilized approximately 2.54 million grid points.

The computations were each run for 15 cycles using one subiteration per time step and 6000 time steps per cycle. Here, a cycle is defined as the time it takes a rotor to travel a circumferential distance equal to one vane pitch. The computations were performed on eight 250-MHz processors of a Silicon Graphics Origin2000 computer located at NASA Ames Research Center. Each computation required approximately 6×10^{-5} s/grid point/iteration computation time (i.e., each iteration takes approximately 28 seconds wall clock time).

Numerical Results

The Mach number at the inlet to the vane is approximately 0.14 and the inlet flow is assumed to be axial. The rotor rotational speed was 11,373 rpm. The free-stream Reynolds number was 197,000 based on the rotor axial chord. A pressure ratio of $P_4/P_{t1}=0.385$ was calculated from the experimental data based on the midspan inlet total pressure and the static pressure in the rotor trailing edge plane.

Baseline Case—CERTS Only. Figures 7–9 show comparisons between the predicted and experimental time-averaged critical velocity ratio distributions, where the critical velocity ratio is defined as

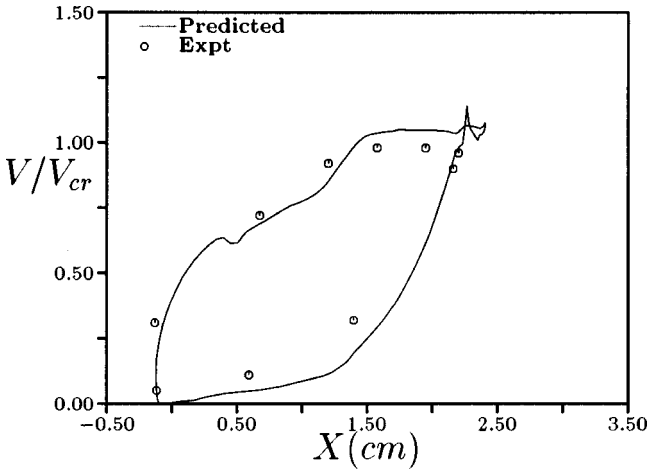

Fig. 7 Critical velocity ratio at the hub of the vane: baseline

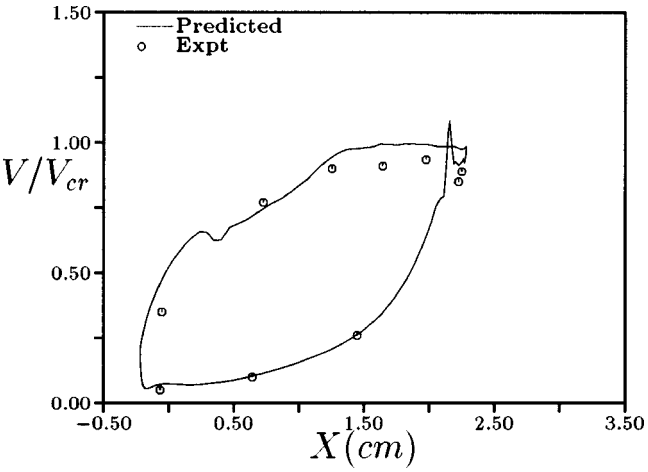

Fig. 8 Critical velocity ratio at midspan of the vane: baseline

$$\overline{V}/V_{cr}=\overline{V}/\sqrt{\frac{2\gamma}{\gamma+1}R\overline{T}_t} \tag{2}$$

and the velocity is based on the isentropic Mach number. There is generally good agreement between the predicted and experimental results, with small differences evident near peak suction. The velocity ratios were similar with and without rotor tip clearance. Therefore, only the results from the tip clearance case are shown.

Figure 10 contains the predicted and experimental radial profiles of circumferentially averaged flow angle 2.5 chord lengths downstream of the rotor. Also included in Fig. 10 is the design-intent flow angle distribution. Both the predicted and experimental results indicate underturning near midspan. A previous study traced the underturning to a large secondary flow region near the hub endwall in the rotor passage [15]. In general, there is good agreement between the predicted and experimental data from 20 to 70 percent span. Near the hub endwall there are discrepancies between the numerical and experimental angles. The differences are due to the extent of the secondary flows in the rotor passage being greater in the experiments than in the simulations. The reduced secondary flows predicted by the analysis may result from the optimistic tendencies of the Baldwin–Lomax turbulence model in separated flow regions. The predicted results do not show the near-constant flow angles that were observed in the experiments from 70 percent span to the outer endwall.

Figure 11 shows the predicted and experimental total pressure

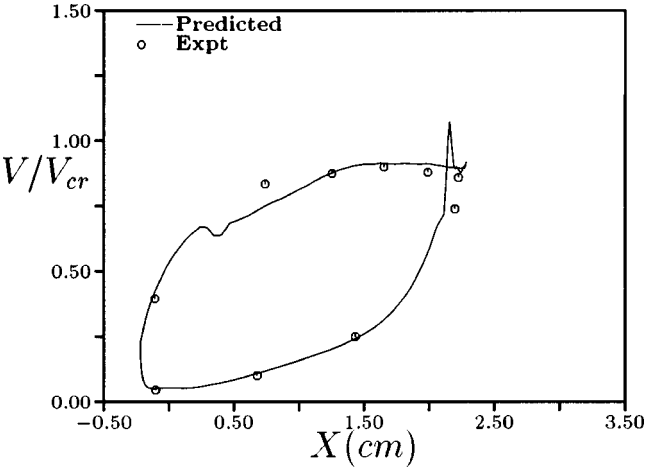

Fig. 9 Critical velocity ratio at the tip of the vane: baseline

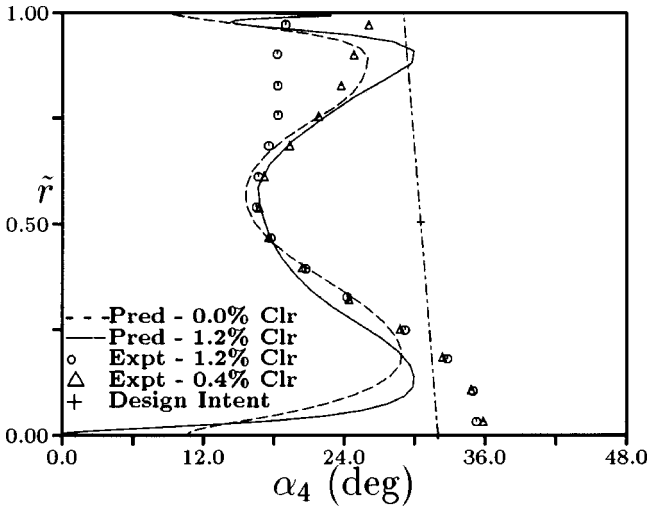

Fig. 10 Absolute circumferential flow angle distribution at the exit of the stage: baseline

distributions 2.5 chord lengths downstream of the rotor. There is good agreement from 40 to 80 percent span. In the outer endwall region the results from the case with 1.2 percent tip clearance case show more loss than the case with 0.0 percent tip clearance, while the discrepancies between the predicted results and the data near the hub are due to the larger secondary flows in the experiments.

Figure 12 contains the predicted and experimental total temperature distributions 2.5 chords downstream of the rotor. The predicted values from both simulations show close agreement with the experimental data, although the case with tip clearance shows better agreement with the data from the hub to 50 percent span and higher temperatures near the outer endwall.

The experimentally determined time-averaged efficiency for this turbine was $\eta=0.883$, while the predicted value was $\eta=0.886$ for 0 percent tip clearance and $\eta=0.875$ with 1.2 percent tip clearance. The total-to-total efficiency, η, is defined as:

$$\eta=\frac{(P_{t4}/P_{t1})^{\gamma-1/\gamma}-1.0}{T_{t1}/T_{t4}-1.0} \tag{3}$$

Cases With CERTS and Hot Streak. Although the experimental study using the CERTS contained a radial temperature

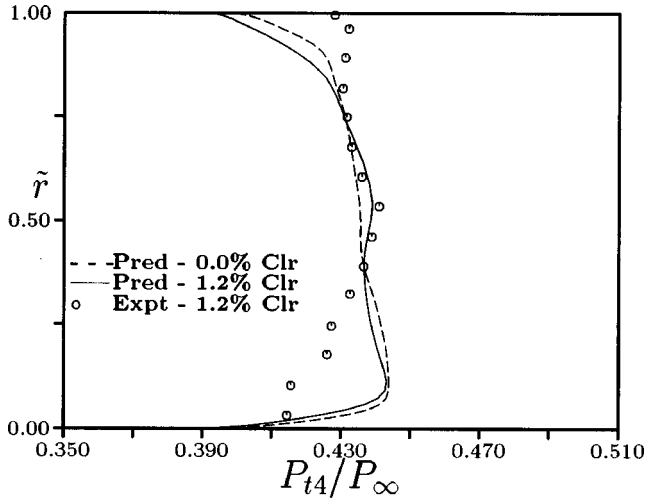

Fig. 11 Total pressure distribution at the exit of the stage: baseline

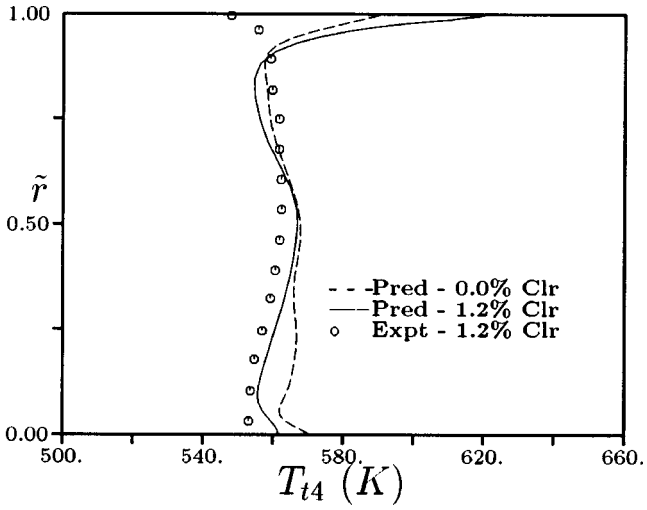

Fig. 12 Total temperature distribution at the exit of the stage: baseline

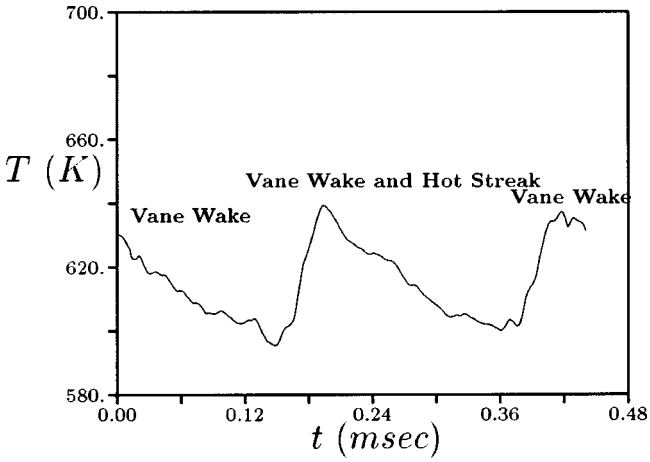

Fig. 14 Temperature history at 42 percent span: clearance

profile, a discrete hot streak was added at the inlet to the turbine to represent a more realistic engine temperature distribution.

Figures 13 and 14 illustrate static temperature traces at the 42 percent span location on the rotor leading edge in the cases without and with tip clearance, respectively. The 42 percent span location corresponds to the impact point of the hot streak in the case without tip clearance, but not for the case with tip clearance. Both figures confirm the periodicity of the solutions (traces at many spanwise locations also showed periodicity). The two figures also illustrate the temperature variations due to the vane wakes, as well as the temperature rise associated with the superimposed hot streak.

Time-averaged static temperature contours on the pressure surface of the rotor for the cases with and without tip clearance are shown in Figs. 15 and 16. The case with tip clearance shows more heating over the majority of the pressure surface. The case with tip clearance also exhibits increased spreading of the hot fluid, especially toward the rotor tip. This is expected because of leakage of flow over the tip from the pressure surface to the suction surface. Figures 17 and 18 show the time-averaged temperature contours on the suction surface of the rotor. Similar to the results for the pressure surface, the case with tip clearance exhibits a more concentrated region of high temperature, as well as a larger spread of the hot fluid. In addition, the case with tip clearance shows more hot fluid entrained in the tip flow. Some of the hot fluid near the suction surface tip is leakage flow from the pressure surface. Overall, the time-averaged rotor surface temperature is higher in the case with tip clearance ($\approx$610.2 K) compared to the case without tip clearance ($\approx$607.5 K).

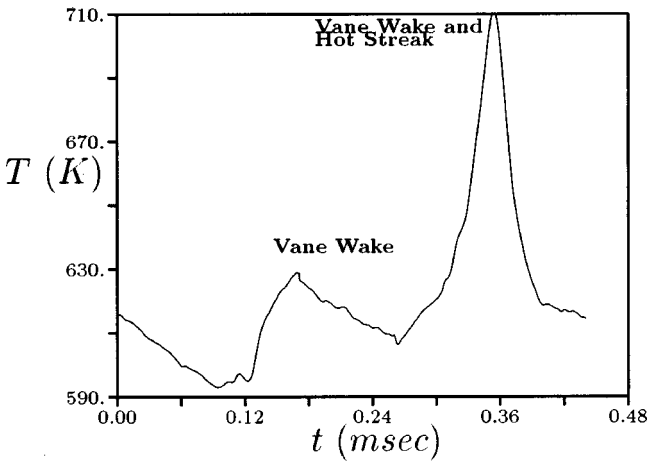

Fig. 13 Temperature history at 42 percent span: no clearance

Figure 19 shows the radial distributions of the circumferentially averaged absolute total temperature at the inlet of the vane with and without the hot streak superimposed on the CERTS profile. The radial distributions of the total temperature at the vane exit are shown in Fig. 20. Both simulations including tip clearance exhibit a high-temperature region at approximately 15 percent span as compared to the cases without tip clearance. The cases with the superimposed hot streak both display elevated temperatures at the vane exit. In the case with tip clearance, the location corresponding to the peak temperature is shifted approximately 5 percent of the span closer to the hub than in the case without tip clearance. In addition, high temperature regions cover a greater portion of the span, which is consistent with Figs. 15 and 16. At the exit of the rotor (see Fig. 21) the cases with tip clearance display elevated temperatures from 80 percent of the span to the outer endwall, indicating less work being extracted near the tip of the rotor. Both simulations with the superimposed hot streaks have elevated temperatures compared to the simulations without a hot streak. The case with tip clearance and the hot streak has lower total temperatures than the case with the hot streak and no tip clearance from approximately 30 to 70 percent of the span.

The absolute total pressure profiles at the vane inlet are shown in Fig. 22. The profiles are similar, which is expected because the total pressure distribution are specified boundary conditions at the inlet. At the exit of the vane passage (see Fig. 23), the cases with the hot streak generate greater losses from approximately 25 percent of the span to 70 percent of the span. The total pressure profiles at the rotor exit are shown in Fig. 24. The profiles in the two cases with tip clearance are similar, while the cases without tip clearance show lower total pressures from approximately 20 to 80 percent of the span.

Figures 25 and 26 show radial profiles of the absolute circumferential flow angle at the exits of the vane and rotor passages, respectively. The vane exit flow angles are similar in all four simulations from 10 to 75 percent of the span. Closer to the outer casing the simulations with tip clearance show generally more flow turning. At the rotor exit the more even temperature distributions in the cases with tip clearance preserve the flow angle deficit originally observed in the CERTS experiments, while in the cases without tip clearance the flow angle deficit is reduced.

Conclusions

A series of four three-dimensional unsteady Navier–Stokes simulations has been performed for the CERTS turbine to study

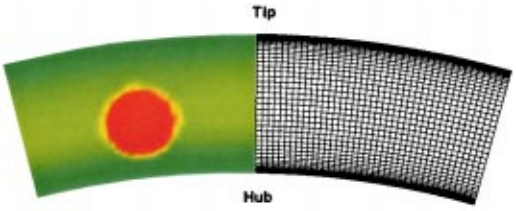

Fig. 3 Computational grid and hot streak definition

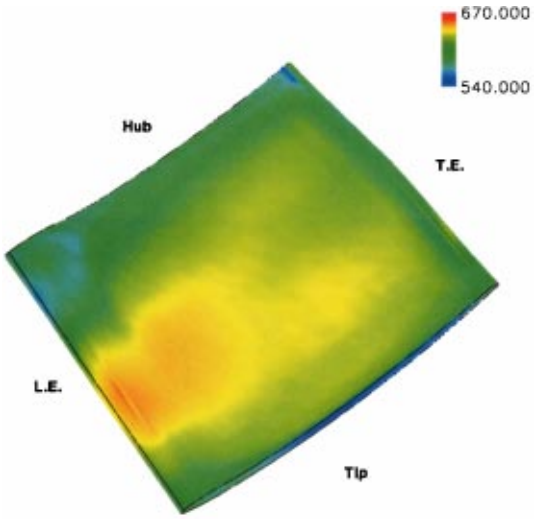

Fig. 15 Time-averaged temperature—pressure surface—no clearance

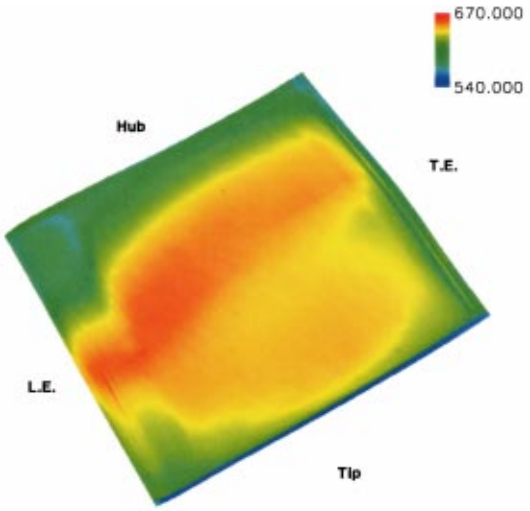

Fig. 16 Time-averaged temperature—pressure surface—clearance

the effects of tip clearance on the migration characteristics of combustor temperature distortions. Two baseline simulations (with and without tip clearance) were performed with the CERTS profiles alone to allow comparisons with the available experimental data. In general, the predicted results showed reasonable agreement with the experimental data. Next, two simulations were performed with a hot streak superimposed onto the CERTS profiles. The predicted results indicate that the inclusion of tip clearance causes the hot fluid to spread out over a greater portion of the

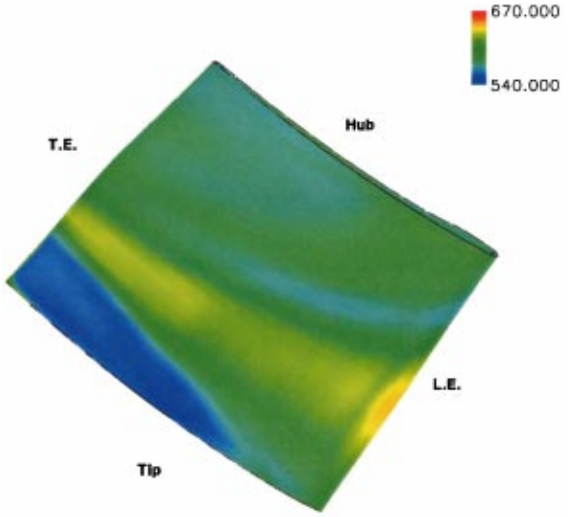

Fig. 17 Time-averaged temperature—suction surface—no clearance

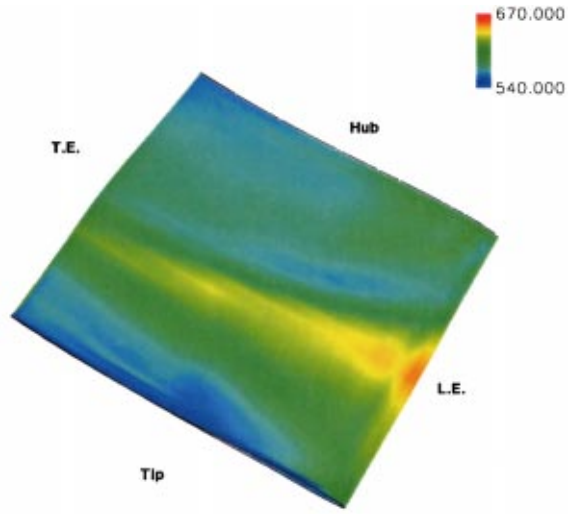

Fig. 18 Time-averaged temperature—suction surface—clearance

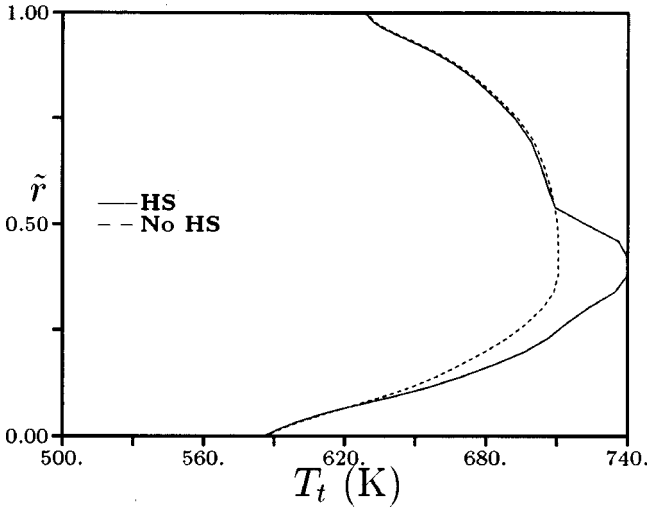

Fig. 19 Total temperature distribution at the inlet of the vane

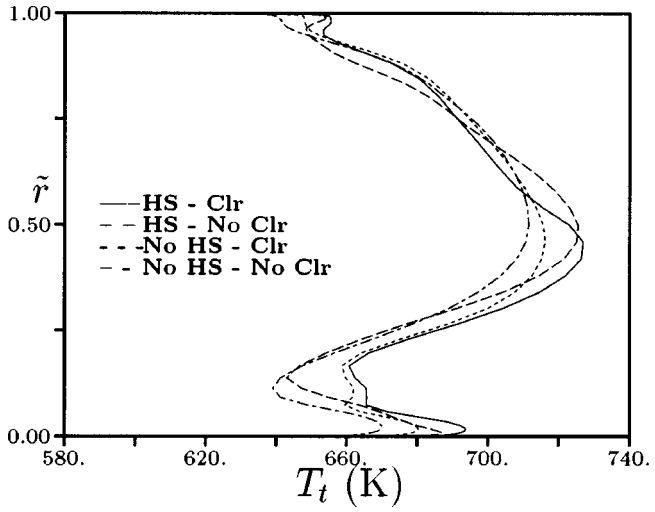

Fig. 20 Total temperature distribution at the exit of the vane

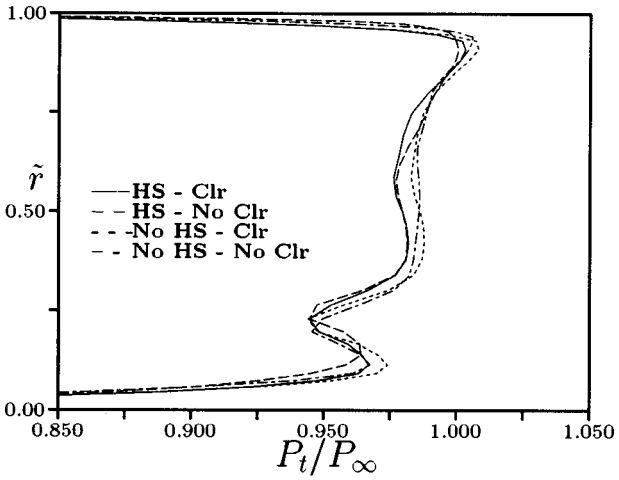

Fig. 23 Total pressure distribution at the exit of the vane

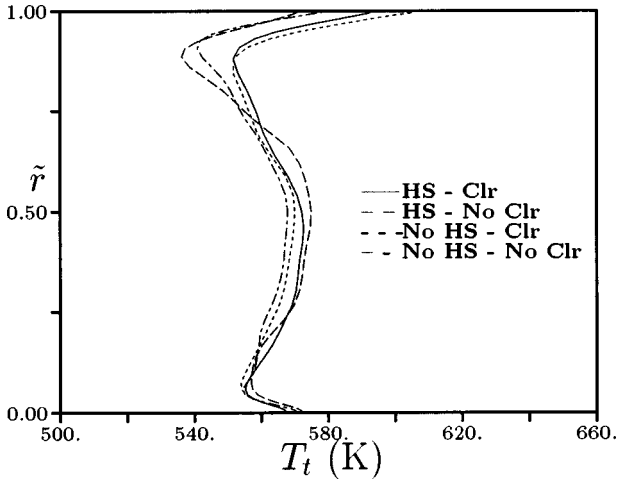

Fig. 21 Total temperature distribution at the exit of the rotor

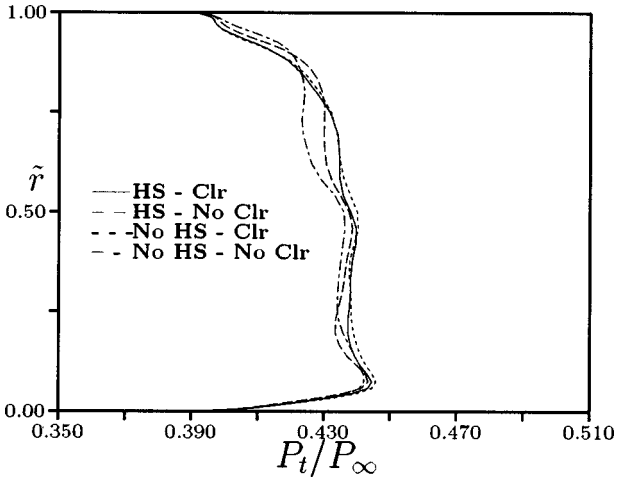

Fig. 24 Total pressure distribution at the exit of the rotor

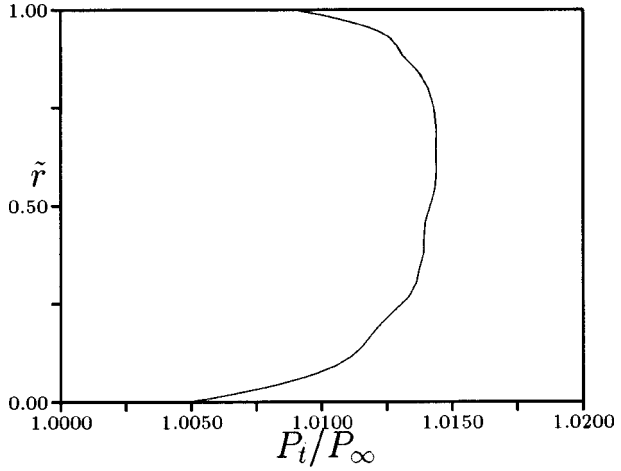

Fig. 22 Total pressure distribution at the inlet of the vane

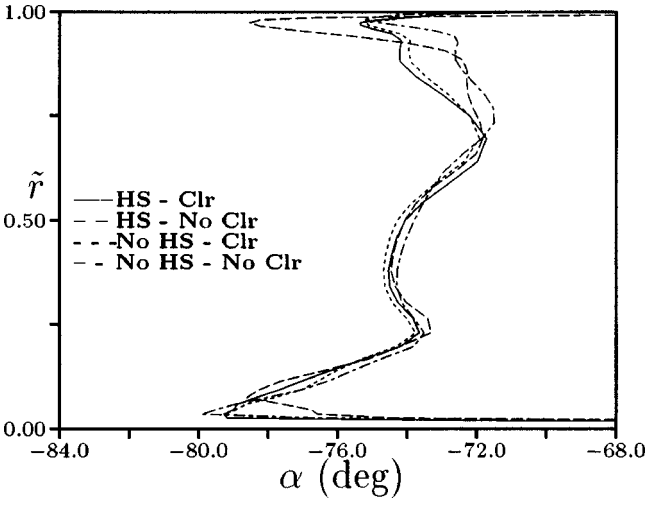

Fig. 25 Circumferential absolute flow angle distribution at the exit of the vane

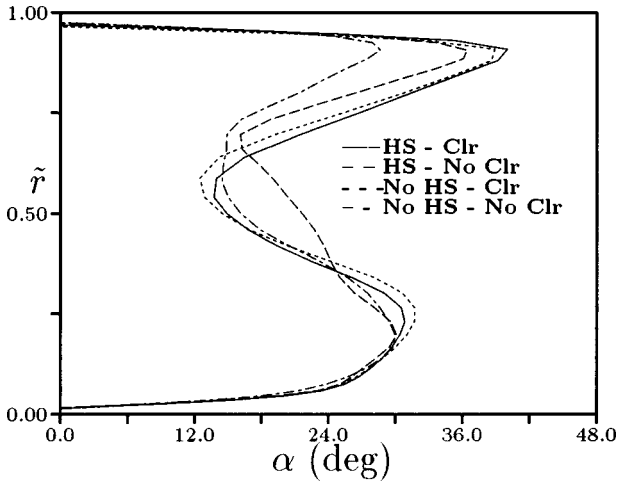

Fig. 26 Circumferential absolute flow angle distribution at the exit of the rotor

rotor surface, and the average rotor surface temperature is increased compared to the simulation without tip clearance. In both simulations, the hot streak had minimal effect on the total pressure distributions. The circumferential flow angle deficit (which was also observed in the experiments) is preserved by the spreading of the hot fluid in presence of tip clearance, while the flow angle deficit is significantly reduced when the tip clearance is removed because the hot fluid is confined to a relatively narrow region near midspan.

Nomenclature

a = speed of sound
bpf = blade passing frequency
f = frequency
P = static pressure
$P.S.$ = pressure surface
$\tilde{r}$ = $(r-r_{\text{hub}})/(r_{\text{tip}}-r_{\text{hub}})$
R = gas constant
$S.S.$ = suction surface
T = static temperature
u = x-direction component of velocity
v = y-direction component of velocity
V = magnitude of the velocity
w = z-direction component of velocity
α = circumferential flow angle (from axial)
γ = ratio of specific heats
η = total-to-total efficiency
ρ = density
$\overline{(\ )}$ = time-averaged value

Subscripts

cr = critical value
hs = hot streak
t = stagnation quantity
1 = vane inlet quantity
4 = exit duct quantity
∞ = free-stream quantity

References

[1] Krouthen, B., and Giles, M. B., 1990, ''Numerical Investigation of Hot Streaks in Turbines,'' AIAAJ. Propul. Power, **6**, No. 6, pp. 769–776.
[2] Rai, M. M., and Dring, R. P., 1990, ''Navier–Stokes Analysis of the Redistribution of Inlet Temperature Distortions in a Turbine,'' AIAA J. Propul. Power, **6**, pp. 276–282.
[3] Takahashi, R. K., and Ni, R. H., 1990, ''Unsteady Euler Analysis of the Redistribution of an Inlet Temperature Distortion in a Turbine,'' AIAA Paper No. 90-2262.
[4] Takahashi, R. K., and Ni, R. H., 1991, ''Unsteady Hot Streak Migration Through a 1-1/2 Stage Turbine,'' AIAA Paper No. 91-3382.
[5] Dorney, D. J., Davis, R. L., Edwards, D. E., and Madavan, N. K., 1992, ''Unsteady Analysis of Hot Streak Migration in a Turbine Stage,'' AIAA J. Propul. Power, **8**, No. 2, pp. 520–529.
[6] Dorney, D. J., and Davis, R. L., 1993, ''Numerical Simulation of Turbine 'Hot Spot' Alleviation Using Film Cooling,'' AIAA J. Propul. Power, **9**, No. 3, pp. 329–336.
[7] Dorney, D. J., and Gundy-Burlet, K. L., 1996, ''Hot Streak Clocking Effects in a 1-1/2 Stage Turbine,'' AIAA J. Propul. Power, **12**, No. 3, pp. 619–620.
[8] Gundy-Burlet, K. L., and Dorney, D. J., 1997, ''Influence of 3D Hot Streaks on Turbine Heat Transfer,'' Int. J. Turbo Jet Eng., **14**, No. 3, pp. 123–132.
[9] Shang, T., and Epstein, A. H., 1997, ''Analysis of Hot Streak Effects on Turbine Rotor Heat Load,'' ASME J. Turbomach., **119**, pp. 544–553.
[10] Whitney, W. J., Stabe, R. G., and Moffitt, T. P., 1980, ''Description of the Warm Core Turbine Facility and the Warm Annular Cascade Facility Recently Installed at NASA Lewis Research Center,'' NASA TM 81562.
[11] Schwab, J. R., Stabe, R. G., and Whitney, W. J., 1983, ''Analytical and Experimental Study of Flow Through an Axial Turbine Stage with a Nonuniform Inlet Radial Temperature Profile,'' AIAA Paper No. 83-1175.
[12] Stabe, R. G., Whitney, W. J., and Moffitt, T. P., 1984, ''Performance of a High-Work Low Aspect Ratio Turbine Tested with a Realistic Inlet Radial Temperature Profile,'' AIAA Paper No. 84–1161.
[13] Baldwin, B. S., and Lomax, H., 1978, ''Thin Layer Approximation and Algebraic Model for Separated Turbulent Flow,'' AIAA Paper No. 78-257.
[14] Roe, P. L., 1981, ''Approximate Riemann Solvers, Parameter Vectors, and Difference Schemes,'' J. Comput. Phys., **43**, pp. 357–372.
[15] Dorney, D. J., and Schwab, J. R., 1995, ''Unsteady Numerical Simulations of Radial Temperature Profile Redistribution in a Single-Stage Turbine,'' ASME J. Turbomach., **118**, pp. 783–791.
[16] Butler, T. L., Sharma, O. P., Joslyn, H. D., and Dring, R. P., 1989, ''Redistribution of an Inlet Temperature Distortion in an Axial Flow Turbine Stage,'' AIAA J. Propul. Power, **5**, pp. 64–71.

Unsteady Effects in Turbine Tip Clearance Flows

Anil Prasad
United Technologies Research Center,
East Hartford, CT 06108

Joel H. Wagner
Pratt & Whitney,
East Hartford, CT 06108

The present study is concerned with the unsteady flow field on the blade outer air seal segments of high-work turbines; these segments are installed between the blade tip and outer casing and are usually subjected to extreme heat loads. Time-resolved measurements of the unsteady pressure on the blade outer air seal are made in a low-speed turbine rig. The present measurements indicate the existence of a separation zone on the blade tip, which causes a vena contracta to form at the entrance of the tip gap. In addition, a careful comparison between the ensemble-averaged pressure measurement and the corresponding result from steady computation suggests that the pressure on the blade outer air seal can largely be described as being due to a steady flow (in the rotating frame) sweeping past a stationary probe. The ensemble deviation measurement indicates that unsteadiness (from one revolution to the next) is confined to the tip gap.
[S0889-504X(00)02304-7]

Introduction

Tip clearance flow in turbomachines has been studied extensively by scores of investigators since the seminal work of Rains [1]. Although Rains' work dealt primarily with compressors, it demonstrated the intricate nature of tip clearance flow and the evolution of the tip vortex. The dynamics of flow through turbine blade passages is further complicated by the existence of secondary flows, which result from flow turning. The tip clearance flow together with the passage secondary flows account for about 25 percent of the total loss incurred in a turbine stage. The general features of secondary flow in turbine cascades are described by Sieverding [2], and mechanisms by which losses are generated in turbine passages are addressed by Bindon [3]. It is generally known that the tip clearance flow is a pressure-driven flow with viscous effect being confined to the vicinity of the wall, except for the limiting case of small tip clearance where viscous effects dominate the entire tip gap region. The flow that leaks over the blade tip emerges from the tip clearance in the form of a wall jet; this jet is then subjected to the pressure gradients present in the blade passage and rolls up into a coherent vortical structure. The details of the flow through the tip gap have been documented by Moore and Tilton [4], Sjolander and Cao [5] and Bindon [3], while the effect of rotation on the tip gap flow was examined by Morphis and Bindon [6]. However, these investigations focused on the tip gap flow measured in turbine cascade environments. The question then remains whether flow features determined from cascade measurements are present in an actual turbine configuration, which is the main aspect of the present work. It is clear that the tip clearance flow in an actual turbine configuration is significantly more complex due to the presence of upstream vane wakes as well as the relative motion between the blade tip and the endwall.

The present work is focused on the flow in ''high-work'' turbines. Market demands require engines with higher power-to-weight ratios and fewer airfoils, which has motivated the design of single-stage turbines that are capable of extracting large amounts of work per stage. High-work turbine designs, which are more suitable as high-pressure turbines, are characterized by low values of flow coefficient. The higher values of blade loading present in high-work turbines results in an intensified tip clearance vortex. It then follows that there is an urgent need to moderate the flow that leaks over the blade tip in order to offset the incurred penalty in turbine performance. Although there exist several methods to moderate this tip leakage, it is nevertheless important to understand the manner in which the flow evolves through the blade tip clearance. The present study utilizes a low-speed turbine rig, the focus being on the time-resolved pressure signature measured on the curved surface of the blade outer air seal, which is installed between the blade tip and the outer casing. In engine applications, this blade outer air seal surface is often film-cooled, but this particular aspect of the flow is beyond the scope of the present experimental investigation.

A secondary motivation for investigating this aspect of the flow arises from the observation that in the engine installation, the blade outer air seal segments are particularly susceptible to heat loads, especially in the region beneath the blade tip. It is therefore of interest to examine the detailed dynamics of the tip gap flow as the blade tip sweeps over the outer air seal. The rig conditions are selected so as to nearly match the Reynolds number ($\mathrm{Re}=3.43\times10^5$ based on blade chord and blade exit relative velocity at midspan) with those present under actual engine conditions. Although engine Mach numbers cannot be simulated in the rig, the purpose of this investigation is to extract characteristic incompressible flow structures that exist in a high-work turbine geometry.

Experimental Details

The experiments were performed in the UTRC Large-Scale Rotating Rig, which has been designated LSRR-2 in previous investigations. The rig bears strong similarities to an earlier large-scale rotating rig used in the extensive turbine investigations of Joslyn and Dring [7]. Only certain relevant features specific to the new configuration are described here.

A blower mounted downstream of the turbine stage drew atmospheric air through a bell-mouth inlet, followed by passage through a series of turbulence manipulation screens and flow straighteners, over an axially positioned inlet cone and finally through the single-stage turbine model into a dump diffuser. The flow coefficient, determined from measurements made upstream of the vane leading edge, was the primary factor used to set flow conditions in the rig. This ensured that airfoil incidence angles were always at their design values and independent of the ambient temperature and pressure. In the present study, axial distances (x) are measured from the blade tip leading edge and normalized by the blade tip axial chord, b_x. The vane trailing edge is located at $x/b_x=-0.93$.

The turbine vanes, blades and blade outer air seal segments were constructed from molded plastic. The molded plastic con-

Contributed by the International Gas Turbine Institute and presented at the 45th International Gas Turbine and Aeroengine Congress and Exhibition, Munich, Germany, May 8–11, 2000. Manuscript received by the International Gas Turbine Institute February 2000. Paper No. 2000-GT-444. Review Chair: D. Ballal.

struction permits a change of turbine geometry in a turnaround time that is significantly less than that required to replace machined metal blading. The plastic airfoils also possess the advantage of being light and easy to instrument extensively. In addition, owing to a simple method of vane and blade installation, the airfoil counts can be easily altered. The nominal value of blade tip clearance was about 0.75 percent of blade span and is comparable to that found in typical engine configurations.

The vanes, blades, and blade outer air seal segments were instrumented extensively. The installed instrumentation consisted of ''steady'' and ''unsteady'' instrumentation to measure respectively the time-averaged and instantaneous flow quantities. The steady instrumentation was comprised of wall static pressure ports on the airfoils and blade outer air seal segments. Pressure ports on the vanes and blades were used to measure airfoil pressure distributions at seven different spanwise locations. The unsteady instrumentation was installed only on the curved surface of the blade outer air seal segments and consists of high-response pressure transducers. The measurement of quantities using this unsteady instrumentation was phase-locked with the rotor and the data acquired are subsequently ensemble processed in order to facilitate comparison with steady computational results generated using a flow solver described by Ni [8] and Davis et al. [9]. The flow solver utilizes a Lax-Wendroff/multiple-grid procedure to compute the solution of the Reynolds-averaged Navier–Stokes equations. The algorithm has second-order spatial accuracy and uses a central difference approach for the spatial derivatives with second- and fourth-order smoothing for stability. The no-slip condition was implemented at the adiabatic solid boundaries and the nonreflecting conditions of Giles [10] were imposed at the downstream end of the domain. The code has been extensively validated as demonstrated in the work of Ni and Bogoian [11], Ni and Sharma [12] and Davis et al. [13]. In the present case, the entire tip region was gridded and turbulence closure was achieved using the Baldwin–Lomax [14] model.

The high-response pressure transducers were calibrated subsequent to installation in the blade outer air seal segments with particular care being exercised to ensure that a frequency response of at least 9 kHz (about 15 times blade-passing frequency) was attained. Five axial locations were selected, shown in Fig. 1, at which these high-response sensors were situated relative to the blade tip footprint. The blade tip footprint refers to the area swept by the blade tip in its motion over the surface of the blade outer air seal. Phase-locked data acquisition, performed by a high-speed analog-to-digital board, was triggered by an optical pickup. The pressure transducer signal was high-pass filtered at 10 Hz to remove the mean component of pressure and any low-frequency flow unsteadiness that was present in the rig. An anti-aliasing low-pass filter with a cutoff frequency of 25 kHz was used since data acquisition was conducted at 50 kHz. Typically 100 ensembles were recorded; this was deemed more than adequate, since little difference was found between the ensemble averages obtained from 50 and 100 ensembles.

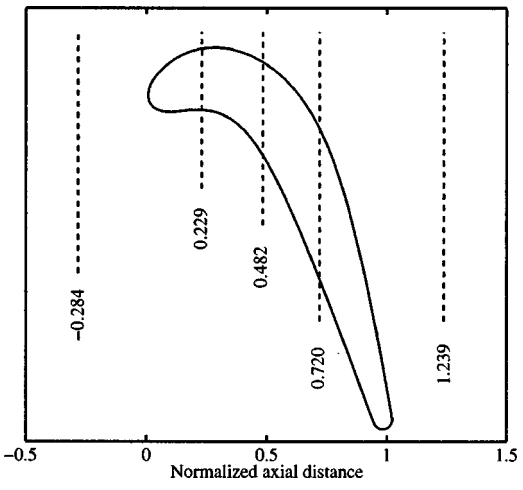

Fig. 1 Location of the high-response instrumentation. Of the five transducers installed on the blade outer air seal, three are located within the blade tip footprint and one each is installed upstream and downstream of the blade. All distances are measured from the blade tip leading edge and normalized by blade chord at the tip.

Airfoil Pressure Distributions

Wall static pressure ports were installed on the vanes and blades to measure steady-state airfoil distributions at the following spanwise locations: 2, 12.5, 25, 50, 75, 87.5, and 98 percent of the airfoil span. Each spanwise set of pressure ports was distributed over two or more airfoils; these instrumented airfoils, no two of which were adjacent, were distributed around the airfoil-pack. Experimental vane pressure distributions are presented in Fig. 2 for selected spanwise locations; the corresponding computational data are also shown. The coefficient of pressure used for the vane pressure distributions is defined as

$$C_{pV}=\frac{P_{T,\mathrm{abs}|_{\mathrm{vn}}}-P}{\frac{1}{2}\rho C_x^2}, \tag{1}$$

where C_x is the midspan axial velocity at the inlet to the turbine model.

The quantity $P_{T,\mathrm{abs}|_{\mathrm{vn}}}$ is the annulus-averaged absolute inlet total pressure; eight Kiel probes distributed uniformly around the annulus and located three vane chords upstream of the vane leading edge provided the total pressure at the inlet to the turbine. The measured pressure data from various vane airfoils situated around the annulus suggest a consistent vane-to-vane flow that is reason-

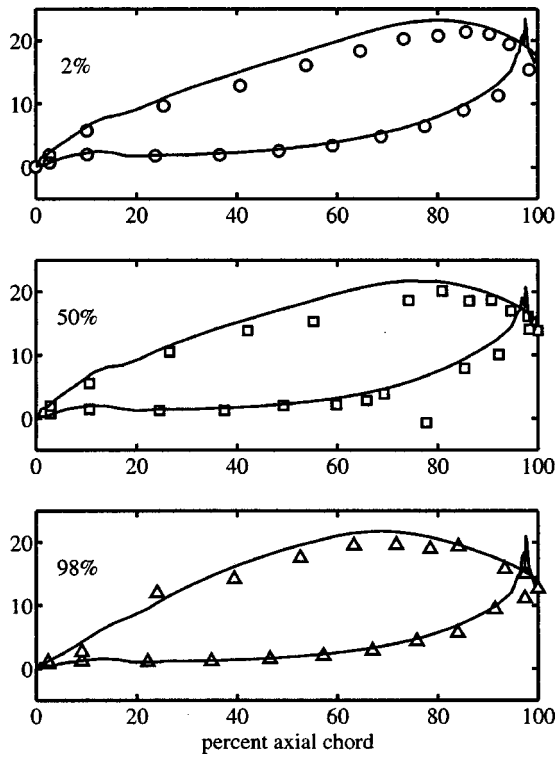

Fig. 2 Typical airfoil pressure distributions on the vane. The ordinate is the pressure coefficient defined in Eq. (1) and the spanwise locations of the distributions are indicated. The solid line is the pressure distribution determined from the computational solution.

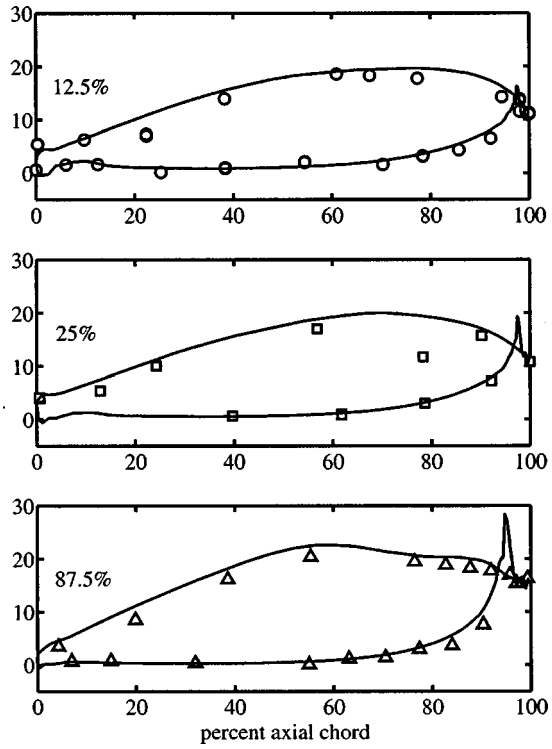

Fig. 3 Typical airfoil distributions on the blade. The ordinate is the pressure coefficient defined in Eq. (2) and the spanwise locations of the distributions are indicated. The solid line is the computational pressure distribution.

ably axisymmetric in the turbine model. The slight mismatch between the experiment and the computation on the vane suction surface is due to a small discrepancy in the vane stagger angle of the molded vanes in comparison with the design value used in the computation. The stagger angle was such that the vane throat areas were slightly larger than the design intent and is consistent with the observed variation of the vane pressure distributions between spanwise locations.

The measured blade pressure distributions, shown in Fig. 3 at three different spanwise locations, are found to compare well with the corresponding superposed results from the computation. In this case, the coefficient of pressure is defined as

$$C_{pB}=\frac{\widehat{P_{T,\mathrm{rel}}}|_{\mathrm{bl}}-P}{\frac{1}{2}\rho C_x^2} \tag{2}$$

where $\widehat{P_{T,\mathrm{rel}}}|_{\mathrm{bl}}$ is the circumferentially pitch-averaged value of the relative total pressure, deduced from traverse measurements in the vane exit plane located at $x/b_x=-0.455$. It should be noted that the relative total pressure is clearly a function of radius and this variation was accounted for in the calculation of the pressure coefficient. The pressure coefficients C_{pV} and C_{pB} are consistent since they are both based on an upstream total pressure measured in the reference frame of the relevant airfoil row.

The measured vane and blade pressure distributions were found to be very repeatable. This implies that the method of setting the rig conditions (by monitoring the flow coefficient) was sufficient to ensure that airfoil loadings were consistent between experimental runs. Moreover, the favorable correspondence between the steady-state experimental airfoil pressure distributions and those predicted by computation indicates that the experimental measurements are similar to that specified in the design. One may then compare certain experimentally measured features of the flow with the corresponding computational result, and eventually interrogate the entire computational flow field in a manner that precludes experimental measurement.

High Response Pressure Measurements on the Blade Outer Air Seal

As discussed above, the fluctuating component of the wall static pressure was measured at five axial locations on the blade outer air seal as shown in Fig. 1, three of which lie beneath the blade tip. The three measurements within the blade tip footprint are compared to results available from the steady computation; the measurements upstream and downstream of the blade tip are included for completeness and do not display any specific characteristics representative of the tip leakage flow. Use is made of the unsteady pressure coefficient,

$$p'=\frac{P-\overline{P}}{\frac{1}{2}\rho C_x^2} \tag{3}$$

where $\overline{P}$ is the time-averaged value of pressure at the axial location under consideration. Recall that the action of high-pass filtering during data acquisition directly results in a measurement of the fluctuating pressure $(P-\overline{P})$. The pressure time traces are analyzed in terms of the conventional phase-locked ensemble average and the root-mean-square deviation of the ensembles from the average.

In Fig. 4, the variation of the unsteady pressure at $x/b_x=-0.284$ upstream of the blade leading edge clearly displays potential pressure fluctuations which are present at the blade-passing frequency, denoted f_B. Figures 5 and 6 depict typical phase-locked ensemble-averaged time variations of the pressure at $x/b_x=0.229$ and $x/b_x=0.482$; both time traces display a periodicity that corresponds to the blade-passing frequency. A certain degree of blade-to-blade variation is evident in the time trace in Fig. 6. It should be noted that the blade-to-blade variations in the traces can be ascribed to rotor blade driven unsteadiness of the vane wake position, and also to blade tip clearance variations, which ranged between 0.7 and 1.0 percent of the blade span. In Fig. 7, the time variation at $x/b_x=0.720$ demonstrates a strong periodicity as well, but the blade-to-blade variations are more apparent and the time trace appears to be more complicated than that shown in Fig. 6; this is attributed to further development of the tip leakage flow. The increase in amplitude of fluctuation of p' is also to be visible for the locations within the blade tip footprint. The fluctuating pressure at $x/b_x=1.239$ downstream of the blade trailing edge, shown in Fig. 8, is comprised of what appears to be

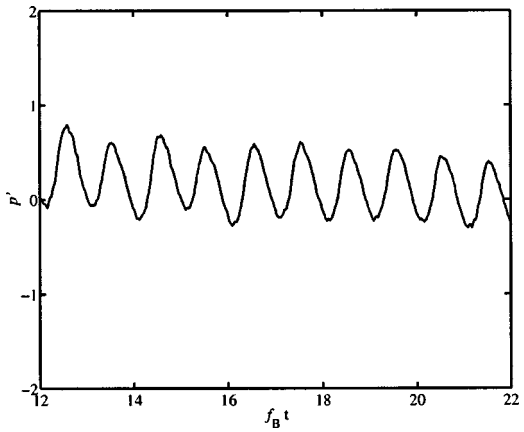

Fig. 4 Time variation of unsteady pressure at $x/b_x=-0.284$ upstream of the blade tip leading edge. The ordinate is defined in Eq. (3).

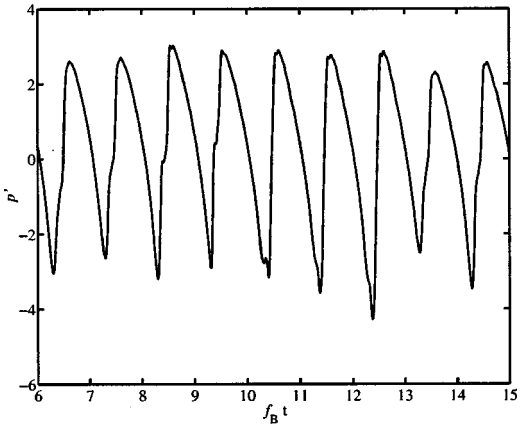

Fig. 5 Time variation of unsteady pressure at $x/b_x=0.229$ within the blade tip footprint. The ordinate is defined in Eq. (3).

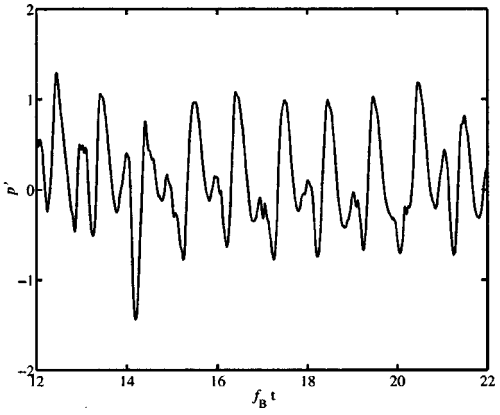

Fig. 8 Time variation of unsteady pressure at $x/b_x=1.239$ downstream of the blade tip trailing edge. The ordinate is defined in Eq. (3).

random noise superposed on an oscillation at the blade-passing frequency, suggesting that turbulence present in the blade wakes is perceptible on the blade outer air seal.

In summary, the high-response measurements demonstrate that the measured static pressure signature on the blade outer air seal (in a stationary reference frame) displays a predominant frequency of oscillation equal to the blade passing frequency. This suggests that the observed unsteadiness may be purely the result of a steady flow moving at this frequency past a stationary transducer. In order to evaluate this suggestion, the experimentally measured time traces are carefully compared with those extracted from the computational solution.

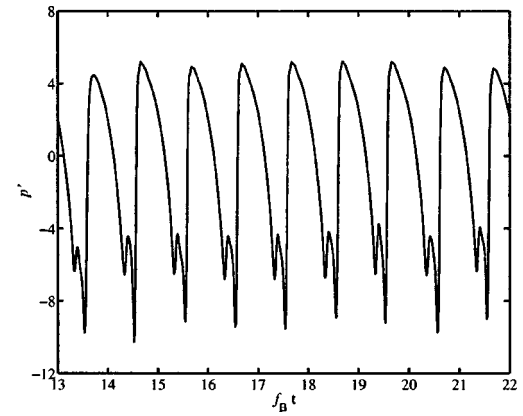

Fig. 6 Time variation of unsteady pressure at $x/b_x=0.482$ within the blade tip footprint. The ordinate is defined in Eq. (3).

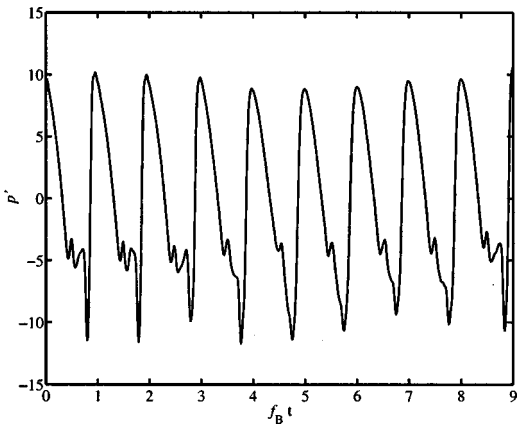

Fig. 7 Time variation of unsteady pressure at $x/b_x=0.720$ within the blade tip footprint. The ordinate is defined in Eq. (3).

Comparison of Steady Computational Results to High Response Measurements

''Time traces'' are generated from the steady computational solution by transforming the circumferential variation of pressure across the blade passage to a temporal one by using the product of the rotor angular speed and radius of curvature of the blade outer seal surface; the resulting computational pressure signature is time-shifted so as to be superimposed on the experimental measurement. The usefulness of comparing the details of the ensemble-averaged pressure measurement with the steady computation in a direct manner is twofold:

1 It is crucial in identifying not only specific flow features but also their location and extent relative to the blade tip, since the location of the latter is known more precisely from the computation than from the measurement.

2 To provide an indication of the level of unsteadiness in the tip clearance flow.

In order to make a meaningful comparison with computational results, measured signatures were selected from a blade for which the tip clearance is most similar to the nominal value (0.75 percent of blade span) used in the computation. In Figs. 9, 10, and 11, comparison is made between the ensemble-averaged measurement and the computational result at the three axial locations within the blade tip footprint, shown in Fig. 1. In each of these figures, the extent and location of the blade tip relative to the time trace are indicated by vertical lines; the vertical line to the left coincides with the blade tip suction surface and that to the right coincides with the pressure surface. Furthermore, the lower panes in the figures show the corresponding time variation of the ensemble root-mean-square deviation.

The figures indicate that the general features of the ensemble-averaged time trace compare well with those from steady computation. The agreement between the experiment and the steady computational result with regard to the amplitude of ensemble-averaged pressure fluctuations and in the overall features of the pressure variation strongly suggests that the flow in the tip region as discerned by a static pressure transducer on the blade outer air seal can largely be described as a steady flow in the reference frame of the rotor. Furthermore, the variation of the ensemble deviation (displayed in the lower panes of the figures) is found to be close to zero except for regions beneath the blade tip. This implies that the flow within the blade passage does not change significantly from one revolution to the next, and lends support for

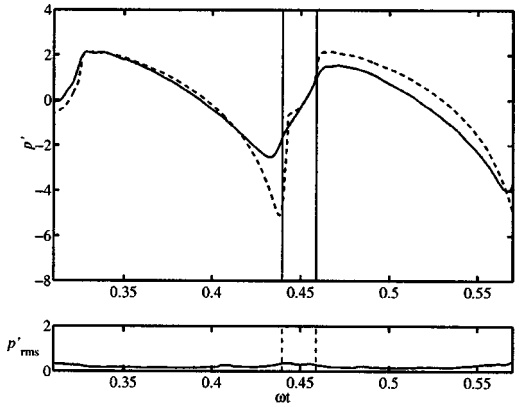

Fig. 9 Pressure signature at $x/b_x=0.229$. In the upper pane, the computational result is shown as the broken line and the ensemble-averaged measurement is shown as the solid line. The lower pane depicts the corresponding variation of the ensemble deviation. The blade tip lies between the two vertical lines indicated.

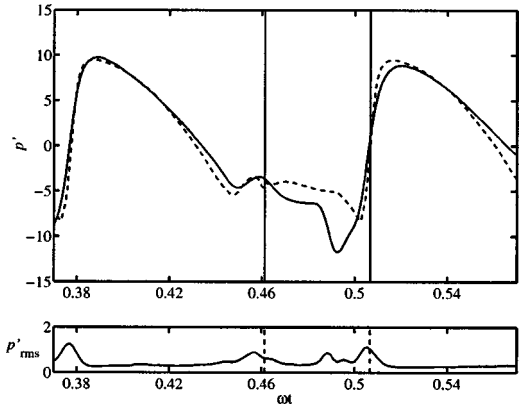

Fig. 11 Pressure signature at $x/b_x=0.720$. In the upper pane, the computational result is shown as the broken line and the ensemble-averaged measurement is shown as the solid line. The lower pane depicts the corresponding variation of the ensemble deviation to the same scale as the upper pane. The blade tip lies between the two vertical lines indicated.

the suggestion that the flow is virtually steady in the rotating reference frame, with the unsteadiness for the most part being confined to the vicinity of the tip gap.

The general features of the experimental time trace agree well with those determined from computation and an attempt is now made to extract physical features of the tip clearance flow from its pressure signature on the blade outer air seal. Contours of static pressure on the blade outer air seal from the computation are shown in Fig. 12, and include the locations of two adjacent blade tips. The presence of the tip vortex imparts a region of low pressure on the blade outer air seal near the suction surface of the airfoil, by virtue not only of the low pressure that exists at the core of a vortex but also because of the streamline curvature that is induced between the vortex and the endwall. Upon careful scrutiny, a region of lower static pressure is observed near the pressure surface of the blade tip (distinguished by the concentration of contours there), which is suggestive of a *vena contracta* in the tip gap. In order to display more clearly the extent of this *vena contracta*, streamline patterns are extracted from the computational solution. The streamline pattern on a plane parallel to the blade tip surface and slightly removed from it is shown in Fig. 13(*a*). It is observed that a reattachment line forms near the pressure surface of the blade tip, and that the flow leaves the tip gap in an almost axial direction. The streamline pattern in a plane perpendicular to the blade tip near the pressure side corner (shown in Fig. 13(*b*)) is employed to visualize the flow in the tip gap. It is clearly seen that flow separation occurs at the edge of the pressure surface with subsequent reattachment on the blade tip surface. The ensuing separation bubble results in a *vena contracta* at the inlet to the tip gap and is responsible for the region of low static pressure near the blade tip pressure surface seen in Fig. 12. Figure 13(*b*) also indicates that the separation bubble (obtained from the steady computational solution) occupies about 20 percent of the radial tip

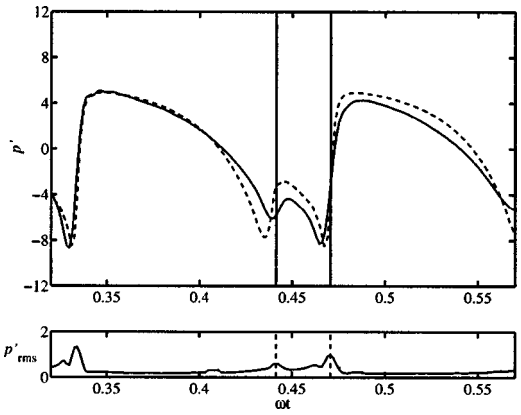

Fig. 10 Pressure signature at $x/b_x=0.482$. In the upper pane, the computational result is shown as the broken line and the ensemble-averaged measurement is shown as the solid line. The lower pane depicts the corresponding variation of the ensemble deviation to the same scale as the upper pane. The blade tip lies between the two vertical lines indicated.

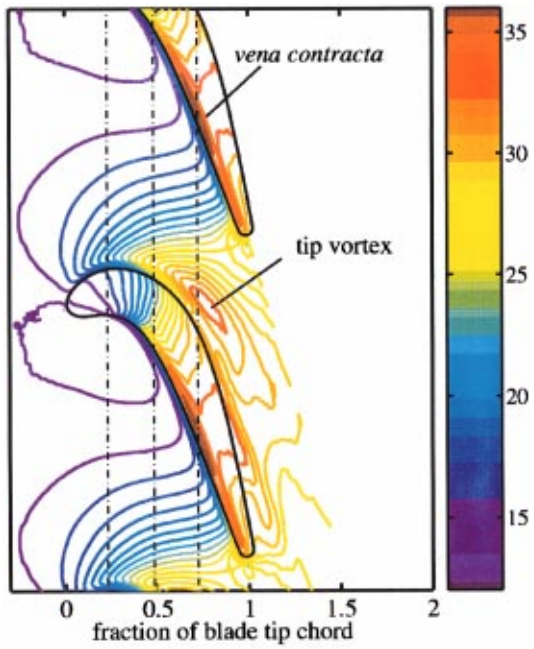

Fig. 12 Static pressure coefficient on the surface of the blade outer air seal. The static pressure coefficient is defined with respect to the turbine inlet total pressure and normalized by the turbine inlet dynamic pressure so that regions indicated by red contour levels correspond to low static pressure and those indicated by blue to higher static pressure. The high-response pressure transducers are located at the axial stations indicated by the broken lines.

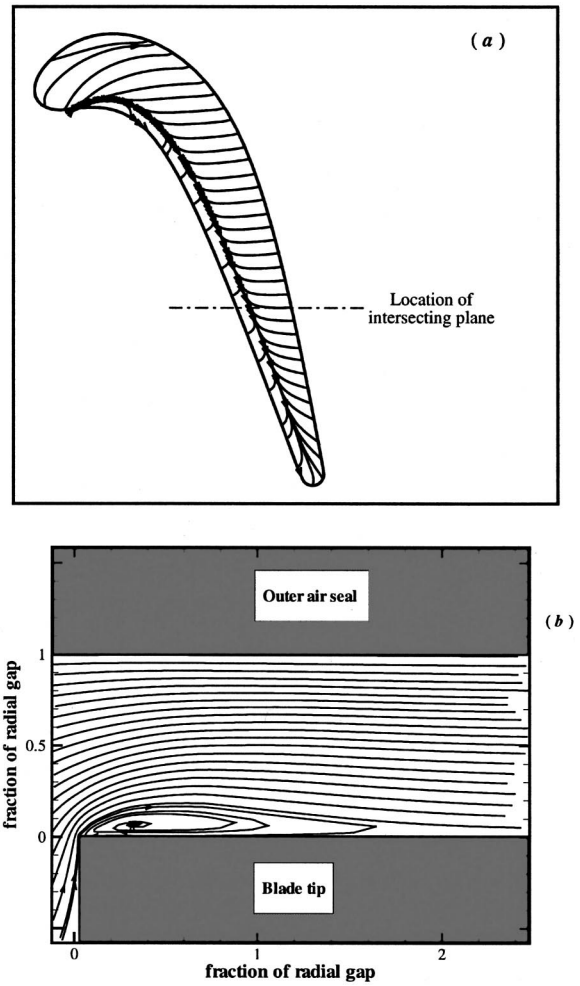

Fig. 13 The streamline pattern determined from the computational solution. (*a*) Streamline pattern on a plane that is parallel to the blade tip surface and a small distance away from it. The location of an axially aligned intersection place is indicated, at which the flow in the tip gap is examined. (*b*) Streamline pattern in the plane, showing clearly the existence of a separation bubble near the edge between the pressure surface and the blade tip.

clearance, which implies that variations in the size of this bubble may affect the instantaneous pressure measured on the blade outer air seal surface.

The contour plot in Fig. 12, when used in conjunction with computational time traces, indicates that the minimum pressure beneath the blade tip is due to the *vena contracta*; furthermore, the local minimum to the left of the blade tip suction surface corresponds to the signature of the tip vortex. If each axial location is considered in turn, it is found that for $x/b_x = 0.229$, the minimum due to the tip vortex appears to be more intense in the computation than that measured experimentally, as shown in Fig. 9.

Further downstream at $x/b_x = 0.482$ in Fig. 10, a somewhat better agreement is observed between the ensemble-averaged measurement and computation for the tip vortex minimum unsteady pressure as well as the minimum pressure due to the *vena contracta*. At this location, it is found that most of the unsteadiness is confined to the tip gap, as indicated by the variation of ensemble deviation within that region.

The pressure time signature at $x/b_x = 0.720$, where the tip vortex has developed to a significant extent, is presented in Fig. 11. The magnitude of the minimum due to the tip vortex is captured reasonably well by the computation. However, the minimum unsteady pressure due to the *vena contracta* and its location relative to the blade tip displays differences between the measurement and computation. The intensity of the experimental *vena contracta* minimum pressure is larger than that predicted from computation, and may be indicative of an unsteady effect. Khan [15] has shown that leading edge separation bubbles on compressor blades also demonstrate unsteadiness induced by the external forcing of upstream vane wakes which causes the bubble to appear larger than its time-averaged value. Furthermore, the measured location at which the *vena contracta* minimum pressure occurs seems to be further within the tip gap region than that predicted by the computation. The experimental minimum is found to occur at about 30 percent of the blade tip thickness at this location. It should be pointed out that the region of nearly constant pressure to the left of this minimum is believed to be due to the shear layer that forms in the tip gap downstream of the *vena contracta*.

Sjolander and Cao [5] and Moore and Tilton [4] have made detailed measurements on the endwall in turbine cascade environments; Sjolander and Cao also present flow visualization on the blade tip surface. Both of these investigations clearly show the existence of a *vena contracta* due to local separation at the pressure surface corner. Moreover, it can be inferred from their measurements that the location of this minimum occurs at about 25–33 percent of the local blade tip thickness, which is in reasonable agreement with the present measurements.

In summary, it can be stated that the main features of the tip clearance flow are discerned on the blade outer air seal pressure signature. Furthermore, the present work indicates that earlier measurements in cascade environments bear strong similarities to that found in a low-speed rotating rig turbine configuration. At higher Mach numbers, one would expect the static pressure field associated with the vane to have a stronger influence on the pressure sensed on the blade outer air seal surface.

Conclusions

Time-resolved measurements on the blade outer air seal are found to capture the presence of the main flow features that exist in the tip region; the signature of the tip clearance vortex as well that of a separation zone that forms on the blade tip near its pressure surface are clearly visible as local minima in the pressure signature. This separation bubble results in a *vena contracta* at the inlet to the tip gap; its existence is confirmed by examination of the steady computational flow field on the blade outer air seal. Careful comparison of phase-locked ensemble-averaged static pressure measurements with these steady computational results demonstrates that much of the flow is largely steady in the rotating frame of reference at the low Mach numbers considered here and that the bulk of unsteadiness is confined to the tip gap. These flow structures, determined in the present study using a low-speed turbine rig, are found to compare well with those determined by earlier investigators in turbine cascade environments.

Acknowledgments

The authors would like to express their gratitude to Gary Stetson and Dick Price, whose extremely helpful suggestions contributed significantly to interpretation of the measured data. Gary Winch was responsible for the maintenance of the rig and assisted in experimental data acquisition.

References

[1] Rains, D. A., 1954, ''Tip Clearance Flows in Axial Flow Compressors and Pumps,'' California Institute of Technology, Hydrodynamics and Mechanical Engineering Laboratories, Report No. 5.

[2] Sieverding, C. H., 1985, ''Recent Progress in the Understanding of Basic Aspects of Secondary Flows in Turbine Blade Passages,'' ASME J. Turbomach., **107**, pp. 248–257.

[3] Bindon, J. P., 1989, ''The Measurement and Formation of Tip Clearance Loss,'' ASME J. Turbomach., **111**, pp. 257–263.

[4] Moore, J., and Tilton, J. S., 1988, ''Tip Leakage Flow in a Linear Turbine Cascade,'' ASME J. Turbomach., **110**, pp. 18–26.
[5] Sjolander, S. A., and Cao, D., 1995, ''Measurements of the Flow in an Idealized Turbine Tip Gap,'' ASME J. Turbomach., **117**, pp. 578–584.
[6] Morphis, G., and Bindon, J. P., 1988, ''The Effects of Relative Motion, Blade Edge Radius and Gap Size on the Blade Tip Pressure Distribution in an Annular Cascade With Clearance,'' ASME Paper No. 88-GT-256.
[7] Joslyn, H. D., and Dring, R. P., 1992, ''Three-Dimensional Flow in an Axial Turbine: Part 1—Aerodynamic Mechanisms,'' ASME J. Turbomach., **114**, pp. 61–70.
[8] Ni, R. H., 1982, ''A Multiple Grid Scheme for Solving Euler Equations,'' AIAA J., **20**, pp. 1565–1571.
[9] Davis, R. L., Ni, R.-H., and Carter, J. E., 1986, ''Cascade Viscous Flow Analysis Using Navier–Stokes equations,'' AIAA Paper No. 86-0033.
[10] Giles, M. B., 1990, ''Nonreflecting Boundary Conditions for Euler Equation Calculations,'' AIAA J., **28**, pp. 2050–2058.
[11] Ni, R. H., and Bogoian, J. C., 1989, ''Predictions of 3-D Multi-stage Turbine Flow Fields Using a Multiple-Grid Euler Solver,'' AIAA Paper No. 89-0203.
[12] Ni, R. H., and Sharma, O. P., 1990, ''Using a 3-D Euler Flow Simulation to Assess Effects of Periodic Unsteady Flow Through Turbines,'' AIAA Paper No. 90-2357.
[13] Davis, R. L., Shang, T., Buteau, J., and Ni, R.-H., 1996, ''Prediction of 3-D Unsteady Flow in Multi-stage Turbomachinery Using an Implicit Dual Time-Step Approach,'' AIAA Paper No. 96-2565.
[14] Baldwin, B. S., and Lomax, H., 1978, ''Thin Layer Approximation and Algebraic Model for Separated Turbulent Flows,'' AIAA Paper No. 78-257.
[15] Khan, R., 2000, ''Boundary Layers on Compressor Blades,'' Ph.D. dissertation (in preparation), Whittle Laboratory, University of Cambridge, Cambridge, England.

Numerical and Experimental Investigation of Unsteady Flow Interaction in a Low-Pressure Multistage Turbine

Wolfgang Höhn
email: wolfgang.hoehn@muc.mtu.de

Klaus Heinig

MTU Motoren- und Turbinen-Union,
München GmbH,
Department of Acoustics and Aeroelasticity,
Dachauer Straße 665,
D-80995 München, Germany

This paper presents results of unsteady viscous flow calculations and corresponding cold flow experiments of a three-stage low-pressure turbine. The investigation emphasizes the study of unsteady flow interaction. A time-accurate Reynolds-averaged Navier–Stokes solver is applied for the computations. Turbulence is modeled using the Spalart–Allmaras one-equation turbulence model and the influence of modern transition models on the unsteady flow predictions is investigated. The integration of the governing equations in time is performed with a four-stage Runge–Kutta scheme, which is accelerated by a two-grid method in the viscous boundary layer around the blades. At the inlet and outlet, nonreflecting boundary conditions are used. The quasi-three-dimensional calculations are conducted on a stream surface around midspan, allowing a varying stream tube thickness. In order to study the unsteady flow interaction, a three-stage low-pressure turbine rig of a modern commercial jet engine is built up. In addition to the design point, the Reynolds number, the wheel speed, and the pressure ratio are also varied in the tests. The numerical method is able to capture important unsteady effects found in the experiments, i.e., unsteady transition as well as the blade row interaction. In particular, the flow field with respect to time-averaged and unsteady quantities such as surface pressure, entropy, and skin friction is compared with the experiments conducted in the cold air flow test rig. [S0889-504X(00)02004-3]

Introduction

Many research activities are presently being conducted in the field of unsteady blade row interaction in axial turbomachines, e.g., [1–4].

The aim of this paper is to present a computational method [5] that quantitatively predicts important unsteady transition effects in a three-stage low-pressure turbine. The Abu-Ghannam/Shaw [6] model is used to predict the onset of transition. It is one of the most widely used models in both external and internal flow simulations [7]. A modification of the Abu-Ghannam/Shaw model conducted by Drela [8] has been implemented into the Navier–Stokes solver [9]. Other approaches found in the literature use either algebraic turbulence models in conjunction with the intermittency approach [10] or two-equation models, especially the low-Reynolds-number $k-\varepsilon$ models [11]. Eulitz and Engel [5] and Ekaterinaris [12] demonstrated for turbomachinery and airfoil applications that the one-equation turbulence model of Spalart and Allmaras [13] is a good compromise between turbulent prediction qualities and computational costs.

The present work is conducted within the German Engine-3E turbine technology program [14]. The final goal of this project is to understand the underlying mechanisms of turbine stator clocking, which denotes the interaction of an upstream stator wake with the next stator, which has the same blade count. Although several studies on turbine clocking have been presented [15,16], the phenomenon is not fully understood yet.

This paper presents a classification of unsteady blade row interaction effects followed by the description of the experimental setup. Thereafter, the computational method used for steady and unsteady computations is explained. The latter needs a steady-state initial solution for the time-accurate computation of the unsteady Reynolds-averaged Navier–Stokes equations. Moreover, the turbulence and transition model are discussed. Finally, the results of the steady-state, time-averaged unsteady and unsteady calculations are compared with experiments conducted in a low-pressure turbine cold flow turbine test rig.

Contributed by the International Gas Turbine Institute and presented at the 45th International Gas Turbine and Aeroengine Congress and Exhibition, Munich, Germany, May 8–11, 2000. Manuscript received by the International Gas Turbine Institute February 2000. Paper No. 2000-GT-437. Review Chair: D. Ballal.

Classification of Effects

An attempt is made to classify the effects in multistage turbomachines that are due to the wake generated by an upstream blade row, i.e., a stator, according to different mechanisms working on the next stator blade row.

Wake-Generating Blade Row. The flow leaving a stator blade row consists of wakes that extend downstream of each individual blade profile. The shape of these wakes differs depending on whether the vorticity in the wake is continuously or discontinuously distributed. A discontinuous distribution of vorticity may be self-induced (vortex shedding) or caused by external effects such as pressure disturbances; see Dorney and Sondak [17]. In both cases, there is interaction between the wake and the downstream blade rows, although in a different manner, and therefore the dissipation process linked to the shear stress takes a different course.

Transformation Blade Row. The first downstream rotor blade row intercepts the continuously shaped wake from the upstream stator as a result of its relative movement and deforms, i.e., twists, upsets, and stretches, the segments of the distributed wake vorticity. During interception, the wake comes into direct contact with the boundary layer of the rotor blade row. This causes velocity disturbances, velocity gradient disturbances, or vorticity disturbances at the edge of the boundary layer; see Valkov and Tan [18] and Platzer and Tuncer [19], which in turn affect the losses in the laminar, transition, and turbulent regions of the boundary layer during convection. The equidistant arrangement of profiles in the wake-generating blade row leads to a periodic wake

at the transformation blade row whose vorticity, as a result, is no longer continuously distributed. Simultaneously, the interception process produces a double vortex, see Fig. 1, which will interact with all downstream blade rows.

Interaction Blade Row. The inflow conditions of the interaction blade row, i.e., a stator, are the discontinuously shaped wakes and the double vortex with boundary layer material from the wake-generating blade row, which convects between two adjacent continuous transformation blade (rotor) wakes.

Experimental Setup

The investigations are performed on a three-stage cold-air LPT rig with various operating conditions and geometry; see Heisler [20]. All three stators carry the same number of vanes, which can be precisely adjusted circumferentially; see Fig. 2. In addition to the Reynolds number, the speed and the pressure ratio can be varied.

Instrumentation and Measurements. The test rig is instrumented in order to study the physics of stator clocking. The total isentropic efficiency is determined by measurements of the mass-weighted representative total pressure and total temperature at the turbine inlet and outlet, where mixing losses are not taken into account. Since the inflow conditions to the downstream stator of each clocking pair vary for the circumferential positions, comprehensive unsteady instrumentation is provided at midspan. The leading edges are fitted with unsteady total pressure transducers, the positions near the transition region with unsteady static pressure transducers, and the suction sides of the profiles with surface mounted hot-film sensors. Static pressure holes are used to measure the time-averaged pressure on the stator blades at midspan.

Computational Method

The unsteady flow equations, i.e., the Reynolds-averaged, compressible Navier–Stokes equations, are solved along the three-dimensional stream-tube with varying radial thickness and radius [5]. The convective fluxes are discretized using Roe's upwind scheme [21] in combination with van Leer's MUSCL approach [22] to obtain second-order accuracy in space. The viscous terms are discretized with central differences. At the solid blade wall the no-slip condition is applied. At the streamtube boundaries toward the tip and the hub, the kinematic boundary condition is applied. The steady-state equations are marched in time using an implicit scheme [9]. The unsteady flow equations are solved using a four-stage Runge–Kutta scheme in combination with He's time accurate two-grid method [23]. For the steady-state solution at the inlet and outlet boundaries of the computational domain, quasi-three dimensional nonreflecting boundary conditions are applied [24]. For the unsteady computations nonreflecting boundary conditions according to Acton and Cargill [25] are used. At the rotor–stator interface the sheared cell technique [26] is employed for the unsteady computations, whereas the circumferentially averaged characteristic variables are exchanged at the steady rotor–stator interface.

The multiblock solver is parallelized based on domain composition and message passing using communication routines of the MPI library. In order to achieve good parallel performance and efficiency, explicit or block local solution strategies are implemented [27].

Turbulence and Transition Modeling. In order to close the Reynolds-averaged equations, the Boussinesq hypothesis is used [28] together with the Spalart and Allmaras one equation turbulence model [13].

Transition onset is determined from a correlation as proposed by Drela [8] for his viscous/inviscid interaction code MISES, which is a modification of the well-known Abu-Ghanam/Shaw [6] criterion. In the laminar part of the boundary layer the transport equation of the one equation turbulence model is solved without turbulent production. When the Drela correlation signals the start of transition, the production term is switched on.

Configuration and Computational Mesh. A low-pressure model turbine with three stages, as shown in Fig. 3, is considered for this study. A blade count ratio of 1 has been assumed in order to limit the computational costs. The rotor blades were geometrically scaled to a blade number of 70, i.e., the number of stator blades, in order to keep loading of the blades the same as in the unscaled case. Moreover, the axial gaps between the blades in the calculations are kept the same as in the experiments. The Mach number at the entry of the turbine is 0.45 and the total pressure ratio is approximately 3. The Reynolds number based on the exit flow and the chord length of the first vane is 90,000. For the turbulent calculation using the transition model, the turbulence level is 1.5 percent at the inlet of the computational mesh. The computational mesh consists of O-blocks around the airfoils and three H-blocks in the blade passage with a total of 18,000 mesh cells for each blade passage. The $y+$ values of the first mesh points off the surface are below 1.5 in order to resolve the turbulent boundary layer accurately and 15 to 20 mesh points are in the boundary layer in the aft section of the blades.

Steady-State Calculation. The steady-state multistage calculation is initialized by linear interpolation of the calculated flow angle and Mach number and pressure for each blade by the values obtained from the S1–S2 design procedure used at MTU. The Reynolds-averaged Navier–Stokes equations are marched in time by a fully implicit time integration scheme [9]. For the fully turbulent calculations approximately 10,000 time steps are needed to achieve full convergence using a CFL number of 80. For the calculations using the transition correlation, the first 1000 time steps are used to develop the turbulent boundary layer and then approximately 10,000 time steps are required to achieve a converged steady-state solution. At the stator–rotor interface, passage-averaged flow quantities are exchanged and the wakes are mixed out at the blade row boundaries. The steady-state calculation is used as initial solution for the unsteady time accurate calculations.

Time-Accurate Calculation. When starting the unsteady cal-

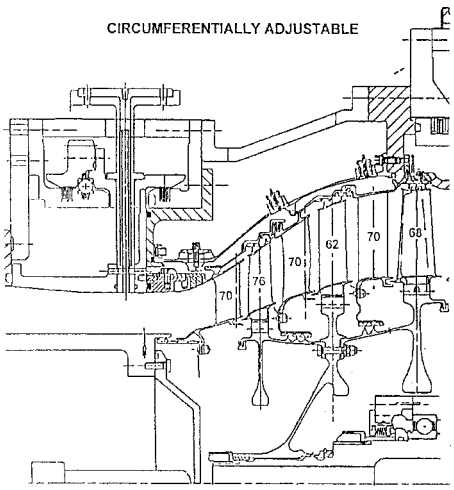

Fig. 2 Experimental setup

Fig. 3 Computational mesh

culation with the steady-state result as initial solution, a time-periodic solution does not evolve until all wakes are convected through the computational domain. Using the two-grid method, the time step can be set to CFL number of 7.0 in the O-grid, where the smallest cells are found in the viscous boundary layer. Eighteen blade passing periods are computed to obtain a periodic unsteady flow field.

Results

Steady-State Results. In order to study the basic performance of the transition model, steady-state calculations are performed for the third stator alone. The boundary conditions for the numerical computations are taken from the S1–S2 design method used at MTU.

Figure 4 shows the surface pressure distribution at midspan normalized with the total inlet pressure. Good agreement between the time-averaged unsteady measurements and the steady calculation is found in general. Close to the trailing edge on the suction side of the blade, the laminar flow separates, transition occurs, and the turbulent flow reattaches. The numerical predictions including the transition model show excellent agreement with the experiments. The transition model correctly predicts the transition of the laminar separated flow to turbulent flow, which can be seen in the surface pressure distribution close to the trailing edge.

Time-Averaged Unsteady Results. Figures 5, 6, and 7 show the time-averaged surface pressure distribution for the experiments and the computations conducted using the fully turbulent Navier–Stokes equations and the simulation incorporating the transition model for the stators of the low pressure rig at midspan. In general, good agreement with the experiments is found, which confirms the applicability of the quasi-three-dimensional method toward the investigated problem. The steady-state results shown in Fig. 4 give better agreement with the experiments because the computations are performed for the third stator alone with the specified boundary conditions according to the experiments before and after the blade. It cannot be expected that the computations for the full rig at midspan, where the boundary conditions are specified according to the experiment in front of the first stator and after the last rotor, give the same accuracy for the numerical predictions. The fully turbulent calculations show no separation on the suction side of the blade for either stator one or stator three. On the other hand, the calculations considering transition give separation for stator one and three at these points. This is indicated by the pressure distribution obtained in the calculation with the transition model close to the trailing edge of stator 1 on the suction side. However, the pressure distribution of stator 3 does not indicate a separation in the calculations with the transition

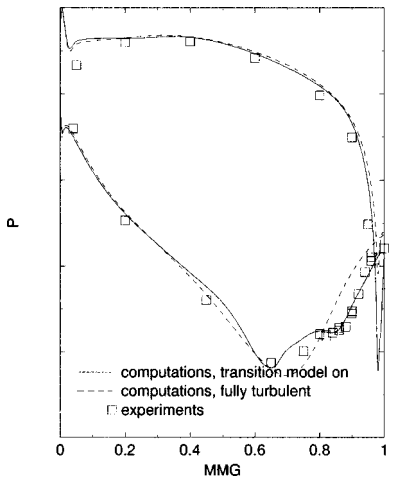

Fig. 4 Steady-state surface pressure distribution, Stator 3

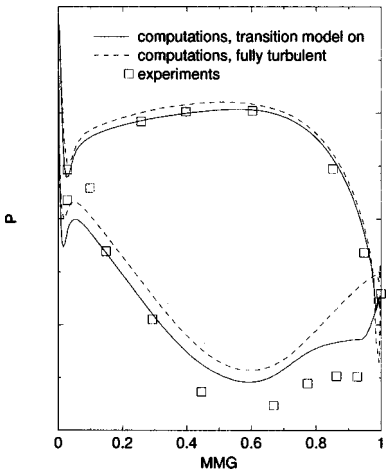

Fig. 5 Time-averaged surface pressure distribution, Stator 3

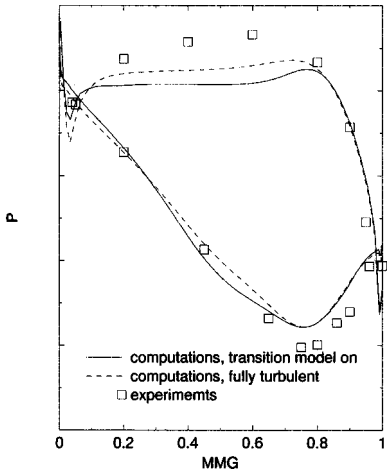

Fig. 6 Time-averaged surface pressure distribution, Stator 2

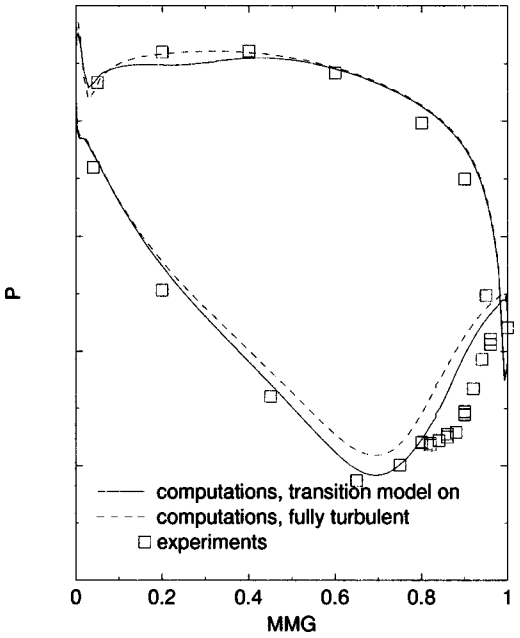

Fig. 7 Time-averaged surface pressure distribution, Stator 3

Fig. 1 Transformation blade row

model as shown in Fig. 4 for the steady calculations. This is probably due to a flat separation bubble in the numerical prediction and will be investigated in future studies. It is expected that transition from laminar to turbulent flow in the separated region will have a considerable influence on the profile loss as well as the overall efficiency predicted by the numerical method. In the other regions, good agreement is found between the fully turbulent calculations and the computations with the transition model. The higher back pressure close to the trailing edge at stator 3 in the numerical results has to be investigated in future studies. The newest results show better agreement between the experiments and the numerical predictions for the suction side of stator one and the pressure side of stator two by improving the streamsurface obtained by the S2 procedure, which is used for the quasi-three-dimensional computations.

Unsteady Results. On the rearward suction-side as well as the forward pressure side of rotor 1, the boundary layer shows a clear tendency to transition induced by flow separation in the calculations using the transition model. However, the fully turbulent calculation does not predict the separation on the suction side of this blade. Due to the interaction of the boundary layer and the wake of the upstream stator, the vortex leaving the rotor has a different shape in the two different calculations. This circumstance is obvious in Figs. 8–11, which show the instantaneous flow fields for the entropy of the whole configuration under investigation for the fully turbulent calculation. Comparing these figures at the same entropy contour levels with the calculations using the transition model at the exit of stator 1, i.e., Figs. 12–15, shows the different vortex structure of the upstream stator wake leaving the rotor 1. These wakes are interacting then with stator 2 and its boundary layer. Consequently, the interaction of the wakes of sta-

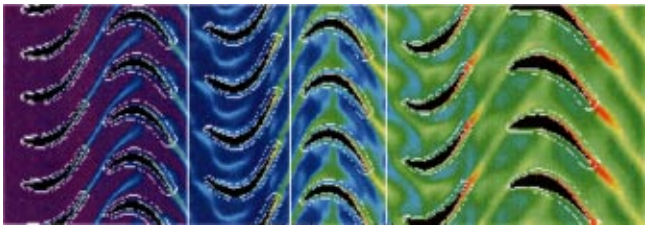

Fig. 8 Entropy, $t=t_0$, fully turbulent

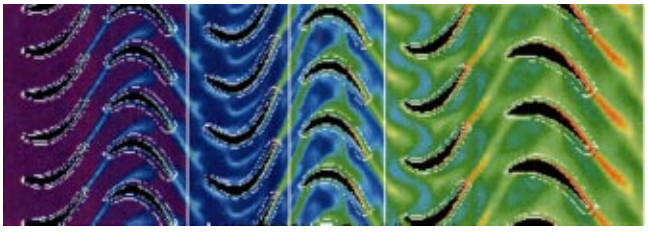

Fig. 9 Entropy, $t=T/4$, fully turbulent

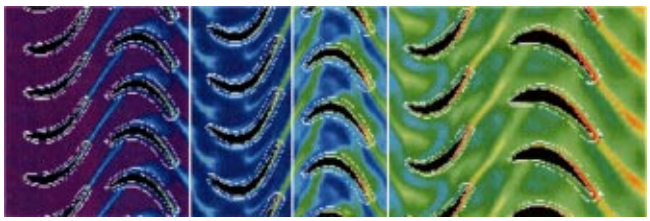

Fig. 10 Entropy, $t=T/2$, fully turbulent

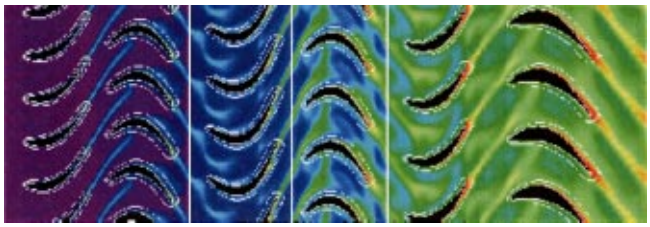

Fig. 11 Entropy, $t=3T/4$, fully turbulent

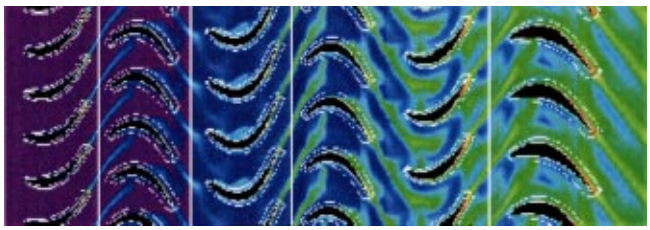

Fig. 12 Entropy, $t=t_0$, transition model on

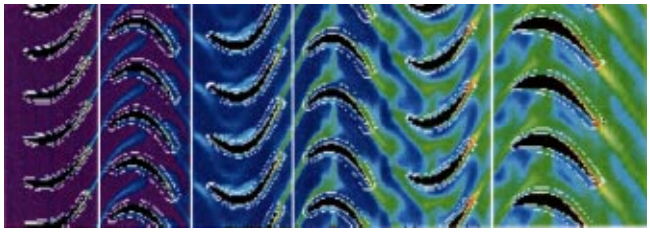

Fig. 13 Entropy, $t=T/4$, transition model on

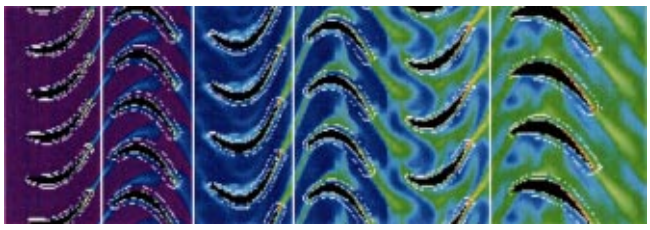

Fig. 14 Entropy, $t=T/2$, transition model on

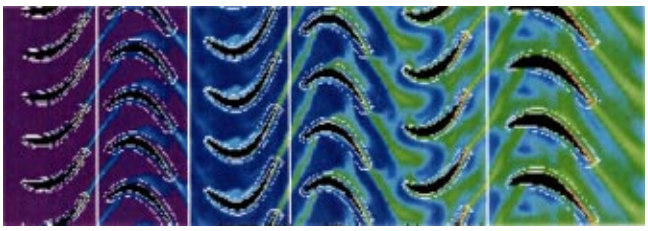

Fig. 15 Entropy, $t=3T/4$, transition model on

tor 1 and stator 2, which is commonly denoted as clocking, seems to be dependent on the modeling of transition. As the wake of stator 1 moves further, it shows some tendency to merge with the wake of stator 2. A very similar interaction process takes place with the next three blade rows, i.e., stator 2, rotor 2, and stator 3. However, due to the interaction of the wakes with the upstream stream wakes, it is more difficult to identify clearly the origin of each wake.

Figures 16 and 17 show the space–time diagram of the wall shear stress on the suction side of the blade for the computation without (fully turbulent) and with transition for five blade passing periods. Figure 16 shows that the flow does not separate for the fully turbulent computations. The calculations give 5 N/m^2 as minimum value for the wall shear stress.

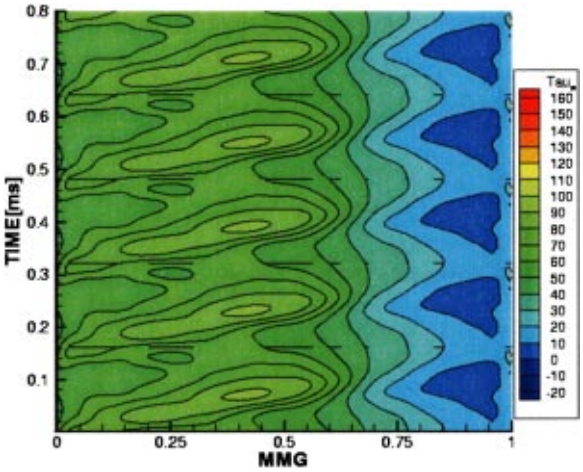

Fig. 16 Wall shear stress, suction side of Stator 3, transition model off

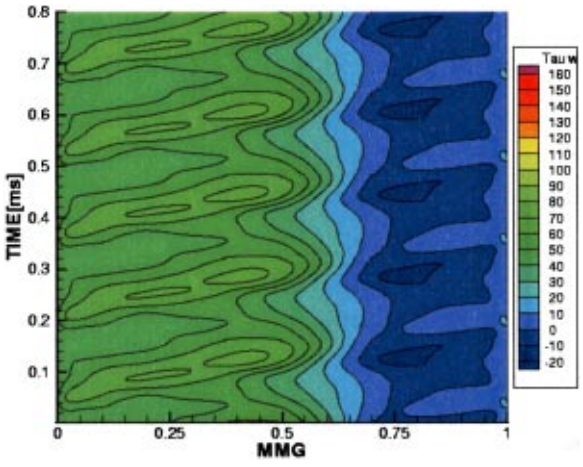

Fig. 17 Wall shear stress, suction side of Stator 3, transition model on

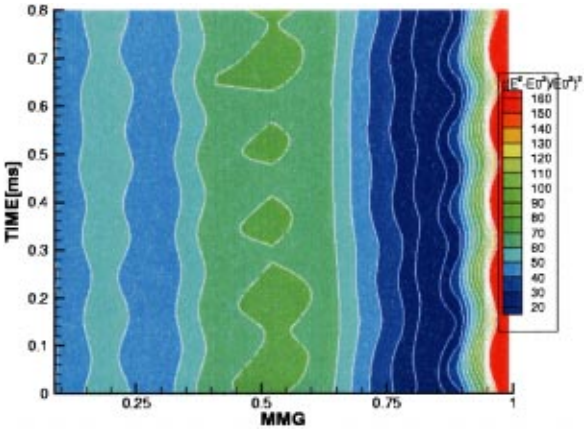

Fig. 18 Quasi wall shear stress, suction side of Stator 3, experiments

On the other hand, the computations with the transition model, see Fig. 17, show separated flow for 0.7 to 0.95 of the meridional coordinate (MMG) and 80 percent of the blade passing time of 0.16 ms. The experimental hot-film results are presented as quasi wall shear stress [29] and are shown in Fig. 18 as a space–time diagram. The figure indicates very low quasi wall shear stress between 0.75 and 0.95 of the meridional coordinate in quite good agreement with the numerical results given in Fig. 17. Since the hot-film measurement technique is not able to detect negative wall shear stresses, flow visualization pictures are used to detect that the flow is separated in this area. The maximum quasi wall shear stress is measured at about 0.51 of the meriodional coordinate against 0.42 for the computations with the transition model. In addition, the wake-induced path can be seen clearly in the experimental and numerical results.

Conclusions

A time-accurate Navier–Stokes solver is applied toward the unsteady flow interaction in a three-stage low-pressure turbine. A modern one-equation turbulence model coupled with a variant of an AGS transition model is used to predict the transition on the blade surface.

The steady and unsteady time-averaged results show, in general, good agreement with the experiments for the surface pressure distribution at midspan. However, efforts are made to achieve better agreement between the experiments and the computations by improving the S2 solution obtained by a throughflow method.

The unsteady interaction of the wake of an upstream stator with the following rotor and the next stator is influenced by the correct prediction of the separated flow on the rotor. The space–time diagrams show that a transition model is needed to predict the state of the boundary layer correctly, i.e., the fully turbulent calculation fails to calculate the boundary layer separation on the suction side of stator three.

Consequently, the influence of a modern transition model on the prediction of the efficiency for stator clocking is presently being investigated.

Acknowledgments

The authors would like to thank Mr. A. Heisler, Mr. F. Lippl, and Mr. H. Kneißl from the MTU test team who carried out the comprehensive test program, Mr. K. Rieger and Mr. B. Patzer for the excellent measurements with unsteady pressure and surface-mounted hot-film sensors, Mr. U. Wiech for the ensemble averaging and data reduction, and Dr. A. Fiala for many useful discussions about the analysis of the measurements. Dr. K. Engel, Mr. F. Eulitz Mr. B. Grüber, and Mr. G. Kahl deserve thanks for assist-

ing in the first steps in performing multiple stage calculations with the present method at MTU. The work is part of the ''Engine 3E 2010 Program'' financed by the German Ministry of Economics and Technology under the contract No. 20T9537. The financial support is gratefully acknowledged.

Nomenclature

t = time variable
P = pressure
T = blade passing period
MMG = meridional coordinate
$((E^2-E_0^2)/E_0^2)^3$ = quasi wall shear stress
τ_w = wall shear stress

Subscripts

e = entrance flow quantity
s = static flow quantity
t = stagnation flow quantity
v = vane

References

[1] Halstead, D. E., Wisler, D. C., Okiishi, T. H., Walker, G. J., Hodson, H. P., and Shin, H.-W., 1997, ''Boundary Layer Development in Axial Compressors and Turbines: Part 1-4,'' ASME J. Turbomach., **119**, pp. 114–127; ibid. **119**, pp. 225–237; ibid. **119**, pp. 426–444; ibid. **119**, pp. 128–139.
[2] Hodson, H. P., 1998, ''Blade Row Interference Effects in Axial Turbomachinery Stages: Blade Row Interactions in Low Pressure Turbines,'' VKI Lecture, Brussels, Feb.
[3] Fan, S., and Lakshminarayana, B., 1996, ''Computation and Simulation of Wake-Generated Unsteady Pressure and Boundary Layers in Cascades, Parts 1 & 2,'' ASME J. Turbomach., **118**, pp. 96–121.
[4] Sharma, O., 1998, ''Blade Row Interference Effects in Axial Turbomachinery Stages,'' VKI Lecture, Brussels, Feb.
[5] Eulitz, F., and Engel, K., 1998, ''Numerical Investigation of Wake Interaction in a Low Pressure Turbine,'' ASME Paper No. 98-GT-563.
[6] Abu-Ghannam, B., and Shaw, R., 1980, ''Natural Transition of Boundary Layers: The Effects of Turbulence, Pressure Gradient and Flow History,'' J. Mech. Eng. Sci., **22**, pp. 213–228.
[7] Coupland, J., 1995, ''Transition Modelling for Turbomachinery Flows,'' ER-COFTAC Bulletin, **24**, pp. 5–8.
[8] Drela, M., 1995, ''MISES Implementation of Modified Abu-Ghannam/Shaw Transition Criterion,'' MIT Aero-Astro, Feb.
[9] Eulitz, F., Engel, K., Nürnberger, D., Schmidt, S., and Yamamoto, K., 1998, ''On Recent Advances of a Massively-Parallel Time-Accurate Navier–Stokes Solver for Unsteady Turbomachinery Flow,'' Proc. ECCOMAS. Athens.
[10] Narasimha, R., 1990, ''Modelling the Transitional Boundary Layer,'' NASA CR-187487; ICASE Report No. 90-90.
[11] Savill, A. M., 1994, ''Transition Modelling for Turbomachinery,'' *Proc. ER-COFTAC Turbomachinery Special Interest Group Seminar and Workshop on 3D Turbomachinery Flow Prediction*, Part 2.
[12] Ekaterinaris, J. A., 1995, ''Numerical Investigation of Dynamic Stall of an Oscillating Wing,'' AIAA J., **33**, No. 10, pp. 1803–1808.
[13] Spalart, P., and Allmaras, S., 1992, ''A One-Equation Turbulence Model for Aerodynamic Flows,'' AIAA Paper No. 92-0439.
[14] Niehuis R., 1997, ''Luftfahrtforschung und -technologie Engine 3E 2010 Programm für zivile MTU-Antriebsprojekte, Turbinen für Triebwerke der unteren Schubklasse Phase A,'' Daimler-Benz Aerospace MTU München.
[15] Dorney, D. J., Sondak, D. L., Ciszmas, P. G. A., Saren, V. E., and Savin, N. M., 1999, ''Full-Annulus Simulations of Airfoil Clocking in a 1 1/2 Stage Axial Compressor,'' ASME Paper No. 98-GT-23.
[16] Huber, F. W., Johnson, P. D., Sharma, O. P., Staubach, J. B., and Gaddis, S. W., 1996, ''Performance Improvement Through Indexing of Turbine Airfoils: Part 1—Experimental Investigation,'' ASME J. Turbomach., **118**, pp. 630–635.
[17] Sondak, D., and Dorney, D. J., 1999, ''Simulation of Vortex Shedding in a Turbine Stage,'' ASME J. Turbomach., **121**, pp. 428–435.
[18] Valkov, T. V., and Tan, C. S., 1999, ''Effect of Upstream Rotor Vortical Disturbances on the Time-Average Performance of Axial Compressor Stators: Part 1—Framework of Technical Approach and Wake-Stator Blade Interactions; Part 2—Rotor Tip Vortex/Streamwise Vortex-Stator Blade Interactions,'' ASME J. Turbomach., **121**, pp. 377–397.
[19] Platzer, M. F., and Tuncer, I. H., 1995, ''Analysis of Unsteady Airfoil Interference Effects Using a Zonal Navier–Stokes Solver,'' AIAA-95-0307.
[20] Heisler, L., 1999, ''E3E, NDT-Rig 448 Bau 03 vorläufige Versuchsergebnisse,'' 27.09.99, MTU, München.
[21] Roe, P., 1981, ''Approximative Riemann Solvers, Parameter Vector and Differences Schemes,'' J. Comput. Phys., **43**, pp. 357–372.
[22] van Leer, B., 1979, ''Towards the Ultimate Conservation Difference Scheme, A Second Order Sequel to Godunov's Method,'' J. Comput. Phys., **32**, pp. 101–136.
[23] He, L., 1993, ''New Two-Grid Acceleration Method for Unsteady Navier–Stokes Calculations,'' AIAA J. Propul. Power, **9**, p. 272.
[24] Saxer, A. P., and Giles, M., 1993, ''Quasi Three Dimensional Nonreflecting Boundary Conditions for Euler Equations Calculations,'' AIAA J. Propul. Power, **9**, No. 2, pp. 263–271.
[25] Acton, E., and Cargill, M., 1988, ''Non-Reflecting Boundary Conditions for Computations of Unsteady Turbomachinery Flow,'' *Proc. 4th Int. Symp. Unsteady Aerodynamics and Aeroelasticity of Turbomachines and Propellers*, pp. 211–228.
[26] Giles, M., 1991, ''UNSFLO: A Numerical Method for the Calculation of Unsteady Flow in Turbomachinery,'' GTL-Report 205, MIT-GTL.
[27] Engel, K., Eulitz, F., Pokorny, S., and Faden, M., 1996, ''Validation of Different TVD-Schemes for the Calculation of the Unsteady Turbomachinery Flow,'' 14. ICNMFD, Bangalore, India.
[28] Boussinesq, T. V., 1877, Mem. Pres, Acad. Sci., 3rd ed. Paris XXIII, p. 46.
[29] Hodson, H. P., Huntsmann, L., and Steele, A. B., 1994, ''An Investigation of Boundary Layer Development in a Mutlistage LP Turbine,'' ASME J. Turbomach., **116**, pp. 375–383.

Separation Bubbles Under Steady and Periodic-Unsteady Main Flow Conditions

Weiliang Lou[1]
e-mail: Weiliang.Lou@muc.mtu.de

Jean Hourmouziadis

Jet Propulsion Laboratory,
Aerospace Institute F1,
Berlin University of Technology,
Marchstr. 12,
D-10587 Berlin, Germany

Based on an experimental investigation carried out in a low-speed test facility at the Berlin University of Technology, this paper describes the formation of separation bubbles under steady and periodic-unsteady main flow conditions. The aim of the investigation was to understand the mechanism of separation, transition, and reattachment, and the effect of main flow unsteadiness on it. Separation bubbles for various main flow conditions were generated over a large flat plate, which experienced a similar pressure distribution to that on the suction surface of blades in turbomachines. The pressure distribution was generated by a contoured wall opposite the plate. Aimed at separating the effect of the velocity and the turbulence wake, this paper considers only the influence of the velocity wake. To this effect, a rotating flap was mounted downstream of the test section to produce periodic oscillations of the main flow. The overall flow field under steady main flow conditions was obtained by hot-wire measurements. Pressure taps were used to measure the pressure distribution over the plate. The Reynolds number effects were determined and compared to the measurement results in the literature. Results for periodic-unsteady separation bubbles are shown using different Strouhal numbers, oscillation amplitudes, and Reynolds numbers. Ensemble-averaged mean velocity profiles and the ensemble-averaged rms velocity profiles are used to demonstrate the development of the periodic boundary layer. Time–space diagrams are plotted to show the development of the periodic-unsteady boundary layers. The characteristic instability frequencies in the free shear layer are identified. The impact of the major parameters, Strouhal number and amplitude, on the bubble formation are discussed. [S0889-504X(00)01204-6]

Introduction

In turbomachines and particularly in aircraft engines, the Reynolds numbers that characterize the development of boundary layers are relatively low. A large part of the blade surface is often covered by laminar and transitional flow. The determination of the transition zone is a very important task in the design process.

The designer of compressors and turbines for aircraft engines is required to achieve two targets simultaneously: high efficiency and low weight. High efficiency should be available under different operating conditions. Figure 1 demonstrates the evolution of losses with Reynolds number of a low-pressure turbine cascade. At high Reynolds number (a) transition occurs far upstream and turbulent separation near the trailing edge produces mixing losses (3), which are added to the shear layer losses (2). With decreasing Reynolds number the turbulent separation disappears (b), transition moves downstream beyond the laminar separation point, and a separation bubble (c) appears on the suction surface. In this region loss generation takes place in the wall shear layers and the wake of trailing edge only. Further down the Reynolds scale, losses increase dramatically (d). Transition has now moved so far downstream that the turbulent free shear layer cannot reattach before the trailing edge. The largest part of the losses now is produced by the mixing out of the separation in the wake (1). The extension of this separation away from the profile wall increases rapidly with decreasing Reynolds number, because transition is shifted downstream. It has a maximum when the transition point in the free shear layer reaches the plane of the trailing edge. Beyond that point (e) rising losses are caused by the growing free shear layer thickness with falling Reynolds number. Laminar separation that does not reattach is the case of the so-called strong viscous/inviscid interaction or separation bubble bursting.

There appears to be a wide Reynolds number range with low losses. The second optimization criterion, however, low weight, demands small size or few airfoils, which means the lowest possible Reynolds number.

The designer has to work very carefully to avoid the risk of an efficiency collapse. This requires an accurate prediction of the development of the separation bubble, e.g., the transition and reattachment point. Failure to achieve this can affect the efficiency by several percent and the life of components by more than an order of magnitude [1].

Current industrial turbomachinery blade design is still largely based on empirical correlation methods for handling transition, primarily within integral boundary layer codes. Such methods work effectively over a range of flow parameters (Reynolds number, turbulence level, etc.) at design conditions, but become less reliable at off-design conditions, when the transition is involved in separation [2].

On the other hand, most transition models are obtained from steady flow experiments. Turbomachinery flow, however, is unsteady. Each blade row produces a nonuniform exit flow field due to both potential and viscous flow effects (Fig. 2). The inlet flow field to the downstream blade row is therefore characterized by periodic changes in entropy, stagnation pressure, Mach number, radial and pitchwise flow angles, and turbulence. Due to the relative motion of adjacent blade rows, a downstream blade row experiences an inlet flow that is periodically unsteady.

As a result of the unsteadiness that arises due to the interaction of the nonuniform exit flow from an upstream blade row with a downstream one, the surface pressure distribution and the boundary layer characteristics of the latter undergo periodic changes. One of the most important of these changes is that which occurs as the boundary layers periodically undergo transition from lami-

[1]Present address: MTU Aero Engines, Dachauer Str. 665, 80995 Munich, Germany.

Contributed by the International Gas Turbine Institute and presented at the 45th International Gas Turbine and Aeroengine Congress and Exhibition, Munich, Germany, May 8–11, 2000. Manuscript received by the International Gas Turbine Institute February 2000. Paper No. 2000-GT-270. Review Chair: D. Ballal.

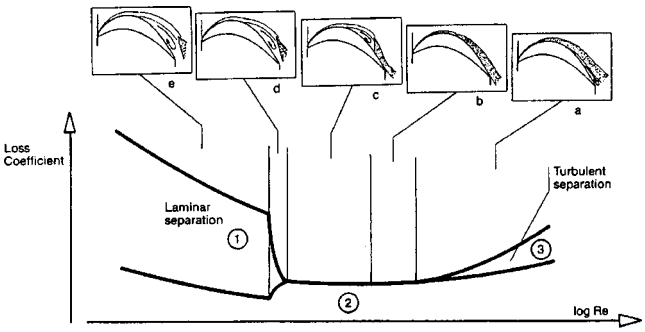

Fig. 1 Reynolds number effects on performance of a turbine cascade [2]

nar to turbulent flow. This unsteady transition affects not only the production of aerodynamic loss but also the heat transfer rates.

The wakes of upstream blades involve a periodic (velocity wake) and a random (turbulence wake) component. Both phenomena have a direct effect on the development of the boundary layers on the downstream blades. The relative importance of these phenomena still remains unclear [3].

There are too many published studies related to boundary layer transition and separation bubble to be cited here. A generally accepted classification [4] shows that there are four important modes of transition in a boundary layer: natural transition, bypass transition, separated flow transition, and reverse transition. Separated flow transition is the mode of transition of which the least is known. Empirical data on the formation of the separation bubbles, under different experimental conditions, have been obtained by many authors such as: Gault [5], Gaster [6], Horton [7], Malkiel and Mayle [8], and others. The influence of the Reynolds number and main flow turbulence level on separated flow behavior was studied by Roberts [9]. The interaction between separation bubbles and transition was observed by Hatman and Wang [10] in a low-speed test facility. A strong influence of upstream wakes on the separation bubble has been found by Dong and Cumpsty [11]. Researchers from GE Aircraft Engines (Halstead, Wisler, Shin), from the Iowa State University (Okiishi), the University of Tasmania (Walker), and the University of Cambridge (Hodson) [12] carried out a comprehensive experimental study of the unsteady wake effects on the downstream blade rows of a compressor and turbine stage in an effort to understand the physics of unsteady transition. Miller and Fejer [13] and Obremski and Fejer [14] have investigated the influence of main flow oscillations on the transition in attached boundary layers over a flat plate. However, no studies separating the effects of the velocity and turbulence wakes on the separation bubbles are known to the authors.

To improve the physical understanding of separation bubbles under steady and periodic-unsteady main flow conditions, the highly loaded blade boundary layer is simulated in a low-speed test facility. A large flat plate and a curved wall opposite the plate were used to generate a boundary layer with a separation bubble. The characteristics of separation, transition, and reattachment were studied. The main flow oscillations were generated by a rotating flap downstream of the test section. This experimental setup simulated the trailing edge velocity wake and permitted a study of this effect alone without the influence of the associated turbulence in the wake.

Experimental Setup

The experiments were conducted at the Berlin University of Technology in an unsteady low-speed wind tunnel (Fig. 3), which is an open circuit wind tunnel of suction type. It incorporates an inlet, a settling chamber fitted with a honeycomb straightener, a square 9:1 contraction, and a square test section of 0.4 m width, 0.4 m height, and 1.5 m length. The test section is followed by a rotating flap and a diffuser.

Under steady flow conditions a velocity range from zero to 40 m/s can be realized in the test section. The variation of the mean flow velocity across the test section is less than 0.75 percent. The turbulence level of the main flow is about 0.5 percent. The oscillating flow is generated by the rotating flap between the test section and the diffuser. The flap closes the passage twice in every cycle of rotation. The rotating flap is a sheet metal plate and can be varied in width so that in the limit case the duct is completely closed. It is driven at a constant speed from 0 to 50 cycles per second, giving a frequency range of flow oscillations of up to 100 Hz [15].

For the boundary layer investigation reported in this paper, a plate of 1 m length is located in the test section, which is shown in Fig. 4. Particular attention was paid to surface finish giving excellent flatness and smoothness. The leading edge has a NACA 0009 profile form to avoid leading edge separation. A contoured wall opposite the test plate is used to generate the required pressure distribution. A one-dimensional potential flow analysis was used for designing the contour to produce a pressure distribution with

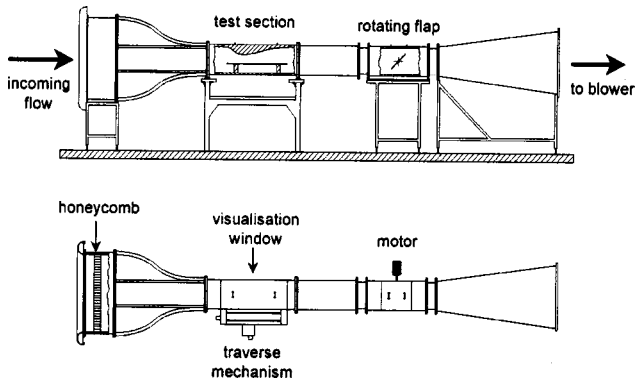

Fig. 3 Periodic-unsteady low-speed wind tunnel

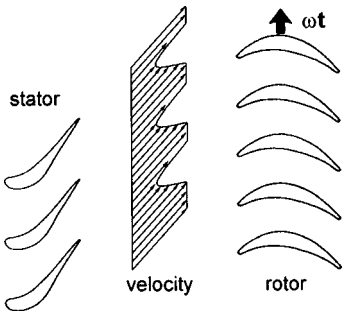

Fig. 2 Rotor/stator interaction of a turbine stage

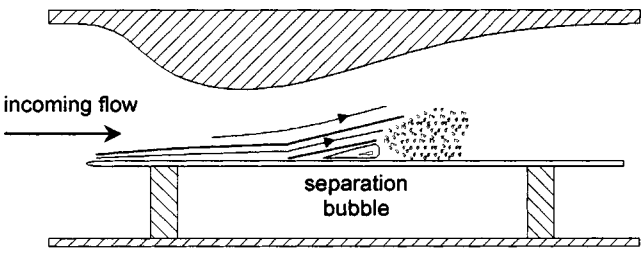

Fig. 4 Test section

minimum surface friction. This method was recommended by Stratford [16] to optimize the turbulent boundary layer for maximum diffusion.

The experimental setup has been designed to reproduce turbomachinery conditions except for compressibility. The Reynolds number covers a range from 1×10^5 to 2×10^6, the Strouhal number from 0 to 3, and the velocity amplitude from 0 to 20 percent.

The distribution of the time-averaged wall static pressure on the test plate was measured at a number of streamwise locations with pressure taps. For the time-resolved measurements, Honeywell pressure transducers (176PC07HD2) were used.

A TSI IFA 300 hot-wire anemometer was used to measure the velocity of the boundary layer. A special three-dimensional traverse mechanism was designed and mounted on the side of the test section to obtain a high spatial resolution of the whole bubble structure.

Experimental Results

The flow structure and the separation bubble formation were analyzed for steady and periodic-unsteady main flow conditions. The data analysis was mainly focused on the major parameters, which determine the evolution of a separation bubble.

Steady Main Flow Conditions. Under steady main flow conditions, four experiments were run using four different Reynolds numbers: $\mathrm{Re}_\infty=U_\infty L/\nu=2.9\times10^5,\ 6.2\times10^5,\ 1.0\times10^6,\ 1.4\times10^6$, where U_∞ is the velocity at the test section inlet, L the plate length, and ν the kinematic viscosity. All four experiments show similar characteristics. This paper describes in detail the flow structure of one case only with $\mathrm{Re}_\infty=6.2\times10^5$. Where necessary, the analysis and discussion will include results of other cases.

For the chosen case, the normalized main flow velocities over the plate derived from the static pressure measurements and measured with hot-wire probes are shown against the streamwise position in Fig. 5. The normalization was done by the incoming flow velocity U_∞ and the plate length. A good agreement in the comparison of the two measurement techniques can be observed. On the other hand, a similar velocity distribution to that of blades can be found here. The main flow over the flat plate is first accelerated up to the velocity peak at $x/L=0.3$ and then diffused by the adverse pressure gradient.

A separation bubble can be clearly identified. The laminar boundary layer separates at $x/L=0.4$, where the adverse pressure gradient is sufficiently strong. From $x/L=0.4$ to 0.455, the main flow velocity remains almost constant, which is typical for the stagnating flow beneath the separated laminar layer. Beyond $x/L=0.455$ transition occurs and the main flow velocity decreases rapidly. Reattachment takes place at $x/L=0.48$.

The plots of the mean velocity field and the rms velocity field normalized with U_∞ in Fig. 6 show the general bubble configuration, consisting of the separated shear layer, the stagnant fluid region, and the area of the rms maximum, which indicates the development of transition and reattachment. The dividing streamline and the line of inflection points in the velocity profiles are marked in both diagrams. The practically static behavior of the fluid in the separation bubble can be verified in the area under the dividing streamline. The relatively higher mean velocity of the turbulent part in the separation bubble is related to the unsteadiness of the transition and reattachment, which was observed by laser-sheet flow visualization. It was also observed that the separation point remains almost constant. From the normalized rms velocity field, one can see that the flow fluctuations originate on the line of inflection points in the velocity profiles. A region of high turbulence can be identified at $x/L=0.485$. The rms velocity decreases downstream to those of the turbulent boundary layer.

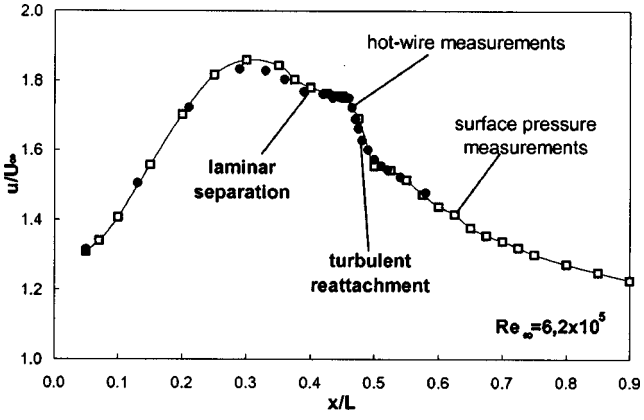

Fig. 5 Velocity distribution over the flat plate

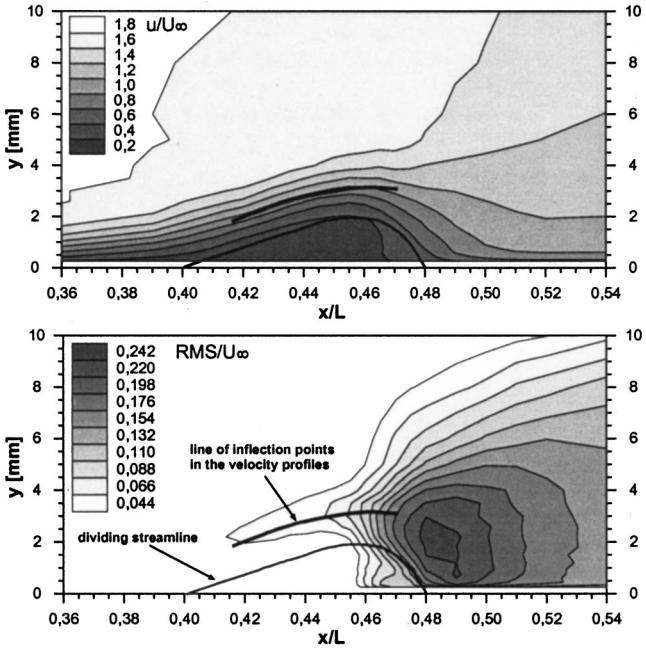

Fig. 6 Velocity field around the separation bubble

Obviously, the line of inflection points in the velocity profiles is significant for the development of transition and reattachment. From the point of view of free shear layer stability theory, points of maximum vorticity are inherently unstable. An evaluation of the frequency spectra contributes to the understanding of these phenomena.

The velocity power spectra at six points along the line of maximum vorticity are shown in Fig. 7. To enhance the differences, the spectra are presented in logarithmic form. At the first location $x/L=0.42$ the flow is laminar. The power spectrum level is quite low. No special events can be found here. At $x/L=0.43$ a frequency range concentrated around 480 Hz shows a distinct amplitude rise while the overall power spectrum remains unchanged. This is caused by the amplification of the free shear layer instability. Farther downstream at $x/L=0.44$ this frequency range becomes more pronounced and the overall levels of the spectrum start rising. At $x/L=0.45$ a second frequency range as the superharmonic of the first one can be observed. This observation is different from that of Malkiel and Mayle [8], who presented the subharmonic instability waves. Farther downstream at $x/L=0.46$, the two frequency ranges are still present, and the high-frequency part of the power spectrum level increases dramatically indicating the transition to turbulence. Turbulent spots and the associated intermittency, like those occurring in attached boundary layers [4], could not be identified in the corresponding time traces, which are not shown in this paper. Transition to turbulence

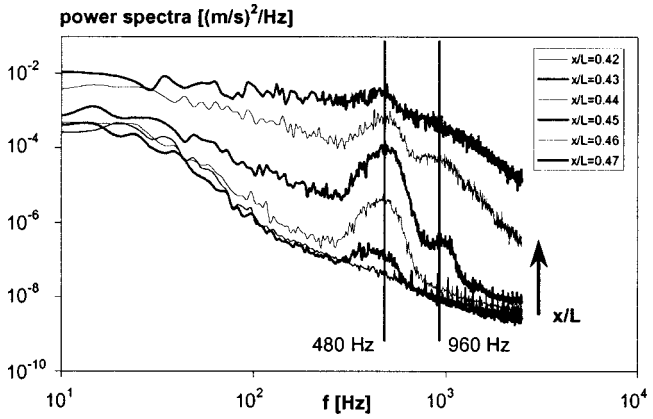

Fig. 7 Velocity power spectra along the line of inflection points in the velocity profiles

Table 1 Parameters describing separation bubble for four test cases

U_∞ [m/s]	4.2	9.0	14.5	19.7
Re_∞	2.9×10^5	6.2×10^5	1.0×10^6	1.4×10^6
X_S/L	0.401	0.401	0.401	0.402
x_{MD}/L	0.490	0.455	0.44	0.435
X_R/L	0.53	0.48	0.46	0.45
$x_{u'max}/L$	0.515	0.485	0.462	0.455
$x_T/L=x_{MD}/L$	0.490	0.455	0.44	0.435
U_s [m/s]	7.38	16.02	26.22	33.50
δ_1 [mm]	2.26	1.48	1.08	0.90
δ_2 [mm]	0.67	0.45	0.36	0.32
H_{12}	3.37	3.29	3.00	2.81
Re_{2S}	339	494	647	734
AC x 10^6	-3.54	-1.61	-1.0	-0.78
Po	-0.086	-0.083	-0.080	-0.084

happens very rapidly within a very short length of the free shear layer. At the last location $x/L=0.47$ the flow is fully turbulent, and the instability waves almost disappear in the overall levels of turbulence.

Summing up these results, the transition process via a separation bubble can be described as follows.

- Free shear layer instability originates at the maximum vorticity point of the velocity profile and energy is transferred from the shear flow to the instability waves.
- The instability waves are amplified downstream and finally trigger transition.
- Due to the turbulent fluctuation, the momentum transfer across the shear layer is increased. This causes the reattachment of the free shear layer.
- The free shear layer apparently has considerably less damping capability then the attached boundary layer. Transition takes place rapidly over an extremely short transition length.

These results agree with the observation by Hatman and Wang [10]. The separation bubble can be identified as one in short mode.

The streamwise distributions of displacement thickness δ_1, momentum thickness δ_2, and the shape factor H_{12} are shown in Fig. 8. The initial growth of the displacement thickness and the shape factor, up to the separation point, is significantly lower than downstream of the separation point and upstream of the maximum displacement location. Within the separation bubble between the separation point x_S and reattachment x_R, the momentum thickness does not demonstrate any unusual behavior. Growth in the turbulent part of the free shear layer after transition, and downstream of the maximum displacement point x_{MD}, is considerably stronger than in the laminar part. This corresponds to the characteristics of the attached boundary layer and is due to the definition of δ_2. The low-velocity separation region does not contribute significantly to the integral parameter. Momentum thickness can be used to treat the free shear layer like a wall boundary layer at incipient separation [17]. Displacement thickness and correspondingly the shape factor contain the displacement of the dead water. They depend on the shape of the wall and have no generalized characteristics.

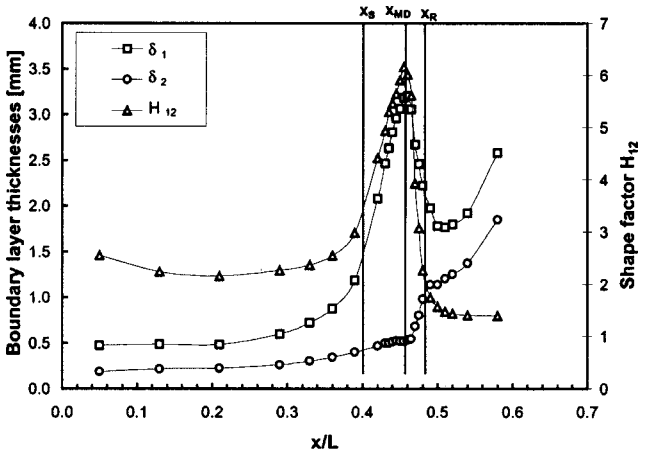

Fig. 8 Boundary layer thicknesses and shape factor

After reattachment, although the resulting turbulent boundary layer may be structurally different from the one resulting from transition in attached flow, the shape factor decreases to a nearly turbulent value $H_{12}=1.4$ for decelerated flows.

The main parameters describing the separation bubble for the four test cases are presented in Table 1. There are some remarkable points to be mentioned. The Reynolds number based on the momentum thickness at the separation point increase with higher overall Reynolds number Re_∞ as expected. The separation points for the four test cases remain the same, while the maximum displacement locations, the reattachment points, and the maximum rms velocity locations vary considerably. The unchanged separation point may contribute to the constant normalized velocity distributions of the main flow for the four test cases. The maximum rms velocity location can be found somewhere near the reattachment point. It lies upstream of the reattachment point at the lowest Reynolds number (2.9×10^5), and downstream of that point at the other three Reynolds numbers.

The shape of the dividing streamlines can be used as a measure for the separation bubble size. Derived from the velocity profile measurements, they are shown in Fig. 9 for the four test cases. The length of the separation bubble can be verified from the main flow velocity distribution (see Fig. 5). Each of them has an almost linear rise downstream of the separation point x_S and upstream of the maximum displacement location x_{MD}.

It can be observed that the bubble length increases with lower Reynolds number. This is due to the delay of transition of the free shear layer. It can also be observed that the rate of displacement growth increases with lower Reynolds numbers. This phenomenon has also been confirmed by laser light sheet flow visualization. The mechanism causing this behavior is not yet understood by the authors.

The shape of the bubble obviously depends both on the Reynolds number and the pressure distribution that would arise without separation. The most suitable nondimensional parameter de-

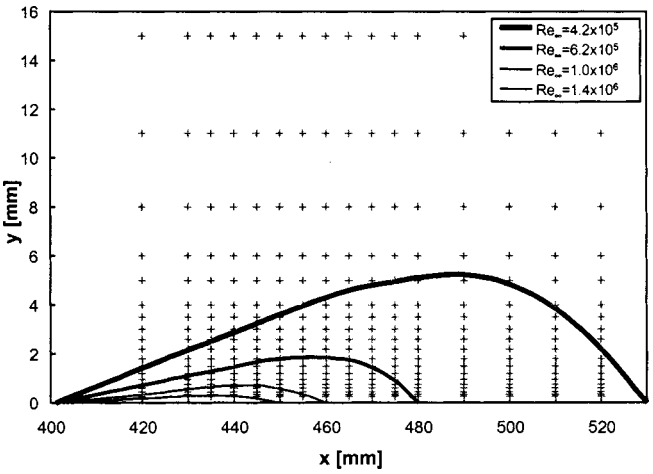

Fig. 9 Separation bubble size of the four test cases

scribing this pressure distribution in the region of the bubble is called acceleration parameter and given by $AC=\nu/U^2(dU/dx)$. This parameter varies between -3.54 and -0.78 for the four test cases. The Pohlhausen parameter at the separation point $Po_S=(Re_2)^2AC_S$ lies between -0.086 and -0.080 for the Reynolds number range investigated and well meets the empirical value -0.082 suggested by Thwaites [18].

A plot of the Reynolds number $Re_{SMD}=U_s(x_{MD}-x_S)/\nu$, based on the conditions at separation and the distance $(x_{MD}-x_S)$ versus the momentum thickness Reynolds number $Re_{2S}=U_s\delta_2/\nu$, is shown in Fig. 10. The data taken from measurements of Gault [4], Gaster [6], and Bellows [19] at low turbulence level, and the empirical formula by Mayle [3]:

$$Re_{SMD}=700\,Re_{2S} \tag{1}$$

are also plotted in this figure as a comparison. The data are in good agreement with previous experiments.

Periodic-Unsteady Main Flow Conditions. Three experiments were run under periodic-unsteady main flow conditions using different Strouhal numbers and oscillation amplitudes at an almost constant Reynolds number typical for turbomachinery blades. This paper describes the flow structure of one case in detail. The analysis and discussion will include results of the other cases without showing the flow structure.

In the interest of the main flow quality, Fig. 6 shows the incoming flow velocity signal and its power spectrum for the present test

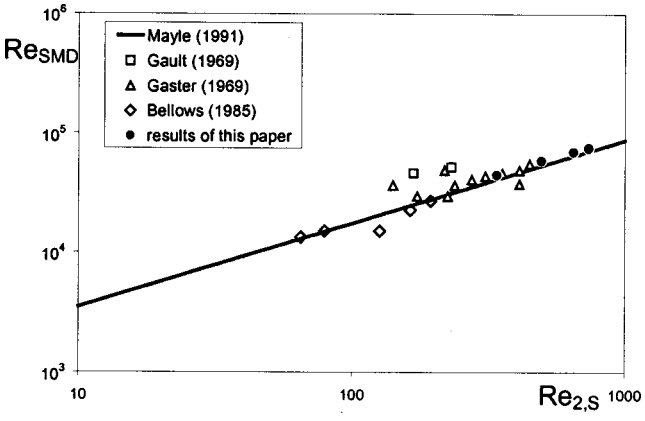

Fig. 10 Reynolds number based on the length from separation to transition as a function of the momentum thickness Reynolds number at separation point

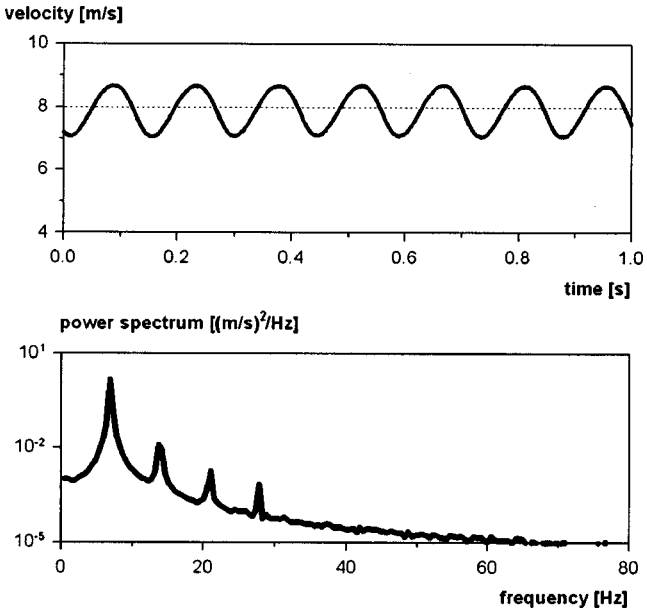

Fig. 11 Incoming flow signal of the periodic-unsteady boundary layer

case. It can be seen that the flow contains a fundamental frequency (equal to twice the flap frequency) and a number of harmonics, which decrease in amplitude rapidly (Fig. 11). The incoming flow can be represented as follows:

$$U_\infty=U_0+U_1\ \sin(2\pi f+\varphi) \tag{2}$$

where U_0 is the time-averaged velocity, U_1 is the oscillation amplitude, f is the oscillation frequency, and φ is the phase shift. The unsteady boundary layer around the test plate is characterized by three nondimensional parameters, i.e., overall Reynolds number Re, Strouhal number Sr, and relative oscillation amplitude A defined as follows:

$$Re=\frac{U_0L}{\nu},\quad Sr=\frac{fL}{U_0},\ \text{and}\ A=\frac{U_1}{U_0} \tag{3}$$

where L is the length of the test plate. In the present case, U_0 was 7.9 m/s and f was 7.0 Hz, corresponding to $Re=5.45\times10^5$ and $Sr=0.89$, respectively. The relative amplitude of the velocity oscillation was 13 percent.

Figure 12 presents the normalized time-averaged mean velocity profiles and a series of velocity time traces of the hot-wire measurements for reference. The velocity profiles of the boundary layer were measured at $x/L=0.39$, 0.41, 0.43, 0.45, 0.47, and 0.49. The time-averaged velocity profiles are shown in the central diagram of this figure. The normalization was done by the time-averaged velocity U_0 of the incoming flow. A separation bubble configuration can be identified from the velocity profiles. The dividing streamline and the line of inflection points in the velocity profiles are marked in this diagram. A similar bubble formation to that of steady flows can be found here. However, in comparison to the separation bubble shown in Fig. 6 for steady flow conditions, one can find a shorter bubble under unsteady conditions, although the overall Reynolds number is lower.

The time-averaged length of the separation bubble shown in Fig. 12 matches well that from surface static pressure measurements, which are not shown in this paper. The typical velocity signals around the separation bubble against time are shown in Fig. 12(*A*, *B*, *C*, *D*, *E*, *F*, and *G*). Three distinct regions of flow can be identified from the measurements. The first, which is stable laminar flow, is plotted in Fig. 12(*A*). At this location, only very low-level random information can be observed in addition to the

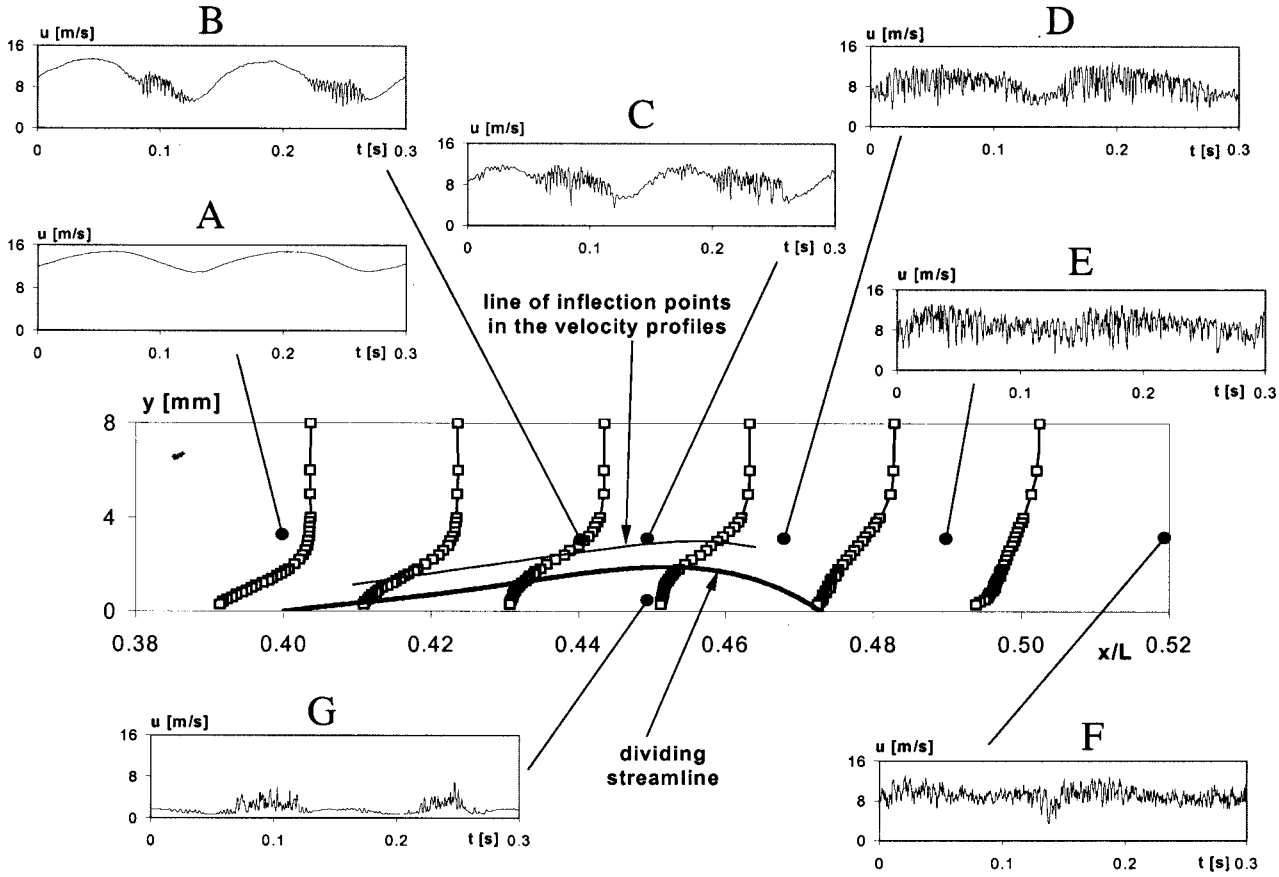

Fig. 12 Time-averaged velocity profiles and typical velocity signals of the periodic-unsteady boundary layer

flow oscillation. The second or intermittent region is shown in Fig. 12(*B*, *C*, and *G*). At these locations, a periodic change between laminar and turbulent flow can be identified. The portion of turbulent flow increases continuously downstream from (*B*) to (*C*). The flow velocity in the separation bubble and its oscillation amplitude plotted in Fig. 12(*G*) are obviously much smaller than those over the bubble plotted in Fig. 12(*B* and *C*). The velocity signals in Fig. 12(*C* and *G*) are measured at the same x position $x/L=0.45$. The flow velocity signals at these three positions contain instability waves. Just as under steady conditions, two harmonic instability frequency ranges can be observed at 350 Hz and 700 Hz. It should be noted that in other test cases the two frequency ranges were nonharmonic [15]. These instability waves occur periodically first in the trough of the velocity trace. They subsequently increase in amplitude and move into the decelerating part of the velocity trace. The associated onset of transition has the same characteristic. To demonstrate the development of the free shear layer instability, the velocity power spectra along the line of inflection points in the time-averaged velocity profiles are shown in Fig. 13. A similar evolution to that for steady flow conditions shown in Fig. 7 can be found here.

The last region is the turbulent region, which is presented in Fig. 12(*D*, *E*, and *F*). In this region the flow is fully turbulent; the random and periodic components of the velocity signal are of similar magnitude. One can see that the magnitude of the random component increases downstream from *D* to *E* at first, and then decreases from *E* to *F*. This will be shown and discussed more clearly with the ensemble-averaged velocity fields in Fig. 14 and 15.

The complexity of the intermittent region comes from the fact that it contains two periodically alternating flow structures: one pertaining to the laminar flow and the other pertaining to the turbulent flow. The best impression of the periodic-unsteady boundary layer with separation bubble can be obtained, if one looks at the normalized ensemble-averaged mean velocity field and the normalized ensemble-averaged rms velocity field. Both of them will be used to demonstrate the temporal and spatial development of the unsteady boundary layer.

Figure 14 shows the normalized ensemble-averaged mean velocity field for the present test case. Eight points in time are presented within an oscillation period. From top to bottom in this figure, the incoming flow experiences a sinusoidal oscillation. The plots of $t/T=0$ and 0.5 stand for the flow field when the main flow reaches its time-averaged velocity; the plot of $t/T=0.25$ presents the flow field for the maximum main flow velocity and plot of $t/T=0.75$ for the minimum main flow velocity. One can see the

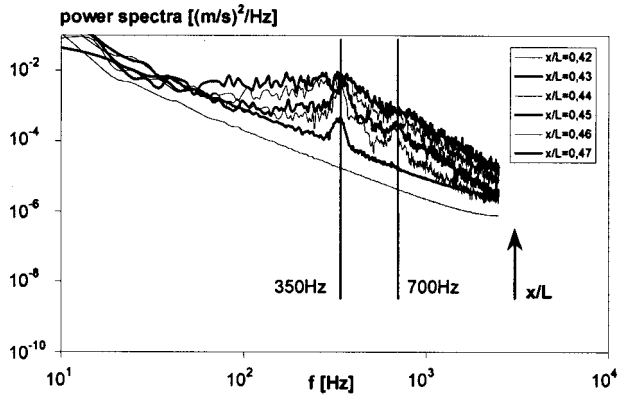

Fig. 13 Velocity power spectra along the inflection point line in the time-averaged velocity profiles

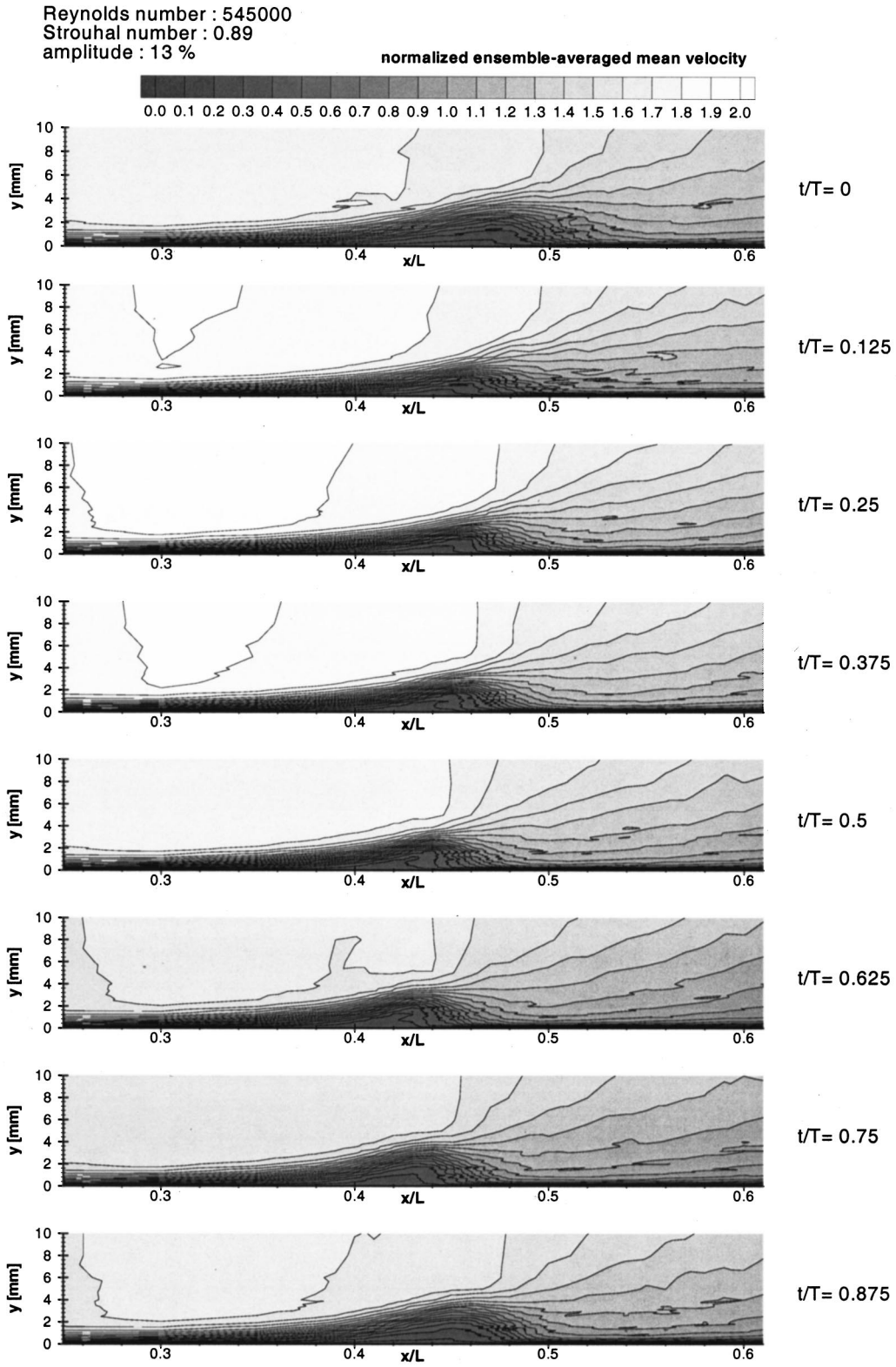

Fig. 14 Normalized ensemble-averaged mean velocity field

streamwise deceleration of the main flow in all plots, and identify the separation bubble through the area of the low velocity. Remarkable is the difference of the bubble size between the plot $t/T=0$ and the plot $t/T=0.5$, although their main flow fields are almost the same. The shortest bubble can be found between $t/T=0.5$ and 0.625, and not at $t/T=0.25$ with the maximum main flow velocity. This indicates the existence of a phase shift between the velocities of the boundary layer and the main flow. The bubble needs some time to respond to the main flow oscillation. Figure 15 shows the normalized ensemble-averaged rms velocity field for the present case. The time allocation is the same as in Fig. 14. In each plot of Fig. 15, one can find a region with unusu-

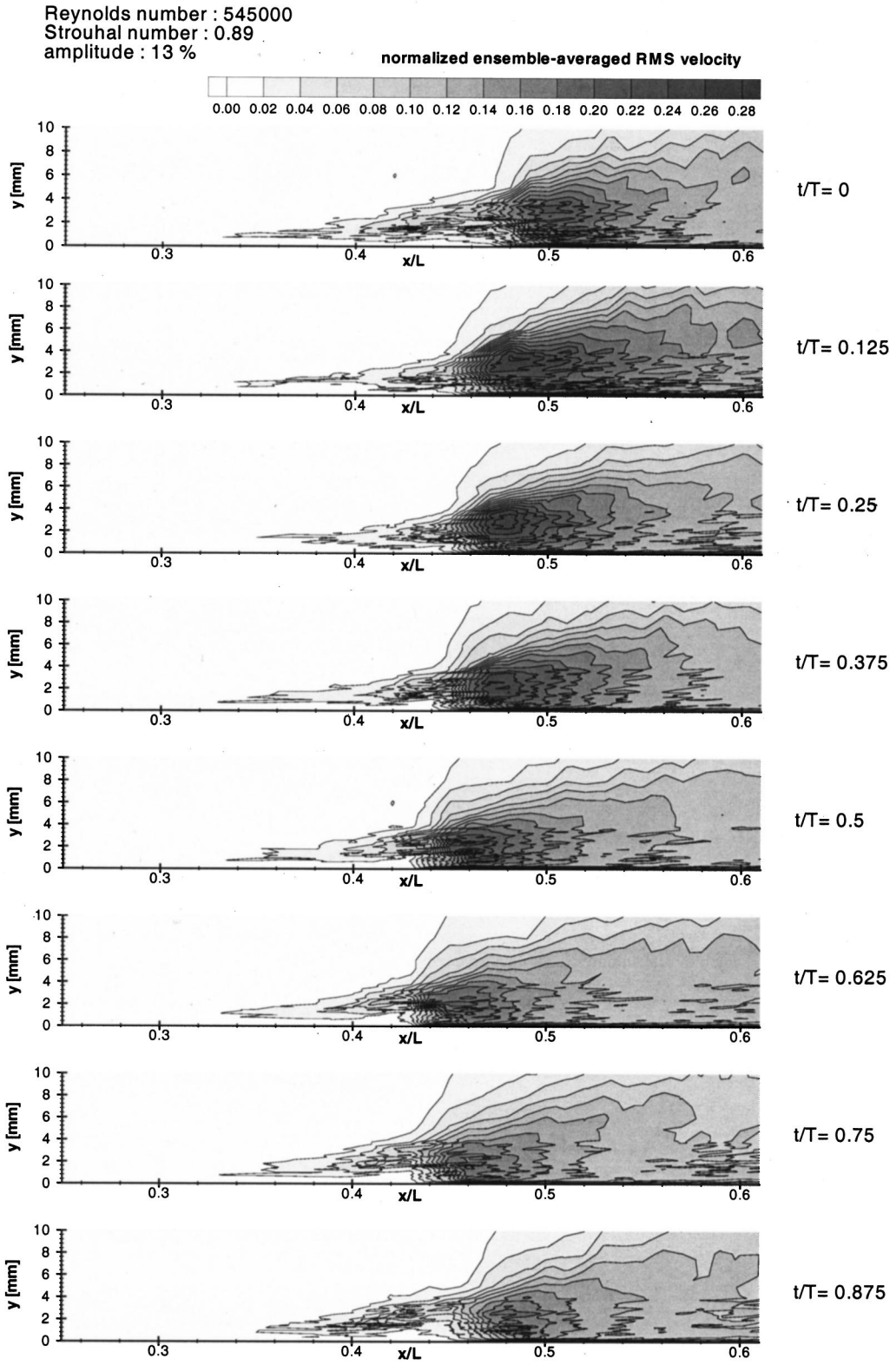

Fig. 15 Normalized ensemble-averaged rms velocity field

ally high turbulence levels similar to that observed under steady flow conditions. An oscillation of this location can also be identified from the plots from top to bottom. The phase shift mentioned above can be verified.

Figure 16 shows the phase shift and the absolute/relative amplitude of the flow oscillation. The relative amplitude a indicates the flow oscillation level in comparison to the time-averaged flow, and is equal to the absolute amplitude u_1 divided by the time-averaged mean flow velocity u_0.

Outside of the separation bubble the flow oscillates in-phase. The amplitude remains almost the same as that of the incoming flow. This well reflects the characteristic of incompressible flow.

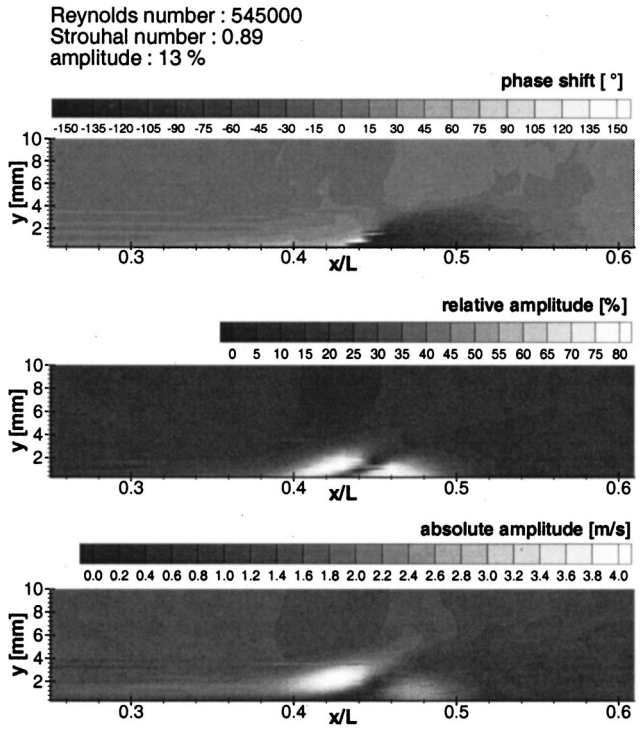

Fig. 16 Oscillation characteristic of the separation bubble

There are two areas with phase shift. The laminar area of the separation bubble has a positive phase shift, while the turbulent one has a negative phase shift. In the transition area no phase shift can be identified. It appears as two masses connected by a spring. During swing a fixed point separates two areas with different phase shift. It can also be observed, that the flow oscillations in the inflection points region and in the reattachment region are relatively strong with larger amplitude. The two regions are extremely sensitive to main flow oscillation. Between these two regions the amplitude of the flow oscillation is almost zero. The flow in this third region can be treated as a steady flow. This location can be defined as the time-averaged transition position.

The time–space diagram presenting the oscillating separation, transition, and reattachment characteristic is shown in Fig. 17. This diagram obtained from velocity measurements agrees with that from surface dynamic pressure measurements, which are not shown in this paper. It can be seen that the laminar separation point does not appear to respond to the unsteadiness of the main flow, whereas the transition and reattachment points show a strong interaction. Laminar flow does not, at any time, appear downstream of the turbulent flow region as in the case of an attached boundary layer measured by Obremski and Fejer [14].

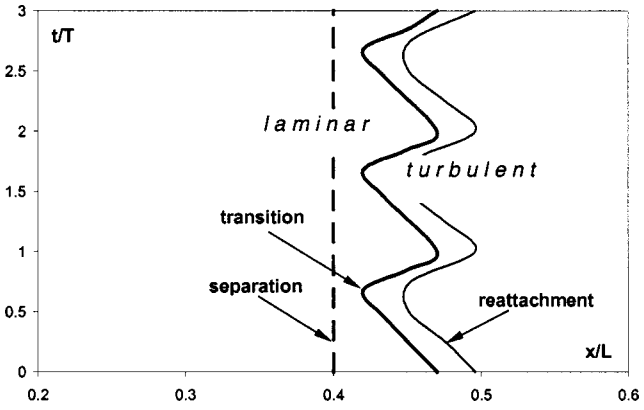

Fig. 17 Time-space diagram of the separation, transition, and reattachment (Re=54,500, Sr=0.89, *A*=13 percent)

The effect of Strouhal number and oscillation amplitude on the separation bubble was also investigated. Lower Strouhal numbers result in a reduction of the phase shift of the separation bubble oscillation. This means that in terms of phase shift the separation bubble responds more slowly to high-frequency oscillations. This result also agrees with the theoretical analysis for attached boundary layer at very high Strouhal numbers [20]. For the limit case of a very low Strouhal number a quasi-steady flow field without phase shift is present. A lower amplitude of the main flow oscillation causes a lower amplitude of the separation bubble oscillation as expected.

Conclusions

The following conclusions may be drawn from the experimental results for steady and periodic-unsteady boundary layers with separation bubble:

- Transition via a separation bubble shows a typical structure of laminar separation, transition of the free shear layer, and reattachment. A region of high turbulence levels can be observed downstream of the transition point both in steady and unsteady flow.
- The dividing streamline of the separation bubble has a quasi-linear rise directly downstream of the separation point. The displacement growth rate of the separation bubble depends on the Reynolds number.
- Momentum thickness in steady flow behaves very similarly to that of an attached boundary layer. It can be used as a major parameter describing the separation bubble.
- Higher Reynolds numbers resulting in earlier transition reduce the length of the separation bubble, while the separation point does not change its location.
- Transition and the associated reattachment via a separation bubble are dominated by the free shear layer instability. Two instability frequency ranges are identified.
- The periodic-unsteady main flow induces an oscillation of the separation bubble. During the oscillation, a fixed laminar separation point can be observed, while all other parameters of the separation bubble oscillate with the main flow. At the separation bubble two areas with opposite phase shift relative to the main flow can be observed. The inflection point region and the reattachment point region respond very strongly to the main flow oscillation in terms of amplitude.
- A shorter time-averaged separation bubble was observed than under steady conditions, although the overall Reynolds number was smaller.
- The Strouhal number of the main flow appears to have only a minor effect on the amplitude of the separation bubble oscillation. But it has an effect on the phase shift. It increases with Strouhal number.

Nomenclature

A, a = relative amplitude; $A=U_1/U_0$; $a=u_1/u_0$
AC = acceleration parameter$=\nu/U^2(dU/dx)$
f = oscillation frequency
H_{12} = shape factor
L = plate length
Po = Pohlhausen parameter$=(\mathrm{Re}_2)^2 AC$
Re = Reynolds number; $\mathrm{Re}_\infty=U_\infty L/\nu$
Sr = Strouhal number$=fL/U_0$
t = time
U, u = flow velocity
x, y, z = Cartesian coordinates
δ_1 = displacement thickness

δ_2 = momentum thickness
ν = kinematic viscosity

Subscripts

∞ = incoming flow
0 = time-averaged values
1 = oscillating amplitude; displacement thickness
2 = momentum thickness
S = separation point
MD = maximal displacement location
R = reattachment point
u' max = the location of maximal rms velocity

References

[1] Hodson, H. P., 1991, ''Aspect of Unsteady Blade-Surface Boundary Layers and Transition in Axial Turbomachines,'' VKI Lecture Series 1991-06, Boundary Layers in Turbomachines, Sept. 2–6.
[2] Hourmouziadis, J., 1989, ''Aerodynamic Design of Low Pressure Turbines,'' AGARD Lecture Series 167.
[3] Walker, G. J., 1993, ''The Role of Laminar–Turbulent Transition in Gas Turbine Engines: A Discussion,'' ASME J. Turbomach., **115**, pp. 207–217.
[4] Mayle, R. E., 1991, ''The Role of Laminar–Turbulent Transition in Gas Turbine Engines,'' ASME J. Turbomach., **113**, pp. 509–537.
[5] Gault, D. E., 1955, ''An Experimental Investigation of Regions of Separated Laminar Flow,'' NACA TN 3505.
[6] Gaster, M., 1969, ''The Structure and Behavior of Laminar Separation Bubbles,'' Aeronautical Research Council, R&M 3595.
[7] Horton, H. P., 1969, ''A Semi-Empirical Theory for the Growth and Bursting of Laminar Separation Bubbles,'' Aeronautical Research Council, C.P. No. 1073.
[8] Malkiel, E., and Mayle, R. E., 1996, ''Transition in a Separation Bubble,'' ASME J. Turbomach., **118**, pp. 752–759.
[9] Roberts, W. B., 1975, ''The Effect of Reynolds Number and Laminar Separation on Axial Cascade Performance,'' ASME J. Eng. Power, **97**, pp. 261–274.
[10] Hatman, A., and Wang, T., 1998, ''Separated-Flow Transition: Parts 1 to 3,'' ASME Paper Nos. 98-GT-461/462/463.
[11] Dong, Y., and Cumpsty, N. A., 1990, ''Compressor Blade Boundary Layers: Parts 1 and 2,'' ASME J. Turbomach., **112**, pp. 222–240.
[12] Halstead, D. E., Wisler, D. C., Okiishi, T. H., Walker, G. J., Hodson, H. P., and Shin, H.-W., 1997, ''Boundary Layer Development in Axial Compressors and Turbines: Part 1— Composite Picture; Part 2—Compressor; Part 3—LP Turbines; Part 4—Computations and Analysis,'' ASME J. Turbomach., **119**, pp. 114–126; 426–444; 225–237; 128–139.
[13] Miller, J. A., Fejer, A. A., 1964, ''Transition Phenomena in Oscillating Boundary Layer Flows,'' J. Fluid Mech., **18**, pp. 438–449.
[14] Obremski, H. J., and Fejer, A. A., 1967, ''Transition in Oscillating Boundary Layer Flows,'' J. Fluid Mech., **29**, pp. 93–111.
[15] Lou, W., and Hourmouziadis, J., 1999, ''Experimental Investigation of Periodic-Unsteady Flat Plate Boundary Layers With Pressure Gradients,'' *Proc. 3rd ASME/JSME Joint Fluids Engineering Division Summer Meeting*, Paper No. FEDSM99-7190.
[16] Stratford, B. S., 1959, ''The Prediction of Separation of the Turbulent Boundary Layer,'' J. Fluid Mech., **5**, pp. 1–16.
[17] Hourmouziadis, J., 1990, ''Selected Unresolved Problems in Turbomachinery Aerodynamics,'' presented at ASME/IGTI Fluid Dynamics of Turbomachinery, Iowa State University, Ames, IA, 13–23 Aug.
[18] Thwaites, B., 1949, ''Approximate Calculation of the Laminar Boundary Layer,'' Aeronaut. Q., 245–280.
[19] Bellows, W. J., and Mayle, R. E., 1986, ''Heat Transfer Downstream of a Leading Edge Separation Bubble,'' ASME J. Turbomach., **108**, pp. 131–136.
[20] Lin, C. C, 1957, ''Motion in the Boundary Layer With a Rapidly Oscillating External Flow,'' *Proc. 9th Int. Congress Appl. Mech.*, **4**, pp. 155–167.

The Use of Hot-Wire Anemometry to Investigate Unsteady Wake-Induced Boundary-Layer Development on a High-Lift LP Turbine Cascade

Stefan Wolff

Stefan Brunner

Leonhard Fottner

Institut für Strahlantriebe,
Universität der Bundeswehr München,
D-85577 Neubiberg, Germany

Recent research has revealed positive effects of unsteady flow on the development of boundary layers in turbine cascades, especially at conditions with a laminar suction side separation bubble at low Reynolds numbers. Compared to steady flow, a reduction of total pressure loss coefficient over a broad range of Reynolds numbers has been shown. Taking into account the positive effects of wake-induced transition already during the design process, new high lift bladings with nearly the same low losses at unsteady inlet flow conditions could be achieved. This leads to a reduction of weight and cost of the whole turbine module for a constant stage loading. Unsteady flow in turbomachines is caused by the relative motion of rotor and stator rows. For simulating a moving blade row upstream of a linear cascade in the High-Speed Cascade Wind Tunnel of the Universität der Bundeswehr München, a wake generator has been designed and built. The wakes are generated with bars, moving with a velocity of up to 40 m/s in the test section upstream of the cascade inlet plane. Unsteady flow causes the transition on the surface of the suction side of a low-pressure turbine blade to move upstream whenever an incoming wake is present on the surface; moreover, a laminar separation bubble can be diminished or even suppressed. In order to detect the effects of wakes on the boundary layer development a new hot wire data acquisition system is required. Due to the fact that hot wires give a good insight into boundary layer development, a new hot-wire data acquisition system has been set up. The anemometry system can acquire four channels simultaneously, therefore being capable of logging a triple hot-wire sensor and a bar trigger simultaneously. One further channel is utilized for a once-per-revolution trigger. The once-per-revolution trigger is used to start the measurement of one data block. Using the well-established ensemble-averaging technique, 300 ensembles each consisting of five wake passing periods have been acquired. Ensemble averaging can be directly performed without any data reduction. The adaptation of this new hot-wire anemometry data acquisition system to the High-Speed Cascade Wind Tunnel of the Universität der Bundeswehr München is pointed out. First, results on unsteady periodic boundary layer development of a highly loaded low-pressure turbine cascade under unsteady inlet flow conditions are presented. During the present investigation four boundary layer traverses, ranging from $x/l_{ax}=0.82$ to $x/l_{ax}=0.99$ (suction side), at steady and unsteady inlet flow conditions ($U_{bar}=10$ m/s) at an outlet Reynolds number of $Re_{2th}=100{,}000$ have been conducted. [S0889-504X(00)00204-X]

Introduction

Positive effects of rotor–stator interaction mainly occur in high-lift low-pressure turbines, where a laminar suction side separation bubble exists, especially at low Reynolds numbers [1,2]. Incoming wakes force the boundary layer of the suction side to undergo transition, whenever the Reynolds number based upon momentum thickness exceeds the range of $Re_\theta=90-150$ [3,4]. Following the wake-induced transitional regions, calmed regions appear, which show laminar-like boundary layer behavior [2,5,6]. With a full velocity profile and low entropy generation the calmed region combines the positive properties of laminar and turbulent boundary layers. It is able to inhibit turbulent spot generation and withstand larger adverse pressure gradients than conventional laminar boundary layers. The calmed region is therefore able to suppress or delay a laminar suction side separation bubble. The replacement of a thick laminar separation bubble that is present at steady inflow conditions with intermittently becalmed or transitional attached flow at unsteady inflow conditions leads to a time mean reduction of loss generation [7–9]. Extra benefit may be gained by setting an optimal sequence of transitional, separated and becalmed regions, hence a favorable reduced frequency [2] of the rotor wakes. In general the positive effect of rotor–stator interaction increases at higher loading [3,7]. Furthermore, the incoming wakes are influencing the whole suction side boundary layer by thickening the boundary layer [10].

Several parameters influence the loss generation of the low-pressure turbine blade: the Reynolds number Re, the Strouhal number Sr, the wake strength (turbulence intensity or velocity deficit within the wake and the wake width), and the loading of the turbine cascade.

The gap of experiments on rotor–stator interaction on high-lift low-pressure turbines between turbine rig testing [5,11,12] and testing at low-speed cascade wind tunnels [1–3,12], was closed by

Contributed by the International Gas Turbine Institute and presented at the 45th International Gas Turbine and Aeroengine Congress and Exhibition, Munich, Germany, May 8–11, 2000. Manuscript received by the International Gas Turbine Institute February 2000. Paper No. 2000-GT-49. Review Chair: D. Ballal.

Acton et al. [13] and Brunner et al. [9] who pointed out a re-establishment of a laminar separation bubble between two wake-induced turbulent patches at design conditions of the investigated high lift blading.

In order to prove the results on a high-lift low-pressure turbine cascade, a HWA measurement technique was set up to determine the steady and periodic unsteady boundary layer development. The ensemble-average technique delivers velocity and turbulence profiles. These time-resolved velocity profiles are taken to evaluate time resolved integral boundary layer parameters. Therefore data [9] taken by pneumatic and hot-film measurements could be verified and supplemented. Furthermore, steady and periodic unsteady integral boundary layer parameters have been calculated in order to optimize design criteria for high-lift low-pressure turbines considering effects of rotor–stator interaction.

Experimental Setup

High-Speed Cascade Wind Tunnel. The experiments were carried out at the High-Speed Cascade Wind Tunnel (Fig. 1) of the Universität der Bundeswehr München. This wind tunnel is an open-loop facility, which can operate continuously and reach Mach numbers up to Ma=1.05 in the test section. Being built inside a large pressure tank, the wind tunnel offers the possibility to vary the Mach and Reynolds numbers in the test section independently [14] in order to simulate the flow conditions correctly inside turbomachines.

The air is supplied by a six-stage axial compressor, driven by a 1.3 MW a.c. electric motor, which is situated outside the pressure tank. The air enters through a diffuser into a settling chamber where it is cooled down to an adjustable constant temperature (30°C to 60°C). A turbulence generator and a nozzle are positioned upstream of the 300-mm-wide test section. It has variable height. The following data were used in order to monitor the flow conditions of the cascade main stream flow [14]: the total temperature in the settling chamber, the static pressure in the tank (downstream conditions), the static pressure, and the total pressure of the main stream flow upstream of the cascade.

Wake Generator. In turbomachines, periodically unsteady flow is caused by the relative motion of rotor and stator rows. A wake generator has been designed and built in order to simulate a moving blade row upstream of the linear turbine cascade in the High-Speed Cascade Wind Tunnel of the Universität der Bundeswehr München (Fig. 2) [13]. The wakes are generated with cylindrical bars moving with a velocity of up to 40 m/s in the test section upstream of the cascade inlet plane (Table 1). As shown by Pfeil and Eifler [15] the far wake of a cylinder is similar to that of an airfoil assumed that both cause the same total pressure losses. With the wake generator an angle of the incoming wake of about 55 deg (Sr=1.06) can be generated, whereas a representative turbine has a wake angle of about 65 deg ($c_{ax}/U=0.85$). Investigations [16] conducted on a turbine cascade showed a strong dependency of the wake-induced transition on the incoming turbulence intensity and less on the angle of the incoming wake. So despite this deviation of the velocity triangle basic investigations on the effects of wake-induced transition on the suction side boundary layer can be performed.

The principle of the wake generator is based on cylindrical bars fastened to two rubber timing belts moving in front of and behind the cascade. The timing belts, having a length of 4000 mm, span two main pulleys with a diameter of 400 mm positioned above and below each cascade. The distance between the trailing edge of each cascade and the returning bars is large enough that the flow in the blade passages is not disturbed and to allow the traverse of all probe types usually employed during the tests. The driving pulley is positioned on the lower main shaft and is connected by a timing belt to the a.c. electric motor using a 1:1 transmission ratio. The water-cooled motor has a nominal maximum power of 10 kW at 3000 rpm. With the motor the bars can be moved in both directions for simulating the rotor–stator interaction of compres-

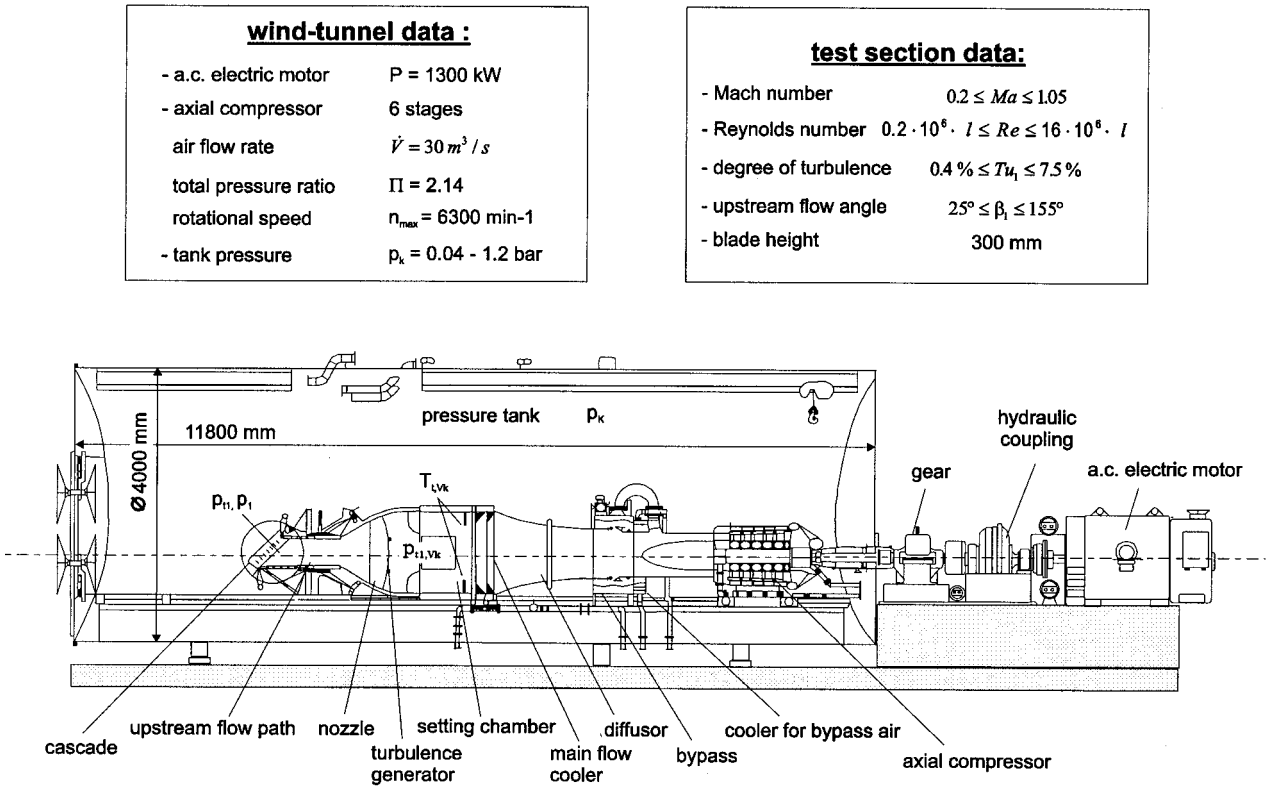

Fig. 1 High-speed cascade wind tunnel

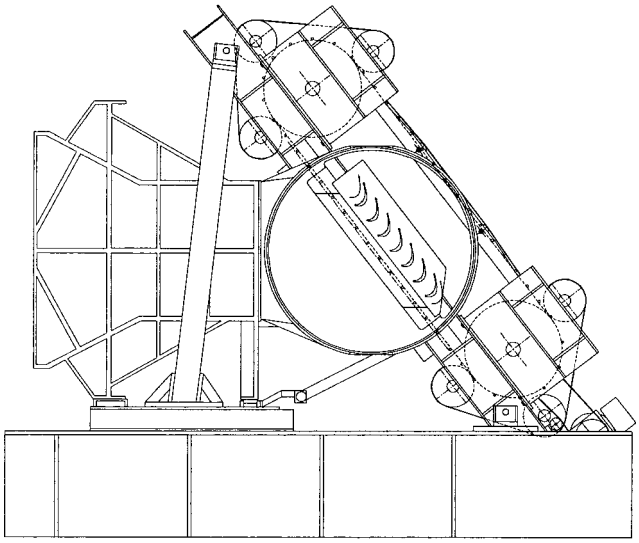

Fig. 2 Generator of unsteady inlet flow conditions

Table 1 Design data for wake generator

Bar diameter	2 mm
Bar pitch	Min. 10 mm
Bar velocity	1–40 m/s
Maximum number of bars	400
Strouhal-numbers in tested cases	Sr = 0.26 – 1.06
Axial gap between bar plane and cascade inlet plane	$0.75 * l_{ax}$

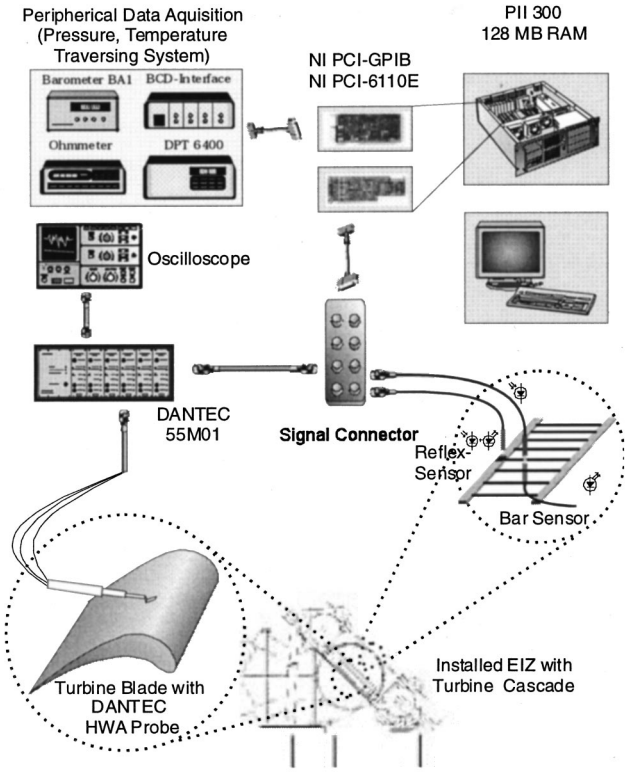

Fig. 3 HWA data acquisition system

sor as well as of turbine stages. The velocity of the motor can be digitally controlled with an accuracy of 0.1 rpm from 100 to 3000 rpm.

In order to avoid disturbances of the inlet flow due to the timing belts in front of the cascades, it was necessary to reduce the width of the test section to 176 mm. Thus, the blade aspect ratio for the used cascade was reduced to 1.76, too. Due to flow visualizations with the oil-and-dye technique on the blade surface of the cascade and with a flow field traverse downstream ($x/l_{ax}=1.5$) of the cascade, a two-dimensional flow at midspan of the turbine cascade had been assured.

Pneumatic Measurements. Measurements of the surface pressure distribution and wake traverses in a plane $x/l_{ax}=1.5$ downstream of the cascade inlet plane have been performed. All measurements have been taken at midspan of the turbine cascade. The surface pressure distribution has been measured utilizing a Scanivalve SDIU-System, and the wake traverses have been conducted with a five-hole probe and a PSI DPT6400-Pressure-Measurement-System evaluated according to Amecke [17] and Ganzert and Fottner [18].

New Hot-Wire Anemometry Data Acquisition System. In order to control the acquisition and evaluation of peripheral and HWA data for steady and periodic unsteady inflow conditions, a software package was developed (WINSMASH [19]).

The software is highly modular and flexible for many different test applications. All features are embedded in a user-friendly Microsoft Windows based graphical user interface. When programming the software, parts of the software for profile pressure distribution measurements (WINPANDA [18]) were used. WINSMASH is able to handle one-dimensional and three-dimensional, steady and periodic unsteady measurements just as measurements with film cooling injection. Furthermore, different traversing applications are possible such as boundary layer profiles and boundary layer planes perpendicular to the profile surface; even wake and field traverses downstream of the cascade are installed. The software package includes probe calibration routines for the velocity and directional (three-dimensional probes) characteristics as well. The data reduction of the peripheral data is performed within the measurement routines in order to monitor the current cascade main flow conditions. The HWA signals are saved in binary files for further off-line evaluation which is implemented as well for one-dimensional and three-dimensional, steady and periodic unsteady measurements.

In order to prove the capacity of WINSMASH first results are shown for one-dimensional steady and periodic unsteady boundary layer profiles of a highly loaded turbine blade.

HWA Measurements. The complete HWA data acquisition system is shown in Fig. 3. The monitoring of the test facility, the traversing system and the HWA data acquisition is controlled by a P II 300 Intel PC. The peripheral data acquisition and the traversing system are controlled via GPIB bus. The turbulence intensity and the velocity deficit due to the bars in each cascade inlet plane have been measured with a standard HD hot-film probe (DANTEC HF-55R01), the boundary layer profiles are measured by hot-wire probes (DANTEC HW-55P15). Both are connected to a constant-temperature bridge of the type DANTEC 55M01. The analog anemometer output is digitized by a National Instruments DAQ board PCI-6110E. The board allows four analog inputs with 5 mega samples per second simultaneous sampled with 12-bit resolution. For the measurements with periodic unsteady inflow conditions a once-per-revolution trigger is used to start the HWA signal acquisition of each data block. The fourth analog input channel is used for the detection of each bar.

The sensor calibration has been performed in the cascade inlet plane of the wind tunnel test section and a fourth-order polynomial has been used for the approximation of the calibration curve.

Glue-on Hot-Film Measurements. Wake induced transition is qualitatively mapped by employing a simultaneous surface hot-

film CTA anemometry system (DANTEC-Streamline) [20]. Twelve SENFLEX hot-film sensors have been logged simultaneously. Totally 24 hot-film sensors spaced 2.5 mm apart have been used to detect the location and the mode of transition by the normalized rms value of the anemometer output signal.

Data Reduction. For both measurements the well-established ensemble average technique has been applied to evaluate the raw data, using 300 ensembles each consisting of five, wake passing periods.

The ensemble average of a time-dependent quantity b is given by:

$$\tilde{b}(t)=\frac{1}{N}\cdot\sum_{j=1}^{N} b_j(t) \tag{1}$$

where N is the number of ensembles and the ensemble rms is given by:

$$\sqrt{\tilde{b}'^2(t)}=\sqrt{\frac{1}{N-1}\cdot\sum_{j=1}^{N}(b_j(t)-\tilde{b}(t))^2} \tag{2}$$

The skewness (third-order moment)

$$\mu_3(t)=\frac{1}{(\tilde{b}(t))^3}\cdot\frac{1}{N-1}\cdot\sum_{j=1}^{N}(b_j(t)-\tilde{b}(t))^3 \tag{3}$$

has also been calculated in order to gain a deeper insight into the boundary layer characteristics.

In the case of the one-dimensional hot-film and hot-wire data, b is set to the velocity and for the glued-on hot-film data to the anemometer output voltage.

For the calculation of the integral boundary layer parameters the boundary layer thickness δ is be determined:

$$\delta(t)=y\cdot\left(\frac{w(y,\,t)}{w_\infty}=0.99\right) \tag{4}$$

The boundary layer displacement thickness δ_1 is calculated from:

$$\delta_1(t)=\int_0^{\delta(t)}\left[1-\frac{\rho(y,\,t)\cdot w(y,\,t)}{\rho(\delta(t),\,t)\cdot w(\delta(t),\,t)}\right]dy \tag{5}$$

The boundary layer momentum thickness δ_2 is obtained from:

$$\delta_2(t)=\int_0^{\delta(t)}\frac{\rho(y,\,t)\cdot w(y,\,t)}{\rho(\delta(t),\,t)\cdot w(\delta(t),\,t)}\left[1-\frac{w(y,\,t)}{w(\delta(t),\,t)}\right]dy \tag{6}$$

The shape factor H_{12} results from the quotient of δ_1 and δ_2:

$$H_{12}(t)=\frac{\delta_1(t)}{\delta_2(t)} \tag{7}$$

For the steady measurements there is no dependence in time.

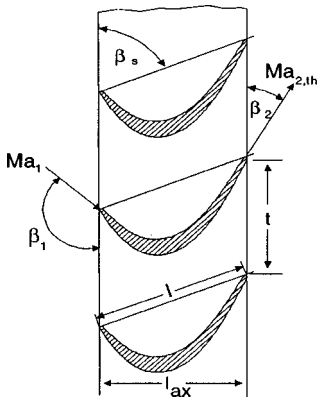

Aerodynamic Design	
β_s	68.69 °
β_1	135 °
β_2	29.5 °
Ma_1	0.38
$Ma_{2,th}$	0.70
$Re_{2,th}$	100000

Fig. 4 Aerodynamic design and exemplary sketch

High Lift Linear LP Turbine Cascade. The measurements have been performed on a highly loaded low-pressure turbine linear cascade (see Fig. 4). The turbine cascade, representing a current high-lift LP turbine design (see [9]), is specifically designed in order to take advantage of the positive effect of rotor–stator interaction on the suction side boundary layer.

Results

The measurements presented in this paper are an extract of a systematic test program. Using different measurement techniques when varying the Reynolds number for steady ($Sr=0$) and periodic unsteady ($Sr=0.26$) inflow conditions deliver manifold opportunities for evaluating the data set. In order to show the options of the data acquisition and evaluation system, the paper focuses on the design conditions of the utilized cascade at $Ma_{2,th}=0.7$ and $Re_{2,th}=10{,}000$.

Wake Intensity. Ensemble-averaged velocity and turbulence intensities for five wake passing periods are shown in Fig. 5. The velocity deficit of $\Delta U/U_{max}$ of about 9 percent as well as the turbulence level of $Tu_1=1.5-2$ percent between two wakes are in a good agreement with realistic LP turbine conditions.

Isentropic Mach Number Distribution. The isentropic Mach number distributions determined by pressure taps at midspan (28 SS; 21 PS) for the steady and unsteady inflow conditions are given in Fig. 6. The overall Mach number level declined for periodic unsteady inflow conditions. Both distributions show a laminar separation bubble on the SS in the trailing edge region ($0.8<x/l_{ax}<1$). As expected the laminar separation bubble seems to be weaker for the periodic unsteady inflow conditions. The transition point moves upstream for periodic unsteady inflow conditions. Hereby the start of a plateau-like distribution of Ma_{is} describes the location of the separation point of a laminar separation bubble detected. The intersection point of the tangents on the Ma_{is} distribution thereby detects the transition point in the region of the laminar separation bubble (see exemplary zoom out Fig. 6, cf. [9]), where an intermittence of 50 percent occurs.

Boundary Layer Profile. Using the ensemble-average evaluation technique, the HWA measurements provide the time-resolved boundary layer velocity and turbulence profile for periodic unsteady inflow conditions. The results at $x/l_{ax}=0.8792$ are shown in Fig. 7. At this position close to the trailing edge the velocity profile is still giving a clue of the passing wake. After a

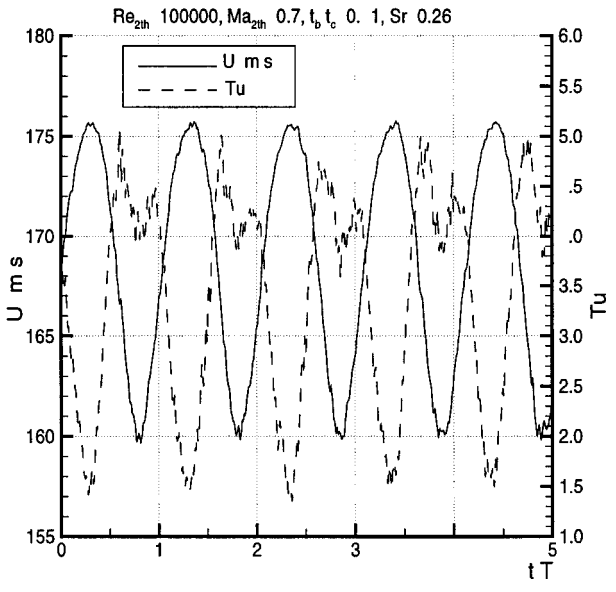

Fig. 5 Wake turbulence intensity and velocity distribution

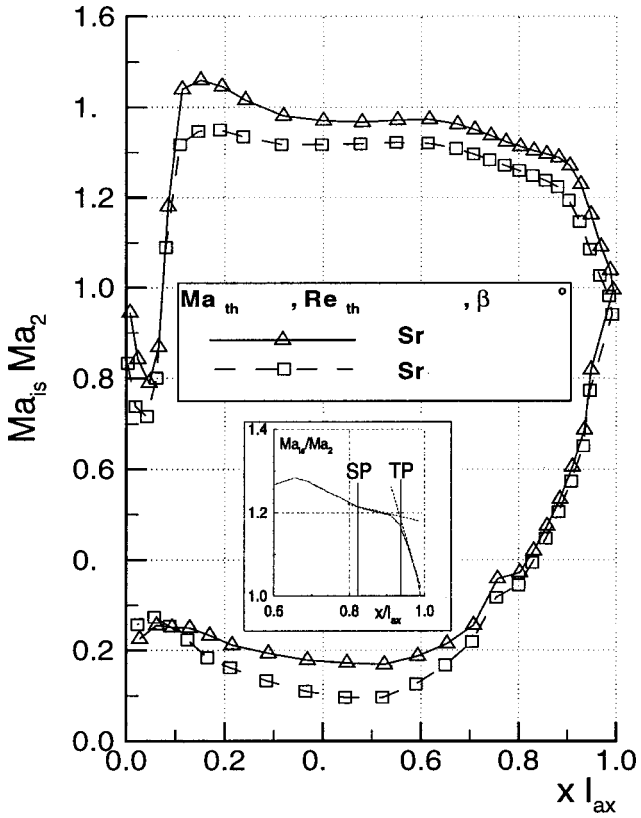

Fig. 6 Isentropic Mach number distributions

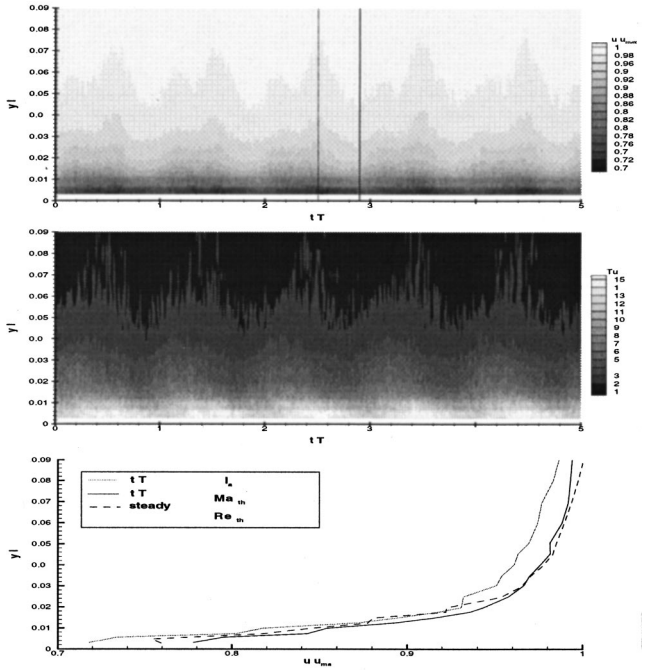

Fig. 7 Boundary layer velocity and turbulence profile

period of high velocities (e.g., $t/T=1.9$) the wake influence is displayed by a deceleration (e.g., $2.1<t/T<2.5$). However, the velocity deficit inside the wake is rather displayed as a double peak. This phenomenon is more distinct farther upstream even though the turbulence intensity seems to be unaffected.

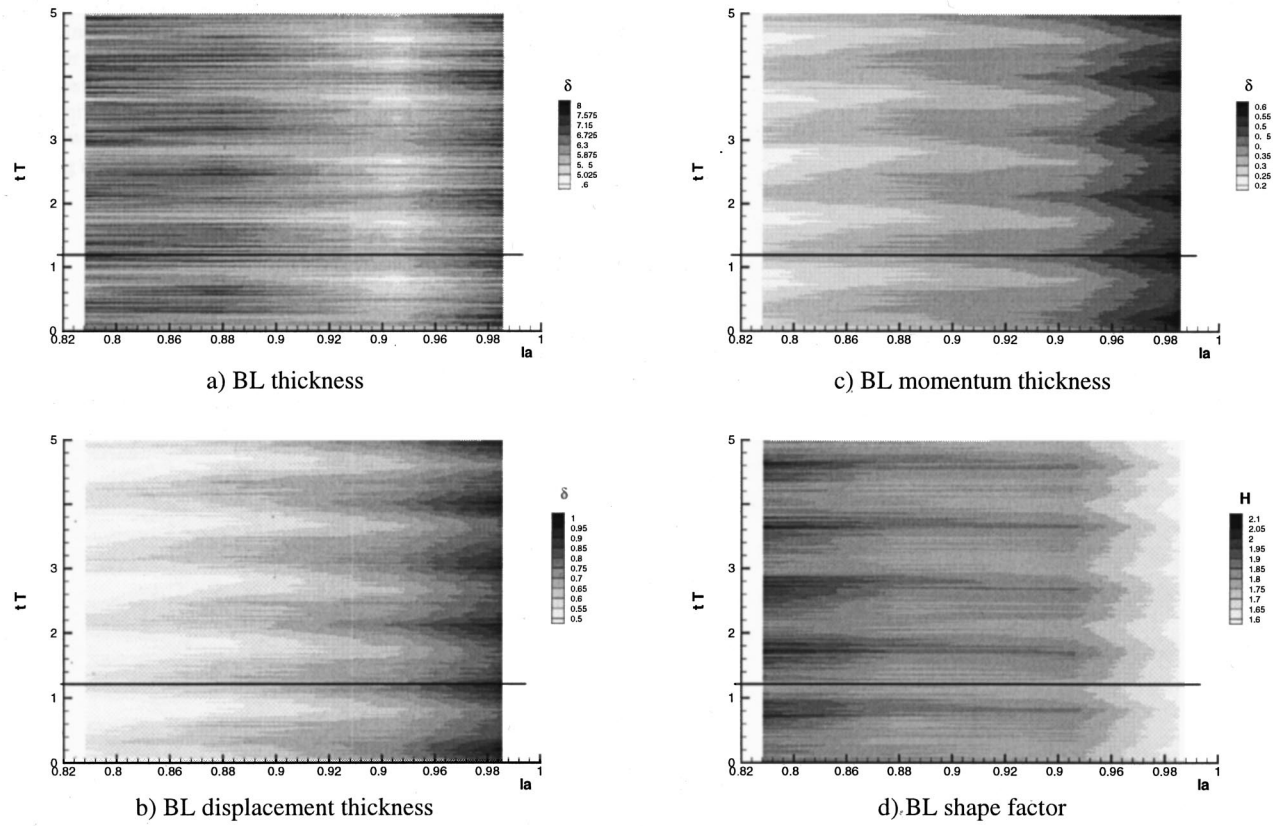

Fig. 8 Time-resolved integral layer parameter

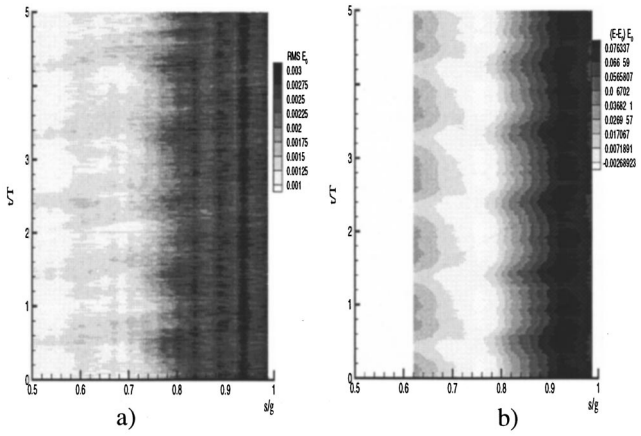

Fig. 9 Ensemble-averaged glue-on hot-film results: (*a*) rms value; (*b*) quasi-wall shear stress distribution

In order to compare the results of steady and periodic unsteady inflow conditions, the boundary layer velocity profiles for two marked time steps and the profile for the steady measurement are plotted in Fig. 7.

As expected the velocity during the wake passing period is lower than for steady inflow conditions, whereas the time step with the highest velocities shows nearly the same values as at steady inlet flow. This could lead to the conclusion that between two wakes passing, a quasi-steady boundary layer, as it would occur at steady inflow conditions, is established.

Integral Boundary Layer Parameters. The time-resolved integral boundary layer parameters result from applying Eqs. (4)–(7) on the ensemble averaged velocity profiles, which are displayed in Fig. 7. The passing wake increases the boundary layer thickness δ (Fig. 8(*a*)) whereas a decrease is induced by the accelerated flow between two wakes. At $x/l_{ax}=0.95$, the periodic unsteady inflow conditions seem to suppress the separation. The rather full velocity profile of the becalmed region, which occurs after a wake has passed, causes a decreasing boundary layer thickness, which increases again farther downstream by the influence of the next passing wake.

On the other hand, the boundary layer displacement thickness δ_1 (Fig. 8(*b*)) increases continuously in the streamwise direction. Nevertheless, the influence of periodic unsteady inflow conditions is much more visible for δ_1 than for δ. Considering the displacement thickness and the momentum thickness δ_2 (Fig. 8(*c*)) it is obvious that the incoming wakes effectuate an increase of the level of these boundary layer parameters.

The momentum thickness, which represents the degree of loss production in the boundary layer, shows that the influence of the wake shifts the high loss production of the boundary layer into an upstream position. Between two wakes the main loss production again occurs mainly in the trailing edge region ($x/l_{ax}\geqslant 0.96$).

The shape factor H_{12} (Fig. 8(*d*)) gives a clue of the velocity distribution inside the boundary layer and is often used as an indicator for the turbulence of a boundary layer. The time–space diagram of the shape factor H_{12} detects a more turbulent boundary layer ($H_{12}\approx 1.7$) in the whole region influenced by the wake. Furthermore, it is shown that the becalmed region, between two wakes passing, can be detected by a higher level of the shape factor ($H_{12}=1.9$; $0.83\leqslant x/l_{ax}\leqslant 0.94$), which indicates a more laminar character of the suction side boundary layer compared to the wake-induced boundary layer.

Ensemble-Averaged Glue-on Hot-Film Results. In Fig. 9 ensemble-averaged glue-on hot-film results are shown. The HWA boundary layer results as well as the measured data of the hot film sensors, glued on the suction side of the investigated turbine cascade, show a clear influence of the passing wakes. High-level the rms values detect the transition region on the suction side. It can be seen that the transition region is shifted upstream by the passing wake. Between two wakes passing the transition moves downstream again, to a position where it would occur at steady inlet flow conditions. Also the quasi-wall shear stress distribution ($(E-E_0)/E_0$) is influenced by the passing wake in such a way that the level of quasi-wall shear stress is increased by the passing wake.

Conclusions

A new data acquisition system for HWA measurements at the High-Speed Cascade Wind Tunnel of the Universität der Bundeswehr München has been implemented and tested successfully. The new software WINSMASH comprises calibrating routines as well as evaluation tools for one-dimensional and three-dimensional HWA probes. Measurements are possible for different traversing tasks. Peripheral data acquisition and main flow monitoring is implemented for steady and periodic unsteady inflow conditions.

The results presented in this paper, focused on a high-lift low-pressure turbine blade at design conditions, showed:

- Periodic unsteady inflow conditions generate a periodically increased boundary layer thickness
- Between two wakes passing quasi-steady flow conditions are re-established
- The high values for the integral boundary layer parameters δ_1 and δ_2 are shifted upstream by the passing wake as well as the transition region (rms/E_0)
- The boundary layer at the trailing edge has a more turbulent character within the region of the passing wake.

It could be pointed out that the results are in a good agreement between the new measurement system and the already established measurement techniques at the Institut für Strahlantriebe. Therefore the new HWA data acquisition and evaluation system is a good supplement for investigating wake-induced transition phenomena and boundary layer development.

Acknowledgments

The reported work was performed within a research project that is part of the national research co-operation ''AG TURBO.'' The project has been supported by the German Ministry of Education, Science, Research and Technology (BMBF) and the BMW Rolls-Royce GmbH. The permission for publication is gratefully acknowledged.

Nomenclature

c_{ax} = axial velocity, m/s
b = variable
E = anemometer voltage, V
f = frequency, Hz
h = airfoil height, m
H_{12} = boundary layer shape factor
l = chord length, m
N = number of ensembles
p, p_t = static pressure, total (stagnation) pressure, Pa
t = pitch, time, m/s
T = time period between two wakes, s
T_t = total (stagnation) temperature, K
Tu = turbulence intensity, percent
U, w = velocity, m/s
x = coordinate along axial chord length, m
y = coordinate normal to the blade surface, m
β = circumferential (pitchwise) flow angle, deg
β_s = stagger angle, deg
δ = boundary layer thickness, m
δ_1 = boundary layer displacement thickness, m

δ_2 = boundary layer momentum thickness, m
ρ = density, kg/m^3
ω = loss coefficient $=(p_{t1}-p_{t2})/(p_{t1}-p_K)$

Subscripts and Superscripts

1, 2 = inlet and outlet flow conditions
2th = downstream conditions for isentropic flow
ax = axial
b = bar
c = cascade
is = isentropic
K = pressure tank
t = total
$\sim$ = ensemble averaged

Abbreviations

BL = boundary layer
CTA = Constant Temperature Anemometry
HWA = Hot Wire Anemometry
Ma = Mach number
Re = Reynolds number
rms = root-mean-square
Sr = Strouhal number $=f^*l/c_{\mathrm{ax}}$
WINSMASH = Windows *S*oftware for Measurement and *A*nalytical Evaluation of Signals from Hot-Wire Anemometry

References

[1] Schulte, V., 1995, ''Unsteady Separated Boundary Layers in Axial-flow Turbomachinery,'' PhD thesis, Cambridge University.
[2] Schulte, V., and Hodson, H. P., 1998, ''Unsteady Wake-Induced Boundary Layer Transition in High Lift LP Turbines,'' ASME J. Turbomach., **120**, pp. 28–35.
[3] Hodson, H. P., 1998, ''Blade Row Interference Effects in Axial Turbomachinery Stages: Bladerow Interactions in Low Pressure Turbines,'' VKI Lecture Series 1998-02.
[4] Mayle, Robert Edward, 1991, ''The 1991 IGTI Scholar Lecture: The Role of Laminar–Turbulent Transition in Gas Turbine Engines,'' ASME J. Turbomach., **113**, pp. 590–537.
[5] Halstead, D. E., Wisler, D. C., Okiishi, T. H., Walker, G. J., Hodson, H. P., and Shin, H.-W., 1997, ''Boundary Layer Development in Axial Compressors and Turbines: Part 3 of 4—LP Turbines,'' ASME J. Turbomach., **119**, pp. 225–237.
[6] Schulte, V., and Hodson, H. P., 1998, ''Prediction of the Becalmed Region for LP Turbine Profile Design,'' ASME J. Turbomach., **120**, pp. 839–846.
[7] Curtis, E. M., Hodson, H. P., Banieghbal, M. R., Howell, R. J., and Harvey, N. W., 1997, ''Development of Blade Profiles for Low-Pressure Turbine Applications,'' ASME J. Turbomach., **119**, pp. 531–538.
[8] Harvey, N. W., Cox, J. C., Schulte, V., Howell, R., and Hodson, H. P., 1999, ''The Role of Research in the Aerodynamic Design of an Advanced Low Pressure Turbine,'' ImechE Conference Transactions/Vol. A: 3rd European Conference on Turbomachinery, C557/043, pp. 123–132.
[9] Brunner, S., Fottner, L., Schulte, V., and Kappler, G., 1999a, ''Investigation of Wake-Induced Transition on a Highly Loaded Low-Pressure Turbine Cascade,'' ImechE Conference Transactions/Vol. A: 3rd European Conference on Turbomachinery, C557/068, p. 231 ff.
[10] Schröder, Th., 1991, ''Investigations of Blade Row Interaction and Boundary Layer Transition Phenomena in a Multistage Aero Engine Low-Pressure Turbine by Measurements With Hot-Film Probes and Surface-Mounted Hot-Film Gauges,'' Von Karman Institute for Fluid Dynamics, Lecture Series 1991-06.
[11] Arndt, N., 1993, ''Blade Row Interaction in a Multistage Low-Pressure Turbine,'' ASME J. Turbomach., **115**, pp. 137–146.
[12] Banieghbal, M. R., Curtis, E. M., Denton, J. D., Hodson, H. P., Huntsmann, I., and Schulte, V., 1995, ''Wake Passing in LP Turbine Blades,'' AGARD CP 571, Paper 23.
[13] Acton, P., and Fottner, L., 1996, ''The Generation of Instationary Flow Conditions in the High Speed Cascade Wind Tunnel,'' 13th Symposium on Measuring Techniques.
[14] Sturm, W., Fottner, L., 1985, ''The High-Speed Cascade Wind-Tunnel of the German Armed Forces University Munich,'' 8th Symposium on Measuring Techniques.
[15] Pfeil, H., and Eifler, J., 1979, ''Turbulenzverhältnisse hinter rotierenden Zylindergittern,'' Forschung im Ingenieurwesen, **42**.
[16] Brunner, S., and Fottner, L., 1999, ''Untersuchungen zum Einfluß der Rotor–Stator Interaktion auf die saugseitige Transition eines hochbelassteten ungekühlten Niederdruck-Turbinengitters,'' DGLR-JT99-078.
[17] Amecke, J., 1967, ''Auswertung von Nachlaufmessungen an ebenen Schaufelgittern,'' Bericht 67A49, AVA Göttingen.
[18] Ganzert, W., and Pottner, L., 1996, ''WINPANDA—an Enhanced PC-Based Data Acquisition System for Wake and Profile Distribution,'' 13th Symposium on Measuring Techniques.
[19] Wolff, S., 1999, ''Konzeption, Programmierung and Erprobung eines PC-gesteuereten Meßsystems zur Aufnahme und Auswertung von 1-D and 3-D-Hitzdraht-Signalen am Hochgeschwindigkeits-Gitterwindkanal als Ersatz des HP-Systems,'' Institute Report WOIB9909.
[20] Brunner, S., Teusch, R., Stadtmüller, P., and Fottner, L., 1998, ''The Use of Simultaneous Surface Hot Film Anemometry to Investigate Unsteady Wake Induced Transition in Turbine and Compressor Cascades,'' 14th Symposium on Measuring Techniques.

Secondary Flow Measurements in a Turbine Passage With Endwall Flow Modification

Nicole V. Aunapu

Ralph J. Volino
email: volino@usna.edu

Karen A. Flack

Ryan M. Stoddard

Department of Mechanical Engineering,
United States Naval Academy,
Annapolis, MD 21402

A flow modification technique is introduced in an attempt to allow increased turbine inlet temperatures. A large-scale two half-blade cascade simulator is used to model the secondary flow between two adjacent turbine blades. Various flow visualization techniques and measurements are used to verify that the test section replicates the flow of an actual turbine engine. Two techniques are employed to modify the endwall secondary flow, specifically the path of the passage vortex. Six endwall jets are installed at a location downstream of the saddle point near the leading edge of the pressure side blade. These wall jets are found to be ineffective in diverting the path of the passage vortex. The second technique utilizes a row of 12 endwall jets whose positions along the centerline of the passage are based on results from an optimized boundary layer fence. The row of jets successfully diverts the path of the passage vortex and decreases its effect on the suction side blade. This can be expected to increase the effectiveness of film cooling in that area. The row of jets increases the aerodynamic losses in the passage, however. Secondary flow measurements are presented showing the development of the endwall flow, both with and without modification. [S0889-504X(00)01004-7]

Introduction

To achieve higher cycle efficiency and increase power from gas turbine engines, turbine inlet temperatures should be as high as possible. Over the past several decades improvements have been made through the use of advanced materials and innovative cooling schemes, allowing turbine inlet temperatures to approach 2000 K [1]. Even with modern cooling techniques, however, ''hot spots'' still occur along the turbine airfoils, due to the complex secondary flow between adjacent blades, limiting a move to even higher temperatures.

Effective film cooling of turbine airfoils is complicated by secondary flows, such as endwall vortices. The dominant features of the secondary flow in a turbine passage are the horseshoe vortex, which forms at the blade leading edge–endwall junction, and the endwall crossflow. These are illustrated in Fig. 1, which is a simplified version of a figure presented by Goldstein and Spores [2]. The features presented in Fig. 1 are those most pertinent to the present study. The actual flow is more complex with additional vortices. Wang et al. [3] provide a more detailed description and illustration of the flow. Langston et al. [4] and others have presented similar models. Sieverding [5] provides a review of several models. All models indicate that a horseshoe vortex forms at the junction of the leading edge of each airfoil and the endwall. The suction side leg of this vortex wraps around the suction surface of the blade, while the pressure side leg migrates across the passage, due to the pressure gradient, combines with the endwall crossflow to form the passage vortex, and impinges upon the suction side of the neighboring airfoil. The passage vortex may merge with the suction side leg of the horseshoe vortex of the adjacent blade [6] or they may remain distinct [2]. In either case, they lift up off the endwall and increase in size. Figure 1 shows the passage vortex impinging upon the suction surface at point *C* and then climbing up the blade as it moves downstream. This vortex washes away the film cooling air on the surface of the blade, thus resulting in a triangular shaped hot spot, as documented by Chung and Simon [7], Goldstein et al. [8], and others.

Secondary flows are also of interest from an aerodynamics standpoint. The highest aerodynamic losses in an engine may occur in the endwall region. Various methods have been developed to study and modify the secondary flow between two adjacent blades. Duden et al. [9] attempted to modify the secondary flow by applying endwall contouring and three-dimensional airfoil design in the endwall region. Their modifications resulted in improvements in the radial extent of the secondary flow and a decrease in secondary losses. The increased blockage caused by these modifications, however, increased profile and inlet losses in the test section. Michelassi et al. [10] conducted a similar study using nonsymmetric endwall contouring. Dossena et al. [11] compared a contoured and a planar configuration of a linear turbine cascade. They found that endwall contouring influenced the gen-

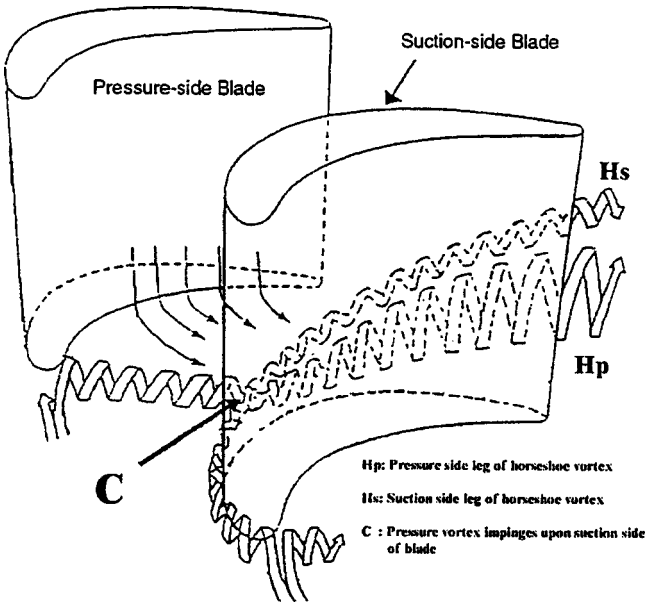

Fig. 1 Schematic of horseshoe vortex impinging upon suction-side blade [2]

Contributed by the International Gas Turbine Institute and presented at the 45th International Gas Turbine and Aeroengine Congress and Exhibition, Munich, Germany, May 8–11, 2000. Manuscript received by the International Gas Turbine Institute February 2000. Paper No. 2000-GT-212. Review Chair: D. Ballal.

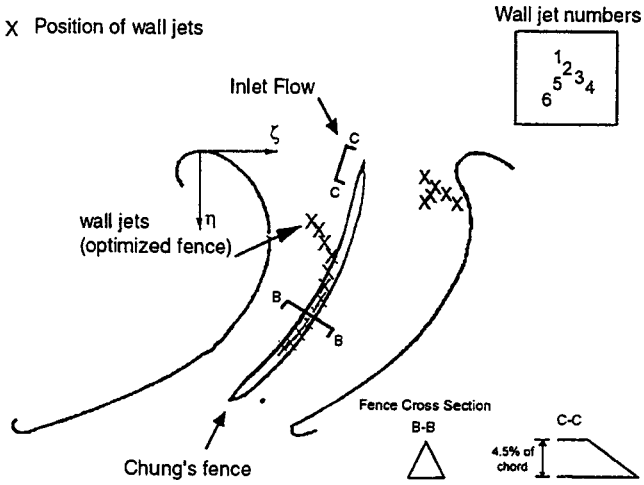

Fig. 2 Top view of test section showing flow control schemes: location of endwall fence as used by Chung and Simon [7]; location of upstream jets (numbered 1–5); location of optimized boundary layer fence and endwall centerline jets

eration of the passage vortex and inhibited its development through strong acceleration, while lowering secondary losses in the passage.

In another study, Chung et al. [7,12,13] used a boundary layer fence, inserted on the endwall between two adjacent blades. The fence cross section was an equilateral triangle. Its height and length were 4.5 and 88 percent of the chord length, respectively. The fence was located as shown in Fig. 2, with its leading edge at the center of a line connecting the leading edges of the pressure and suction side airfoils. The fence acted like a ramp to lift the vortex up off the endwall to be washed away by the main flow. It was effective in preventing the vortex from growing to its full potential strength and diverting it away from the suction surface. Since the influence of the secondary flow on the suction wall was reduced, film cooling would be more effective in that area. The fence also reduced aerodynamic losses due to secondary flow within the passage. In practice problems may arise due to a need to cool the fence itself [12].

The objective of the present study was to develop a method to reduce the harmful effects of secondary flow in a turbine passage without adversely affecting the aerodynamic performance of the turbine. As with the fence used by Chung and Simon [7], an attempt was made to divert the path of the passage vortex so that it would be washed away by the main free-stream flow. This would increase the effectiveness of film cooling, and the weakening of the vortex might decrease the aerodynamic losses in the passage. A second objective was to provide documentation of the secondary flow both with and without modification. Several studies have described endwall flows, and a few such as Gregory-Smith and Cleak [14] and Kang and Thole [15] provide quantitative data on mean flow and turbulence quantities. The present study continues this documentation, and by considering cases with modified flow, may provide further insight into the flow behavior.

Endwall blowing was used in an attempt to achieve these objectives. It was hypothesized that jets might be used to manipulate the secondary flow, either by blowing the passage vortex away from the endwall, or diverting it away from the suction surface, similar to the action of a boundary layer fence. Holes for jets could be machined into the endwall, similar to film cooling holes, and used with compressor bleed air. Alternatively, a slot might be used, possibly utilizing the gap leakage flow between adjacent airfoils. Chyu et al. [16] provide a study of gap leakage. Unlike film cooling injection, which typically utilizes shallow injection angles and low blowing rates to provide a film of cooling air on a surface, jets for vortex control would be blown normal to the endwall with sufficient momentum to influence the secondary flow.

The use of jets would circumvent the problem of having to manufacture and cool a fence. Unlike endwall contouring, there would be no need to change the geometry of a passage, which might be beneficial from an aerodynamics standpoint.

A few studies have considered the interaction between endwall blowing and a vortex. Ligrani and Mitchell [17] considered the effect of a vortex on film cooling. The airflow from the film cooling holes was relatively weak, so it did not affect the vortex dynamics. Johnston and Nishi [18] used ''vortex generator jets'' to create a vortex. To the authors' knowledge, there have been no previous attempts to control or suppress an existing vortex with wall jets.

Results are presented below for cases with two jet configurations and an optimized boundary layer fence, which was used to guide the second jet configuration.

Experimental Apparatus

Wind Tunnel and Turbulence Generator. Experiments were conducted in a low-speed, blown type wind tunnel located in the Aeronautics Laboratory at the United States Naval Academy. Three blowers draw air at room temperature into the wind tunnel. The blowers are followed by a diffuser, a settling chamber with a honeycomb, a screen pack, a second settling chamber, and a nozzle. The nozzle is a three-dimensional contraction, which reduces the wind tunnel cross-sectional area by a factor of 9.8 from 109 cm×109 cm to 18 cm×69 cm. The long dimension is vertical. A turbulence generator is attached to the nozzle and contains a two-dimensional bar grid. The grid is based on one used by Kim et al. [19] and consists of one vertical 3.8-cm-dia PVC pipe and six horizontal 3.2-cm-dia PVC pipes, evenly spaced across the nozzle outlet. The grid is followed by a 1-m-long rectangular settling chamber, which allows the flow to become uniform before entering the test section. Exiting the settling chamber, the free-stream turbulence intensity is 8 percent. The mean flow is uniform to within 3 percent, and the turbulence is isotropic and uniform to within 4 percent. For the conditions of the present study, the turbulence had integral length scales of 3 cm in the streamwise component and 1.3 cm in the vertical component.

Test Section. A large-scale, two half-blade test section is used to simulate a turbine passage, following the design and geometry of Chung and Simon [20]. It contains two turbine half-blades for suction and pressure sidewalls, a top and bottom endwall, and two flaps to guide the flow into the test section. Each

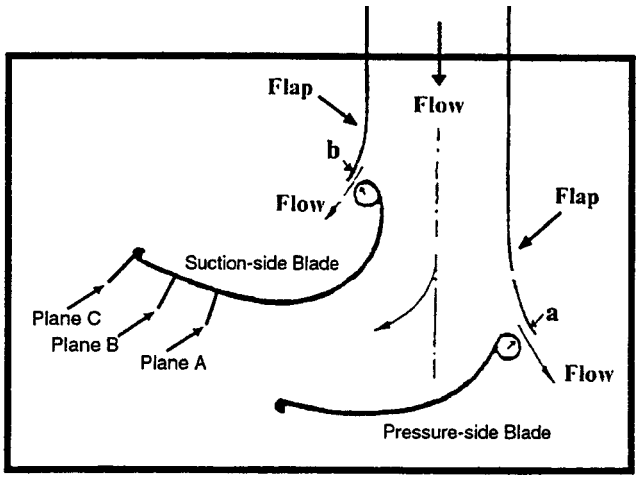

Fig. 3 Schematic of test section (top view) showing location of measurement planes A, B, and C

Table 1 Test section geometry and test conditions

	Chung (1992)	Present study
Chord (mm)	231	328
Pitch (mm)	178	252
Span (mm)	610	665
Aspect Ratio (H/C)	2.64	2.02
Solidity (C/P)	1.30	1.30
Inlet Angle (deg)	44.3	46
Outlet Angle (deg)	62.7	62
FSTI (%)	~10	~8
Re_c	2.1×10^5	1.8×10^5
Endwall δ_2/C at pressure-blade leading edge	0.011	0.010

half-blade has full leading and trailing edges, which along with the flaps provide the correct leading edge flow for each blade. A schematic of the test section is shown in Fig. 3. The geometry of the test section and the test conditions are summarized and compared with Chung and Simon's [7] test section geometry and conditions in Table 1. Chung and Simon closely match the multiblade cascade study of Chen and Goldstein [21].

The test section blade shape is the General Electric CF6-50 rotor profile, scaled up to have a chord length of 328 mm. The CF6-50 shape, while not particularly modern, allows direct comparison to previous studies. The full leading and trailing edges of the pressure-side blade are machined out of high-density foam and connected with transparent Plexiglas. The suction-side blade is machined out of foam. Eleven 0.3-mm-dia pressure taps are located along each half-blade, 356 mm above the endwall in a region where the flow is two dimensional.

The endwalls are constructed of 6.4-mm-thick clear Plexiglas. Both the top and bottom endwall have sharp leading edges that extend to the edge of the turbulence generator settling section. The height of the test section is 20 mm shorter than the exit of the settling section, providing 10 mm gaps at each endwall leading edge to remove the boundary layers which develop upstream. Two transparent Plexiglas flaps extend from the sides of the settling section to direct the flow into the test section. The flaps curve out past the leading edge of each half-blade. The gaps between the blades and the flaps, labeled *a* and *b* in Fig. 3, are adjustable. These gaps allow air to escape the test section. By controlling the size of the gaps, the flow around the leading edges of the blades is controlled. This affects the flow conditions, particularly the development of secondary flows, in the test section. The flaps were necessary to match the leading edge and secondary flow in an actual turbine or multiblade cascade.

Wall Jets. All wall jets used in this study were of the same type, but used in varying configurations. Holes were drilled and tapped into the bottom endwall to hold fittings for 6-mm-dia jets. Shop air was blown into a 9 liter Nalgene bottle, which served as a plenum. Twelve fittings were installed in the bottle wall and connected to the wall jet fittings with 4.8-mm-dia tubing. Jet velocity was controlled with a pressure regulator on the plenum inlet. When multiple jets were used simultaneously, clamps were placed on the tubing for each jet for individual adjustment. This insured that all jets had the same velocity to within 6 percent.

Instrumentation. A pressure transducer with a range of 0–3.5 in. H_2O was calibrated using a micromanometer and used for all pressure measurements. A Kiel probe was used for total pressure surveys. Kiel probes are total pressure probes designed for insensitivity to flow angle, making them suitable for use in regions of strong secondary flow.

A single sensor, boundary layer type hot-wire probe (TSI 1218-T1.5) and a hot-wire anemometer (TSI IFA 100) were used to measure the streamwise component of the test section inlet and outlet velocities, and the velocities of the wall jets. A cross-wire (TSI 1243-T1.5) was used to check the inlet free-stream turbulence isotropy and acquire data for spectra and length scale calculations.

Secondary flow velocities were measured using a single component Laser Doppler Velocimeter (LDV). The LDV system (Dantec Flowlite) uses a 10 mW helium neon laser with Gaussian beam diameter of 0.168 mm and crossing angle of 5 deg. Each plane of interest was surveyed twice with the beams in two different orientations to obtain two velocity components.

A sonic nozzle water sprayer was used to seed the flow for the LDV. The water sprayer used compressed shop air to jet-pump distilled water and produce a fine spray (droplets<5 μm in diameter). The spray was injected through a 3.8 cm hole at the bottom of the wind tunnel, upstream of the contraction. The seeding had no measurable effect on the flow turbulence when the turbulence grid was in use.

Flow Visualization. Various tufts were used to show the direction of shear stress on the endwall and the location of the passage vortex. A long tuft of about the chord length was particularly illustrative when placed near the endwall. The tuft would become entrained in the passage vortex, wrapping around it as it crossed the passage, grew in size, and climbed the suction surface. A vorticity detector was also used to locate the vortex. This detector is a small pinwheel with paddles parallel to the axis of rotation. The vorticity detector is placed in the test section with its axis pointed upstream. The spinning of the pinwheel indicates the location of a vortex. Both the tuft probe and the vorticity detector were used as preliminary tools to visualize the flow in the passage. The locations and cases that appeared interesting were then documented with more permanent techniques such as ink dot visualization.

The ink dot flow visualization technique was used on the suction surface as well as the endwall. This technique, introduce by Langston and Boyle [22], provides a permanent record of the endwall shear stress as shown by ink traces. A grid pattern of dots was placed on a sheet of contact paper with a permanent marker. The contact paper was then taped to the endwall or blade and sprayed with a uniform thin layer of 99.5 percent isopropyl alcohol. In their study, Langston and Boyle used oil of wintergreen as a solvent. Simon et al. [23] substituted isopropyl alcohol and found that it would also suffice. The alcohol dissolves the ink dots, the wind tunnel is turned on, and upon exposure to flow, the ink moves in the direction of the shear stress on the wall. The alcohol evaporates and the ink traces dry, leaving a permanent record of the wall shear stress. About 45 seconds are required per run. This technique is useful for showing the endwall flow pattern and the effect of the passage vortex on the suction surface.

Results

Baseline Case—No Flow Modification. The main characteristics of the flow in the passage were matched to those of Chung and Simon [7] to qualify the test section and provide a comparison case for evaluation of flow modification techniques. The Reynolds number, based on inlet velocity and chord length, was set at 2×10^5. This is a somewhat low but still representative Reynolds number for a high pressure turbine. The normalized velocity distribution along the airfoil surfaces (computed from local pressure measurements along the blades) is presented in Fig. 4. Also shown for comparison are results from Chung [13] and predicted values supplied by General Electric. The present case compares well with the expected values, matching to within 9 percent.

To insure that the proper secondary flow was modeled in the passage (as opposed to simply the flow in a curved channel), several steps were taken. As noted above, the full leading edges of both the pressure and suction side blades were modeled. Bleed air was allowed to escape the passage around the leading edges, as shown in Fig. 3. This insured that horseshoe vortices would form at the leading edge–endwall junctions. The endwall boundary

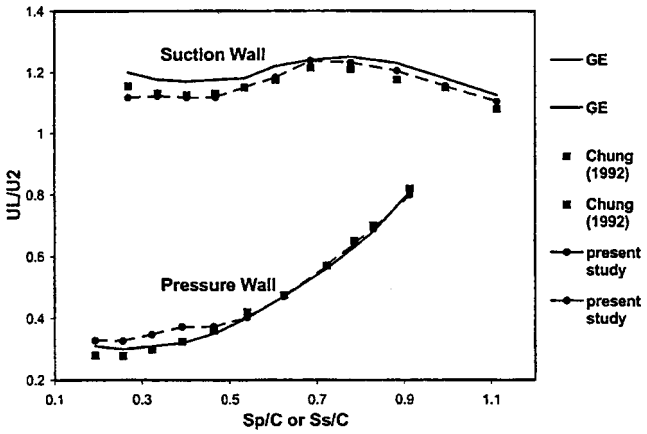

Fig. 4 Normalized velocity distribution along the blade surfaces

layer thickness also plays an important role in determining the secondary flow in the passage. The LDV was used to measure the boundary layer thickness at a location 25.5 cm upstream of the leading edge of the pressure-side blade, near the center of the passage. Following the procedure of Chung and Simon [7], δ_2/C was calculated and extrapolated to the leading edge of the pressure-side blade, assuming flat plate, zero pressure gradient, turbulent boundary layer growth. The boundary layer was tripped using a 3-mm-dia Tygon tube at the entrance of the test section, just after the settling section. The size of the trip was selected so that δ_2/C matched the value reported by Chung and Simon [7], as shown in Table 1.

The ink dot flow visualization technique was employed on the endwall to determine the location of the saddle point (the intersection of separation and reattachment lines of the endwall boundary layer) and is shown in Fig. 5. The endwall shear stress pattern matches those of Chung and Simon [20] and the cascade study of Chen and Goldstein [21], providing confidence that the desired secondary flow has been created. The location of the passage vortex can be seen downstream of the saddle point, near the

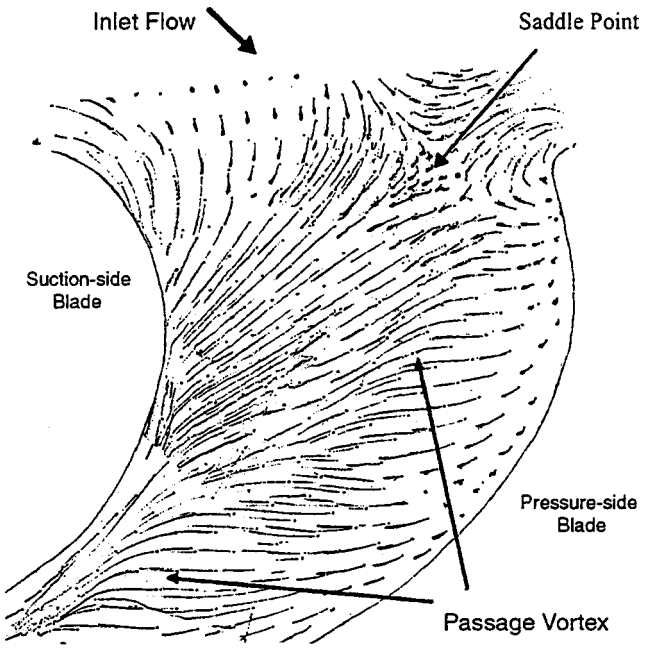

Fig. 5 Ink dot flow visualization on the endwall: baseline case

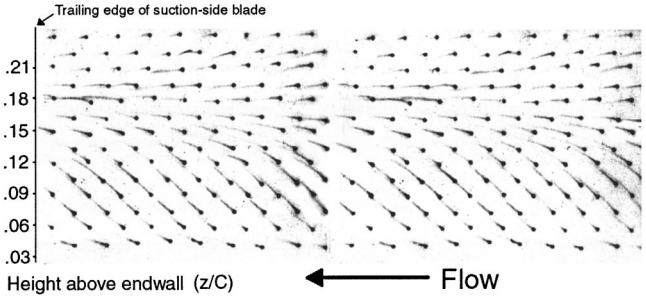

Fig. 6 Ink dot flow visualization on the suction-side blade: baseline case

leading edge of the pressure-side blade, and continuing across the passage toward the suction-side blade. The ink dot traces show the clockwise sense of rotation of the passage vortex (view looking upstream). This is the sense of rotation of the vorticity of the inlet boundary layer as discussed by Langston et al. [22]. Oil and lampblack visualization was also used to confirm the path of the vortex.

Ink dot visualization also provides a clear image of the shear stress on the suction surface, as shown in Fig. 6. The technique was applied to a region 225 mm long (from $S_s/C=0.62$ to 1.31) and 100 mm high ($z/C=0$ to 0.30), flush with the endwall and extending to within 4 mm of the trailing edge of the blade. This is the region where the passage vortex impacts the suction surface. The clockwise rotation of the vortex moves the ink traces in an upward motion. Although each ink trace shows the direction of shear stress, not the magnitude, a general idea of the strength of the vortex can be deduced by the angle of inclination of the trace. The ink traces above the vortex are straight lines in the direction of the main flow, indicating that the passage vortex has no effect in this area. The slight downward inclination of some traces may be due to the fact that the ink dissolves in the alcohol and starts to run down, as a result of gravity, before the wind tunnel reaches its full velocity. It is also possible that the downward inclination of these traces may be due to smaller vortices such as the suction-side leg of the horseshoe vortex or the wall vortex, as documented by Wang et al. [3].

The secondary velocity field was measured in three planes, shown in Fig. 3 as Planes A, B, and C. Each plane was perpendicular to the suction surface and the endwall, and extended from the blade-endwall junction to at least 65 mm ($y/C=0.20$) away from the suction surface and 105 mm ($z/C=0.32$) above the endwall. Plane A was located at $S_s/C=0.80$, 171 mm upstream of the trailing edge of the suction surface, as measured along the surface. Plane B was at $S_s/C=0.99$, 106 mm upstream of the trailing edge, and Plane C was at the trailing edge ($S_s/C=1.32$). Figure 7 shows the mean velocity field in each plane. The length of the velocity vectors is proportional to the magnitude of the velocity in that direction. The center of the vortex can be seen near the junction of the endwall and the suction surface in Plane A. As the vortex moves downstream, Planes B and C clearly show how it impinges upon the suction surface, increases in size and moves up the blade. The vortex location agrees with that indicated by the suction surface ink dots traces (Fig. 6). Secondary kinetic energy loss coefficients were calculated from the velocity field using the equation:

$$C_{\mathrm{SKE}}=\frac{V^2+W^2}{U_1^2} \tag{1}$$

and are shown in the second row of Fig. 7. Note the high values along the suction surface, which again shows the action of the vortex on the blade, in agreement with Fig. 6.

Total pressure was measured in the same planes as the secondary velocity. Total pressure losses were computed as:

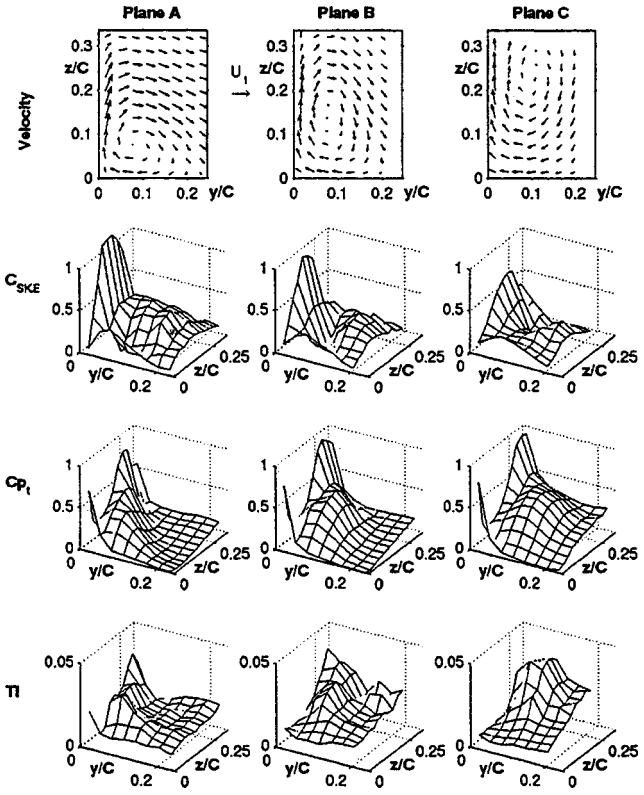

Fig. 7 Secondary flow measurements at Planes A, B, and C (see Fig. 3) for baseline case. Top row: secondary velocity; second row: secondary kinetic energy loss coefficient; third row: total pressure loss coefficient; bottom row: turbulence intensity. Dimensions *y* (distance from suction wall) and *z* (distance from endwall) normalized on chord.

$$Cp_t = \frac{P_t - P_{tr}}{0.5\rho U_1^2} \tag{2}$$

and are shown in the third row of Fig. 7. Comparing to the velocity fields, it can be seen that high Cp_t corresponds to the center of the passage vortex. This result is expected and agrees with Chung and Simon [7].

Turbulence intensity was computed as:

$$TI = \sqrt{\frac{v'^2 + w'^2}{2U_1^2}} \tag{3}$$

and is shown in the fourth row of Fig. 7. High turbulence regions correspond to the core of the passage vortex, in agreement with the total pressure losses.

Case 2—Wall Jets Near the Saddle Point. Six wall jets were installed near the saddle point in the locations illustrated in Fig. 2. In terms of the fixed coordinates ζ and η, shown in Fig. 2, wall jet #1 was located at $\zeta/C=0.62$, $\eta/C=0.14$; jet #4 at $\zeta/C=0.72$, $\eta/C=0.23$; and jet #6 at $\zeta/C=0.58$, $\eta/C=0.22$. These jets were used in an attempt to redirect the passage vortex near its point of origin. Analysis of the secondary flow with a tuft probe revealed that the passage vortex still impinged upon the suction surface, as in the case without any jets. The vorticity detector showed that when jet #4 was not operating, the passage vortex appeared to travel around the jets toward the pressure-side blade and then migrate across the passage. When jet #4 was operating, the vortex path was less clear, but it still traveled across the passage to the suction-side blade. Ink dot flow visualization on the suction-side blade revealed no significant difference from Fig. 6, the baseline case. Increasing the velocity ratio, V_{jet}/U_1, was not helpful. There was some evidence that the vortex could be temporarily diverted, but it was not blown off the endwall. Because the wall jets near the saddle point had no significant effect on the secondary flow, no further efforts were made with this case, and it was not quantitatively documented.

Case 3—Optimized Fence. A clay fence of the same length (88 percent of chord), height (4.5 percent of chord), cross section (equilateral triangle), and orientation as used by Chung and Simon [7] was positioned in the test section, as shown in Fig. 2. The leading edge of the fence was at $\zeta/C=0.37$, $\eta/C=0.08$, and the trailing edge was at $\zeta/C=0$, $\eta/C=0.79$. Ink dot flow visualization on the suction surface clearly showed that the fence reduced the effects of the passage vortex on the suction-side blade. This result is consistent with that of Chung and Simon [7]. They concluded that with the fence, the passage vortex could not reach the suction surface. Instead, it was lifted by the fence and washed away by the mainstream flow. Evaluation of the flow with a tuft probe and the vorticity detector led to the same conclusion.

The fence was then modified to minimize its length. This was done in preparation for the use of a row of wall jets. The wall jets were to be installed in place of the fence at the same location as the fence. By minimizing the length of the fence, the number of wall jets could be reduced, thereby reducing the amount of air required. The fence was split into sections. Ink dot flow visualization was done on the suction surface to see the effect of the removal of each section of the fence. If too much of the fence was removed, the remaining sections either failed to intercept the vortex on the upstream end, or allowed it to move across the passage downstream of the trailing end. With the removal of 50 percent of the fence (30 percent from the upstream end and 20 percent from the downstream end), and a slight reorientation of the upstream end, the remaining sections still proved to be effective in diverting the passage vortex. This is evident in the blade ink dot traces shown in Fig. 8. The region shown is the same as in Fig. 6. Note that the ink traces are parallel to the main flow and do not exhibit the upward inclination seen in Fig. 6. The optimized fence length was 44 percent of the chord length. Its leading and trailing edges were located at $\zeta/C=0.35$, $\eta/C=0.36$ and $\zeta/C=0.10$, $\eta/C=0.72$ respectively. A schematic depicting its location and orientation is shown in Fig. 2. Notice the leading edge of the fence is slightly turned toward the suction-side blade. In this position the passage vortex is intercepted and forced to follow a path along the fence.

Oil and lampblack visualization was conducted on the endwall with the modified fence in place. The saddle point could be seen at the same location as the baseline case. The path of the passage vortex could be seen as it was intercepted by the fence, and forced to travel the length of the fence before exiting the test section.

Flowfield measurements were acquired in Planes A, B, and C (the same locations used in the baseline case) for cases with the original and optimized fences. The results with the two fences were nearly indistinguishable, and are presented in Fig. 9 for the

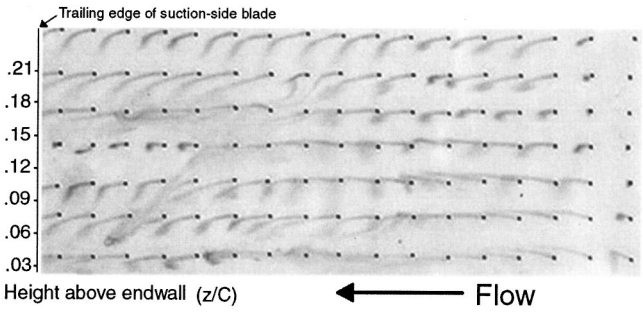

Fig. 8 Ink dot flow visualization on suction-side blade: optimized fence

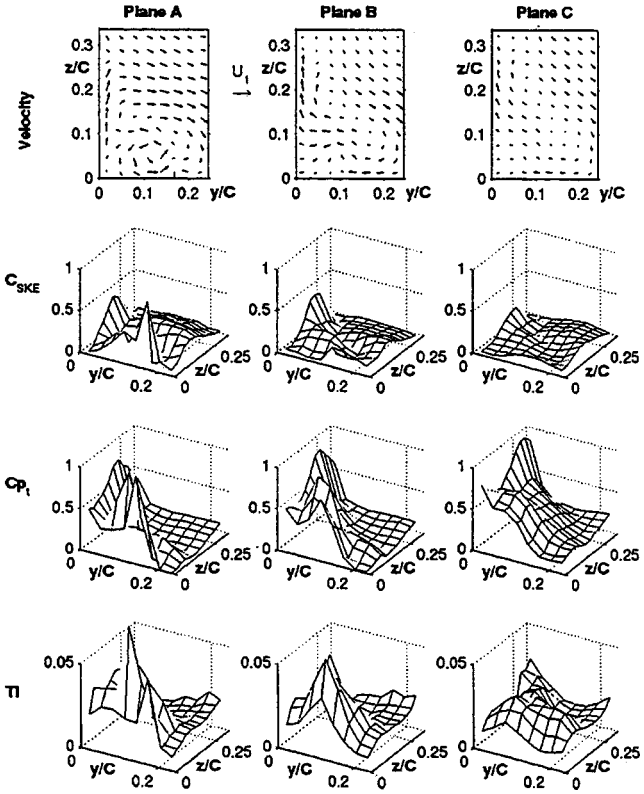

Fig. 9 Secondary flow measurements at Planes A, B, and C (see Fig. 3) for case with optimized fence

optimized fence case. The passage vortex develops in the same location as the baseline case, but the fence inhibits the development of the vortex as it moves downstream, from Plane A to Plane C. Inspection of the velocity field shows that the vortex does not impinge upon or climb the suction surface. Rather, it remains away from the blade and its strength is greatly decreased from the baseline case (Fig. 7). A weak counterrotating vortex is present near the blade–endwall junction. This may be the suction-side leg of the horseshoe vortex. The fence prevents its entrainment by the passage vortex.

A weaker vortex means lower secondary kinetic energy losses. Averaging over Plane C, the average C_{SKE} is reduced to 30 percent of the baseline case level. Total pressure losses increase by about 30 percent with the fence, but the combined C_{SKE} and Cp_t losses are about 10 percent lower with the fence than in the baseline case. Note that the losses are only averages over the planes shown, and are not stage losses. If larger measurement planes had been used, including regions less affected by secondary flow, the differences between cases would be less.

The locations of high total pressure losses and also high turbulence intensity do not follow the core of the passage vortex. Instead they remain near the blade–endwall junction at the location of the counterrotating vortex noted in the velocity fields. It appears that losses may not be generated so much by the passage vortex as by upstream activity in the suction-surface-endwall region. In the unmodified flow this region of losses is entrained by the passage vortex and moved. With the fence, the high loss area remains in the corner.

Case 4—Centerline Wall Jets. Twelve wall jets were installed in place of the modified fence. It was hypothesized that the wall jets would perform the same function as the fence by lifting the passage vortex off the endwall and diverting it from the suction surface. The configuration of the twelve wall jets is shown in Fig. 2.

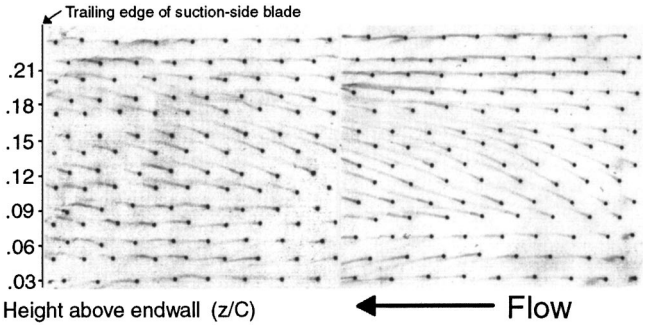

Fig. 10 Ink dot flow visualization on suction-side blade: centerline wall jets

The ink dot technique was used to evaluate the effectiveness of the wall jets. Nine jet velocities were tested by varying the jet supply pressure from 14 kPa to 70 kPa in 7 kPa increments. It was concluded, by inspection of the suction surface ink traces, that a jet velocity of 24 m/s ($V_{\mathrm{jet}}/U_1 = 2.7$) was sufficient to divert the passage vortex successfully. An image of the ink traces on the suction surface, with the jets at this velocity, is shown in Fig. 10. Note that the ink traces are more parallel to the main flow than in the baseline case (Fig. 6). There is, however, some upward inclination of the traces in the region between 30 and 70 mm from the endwall, which will be explained below. Since the jets and main flow have the same temperature and density in the experiment, the jets have a blowing ratio, $(\rho_{\mathrm{jet}}V_{\mathrm{jet}})/(\rho_1 U_1)$, of 2.7, and a momentum ratio, $(\rho_{\mathrm{jet}}V_{\mathrm{jet}}^2)/(\rho_1 U_1^2)$, of 7.3. These ratios would be lower if based on local free-stream velocities at the jet locations, dropping toward 1.8 and 3.2 at the test section exit. Typical blowing ratios, based on local velocity, for film cooling are well below 1, but this is due to the fact that film cooling is more effective at lower blowing ratios. In theory, a velocity ratio approaching 1 should be possible even in the first-stage vane of a high pressure turbine. In practice, a somewhat lower limit would be expected. Assuming a density ratio approaching 3 in an engine, blowing and momentum ratios of 3 would be the limit in the first stage. The blowing and momentum ratios of the present study are too high for use in the first stage, but are of the right order of magnitude for a workable design. It is conceivable that with refinement and optimization, wall jets could be made to work at a blowing ratio which would be achievable in an engine. Downstream of the first stage, even the high ratios of the present study should be achievable. To determine more precisely the blowing and momentum ratios needed for the jets, further experiments should be done with jets at a higher density ratio.

The mass flow from all 12 jets corresponds to 1 percent of the mass flow through the present test section. If one assumes an aspect ratio of 1 and blowing from both endwalls, the jet air requirement would correspond to 4 percent of the mass flow through a typical turbine passage. The wall jet flow would be in addition to the mass flow introduced through film cooling. Lakshminarayana [1] states that the typical cooling requirement in the first-stage nozzle is about 6 percent of the core engine inlet flow. Therefore the mass flow of the jets in the present study, while high, is conceivable for engine application, and if the jets are successful in reducing secondary flow effects and making film cooling more effective, it may be possible to reduce the film cooling mass flow, somewhat offsetting the extra mass flow needed for the wall jets.

The ink dot technique was applied over the endwall with the jets in operation. The results are shown in Fig. 11. This figure shows that the main characteristics of the flow, excluding the passage vortex path, are similar to the baseline case. The saddle point is located in the same position. The endwall crossflow due to

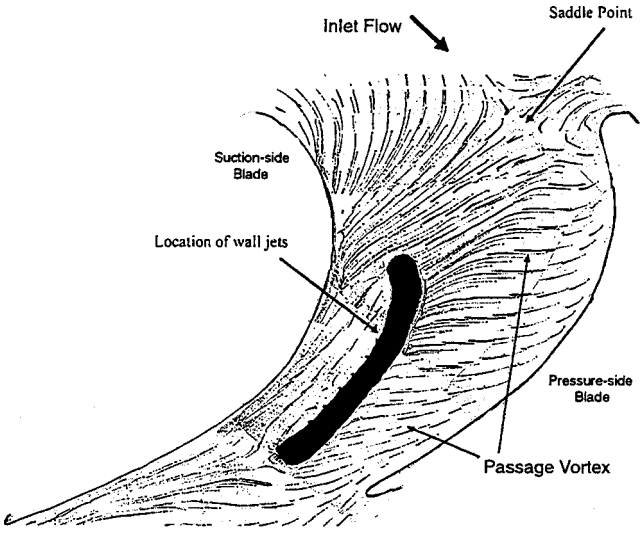

Fig. 11 Ink dot flow visualization on the endwall: centerline wall jets

the pressure gradient from the pressure-side blade to the suction-side blade is clearly indicated. The passage vortex is observed downstream of the saddle point, near the leading edge of the pressure-side blade. The vortex begins to migrate across the passage, toward the suction-side blade, but is intercepted by the wall jets. The vortex is pushed along the length of the wall jet row and out of the test section without impinging on the suction surface. Oil and lampblack visualization showed similar results.

Flow field quantities from Planes A, B, and C are shown in Fig. 12. As the vortex moves downstream, it is lifted up off the endwall and kept away from the suction-side blade. The strength of the vortex is about the same as in the baseline case (compare to Fig. 7). A small counterrotating vortex is apparent in the endwall–suction surface corner in Planes A and B, but it has been overwhelmed by the passage vortex by Plane C. Average C_{SKE} are about the same with the jets as in the baseline case. Near the suction surface, however, a comparison of C_{SKE} in Figs. 7 and 12 shows much lower secondary velocity near the suction wall with the jets. This indicates that the vortex is having less of an effect on the suction surface, in agreement with the ink dot visualization of Fig. 10. The area on the suction surface from the endwall to a height of $z/C=0.09$ shows little influence of the passage vortex, as indicated by the ink traces parallel to the endwall. The upward motion of the vortex, shown by the velocity field in the region between $z/C=0.09$ and 0.21 up the suction surface, corresponds to the inclined ink traces in that same region. This supports the conclusion that the passage vortex has a weaker effect in the case with the jets and is farther from the suction surface. This would presumably allow for more effective film cooling on the suction surface.

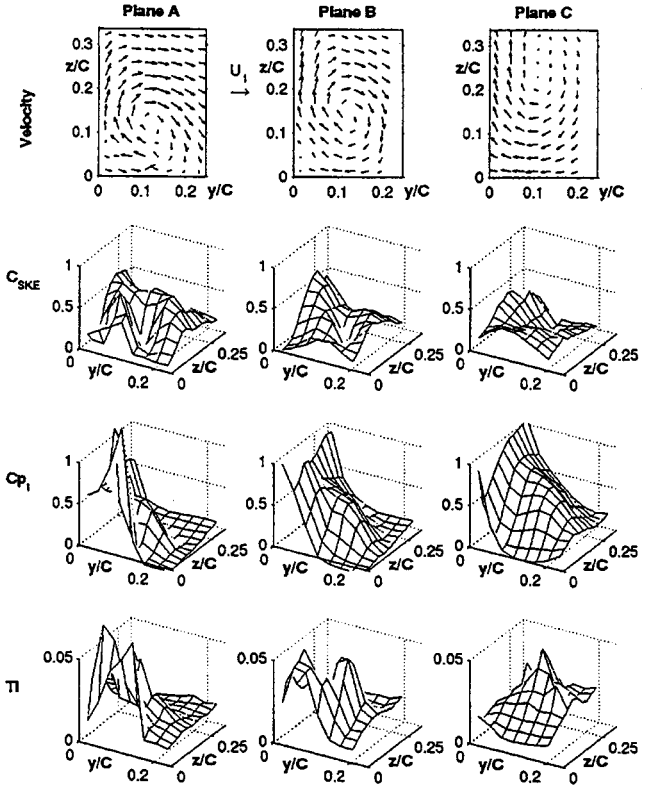

Fig. 12 Secondary flow measurements at Planes A, B, and C (see Fig. 3) for case with centerline wall jets

Total pressure losses show characteristics of both the baseline case and the optimized fence case, with high Cp_t in both the corner, at the location of the counterrotating vortex noted above, and the core of the passage vortex. Average pressure losses are about 50 percent higher than in the baseline case. Combined Cp_t and C_{SKE} losses are about 30 percent higher than the baseline case.

The drop in losses observed with the optimized fence suggested that similar behavior might be expected with the jets. This was not the case, and the turbulence intensity measurements may provide an explanation. The turbulence intensity follows the pressure loss behavior, with a peak in the blade–endwall corner in Plane A, a double peak in the corner and passage vortex core in Plane B, and a peak at the passage vortex core in Plane C. Comparison of Figs. 7 and 12 shows that the turbulence intensity in the jet case is considerably higher than in the baseline case, particularly in Planes A and B. The jets are disturbing the main flow and creating turbulence. Much of this extra turbulence has been dissipated by Plane C, and the dissipation has resulted in higher losses.

From a heat transfer standpoint, the centerline jets appear to have the desired effect of providing a more favorable situation for film cooling on the suction surface. From an aerodynamics standpoint, the jets have the undesirable effect of increasing losses. These two effects, along with the cost associated with supplying the jet air, would need to be balanced to determine the overall effect on engine efficiency. Further experiments to quantify stage losses and the benefits to film cooling and heat transfer would be needed to make this comparison. More work to optimize jet size and spacing might also be beneficial for reducing jet air requirements.

Conclusions

Endwall jets located in the center of a turbine passage were effective in altering the path of the pressure-side leg of the horseshoe vortex. The vortex was not significantly weakened, but its migration across the passage toward the suction surface was partially blocked. Jet airflow requirements were comparable to those used for film cooling.

The jets appear to provide an improved situation for airfoil cooling, but result in higher secondary losses due to the turbulence generated by the jets.

A boundary layer fence was effective in altering the path, reducing the strength, and minimizing the harmful effects of the pressure-side leg of the horseshoe vortex in a turbine passage. The fence length could be reduced to half that used in previous studies, with no significant change in results.

Total pressure losses appear to be generated primarily near the

suction surface–endwall corner, and are not directly attributable to the passage vortex. The passage vortex entrains the fluid in this high loss area when it reaches the suction surface.

Acknowledgments

The assistance of the Technical Support Department at the Naval Academy is appreciated. Roy Goddard constructed the wind tunnel and Bill Beaver fabricated the test section. Ron Wheeler and Louise Becnel provided technical help in the laboratory. Christine Jamison and Karen Lambert of the Educational Resource Center assisted with the production of the figures in this paper. This work was supported by the Trident Scholar Program at the United States Naval Academy.

Nomenclature

C = chord
C_{SKE} = secondary kinetic energy loss coefficient
Cp_t = total pressure loss coefficient
FSTI = free-stream turbulence intensity
H = span
H_p = pressure side leg of horseshoe vortex
H_s = suction side leg of horseshoe vortex
P = pitch
P_s = static pressure
P_t = total pressure
P_{tr} = total pressure in free-stream upstream of cascade
Re_c = Reynolds number based on chord and U_1
S_p = curvilinear distance from leading edge along pressure side
S_s = curvilinear distance from leading edge along suction side
TI = local turbulence intensity
U_L = local free-stream velocity along the airfoil $= \sqrt{2/\rho^*(P_{tr}-P_s)}$, m/s
U = free-stream velocity, m/s
V = flow velocity in y direction, m/s
V_{jet} = wall jet velocity, m/s
v' = rms fluctuating velocity in y direction
W = flow velocity in z direction, m/s
w' = rms fluctuating velocity in z direction
y = distance away from suction surface
z = distance away from endwall
δ_2 = momentum thickness
η = axial distance from suction side leading edge (Fig. 2)
ρ = density
ζ = pitchwise distance from suction side leading edge (Fig. 2)

Subscripts

1 = inlet condition
2 = exit condition

References

[1] Lakshminarayana, B., 1996, *Fluid Dynamics and Heat Transfer of Turbomachinery*, Wiley, New York, p. 617.
[2] Goldstein, R. J., and Spores, R. A., 1988, ''Turbulent Transport on the Endwall in the Region Between Adjacent Turbine Blades,'' ASME J. Heat Transfer, **110**, pp. 862–869.
[3] Wang, H. P., Olson, S. J., Goldstein, R. J., and Eckert, E. R. G., 1997, ''Flow Visualization in a Linear Turbine Cascade of High Performance Turbine Blades,'' ASME J. Turbomach., **119**, pp. 1–8.
[4] Langston, L. S., Nice, M. L., and Hooper, R. M., 1977, ''Three-Dimensional Flow Within a Turbine Cascade Passage,'' ASME J. Eng. Power, **99**, pp. 21–28.
[5] Sieverding, C. H., 1985, ''Recent Progress in the Understanding of Basic Aspects of Secondary Flows in Turbine Blade Passages,'' ASME J. Eng. Gas Turbines Power, **107**, pp. 248–257.
[6] Sharma, O. P., and Butler, T. C., 1987, ''Reynolds Stresses and Dissipation Mechanisms Downstream of a Turbine Cascade,'' ASME J. Turbomach., **109**, pp. 229–236.
[7] Chung, J. T., and Simon, T. W., 1993, ''Effectiveness of the Gas Turbine Endwall Fences in Secondary Flow Control at Elevated Freestream Turbulence Levels,'' ASME Paper No. 93-GT-51.
[8] Goldstein, R. J., Wang, H. P., and Jabbari, M. Y., 1995, ''The Influence of Secondary Flows Near the Endwall and Boundary Layer Disturbance on Convective Transport From a Turbine Blade,'' ASME J. Turbomach., **117**, pp. 657–665.
[9] Duden, A., Raab, I., and Fottner, L., 1999, ''Controlling the Secondary Flow in a Turbine Cascade by Three-Dimensional Airfoil Design and Endwall Contouring,'' ASME J. Turbomach., **121**, pp. 191–199.
[10] Michelassi, V., Martelli, F., and Corradini, U., 1998, ''Secondary Flow Decay Downstream of Turbine Inlet Guide Vane With Endwall Contouring,'' ASME Paper No. 98-GT-95.
[11] Dossena, V., Perdichizzi, A., and Savini, M., 1999, ''The Influence of Endwall Contouring on the Performance of a Turbine Nozzle Guide Vane,'' ASME J. Turbomach., **121**, pp. 200–208.
[12] Chung, J. T., Simon, T. W., and Buddhavarapu, J., 1991, ''Three-Dimensional Flow Near the Blade/Endwall Junction of a Gas Turbine: Application of a Boundary Layer Fence,'' ASME Paper No. 91-GT-45.
[13] Chung, J. T., 1992, ''Flow and Heat Transfer Experiments in the Turbine Airfoil/Endwall Region,'' Ph.D. Thesis, Department of Mechanical Engineering, University of Minnesota, Minneapolis, MN.
[14] Gregory-Smith, D. G., and Cleak, J. G. E., 1992, ''Secondary Flow Measurements in a Turbine Cascade With High Inlet Turbulence,'' ASME J. Turbomach., **114**, pp. 173–183.
[15] Kang, M. K. B., and Thole, K. A., 2000, ''Flowfield Measurements in the Endwall Region of a Stator Vane,'' ASME J. Turbomach., **122**, pp. 458–465.
[16] Chyu, M. K., Hsing, Y. C., and Bunker, R. S., 1998, ''Measurements of Heat Transfer Characteristics of Gap Leakage Around a Misaligned Component Interface,'' ASME Paper No. 98-GT-132.
[17] Ligrani, P. M., and Mitchell, S. W., 1994, ''Interaction Between Embedded Vortices and Injectant From Film Cooling Holes With Compound Angle Orientations in a Turbulent Boundary Layer,'' ASME J. Turbomach., **116**, pp. 709–720.
[18] Johnston, J. P., and Nishi, M., 1990, ''Vortex Generator Jets. Means for Flow Separation Control,'' AIAA J., **28**, pp. 989–994.
[19] Kim, J., Simon, T. W., and Russ, S. G., 1992, ''Free-Stream Turbulence and Concave Curvature Effects on Heated Transitional Boundary Layers,'' ASME J. Heat Transfer, **114**, pp. 338–347.
[20] Chung, J. T., and Simon, T. W., 1990, ''Three-Dimensional Flow Near the Blade/Endwall Junction of a Gas Turbine: Visualization in a Large-Scale Cascade Simulator,'' ASME Paper No. 90-WA/HT-4.
[21] Chen, P. H., and Goldstein, R. J., 1992, ''Convective Transport Phenomena on the Suction Surface of a Turbine Blade Including the Influence of Secondary Flows Near the Endwall,'' ASME J. Turbomach., **114**, pp. 776–787.
[22] Langston, L. S., and Boyle, M. T., 1982, ''A New Surface-Streamline Flow Visualization Technique,'' J. Fluid Mech., **125**, pp. 53–57.
[23] Simon, T. W., Qiu, S., and Yuan, K., 2000 ''Measurements in a Transitional Boundary Layer Under Low-Pressure Turbine Airfoil Conditions,'' NASA/CR-2000-209957.

Flow Measurements in a Nozzle Guide Vane Passage With a Low Aspect Ratio and Endwall Contouring

Steven W. Burd

Terrence W. Simon

Heat Transfer Laboratory,
University of Minnesota,
Minneapolis, MN 55455

Most turbine cascade studies in the literature have been performed in straight-endwall, high-aspect-ratio, linear cascades. As a result, there has been little appreciation for the role of, and added complexity imposed by, reduced aspect ratios. There also has been little documentation of endwall profiling with these reduced spans. To examine the role of these factors on cascade hydrodynamics, a large-scale nozzle guide vane simulator was constructed at the Heat Transfer Laboratory of the University of Minnesota. This cascade is comprised of three airfoils between one contoured and one flat endwall. The geometries of the airfoils and endwalls, as well as the experimental conditions in the simulator, are representative of those in commercial operation. Measurements with hot-wire anemometry were taken to characterize the flow approaching the cascade. These measurements show that the flow field in this cascade is highly elliptic and influenced by pressure gradients that are established within the cascade. Exit flow field measurements with triple-sensor anemometry and pressure measurements within the cascade indicate that the acceleration imposed by endwall contouring and airfoil turning is able to suppress the size and strength of key secondary flow features. In addition, the flow field near the contoured endwall differs significantly from that adjacent to the straight endwall. [S0889-504X(00)01104-1]

Introduction

The most interesting and plaguing characteristics of cascade fluid mechanics are the secondary flows. As a result, secondary flow field documentation in gas turbine cascades has been the center of many studies. Sieverding [1] presented a review of numerous investigations. In general, studies have shown that the passage flow field is extremely complicated as it consists of horseshoe vortices, passage vortices, and endwall secondary flows, which are due to pressure gradients formed with curvature. The generally accepted flow patterns within cascades are shown in Fig. 1, a three-dimensional cascade flow model that was developed by Langston [2]. As the flow travels through a cascade, it experiences aerodynamic losses. These arise from viscous effects. Profile losses are generated in the airfoil boundary layers well away from the endwalls. Endwall and secondary flow losses arise from endwall boundary layer flow and the secondary flows generated as boundary layers pass through the airfoil row. For turbines, secondary flow losses contribute one-third [3] to nearly two-thirds [4] of the total aerodynamic loss.

Nozzle designs in high-pressure turbines tend to have low aspect ratios, sharp flow turning, high exit Mach numbers, and large trailing edge blockages. These features can combine to produce prominent secondary flows that may seriously affect nozzle efficiency as well as the performance of the downstream high-work rotor. In contemplating methods of improving the performance of such nozzles, considerable attention has been paid to endwall contouring. Contouring offers the possibility of reducing exit flow profile distortion as well as controlling secondary flow development by reduction of cross-channel and radial static pressure gradient effects. Researchers have investigated the effects of endwall contours for a variety of contour profiles and positions of these contours relative to the airfoil chords. Contouring has shown promise as an effective passive flow management method. Deich et al. [5] and Ewen et al. [6] have reported obtaining increases in efficiency approaching 3.5 percent with meridional endwall profiling (i.e., contoured axially) within nozzle airfoil rows. Morris and Hoare [7] described experimental work on a linear cascade of airfoils fitted with several forms of meridional endwall profiles and varied airfoil aspect ratios. It was found that symmetric-cubic wall profiling could reduce overall secondary loss up to 25 percent with a small aspect ratio and thin inlet boundary layers. The loss reduction occurred almost exclusively near the flat, non-profiled endwall, and was attributed to changes in airfoil pressure distributions due to profiling. Kopper et al. [8] investigated the benefit of endwall profiling in a cascade with one planar and one contoured endwall, a design similar to that documented in this paper. Their design demonstrated a 17 percent reduction of the full-passage, mass-averaged loss relative to a planar cascade, primarily due to lower secondary losses on the planar wall side of the cascade. Boyle and Haas [9], Timko [10], Tipton [11], and Boyle et al. [12] also studied contoured endwalls. In spite of this work, more insight into the benefits of these designs is needed. Moustapha and Williamson [13] studied the effects of two meridionally profiled endwalls. Boletis [14] and Arts [15] published a two-part, experimental-numerical study of the effect of tip endwall contouring on the three-dimensional flow field in a low-speed, low-aspect-ratio, annular turbine nozzle guide vane. They concluded that passage losses are reduced by tip contouring. Boletis and Sieverding [16] employed a cubic, meridional-contoured endwall in their investigation with a low-aspect-ratio stator geometry.

Nonaxisymmetric endwall profiles have also been investigated. These used shaped endwalls in both the axial and circumferential directions. Nonaxisymmetric designs of Morris and Hoare [7] and Atkins [17] showed limited success. The nonaxisymmetric profile of Morris and Hoare, for instance, produced a large reduction of losses in the half-span adjacent to the flat wall but increased considerably the losses near the profiled wall. To the contrary, the ''Russian kink'' of Warner and Tran [18] yielded improved efficiencies in low-aspect-ratio turbines. Rose [19] showed promising results for several types of three-dimensional endwall shapes. Du-

Contributed by the International Gas Turbine Institute and presented at the 45th International Gas Turbine and Aeroengine Congress and Exhibition, Munich, Germany, May 8–11, 2000. Manuscript received by the International Gas Turbine Institute February 2000. Paper No. 2000-GT-213. Review Chair: D. Ballal.

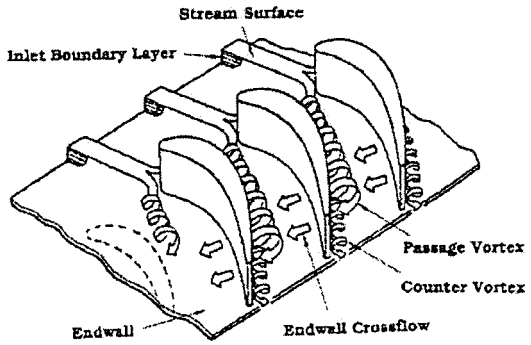

Fig. 1 Cascade secondary flow model [2]

den et al. [20], Duden and Fottner [21], Yan et al. [22], Harvey et al. [23] and Hartland et al. [24] have investigated nonaxisymmetric profiles more recently.

Several profiles hold more promise than others. A successful and very popular contour in guide vanes is one that imposes a reduction in passage span in approaching the trailing edges of the airfoils, permitting most of the flow turning to be achieved at lower velocities around the initial region of the vane. Subsequent flow acceleration is then available to reduce flow profile distortion and boundary layer growth. The cubic-type profiles of Morris and Hoare [7], Kopper et al. [8], and Boyle and Haas [9] fall in this category. Unfortunately, the understanding of contouring effects is still limited. Very few data are available for the flow field velocity, turbulence, and vorticity within the passage and secondary flow mechanisms are not clear. In this paper, the flow field and secondary flows are documented and losses are quantified.

Experimental Facility

The test facility (Fig. 2) was designed and constructed to simulate the geometry of, and the flow through, the inlet guide vanes of the high-pressure turbine stage of a modern, midsized, industrial gas turbine engine. In the facility, filtered air is supplied by a centrifugal blower into a turning header. Downstream of the header, the flow enters an axial fan and then travels through a heat exchanger element to the turbulence generator. The two fans in series supply the core flow through a grid of eight rectangular openings (5.08 cm×15.2 cm) while a third supplies the jet flow for mixing in the combustor simulator. Air jets issue from the sides of the generator through two axial rows of 4.13-cm-dia holes to simulate the primary and dilution jets. The mixing of these jets with the core flow produces high-level, large-scale turbulence. Additional 4.13 cm holes are cut in the top and bottom of the generator to supply more jet flow to improve uniformity in velocity and scales. There are 48 holes in total. The generator follows the designs of Ames [25] and Wang [26]. The combined flows exit the generator, travel through a 2.25:1 contraction nozzle, and through a straight-walled section to the nozzle guide vane simulator. There is a separate, secondary flow loop attached to the facility that is capable of supplying bleed cooling to the cascade test section. This loop was inactive for the present measurements but was used by Burd and Simon [27] and Burd et al. [28].

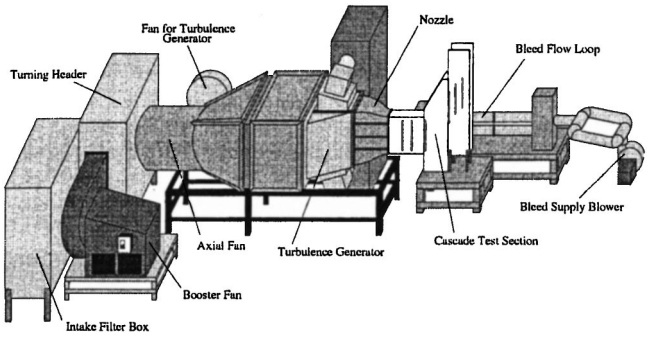

Fig. 2 Experimental test facility

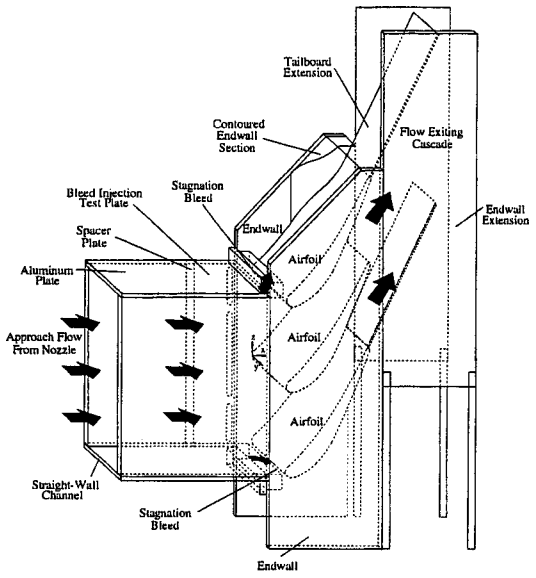

Fig. 3 Nozzle guide vane simulator test facility

The most important constituent of the facility is the nozzle guide vane simulator (Fig. 3), which serves as the test section. It consists of a three-airfoil, two-passage cascade. The airfoils are expanded-scale models of the actual engine nozzle mid-passage section. The airfoils are fabricated of low-thermal conductivity silicon-reinforced phenolic. One endwall is flat and made with 1.27-cm-thick acrylic. The other is fabricated with significant profiling in the axial direction and is constructed of phenolic. The contour of this endwall starts at roughly 25 percent of the axial chord downstream of the leading edge plane and, moving axially, is concave over the first half and convex over the latter half. The profile creates a 25 percent reduction in exit plane span relative to the inlet plane. Geometric parameters of the simulator are in Table 1. The limited number of airfoils and the large size of the components allows high-resolution measurements of flow features (i.e., boundary layers and vortices).

The small number of airfoils and passages is not without complications. The three airfoil arrangement used in this facility tends to produce higher static pressures for the lower passage than in the upper passage, as would naturally be expected for any bend. To minimize this effect, the facility was fashioned with stagnation-region, leading-edge suction bleeds and tailboards. These were manipulated to obtain acceptable flow patterns and to produce identical and proper stagnation streamlines into the leading edges of all three airfoils. From the center of the trailing edges, the tailboards project at an angle of 67 deg relative to the axial coordinate; nearly tangent to the camber line. The upper of the two passages is reserved for testing and measurements are based upon the bulk flow through it.

Other cascades of the same type have been studied in the Heat Transfer Laboratory at the University of Minnesota. Chung and

Table 1 Guide vane simulator design parameters

Airfoil True Chord=44.7 cm	Camber Angle=59.59°
Airfoil Pitch=31.8 cm	Stagger Angle=55.8°
Airfoil Axial Chord=25.5 cm	Aspect Ratio (Inlet)=S_1/C=0.58
Solidity = C/P=1.41	Aspect Ratio (Exit)=S_2/C=0.43
Airfoil Span (Inlet)=S_1=25.9 cm	Angle of Incidence=10°
Airfoil Span (Exit)=S_2=19.3 cm	Fillet Radii=1.27 cm

Simon [29,30], for instance, compared the flow field and endwall shear stresses in their cascade simulator to those in a true cascade Realistic flow field patterns, including secondary flow features, and endwall shear stress distributions were reproduced by their simulator. In addition, the stagnation streamlines were oriented using bleed slots adjacent to the leading edges as in the present facility. The leading edge horseshoe vortex and the evolution of secondary flows in the passage were not affected by this type of stagnation bleed.

An x, y, z-coordinate system (Fig. 2) is used to describe measurement locations. The streamwise coordinate, x, is in the direction of approaching core flow, with $x=0$ taken at the airfoil leading edges. The endwall-normal coordinate, y, is perpendicular to x and to the flat endwall. At each x, the contoured endwall surface is $y=0$ with positive y values extending toward the flat endwall. The limits of y are therefore $y/S=0.0$ and 1.0. The pitchwise or cross-stream coordinate, z, is perpendicular to both x and y. The z-origin ($z=0$) follows the leading edge of the center airfoil and continues along the pressure surface of the center airfoil. Positive z values correspond to the upper passage.

Experimental Procedure

Hot-Wire Measurements. A single-wire, hot-wire probe (TSI Model 1218-T1.5) was used for measurements of mean effective velocities and fluctuations about mean values. The probe had a 3.81-μm-diam tungsten sensor with a length-to-diameter ratio of 480. The active length is approximately 67 percent of the total length. A triple-sensor, hot-film probe (TSI Model 1299BM-20) was used to obtain three-dimensional velocity and turbulence measurements. Each sensor in this probe had a diameter of 50.8 μm and an active sensing length of 1.02 mm. The probe spatially averages over a spherical volume of approximately 2 mm in diameter. Both the single-wire and triple-film probes were driven by IFA-100 anemometer bridges. Data were sampled at 5 kHz sampling rate for 52.4 s (262,144 data points) for each measurement point. Voltages were recorded with an IOTech ADC-488/8SA A/D converter. Spectra were taken with both sensors with 1.1 million data points recorded at sampling frequencies of 50 kHz, 5 kHz, 500 Hz, 50 Hz, and 5 Hz and low-pass filtering at 40 percent of the sampling frequency. An automatic, two-axis traverse system with a 25 μm resolution was used to position the probes during experimentation.

Hot-wire uncertainty comes from precision and bias errors. Such uncertainties, which arise during calibration and measurement, are larger at smaller velocities. They arise from changes in fluid properties between calibration and measurement, near-wall effects, and sensor drift. For the triple-wire, measurements are sensitive to sensor alignment. A standard propagation, as detailed by Kline and McClintock [31], of uncertainty contributions assigned for these various effects yields a combined uncertainty in mean values of 5 percent for the single-wire and 5–7 percent for the triple-film. The rms-velocity fluctuations have nominally the same uncertainty level. Errors in turbulent shear stresses measured with the triple-film are 10 percent. Due to the large sampling sizes and long sampling times, stochastic errors associated with sampling are negligible in comparison to the deterministic errors. These calculated uncertainties are corroborated through turbulent pipe flow measurements, which were compared to the data of Laufer [32].

Pressure Measurements. Static and total pressures are measured using a standard pitot-static pressure probe (United Sensor Model PCD-12-KL), miniature total pressure probes, and static pressure taps. The miniature total pressure probes include a telescoping boundary layer probe with a 0.71 mm sensing hole diameter that was constructed by Hanna [33] and two similar designs that were fabricated with 90 deg bends in the support arms. The probe selected for measurements depends on measurement location. Variable reluctance pressure transducers, Validyne Model DP45 (8.9 cm water) and DP15 (14.0 cm water) are used to record differential pressures. A Validyne Sine Wave Carrier Demodulator (Model CD15), with 1 kHz response, provides a DC output from the transducers. This DC voltage output is recorded by a Hewlett-Packard Data Acquisition Unit (Model 3412A). For each individual pressure measurement, a total of 20 to 100 voltage readings is recorded at a sampling frequency of 2 Hz. A transducer calibration equation was used to deduce pressure magnitudes from processed voltages. Probes are aligned by rotating the probe in the direction of the mean total velocity and so that maximum local total pressures are recorded.

Uncertainties, accounting for calibration and bias errors, in pressure measurements are as low as 0.5 percent of full scale (0–5.1 cm water) to as high as 0.9 percent of full scale (exceeding 5.1 cm water). The miniature total pressure probes have square-edged openings and yield correct readings for angles of attack less than ± 10 deg. Through careful positioning of the probes, this angle of attack limit is not exceeded. When significant, corrective measures for turbulence effects are taken [34]. Effects associated with Mach number, Reynolds number, or shear displacement effects were not important.

Cascade Flow Orientation. Inlet mean velocity and turbulence distributions were measured at three positions upstream of the airfoil leading edges using single-wire anemometry (75 percent, 45 percent, and 10 percent of the axial cord upstream of the cascade). These data show that the cascade flow in the facility is highly elliptic and that flow patterns that develop as the flow approaches the passage are dominated by the pressure gradients. Data at 75 percent C_{ax} upstream of the airfoil leading edges are used to characterize the inlet conditions to the cascade. The flow at this location is fairly insensitive to the downstream presence of the cascade and velocity and turbulence distributions show uniform values across the measurement zone. A spatially averaged velocity over the region $y/S=0$ to $y/S=1.0$ and $z/P=0$ to $z/P=1.0$, $U_1=12.6$ m/s, was calculated via integration of the velocity. The inlet Reynolds number based on the airfoil actual chord and U_1 is approximately 350,000. The turbulence level normalized on U_1 is 9.5 percent.

At $x/C_{ax}=-0.45$, the data begin to show the elliptic nature of this approach flow. Low velocities are found upstream of the leading edges ($z/P=0$). Increased velocities (relative to $x/C_{ax}=-0.75$ values) are found above and below this low-velocity region suggesting mild acceleration of flow around it. The distributions clearly show that pressure gradients have begun to form and influence the flow at this point.

Velocity and turbulence distributions measured just upstream of the airfoil leading edge plane, $x/C_{ax}=-0.10$, are in Fig. 4. Data are collected over the area spanning from $y/S=0.06$ to $y/S=0.94$ and $z/P=0.03$ to $z/P=0.94$. A total of 70 data points, in a 7×10 $y\times z$ measurement grid, was recorded. The data show that at this location the pressure gradients that develop within the cascade dominate the flow pattern. In Fig. 4(A), high velocities at $z/P=0.15$ and $z/P>0.8$ clearly indicate that the core flow has begun to accelerate around the blockage created by the airfoil leading edge. The velocities progressively decrease in moving toward the center of the passage, however. The lowest velocities are found at $z/P=0.5$. Low velocities are also observed at $z/P=0$, revealing that the flow is decelerating as it approaches stagnation. Turbulence intensity (Fig. 4(B)) appears to depend strongly on the acceleration of the core flow as it enters the cascade. The regions of high acceleration have reduced turbulence intensities relative to the upstream values. In approaching the leading edge, the flow decelerates and turbulence is augmented. Given that the turbulence is normalized on the local streamwise velocity, most of the variations are attributed to changes in the mean flow.

Near-wall velocity profiles were measured in the approach flow to assess the thickness and growth of the boundary layers ap-

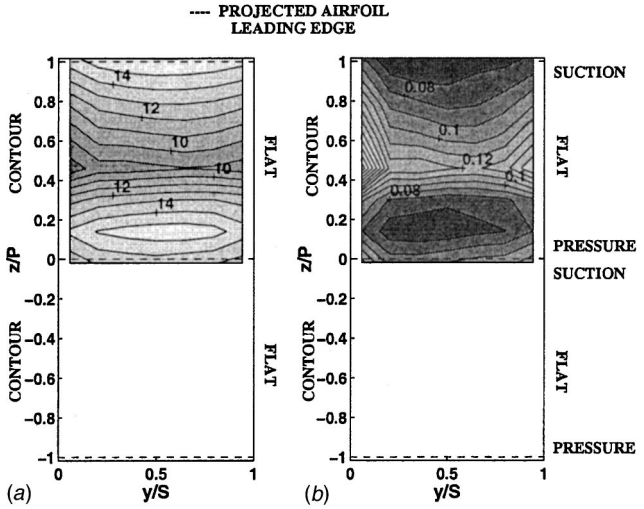

Fig. 4 Approach flow at $x/C_{ax}=-0.10$: (*A*) streamwise velocity, *U* (m/s); (*B*) turbulence, u'/U

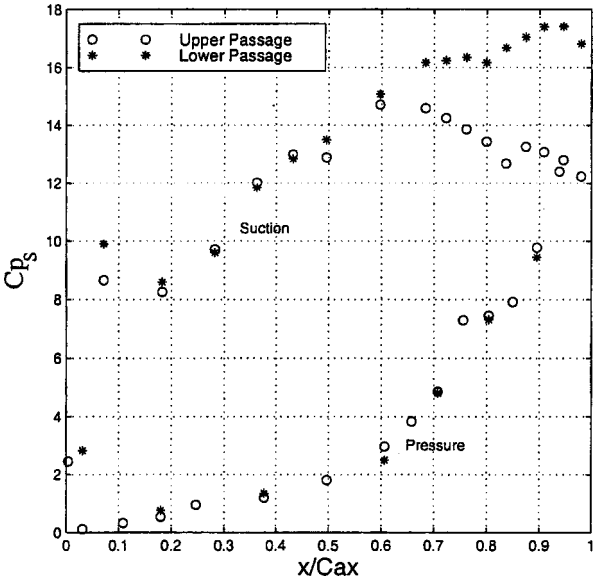

Fig. 5 Airfoil surface static pressure coefficient, Cp_s, distributions in the cascade facility

proaching the cascade. Three profiles were taken: $x/C_{ax}=-0.75$ and $y/P=0.25$, 0.5, and 0.75. The momentum and displacement thicknesses are listed in Table 2.

To document the scales in the approach flow, filtered velocity wave forms were measured along the center span ($y/S=0.5$) upstream of the test passage at several locations. Spectral analyses were then performed. Integral lengths scales ranging from 6.3–8.4 cm ($0.14<\Lambda/C<0.19$) are calculated. These large values are considered to be representative of the macroscales entering the guide vane in the engine [35]. Such large scales are not easy to generate in an experimental setting. With the assumption that the turbulence of the inertial subrange in this flow is isotropic, dissipation rates of turbulence kinetic energy and associated energy scale were calculated from these spectra [36]. Representative values for these quantities at $x/C_{ax}=-0.75$, $z/P=0.5$ are listed in Table 2.

Static pressure distributions were measured along the four airfoil surfaces in the cascade. The data were recorded for pressure taps located along a line parallel to the straight endwall and passing through the center of the exit span. Data were measured for the 15 taps on the suction surfaces in both the upper and lower channels, 14 taps on the pressure surface in the upper channel, 7 taps on the pressure surface in the lower channel, and the taps near the respective leading edges. Given the nonuniformity of static pressures upstream of the airfoil leading edges, equal absolute pressures on the surfaces with the two channels was not expected. Local static pressure coefficients based on the inlet total pressure, inlet static pressure upstream of each passage ($x/C_{ax}=-0.75$ at $z/P=-0.5$ and 0.5), and locally measured airfoil surface static pressures are shown in Fig. 5.

In general, the data from the same surfaces of neighboring airfoils compare well. The pressure surface data appear to match from channel to channel. There is some disparity in the vicinity of the leading edge. The suction surface data appear to match over the first 60 percent of the axial cord. Local diffusion, indicated by the drop in static pressure coefficients in the upper passage, is expected. Values measured near the trailing edges of the airfoils in the lower passage, though, begin to deviate from those in the upper passage. This is primarily due to the presence of the tailboard. Measurements using static endwall taps indicate that the tailboard appears to create a more prominent zone of high static pressure in the vicinity of the pressure surface trailing edge than observed for the upper cascade. This results in acceleration of flow toward the suction surface trailing edge yielding pressures that are lower relative to those in the upper passage. For this reason, all measurements presented in this paper were taken in the upper passage.

Table 2 Boundary layer parameters and turbulence parameters from spectra

x/C_{ax}	z/P	$\theta/C_{ax}\times10^3$	$\delta^*/C_{ax}\times10^3$	H	Re_θ
-0.75	0.25	6.82	9.71	1.42	1400
-0.75	0.50	6.05	8.61	1.42	1315
-0.75	0.75	5.46	7.66	1.40	1200

x/C_{ax}	z/P	U (m/s)	k (m^2/s^2)	Λ/C	ε (m^3/s^2)	L_u/C
-0.75	0.25	13.04	1.52	0.140	40.26	0.085
-0.75	0.50	13.33	1.69	0.180	41.05	0.098
-0.75	0.75	12.83	2.25	0.188	65.58	0.094

Results

The measurements presented in the following sections include velocity distributions, turbulence field measurements, and aerodynamic loss coefficients. From these, a general appreciation for the fluid mechanics and aerodynamics in the simulator can be obtained. Since this configuration is constructed with one contoured endwall, effects of contouring can be deduced. It must be realized, however, that both endwall flows experience the same streamwise acceleration, so the differences between the two endwalls cannot be interpreted as an endwall contouring effect.

Flow Field Measurements. Flow field measurements were taken near the exit plane of the cascade, $x/C_{ax}=0.90$, using triple-sensor, hot-film anemometry. The probe was oriented 65 deg relative to the axial direction and parallel to the flat endwall. This angle was used to locate the probe in the direction of the average exit flow angle, using a nulling method. A total of 597 data points was taken over the measurement plane with fine resolution near the suction surface ($z/P=1.0$) and the near-endwall ($y/S=0$ and 1.0) regions. Near the endwall–airfoil corner, data are limited, given the size of the triple-film sensor and the corner fillets. Coarse spatial resolution is accepted in the center of the passage where gradients are weak. Data from the triple-sensor include the mean and rms-fluctuating streamwise (i.e., bulk flow direction) components of velocity, *U* and u', as well as mean and rms-fluctuating cross-stream components of velocity. The cross-stream components perpendicular to both *U* and the flat endwall surface

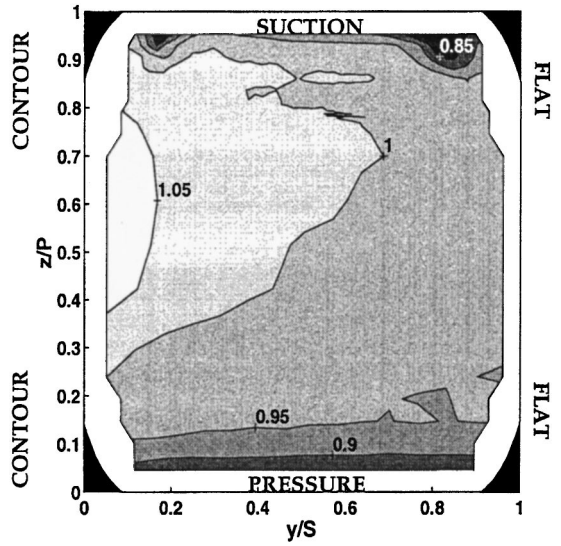

Fig. 6 Exit streamwise velocities, U/U_2, at $x/C_{ax}=0.9$

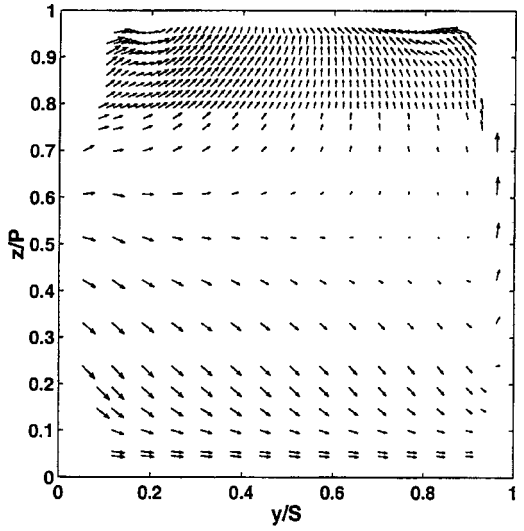

Fig. 7 Cross-stream ($V-W$) velocity vectors at $x/C_{ax}=0.9$

are V and v', with a positive value indicating motion from the contoured to the flat endwall. The cross-stream components perpendicular to U and V are W and w', with a positive value indicating motion from the pressure side toward the suction surface. Correlations of the rms-fluctuating components enable documentation of the primary turbulent Reynolds shear stress, $\overline{u'v'}$, $\overline{u'w'}$, and $\overline{v'w'}$.

Streamwise Velocity. A distribution of streamwise velocity at $x/C_{ax}=0.90$ is provided in Fig. 6. This distribution is normalized on the streamwise velocity at the center ($y/S=0.5$ and $z/P=0.5$) of the passage, U_2 (46 m/s) This distribution highlights several features of this flow including: (1) the clear existence of boundary layers along the airfoil surfaces ($z/P=0$ and 1.0); (2) accelerated or high-speed flow in the vicinity of the contoured endwall ($y/S=0$); and (3) two secondary flow structures along the suction surface, one positioned near each suction-endwall corner. The two structures, identifiable as distinct regions of reduced streamwise momentum (compared to the bulk core flow velocity), are of different size and strength. In general, the structure adjacent to the flat endwall ($y/S=1.0$) is larger, but less concentrated. This structure imposes a large region extending from $y/S=0.7$ to 0.9 over which $U/U_2 \leqslant 0.9$. The smaller, concentrated nature of the other structure ($y/S=0$) appears to be the direct result of streamwise acceleration associated with endwall contouring. The zone of $U/U_2 \leqslant 0.9$ for this feature is about one-half that of the structure near the flat endwall. It is speculated that the curvature of and acceleration along the contoured endwall would thin the endwall boundary layer and, thus, stretch and suppress the growth of any secondary flow structures that form within it. The acceleration would have a similar effect on the flow near the straight endwall.

Cross-Stream Velocities. The mean cross-stream velocities, V and W, are presented in Fig. 7 as a vector plot. The two secondary flow structures observed in Fig. 6 are again evident here. They appear as regions of short arrows adjacent to regions of large arrows. Due to rotation, portions of these structures oppose the cross-stream motion and others add to the cross-stream motion. The structures near the two endwalls appear to have opposing circulation directions; clockwise for the contoured endwall structure and counterclockwise for the flat endwall counterpart. They are consistent with expectations for passage vortices along these surfaces. The vortices differ in strength and size of their region of influence. In terms of general cross-stream velocities, the figure shows that: (1) with contouring, the flow coming off the profiled surface has a considerable V (contoured endwall to straight endwall) velocity component, (2) with some diffusion downstream from the throat, the flow from the channel center is migrating toward the two airfoil surfaces; the suction surface for $z/P>0.5$ and the pressure surface for $z/P<0.5$, (3) flow moves from each suction–endwall corner ($y/S=0$ and 1.0; $z/P=1.0$) toward the center span, and (4) flow moves strongly from the pressure to suction surface along the flat endwall ($y/S=1.0$).

The mean cross-stream velocities are also useful in determining the deviation of the flow from the bulk streamwise direction. In general, deviation is modest in this facility, remaining below ± 8 deg. For brevity, plots of deviation magnitudes are not presented. Low exit profile distortion was expected with the contour-imposed acceleration within the aft portion of the cascade.

Turbulence and Velocity Fluctuations (Not Shown). Also, turbulence distributions were measured at $x/C_{ax}=0.9$. Over the majority of the flow field, the rms-fluctuations of velocity are small (<2.0 percent of U_2) and comparable in magnitude to those of the approach flow to the cascade. At this position, the magnitude of u' decreased from the approach flow values, however, due to dissipation of streamwise turbulent kinetic energy and strain in the direction of the bulk fluid motion. The magnitudes of v' and w' were larger than u' values, except near the suction surface ($z/P=1.0$). This is understandable, given the highly three-dimensional nature of the flow field at this location. The two secondary flow structures are clearly visible as regions of elevated u', v', and w' near the suction–endwall corners. In these regions, u' values are the highest, primarily due to wall damping of v' and w' in this region.

Turbulent Reynolds Shear Stresses. Turbulent Reynolds shear stress distributions (normalized on U_2^2) are given in Figs. 8 and 9. Regions of high shear stress are of primary concern to this study. It is well known that large magnitudes of turbulent Reynolds shear stresses will accompany regions of strong shear. Secondary vortex structures are regions of enhanced shear. As such, coherent longitudinal vortices are easily identified via plots of $\overline{u'v'}$ and $\overline{u'w'}$. Generally, the center is a local minimum in the turbulent shear stress field with higher levels about this center. If diffusion is nearly isotropic, the vectors $\overline{u'v'}j+\overline{u'w'}k$ point radially outward from the center and perpendicular to the velocity gradients. Considering $\overline{u'v'}$ and $\overline{u'w'}$ separately, a plot of $\overline{u'v'}$ would, therefore, be expected to have a reversal in sign, with the reversal following a line perpendicular to y. Likewise, a coherent longitudinal vortex structure would be expected to also have a reversal in

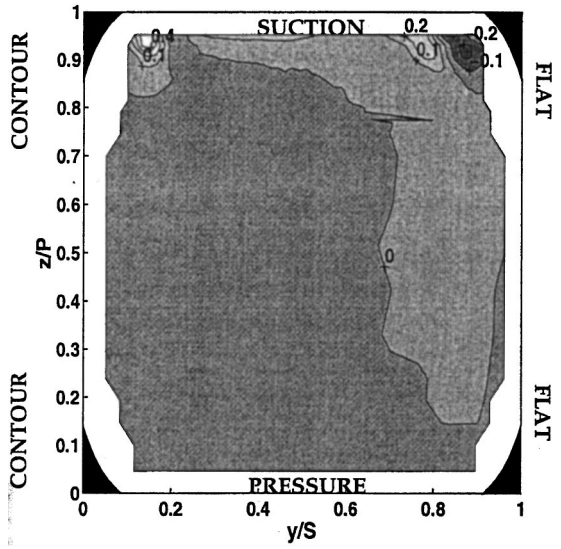

Fig. 8 Turbulent shear stress, $\overline{u'v'}/U_2^2\times100$, at $x/C_{ax}=0.9$

sign of $\overline{u'w'}$, with the reversal along a line perpendicular to *z*. In theory, the crossing point of the two reversal lines would signify the vortex center of rotation.

The plot of $\overline{u'v'}$ (Fig. 8) clearly shows the existence of two distinct regions of concentrated high $\overline{u'v'}$ stresses. These regions are coincident with the low-momentum regions observed in plots of the mean streamwise velocity (Fig. 6). The region of high stresses near the suction-flat-endwall corner ($y/S=1.0$; $z/P=1.0$) is believed to be the passage vortex along the flat endwall. The $\overline{u'v'}$ stresses indicate that this structure is vortical and reasonably coherent since there is a reversal in shear stress sign. Since the reversal in sign of $\overline{u'v'}$ does not fall along a line normal to the suction surface, it is believed that this vortex is slightly skewed and elliptic in shape, however. The structure near the suction-contoured endwall corner ($y/S=0$; $z/P=1.0$) is different. The stresses for this structure are biased favoring positive $\overline{u'v'}$ (diffusion away from the contoured endwall) with only a small region of negative $\overline{u'v'}$ (Note: This region has a magnitude slightly greater than -0.01 and does not appear on the plot, given contour increments of 0.01.) As a result, a pronounced line of sign reversal is not evident. The $\overline{u'v'}$ shear stress behavior for this structure suggests that there is likely a coherent vortex structure present in this region (i.e., weak passage vortex) but it is washed out, to a great extent, by the secondary endwall and suction surface motions in planar shear within the core flow. The peak shear stresses are much higher, though, than those for the flat endwall structure (0.4 for contoured and 0.2 for flat).

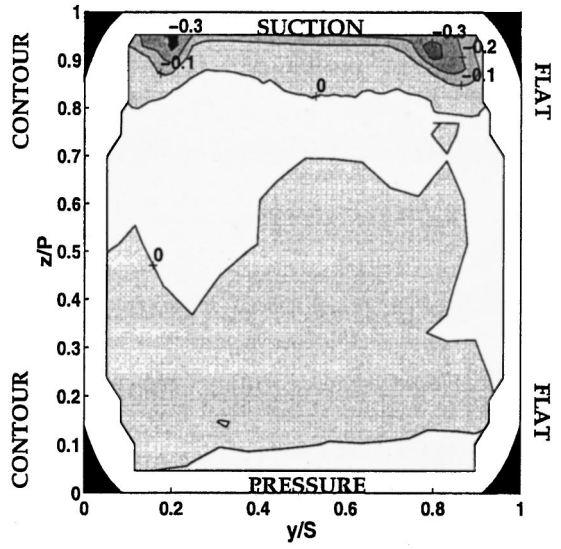

Fig. 9 Turbulent shear stress, $\overline{u'w'}/U_2^2\times100$, at $x/C_{ax}=0.9$

The distribution of $\overline{u'w'}$ shear stress (Fig. 9) shows also the two structures discussed above. These structures are visible as high negative $\overline{u'w'}$ values (diffusion away from suction surface). It is speculated that regions of positive $\overline{u'w'}$ would be found nearer to the suction surface if background stresses were removed and near-wall stresses measured. The magnitudes of normalized $\overline{u'w'}$ are comparable to the normalized $\overline{u'v'}$ values.

Magnitudes of $\overline{v'w'}$ (not shown) are small, as expected. These terms represent the *z* diffusion of *y* momentum. In the context of this study, these quantities are not important.

Key Observations From Velocity Measurements. These plots clearly indicate the existence of two structures adjacent to the airfoil suction surface and in the vicinity of the airfoil–endwall corners. They are clearly related to secondary flows and resemble passage vortices. The two are of different size and strength, with the passage vortex adjacent to the flat endwall being larger and less concentrated. That both structures are smaller than expected and smaller than those found in a large-aspect ratio, linear cascades (e.g., [29,30,37]), appears to be the direct result of the streamwise acceleration and boundary layer thinning on both endwalls associated with the contouring of one endwall. This is not merely a high free-stream turbulence effect for Chung documented strong structures with both high and low free-stream turbulence.

Aerodynamic Loss Evaluation

Total Pressure Loss. Total pressures are measured upstream (at $x/C_{ax}=-0.7$) and slightly downstream ($x/C_{ax}=1.02$) of the cascade. The upstream measurement is a single-point measurement with the pitot-static probe. A single point measurement in the upstream position is justified since p_o at any *x* upstream of the cascade has been verified to be nominally uniform. Total pressures at $x/C_{ax}=1.02$ are taken over the entire exit plane of the test passage and about the trailing edge of the center airfoil with miniature total pressure probes via a total of 1298 (892 in one set; 404 in another) measurement points. The measurement plane in the test passage encompasses nearly 98 percent of the total flow area. The total pressures, coupled with the velocity head of the approach flow, $1/2\rho U_1^2$, are used to calculate a total pressure loss coefficient, Cp_o at each measurement location at $x/C_{ax}=1.02$. A distribution of these values is given in Fig. 10. This figure shows that over the vast majority of the exit plane, Cp_o values are small ($Cp_o=0$) since flow distant from airfoil and endwall surfaces would closely follow inviscid flow patterns. The endwall boundary layers, though, have thin regions of high loss coefficients. The largest Cp_o ($Cp_o>4.0$) values are found in the vicinity of the trailing edge and the airfoil boundary layers. The two secondary flow structures along the suction surface have clearly identifiable contributions to this loss. The structure near the contoured endwall, centered about $y/S=0.15$, has a more substantial total pressure loss than the one near the flat endwall ($y/S\sim0.75$). The Cp_o values in the suction-contoured-endwall ($y/S=0$; $z/P=1.0$) corner adjacent to this structure are also much larger than those for the suction-flat-endwall corner ($y/S=1.0$; $z/P=1.0$). In addition, there is some indication of lower Cp_o values in the trailing edge region wake closest to the flat endwall. A reasonable conclusion from this distribution, therefore, is that the contouring of one endwall assists in reducing the total pressure losses in the vicinity of both the flat and contoured endwalls with the flat endwall region

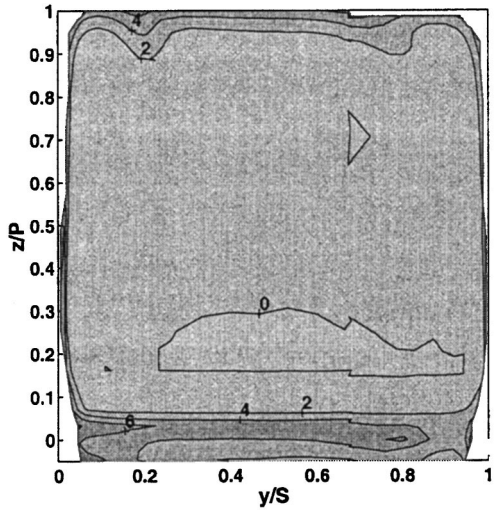

Fig. 10 Total pressure loss coefficients, Cp_0, at $x/C_{ax}=1.02$

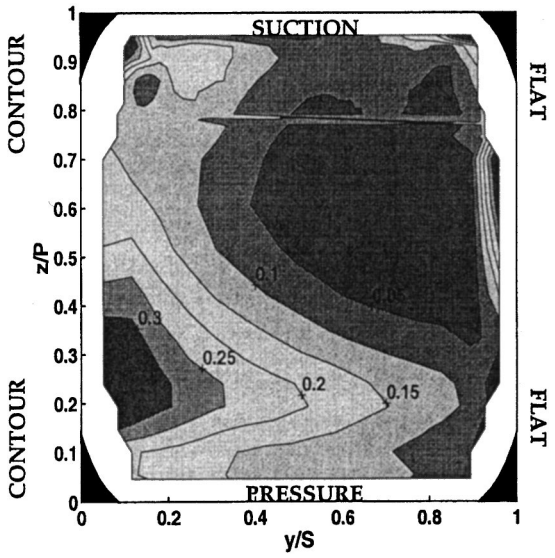

Fig. 11 Secondary kinetic loss coefficients, C_{ske}, at $x/C_{ax}=0.9$

receiving more benefit relative to that of the profiled endwall. Lower loss near the flat endwall is an observation that is consistent with the findings of other researchers who have investigated profiling [7,8].

The distribution of total pressure loss coefficients at the exit plane ($x/C_{ax}=1.02$) of the test passage are integrated over both the span and pitch, including the trailing edge region, to yield a spatially averaged, total pressure loss coefficient, $\overline{Cp_o}$. This quantity is a single parameter that can be used to evaluate and quantify a substantial portion of the aerodynamic loss through the cascade. The $\overline{Cp_o}$ value calculated for the configuration is 0.47. This indicates that the average total pressure loss in this cascade is 47 percent of the approach dynamic head or 3.0 percent of the departure flow dynamic head. Uncertainty in this quantity is estimated to be 2.0 percent of the approach dynamic head.

Secondary Kinetic Energy Loss. Using the mean streamwise and cross-stream velocities from triple-film measurements, loss coefficients associated with the secondary kinetic energy, C_{ske}, can be calculated. A distribution of C_{ske} at $x/C_{ax}=0.9$ is given in Fig. 11. It is believed that the C_{ske} distribution at $x/C_{ax}=1.02$ would closely resemble these values but would have additional loss contributions in the trailing edge wake region. In general, relative to peak total pressure loss coefficients, C_{ske} values tend to be small ($C_{ske}\leqslant 0.35$). C_{ske} values are highest near the contoured endwall, adjacent to the flat endwall, and in the pressure-surface-contoured-endwall corner region. Only in the center of the passage where Cp_o values (Fig. 10) approach zero but secondary motion remains strong are C_{ske} dominant contributors to the total loss. On average, secondary kinetic energy loss is about 25 percent of the total loss.

Conclusions

A large-scale experimental test facility, which simulates the geometry of, and flow within, the inlet nozzle guide vane section of a modern gas turbine, has been constructed and qualified. The facility is a three-airfoil, two-passage design. The airfoils are encased between one contoured and one flat endwall which reduce the cascade span by 25 percent, from inlet to exit. Testing was performed under high-level (9.5 percent) and large-scale core-flow-turbulence conditions with an inlet Reynolds number based on true chord length of 350,000.

With this facility, a detailed experimental investigation of the fluid mechanics and aerodynamics inherent to the guide vane design was conducted. Many of the fundamental flow features inherent to the nozzle guide vane passage design have been characterized. These features have been captured via measurements of mean streamwise and cross-stream velocities, turbulence, and turbulent shear stresses. As anticipated, measurements indicate that the flow field is three dimensional and that distinct secondary flow patterns develop within the cascade. Contrary to related studies in the literature, these secondary flow features are relatively small, localized, and difficult to characterize. The most important of these secondary flow features, resembling passage vortices, are still visible. With contouring of one endwall, these structures are not symmetric and differ considerably in their sizes and strengths. The structure near the suction-surface-flat-endwall corner is large in size but fairly weak in strength while the contoured-endwall counterpart is more concentrated in size and stronger. Boundary layer thinning and streamwise acceleration imposed by the contoured endwall are believed responsible for these differences. Both endwalls experience the same pressure gradient but differ in their curvature profiles. This curvature apparently has a profound effect on the secondary flow development. Aerodynamic loss assessment, including total pressure and secondary kinetic energy losses, suggests that the losses along the flat endwall in the suction corner region are lower relative to those near the contoured-endwall corner. The structure strength measurements support this conclusion. Although data document the flow field in a contoured-endwall cascade, the relative influence of contouring was not evaluated in this study. In fact, it would not be possible to do so because merely straightening the curved endwall has far-reaching effects beyond contouring, including changing the reaction of the stage.

Acknowledgments

This paper is part of a research project funded under the ATS program of DOE by Solar Turbines, Inc., and AGTSR. The AGTSR grant monitor was Dr. Daniel Fant and the Solar Turbines Technical Monitor was Dr. Luzeng Zhang. Additional guidance was provided by Dr. Boris Glezer and Mr. Loris Bedrosyan of Solar Turbines, Inc. The authors appreciate also the support of the Civilian Research and Development Foundation and the advice given by the co-researchers on the program in the Ukraine.

Nomenclature

C = airfoil actual or true chord
C_{ax} = airfoil axial chord
Cp_o = total pressure loss coefficient$=(p_{o1}-p_{o2})/(0.5\rho_1 U_1^2)$

$\overline{Cp_o}$ = spatially averaged total pressure loss coefficient
Cp_s = static pressure coefficient $=(p_{o1}-p_s)/(0.5\rho_1 U_1^2)$
C_{ske} = secondary kinetic energy loss coefficient $=(V_2^2+W_2^2)/U_1^2$
H = shape factor $=\delta^*/\theta$
k = turbulent kinetic energy
L_u = dissipation or energy scale
P = airfoil pitch
p = pressure
Re_θ = Reynolds number based on mean streamwise velocity external to boundary layer and momentum thickness
S = airfoil span
S_1 = inlet airfoil span
S_2 = exit airfoil span
U = time-averaged local streamwise (axial) velocity
U_1 = characteristic inlet velocity to test passage ($x/C_{ax}=-0.75$)
U_2 = characteristic exit velocity of test passage ($x/C_{ax}=0.90$)
U_∞ = free-stream velocity
u' = time-averaged, rms streamwise (axial) velocity fluctuation
$\overline{u'v'}$ = streamwise-endwall normal turbulent shear stress
$\overline{u'w'}$ = streamwise-pitchwise turbulent shear stress
V = time-averaged endwall-normal velocity
V_1 = inlet mean endwall-normal velocity
V_2 = exit mean endwall-normal velocity
v' = time-averaged, rms endwall-normal (radial) velocity fluctuation
$\overline{v'w'}$ = endwall-normal-pitchwise turbulent shear stress
W = time-averaged pitchwise velocity
W_1 = inlet mean pitchwise velocity
W_2 = exit mean pitchwise velocity
w' = time-averaged, rms pitchwise velocity fluctuations
x = axial coordinate
y = endwall-normal coordinate
z = pitchwise coordinate
δ_{99} = boundary layer thickness (99 percent)
δ^* = displacement thickness
ε = dissipation of turbulent kinetic energy
θ = momentum thickness
Λ = integral length scale
ρ = air density at measurement
ρ_1 = approach/inlet core flow air density

Subscripts

1 = inlet or approach condition
2 = exit condition
lower = referring to lower cascade passage
o = stagnation or total
s = static
upper = referring to upper (test) cascade passage

References

[1] Sieverding, C. H., 1985, ''Recent Progress in Understanding of Basic Aspects of Secondary Flows in Turbine Blade Passages,'' ASME J. Eng. Gas Turbines Power, **107**, pp. 248–257.
[2] Langston, L. S., 1980, ''Crossflow in a Turbine Cascade Passage,'' ASME J. Eng. Power, **102**, pp. 866–874.
[3] Denton, J. D., 1993, ''The 1993 IGTI Scholar Lecture: Loss Mechanisms in Turbomachines,'' ASME J. Turbomach., **115**, pp. 621–656.
[4] Prumper, H., 1972, ''Application of Boundary Layer Fences in Turbomachinery,'' AGARDograph No. 164, Paper II-3, pp. 311–331.
[5] Deich, M. E., Zaryankin, A. E., Fillipov, G. A., and Zatsepin, M. F., 1960, ''Method of Increasing the Efficiency of Turbine Stages and Short Blades,'' Teploenergetika, No. **2**, Feb., translation No. 2816, Associated Electrical Industries (Manchester), Ltd., April 1960.
[6] Ewen, J. S., Huber, F. W., and Mitchell, J. P., 1973, ''Investigation of the Aerodynamic Performance of Small Axial Turbines,'' ASME Paper No. 73-GT-3.
[7] Morris, A. W. H., and Hoare, R. G., 1975, ''Secondary Loss Measurements in a Cascade of Turbine Blades With Meridional Wall Profiling,'' ASME Paper No. 75-WA/GT-13.
[8] Kopper, F. C., Milano, R., and Vanco, M., 1980, ''An Experimental Investigation of Endwalls Profiling in a Turbine Vane Cascade,'' AIAA Paper No. 80–1089.
[9] Boyle, R. J., and Haas, J. E., 1982, ''Comparison of Experimental and Analytical Performance for Contoured Endwall Stators,'' AIAA Paper No. 82–1286.
[10] Timko, L. P., 1982, ''Energy Efficient Engine: High Pressure Turbine Component Test Performance Report,'' NASA CR-168289.
[11] Tipton, D. L., 1981, ''Experimental Investigation of Turbine Endwall Contouring,'' Detroit Diesel Allison Report AX0400 174, General Motors Corp., AVRADCOM Tech. Report 81-D-19.
[12] Boyle, R. J., Rholik, H. E., and Goldman, L. J., 1981, ''Analytic Investigation of End-Wall Contouring on Stator Performance,'' NASA TP-1943.
[13] Moustapha, S. H., and Williamson, R. G., 1985, ''Effect of Two Endwall Contours on the Performance of an Annular Nozzle Cascade,'' AIAA J., **24**, No. 9. pp. 1524–1530.
[14] Boletis, E., 1985, ''Effects of Tip Endwall Contouring on the Three-Dimensional Flow Field in an Annular Turbine Nozzle Guice Vane: Part 1—Experimental Investigation,'' ASME J. Eng. Gas Turbines Power, **107**, pp. 983–990.
[15] Arts, T., 1985, ''Effects of Tip Endwall Contouring on the Three Dimensional Flow Field in an Annular Turbine Nozzle Guide Vane, Part 2—Numerical Investigation,'' ASME Paper No. 85-GT-108.
[16] Boletis, E., and Sieverding, C. H., 1991, ''Experimental Study of the Three-Dimensional Flow Field in a Turbine Stator Preceded by a Full Stage,'' ASME J. Turbomach., **113**, pp. 1–9.
[17] Atkins, M. J., 1987, ''Secondary Losses and End-wall Profiling in a Turbine Cascade,'' I. Mech. E. Turbo Conference 1987 C255/87.
[18] Warner, R. E., and Tran, M. H., 1987, ''Recent Developments to Improve High-Pressure and Intermediate-Pressure Turbine Efficiency,'' I. Mech. E. Turbo Conference 1987 C275/87.
[19] Rose, M. G., 1994, ''Non-Axisymmetric Endwall Profiling in the HP NGV's of an Axial Flow Gas Turbine,'' ASME Paper No. 94-GT-249.
[20] Duden, A., Raab, I., and Fottner, L., 1999, ''Controlling the Secondary Flow in a Turbine Cascade by Three-Dimensional Airfoil Design and Endwall Contouring,'' ASME J. Turbomach., **121**, pp. 191–199.
[21] Duden, A., and Fottner, L., 1999, ''The Secondary Flow Field of a Turbine Cascade With 3D Airfoil Design and Endwall Contouring at Off-Design Incidence,'' ASME Paper No. 99-GT-211.
[22] Yan, J., Gregory-Smith, D. G., and Walker, P. J., 1999, ''Secondary Flow Reduction in a Nozzle Guide Vane Cascade by Non-axisymmetric End-wall Profiling,'' ASME Paper No. 99-GT-339.
[23] Harvey, N. W., Rose, M. G., Taylor, M. D., Shahpar, S., Hartland, J., and Gregory-Smith, D. G., 2000, ''Non-Axisymmetric Turbine End Wall Design: Part I—Three-Dimensional Linear Design System,'' ASME J. Turbomach., **122**, pp. 278–285.
[24] Hartland, J. C., Gregory-Smith, D. G., Harvey, N. W., and Rose, M. G., 2000, ''Nonaxisymmetric Turbine End Wall Design: Part II—Experimental Validation,'' ASME J. Turbomach., **122**, pp. 286–293.
[25] Ames, F. E., 1994, ''Experimental Study of Vane Heat Transfer and Aerodynamics at Elevated Levels of Turbulence,'' NASA CR-4633.
[26] Wang, L., 1996, ''A Study of Gas Turbine Flows, Turbulence Generation, and Film Cooling Flow Measurement,'' M. S. Thesis, Department of Mechanical Engineering, University of Minnesota.
[27] Burd, S. W., and Simon, T. W., 2000, ''Effects of Slot Bleed Injection Over a Contoured Endwall on Nozzle Guide Vane Performance: Part I—Flow Field Measurements,'' ASME Paper No. 2000-GT-199.
[28] Burd, S. W., Satterness, C. J., and Simon, T. W., 2000, ''Effects of Slot Bleed Injection Over a Contoured Endwall on Nozzle Guide Vane Performance: Part II—Thermal Measurements,'' ASME Paper No. 2000-GT-200.
[29] Chung, J. T., and Simon, T. W., 1990. ''Three-Dimensional Flow Near the Blade/Endwall Junction of a Gas Turbine: Visualization in a Large-Scale Cascade Simulator,'' ASME Paper No. 90-WA/HT-4.
[30] Chung, J. T., and Simon, T. W., 1991. ''Three-Dimensional Flow near the Blade/Endwall Junction of a Gas Turbine: Appliation of a Boundary Layer Fence,'' ASME Paper No. 91-GT-45.
[31] Kline, S. J., and McClintock, F. A., 1953, ''Describing Uncertainties in Single-Sample Experiments,'' Mech. Eng. (Am. Soc. Mech. Eng.), Jan., pp. 3–8.
[32] Laufer, J., 1953, ''The Structure of Turbulence in Fully-Developed Pipe Flow,'' NACA Report 1174.
[33] Hanna, J. A., 1982, ''Design and Analysis of a Boundary Layer Velocity Probe,'' Plan B Paper, Dept. of Mechanical Engineering, University of Minnesota.
[34] Dean, R. C., 1953, ''Aerodynamic Measurements,'' Gas Turbine Laboratory, Massachusetts Institute of Technology, Cambridge, MA.
[35] Moss, R. W., 1992, ''The Effects of the Turbulence Length Scale on Heat Transfer,'' Department of Engineering Science, University of Oxford, Report OUEL 1924, Ph.D. Dissertation.
[36] Ames, F. E., 1998, ''Aspects of Vane Film Cooling With High Turbulence: Part I—Heat Transfer,'' ASME J. Turbomach., **120**, pp. 768–776.
[37] Chung, J. T., 1992, ''Flow and Heat Transfer Experiments in the Turbine Airfoil/Endwall Region,'' Ph.D. Thesis, Department of Mechanical Engineering, University of Minnesota.

A Numerical Study of Secondary Flow in Axial Turbines With Application to Radial Transport of Hot Streaks

Dilip Prasad
United Technologies Research Center,
East Hartford, CT 06108

Gavin J. Hendricks
Pratt & Whitney,
East Hartford, CT 06108

The flow field in a low-speed turbine stage with a uniform inlet total pressure is studied numerically. A circular hot streak is superposed on the vane inlet flow. In agreement with previous experimental and numerical work, it is observed that while the streak passes through the vane unaltered, significant radial transport occurs in the rotor. Furthermore, despite the unsteady nature of the flow field, the steady theory of Hawthorne (1974) is found to predict the radial transport velocity well. Making use of this theory, it is shown that the secondary vorticity in the rotor may be attributed to the effects of density stratification, the spatial variation of the vane exit flow angle, and the relative eddy. It then follows that the extent of radial transport in the rotor may be influenced by altering the vane exit flow angle distribution. The present study examines one means by which this may be effected, viz., varying the vane twist across the span. It is shown that a ''reverse'' twist, wherein the flow angle at the vane exit is larger near the tip than it is at midspan, reduces the secondary flow (and consequently, radial transport) in the blade passage. On the other hand, ''positive'' twist, in which the vane exit flow angle decreases with span, is found to worsen the radial transport in the blade markedly. It is to be noted that varying the vane twist is but one method to obtain the desired exit flow angle; possibilities for altering other aspects of the vane geometry also exist. [S0889-504X(00)00104-5]

Introduction

The flow at the exit of gas turbine combustors is known to exhibit circumferential and radial variations in temperature, as shown by Elmore et al. [1] from measurements in an engine. The temperature within these nonuniformities, generally referred to as hot streaks, can vary from compressor discharge to stoichiometric levels. The continuous quest for more efficient engines with higher thrust–weight ratios has led over the years to ever-increasing turbine inlet temperatures. As a consequence, the high-pressure turbine is subjected to large heat loads, which can result in thermal distress, particularly in the rotor. The first systematic investigation of hot streak transport was undertaken by Butler et al. [2], who conducted experiments in a single-stage, low-speed rig. In this study, a circular hot streak was introduced into the vane inlet flow field; the total pressure across the inlet plane was kept uniform. The reason for this is based on the result of Hawthorne [3] that the secondary vorticity induced in a vane passage is proportional to the total pressure gradient. Thus, the absence of this gradient ensures that the secondary flow and consequent transport in the vane are minimized so that attention can be focused on transport in the rotor passage. The results of these experiments demonstrated that the hot fluid segregates toward the pressure surface of the blade passage and moves radially outward in the direction of the blade tip.

Rai and Dring [4] and Krouthen and Giles [5] attempted to model the results of Butler et al. [2] using the two-dimensional Navier–Stokes equations. It was found that the experimental trend of migration of hot fluid toward the pressure surface of the rotor passage was captured; there were, however, significant quantitative differences. Specifically, the numerical prediction of the temperature was higher on the suction surface than the experimental values, while that on the pressure surface was lower. It is, therefore, evident that three-dimensional effects are important in order to understand the transport processes in the rotor.

Dorney et al. [6] and Takahashi and Ni [7] performed the first three-dimensional Navier–Stokes analyses of the configuration of Butler et al. [2]. The agreement with the experimental data was found to be excellent. These simulations, in conjunction with the experiments of Butler et al. [2], have resulted in a better understanding of the flow processes in the turbine rotor. This has, in turn, led to the investigation of techniques to reduce hot streak transport in the rotor. In particular, Dorney and Gundy-Burlet [8] and Takahashi et al. [9] have proposed the use of fuel-nozzle indexing, wherein the combustor nozzles are arranged such that the hot streak impinges on the vane instead of passing through the stator passage. This method was shown to be very effective in reducing the heat loads in the rotor and has been verified experimentally by Roback and Dring [10].

Although the principal physical processes that influence hot streak transport were identified by Butler et al. [2], additional mechanisms may be present in the engine environment. This was exemplified by Shang and Epstein [11] in their numerical study of hot streaks in a transonic turbine stage, where it was found that the potential interaction between the vane and the blade causes the hot streak to wobble. This unsteady interaction was shown to render the time-averaged total temperature at the rotor inlet plane circumferentially non-uniform, resulting in enhanced heat loads on the blade. It was further demonstrated that the magnitude of the rotor-stator interaction and its effect on the rotor heat load may be reduced by adjusting the vane-blade count ratio to an optimum value. Shang & Epstein [11] also observed significant radial migration in their simulations. However, unlike the experiments of Butler et al. [2], the streak was found to migrate toward the hub radius of the blade passage; this was attributed to buoyancy effects.

Despite the large body of numerical and experimental data that has been accumulated since the pioneering study of Butler et al.

Contributed by the International Gas Turbine Institute and presented at the 45th International Gas Turbine and Aeroengine Congress and Exhibition, Munich, Germany, May 8–11, 2000. Manuscript received by the International Gas Turbine Institute February 2000. Paper No. 2000-GT-448. Review Chair: D. Ballal.

[2], several important issues remain outstanding. With the exception of the work of Shang and Epstein [11], the focus of the studies described earlier was on the *circumferential* redistribution of temperature, although the experimental data clearly demonstrate that spanwise migration of the streak also occurs. In the present investigation, we examine the fundamental transport processes that cause this transport, with a view to developing means by which it may be controlled. Numerical experiments were conducted to investigate the flow through a turbine stage. Previous work has indicated that the transport processes are primarily convective in nature, and for this reason, attention is focused on a low-speed configuration that seeks to replicate the Reynolds number but not the Mach number in a typical contemporary engine. As in prior numerical and experimental studies, we assume that the total pressure at the vane inlet plane is uniform. While this is clearly not valid for engine flows, it serves nevertheless to identify the basic transport mechanisms in the rotor, as pointed out by Butler et al. [2]. It will be demonstrated that although the flow field is unsteady, an excellent quantitative estimate of spanwise transport may be obtained from an analysis that assumes the flow in the rotor frame to be steady. This makes it possible to employ theoretical constructs to provide design guidelines for the management of secondary flow in the rotor and thereby to influence radial transport of hot streaks.

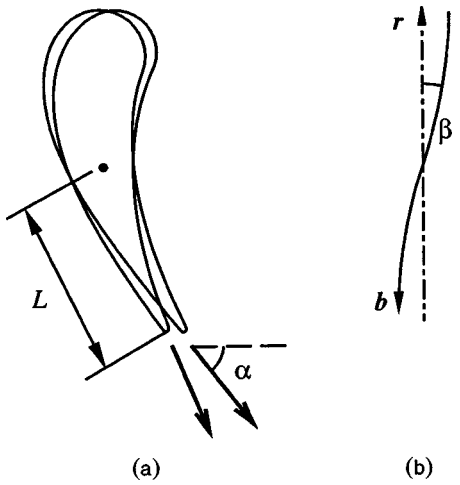

Fig. 1 (***a***) **Illustration of vane exit geometry and nomenclature;** (***b***) **view of the vane trailing edge looking upstream; solid line represents the trailing edge**

Transport Mechanisms in the Rotor

It is well known that secondary flows can have a substantial effect on the flow in turbine passages. Consider first the flow through a vane passage. This may be described in terms of the theory of steady secondary flow, developed in a seminal investigation by Hawthorne [3], who showed that a flow with an initial vorticity normal to the direction of the primary flow will, upon transport through the passage, generate a component of streamwise vorticity. This occurs as a result of the turning and stretching of vortex lines as they are convected through the curved channel. The boundary layers on the hub and casing represent one source of normal vorticity. In addition, when the flow is density-stratified owing to the presence of a hot streak at the vane inlet, the (inviscid) baroclinic torque that is caused by the non-parallelism of the density and pressure gradients gives rise to another source of normal vorticity. Alternatively, this may be thought of in terms of the lower density fluid within the streak being accelerated more than the colder fluid, leading to a jetlike velocity profile at the vane exit.

The work of Hawthorne [3] has been generalized to include the effects of compressibility, density stratification, and rotation; these developments are summarized in the review by Horlock and Lakshminarayana [12]. As shown by Lakshminarayana and Horlock [13] and Hawthorne [14], it proves convenient to employ both cylindrical polar (z, r, θ) and intrinsic (s, n, b) coordinates; here s, n, and b denote, respectively, coordinates in the direction of the relative streamline, the inward direction of its principal normal, and the binormal direction. Following Hawthorne [14], the rate of change of the component of absolute vorticity along a relative streamline, Ω_s, is given by

$$\frac{\partial}{\partial s}\left(\frac{\Omega_s}{W}\right)=\frac{2}{\rho W^2 R_n}\left[\frac{\partial p^*}{\partial b}+\frac{\omega^2 r^2}{2}\frac{\partial \rho}{\partial b}\right]+\frac{2\omega}{\rho W^3}\left[\frac{\partial p^*}{\partial z}+\frac{1}{2}(W^2+\omega r V_\theta)\frac{\partial \rho}{\partial z}-\frac{\omega W_Z}{2}\frac{\partial \rho}{\partial \theta}\right], \tag{1}$$

where ω is the *magnitude* of the angular wheel speed, $\vec{W}=(W_z, W_r, W_\theta)$ and $V=(V_z, V_r, V_\theta)$ are the relative and absolute flow velocities, ρ is the density, and R_n is the principal radius of curvature of the relative streamline. The quantity p^* that appears in Eq. (1) is the rotary total pressure, defined by

$$p^*=p+\frac{1}{2}\rho(W^2-\omega^2 r^2), \tag{2}$$

where p is the static pressure. It is evident from Eqs. (1) and (2) that in a stationary passage ($\omega=0$), the generation of streamwise vorticity depends only on the gradient of the total pressure. This is the well-known substitution principle of Munk and Prim [15] for steady isentropic flows, which states that for a specified geometry and total pressure distribution, the streamline pattern will remain unchanged by alterations in the total temperature distribution.

Next, attention is focused on the flow conditions at the interfacial plane between the stator and rotor. The vane can be considered to be comprised of radially stacked two-dimensional airfoil sections that are twisted about a radial axis so that the exit flow angle, α, depends on r, as shown in Fig. 1. We denote by $\beta=\beta(r)$ the angle between the radial direction and the spanwise locus of points along the vane trailing edge. Considering now the flow at the rotor inlet, the binormal direction is given by

$$db=-dr\cos\beta-r\,d\theta\sin\beta \tag{3}$$

It may be shown from geometry that the angles α and β are related by

$$\tan\beta=L\frac{\partial \alpha}{\partial r}, \tag{4}$$

where L is the distance from the twist axis to the vane trailing edge. We assume that the amount of twist is small so that $L\partial\alpha/\partial r=\epsilon\ll 1$: it then follows from Eq. (4) that $\cos\beta=1+O(\epsilon^2)$. In addition, the following approximations are made upstream of the rotor:

1 circumferential and axial variations in the flow quantities are negligible in comparison with those in the radial direction,
2 the (absolute) total pressure is uniform,
3 the flow is essentially in radial equilibrium so that the radial velocity is small, $V_r\ll V$.

Then, upon making use of Eqs. (3) and (4), it is found that Eq. (1) yields to leading order in ϵ:

$$\frac{W^2 R_n}{2\omega}\frac{\partial}{\partial s}\left(\frac{\Omega_s}{W}\right)=\left(V\cos\alpha-\frac{\omega r}{2}\right)\frac{r}{\rho}\frac{\partial \rho}{\partial r}+\cos\alpha\frac{\partial}{\partial r}(rV)-rV\sin\alpha\frac{\partial \alpha}{\partial r}. \tag{5}$$

Making use of the uniformity of total pressure and the condition of radial equilibrium, it may be shown that

$$\frac{\partial V}{\partial r} = -\frac{V}{r}\cos^2\alpha - \frac{V}{2\rho}\frac{\partial \rho}{\partial r}. \tag{6}$$

Finally, Eqs. (5) and (6) may be combined to give

$$\frac{W^2 R_n}{2\omega}\frac{\partial}{\partial s}\left(\frac{\Omega_s}{W}\right) = \frac{1}{2}(V\cos\alpha - \omega r)\frac{r}{\rho}\frac{\partial \rho}{\partial r} + V\sin^3\alpha\frac{\partial}{\partial r}(r\cot\alpha). \tag{7}$$

Equation (7) shows that the generation of secondary vorticity in the rotor passage is influenced by: (*a*) density gradients induced by the hot streak, and (*b*) the vane exit flow angle distribution. The last parameter depends on (among other quantities) the spanwise twist distribution of the vane, a point that we will revisit.

In addition to the dynamic mechanisms of secondary flow generation described above, it is also necessary to take account of the kinematic circulation that exists in the rotor blade passage owing to the so-called ''relative eddy.'' The *relative* streamwise vorticity ζ_s is then given by

$$\zeta_s = \Omega_s + 2\omega\hat{i}\cdot\vec{s},$$

where $\hat{i}$ is the unit vector along the axial direction. Note that the sign of the second term in this equation is positive since ω is taken here to represent the magnitude of the angular wheel speed.

In Eq. (7), the first term on the right-hand side is of the same sign as $\partial\rho/\partial r$ since $V\cos\alpha > \omega r$ (see Fig. 7). For a radially uniform vane exit flow angle distribution, the second term is positive and hence the two terms reinforce each other in the upper portion of the streak where $\partial\rho/\partial r > 0$. On the other hand, these terms produce opposing effects in the lower portion of the streak where $\partial\rho/\partial r < 0$; semi-quantitative estimates for the hot streak considered here indicate that the effect of density stratification dominates so that the right-hand side of Eq. (7) is in fact negative in this part of the streak. A qualitative picture of the flow field in the rotor passage is depicted in Fig. 2; here the crossflow generated by the streamwise vorticity is represented schematically by the trajectory of its induced circulation. Based on the previous discussion, it is seen that the generated streamwise vorticity is positive (negative) in the upper (lower) part of the passage. The relative eddy contributes an additional positive gross circulation as illustrated. In reality, additional flow-altering features such as horseshoe vortices will be present in the blade passage. We expect nevertheless that the essential features of the flow depicted in Fig. 2 should be reproduced by the numerical simulations. In particular, we observe that close to the pressure surface, the contributions to the radial velocity from the secondary flow and relative eddy are both positive in the upper portion of the passage, while they are in opposite directions in the lower part of the passage. Thus, it is expected that the pitch angle will be asymmetrically distributed across the span, and will be significantly larger near the tip than the hub.

Baseline Geometry: Flow Analysis

The computational tool employed here is based on the scheme described by Ni [16] and Davis et al. [17]. For the transient problem, the time-dependent, Reynolds-averaged, Navier–Stokes equations are solved using an implicit, dual time-step approach coupled with a Lax–Wendroff/multiple-grid procedure. In the steady case, only the Lax–Wendroff/multiple-grid procedure is used. The algorithm has second-order spatial and temporal accuracy, using centered differences for the spatial derivatives with second- and fourth-order smoothing for stability. Turbulence closure is achieved using the Baldwin–Lomax [18] model. No-slip and adiabatic boundary conditions were implemented at the solid boundaries while the nonreflecting conditions of Giles [19] were employed at the downstream boundary. At the interblade row boundaries, where the computational grid sectors move relative to each other, the pseudo-time rate of change of the primary variables is interpolated from the adjacent blade row and added to that determined from the Lax–Wendroff discretization. The code has been extensively validated and further details may be found in the works of Takahashi and Ni [7], Davis et al. [20], Ni [16], Ni and Bogoian [21], and Ni and Sharma [22].

Numerical simulations were carried out for a low-speed, single-stage turbine geometry. The stator consists of radially stacked airfoil sections designed to produce a spanwise variation of the exit flow angle at midpassage, as shown in Fig. 3. In presenting our results, the temperature data are normalized using the background total temperature at the vane inlet. A circular hot streak was superposed upon the otherwise uniform vane inlet conditions. The total temperature distribution at the (computational) inlet boundary when the streak is centered at 50 percent-span is illustrated in Fig. 4; the peak value of 1.3 is representative of that in a typical modern engine. In all of the calculations presented, the total pressure at the vane inlet was assumed to be uniform, mimicking the experimental conditions of Butler et al. [2], so that Eq. (7) applies.

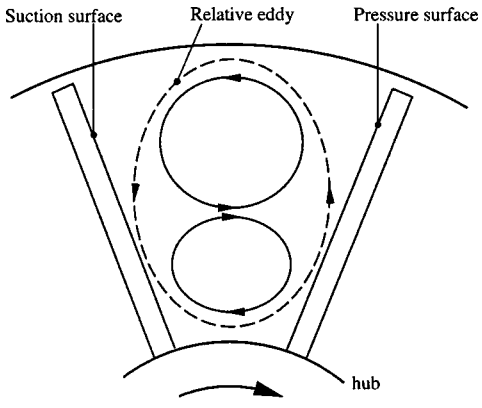

Fig. 2 Schematic illustration of the secondary flow in the rotor passage. The direction of the primary flow is out of the plane. Note that in the upper part of the blade passage, the radial velocity contribution from the secondary flow (solid line) reinforces that from the relative eddy (broken line) near the pressure surface.

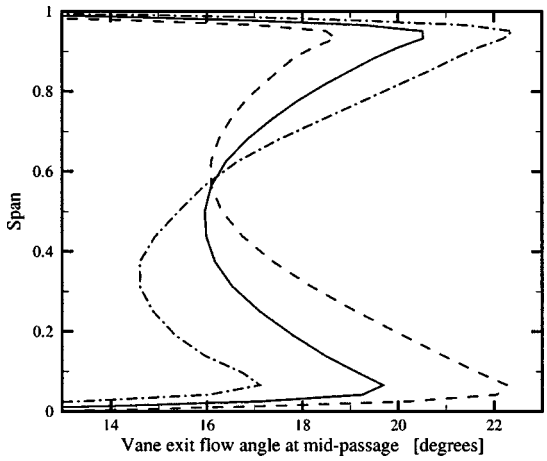

Fig. 3 Variation of the vane exit flow angle at midpassage as a function of span. The solid line illustrates the vane exit flow angle for the baseline geometry, while – – – and ·–· represent positive and reverse twist (see ''Secondary Flow Control''), respectively.

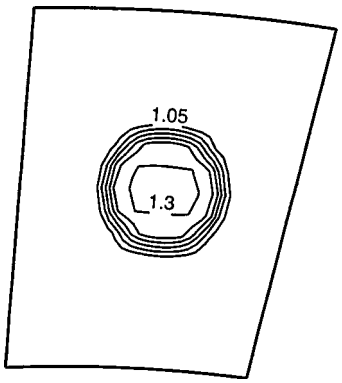

Fig. 4 Contours of total temperature at the inlet boundary; values range from 1.05 to 1.3 in steps of 0.05

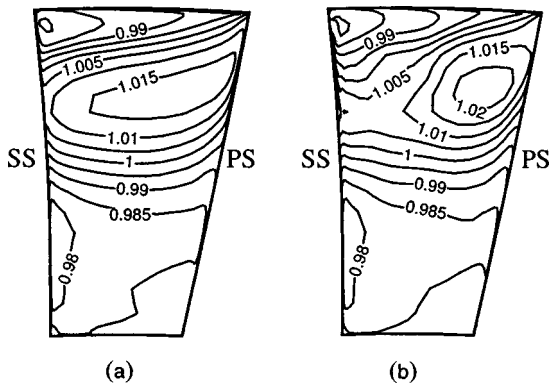

Fig. 6 Temperature distribution in blade at 33 percent chord: (*a*) steady computation, (*b*) time-averaged unsteady computation. The segregation of the hot fluid toward pressure surface (on the right side) is evident.

Unsteady Flow Effects. The primary obstacle to using the secondary flow theory is that it is valid only for steady flow. While this assumption is true for the stator, it is evident that its applicability to the rotor flow field is questionable. In order to clarify this issue, two sets of calculations were carried out with a hot streak directed into the center of a vane passage at 75 percent span. In the first run, steady inlet boundary conditions were imposed on the stator, while the rotor inlet conditions were obtained by carrying out a circumferential average of the flow quantities at the interfacial plane between the stator and rotor. This procedure determined a ''steady'' flow in the turbine stage. The second set of computations comprised a full unsteady run, which was then time-averaged in order to facilitate a comparison with the first calculation. The results are presented in terms of the pitch angle, defined as $\tan^{-1}(W_r/W_z)$.

We illustrate in Fig. 5 the distributions of the pitch angle on a plane perpendicular to the turbine axis located 0.33 chord lengths downstream of the blade leading edge; numerical data are presented along radial lines that lie close to the pressure and suction surfaces and at midpassage. It is evident that the flow distortion by the secondary vorticity is well predicted by the steady model. Specifically, we observe that the region of relatively large pitch angle variation in the vicinity of the pressure surface is common to both computations. Furthermore, the direction of radial transport near the pressure surface is toward the blade tip. These features are in accord with our qualitative conclusions based on Fig. 2. The agreement between the results of the two computational

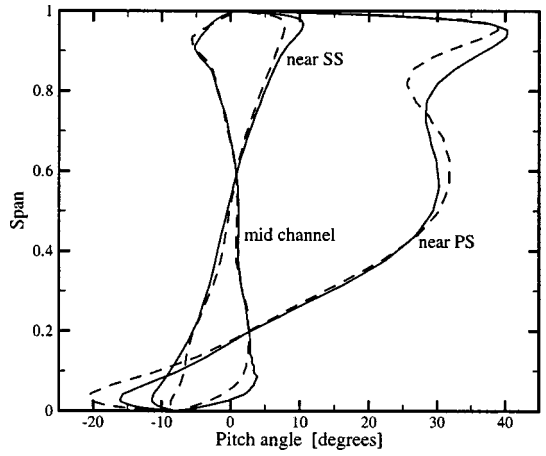

Fig. 5 Spanwise variation of pitch angle at three circumferential locations. The solid lines represent the results of the steady run, while the broken lines represent those for the time-averaged unsteady run.

procedures is significant because it implies that the dynamics of the secondary flow may be understood in terms of the steady theory of Hawthorne [14] described earlier. Furthermore, it now becomes possible to compare differing blade designs with regard to their secondary flow properties by carrying out comparatively inexpensive steady-state computations.

We also note that it is not possible to make a general statement about the direction of radial transport since it depends crucially on the secondary flow in the passage. Thus, it is entirely possible that the streak may be transported toward the hub instead of the tip, depending on the temperature of the streak and the aerodynamics of the stage. In particular, under the approximations described earlier, we observe from Eq. (1) that the secondary flow in the blade passage is driven by the rotary total pressure gradient and the centrifugal (buoyancy) force. In the investigation of Shang and Epstein [11], the trajectory of the streak was found to be well predicted using an analysis that considered only the buoyancy effect, suggesting its dominance for their configuration. This is, however, not always the case, and both terms must be included in general.

Despite the fact that the steady theory provides a good estimate of the radial transport velocity, it should not be expected that this would hold true for the temperature distribution. Indeed, the temperature distributions on the tangential planes at 0.33 chord for the steady-state and time-averaged computations, shown in Fig. 6, illustrate that although the general features of the field are captured by the latter, there is a significant circumferential variation that is not. The reason for this discrepancy is understood when one considers the segregation effect of Kerrebrock and Mikolajczak [23], wherein the requirements of circumferential uniformity of total and static pressure and absolute flow angle at the vane exit plane give rise to an increase in the relative angle of attack on the blade with fluid temperature. This causes accumulation of hot fluid on the pressure side of the blade. The procedure used to obtain the ''steady'' flow solution performs a circumferential average of the rotor inlet quantities, resulting in a loss of information concerning the tangential variation. The experiments of Butler et al. [2] were the first to demonstrate this segregation; the phenomenon has also been observed in previous numerical work, as noted earlier.

Radial Transport in the Rotor. The transport of the hot streak in the rotor passage is now examined using the results of the steady computation. In the reference frame of the rotor, the rotary total temperature is defined by,

$$T^* = T + \frac{1}{2c_p}(W^2 - \omega^2 r^2),$$

where c_p is the specific heat at constant pressure. It may be shown that this quantity is conserved along streamlines for steady, inviscid, adiabatic flow (see, for example [24]). Since the Reynolds number of the flow under consideration is large, diffusive effects are small and thus T^* is (approximately) convected with the flow. Hence, the rotary total temperature field is indicative of the streamline pattern in the rotor. The distribution of T^* on a plane parallel to and near the pressure surface but outside its boundary layer is illustrated in Fig. 9(*b*). The hot fluid within the streak is observed to move toward the blade tip, indicating radial distortion of the streamlines. Thus we conclude that the radial velocity induced by the secondary flow in the rotor passage of this low-speed configuration is capable of transporting hot fluid to the tip region.

Secondary Flow Control

Theoretical Considerations. We have thus far examined the physical phenomena underlying radial transport in the turbine, viz., secondary flows induced by flow turning, density stratification, and rotation. Here, we examine one possible means by which this secondary flow can be altered. It is observed from Eq. (7) that the rate of generation of streamwise vorticity depends on the vane exit flow angle, $\alpha=\alpha(r)$. This suggests that it is possible to affect the secondary flow in the blade passage by varying the vane exit metal angle. In the present study, this is accomplished by twisting the defining airfoil sections about the stacking axis. Consider now the velocity triangle at a typical radial section, as shown in Fig. 7. It is evident that $V\cos\alpha>\omega r$ and therefore the first term on the right-hand side of Eq. (7) is positive (negative) in the upper (lower) portion of the streak where the density is an increasing (decreasing) function of the radial coordinate. Recalling that the relative eddy contributes a further positive quantity to the relative streamwise vorticity in the blade passage, it appears that in order to reduce radial transport in the upper portion of the blade passage, one must require generally that the remaining term in Eq. (7) be negative. This results in a vane exit flow angle, α, which increases along the radial direction in the upper portion of the passage, where the temperature decreases with radius. This will henceforth be referred to as ''reverse twist'' whereas the complementary geometry, where α decreases with r will be called ''positive twist.'' In what follows, we apply both types of twist to the nominal vane; for simplicity, the twist is imposed linearly in a symmetric manner across the span. Semi-quantitative estimates

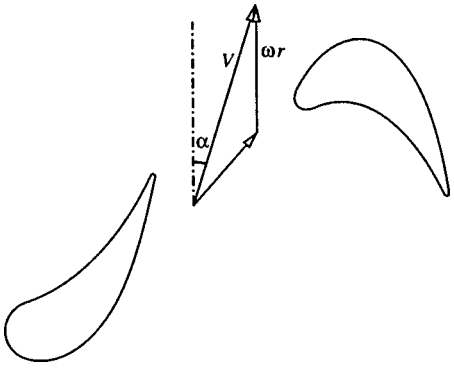

Fig. 7 Velocity triangle at vane exit

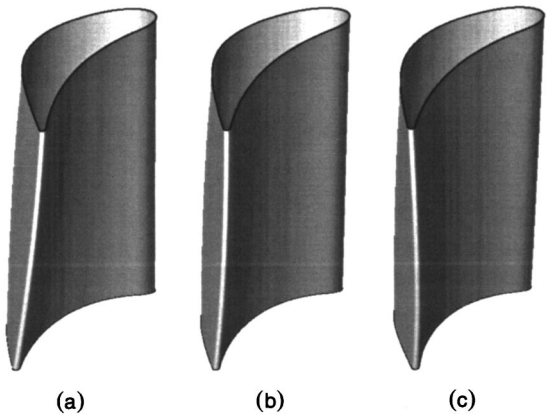

Fig. 8 Illustration of (*a*) positive, (*b*) nominal, and (*c*) reverse twist

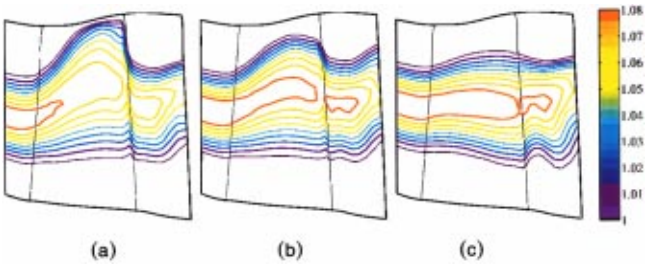

Fig. 9 Steady-state temperature distribution close to the pressure surface of the blade passage for vanes with: (*a*) positive twist, (*b*) nominal twist, and (*c*) reverse twist

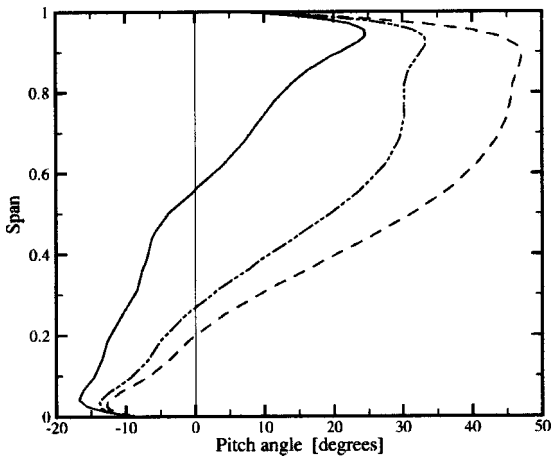

Fig. 10 Pitch angle at a streamwise distance of 0.33 chord downstream of the leading edge of the rotor blade, along a radial line close to the pressure surface; the nominal case is represented by –···–, while – – – and — represent the positive and reverse twist cases, respectively

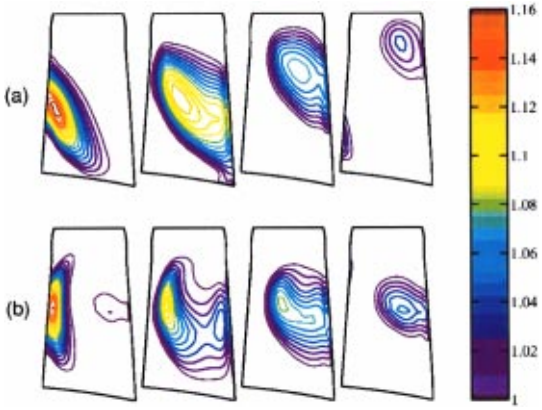

Fig. 11 Instantaneous view of temperature contours in four successive blade passages for vanes with: (*a*) positive twist, and (*b*) reverse twist

based on Eq. (7) indicate that a twist amplitude (from midspan to hub/tip) of 5 deg is sufficient to reduce the radial transport in the blade significantly. The vane geometries obtained upon applying positive and reverse twists of amplitude 5 deg are shown in Fig. 8 together with the nominal design. The resulting exit flow angle variations at midpassage are illustrated in Fig. 3.

Numerical Results. Computational runs were carried out with the streak positioned at 50 percent span. Since the new geometries are motivated by steady theory, we commence our study with steady-state calculations. Furthermore, a one-streak/one-vane/one-blade configuration was employed; this enables the relative merits of the three configurations to be compared at a reduced computational cost.

As we have pointed out earlier, the rotary total temperature, T^*, is convected with the steady flow in the rotor and is thus indicative of the magnitude of radial transport. In Fig. 9, we illustrate for each of the vanes in Fig. 8 contours of T^* on a computational surface parallel to the rotor pressure surface and close to it but outside the boundary layer. It is evident that positive twist enhances the secondary flow in the rotor significantly and the temperature distribution in the tip region indicates increased radial transport compared to the nominal case. Conversely, reverse twist has the opposite effect on radial transport: The outward curvature of the streamlines is diminished and the streak is directed toward the center of the blade passage. Illustrated in Fig. 10 are radial profiles of the pitch angle along a line that is located 0.33 chord lengths downstream of the leading edge and just outside the boundary layer on the pressure surface. These profiles demonstrate that the effect of reverse or positive twist is to decrease or increase the pitch angle by as much as 50 percent in comparison with the nominal case.

Having verified that the effect of vane twist on the steady flow in the rotor is in agreement with the theory, the behavior of the streak under fully unsteady conditions is studied. The configuration employed reflects the real geometry and consists of a one-streak/three-vane/four-blade configuration. The unsteady temperature field is visualized on the same plane as in Fig. 10. A view of the temperature contours is shown in Fig. 11(a,b) at an instant when the temperature uniformity enters the first blade passage. The position of the temperature contours in the other passages then illustrates the trajectory that is followed by the streak.[1] In both cases, the streak tends to diffuse. It is nevertheless clear that the streak is transported to the periphery of the blade when a positive twist is imposed on the vane, whereas in the case of reverse twist, the radial position of the streak at the middle of the blade span is maintained. Thus, the results of the earlier steady-state calculation are observed to carry over to the unsteady case and we conclude that radial migration of the streak can be effectively controlled by modifying the vane exit flow angle distribution via the twist.

Discussion

The present investigation was motivated by the need to provide a clear understanding of the fluid dynamic mechanisms that are responsible for radial transport of hot streaks in turbine rotors. This transport is caused by the secondary flow in the blade passage and since the processes are believed to be primarily convective in nature, a low-speed turbine configuration is used as a model. Making use of the results of Hawthorne [14], it is seen that the secondary flow is driven by hot streak-induced density gradients and by spatial variations in the flow angle entering the rotor. Computations were carried out to examine the relevance to the rotor flow of Hawthorne's [14] theory of steady secondary flow. Despite the unsteady nature of the relative flow entering the rotor, it is found that the steady theory provides a very good estimate of the radial transport velocity. Hence we conclude that it is possible to compare the relative merits of competing designs using inexpensive steady computations.

The occurrence of radial transport assumes particular importance in modern engines with very high turbine inlet temperatures. The transport of hot fluid toward the periphery of the blade results in large thermal loads on the blade tip and the outer air seal. We have shown that it is possible to influence the secondary flow and thus the thermal loads in the blade passage by suitably altering the vane exit flow angle. One way by which this may be effected is to vary the spanwise twist distribution. This technique was investigated in detail and was found to be very effective in controlling the trajectory of the hot streak through the passage. It was found that a ''reverse'' twist, wherein the vane exit flow angle increases with span, is necessary to diminish radial transport. It is to be emphasized, however, that the specification of a vane twist distribution is merely a vehicle by which the vane exit flow angle may be altered; the same distribution of the vane exit flow angle could have been obtained by suitably altering other aspects of the vane geometry.

The present study has focused on a configuration that is representative of the Reynolds number and flow coefficient of modern engines and thus captures the essential convective mechanisms. However, the direct application of the present results to the actual engine environment must be done with care, primarily because of compressibility effects. For example, as we have noted earlier, the potential (bow-wave) rotor–stator interaction in a high-speed turbine can significantly influence the flow field [11]. In addition, alteration of the vane exit flow angle distribution will change the rotor thermal and aerodynamic loading so that a redesign of the blade may become necessary. Finally, the results concerning vane exit angle as a means of altering the rotor secondary flow were derived on the assumption of a uniform vane inlet total pressure. While this is not strictly true for engine flows, it is expected nevertheless that the general trend of requiring a larger vane exit angle at the tip than at midspan should hold.

Acknowledgments

The authors are indebted to Professor E. M. Greitzer (MIT) and Dr. J. S. Sabnis (Pratt & Whitney) for many stimulating discussions on this topic. The assistance provided by Dr. J. A. Busby and Dr. C. G. Fotache in performing the simulations described here is also greatly appreciated.

References

[1] Elmore, D. L., Robinson, W. W., and Watkins, W. B., 1983, ''Dynamic Gas Temperature Measurement System,'' NASA CR 168267.
[2] Butler, T. L., Sharma, O. P., Joslyn, H. D., and Dring, R. P., 1989, ''Redistribution of an Inlet Temperature Distortion in an Axial Flow Turbine Stage,'' J. Propul. Power, **5**, pp. 64–71.
[3] Hawthorne, W. R., 1951, ''Secondary Circulation in Fluid Flow,'' Proc. R. Soc. London, Ser. A, **206**, pp. 374–387.
[4] Rai, M. M., and Dring, R. P., 1990, ''Navier–Stokes Analysis of the Redistribution of Inlet Temperature Distortions in a Turbine,'' J. Propul. Power, **6**, pp. 276–282.
[5] Krouthen, B., and Giles, M. B., 1988, ''Numerical Investigation of Hot Streaks in Turbines,'' AIAA Paper No. 88-3015.
[6] Dorney, D. J., Davis, R. L., and Edwards, D. E., 1992, ''Unsteady Analysis of Hot Streak Migration in a Turbine Stage,'' J. Propul. Power, **8**, pp. 520–529.
[7] Takahashi, R. K., and Ni, R.-H., 1991, ''Unsteady Hot Streak Migration Through a $1\frac{1}{2}$-Stage Turbine,'' AIAA Paper No. 91-3382.
[8] Dorney, D. J., and Gundy-Burlet, K. L., 1995, ''Hot Streak Clocking Effects in a $1\frac{1}{2}$-Stage Turbine,'' J. Propul. Power, **12**, pp. 619–620.
[9] Takahashi, R. K., Ni, R.-H., Sharma, O. P., and Staubach, J. B., 1996, ''Effect of Hot Streak Indexing in a $1\frac{1}{2}$-Stage Turbine,'' AIAA Paper No. 96-2796.
[10] Roback, R. J., and Dring, R. P., 1993, ''Hot Streaks and Phantom Cooling in a Turbine Rotor Passage: Part 1—Separate Effects,'' ASME J. Turbomach., **115**, pp. 657–666.
[11] Shang, T., and Epstein, A. H., 1997, ''Analysis of Hot Streak Effects on Turbine Rotor Heat Load,'' ASME J. Turbomach., **119**, pp. 544–553.
[12] Horlock, J. H., and Lakshminarayana, B., 1973, ''Secondary Flows,'' Annu. Rev. Fluid Mech., **5**, pp. 247–279.

[1]This was also verified using animations of the unsteady motion of the streak through the rotor passages.

[13] Lakshminarayana, B., and Horlock, J. H., 1973, ''Generalized Expressions for Secondary Vorticity Using Intrinsic Coordinates,'' J. Fluid Mech., **59**, pp. 97–115.
[14] Hawthorne, W. R., 1974, ''Secondary Vorticity in Stratified Compressible Fluids in Rotating Systems,'' CUED/A-Turbo/TR 63, University of Cambridge.
[15] Munk, M., and Prim, R. C., 1947, ''On the Multiplicity of Steady Gas Flows Having the Same Streamline Pattern,'' Proc. Natl. Acad. Sci. U.S.A., **33**, pp. 137–141.
[16] Ni, R.-H., 1982, ''A Multiple Grid Scheme for Solving the Euler Equations,'' AIAA J., **20**, pp. 1565–1571.
[17] Davis, R. L., Ni, R.-H., and Carter, J. E., 1986, ''Cascade Viscous Flow Analysis Using Navier–Stokes Equations,'' AIAA Paper No. 86-0033.
[18] Baldwin, B. S., and Lomax, H., 1978, ''Thin Layer Approximation and Algebraic Model for Separated Turbulent Flows,'' AIAA Paper No. 78-257.
[19] Giles, M. B., 1990, ''Nonreflecting Boundary Conditions for Euler Equation Calculations,'' AIAA J., **28**, pp. 2050–2058.
[20] Davis, R. L., Shang, T., Buteau, J., and Ni, R.-H., 1996, ''Prediction of 3-D Unsteady Flow and Multi-Stage Turbomachinery Using an Implicit Dual Time-step Approach,'' AIAA Paper No. 96-2565.
[21] Ni, R.-H., and Bogoian, J. C., 1989, ''Predictions of 3-D Multi-stage Turbine Flow Fields Using a Multiple-Grid Euler Solver,'' AIAA Paper No. 89-0203.
[22] Ni, R.-H., and Sharma, O. P., 1990, ''Using a 3-D Euler Flow Simulation to Assess Effects of Periodic Unsteady Flow Through Turbines,'' AIAA Paper No. 90-2357.
[23] Kerrebrock, J. L., and Mikolajczak, A. A., 1970, ''Intra-stator Transport of Rotor Wakes and its Effect on Compressor Performance,'' ASME J. Eng. Power, **92**, pp. 359–368.
[24] Cumpsty, N. A., 1989, *Compressor Aerodynamics*, Longman.

A Study of the Effects of Tip Clearance in a Supersonic Turbine

Daniel J. Dorney
Department of Mechanical Engineering,
Virginia Commonwealth University,
Richmond, VA 23284-3015

Lisa W. Griffin
Fluids Dynamics Analysis Branch,
NASA Marshall Space Flight Center,
Marshall Space Flight Center, AL 35812

Frank W. Huber
Riverbend Design Services,
Palm Beach Gardens, FL 33418

Flow unsteadiness is a major factor in turbine performance and durability. This is especially true if the turbine is a high work design, compact, transonic, supersonic, counterrotating, or uses a dense drive gas. The vast majority of modern rocket turbine designs fall into these categories. In this study a parallelized unsteady three-dimensional Navier–Stokes analysis has been used to study the effects of tip clearance on the transient and time-averaged flow fields in a supersonic turbine. The predicted results indicate improved performance in the simulation including tip clearance. The main sources of the performance gains were: (1) a weakened shock system in the case with tip clearance, and (2) the fact that the reductions in the shock losses were greater than the losses introduced by tip clearance. [S0889-504X(00)02404-1]

Introduction

Flow unsteadiness is a major factor in turbine performance and durability. This is especially true if the turbine is a high work design, compact, transonic, supersonic, counterrotating, or uses a dense drive gas. The vast majority of modern rocket turbine designs fall into these categories. For example, the STME (Space Transportation Main Engine) fuel turbine, a high work, transonic design, was found to have an unsteady interrow shock, which reduced efficiency by 2 points and increased dynamic loading by 24 percent. The Revolutionary Reusable Technology Turbopump (RRTT), which uses full flow oxygen for its drive gas, was found to shed vortices with such energy as to raise serious blade durability concerns. In both cases, the sources of the problems were uncovered (before turbopump testing) with the application of validated, unsteady computational fluid dynamics (CFD) to the designs. In the case of the RRTT and the Alternate Turbopump Development (ATD) turbines, the unsteady CFD codes have been used not just to identify problems, but to guide designs that mitigate problems due to unsteadiness. Using unsteady flow analyses as a part of the design process will lead to turbine designs with higher performance (which affects temperature and mass flow rate) and fewer dynamics problems. The works of Griffin et al. [1–4], Garcia et al. [5], and Griffin and Dorney [6] are examples of the application of unsteady CFD to rocket turbine designs.

In practice, some supersonic turbines are designed with rotating shrouds, while others are designed with tip clearance. While extensive research has been performed to understand tip clearance flows in subsonic and transonic turbomachines (e.g., Foley and Ivey [7]; Suder and Celestina [8]; Kang and Hirsch [9]; Chima [10]), much less effort has been put into studying tip clearance flows in supersonic turbines. An improved understanding of the influence of tip clearance on the flow field in supersonic turbines will help designers improve both durability and performance. In this study a parallelized unsteady three-dimensional Navier–Stokes analysis has been used to investigate the effects of tip clearance on the performance of a candidate turbine for the next generation reusable launch vehicle.

Numerical Algorithm

The governing equations considered in this study are the time-dependent, three-dimensional Reynolds-averaged Navier–Stokes equations. To extend the equations of motion to turbulent flows, an eddy viscosity formulation is used. The turbulent viscosity is calculated using the two-layer Baldwin–Lomax algebraic turbulence model [11].

The numerical algorithm used in the three-dimensional computational procedure consists of a time-marching, implicit, finite-difference scheme. The procedure is third-order spatially accurate and second-order temporally accurate. The inviscid fluxes are discretized according to the scheme developed by Roe [12]. The viscous fluxes are calculated using standard central differences. An alternating direction, approximate-factorization technique is used to compute the time rate changes in the primary variables. Newton subiterations are used at each global time step to increase stability and reduce linearization errors. For all cases investigated in this study, two Newton subiterations were performed at each time step. The Message Passing Interface (MPI) software has been implemented into the numerical analysis to reduce the computation time for large-scale three-dimensional simulations.

The Navier–Stokes analysis uses O- and H-type zonal grids to discretize the flow field and facilitate relative motion of the rotating components (see Fig. 1). The O-grids are body-fitted to the surfaces of the airfoils and generated using an elliptic equation solution procedure. They are used to resolve the viscous flow in

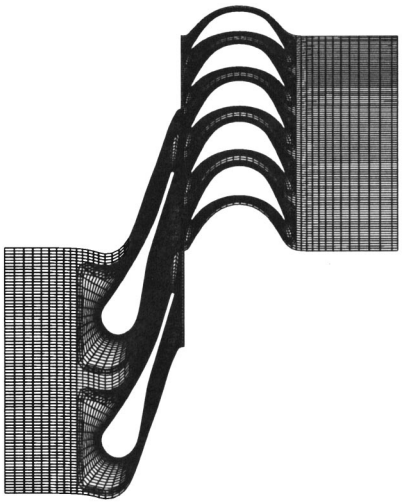

Fig. 1 Midspan section of O–H grid topology for the turbine

Contributed by the International Gas Turbine Institute and presented at the 45th International Gas Turbine and Aeroengine Congress and Exhibition, Munich, Germany, May 8–11, 2000. Manuscript recieved by the International Gas Turbine Institute February 2000. Paper No. 2000-GT-447. Review Chair: D. Ballal.

the blade passages properly and to apply the algebraic turbulence model easily. The algebraically generated H-grids are used to discretize the remainder of the flow field.

The computational analysis has been validated on several cases including tip clearance (e.g., Dorney et al. [13]; Dorney and Schwab [14]). Further details on the numerical procedure can be found in [6,13].

Boundary Conditions

The theory of characteristics is used to determine the boundary conditions at the inlet and exit of the computational domain. For subsonic inlet flow four quantities are specified and one is extrapolated from the interior of the computational domain. In particular, the total pressure, total temperature, and the circumferential and radial flow angles are specified as a function of the radius. The upstream running Riemann invariant, $R_2 = u - (2a/\gamma - 1)$, is extrapolated from the interior of the computational domain.

For subsonic outflow, one flow quantity is specified and four are extrapolated from the interior of the computational domain. The circumferential and radial flow angles, total pressure, and the total temperature are extrapolated from the interior of the computational domain. The pressure ratio, P_2/P_{t0}, is specified at midspan of the computational exit and the pressure at all other radial locations at the exit is obtained by integrating the equation for radial equilibrium. For supersonic outflow all the flow variables are extrapolated. Periodicity is enforced along the outer boundaries of the H-grids in the circumferential direction.

For viscous simulations, no-slip boundary conditions are enforced along the solid surfaces. It is assumed that the normal derivative of the pressure is zero at solid wall surfaces. In addition, a specified heat flux distribution is held constant in time along the solid surfaces.

The flow variables at zonal boundaries are explicitly updated after each time step by interpolating values from the adjacent grid.

Geometry and Grids

The turbine configuration consists of 21 nozzle airfoils and 52 rotor blades. In the current effort a two-nozzle/five-rotor blade count approximation has been made. To keep the pitch-to-chord ratio constant, the nozzle airfoils were scaled by factor of 21/20 and the rotor blades were scaled by a factor of 52/50.

Two simulations have been performed for the turbine, one with the design tip clearance of approximately 2.5 percent span (Case 1) and one with no tip clearance and a rotating shroud (Case 2). In the current study it has been assumed, as a design constraint, that the endwall profiles are similar in both cases. Therefore, the rotor blades in the case without tip clearance extend 2.5 percent more in the spanwise direction than the rotor blades in the tip clearance case. Note, the endwall flowpath diverges between the vane and rotor passages such that the rotor airfoils have a larger span than the vanes.

The grid densities (number of passages$\times i \times j \times k$) for the turbine simulations are presented in Table 1. The total number of grid points used to discretize the turbine in Case 1 was 1,411,422 and the total number of points used in Case 2 was 1,363,022. Figures 1 and 2 illustrate $(x-y)$ and $(z-y)$ views of the grids (note, every second grid point has been removed for clarity), while Fig. 3 illustrates the grids used to discretize the tip clearance region. Figure 4 shows a perspective view of one nozzle airfoil and one rotor blade. The average value of y^+, the nondimensional distance of the first grid line above the surface was approximately 1.5 for the airfoils surfaces and 3.5 for the endwall surfaces. The grid densities were determined based on a compromise between the need for accurately modeling the correct blade count ratio and the computation time. Previous simulations suggested that 38 spanwise planes are adequate to resolve the predominant flow features [6].

The simulations were run on seven (250 MHz) processors of an SGI Origin2000 computer located at NASA Ames Research Center. Each simulations was run for 5.0 global cycles at 25,000 iterations per cycle. A global cycle is defined as the time it takes for the five rotor blades to pass by the two nozzle airfoils. The value of 25,000 iteration per cycle was chosen to resolve all the (expected) frequencies of interest. Each iteration required approxi-

Table 1 Grid dimensions for the two-nozzle/five-rotor simulations

Case 1 Grid Type	Nozzle	Rotor
O	2x121x31x38	5x121x21x38
H	2x86x41x38	5x82x21x38
Tip	–	5x121x16x5
Total Points	553,052	858,370
Case 2 Grid Type	**Nozzle**	**Rotor**
O	2x121x31x38	5x121x21x38
H	2x86x41x38	5x82x21x38
Tip	–	–
Total Points	553,052	809,970

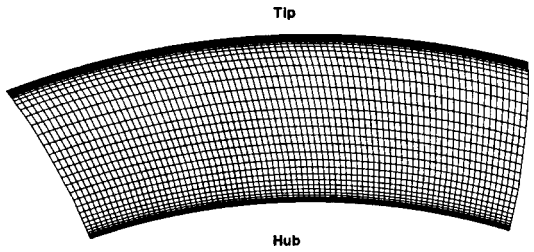

Fig. 2 Axial-direction view of the computational grids for the turbine

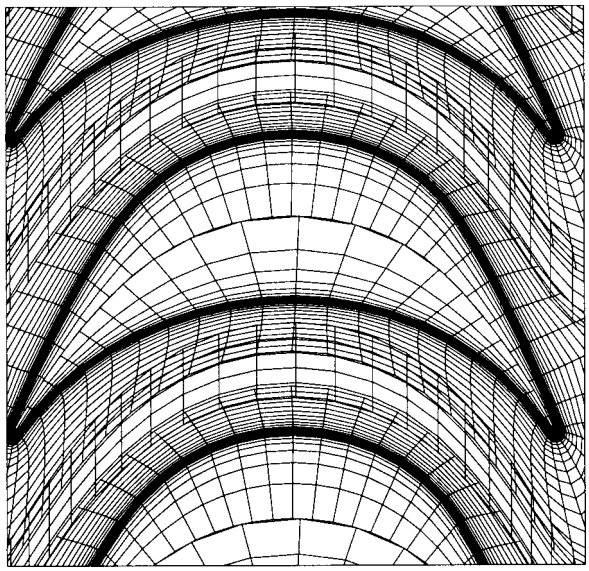

Fig. 3 Tip clearance grids for the turbine

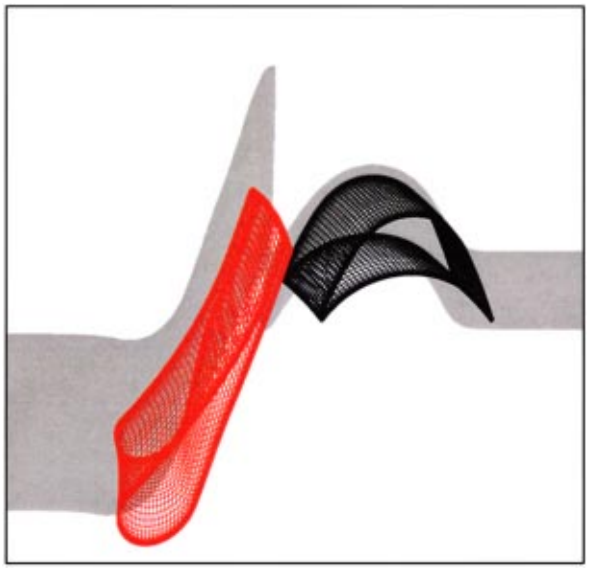

Fig. 4 Perspective view of the nozzle and rotor grids for the turbine

mately 16 seconds computation time on seven processors. The time periodicity of the solutions was determined by interrogating pressure traces at different points along the airfoil surfaces (this is shown in the next section).

Numerical Results

The candidate turbine under consideration has a design inlet Mach number of $M_0 = 0.12$, an inlet static pressure of 15.2 MPa, and an inlet static temperature of approximately $T_0 = 1232$ K. The rotor rotates at $\Omega = 31{,}300$ rpm, the Reynolds number (based on the inlet conditions and the rotor axial chord) is approximately 5×10^5, and the ratio of the rotor exit static pressure to vane inlet total pressure is $P_2 / P_{t0} = 0.1875$. Air, with a specific heat ratio of $\gamma = 1.3537$, was used as the operating gas in the current study.

Figures 5 and 6 illustrate time-averaged nondimensional entropy contours for Cases 1 and 2, respectively, at 50 percent span. The contours in the case without tip clearance indicate thicker

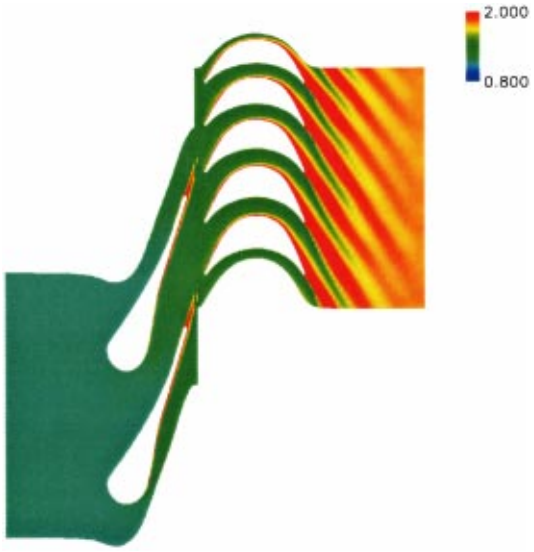

Fig. 5 Time-averaged entropy contours—50 percent span—Case 1

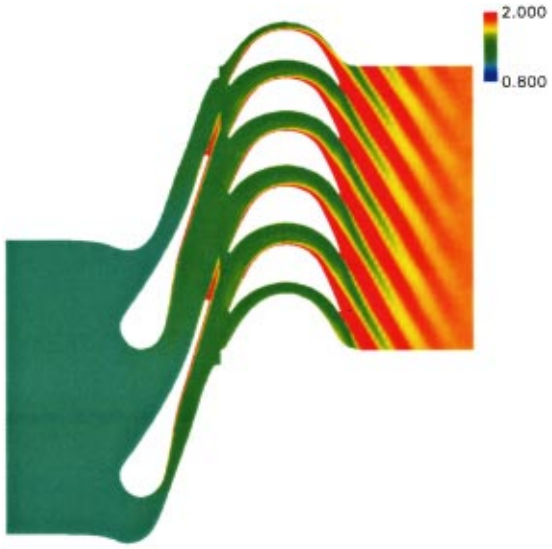

Fig. 6 Time-averaged entropy contours—50 percent span—Case 2

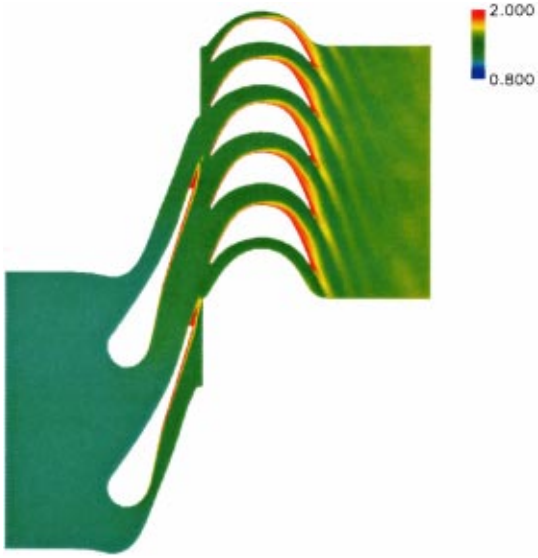

Fig. 7 Time-averaged entropy contours—75 percent span—Case 1

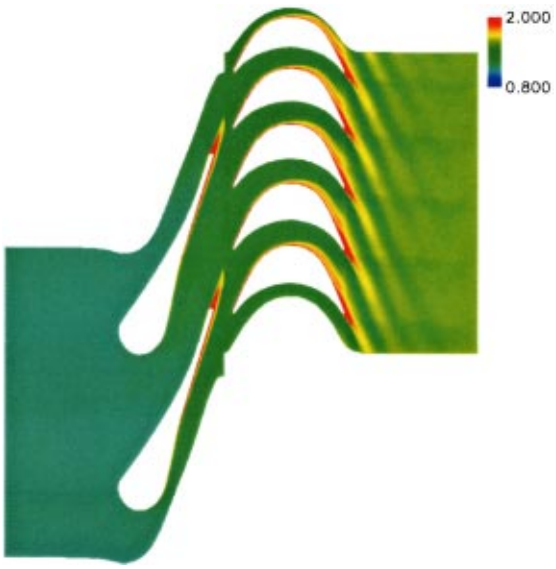

Fig. 8 Time-averaged entropy contours—75 percent span—Case 2

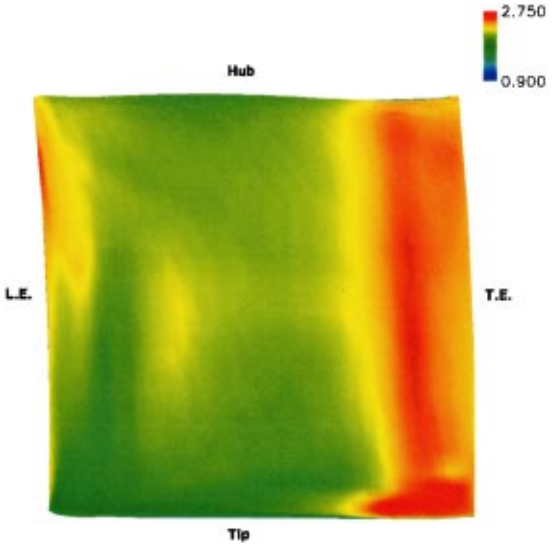

Fig. 9 Time-averaged entropy contours on rotor S.S.—Case 1

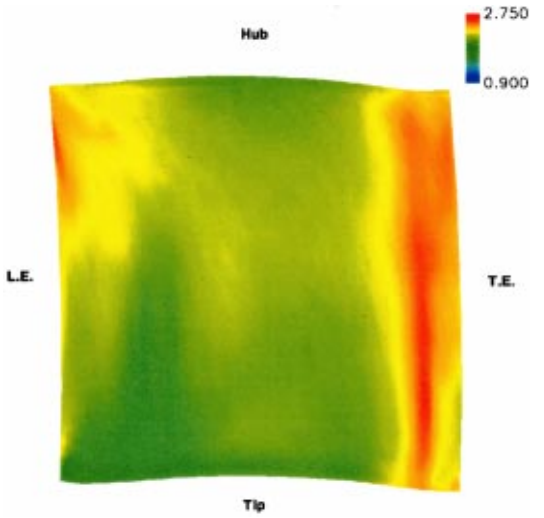

Fig. 10 Time-averaged entropy contours on rotor S.S.—Case 2

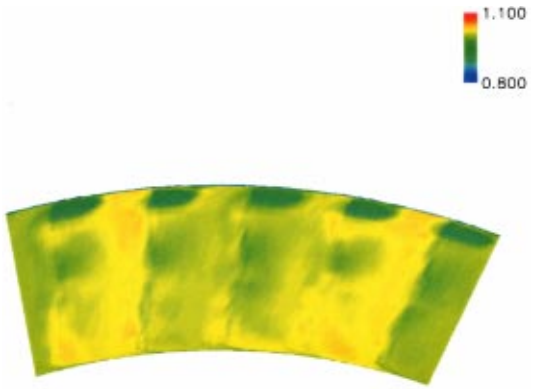

Fig. 11 Time-averaged total temperature contours at rotor passage exit—Case 1

vane and rotor wakes. Both cases display some passage-to-passage time-averaged flow variations in the rotor, both underscoring the need for accurate blade count approximations and indicating the presence of unsteadiness at frequencies other than the blade-passing frequency. Time-averaged entropy contours at 75

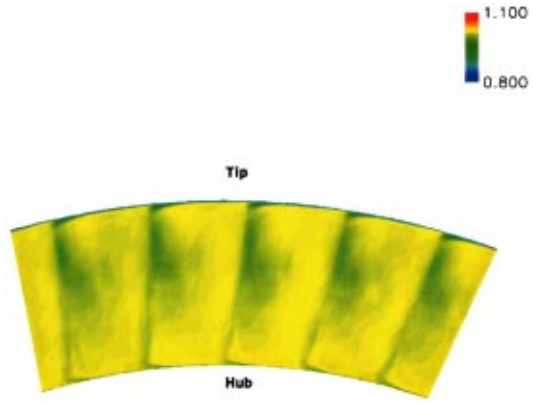

Fig. 12 Time-averaged total temperature contours at rotor passage exit—Case 2

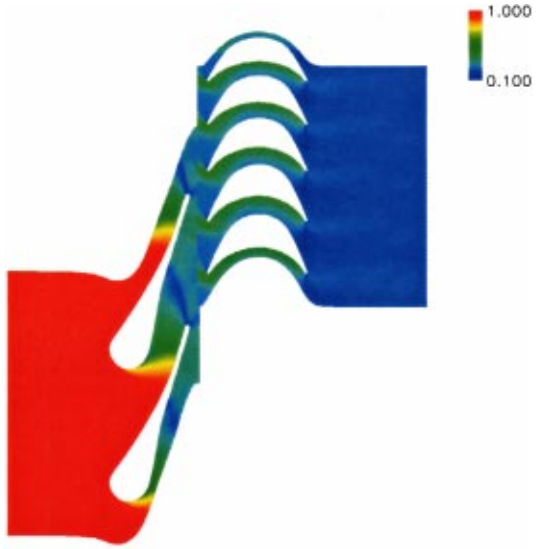

Fig. 13 Time-averaged pressure contours—50 percent span—Case 1

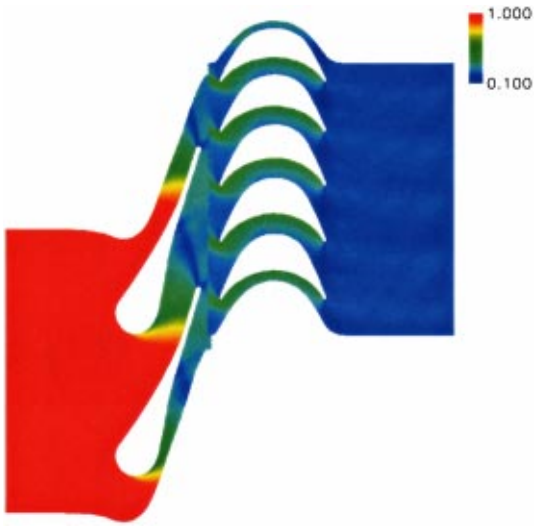

Fig. 14 Time-averaged pressure contours—50 percent span—Case 2

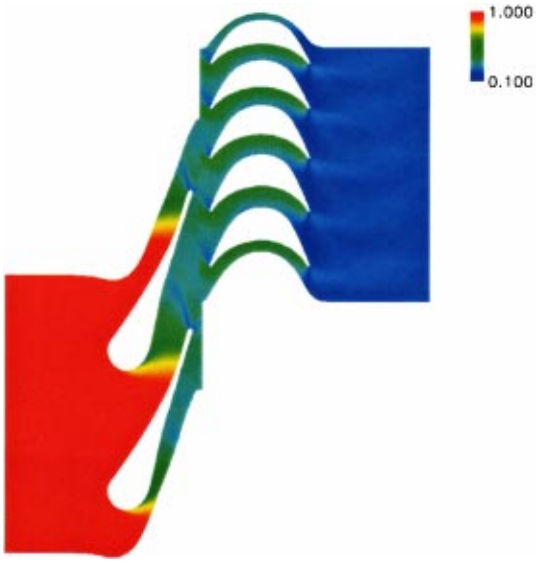

Fig. 15 Time-averaged pressure contours—75 percent span—Case 1

percent of the span are shown in Figs. 7 and 8. At this spanwise location the wakes are still thicker in the case without tip clearance.

Figures 9 and 10 show time-averaged entropy contours on the suction surface of the rotor for Cases 1 and 2, respectively. Both figures show increased entropy levels associated with the flow separation near the trailing edge of the suction surface. The case with tip clearance shows additional entropy generated near the trailing edge at the tip, and is due to the clearance vortex. Figures 9 and 10 also indicate increased entropy levels near the leading edge in the hub region, although the region is more extensive in the case without tip clearance. Figures 11 and 12 contain time-averaged absolute total temperature contours just downstream of the rotor trailing edge plane. The case without tip clearance is characterized by a relatively uniform total temperature distribution across the span, except for reduced values in the endwall and wake regions. The case with tip clearance shows strong gradients in the circumferential direction near the tip. The overall average

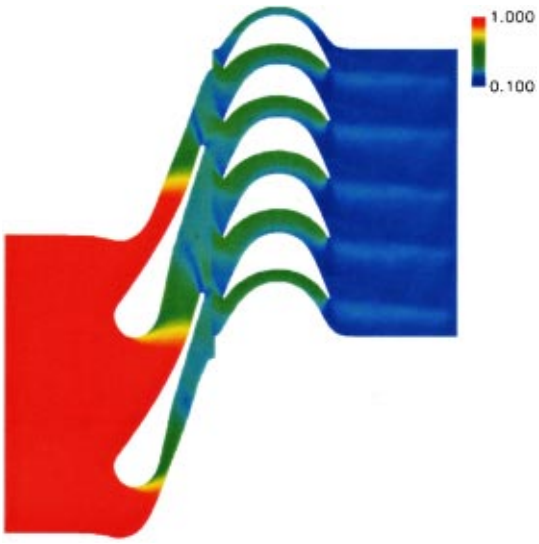

Fig. 16 Time-averaged pressure contours—75 percent span—Case 2

Table 2 Turbine time-averaged flow quantities

	Case 1		Case 2	
Variable	Nozzle	Rotor	Nozzle	Rotor
M_{in}	0.12	1.35	0.12	1.46
M_{out}	1.35	0.90	1.46	0.95
$(P/P_\infty)_{in}$	0.999	0.285	0.999	0.263
$(P/P_\infty)_{out}$	0.285	0.189	0.263	0.189
Tt_{in}	1235^o K	1234^o K	1235^o K	1234^o K
Tt_{out}	1234^o K	1020^o K	1234^o K	1029^o K
$(Pt/P_\infty)_{in}$	1.008	0.829	1.008	0.889
$(Pt/P_\infty)_{out}$	0.829	0.320	0.889	0.337
α_{in}	0.0^o	71.7^o	0.0^o	71.9^o
α_{out}	71.7^o	-51.6^o	71.9^o	-48.4^o
η_{tt}	–	0.671	–	0.667
η_{ts}	–	0.479	–	0.470

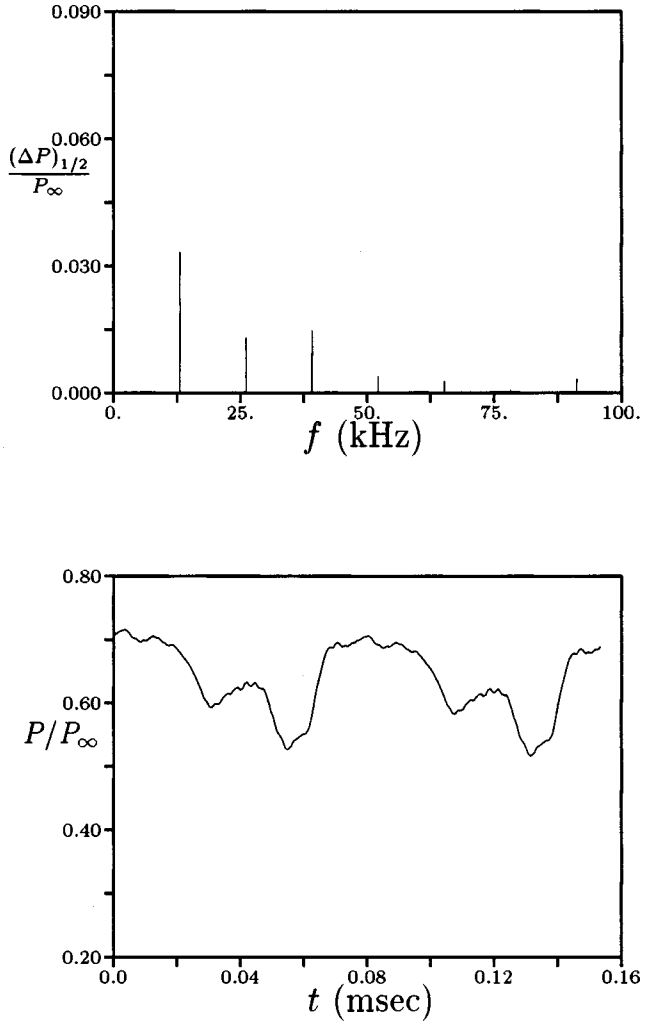

Fig. 17 Unsteady pressure history and decomposition—60 percent span leading edge—Case 1—rotor

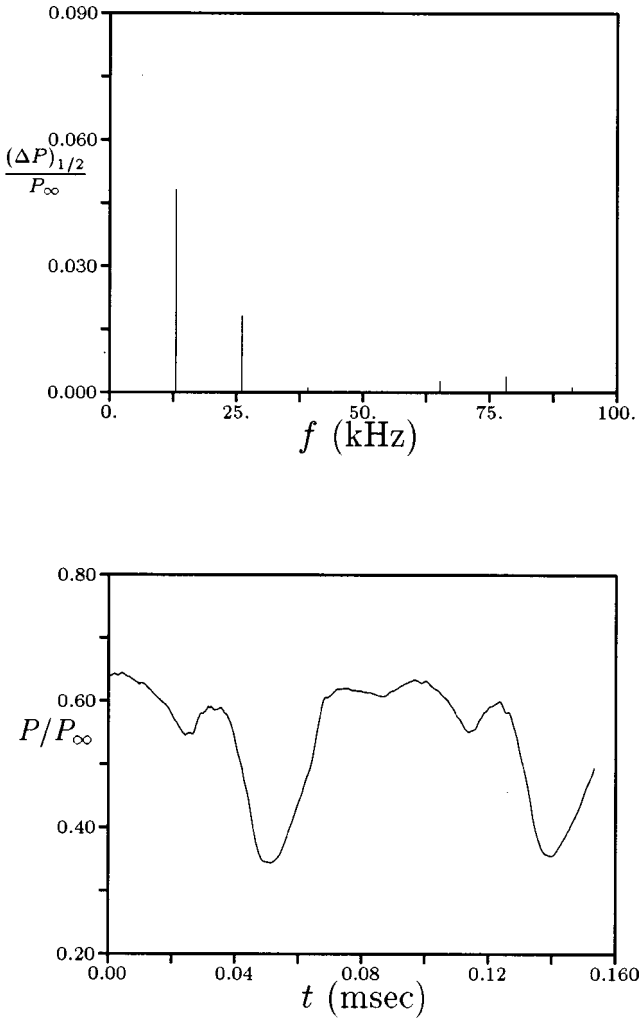

Fig. 18 Unsteady pressure history and decomposition—60 percent span leading edge—Case 2—rotor

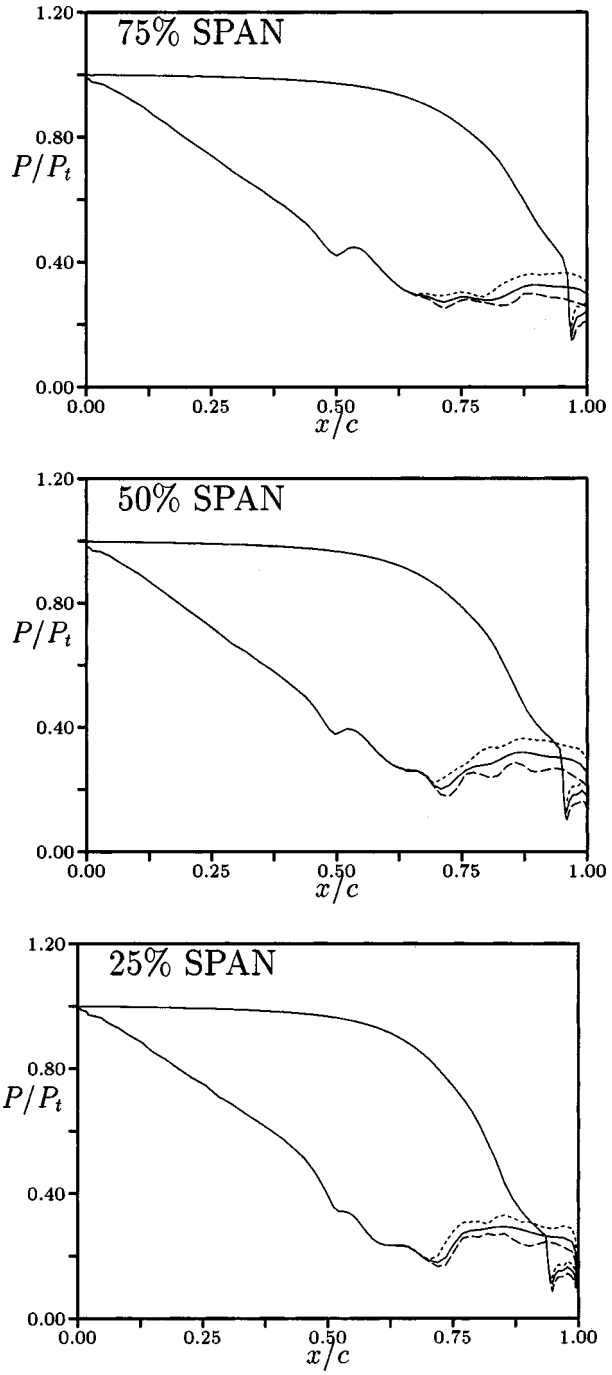

Fig. 19 Unsteady pressure envelope—Case 1—vane; –– min, —— avg, - - - max

total temperature in the tip clearance region is higher than in the case with tip clearance, indicating less work being extracted from the flow in this region.

Figures 13–16 show time-averaged nondimensional (nondimensionalized by the inlet static pressure) static pressure contours at 50 and 75 percent span for the two cases. At 50 percent span the vane trailing edge expansion wave pattern is stronger in the case without tip clearance (Case 2). This in turn leads to a stronger shock in the rotor. Both simulations contain a standing shock near the exit of the rotor passage. In Case 1, the expansion and shock wave patterns weaken considerably by 75 percent span (see Fig. 15), while the wave patterns are still strong in Case 2. The differences in the pressure fields are mirrored by the values of the time-averaged Mach numbers at a plane midway between the vane and rotor airfoils (see Table 2). Henceforth, the term ''inlet'' to the rotor will refer to this plane midway between the vane and rotor airfoils. The absolute Mach number at the rotor inlet is significantly lower in the case with tip clearance. The increased Mach number in the case without tip clearance may be caused by the fact that the rotor span is 2.5 percent greater than in the case with tip clearance. In addition, the effective area in Case 1 must be smaller, generating a back pressure effect on the vane.

Thus, the time-averaged entropy and pressure contours suggest that the flow fields are different in the two cases. Referring to Table 2, these differences result in the time-averaged total-to-static stage efficiency being higher in the simulation with tip clearance ($\eta_{ts}=0.479$) than in the simulation without tip clearance ($\eta_{ts}=0.470$). Note, a mean-line analysis for the turbine (which accounts for tip leakage) yielded a predicted total-to-static stage efficiency of $\eta_{ts}=0.472$. Thus, the additional losses generated by the stronger expansion wave/shock system (which results in higher rotor inlet Mach numbers) in Case 2 overwhelm the losses associated with the introduction of tip clearance. It is interesting to note that, although the Mach number entering the rotor is significantly lower in Case 1, the Mach numbers are closer at the exit of the rotor.

Figures 17 and 18 contain Fourier decompositions and time histories of the unsteady pressure at 60 percent span near the leading edge on the rotor pressure surface for Cases 1 and 2,

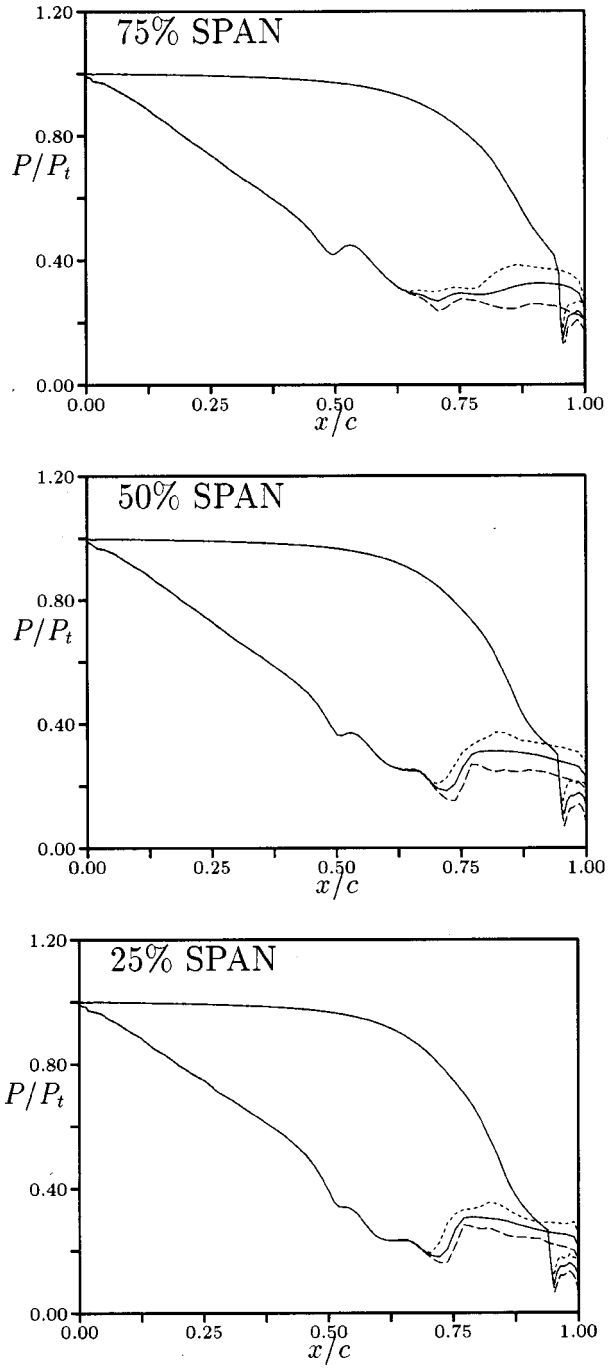

Fig. 20 Unsteady pressure envelope—Case 2—vane; – – min, —— avg, - - - max

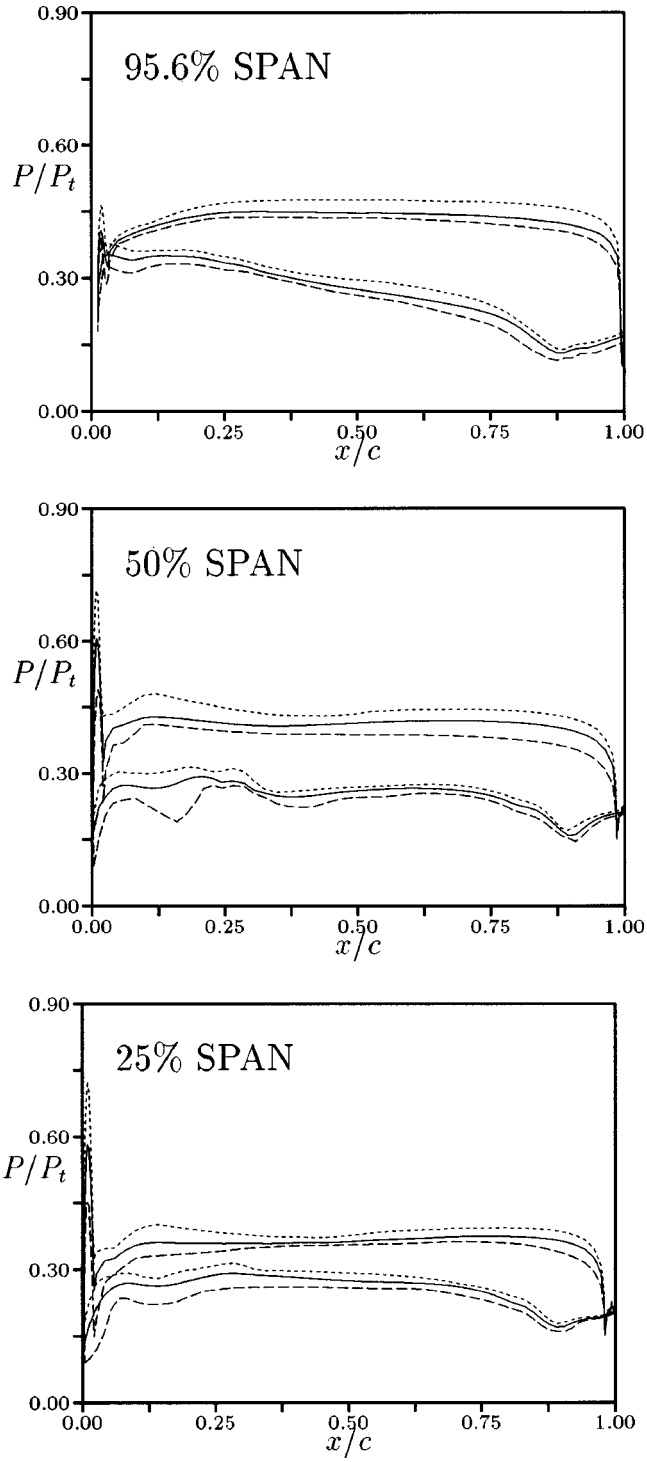

Fig. 21 Unsteady pressure envelope—Case 1—rotor; – – min, —— avg, - - - max

respectively. This location corresponds to the location of maximum unsteadiness at the blade passing frequency in Case 2. Both cases display significant unsteadiness at the vane passing frequency (approximately 13 kHz) and at twice the vane passing frequency. The pressure histories for the two cases demonstrate the time periodicity of the solutions (pressure histories were interrogated at many points to confirm the supposition). The presence of the stronger shock system in Case 2 is evident by the large pressure drop at approximately 0.05 ms (see Fig. 18).

Figures 19 and 20 contain unsteady pressure envelopes on the vane at 25, 50, and 75 percent of the span for Cases 1 and 2, respectively. At the 50 and 75 percent spanwise locations, the case without tip clearance exhibits a stronger shock than the case with tip clearance. The pressure at the trailing edge is higher in Case 1, which agrees with the stronger expansion waves in Case 2. Although the only significant unsteadiness in both cases is located on the suction surface downstream of the throat, the unsteadiness is larger in the case without tip clearance. Figures 21 and 22 illustrate unsteady pressure envelopes on the rotor at 25, 50, and 95.6 percent of the span for Cases 1 and 2. There are several distinguishing features in these two figures. First, both cases display a large amount of unsteadiness, especially near the leading edge on the suction surface (with more overall unsteadiness being

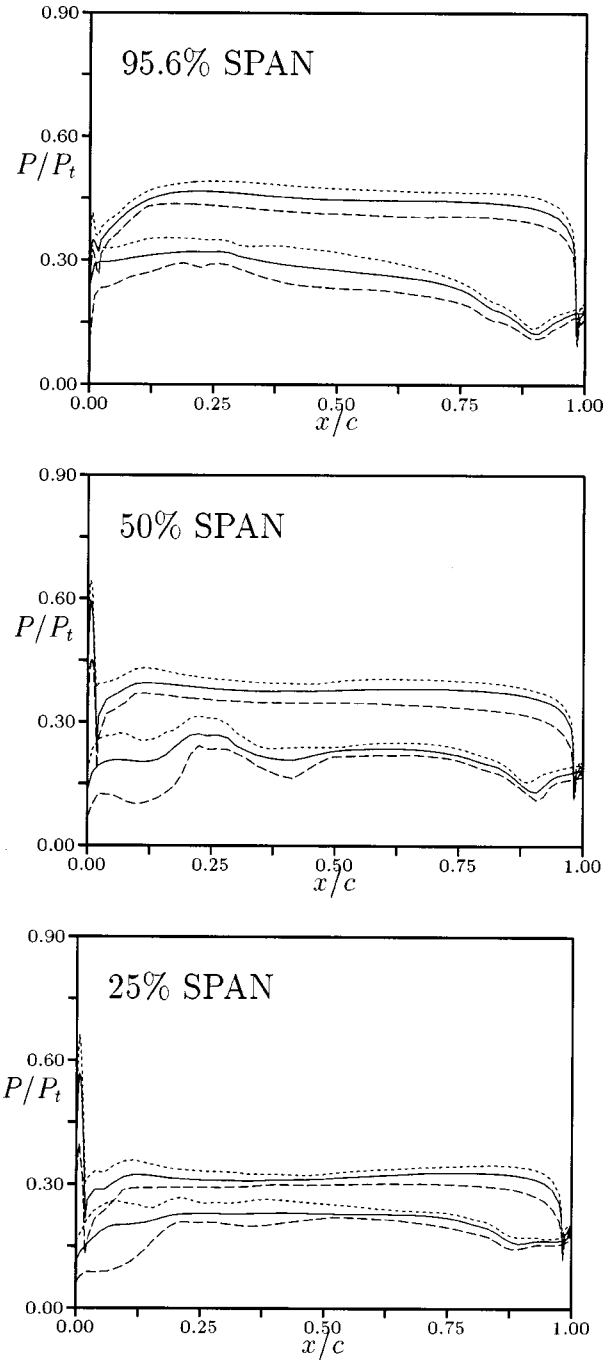

Fig. 22 Unsteady pressure envelope—Case 2—rotor; – – min, —— avg, - - - max

exhibited by Case 2). Second, the case with tip clearance becomes increasingly unloaded near leading edge at the tip. To compensate for the reduced loading in the tip region, the rotor in Case 1 shows increased loading from the hub to approximately 60 percent span.

Radial profiles of the circumferentially averaged absolute Mach number at the vane exit/rotor inlet are shown in Fig. 23. The average Mach number at the vane exit is higher in the case without tip clearance, which is consistent with the stronger shock system shown in Figs. 14 and 16. The shapes of the two profiles at the rotor exit are similar from the hub to approximately 80 percent of the span (see Fig. 24). In the tip region the Mach number is lower in Case 1 due to the effects of the tip clearance flows. Radial profiles of the absolute circumferential flow angle at the exits of the vane and rotor are shown in Figs. 25 and 26, respectively. The case without tip clearance displays a gradual decrease in the flow angle with increasing span (other than in the endwall regions) at the vane exit. The case with tip clearance shows large flow angle deficits in both the hub and outer case regions, while the flow angles in the region from 20 to 70 percent span are similar to those in the case without tip clearance. The average flow angles, however, are within 0.2 deg for the two cases (see Table 2). At the rotor exit the average flow angles are more negative in Case 1 (see Table 2), except near the tip, indicating more flow turning and more work. This fact is consistent with the higher efficiency and larger total temperature drop in Case 1.

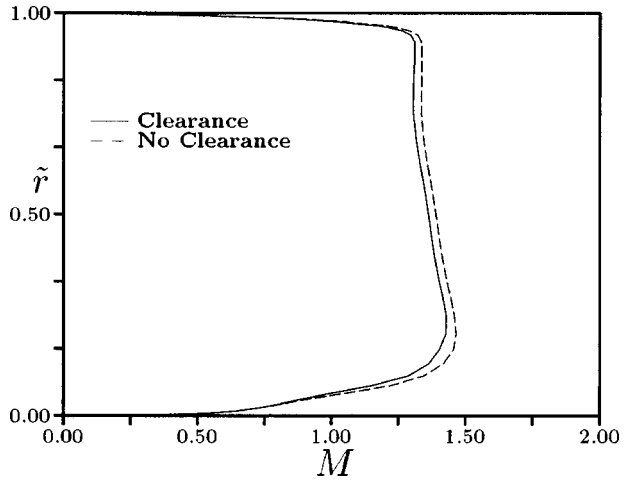

Fig. 23 Radial profile of circumferentially averaged absolute Mach number—vane exit

Radial profiles of the circumferentially averaged absolute total pressure at the vane exit/rotor inlet are illustrated in Fig. 27. The profiles are similar, although Case 1 shows slightly higher losses from the hub to 85 percent span. At the rotor exit both distributions have similar shapes except for the tip region (see Fig. 28), where the losses are greater in Case 1 due to the clearance vortex. Figures 29 and 30 show radial profiles of the circumferentially averaged absolute total temperature at the exit of the vane and rotor, respectively. At the exit of the vane the total temperature distributions are similar. As the flow exits the rotor, the case with tip clearance exhibits lower total temperatures from the the hub to 80 percent span (indicating more work being extracted from the

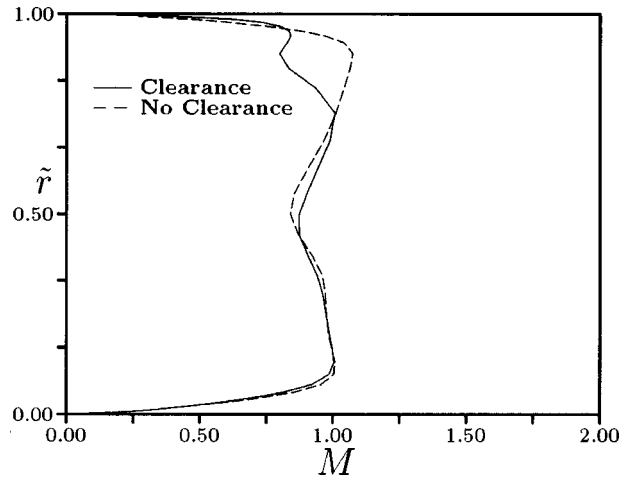

Fig. 24 Radial profile of circumferentially averaged absolute Mach number—rotor exit

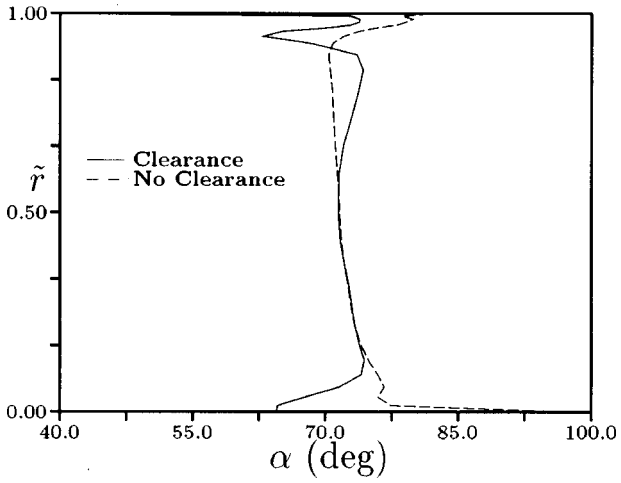

Fig. 25 Radial profile of circumferentially averaged absolute circumferential flow angle—vane exit

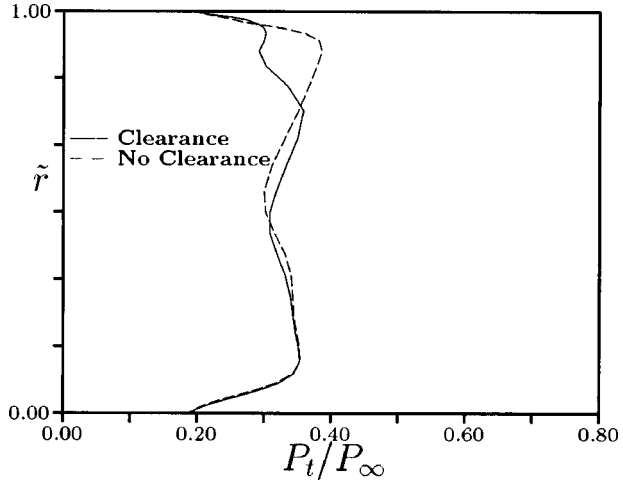

Fig. 28 Radial profile of circumferentially averaged absolute total pressure—rotor exit

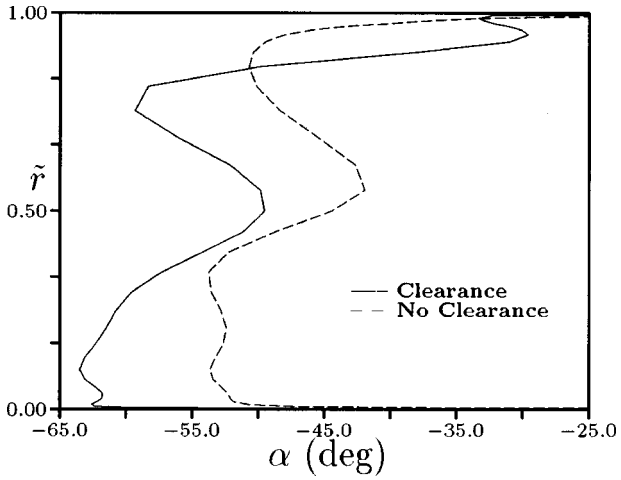

Fig. 26 Radial profile of circumferentially averaged absolute circumferential flow angle—rotor exit

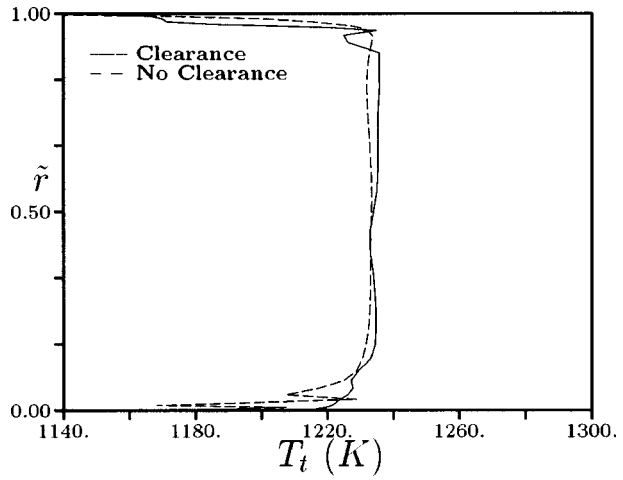

Fig. 29 Radial profile of circumferentially averaged absolute total temperature—vane exit

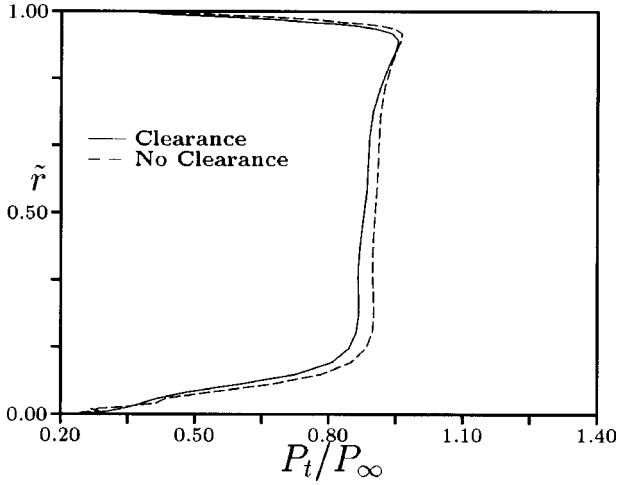

Fig. 27 Radial profile of circumferentially averaged absolute total pressure—vane exit

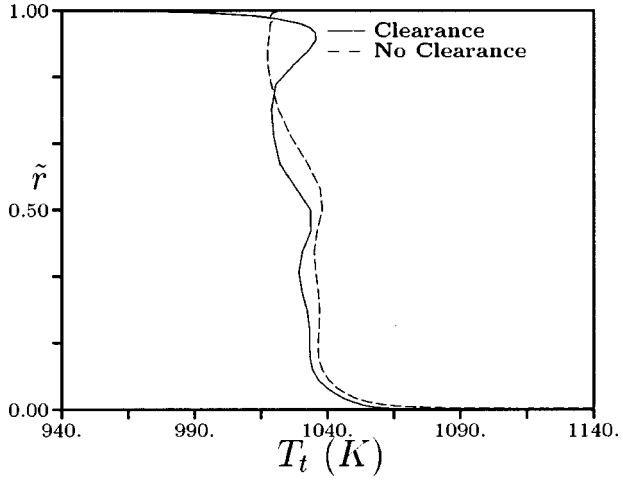

Fig. 30 Radial profile of circumferentially averaged absolute total temperature—rotor exit

flow) and higher total temperatures near the tip (indicating less work being extracted in this region due to the clearance flows).

Conclusions

A set of unsteady three-dimensional Navier–Stokes simulations has been used to investigate the effects of tip clearance on the performance of a candidate turbine for the reusable launch vehicle. The predicted results showed improved efficiency (and work) in the configuration with tip clearance. The improved performance was traced to several sources: (1) an unloading of the rotor in tip region, which reduces the losses induced by the secondary flows, (2) a reduction in the strength of the shock system in the vane/rotor, and (3) for the current turbine geometry, the reduction in the losses associated with the shock system were greater than the losses introduced by adding tip clearance. Further work is necessary to understand better the fundamental physics associated with the flow in the tip clearance region, and to determine the generality of the current results.

Acknowledgments

This work was supported by the Advanced Space Transportation Program at NASA Marshall Space Flight Center under NRA 8-21.

Nomenclature

a = speed of sound
c = axial chord
f = frequency
M = Mach number
P = static pressure
ΔP = amplitude of pressure variation
$P.S.$ = pressure surface
$S.S.$ = suction surface
$\tilde{r}$ = $(r-r_{\text{hub}})/(r_{\text{tip}}-r_{\text{hub}})$
t = time
T = static temperature
x, y, z = Cartesian coordinates
u, v, w = x, y, z components of velocity
α = absolute circumferential angle
η = efficiency
ρ = density
Ω = rotor rotational speed

Subscripts

in = inlet
out = outlet
t = stagnation quantity, time derivative
ts = total-to-static
tt = total-to-total
0 = nozzle inlet
2 = rotor exit
1/2 = half-amplitude
∞ = free stream

Superscripts

$(\tilde{\ })$ = relative frame
$(\ )^*$ = nondimensional

References

[1] Griffin, L. W., and Rowey, R. J., 1993, ''Analytical Investigation of the Unsteady Aerodynamic Environments in Space Shuttle Main Engine (SSME) Turbines,'' ASME Paper No. 93-GT-363.
[2] Griffin, L. W., and Huber, F. W., 1993, ''Advancement of Turbine Aerodynamic Design Techniques,'' ASME Paper No. 93-GT-370.
[3] Griffin, L. W., Huber, F. W., and Sharma, O. P., 1996, ''Performance Improvement Through Indexing of Turbine Airfoils: Part 2—Numerical Simulation,'' ASME J. Biomech. Eng., **118**, No. 4, pp. 636–642.
[4] Griffin, L. W., and Nesman, T., 1996, ''Prediction of the Unsteady Aerodymanic Environment in the RRTT Turbine,'' presented at the 14th Workshop for Fluid Dynamic Applications in Rocket Propulsion and Launch Vehicle Technology, NASA/Marshall Space Flight Center, Apr. 23–25.
[5] Garcia, R., Griffin, L. W., Benjamin, T. G., Cornelison, J. W., Ruf, J. H., and Williams, R. W., 1995, ''Computational Fluid Dynamics Analysis in Support of the Simplex Turbopump Design,'' NASA CP-3282, **1**, pp. 462–470.
[6] Griffin, L. W., and Dorney, D. J., 2000, ''Simulations of the Unsteady Flow Through the Fastrac Supersonic Turbine,'' ASME J. Turbomach., **122**, pp. 225–233.
[7] Foley, A. C., and Ivey, P. C., 1996, ''Measurement of Tip-Clearance Flow in a Multistage, Axial Flow Compressor,'' ASME J. Turbomach., **118**, pp. 211–217.
[8] Suder, K. L., and Celestina, M. L., 1996, ''Experimental and Computational Investigation of the Tip Clearance Flow in a Transonic Axial Compressor Rotor,'' ASME J. Turbomach., **118**, pp. 218–229.
[9] Kang, S., and Hirsch, C., 1996, ''Numerical Simulation of Three-Dimensional Viscous Flow in a Linear Compressor Cascade With Tip Clearance,'' ASME J. Turbomach., **118**, pp. 492–505.
[10] Chima, R. V., 1998, ''Calculation of Tip Clearance Effects in a Transonic Compressor Rotor,'' ASME J. Turbomach., **120**, pp. 131–140.
[11] Baldwin, B. S., and Lomax, H., 1978, ''Thin Layer Approximation and Algebraic Model for Separated Turbulent Flow,'' AIAA Paper No. 78–257.
[12] Roe, P. L., 1981, ''Approximate Riemann Solvers, Parameter Vectors, and Difference Schemes,'' J. Comput. Phys., **43**, pp. 357–372.
[13] Dorney, D. J., Davis, R. L., Edwards, D. E., and Madavan, N. K., 1992, ''Unsteady Analysis of Hot Streak Migration in a Turbine Stage,'' AIAA J. Propul. Power, **8**, No. 2, pp. 520–529.
[14] Dorney, D. J., and Schwab, J. R., 1996, ''Unsteady Numerical Simulations of Radial Temperature Profile Redistribution in a Single-Stage Turbine,'' ASME J. Turbomach., **118**, pp. 783–791.

Influence of Vane/Blade Spacing on the Heat Flux for a Transonic Turbine

M. G. Dunn

C. W. Haldeman

R. S. Abhari[1]

M. L. McMillan[2]

The Ohio State University,
Gas Turbine Laboratory,
Columbus, OH 43235

An experimental and analytical research program determining the influence of vane/blade spacing on the vane and blade time-averaged and unsteady heat flux for a full-scale rotating turbine stage was performed. The turbine stage was operated at a transonic vane exit condition, with pressure and heat flux measurements obtained throughout the stage. This paper focuses on the midspan heat flux measurements for both the vane and blade at three vane/blade axial spacings: 20, 40, and 60 percent of vane axial chord. The time-averaged heat flux results for the vane and the blade are compared with predictions obtained using a two-dimensional, Reynolds-averaged multiblade row code, UNSFLO, developed by Giles (1984). The measured and predicted unsteady heat flux envelopes (as a function of vane/blade spacing) are also compared with predictions. For selected locations on the blade, a direct comparison between the measured phase-averaged surface pressure and the measured phase-averaged Nusselt number history is presented. At some locations along the surface the pressure and the heat flux are shown to be in phase, but at other locations they are not. The influence of vane/blade spacing on the blade heat load was found to be small, and much less than the differences caused by changes in the Reynolds number during the experimental matrix. [S0889-504X(00)00904-1]

1.0 Introduction

The current design trend for high-performance machines within the gas turbine community is to reduce the weight of the turbine by decreasing vane/blade spacing, and operating at vane or blade transonic exit conditions. Improving computational capabilities to predict the adverse effects of this aggressive design trend is critical to the success of any new machine. Dring et al. [1] reported the results of an investigation (performed using a large low-speed rotating rig) designed to assess the influence of vane/blade spacing on blade pressure loading. Rao and Delaney [2] and Dunn et al. [3] reported the results of a combined experimental and computational program determining the unsteady pressure loading for a transonic turbine. The unsteady pressures resulting from the interaction of the blade and the shock wave coming from the vane represent the forcing function for potential high-cycle fatigue. More recently, Venable et al. [4] and Busby et al. [5] reported the results of a combined experimental and analysis program. That research was performed using the same transonic turbine, and was designed to determine the influence of vane/blade spacing (20, 40, and 60 percent vane axial chord) on the time-averaged and time-resolved surface pressure for the vane and blade. The heat transfer results reported here were obtained simultaneously with the pressure data just noted.

Rao et al. [6] reported heat transfer results for the same turbine used in this measurement program for a fixed vane–blade spacing of 40 percent vane axial chord at the transonic vane exit Mach number condition. The time-averaged and time-resolved surface pressure measurements corresponding to the heat transfer results reported in Rao et al. [6] are described in Dunn et al. [3].

Hilditch and Ainsworth [7] investigated the unsteady heat transfer on the blade of a rotating turbine operating at design corrected conditions. They compared their results with data from a previous two-dimensional simulation of a wake-passing flow on the midspan of the same blade. Frequency spectra for selected blade locations were reported. Abhari et al. [8] reported the results of a combined experimental and computational program that used a full-stage rotating turbine operating at corrected design conditions. They included the unsteady heat transfer for selected blade locations. Neither of these papers measured surface pressure on the blades, nor did they investigate the influence of vane/blade spacing on the heat transfer results.

2.0 Description of Experiment

The experimental data were obtained using a short-duration shock tunnel facility to provide the source of heated and pressurized air that is expanded in a conical nozzle (to lower the total pressure). This experimental technique has been described previously in the literature, e.g., [9–12], and only those aspects of the operating procedure essential for the discussion of the effort reported here will be described. A sketch of the turbine configuration and the instrumentation suite is given in both Dunn et al. [3] and Rao et al. [6].

Figure 1 is a sketch of the turbine stage located in the shock-tunnel facility. The turbine stage is located in a device designed to pass the proper turbine weight flow at the desired inlet total pressure and total temperature so that the stage design flow function is duplicated. Only a small portion of the shock-processed airflow is captured by the inlet and then passed through the turbine stage. The remainder of the gas bypasses the device. The initial speed of the rotor was controlled using an air motor. Initially the dump tank is evacuated, thus permitting the rotor to be easily brought to the proper speed. Just prior to rupturing the diaphragms and initiating the flow in the shock tube, the air supply to the motor is turned off and the rotor is free-wheeling. Between the time that the air motor is turned off and the diaphragms break, there is very little change in rotor speed. However, the speed of the rotor is measured continuously during the experiment.

The rotor blades were instrumented with both thin-film heat flux gages and flush-mounted miniature Kulite pressure transducers. Figure 2 is a photograph of the instrumented rotor. The turbine stage geometry consists of 30 vanes and 45 blades. Instrumenting every third blade (skipping two) insures that each blade is in the same relative position in the vane passage (although in a

[1]Current address: ETH Zurich, Institute of Energy Technology.

[2]Current address: Boeing Aerospace, St. Louis, MO.

Contributed by the International Gas Turbine Institute and presented at the 45th International Gas Turbine and Aeroengine Congress and Exhibition, Munich, Germany, May 8–11, 2000. Manuscript received by the International Gas Turbine Institute February 2000. Paper No. 2000-GT-206. Review Chair: D. Ballal.

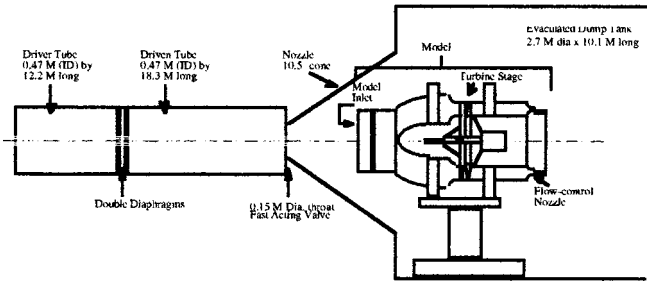

Fig. 1 Sketch of Allison VBI turbine located in OSU GTL shock tunnel

different vane passage). Figure 2 shows that the blades containing surface pressure instrumentation, the contoured leading edge heat flux gage inserts, and the pressure surface button-type thin-film heat flux gages were all located in this configuration so that no correction for phase angle was required. However, because of a desire to measure the heat flux in a single blade passage, the blade with the suction surface heat flux gages requires a phase shift when comparing the unsteady data.

2.1 Heat-Flux Instrumentation. Button-type thin-film heat flux gages were located at midspan on the pressure and suction surfaces of the vane. The rotor blades contained two contoured leading-edge inserts at midspan with each containing several thin-film gages in addition to button-type thin-film gages located at: midspan on both suction and pressure surfaces, at 96 percent span on the suction surface, on the platform, and in the recessed tip of the blade. Photographs of the midspan instrumentation are presented in Rao et al. [6]. The predictions and the discussion of the measurement program presented in this paper will be confined to the midspan data.

The question of a potential ''heat island effect'' requiring a correction factor for the button-type heat flux gages has been raised by [13–15]. The three papers rely on a two-dimensional calculation to predict the magnitude of the potential effect. More recently, Zilles and Abhari [16] experimentally investigated the magnitude of the ''heat island effect'' for conditions consistent with the present experiments. In their experiments, they operated double sided Kapton heat flux gages (for which there is no potential heat-island effect) side-by-side with thin-film button-type heat flux gages. They used a flat plate placed in a blowdown facility duplicating the fluid flow conditions of interest in this work. Zilles and Abhari arrived at a correction factor for the heat-island effect over a wide range of conditions.

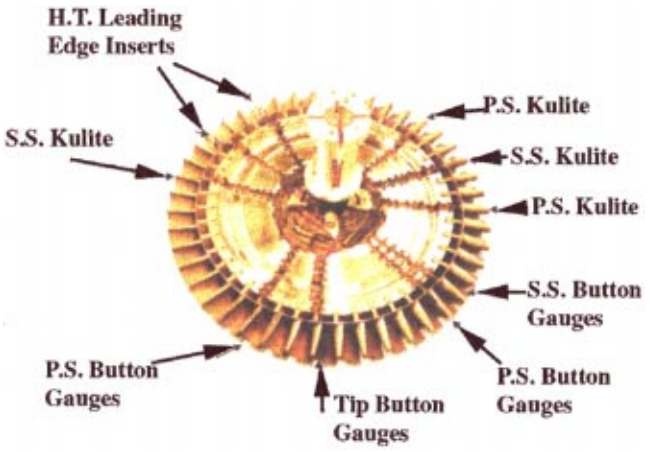

Fig. 2 General instrumented blade locations on VBI turbine

Dunn et al. [17] report the results of a measurement program for which the button-type gages were run simultaneously with three contoured strip inserts (at the Reynolds number conditions of interest in these experiments). The strip insert imbedded in the component removes the heat island influence. These measurements were performed on the vane portion of a full-stage turbine operating at design corrected conditions. The results demonstrated agreement between the heat flux (or Stanton number) data obtained using the button-type thin-film gages and the contoured strip insert thin-film gages to within the stated experimental uncertainty of ± 5 percent.

For this paper the correction factor suggested by Zilles and Abhari [16] was applied to the vane and blade data to assess the magnitude of the potential correction for the turbine and specific test conditions. Equations (15) and (13) of Zilles and Abhari [16], which are given below, are used to perform the correction:

$$\frac{\mathrm{Nu}_b}{\mathrm{Nu}_{KT}} = 1 + \Theta(1-f),$$

where

$$\Theta = \frac{T_f - T_w}{T_T - T_w} \quad \text{and} \quad f = \left(1 - \left(\frac{x_0}{x}\right)^{0.9}\right)^{-1/9} \tag{1}$$

The heat flux gages were calibrated in a temperature-controlled environment prior to and after the measurement program for calibration constants. In addition, prior to each experiment the resistance of each gage at a known temperature was measured so that the calibration could be updated. The uncertainty in the heat flux measurements reported in this paper is estimated to be ± 5 percent.

2.2 Flowpath Pressure Instrumentation. In addition to surface pressure measurements made on the vane and blade (which were reported earlier in Busby et al. [5] and Venable et al. [4]), flowpath static and total pressure measurements were also obtained using Kulite pressure transducers. Static pressure was measured at the inner and outer diameter at the turbine inlet and exit planes and between the vane and blade rows. Also, inlet and exit rakes were used to obtain flow field total pressure measurements upstream of the vane inlet and downstream of the turbine exit, and total temperature measurements upstream of the vane inlet and downstream of the turbine exit.

All of the pressure transducers were calibrated through the entire data system on a daily basis. As a very conservative number, the data can be assumed to lie within ± 0.2 psia (± 1.379 kPa) with a standard deviation of ± 0.067 psia (± 0.46 kPa). More detail regarding the pressure instrumentation can be found in Haldeman and Dunn [18] and Busby et al. [5].

2.3 Turbine Parameters and Operating Conditions. This turbine stage has been designed and constructed such that the vane exit angle can be changed easily to achieve a subsonic or a transonic vane exit Mach number. The vane/blade spacing can also be changed easily. The desired Mach number setting is obtained by rotating the vane externally and inserting a pin in the vane stem. Use of this technique results in a gap of approximately 0.004 in. (1×10^{-4} m) between the vane tip and hub endwalls. For the results reported here, the vane position was set to the transonic vane exit configuration such that the vane exit Mach number was approximately 1.1. In addition, the hardware surrounding the turbine stage was constructed such that the vane/blade spacing can be changed without influencing the rotating system by removing split-casing spacers from in front of the vane row and re-inserting these same spacers behind the vane row. Three separate spacings were used for the results reported here: 20, 40, and 60 percent of vane axial chord.

Table 1 provides a description of the relevant stage geometry, and Table 2 gives the relevant parameters for the three separate experimental conditions relevant to the data reported in this paper.

Table 1 Turbine stage geometry

Parameter	Vane	Blade
number of airfoils	30	45
axial chord, in. (mm)	2.66(67.6)	1.87 (47.5)
spacing, in. (mm)	2.03(51.6)	1.34 (34.0)
chord/spacing	1.32	1.39
mean radius, in. (mm)	9.73(247.1)	9.70 (246.4)
aspect ratio	0.72	1.10
L.E. mean radius, in. (mm)	0.18 (4.6)	0.09 (2.3)
T.E. mean radius, in. (mm)	0.03 (0.8)	0.03 (0.8)
hub/tip radius	0.82	0.81
tip radius, in. (mm)	10.64 (270.3)	10.64 (270.3)
T.E. blockage (%)	9.44	8.94

Table 2 Turbine operating conditions

Parameter	20% (spacing)	40% (spacing)	60% (spacing)
speed (rpm)	11,843	11,795	11,763
$p_{t\ 1}$, psia (KPa)	43.2 (298.1)	43.7 (301)	39.8 (274.7)
p_4, psia (KPa)	10.0 (69.1)	10.3 (71.3)	9.4 (64.8)
$T_{t\ 1}$, R (K)	1108 (615.5)	1173 (651.7)	1176 (653.4)
$T_{vane\ avg}$ R (K)	604 (335.5)	596.3 (331.3)	589 (327.3)
$T_{blade\ avg}$ R (K)	575.8 (319.9)	563.8 (313.2)	563.8 (313.2)

3.0 Discussion of Results

In the remainder of the paper, time-averaged and unsteady heat transfer results for the vane and blade are compared with the results of predictions obtained using the numerical code UNSFLO [19]. In addition, for selected locations on the blade, comparisons are presented between phase-resolved Nusselt number and surface pressure versus position in a vane passage for locations on both the pressure and suction surface of the blade.

3.1 Time-Averaged Heat Transfer Results; Prediction Versus Data for Midspan Region of Vane and Blade. The numerical procedure used to obtain the heat flux predictions presented herein is two-dimensional Reynolds-averaged, unsteady multiblade row code UNSFLO, developed by Giles [20]. This is a coupled viscous/inviscid code in which the thin shear layer Navier–Stokes equations are solved on a body-fitted boundary layer grid using an implicit algorithm, while the Euler equations are solved on an outer inviscid grid using an explicit algorithm. The code utilizes a Baldwin–Lomax algebraic turbulence model in the viscous region. More details can be found in Giles and Haimes [21] and Abhari et al. [22].

A grid independence study demonstrated that the solution presented herein was independent of the mesh density. Solutions were generated for both the vane and the blade for six different grids. Three solutions with 20,000, 45,000, and 60,000 grid points in the inviscid, unstructured mesh were compared. The influence on the steady vane surface Nusselt number was minimal, being less than 2 percent for 45,000 versus 60,000. The blade was even less sensitive to the number of grid points than was the vane. After the grid study, a 45,000 point grid was an acceptable compromise between obtaining accuracy and efficiently using the available computational resources.

The remaining solutions were generated to examine the effect of grid resolution in the viscous *O*-grid region (closely coupled grid that wraps around the airfoil), specifically the effect of increasing the thickness of the viscous *O*-grid on the surface Nusselt number distribution. Thicknesses of 2.0, 2.7, and 3.4 percent of the vane axial chord were considered. The number of points that spanned the *O*-grid was held constant at 19. Thus, increasing the thickness of the *O*-grid decreased the grid packing within the viscous region. It was necessary to maintain a thickness of at least 2.0 percent vane axial chord to contain the vane/blade boundary layer. All three *O*-grids contained adequate viscous packing of grid cells near the surface to resolve the boundary layer. In addition, utilizing the largest of the three viscous grid sizes provided the best transition from the viscous grid to the inviscid grid. Cells in the outermost region of the viscous grid were more than half the thickness of those in the innermost region of the inviscid grid. An *O*-grid thickness of 3.4 percent of vane axial chord was used for the computational results presented herein.

The experimental data are presented as a Nusselt number based on a reference length as defined in the normal manner by the following equation:

$$\mathrm{Nu}_b = \frac{QL}{K_f(T_{\mathrm{Ref}} - T_f)} \tag{2}$$

where L is a reference length: 1 in. (0.0254 m) in this case. K_f if the thermal conductivity of the fluid evaluated at the gage temperature (T_{gage}), and T_{Ref} is a reference temperature, taken as the stage inlet total temperature. The uncertainty in the experimental data is evaluated using the following formula:

$$\frac{\Delta \mathrm{Nu}_b}{\mathrm{Nu}_b} = \sqrt{\left(\frac{\Delta Q}{Q}\right)^2 + \left(\frac{\Delta T_f}{T_f}\right)^2 \left(1 + \frac{A^2}{(1-A)^2}\right) + \frac{1}{(1-A)^2}\left(\frac{\Delta T_{\mathrm{Ref}}}{T_{\mathrm{Ref}}}\right)^2}$$

$$A = \frac{T_f}{T_{\mathrm{Ref}}} \tag{3}$$

which is a simple ''error'' propagation formula, with the much smaller terms eliminated from the equation, yielding a percentage uncertainty in the Nusselt number as a function of the main independent variables used in the calculation.

Each experimental point presented in Figs. 3–10 is a value averaged over approximately 10 ms of test time (or about 1000 data points). Thus, for this uncertainty analysis, the percentage uncertainty in each of the input variables is taken as the standard deviation of that quantity divided by the average value of that quantity over the time period, with the exception of the heat flux in which the standard measurement error (± 5 percent) is used. The uncertainty is taken as twice the value reported in Eq. (3), which encompasses about 95 percent of the data spread (i.e., ± 2 standard deviations). Multiple runs were combined using a weighted average technique. In general, the uncertainty in the Nusselt number is dominated by the uncertainty in the heat flux measurements.

Figures 3, 4, and 5 present the midspan measured Nusselt numbers versus the predicted time-averaged unsteady predicted Nusselt numbers obtained for the vane at vane/blade spacings of 20, 40, and 60 percent of vane axial chord, respectively. All of the data shown in these figures were obtained using button-type gages and both the uncorrected and corrected (using [16]) data are presented on the figures. The maximum value of the correction was on the order of 10 percent and occurred at 92 percent wetted distance on the pressure surface. The suction surface heat flux gages beyond 30 percent wetted distance were damaged early in the measurement program and could not be repaired in place.

For the vane predictions, boundary layer transition was set at 25 percent wetted distance on the suction surface (based on a best fit to the data), and fully turbulent boundary layer was set at 50 percent wetted distance. A fully turbulent boundary layer was assumed for the pressure surface calculation from the stagnation point to the trailing edge. The results at all three spacings suggest that the flow on the suction surface was laminar until about 25 percent wetted distance at which location transition occurred. The agreement between prediction and the experimental data is good on that portion of the suction surface for which data are available.

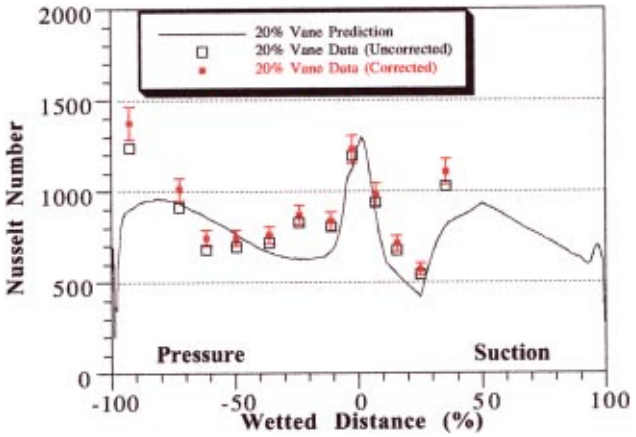

Fig. 3 Vane time-averaged Nusselt number (20 percent spacing)

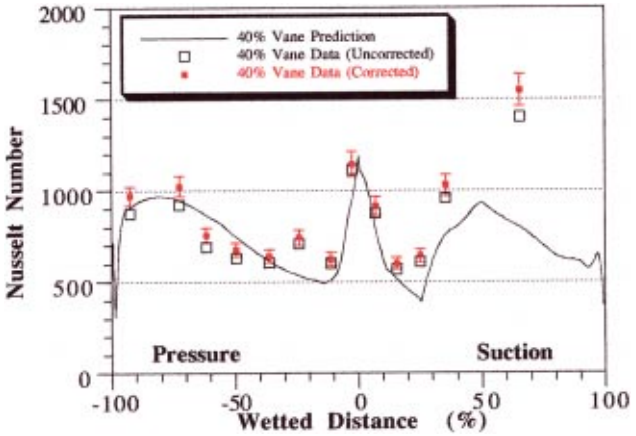

Fig. 4 Vane time-averaged Nusselt number (40 percent spacing)

On the pressure surface, the trends of the experimental and predicted Nusselt number distributions are consistent, with reasonably good agreement, with some data falling above and below the prediction. The one main exception to this is the data at −90 percent for the 20 percent spacing, that seems abnormally high. Since later measurements from the same sensor are in closer agreement with the prediction (and the general data trend), this point is suspect. However, detailed review of the experimental data provided no reason to judge the data point to be in error, so it has been retained.

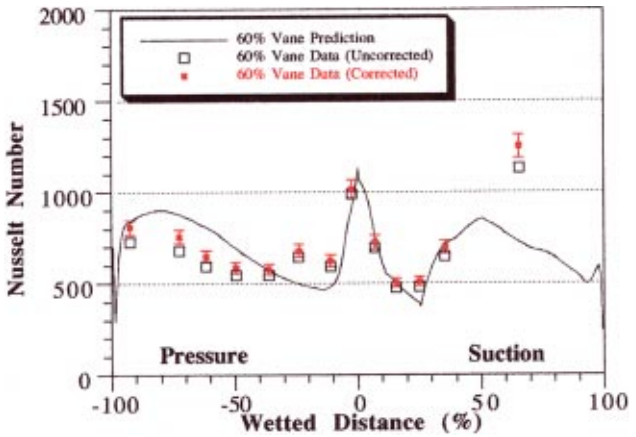

Fig. 5 Vane time-averaged Nusselt number (60 percent spacing)

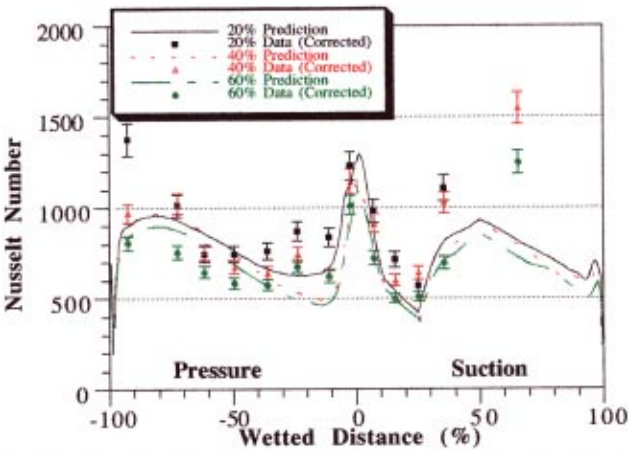

Fig. 6 Composite plot of vane Nusselt number for different spacings

Figure 6 presents a composite plot of the experimental data corrected for potential heat-island effect and the time-averaged unsteady predictions for the vane obtained for 20, 40, and 60 percent vane/blade spacing. The magnitude of the vane/blade spacing should have no significant influence on the predicted Nusselt number distribution for the vane pressure surface and for the initial 23 percent (wetted distance) of the suction surface since the vane is choked for these conditions. This can be verified by integrating the area under the curves (for both the predictions and the data). To make the comparisons more meaningful, an area from −72.5 to 35.5 percent was used for this calculation, which corresponds to the range where most of the data exist for all runs. This also eliminates the edge effects of the prediction. Performing this integration on the predictions shows that the heat flux load is reduced by about 5 percent as the spacing changes from 20 to 40 percent, and about 9 percent from 40 to 60 percent spacing. As seen from Table 2, the Reynolds numbers for these spacings also changed (about 6 percent for the 20 to 40 percent spacing and 9 percent for the 40 to 60 percent spacing). Thus, it would appear that the main driver for the variation in the heat load to the vanes is the change in the experimental Reynolds number rather than the vane–blade spacing. This is consistent with the hypothesis that there should be little interaction because the flow is choked.

Figures 7–9 present a comparison between the UNSFLO time-

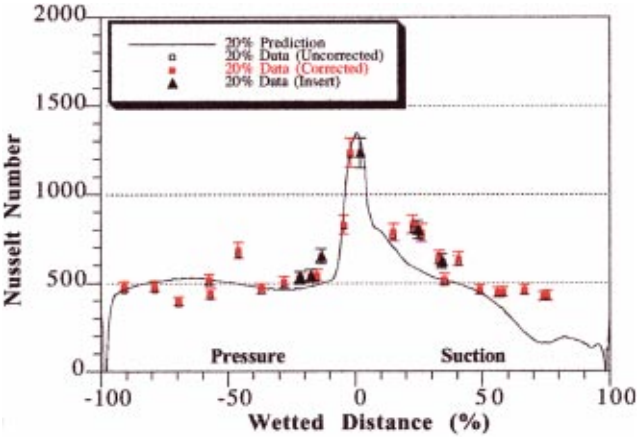

Fig. 7 Blade time-averaged Nusselt number (20 percent spacing)

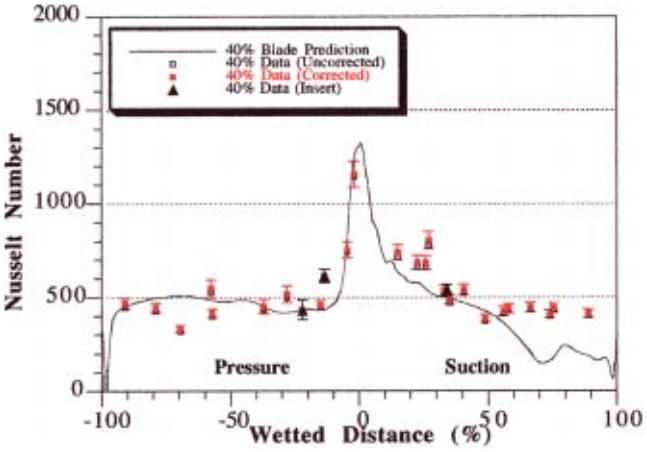

Fig. 8 Blade time-averaged Nusselt number (40 percent vane–rotor spacing)

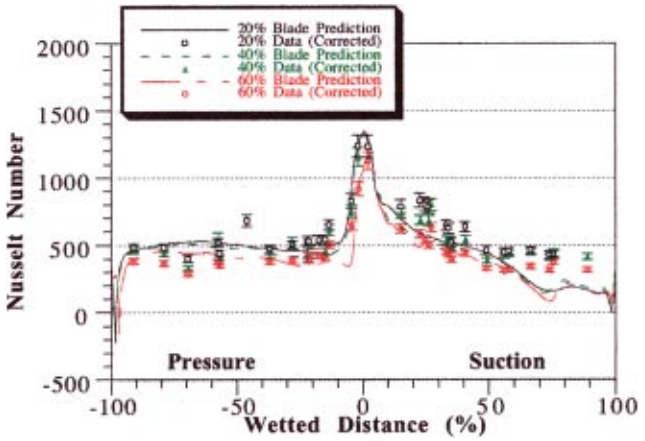

Fig. 10 Composite plot of blade Nusselt number for different spacings

averaged unsteady predicted Nusselt number distribution and the Nusselt numbers deduced from the experimental data for the blade at 20, 40, and 60 percent vane–blade spacing, respectively. Once again, the button-type gage heat flux data have been corrected for the potential ''heat-island effect'' using the correction factor of Zilles and Abhari [16] as indicated by the dark filled symbols. No correction is needed for the strip-insert data since the heat-island effect is not present with this type of installation. The data obtained from the inserts are shown as triangular symbols in these plots. On the blade, the maximum value of the correction was 5 percent and occurred at 91 percent wetted distance on the pressure surface. Both the corrected and uncorrected data are shown. In general, the magnitude of the correction is less than the experimental uncertainty, which agrees well with the observation [17] that there is little difference between the insert and button data.

The calculations assumed the boundary layer to be fully turbulent for both the pressure and suction surfaces of the blade. For all three cases, the prediction and the experimental results are in reasonable agreement over the entire midspan region of the blade suction surface. For the suction surface, the most notable difference between the experimental data and the prediction occurs passed 50 percent wetted distance. At this point the code underpredicts the data for all spacings. For the pressure surface, the predictions underestimate the data closer to the stagnation point, but come into better agreement farther along the blade although these deviations are minor. The trends shown here are consistent with the result presented in Rao et al. [16]. Abhari et al. [8] presented a comparison between experiment and the UNSFLO prediction for another turbine and they also found the data to be above the prediction early on the pressure surface, but better agreement with increasing distance. The comparison on the suction surface also indicated the data to be above the prediction for wetted distances less than 30 percent. There are obvious differences between the turbine stages and the operating conditions so some differences are not unexpected.

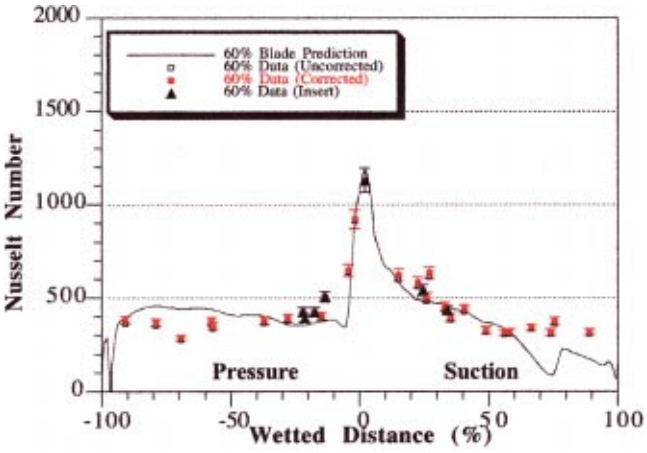

Fig. 9 Blade time-averaged Nusselt number (60 percent spacing)

Figure 10 presents a composite plot of the predictions versus the corrected and insert experimental data obtained at the three different vane/blade spacings. Once again, the 20 percent spacing results in the higher overall predicted and measured Nusselt number distribution than the 60 percent. The trends in the experimental results are consistent with the predicted trends, as they were for the vane results discussed earlier. However, as noted above for the vane results, the difference in the experimental conditions accounts for a significant portion of the difference between the predicted (and experimental) results at the various vane/blade settings. Once again, the areas under the predicted and measured Nusselt number distributions were determined (although on the blade because of the greater number of gages, the integration area was from −91 to 89 percent). In increasing the spacing from 20 to 40 percent the predicted decrease in the blade heat load is 4 percent, whereas the experimental result is a reduction of 7 percent. In changing the spacing from 40 to 60 percent the predicted reduction in heat load is 12 percent whereas the experimental result is 15 percent. As noted earlier, the reduction in Reynolds number from the 20 percent spacing to the 40 percent spacing is about 6 percent and from 40 to 60 percent spacing the change is 9 percent. While the drop in the blade heat loading is greater than that recorded for the vanes for the same spacing changes, the ratio of change in heat loading to change in Reynolds number is remarkably consistent. About 32–37 percent of the total change in heat loading (from 20 to 60 percent spacing) occurs in the change from 20 to 40 percent for both the blade and vanes. And about 40 percent of the change in the Reynolds number (from 20 to 60 percent) occurs in the 20 to 40 percent spacing case. Thus, one concludes that changes in the Reynolds number are the driving force behind the changes in the heat loadings on the blade, dominating whatever vane/blade spacing effects there may be. The Reynolds number effect is higher for the blades than the vanes, as can be seen by the greater changes in the blade heat loading calculated from the data. The data show that the heat load to the blade as the spacing changed from 20 to 60 percent is a little less than twice that measured at the vane. The predictions also suggest a value of about two for the same conditions, thus re-emphasizing that the code is capturing the main heat flux mechanisms.

3.2 Comparison of Measured Unsteady Surface Pressure and Measured Heat Flux at Selected Locations on the Blade. In an earlier paper, Abhari et al. [8] compared the calculated blade surface pressure (obtained using UNSFLO) and the measured surface heat flux on blades near the stagnation point. These comparisons demonstrated that, for that specific portion of the blade, the surface pressure and the heat flux were approximately in phase. Abhari et al. [8] did not present comparisons of other blade locations. Rigby et al. [23] and Johnson, et al. [24] have both reported studies of the relationship between unsteady heat transfer and unsteady surface pressure. In their work, they created the shock waves interacting with the blade using a stationary blade and a rotating series of bars. Rigby et al. [23] argue that it should be possible to determine the local Nusselt number enhancement for a given unsteady pressure signal at various wall temperature ratios using temperature scaling. For this to be true, there must be a linear relationship between the local unsteady Nusselt number history and the local unsteady pressure history. It will be demonstrated below that for some blade locations, such a relationship is true. At other locations, however, the relationship breaks down.

In this work, both the measured unsteady surface pressure and the measured unsteady heat flux were available for comparison. Thus, it was not necessary to rely on the computed surface pressure to compare the inviscid versus viscous flow effects. In addition, the blades were rotating at corrected design speed and the shock waves interacting with the blades were the result of the upstream choked vanes. This section of this paper presents these comparisons for several locations on the blade suction and pressure surfaces. For the purposes of this paper the correlation between measured surface pressure and heat flux at several specific locations on the blade will be presented.

The heat flux gage output was sampled at a frequency of 100 kHz so that temporal resolution of the unsteady wave propagation through the stage could be resolved. Spatial resolution was achieved by phase locking the data to a shaft encoder that generates 500 pulses/revolution resulting in 16.667 samples/vane passage. The unsteady heat flux data were ensemble averaged at 50 independent positions in a vane passage. The first three harmonics were used for the comparisons in this section. The turbine configuration of 30 vanes and 45 blades causes a geometric global cycle every three blades.

An attempt was made to use the heat flux gages and the pressure transducers that were as close to the same physical location on the blade as possible. Instrument mortality resulted in not always having an active pressure transducer and an active heat flux gage at the identical blade location. Figure 11 presents a comparison of the measured unsteady surface heat flux at 2 percent wetted distance on the suction surface with the measured unsteady surface pressure at 0 percent wetted distance.

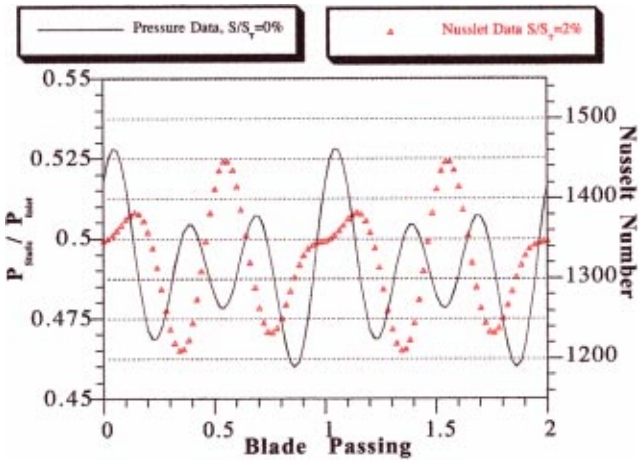

Fig. 11 Blade suction surface data near stagnation point (20 percent spacing)

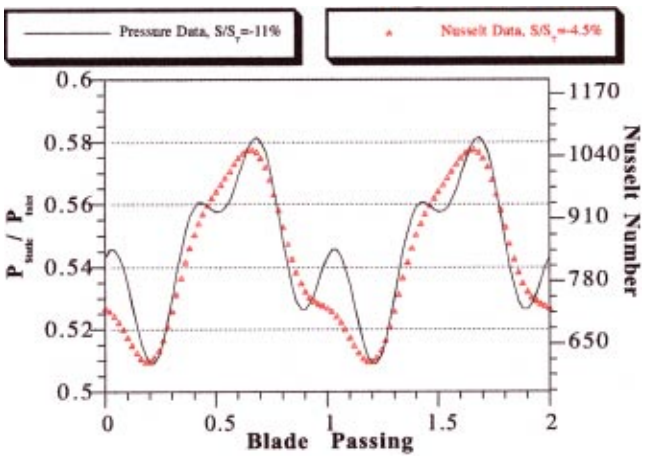

Fig. 12 Blade pressure surface data near stagnation point (20 percent spacing)

The left ordinate is local surface pressure normalized by vane inlet total pressure, the right ordinate is local Nusselt number, and the abscissa is relative position in the passage from 0 to 2 with 2 representing one complete global cycle. A comparison of the phase-averaged unsteady surface pressure and the predicted unsteady surface pressure was presented in Busby et al. [5], and will not be repeated here. The Busby et al. [5] paper also illustrates the harmonics of the surface pressure data. These results, presented in Fig. 11, illustrate that in the leading edge stagnation region the pressure signal contains two distinct peaks near midpassage while the heat flux data show only one peak at the same passage location. At the blade leading edge the flow situation is complicated, due to the interactions between the vane wakes and the shock wave structure; thus, the result was not unanticipated.

Figure 12 presents a comparison between the surface pressure at 11 percent and the heat flux at 4.5 percent on the blade pressure surface. The pressure history illustrates more detail than the heat flux, but the characteristics of the phase response of the pressure and the heat flux are consistent for this particular location. Figure 13 presents a similar comparison for a location a little farther along the blade pressure surface at 37 percent wetted distance. At this location, there is some similarity between the surface pressure and the heat flux behavior in that the peaks and valleys are generally similar, but out of phase.

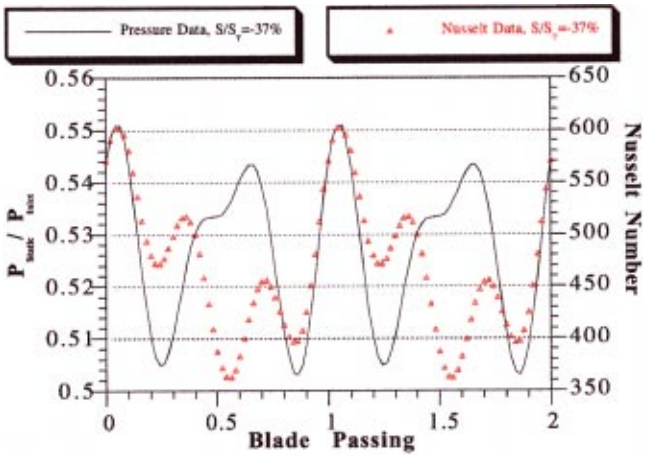

Fig. 13 Blade pressure surface data (20 percent spacing)

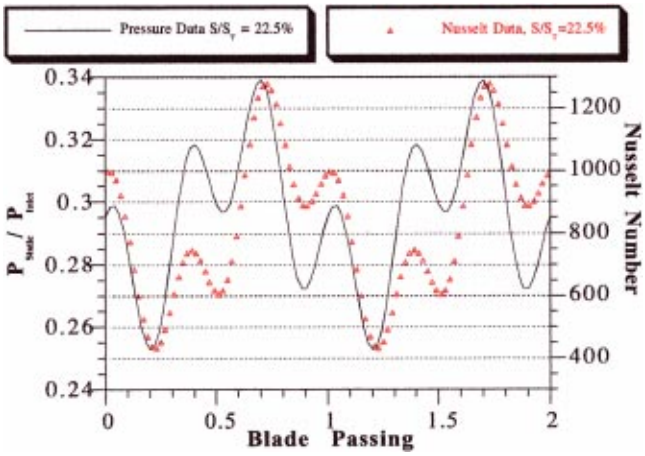

Fig. 14 Blade suction surface data (20 percent spacing)

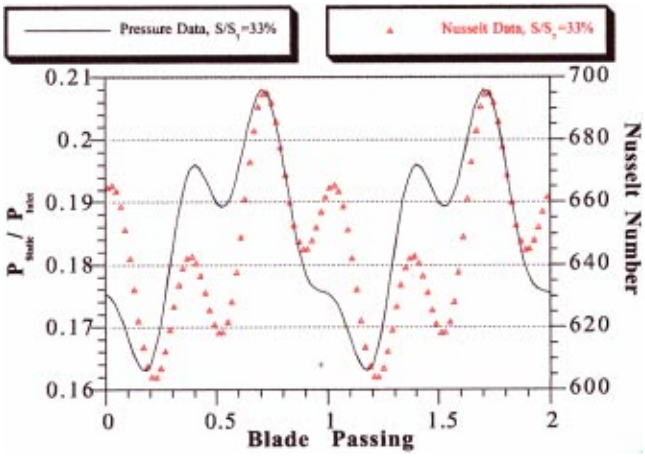

Fig. 15 Blade suction surface data (20 percent spacing)

Near the blade leading edge on the suction surface, there is once again reasonable comparison between the surface pressure and heat flux phase information, as illustrated in Fig. 14 for a wetted distance of 22.5 percent. This comparison is comparable to that shown on Fig. 12 for the pressure surface at 11 percent wetted distance.

The favorable comparison between surface pressure and heat flux phase information continues for the suction surface at 33 percent wetted distance as shown on Fig. 15. The passage shock wave is striking the blade in the vicinity of the 33 percent wetted distance location and moving forward with time as shown by the sketch provided in Busby et al. [5] for this experimental condition. Beyond 37 percent wetted distance on the suction surface, the harmonics of the heat flux signal were sufficiently small that a meaningful comparison with the pressure signal could not be obtained. This result is consistent with the magnitude of the unsteady heat flux as a function of blade position described in Rao et al. [6] for similar operating conditions at the 40 percent spacing. Further, the relationship between the phase of the unsteady surface pressure and the unsteady heat flux on the blade suction surface is consistent with the results of Abhari et al. [8].

Figures 16 and 17 present a comparison of the predicted and measured unsteady envelope of Nusselt number for the blade at 20 and 60 percent vane axial spacing, respectively. Also included on these figures is the average value of the unsteady envelope. In general, the predicted and measured unsteady values are in reasonable agreement for both spacings. The unsteady envelope is predicted to be the largest on the suction surface at wetted distances between 0 and 50 percent, and to be relatively constant in magnitude over the pressure surface. The experimental results are consistent with the predicted trend.

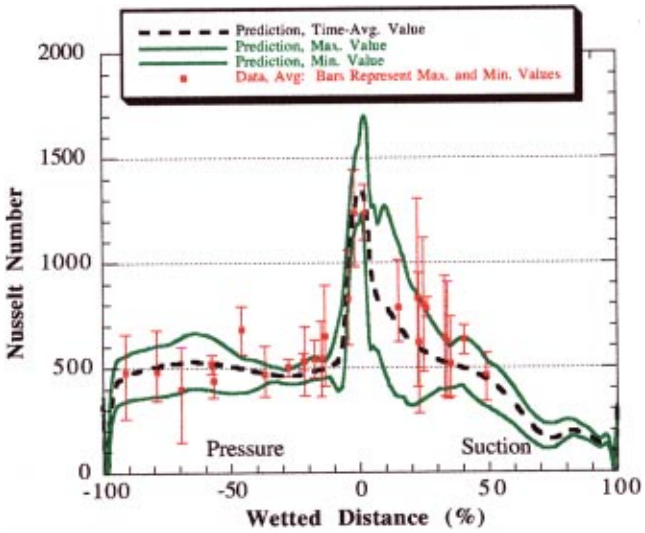

Fig. 16 Unsteady Nusselt number envelopes for 20 percent spacing

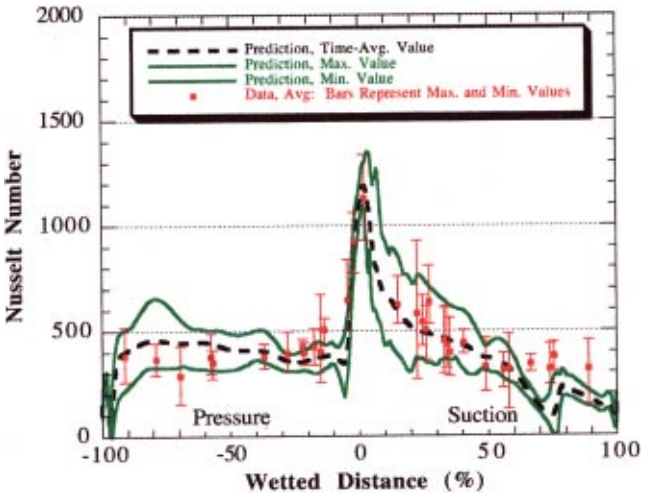

Fig. 17 Unsteady Nusselt number envelopes for 60 percent spacing

4.0 Conclusions

For the particular turbine and the range of vane/blade spacing used for these experiments, the observed drop in heat flux as the spacing changes comes not from the spacing change, but rather from the change in the experimental Reynolds number. The effect is consistent for both the vane and the blade, with the Reynolds number effect being about twice as large on the blade as on the vane. These trends are captured by the predictions also. The CFD code UNSFLO was used to illustrate good comparisons between the time-averaged unsteady predicted and the measured Nusselt number distributions for both the vane and blade.

For some locations on the blade, reasonable agreement was demonstrated between the phase-resolved surface pressure and the corresponding Nusselt number as the blade moved through the vane passage. Near the blade stagnation point there is not good

agreement, but at 11 percent wetted distance on the pressure surface and at 22 and 33 percent on the suction surface reasonable agreement is demonstrated.

Good agreement was found between the predicted and the measured unsteady envelopes of Nusselt number for both the 20 and 60 percent vane–blade spacing data. The most significant unsteadiness occurs on the blade suction surface at wetted distances less than 50 percent. The magnitude of the unsteadiness on the blade pressure surface was found to be relatively constant. By contrast, the magnitude of unsteadiness on the suction surface was very position dependent.

Acknowledgments

This research reported in this paper was funded under support of NASA Grant No. NAG3-1999 and Grant No. NAG3-2157 entitled ''Unsteady Effects (Including Film Cooling) on High-Pressure Turbine Design: An Analytical and Experimental Program.'' The authors would like to thank NASA for permission to publish these results and Dr. Robert J. Boyle for serving as the technical monitor on this program. The support of Kestutis C. Civinskas throughout both of these grant activities is greatly appreciated.

The authors would also like to express their appreciation to Mr. Jeffrey Barton of The Ohio State University Gas Turbine Laboratory for his dedicated help during the experimental phase of this program.

Nomenclature

f = defined by Eq. (1) (or Eq. (13) of [16])
Nu_b = Nusselt number of button-type gage
Nu_{KT} = Nusselt number of double-sided Kapton gage
T_f = temperature of platinum film
T_w = wall temperature of flat plate
T_T = total temperature of external flow
x_0 = distance from leading edge of plate to edge of hole containing heat flux gage
x = distance from leading edge of plate to leading edge of Pyrex heat flux gage
Θ = $(T_f - T_w)/(T_T - T_w)$
L = reference length 1 in. (0.0254 m)
K_f = thermal conductivity of fluid
T_{Ref} = reference temperature, inlet stagnation temperature

References

[1] Dring, R. P., Joslyn, H. D., Hardin, L. W., and Wagner, J. J., 1981, ''Research on Turbine Rotor–Stator Interaction and Rotor Negative Incidence Stall,'' AFWAL-TR-81-2114.
[2] Rao, K. V., and Delaney, R. A., 1990, ''Investigation of Unsteady Flow Through Transonic Turbine Stage, Part I: Analysis,'' AIAA Paper No. 90-2408.
[3] Dunn, M. G., Bennett, W. A., Delaney, R. A., and Rao, K. V., 1990, ''Investigation of Unsteady Flow Through a Transonic Turbine Stage: Part II—Data/Prediction Comparison for Time-Averaged and Phase-Resolved Pressure Data,'' AIAA Paper 90-2409.
[4] Venable, B. L., Delaney, R. A., Busby, J. A., Davis, R. L., Dorney, D. J., Dunn, M. G., Haldeman, C. W., and Abhari, R. S., 1999, ''Influence of Vane–Blade Spacing on Transonic Turbine Stage Aerodynamics: Part I—Time-Averaged Data and Analysis,'' ASME J. Turbomach., **121**, pp. 663–672.
[5] Busby, J. A., Davis, R. L., Dorney, D. J., Dunn, M. G., Haldeman, C. W., Abhari, R. S., Venable, B. L., and Delaney, R. A., 1999, ''Influence of Vane–Blade Spacing on Transonic Turbine Stage Aerodynamics: Part II—Time-Resolved Data and Analysis,'' ASME J. Turbomach., **121**, pp. 673–682.
[6] Rao, K. V., Delaney, R. A., and Dunn, M. G., 1994, ''Vane–Blade Interaction in a Transonic Turbine, Part II: Heat Transfer,'' J. Propul. Power, **10**, No. 3, pp. 312–317.
[7] Hilditch, M. A., and Ainsworth, R. W., 1990, ''Unsteady Heat Transfer Measurements on a Rotating Gas Turbine Blade,'' ASME Paper No. 90-GT-175.
[8] Abhari, R. S., Guenette, G. R., Epstein, A. H., and Giles, M. B., 1992, ''Comparison of Time-Resolved Turbine Rotor Blade Heat Transfer Measurements and Numerical Calculations,'' ASME J. Turbomach., **114**, pp. 818–827.
[9] Dunn, M. G., and Hause, A., 1982, ''Measurement of Heat Flux and Pressure in a Turbine Stage,'' ASME J. Eng. Power, **104**, pp. 215–223.
[10] Dunn, M. G., Rae, W. J., and Holt, J. L., 1984, ''Measurement and Analyses of Heat Flux Data in a Turbine Stage: Part I—Description of Experimental Apparatus and Data Analysis,'' ASME J. Eng. Gas Turbines Power, **106**, pp. 229–233.
[11] Dunn, M. G., 1984, ''Time-Resolved Heat-Flux Measurements for a Full-Stage Turbine,'' AFWAL-TR-84-2025.
[12] Dunn, M. G., Seymour, P. J., Woodward, S. H., George, W. K., and Chupp, R. E., 1989, ''Phase-Resolved Heat-Flux Measurements on the Blade of a Full-Scale Rotating Turbine,'' ASME J. Turbomach., **111**, pp. 8–19.
[13] Kim, J., Ross, R. A., and Dunn, M. G., 1996, ''Numerical Investigation of the Heat-Island Effect for Button-Type, Transient, Heat-Flux Gage Measurements,'' *Experimental Methods in Heat Transfer*, ASME HTD-Vol. 327, pp. 33–39.
[14] Eaton, J. K., Mukerji, D., and Moffat, R. J., 1997, ''3-D Convection in 2-D Boundary Layers: First Progress Report,'' *Development and Application of Heat Flux Calibration Standards and Facilities*, ASME HTD-Vol. 353, pp. 187–189.
[15] Mukerji, D., Eaton, J. K., and Moffat, R. J., 1998, ''A New Correlation for Temperature Rise Correction of Heat Flux Gages,'' *Numerical and Experimental Methods in Heat Transfer*, ASME HTD-Vol. 361-5, pp. 631–636.
[16] Zilles, D. A., and Abhari, R. S., 1999, ''Influence of Non-Isothermal Button Gage Surface Temperature in Heat Flux Measurement Applications,'' *Symposium on Calibration, Error Analysis, and Modeling of Heat Flux Sensors*, ASME HTD-Vol. 364-4, pp. 85–91.
[17] Dunn, M. G., Kim, J., and Rae, W. J., 1997, ''Investigation of the Heat-Island Effect for Heat-Flux Measurements in Short Duration Facilities,'' ASME J. Turbomach., **119**, pp. 753–760.
[18] Haldeman, C. W., and Dunn, M. G., 1998, ''High-Accuracy Turbine Performance Measurements in Short-Duration Facilities,'' ASME J. Turbomach., **120**, pp. 1–9.
[19] Giles, M. B., 1984, ''Stator/Rotor Interaction in a Transonic Turbine,'' AIAA Paper 88-3093.
[20] Giles, M. B., 1988, ''UNSFLO: A Numerical Method for Unsteady Inviscid Flow in Turbomachinery,'' MIT Gas Turbine Laboratory Report No. 195.
[21] Giles, M. B., and Haimes, R., 1993, ''Validation of a Numerical Method for Unsteady Flow Calculations,'' ASME J. Turbomach., **115**, pp. 110–117.
[22] Abhari, R. S., Guenette, G. R., Epstein, A. H., and Giles, M. B., 1992, ''Comparison of Time-Resolved Turbine Rotor Blade Heat Transfer Measurements and Numerical Calculations,'' ASME J. Turbomach., **114**, pp. 818–827.
[23] Rigby, M. J., Johnson, A. B., Oldfield, M. L. G., and Jones, T. V., 1989, ''Temperature Scaling of Turbine Blade Heat Transfer With and Without Shock Wave Passing,'' *Proc. of the 9th International Symposium on Air Breathing Engines*, Athens, Greece.
[24] Johnson, A. B., Rigby, M. J., Oldfield, M. L. G., Ainsworth, R. W., and Oliver, M. J., 1989, ''Surface Heat Transfer Fluctuations on a Turbine Rotor Blade Due to Upstream Shock Wave Passing,'' ASME J. Turbomach., **111**, pp. 105–115.

Time-Averaged Heat Flux for a Recessed Tip, Lip, and Platform of a Transonic Turbine Blade

M. G. Dunn

C. W. Haldeman

The Ohio State University Gas Turbine Laboratory, Columbus, OH 43235

The results of an experimental research program determining the blade platform heat-flux level and the influence of blade tip recess on the tip region heat transfer for a full-scale rotating turbine stage at transonic vane exit conditions are described. The turbine used for these measurements was the Allison VBI stage operating in the closed vane position (vane exit Mach number≈1.1). The stage was operated at the design flow function, total to static pressure ratio, and corrected speed. Measurements were obtained at several locations on the platform and in the blade tip region. The tip region consists of the bottom of the recess, the lip region (on both the pressure and suction surface sides of the recess), and the 90 percent span location on the blade suction surface. Measurements were obtained for three vane/blade spacings; 20, 40, and 60 percent of vane axial chord and for a single value of the tip gap (the distance between the top of the lip and the stationary shroud) equal to 0.0012 m (0.046 in) or 2.27 percent of blade height.
[S0889-504X(00)00604-8]

1.0 Introduction

The tips of axial turbine blades rotate in close proximity to a stationary outer seal or shroud. Differential thermal expansion between the rotating turbine wheel and blades and the stationary outer shroud causes variations in the magnitude of the clearance gap at the blade tip during engine operation. Some engine companies elect to utilize shrouded blades and eliminate this problem. Other companies use either flat-tip blades or recessed-tip blades. For those aircraft engines using flat or recessed tips, significant variations in clearance occur at different operating conditions such as takeoff and cruise; even with active clearance control, the gap is never eliminated at all operating conditions. Using recessed tips allows turbine operation with less clearance and a reduced probability of severe blade damage in the event of a tip rub. Clearance gaps in modern axial gas turbines are typically less than 1 percent of the blade height for large engines, ranging up to 1.5 percent or more for smaller engines with low-aspect-ratio blades. Even with the tightest possible tolerances, the leakage flow has significant effects on stage aerodynamic performance and on the structural durability of the blade. The blade tip area has high convective heat transfer and thermal loads that must be mitigated by the blade internal cooling along with heat conduction to the blade pressure and suction side surface areas.

A significant portion of the literature relevant to tip gap flows has dealt with flat tip blades, and in many cases the measurements were performed for very low (or no) relative tip to shroud motion. The early work of Metzger and Rued [1,2] was designed to obtain detailed information relevant to the source (pressure surface side) of the tip flow and similar information on the sink (suction surface side), and the modeling experiments were conducted in a water tunnel. Several researchers have also investigated methods of reducing performance losses by controlling tip leakage flow [3–6] and others have concentrated on the heat transfer in the tip region [7]. The work of Booth et al. [3] and Wadia and Booth [4] was also conducted using water tunnels as the test bed. Sjolander and Cao [5] use a single blade and shims to change the value of the gap to study the structure of the gap flow in the absence of relative motion. In a later study, Yaras et al. [6] used a cascade of three blades and added a moving outer belt to simulate the influence of rotation on tip leakage. This study indicated that the addition of relative motion results in significant changes in the tip leakage vortex and passage vortex structures from stationary flows. It was concluded that the strength of the tip vortex was reduced considerably with the introduction of wall motion. In addition, the passage vortex was enhanced by the scraping effect of the blades. Both were dragged toward the suction side of the passage and appeared partially to block the outlet flow from the tip gap. Heyes and Hodson [8] presented the results of an experimental study using linear cascades in the absence of a moving outer wall, and suggested a relative simple model that could be used in conjunction with a three-dimensional code to calculate the tip gap flow. One significant finding of their study was that the pressure gradients along the blade chord are a major factor influencing the tip leakage flow.

There are very few experimental data in the literature for the heat transfer distributions in the vicinity of recessed tips that have been obtained for full-scale rotating turbines operating at the design-corrected conditions. It is well known that the pressure difference between the convex and concave sides of the blade drives flow through the clearance gap. However, because of the recessed cavity in the tip, the flow field associated with the recess is significantly more complicated than one would encounter on a flat tip blade. Near the leading edge of the blade, a strong vortex flow exiting the vane near the stationary shroud enters the tip region from head on or from the suction surface side of the blade. Ameri et al. [9] demonstrate in their calculation of the tip region flow for a recessed tip geometry (similar to that of the VBI blade) that the flow field is very three dimensional with many interacting vortices. Their results suggest that there are at least two distinct vortices existing in the cavity region, and they persist throughout the length of the cavity. Their modeling of this flow suggests that one of the vortices is a result of separation off of the pressure side of the lip and that this vortex hugs the cavity pressure sidewall. The second vortex is the result of a flow separation again at the lip on the blade suction side. There appears to be a dividing streamline after which the mainstream flow is turned into the gap from the pressure side of the blade. Once again, flow separation occurs as a result of the lip. Strong secondary flows can be expected to be present in the gas path as a whole, and this can have the effect of bringing very hot portions of the mainstream to the vicinity of the clearance gap, especially just downstream of the blade leading

Contributed by the International Gas Turbine Institute and presented at the 45th International Gas Turbine and Aeroengine Congress and Exhibition, Munich, Germany, May 8–11, 2000. Manuscript received by the International Gas Turbine Institute February 2000. Paper No. 2000-GT-197. Review Chair: D. Ballal.

edge lip. This lip acts like a rearward-facing step with resulting flow separation and attachment in the recessed cavity. As the flow emerges from the suction side of the gap, it is usually visualized as rolling into a vortex as it meets the oncoming shroud wall flow [10,11]. Thus, near the tip on the aft portion of the suction surface, the local heat transfer rates can become quite high, causing trailing edge tip burn out. For this reason, the blades used in this study were instrumented in the 90 percent span region.

Until his death, Metzger and his students published many low-speed outer wall studies applicable to the tip region heat transfer in recessed tips [12–14]. Ameri et al. [9] applied their calculation technique to the Metzger tip cavity data and obtained reasonably good results for cavity depth/cavity width ratios of 0.2 and 0.5 at a tip clearance/cavity width ratio of 0.1. For reference purposes, the depth/width ratio of the cavity used in this study ranged from 0 to 0.21 with a tip clearance/cavity width ratio of 0.14. The experimental data and the results of the Ameri et al. [9] calculation for the geometry closest to that used herein suggested that the peak Nusselt number occurred on the lip with the Nusselt numbers in the bottom of the cavity being about 42 percent of the lip values. In this same paper, the authors have performed tip region calculations to simulate the fluid flow and heat transfer in the tip region for the GE-E^3 high-pressure turbine. Their calculations were performed for a smooth tip, a 2 percent recess, and a 3 percent recess. The measurements used in this paper have a 3 percent recessed tip.

In a more recent paper Bunker et al. [15] and Ameri and Bunker, [16] report the results of a combined experimental and computational study designed to investigate the heat transfer to the first stage blade tip (flat tip configuration) of a power generation gas turbine. The experiment utilized a three-blade linear cascade with no outer shroud motion. Using liquid crystals in the tip region, the authors were able to obtain a rather detailed distribution of heat transfer in the tip region. The computational phase of the effort used to support the experiments utilized the code reported in Rigby et al. [17] and Ameri et al. [9]. The authors showed good comparison between experiment and computation.

Two previous experimental/computational analysis of flow in the tip region for a flat tip blade were reported by Metzger et al. [18], and Ameri and Steinthorsson [19]. For the Metzger et al. paper, time-resolved heat transfer measurements obtained on the blade tip and simultaneously obtained time-resolved heat transfer and surface pressure measured on the adjoining stationary shroud for the full-stage Garrett TFE-731-2 turbine were compared with the results of a CFD analysis. Ameri and Steinthorsson [20] reported the results of time-averaged heat transfer calculations compared to the data of Dunn et al. [21], for the Garrett TFE-731 turbine and a similar comparison for the data of Dunn et al. [21], obtained on the first blade of a full two-stage Space Shuttle main engine hydrogen side turbopump. Both the predictions of Metzger et al. and the predictions of Ameri and Steinthorsson showed good agreement with the experimental results. However, the subject of this paper is the case for which the blade tip has a cavity (squealer) rather than being flat and the accompanying flow field is entirely different.

2.0 Description of Experiment

A brief description of the facility, a description of the turbine stage, and a more detailed description of the tip cavity recess and associated instrumentation, the platform instrumentation, and the instrumentation located at 90 percent span on the blade suction surface will be provided in this section.

2.1 Description of Facility. The facility used for this measurement program utilized a shock-tunnel to produce a short-duration source of heated and pressurized gas that was directed through the rotating turbine. Air was used for the test gas. The experimental apparatus consisted of a shock tube, an expansion nozzle, a large dump tank, and a device that housed the turbine

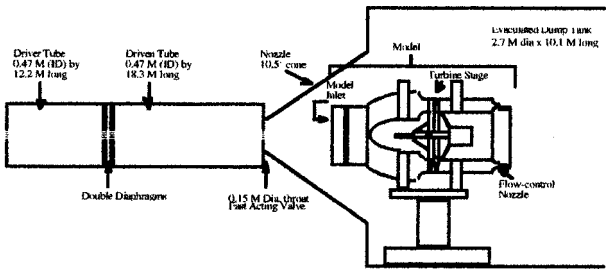

Fig. 1 Sketch of Allison VBI model in OSU GTL shock tunnel

stage and provided the flow path geometry for the stage. The shock tube has a 0.47-m (18.5-in) diam by 12.2-m (40-ft) long driver tube and 0.47-m (18.5-in) diam by 18.3-m (60-ft) long driven tube. The driver tube was designed to be sufficiently long so that the wave system reflected from the driver endwall would not terminate the test time prematurely. The turbine is housed in a device located in the expansion nozzle of the shock-tunnel facility, as illustrated in Fig. 1. This device consists of an inlet duct, an exit nozzle designed to govern the flow through the turbine rig, a 200 channel slip ring, and an air motor drive system. This particular turbine configuration has spacers that can be moved relative to the vane row in order to change the vane/blade spacing.

In order to initiate an experiment, the test section is evacuated, while the driver and the driven tube are pressurized to predetermined values. Pressure values are selected to duplicate the design flow conditions. The flow function ($\dot{w}\sqrt{\theta}/\delta$), wall-to-total temperature ratio (T_w/T_0), stage pressure ratios, and corrected speed are duplicated. The value of T_0 can be set at almost any desired value in the range of 800–3500°R. The design pressure ratio across the turbine is established by altering the throat diameter of a flow control nozzle located near the exit end of the device housing the turbine.

The heat-flux measurements were performed using thin-film resistance thermometers. The thin-film gages were made of platinum (~100 Å thick) and were hand painted on an insulating Pyrex 7740 substrate. The response time of these thin films is on the order of 5×10^{-8} s. The gage substrates were attached to the metal blade by epoxy.

2.2 Description of Turbine Stage. The turbine stage used was the Allison Vane/Blade Interaction (VBI) turbine. This is an advanced turbine and is designed so that one can select either subsonic (Mach No.=0.85) or transonic (Mach No.=1.1) vane exit conditions. The vane exit condition for this measurement program was a Mach No.=1.1.

The geometry of the turbine rig is given in Table 1. Aerodynamic data for the measurement program are given in Table 2.

2.3 Description of Blade Instrumentation and Tip Recessed Cavity. The blades of the rotor were instrumented with both thin-film heat-flux gages and with flush-mounted miniature Kulite pressure transducers. Figure 2 is a photograph of the instrumented rotor. The turbine geometry is such that there are 30 vanes and 45 blades. Thus, instrumenting every third blade results in instruments on different blades being in the same relative position in a vane passage. All of the vane and blade surface pressure measurements were obtained at midspan of the respective component. The time-averaged surface pressure data for all three vane-blade spacings are reported in Venable et al. [22], and the time-resolved pressure data are reported in Busby et al. [23]. On-blade surface pressure data in the recessed cavity are not available for this turbine stage.

As can be seen from Fig. 2, the blades containing surface pressure instrumentation, the blades containing the contoured leading edge heat-flux gage inserts, and the blade with the pressure sur-

Table 1 Turbine stage geometry

Parameter	Vane	Blade
number of airfoils	30	45
axial chord, in. (mm)	2.66(67.6)	1.87 (47.5)
spacing, in. (mm)	2.03(51.6)	1.34 (34.0)
chord/spacing	1.32	1.39
mean radius, in. (mm)	9.73(247.1)	9.70 (246.4)
aspect ratio	0.72	1.10
L.E. mean radius, in. (mm)	0.18 (4.6)	0.09 (2.3)
T.E. mean radius, in. (mm)	0.03 (0.8)	0.03 (0.8)
hub/tip radius	0.82	0.81
tip radius, in. (mm)	10.64 (270.3)	10.64 (270.3)
T.E. blockage (%)	9.44	8.94

Table 2 Turbine operating conditions

Parameter	20% (spacing)	40% (spacing)	60% (spacing)
speed (rpm)	11,843	11,795	11,763
$p_{t\ 1}$, psia (kPa)	43.2 (298.1)	43.7 (301)	39.8 (274.7)
p_4, psia (kPa)	10.0 (69.1)	10.3 (71.3)	9.4 (64.8)
T_{t1}, R (K)	1108 (615.5)	1173 (651.7)	1176 (653.4)
$T_{vane,avg}$ R (K)	604 (335.5)	596.3 (331.3)	589 (327.3)
$T_{blade\ avg}$ R (K)	575.8 (319.9)	563.8 (313.2)	563.8 (313.2)

face button-type gages were all placed so that no correction for phase angle was required. However, there was a desire to place the button-type heat-flux gages so that the heat flux in a given blade passage could be measured. Thus, the blade with the suction-surface button-type heat-flux gages required a shift to obtain the proper phase orientation.

The rotor wiring was connected to a PolyScientific 200-channel gold-on-gold slip ring unit located on the opposite end of the drive shaft from the air motor. The wires from the blade heat-flux gages pass down the front surface of the disk (as shown in the photograph of Fig. 2) and then through a hollow shaft connector to the slip ring unit. The slip ring unit was continuously cooled and

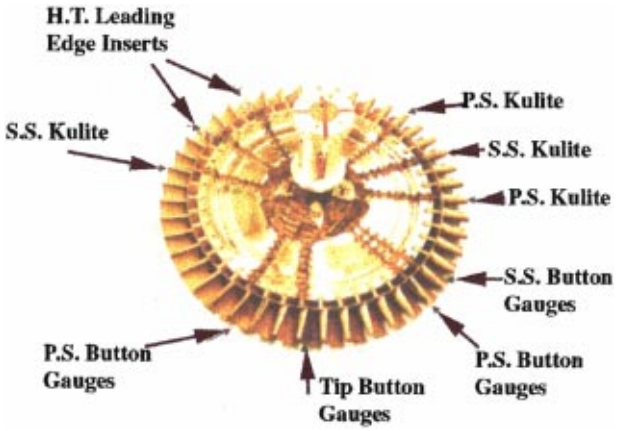

Fig. 2 Instrumented rotor of VBI turbine

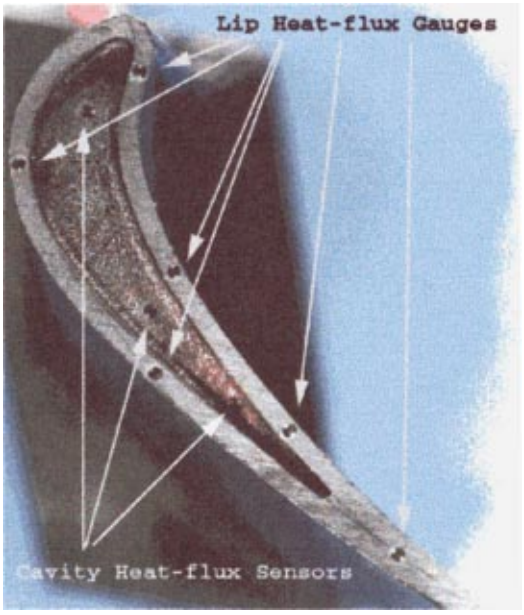

Fig. 3 Photograph of cavity and lip heat-flux gages

lubricated using a positive displacement pump to force Asahiklin AK-225 diluted with a small amount of silicone oil through the closed system as the medium.

The recessed cavity is shown in the photograph of Fig. 3. The lip of the recess is 1.5×10^{-3}-m (0.060-in) wide by 1.5×10^{-3}-m (0.060-in) deep and extends over approximately 67 percent of blade chord. There are three heat-flux gages located in the pressure side lip at wetted distances of approximately 6.5, 32, and 57 percent, two heat-flux gages in the suction side lip at wetted distances of approximately 24.5 and 51 percent three heat-flux gages in the recessed cavity at wetted distances of approximately 12, 39.5, and 55 percent, and one heat-flux gage in the trailing edge downstream of the cavity at a wetted distances of approximately 78 percent. Unfortunately, there were no heat-flux gages located in the lip sidewall on the inside of the cavity nor were there surface pressure transducers located in the tip region. The width of the cavity at the widest point (near the suction side lip heat-flux gage located at 24.5 percent wetted distance) is 7×10^{-3} (0.278 in.). As illustrated in Fig. 2, the cavity width takes on a shape similar to the blade over the remainder of the tip region. Early in the experiments, one of the gages in the pressure side lip failed as did one on the suction side lip, and the one in the trailing edge.

There are four heat-flux gages located on the platform (two on the blade suction surface side and two on the pressure surface side) as shown in the photograph of Fig. 4. The two gages on the

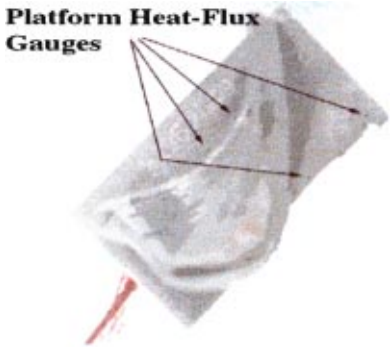

Fig. 4 Photograph of platform heat-flux gages

pressure surface side of the platform were placed relatively close to the blade surface at approximately 41.5 and 57 percent wetted distance. The two gages on the suction surface side of the blade were placed farther away from the surface with the one nearest the suction surface being at approximately 53 percent wetted distance and the second one at the trailing edge near the outer edge of the platform.

There are three heat-flux gages located on the suction surface at the 90 percent span position at wetted distances of approximately 45.5, 57, and 81.5 percent. The positions of these gages were selected so as to be in close proximity to the gages on the suction surface side lip.

3.0 Discussion of Results

Although the intent of this paper is to present the heat-flux measurements obtained on the rotating blade for the floor of the tip cavity, the tip lip region, on the platform, and the suction side of the blade at 90 percent span, the results obtained at midspan [24] are presented in Fig. 5 for reference purposes. The midspan heat-flux data are presented for all three vane/blade spacings.

The experimental data is presented as a Nusselt number based on a reference length as defined in the normal manner by the following equation:

$$\mathrm{Nu}_b = \frac{QL}{K_f(T_{\mathrm{Ref}} \pm T_f)}; \tag{1}$$

where L is a reference length; $L=1$ in (0.0254 m) in this case. K_f is the thermal conductivity of the fluid evaluated at the gage temperature (T_{gage}), and T_{Ref} is a reference temperature, taken as the stage inlet total temperature. The uncertainty in the experimental data is evaluated using the following formula:

$$\frac{\Delta \mathrm{Nu}_b}{\mathrm{Nu}_b} = \sqrt{\left(\frac{\Delta Q}{Q}\right)^2 + \left(\frac{\Delta T_f}{T_f}\right)^2 \left(1 + \frac{A^2}{(1 \pm A)^2}\right) + \frac{1}{(1 \pm A)^2}\left(\frac{\Delta T_{\mathrm{Ref}}}{T_{\mathrm{Ref}}}\right)^2}$$

$$A = \frac{T_f}{T_{\mathrm{Ref}}} \tag{2}$$

which is a simple ''error'' propagation formula, with the much smaller terms eliminated from the equation. These yields a percentage uncertainty in the Nusselt numbers as a function of the main independent variables used in the calculation.

Each experimental point presented in Figs. 3–10 is a value averaged over approximately 10 ms of test time (or about 1000 data points). Thus for this uncertainty analysis, the percentage uncertainty in each of the input variables is taken as the standard deviation of that quantity divided by the average value of that quantity over the time period, with the exception of the heat-flux in which the standard measurement error (± 5 percent) is used. The uncertainty is taken as twice the value reported in Eq. (1), which encompasses about 95 percent of the data spread (i.e., ± 2 standard deviations). Multiple runs were combined using a weighted average technique. In general, the uncertainty in the Nusselt number is dominated by the uncertainty in the heat-flux measurements.

For the purposes of the tip region data reduction, it would have been helpful to have had detailed gas temperature measurements in the tip region of the blade. Temperature measurements were obtained in the gas flow path just upstream of the vane inlet region, but unfortunately, such measurements were not available for the tip region. Thus, in the absence of tip region temperature measurements, the Nusselt number data reported herein have been reduced in the same manner as the midspan results. That is, the Nusselt number is based on the midspan average gas temperature ahead of the inlet vane row.

A question related to the possible necessity for a correction factor for the button-type gages has been raised in the literature by Kim et al. [25], Eaton et al. [26], and Mukerji et al. [27]. This question has arisen because of a potential ''heat island effect.'' More recently, Zilles and Abhari [28] described the results of an experimental investigation designed to determine the magnitude of the ''heat island effect'' for Reynolds number and temperature conditions consistent with the conditions experienced in the present experiments. A more complete discussion of this potential ''heat island'' and the magnitude of such a correction for the experimental conditions described herein is given in Dunn et al. [24]. It suffices here to note that for the purposes of the measurements presented in this paper, that the magnitude of the correction that would have to be applied to the tip region data presented is less than 2 percent, so the correction was ignored.

Figure 6 presents the cavity floor Nusselt number distribution for all three vane/blade spacings. The highest value of Nusselt number occurs just aft of the leading edge lip (gage #HR 78) and decreases from that location to the rear of the recess (gages #HR 79 and #HR 80) for all three vane/blade spacings. This elevated Nusselt number near the leading edge of the cavity is consistent with a flow separation and reattachment as a result of the lip. Observation of turbine flight hardware with recessed cavities will

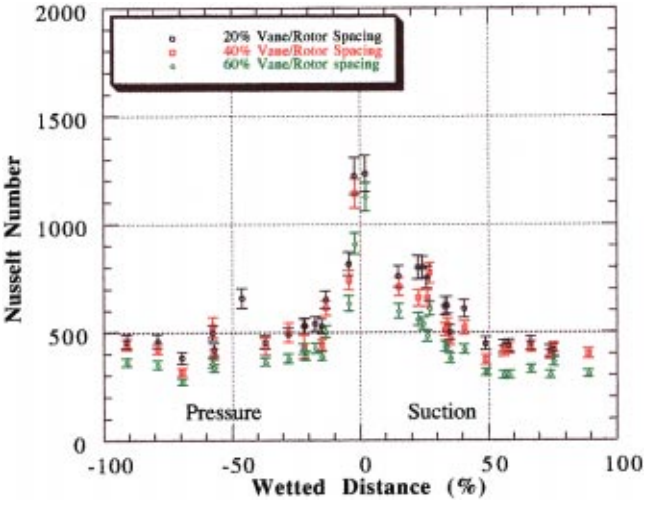

Fig. 5 Time-averaged Nusselt number for rotor blade (50 percent span) versus vane/blade spacing

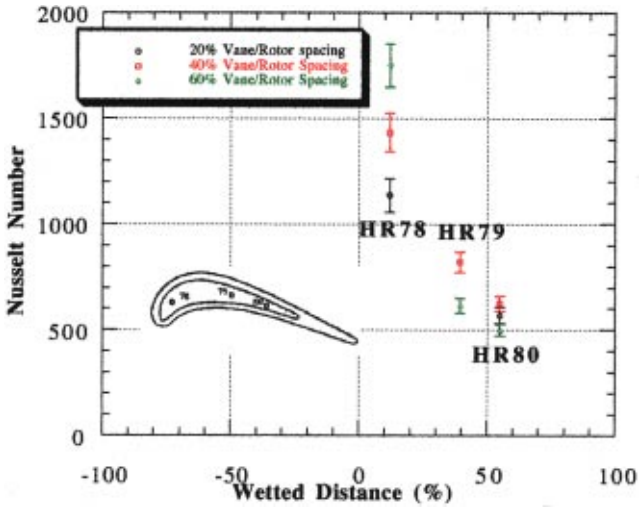

Fig. 6 Nusselt number on blade tip cavity

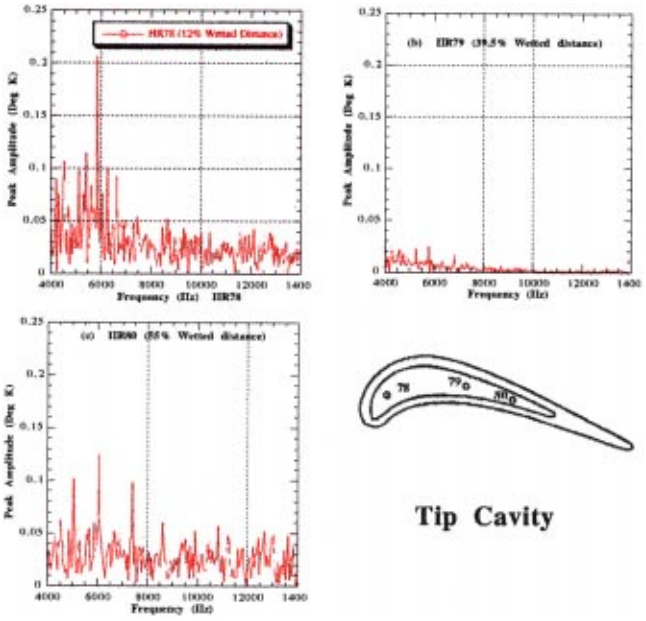

Fig. 7 FFT's of heat-flux gage temperature data: 60 percent vane/blade spacing

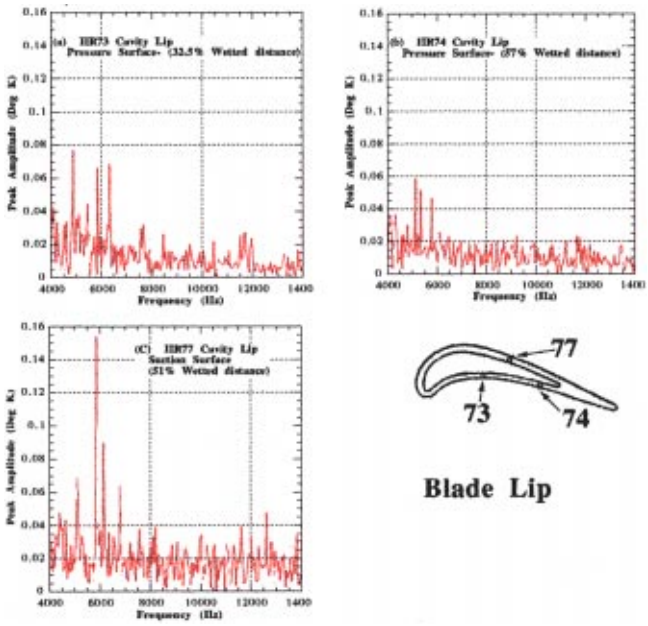

Fig. 9 FFT's of heat-flux gage temperature data: 60 percent vane/blade spacing

generally show a cooling hole at very nearly the same physical location in the cavity. The reason for this is that the location corresponds closely with the top of the leading edge cooling tube for which a relief hole is normally drilled at the tip location. Thus it is unlikely that experience would show blade distress at this location in spite of the very elevated heat load. At this most forward cavity floor location, the Nusselt number decreased with decreasing vane/blade spacing, suggesting that the tip region vortex exiting the vane had a much stronger interaction with the blade cavity with increasing distance of vane/blade separation. At the mid and rear portions of the cavity floor, the Nusselt number is on the same order as the blade midspan value, as can be seen by comparison with the data shown on Fig. 5. In an engine application, these values of Nusselt number are sufficiently large to require that cooling air be supplied to the region.

Figure 7 presents the FFT plots for the three cavity heat-flux gages with the peak amplitude plotted on the same scale so that a relative importance as a function of position can be observed. The wake cutting frequency for this experimental condition for which the vane is operating at an exit Mach number ≈ 1.1 is about 5.8 kHz. The heat-flux gage located at the front of the cavity floor just downstream of the lip shows a strong signal at 5.8 kHz as illustrated in Fig. 7(*a*). However, the magnitude of the signal at the fundamental wake cutting frequency for the second cavity floor gage is very small as can be seen from Fig. 7(*b*). Figure 7(*c*) illustrates that the magnitude of the first harmonic at the last gage location in the cavity is a little more than one half of the first cavity gage and that the frequency has been shifted very slightly higher.

Figure 8 presents the Nusselt numbers for three lip gages (or rim), two on the pressure side (gage #HR 73 and #HR 74) and one on the suction side (gage #HR 77), for all three vane/blade spacings (see Fig. 3 for a photograph of the relative location of these gages). The peak value of Nusselt number occurred at the suction side lip, and for all three vane/blade spacings the magnitude was greater than the blade stagnation point value. In addition, the

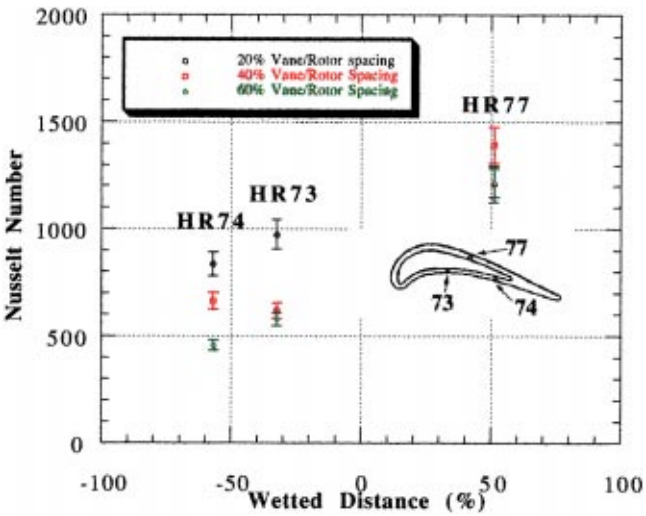

Fig. 8 Nusselt number on blade tip

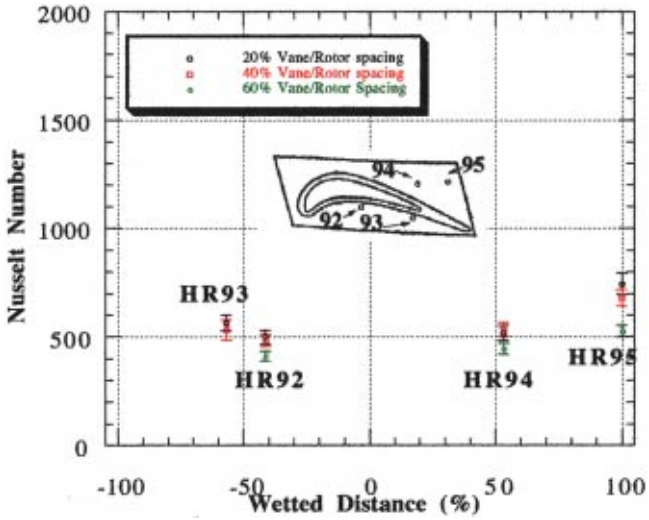

Fig. 10 Nusselt number on blade platform

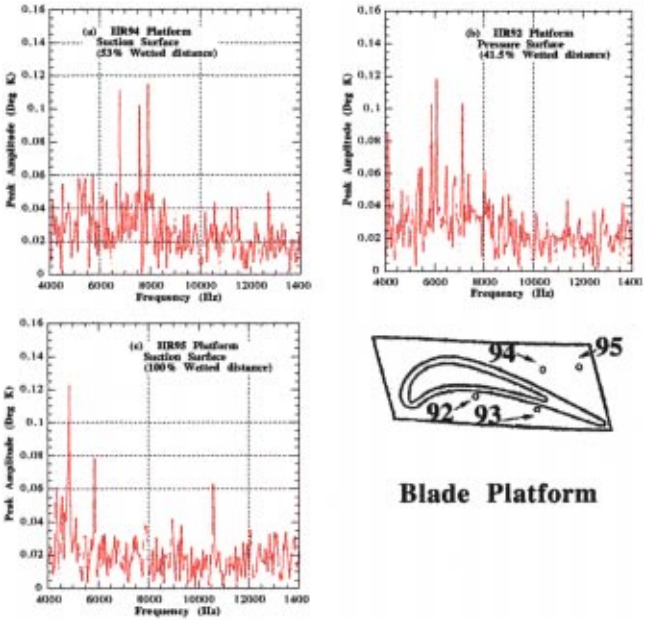

Fig. 11 FFT's of heat-flux gage temperature data: 60 percent vane/blade

larger values of Nusselt number were obtained for the close vane/blade spacings with decreasing values for the intermediate and far spacings. Although the pressure side lip values of Nusselt number were less than the suction side value, they were still significantly greater than representative blade midspan values. The magnitude of the Nusselt number for the suction side lip gage is significantly greater than the pressure side lip values, but not quite as large as the value corresponding to the first gauge of the cavity floor. The pressure side lip gages illustrate Nusselt number values consistent with the middle and aft portion of the cavity floor gages. However, because of the limited instrumentation in the lip and cavity regions, it is difficult to make any further comparisons with the detailed calculations of Ameri et al. [9]. However, Chyu et al. [12] and Ameri et al. [9] both reported results for which the heat transfer rate at the bottom of the cavity was higher than compared to the rim values, which is consistent with the results found here.

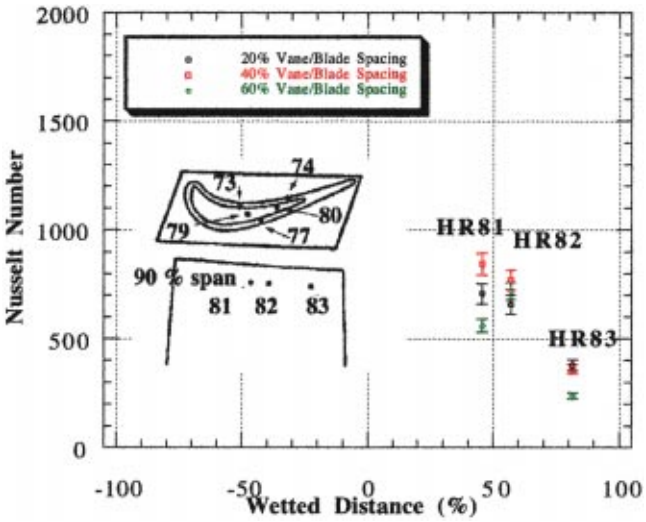

Fig. 12 Nusselt number on blade suction surface (90 percent span)

Figure 9 presents FFT's of these lip heat-flux gages with the peak amplitude plotted on the same scale for all three gages so that the relative importance as a function of position can be observed. The suction side lip gage shows a strong peak at the wake cutting frequency of 5.8 kHz. The pressure side lip gages also show a peak at 5.8 kHz, but the magnitude of the peak is less than one half of the suction side value.

Figure 10 presents the Nusselt number results for the four platform heat-flux gages for all three vane/blade spacings. Figure 4 is a photograph of the platform instrumentation installation showing the relative location of the heat-flux gages. Gage #HR 95, which is located near the blade trailing edge and much closer to the pressure surface than to the suction surface, illustrated the highest values of Nusselt number for all three spacings. The other three gages (#HR 92, #HR 93, and #HR 94) all produced Nusselt numbers that are in excess of representative midspan values.

Figure 11 presents the FFT plots for three of the four platform gages, once again presented so that the magnitudes of the harmonics are on the same relative scale. The suction surface side gage at 53 percent wetted distance does not illustrate a harmonic at the fundamental wake cutting frequency. However, the gage at 41.5 percent wetted distance on the pressure surface and the gage at 100 percent wetted distance on the suction side do show strong signals at the 5.8 kHz wake cutting frequency.

Figure 12 presents the Nusselt number results for the heat-flux measurements made on the suction side of the blade at 90 percent span for all three vane/blade spacings. The two gages near the 50 percent wetted distance location are relatively close to the suction surface lip gage, #HR 77 (see Fig. 8). The magnitude of the Nusselt number at the 90 percent span location is not as large as the tip value, but it is a factor of two larger than the corresponding value at blade midspan. At greater values of wetted distance, the Nusselt number is shown to decrease significantly, but the value is still large, being approximately 25 percent greater than the midspan value. The Nusselt number results obtained for the close spacing were generally higher than the intermediate and far spacing. Figure 13 presents the FFT's for the heat-flux gages located at the 90 percent span location. At this particular location, the peak of the fundamental harmonic occur at 5.2 and 6 kHz instead of at the anticipated 5.8 kHz fundamental wake cutting frequency. It is not clear at this time why there is this observed shift in the harmonic frequency.

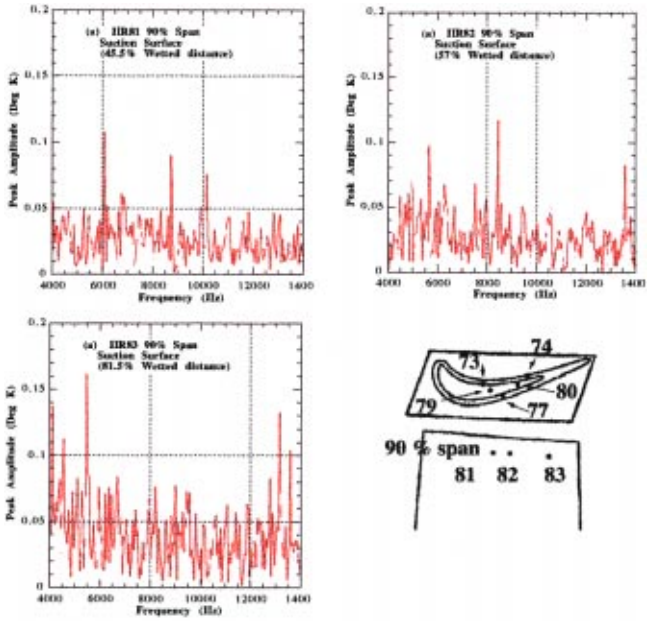

Fig. 13 FFT's of heat-flux gage temperature data: 60 percent vane/blade

4.0 Summary Remarks

Heat-flux measurements have been presented for the tip region of a rotating blade with a recessed tip for a full-stage rotating turbine. Nusselt number values on the floor of the recess near the leading edge of the blade and on the suction side lip were found to be in excess of the blade stagnation value. The peak value on the floor of the recess occurred for the 60 percent spacing condition and was shown to decrease with increasing distance along the cavity and with decreased spacing. On the suction side lip, the Nusselt number results were of the same order for the 40 and 60 percent spacings but decreased for the 20 percent spacing. The highest values of Nusselt number for the platform region occurred on the suction side of the blade at the trailing edge. The peak Nusselt numbers at the 90 percent span location on the blade suction side occurred near the 45 percent wetted distance point and was of the same order as the blade stagnation point value. For the 55 percent wetted distances location at 90 percent span the 40 and 60 percent spacing results were reasonably close to each other with the 20 percent result being significantly lower. However, at 82 percent wetted distance the 20, 40, and 60 percent spacing resultswere relatively close to each other.

The FFT of the cavity floor heat-flux data showed significant amplitude at the wake cutting frequency for the position nearest the leading edge (12 percent wetted distance), little evidence of wake cutting at 39.5 percent wetted distance, and a weak effect near the end of the cavity. The FFT's of the lip data had a strong peak at wake cutting frequency for the suction side heat-flux gage, but a weak signal at the wake cutting frequency for the pressure side locations.

Acknowledgments

The research reported in this paper was funded under support of NASA Grant No. NAG3-1999 and Grant No. NAG3-2157 entitled ''Unsteady Effects (Including Film Cooling) on High-Pressure Turbine Design: An Analytical and Experimental Program.'' The authors would like to thank NASA for permission to publish these results and Dr. Robert J. Boyle for serving as the technical monitor on this program. The support of Kestutis C. Civinskas throughout both of these grant activities is greatly appreciated.

The authors would also like to express their appreciation to Mr. Jeffrey Barton of The Ohio State University Gas Turbine Laboratory for his dedicated help during the experimental phase of this program.

Nomenclature

k_f = thermal conductivity of fluid
L = unit length (meter)
Nu/L = $q/k_f(T_0 - T_g)$
P_0 = total pressure
P_{Ref} = 1.01×10^5 Pa (14.7 psia)
T_g = thin-film temperature during evaluation interval
T_w = wall temperature
T_0 = total temperature
$\dot{w}\sqrt{\theta}/\delta$ = flow function
θ = T_0/T_{ref}
T_{ref} = 294 K (530°R)
δ = P_0/P_{Ref}

References

[1] Metzger, D. E., and Rued, K., 1989, ''The Influence of Turbine Clearance Gap Leakage on Passage Velocity and Heat Transfer Near Blade Tips: Part I—Sink Flow Effects on Blade Pressure Side,'' ASME J. Turbomach., **111**, pp. 284–292.

[2] Metzger, D. E., and Rued, K., 1989, ''The Influence of Turbine Clearance Gap Leakage on Passage Velocity and Heat Transfer Near Blade Tips: Part II—Source Flow Effects on Blade Suction Sides,'' ASME J. Turbomach., **111**, pp. 293–300.

[3] Booth, T. C., Dodge, P. R., and Hepworth, H. K., 1982, ''Rotor-Tip Leakage: Part I—Basic Methodology,'' ASME J. Eng. Power, **104**, pp. 154–161.

[4] Wadia, A. R., and Booth, T. C., 1982, ''Rotor Tip Leakage: Part 2—Design Optimization Through Viscous Analysis and Experiment,'' ASME J. Eng. Power, **104**, pp. 162–169.

[5] Sjolander, S. A., and Cao, D., 1995, ''Measurement of the Flow in an Idealized Turbine Tip Gap,'' ASME J. Turbomach., **117**, pp. 578–584.

[6] Yaras, M. I., Sjolander, S. A., and Kind, R. J., 1992, ''Effects of Simulated Rotation on Tip Leakage in a Planar Cascade of Turbine Blades,'' ASME J. Turbomach., **114**, pp. 652–659.

[7] Mayle, R. E., and Metzger, D. E., 1982, ''Heat Transfer at the Tip of an Unshrouded Turbine Blade,'' *Proc. 7th International Heat Transfer Conference*, **3**, pp. 87–92.

[8] Heyes, F. J. G., and Hodson, H. P., 1993, ''Measurement and Prediction of Tip Clearance Flow in Linear Turbine Cascades,'' ASME J. Turbomach., **115**, pp. 376–382.

[9] Ameri, A. A., Steinthorsson, E., and Rigby, D. L., 1998, ''Effect of Squealer Tip on Rotor Heat Transfer and Efficiency,'' ASME J. Turbomach., **120**, pp. 753–759.

[10] Bindon, J. P., 1986, ''Pressure and Flowfield Measurements of Axial Turbine Tip Clearance Flow in a Linear Cascade,'' Cambridge University Engineering Department, TR 123.

[11] Allen, H. W., and Kofskey, M. G., 1955, ''Visualization Studies of Secondary Flows in Turbine Rotor Tip Regions,'' NACA TN 3519.

[12] Chyu, M. K., Metzger, D. E., and Hwan, C. L., 1987, ''Heat Transfer in Shrouded Rectangular Cavities,'' J. of Thermophysics, **1**, No. 3, pp. 247–252.

[13] Chyu, M. K., Moon, H. K., and Metzger, D. E., 1989, ''Heat Transfer in the Tip Region of Grooved Turbine Blades,'' ASME J. Turbomach., **111**, pp. 131–138.

[14] Metzger, D. E., Bunker, R. S., and Chyu, M. K., 1989, ''Cavity Heat Transfer on a Transverse Grooved Wall in a Narrow Flow Channel,'' ASME J. Heat Transfer, **111**, pp. 73–79.

[15] Bunker, R. S., Bailey, J. C., and Ameri, A. A., 1999, ''Heat Transfer and Flow on the First Stage Blade Tip of a Power Generation Gas Turbine, Part 1: Experimental Results,'' NASA TM 1999-209152.

[16] Ameri, Ali A., and Bunker, R. S., 2000, ''Heat Transfer and Flow on the First Stage Blade Tip of a Power Generation Gas Turbine: Part 2—Simulation Results,'' ASME J. Turbomach., **122**, pp. 272–277.

[17] Rigby, D. L., Ameri, A. A., and Steinthorrson, E., 1996, ''International Passage Heat Transfer Prediction Using Multiblock Grids and $k-W$ Turbulence Model,'' ASME Paper No. 96-GT-188.

[18] Metzger, D. E., Dunn, M. G., and Hah, C., 1991, ''Turbine Tip and Shroud Heat Transfer,'' ASME J. Turbomach., **113**, pp. 502–507.

[19] Ameri, A. A., and Steinthorsson, E., 1995, ''Prediction of Unshrouded Rotor Blade Tip Heat Transfer,'' ASME Paper No. 95-GT-142.

[20] Ameri, A. A., and Steinthorsson, E., 1996, ''Analysis of Gas Turbine Rotor Blade Tip and Shroud Heat Transfer,'' ASME Paper No. 96-GT-189.

[21] Dunn, M. G., Kim, J., Civinskas, K. C., and Boyle, R. J., 1994, ''Time-Averaged Heat Transfer and Pressure Measurements and Comparison With Prediction for a Two-Stage Turbine,'' ASME J. Turbomach., **116**, pp. 14–22.

[22] Venable, B. L., Delaney, R. A., Busby, J. A., Davis, R. L., Dorney, D. J., Dunn, M. G., Haldeman, C. W., and Abhari, R. S., 1999, ''Influence of Vane-Blade Spacing on Transonic Turbine Stage Aerodynamics, Part I: Time-Averaged Data and Analysis,'' ASME J. Turbomach., **121**, pp. 663–672.

[23] Busby, J. A., Davis, R. L., Dorney, D. J., Dunn, M. G., Haldeman, C. W., Abhari, R. S., Venable, B. L., and Delaney, R. A., 1999, ''Influence of Vane-Blade Spacing on Transonic Turbine Stage Aerodynamics, Part II: Time-Resolved Data and Analysis,'' ASME J. Turbomach., **121**, pp. 673–682.

[24] Dunn, M. G., Haldeman, C. W., Abhari, R. S., and McMillan, M. L., 2000, ''Influence of Vane/Blade Spacing on the Heat Flux for a Transonic Turbine,'' ASME J. Turbomach., **122**, this issue, pp. 684–691.

[25] Kim, J., Ross, R. A., and Dunn, M. G., 1996, ''Numerical Investigation of the Heat-Island Effect for Button-Type, Transient, Heat Flux Gage Measurements,'' *Proc 31st National Heat Transfer Conference*, ASME HTD-Vol. 5, pp. 33–39.

[26] Eaton, J. K., Mukerji, D., and Moffat, R. J., 1997, ''3-D Convection in 2-D Boundary Layers: First Progress Report,'' *Proc ASME Heat Transfer Division*, ASME HTD-Vol. 353, pp. 187–189.

[27] Mukerji, D., Eaton, J. K., and Moffat, R. J., 1998, ''A New Correlation for Temperature Rise Correction of Heat Flux Gages,'' *Numerical and Experimental Methods in Heat Transfer*, ASME HTD-Vol. 361-5, pp. 631–636.

[28] Zilles, D. A., and Abhari, R. S., 1999, ''Influence of Non-Isothermal Button Gage Surface Temperature in Heat Flux Measurement Applications,'' *Proc. IMECE99*, Nashville, TN.

High Free-Steam Turbulence Effects on Endwall Heat Transfer for a Gas Turbine Stator Vane

R. W. Radomsky[1]

K. A. Thole

Mechanical Engineering Department,
Virginia Polytechnic Institute
and State University,
Blacksburg, VA 24060

High free-stream turbulence along a gas turbine airfoil and strong secondary flows along the endwall have both been reported to increase convective heat transfer significantly. This study superimposes high free-stream turbulence on the naturally occurring secondary flow vortices to determine the effects on the flowfield and the endwall convective heat transfer. Measured flowfield and heat transfer data were compared between low free-stream turbulence levels (0.6 percent) and combustor simulated turbulence levels (19.5 percent) that were generated using an active grid. These experiments were conducted using a scaled-up, first-stage stator vane geometry. Infrared thermography was used to measure surface temperatures on a constant heat flux plate placed on the endwall surface. Laser-Doppler Velocimetry (LDV) measurements were performed of all three components of the mean and fluctuating velocities of the leading edge horseshoe vortex. The results indicate that the mean flowfields for the leading edge horseshoe vortex were similar between the low and high free-stream turbulence cases. High turbulence levels in the leading edge–endwall juncture were attributed to a vortex unsteadiness for both the low and high free-stream turbulence cases. While, in general, the high free-stream turbulence increased the endwall heat transfer, low augmentations were found to coincide with the regions having the most intense vortex motions. [S0889-504X(00)00704-2]

Introduction

Along a turbine airfoil surface, elevated convective heat transfer coefficients occur as a result of high turbulence levels exiting a combustor in a gas turbine engine. The platform of an airfoil (endwall), a critical surface where durability can be an issue, also has high convective heat transfer levels with a complex footprint. The complexity occurs from the secondary flows that develop in the form of vortices that sweep the platform surface. Both of these effects, high free-stream turbulence effects on airfoil heat transfer and secondary flow effects on endwall heat transfer, have been discussed in the literature. What is missing from the literature is the combined effects of combustor level free-stream turbulence and secondary flows on endwall heat transfer.

Turbulence measurements taken at the exit of a variety of gas turbine combustors have shown that the levels can range between 8 percent and 40 percent [1–3] with some indication that the integral length scale scales with the diameter of the dilution holes in the combustor [4]. As these high levels progress through the downstream turbine vane passage, there is a production of turbulence resulting in high turbulent kinetic energy levels at the exit of the passage [5]. The effect that these high turbulence levels have on the airfoil itself is to increase the heat transfer significantly along the leading edge and pressure side surfaces as well as move the transition location forward on the suction side surface.

The secondary flows previously mentioned take the form of a leading edge horseshoe vortex. This vortex splits into one leg that wraps around the suction surface and another leg that wraps around the pressure surface, with the latter ultimately forming a passage vortex. As the flow progresses downstream, the flow is dominated by the passage vortex. Gaugler and Russell [6] identified, through flow visualization and surface heat transfer, that high convective heat transfer coefficients coincided with the most intense vortex action. Kang and Thole [7] showed through flowfield and heat transfer measurements that the peak heat transfer coincided with the downward legs of both the horseshoe vortex and passage vortex. The downward leg of these vortices brings high speed free-stream fluid toward the endwall and thins the boundary layer to ultimately increase the local heat transfer coefficients. As seen in several past endwall heat transfer studies [8–10] the peak heat transfer on the passage endwall sweeps from the pressure side of the airfoil to the suction side of the adjacent airfoil as the passage vortex moves in that direction.

Although there have been a number of studies documenting high free-stream turbulence effects on airfoil heat transfer and there have been a number of endwall flowfield and heat transfer studies, there are no studies documenting endwall heat transfer at combustor level free-stream turbulence. The work presented in this paper investigates the effect that high turbulence has on endwall heat transfer. In particular, one of the regions having the highest heat transfer is the leading edge–endwall juncture. Three-dimensional flowfield measurements were made in this juncture region such that a comparison of the mean and turbulent flowfields can be made between low and high free-stream turbulence cases.

Past Studies

One of the only flowfield studies to address high free-stream turbulence effects in an endwall region was that of Gregory-Smith and Cleak [11]. They were interested in determining the changes to the flowfield in a rotor blade cascade with a passive grid placed upstream. The passive grid generated an inlet turbulence level of 5 percent. Their primary finding was that the mean flow was not significantly affected by the elevated turbulence level. They also found that there was a net increase of turbulence production as the flow progressed through the channel. They attributed this net increase to the production from the Reynolds shear stresses.

To the authors' knowledge the only endwall heat transfer measurements at elevated turbulence levels reported in the open literature are those of [12–14]. Spencer et al. [12] made endwall heat transfer measurements at an inlet free-stream turbulence level of 9 percent but were not able to contrast that with a low free-

[1]Present address: United Technologies Research Center, 411 Silver Lane, East Hartford, CT 06108.

Contributed by the International Gas Turbine Institute and presented at the 45th International Gas Turbine and Aeroengine Congress and Exhibition, Munich, Germany, May 8–11, 2000. Manuscript received by the International Gas Turbine Institute February 2000. Paper No. 2000-GT-201. Review Chair: D. Ballal.

stream turbulence case since they did not acquire those data. Giel et al. [13] measured convective heat transfer coefficients for a linear rotor cascade with an inlet free-stream turbulence level of 7 percent. Their results indicated, quite surprisingly, that elevated turbulence levels actually decreased the endwall heat transfer levels in several regions along the endwall as compared to their low turbulence level case. This effect, however, may have been due to the fact that the turbulence grid caused a reduction to the inlet boundary layer thickness for the elevated turbulence case. With a thinner boundary layer, the endwall secondary flows are weaker, causing a reduction in the endwall heat transfer. This reduction due to weaker secondary flows would compete with the high turbulence effects that are expected to increase the endwall heat transfer. Khalatov et al. [14] presented an analysis that indicated the augmentation of heat transfer due to high free-stream turbulence along the endwall continually increased as turbulence levels increased up to a turbulence level of 16 percent, beyond which the augmentation leveled off. There were not enough details given in their paper to determine the flow parameters for their experiments.

Endwall flowfield measurements under low free-stream turbulence conditions indicate extremely high turbulence levels in the core of both the leading edge and passage vortices for an asymmetric airfoil as reported by Moore et al. [15], Gregory-Smith et al. [16], and Kang et al. [10]. The reported peak turbulence levels, based on the inlet velocity, range from 25 to 29 percent in the core of the vortex. Results from Devenport and Simpson [17], who used a symmetric airfoil, and from Praisner et al. [18], who used a rectangular block, pointed out that it is improbable that the high turbulence levels in the core are purely a result of turbulent mixing. Devenport and Simpson [17] showed that the peak positive turbulence production coincided with regions having highly bimodal flow as indicated by their streamwise velocity histograms. Based on the analyses, Devenport and Simpson attributed the high turbulence to the large-scale unsteadiness rather than the fluid-wall generated shear layer.

From past studies, there is a clear need to investigate further the heat transfer characteristics of the endwall under high turbulence levels. At this point, the data given in the literature are quite sparse for the effects of high free-stream turbulence on endwall heat transfer.

Experimental Design and Measurements

The construction and the development of the scaled-up turbine stator vane and the test section have been previously documented by a number of studies including Kang et al. [10], Kang and Thole [7], and Radomsky and Thole [5]. The wind tunnel used in this study is recirculating with a corner test section shown in Fig. 1. A description of the vane is indicated in the attached table in Fig. 1. While the inlet Reynolds number for the wind tunnel was matched to that of the engine, the inlet Mach number was not matched (Ma=0.017 for the wind tunnel case and Ma=0.12 for the engine case). This test section contains a central turbine vane with two adjacent vanes that have all been geometrically scaled up by a factor of nine to allow for highly resolved data acquisition. The outside adjacent vane was constructed by attaching a leading edge to a plexiglass sidewall, allowing for optical access. The placement of this flexible wall exactly matches the surface of an adjacent vane. Beyond the point where the adjacent vane geometry stops, the flexible wall was positioned such that the central vane matched a predicted pressure distribution. The computational predictions were made for two-dimensional, inviscid, periodic vanes at low-speed conditions. Pressure measurements on the central vane were made to insure that the flexible wall and stagnation point were correctly positioned.

An active grid turbulence generator, described in detail by Radomsky and Thole [5], was used to generate the high turbulence levels. The active grid consisted of vertical hollow square bars with jets injecting into the mainstream in both the upstream and downstream directions. The bars were 1.27 cm square with the jet

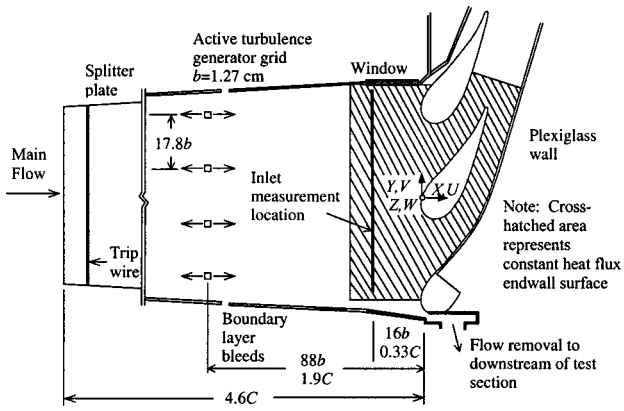

Scaling factor	9
Scaled-up true chord length	59.4 cm
Pitch / true chord	0.77
Span / true chord	0.93
Re_{in}	2.3×10^5
U_∞	5.85 m/s
T_∞	20°C
Inlet flow angle	0°
Trailing edge metal angle	72°
Approach length / chord	4.6

Fig. 1 Schematic of corner test section containing the stator vane cascade

holes having a diameter of 1.5 mm and vertically spaced 3.05 cm apart. These hollow bars were installed 88 bar widths upstream of the stator vane stagnation position or, in terms of vane coordinates, at 1.9 chords in front of the stagnation position. A compressed air supply fed a plenum that supplied each of the bars. The turbulence generated from this active grid was 19.5 percent measured at 0.33 chords upstream of the vane stagnation location. The integral length scale at 0.33 chords upstream was $\Lambda_x/P = 0.12$ and was uniform across the span to within 4 percent. A detailed discussion of the inlet flow quality will be given later in the paper.

Flowfield Measurements. The flowfield was measured for a plane at the endwall–vane juncture parallel with the incoming flow direction that intersects the stagnation location of the vane. This plane was chosen to compare with that previously reported by Kang et al. [10] at low turbulence conditions. The two-component back-scatter fiber optic LDV system used in this study consisted of a 5 W laser used in conjunction with a TSI model 9201 Colorburst beam separator. Velocity data were processed using TSI model IFA 755 Digital Burst Correlator controlled using TSI's FIND software. All three velocity components (U, V, and W) were measured with a two-component laser-Doppler velocimeter (LDV) positioned in two different orientations. A 750 mm focusing lens with a beam expander was used on the end of the fiber optic probe to make measurements of the streamwise (U) and pitchwise (V) components through the top endwall; and the streamwise (U) and spanwise (W) components through the sidewall. Coincident measurements were made through the sidewall to quantify the Reynolds shear stress, $\overline{u'w'}$. The probe volume length and diameter for the 750 mm lens with the beam expander were 0.85 mm and 72 microns. The data were corrected for velocity bias effects by applying residence time weighting.

Endwall Heat Transfer Measurements. The heat transfer results for the high free-stream turbulence conditions were measured in the same facility as for the low free-stream turbulence conditions [10]. These measurements were obtained with a con-

stant heat flux plate placed on the bottom endwall, as indicated by the cross-hatched area in Fig. 1, surrounding the Styrofoam stator vane. The constant heat flux plate consisted of a 50-μm-thick copper layer on top of a 75-μm-thick kapton layer in which 25-μm-thick inconel heating elements were embedded in a serpentine pattern. This heater was placed onto a 1.9-cm-thick wooden surface using double-sided tape. Just below the wood was a 2.54 cm thick *R*-5 extruded Styrofoam board. The total heating area for the plate was 0.549 m^2 and the input power was adjusted to give a heat flux of 980 W/m^2. The lateral conduction was estimated to be less than 1 percent within the averaging spot size for the infrared camera. The top surface of the heater plate was painted black giving an emissivity of 0.94.

Surface temperature data was acquired using a calibrated infrared camera (Inframetrics Model 760). The camera was calibrated in situ using type *E* ribbon thermocouples that were painted black and placed on the heated surface. The calibration procedure was performed to obtain the correct plate emissivity and background temperature and insure a linear relationship between the infrared camera measurements and the thermocouple reading over the required operating temperature range. To perform these measurements, the top endwall was replaced with a plate having 13 viewing ports in which an 11.43-cm-dia crystal fluoride window or, when not making measurements from that port, a lexan insert could be placed. Each endwall temperature resulted from an average of 16 images and, based on an uncertainty analysis, it was determined that five of these 16 averaged images were enough to get a good average. Small positioning crosses were placed on the endwall to identify where each of the 13 images were relative to the turbine vane. An in-house processing routine allowed the 13 images to be assembled into one complete endwall temperature distribution. The infrared camera performed a spatial averaging over 0.37 cm and operated at its maximum viewing area of 21.5 cm$\times$16 cm represented by 255$\times$206 pixels.

The input heat flux was corrected for radiation losses, which amounted to between 7–23 percent of the input power, and conduction losses, which amounted to 1.7–3.5 percent of the input power. No correction was necessary regarding heat losses from conduction to the turbine vane itself because the vane was constructed using Styrofoam. Using the measured temperatures and the remaining convective heat flux, the heat transfer coefficients were computed and reported as Stanton numbers.

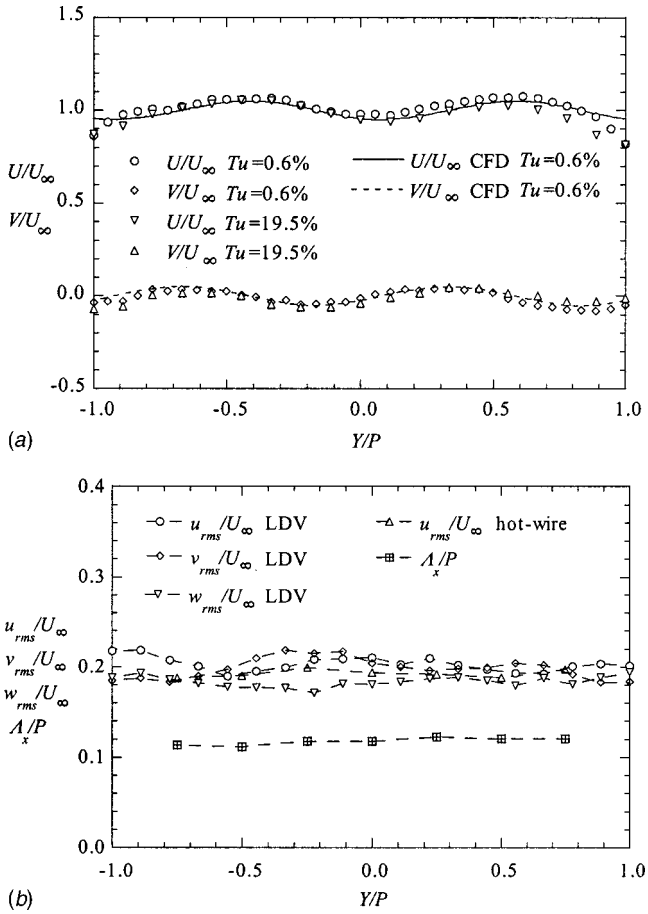

Fig. 2 (*a*) Comparison of measured and predicted normalized mean streamwise and pitchwise velocity profiles at one-third chord upstream of the vane stagnation; (*b*) normalized rms levels of all three velocity components and integral length scale measured at one-third chord upstream of the vane stagnation point

Uncertainty Estimates

The partial derivative and sequential perturbation methods, described by Moffat [19], were used to estimate the uncertainties of the measured values. Uncertainties were calculated based on a 95 percent confidence interval. For each velocity component 15,000 data points were used to compute the mean and turbulence quantities whereas when coincidence data was acquired 20,000 data points were acquired. The estimate of bias and precision uncertainties for the mean velocities were 1 percent while the precision of the rms velocities was 2.1 percent for u_{rms}, 1.7 percent for the v_{rms}, and 3.2 percent for w_{rms}. The precision uncertainties of the Reynolds shear stress and correlation coefficient were 12.8 and 13.4 percent. Note that these uncertainty estimates were made for the near endwall region where the highest uncertainties arise. The uncertainty in the Stanton number was 4.5 percent, which was determined for the lowest measured temperature difference which dominated the uncertainty.

Inlet Flow Conditions

The inlet flow conditions for the high free-stream turbulence case are the same as those previously reported by Radomsky and Thole [5] and are repeated in Figs. 2(*a*) and 2(*b*) for completeness. These profiles were taken at the vane mid-span location at one-third chord upstream of the vane stagnation. Figure 2(*a*) shows measured inlet mean velocity profiles across the entire width of the wind tunnel for the low and high free-stream turbulence cases. The computed profiles, also shown in Fig. 2(*a*), are results from a two-dimensional simulation using FLUENT [20] (see [5] for details). These profiles reveal that the flow is already reacting to the upcoming vane and, more importantly, is quite periodic across the two airfoil pitches. It is also evident that the high free-stream turbulence generator is not affecting the mean flow conditions given the fact that the high and low turbulence cases agree. The vertical uniformity across the span of the airfoil indicate that the maximum deviation normalized by the average velocity was 1.6 and 3.5 percent for the low and high turbulence cases. The measured turbulence conditions at one-third chord upstream, revealed in Fig. 2(*b*), indicate uniformity across the pitch and fairly isotropic conditions with the average spanwise rms (w_{rms}) levels being 91 percent of the average streamwise rms (u_{rms}) levels and 93 percent of average cross-stream rms (v_{rms}) levels. The maximum deviation of the rms velocities across the span of the turbine vane was 2.8 percent. The average turbulence level at this location is 19.5 percent. The integral length scale, also shown in Fig. 2(*b*), is nominally 12 percent of the vane pitch and is relatively uniform across the pitch.

As previously discussed, the high free-stream turbulence was generated using active bar grids with a bar width of 1.27 cm and located 88 bar widths (*b*) upstream of the vane. These bars extended the entire span of the test section, meaning that the bars were also present in the developing endwall boundary layer. To insure that the bars did not create spanwise variations of the boundary layer, boundary layer measurements were made behind

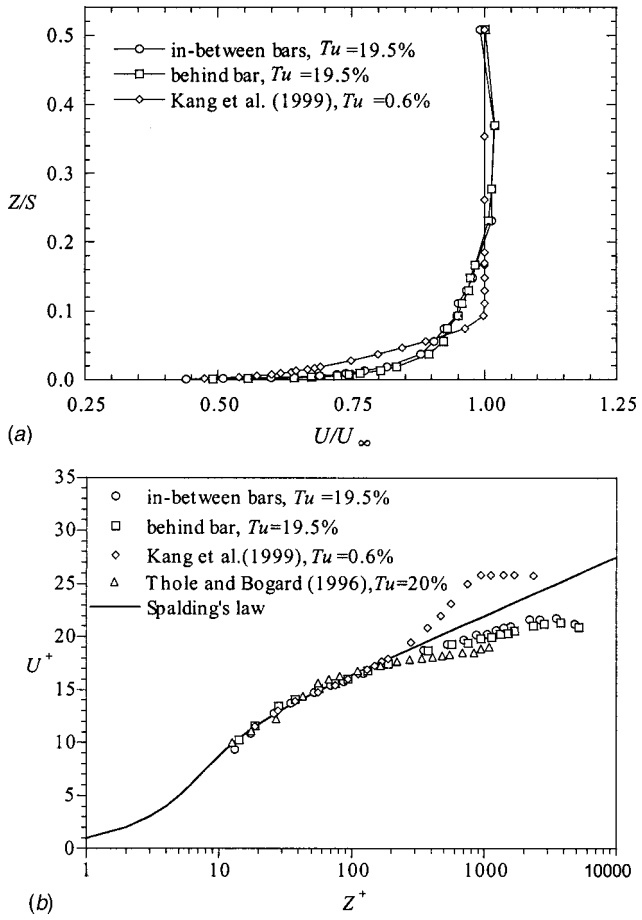

Fig. 3 (*a*) Comparison of measured streamwise boundary layer profiles at low and high free-stream turbulence levels plotted in terms of free-stream parameters; (*b*) comparison of measured streamwise boundary layer profiles at low and high free-stream turbulence levels plotted in terms of inner wall scaling parameters

a bar and in between two bars at one-third of a chord upstream of the airfoil. This location corresponds to 1.6 chords and 59 bar widths downstream of the bars. These boundary layer measurements are shown in Fig. 3(*a*) using free-stream parameters and in Fig. 3(*b*) using inner wall scaling parameters. Comparison of these two profiles indicates no noticeable difference between that measured behind the bar and in between bars. These results demonstrate the fact that the presence of the bars does not affect the endwall boundary layer development. Figures 3(*a*) and 3(*b*) also shows the boundary layers measured at the low free-stream turbulence conditions by Kang et al. [10]. Comparison of the low and high free-stream turbulence boundary layers shows the typical differences, such as the depressed wake, that would be expected for a boundary layer subjected to 20 percent free-stream turbulence levels.

To minimize any boundary layer effects, it is desirable to match the boundary layer momentum Reynolds number between the low and high free-stream turbulence cases. The momentum Reynolds number for the two locations (behind the bar and in between the bars) are shown in Table 1 for the high turbulence cases and the low turbulence case previously given by Kang et al. [10]. For the data given by Kang et al. [10], the boundary layer characteristics were measured at one chord upstream of the vane, whereas for the high free-stream turbulence case the characteristics were measured at one-third of a chord upstream. Based upon the boundary layer virtual origin and turbulent boundary layer correlations, it is expected that the momentum thickness Reynolds number would

Table 1 Boundary layer characteristics for high and low turbulence cases

	Tu = 20% Behind Bars *X/C*=-0.33	Tu = 20% Between Bars *X/C*=-0.33	Tu = 0.6% (Kang, et al. 1998) *X/C*=-1
δ(cm)	9	9	5
δ* (mm)	8.2	9.1	10.6
θ(mm)	6.7	7.2	7.1
H	1.22	1.26	1.50
Re_θ	2653	2704	3340

be Re_θ=3630 at one-third chord upstream relative to Re_θ=3340 at one chord upstream for the low free-stream turbulence case. This would result in a difference in momentum thickness Reynolds number of 25 percent between the low and high free-stream turbulence cases. Using the standard correlations for turbulent boundary layer heat transfer, this difference in Reynolds number should result in a difference in Stanton numbers of 9.5 percent. As will be shown in the results, the augmentation due to high free-stream turbulence was much more than 9.5 percent.

Comparisons made to previously reported data for a boundary layer affected by 20 percent free-stream turbulence levels are also shown in Figs. 3(*b*), 4(*a*), and 4(*b*). The previously reported measurements of Thole and Bogard [21] had the same free-stream turbulence level, but were for a significantly lower momentum Reynolds number of Re_θ=580 as compared with the present study. There is good agreement in the scaling of the boundary layers affected by the high free-stream turbulence and, as expected, the profiles indicate a very depressed wake region.

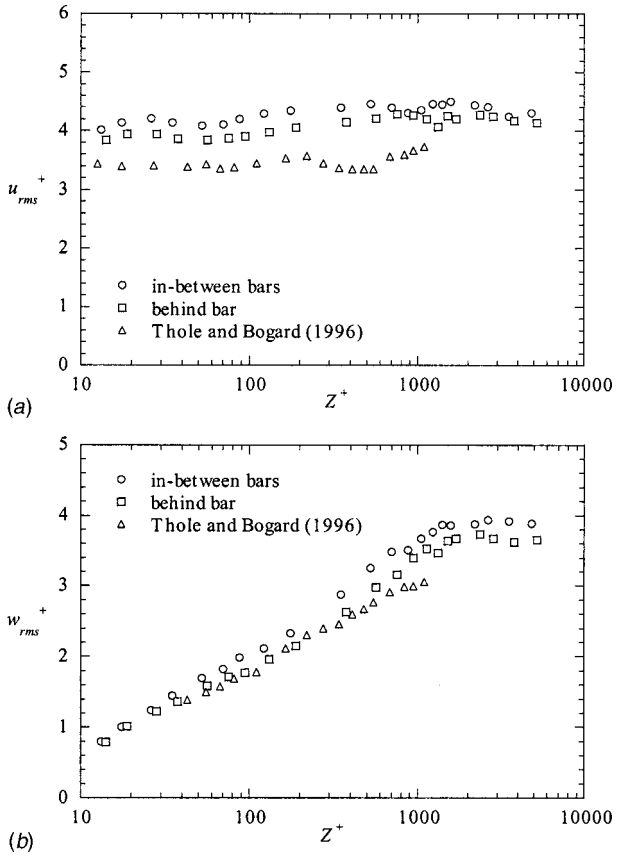

Fig. 4 (*a*) The rms levels of streamwise velocity fluctuations in the boundary layer in terms of inner wall scaling parameters; (*b*) rms levels of spanwise velocity fluctuations in the boundary layer in terms of inner wall scaling parameters

Figures 4(*a*) and 4(*b*) show the streamwise and vertical fluctuations scaled in inner wall coordinates, u^+_{rms} and w^+_{rms}, for the turbulent boundary layers affected by 20 percent turbulence. It is clear that the data for the behind and in between bars are very much the same. Also shown is good agreement with the data given by Thole and Bogard [21] for their 20 percent turbulence cases. The largest difference occurs for the u^+_{rms} measurements indicating values 13 percent higher than the data given by Thole and Bogard [21].

Flowfield Measurements at the Leading Edge Endwall Juncture at High Turbulence Levels

A comparison of the leading edge horseshoe vortices for low and high free-stream turbulence cases shown in Figs. 5(*a*) and 5(*b*). Recall this measurement plane is parallel with the incoming flow direction and intersects the vane surface at the stagnation location. Superimposed on the velocity vectors (U and W) are contours of the streamwise (U/U_∞) velocity. The primary difference between the low and high free-stream turbulence cases is that for the high free-stream turbulence case the vortex is located slightly closer to the vane surface and there is more of a complete roll-up than for the low free-stream turbulence case. The heights of the vortex core for the two cases are very similar with the location being in the near-wall region at approximately $Z/S = 0.015$. Having the vortex pushed closer to the vane for the high turbulence case may be explained by the fact that near the wall, the fluid velocity is faster for the high free-stream turbulence case as compared with the low free-stream turbulence case, as shown in Fig. 3(*a*). This is an affect of the high free-stream turbulence flattening out the approaching boundary layer profile. This higher speed fluid would tend to push the vortex closer to the vane surface.

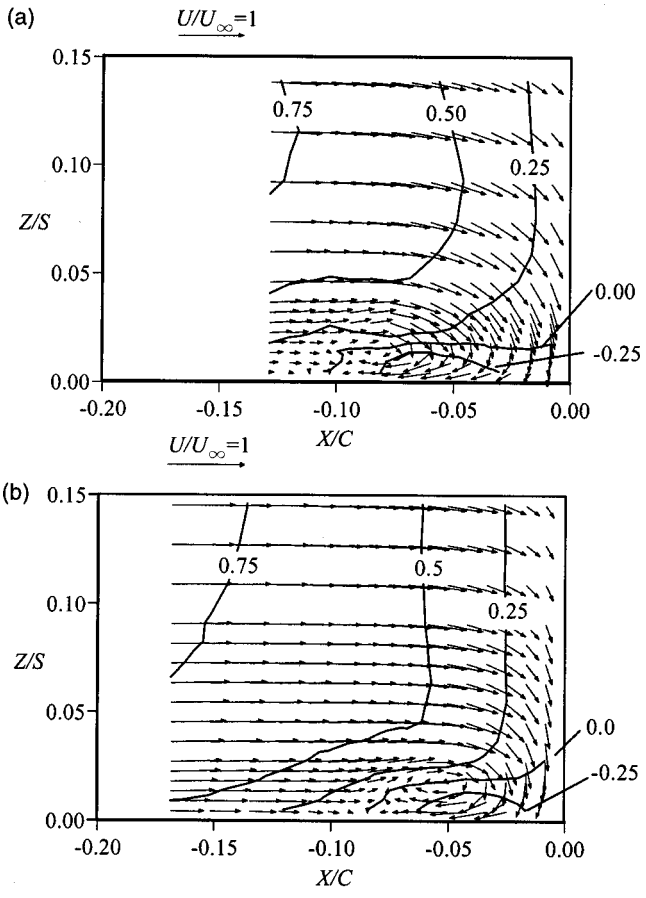

Fig. 5 Leading edge horseshoe vortex with contours of streamwise velocity at: (*a*) *Tu*=0.6 percent [10], and (*b*) *Tu*=19.5 percent

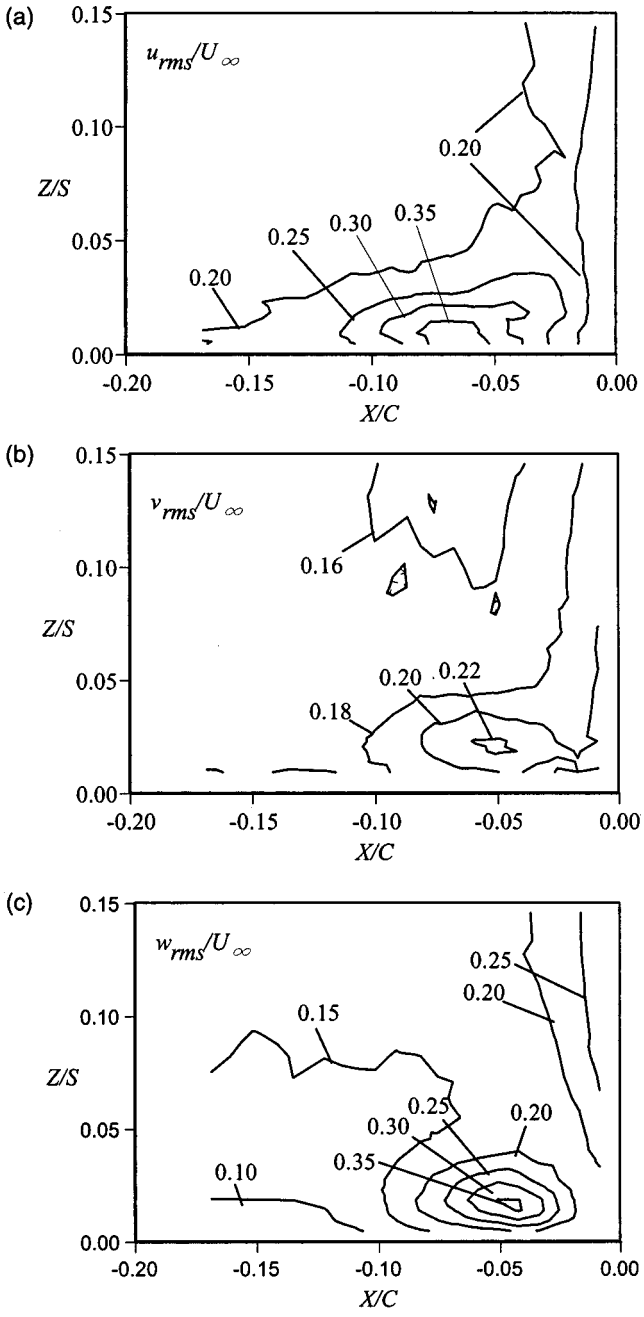

Fig. 6 Contour levels of: (*a*) streamwise, (*b*) pitchwise, and (*c*) spanwise turbulence components at *Tu*=19.5 percent

Figures 6(*a*), 6(*b*), and 6(*c*) depict the turbulence components for the high free-stream turbulence case while Figs. 7(*a*) and 7(*b*) compare the normalized turbulent kinetic energy contours for low and high free-stream turbulence cases. The high turbulence levels away from the endwall at the midspan agree well with the previously reported measurements for the high free-stream turbulence case [5]. Near the endwall, it is clear that the levels are significantly higher than those occurring near the midspan and are higher than those previously reported by [10] for the low free-stream turbulence case. In comparing the relative peak contour levels for the high free-stream turbulence case, the u_{rms}/U_∞ and w_{rms}/U_∞ peak levels are much the same while the cross-stream velocity fluctuations, v_{rms}/U_∞, are somewhat lower. The profiles

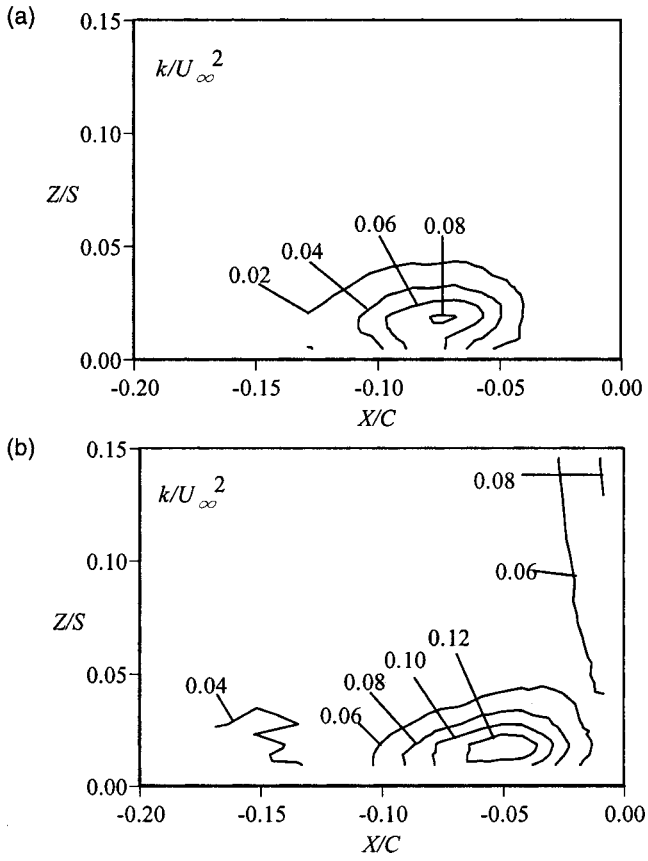

Fig. 7 Contour levels of normalized turbulent kinetic energy at: (*a*) *Tu*=0.6 percent, and (*b*) *Tu*=19.5 percent

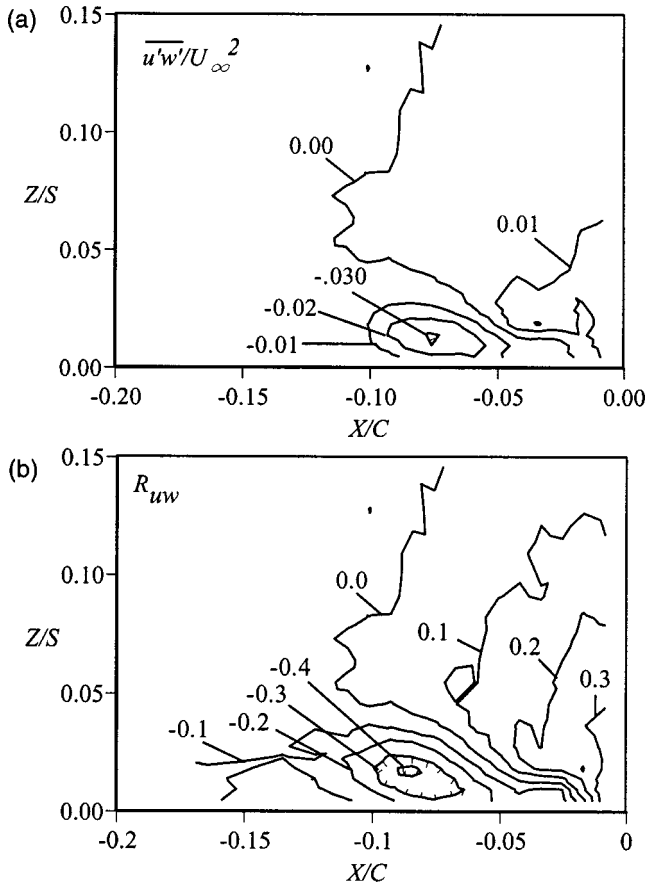

Fig. 8 Contour levels of: (*a*) normalized Reynolds shear stress, and (*b*) correlation coefficients at high free-stream turbulence

also reveal that the locations of these peak values coincide closely with the center of the vortex, with only the peak streamwise fluctuations occurring slightly upstream of the vortex center. If one compares the level of streamwise fluctuation with those found in a canonical turbulent boundary layer where the peak level is less than 15 percent, it is evident that the fluctuations are much higher in the vortex region. These high levels are in agreement with the data previously presented by Devenport and Simpson [17] who also reported very high levels in the vortex region. It appears that an unsteady motion of the horseshoe vortex accounts for the increased turbulence measured near the horseshoe vortex.

The turbulent kinetic energy contours shown in Figs. 7(*a*) and 7(*b*) for the low and high free-stream turbulence conditions indicate that the primary difference is higher turbulent kinetic energy levels occurring for the high turbulence case. Compared with the low free-stream turbulence case, the peak turbulent kinetic energy levels are located closer to the vane surface. This is consistent with the vortex center being closer to the vane surface.

Coincident velocity measurements were made for the streamwise and spanwise velocity components for the high turbulence case to give the Reynolds shear stress component, $\overline{u'w'}/U_\infty^2$, and the correlation coefficient, R_{uw}. The Reynolds shear stress contours given in Fig. 8(*a*) indicate low negative values approaching the vane on the endwall. The peak shear stress value of $\overline{u'w'}/U_\infty^2 = -0.03$ occurs on the front edge of the upturn of the horseshoe vortex. On the downturn side of the vortex positive shear stresses occur, but with much lower values than the negative peak stress values. On the downturn side of the vortex in the vane-endwall juncture the positive stresses coincide with a negative spanwise velocity gradient, $\partial W/\partial Z$, which is the largest turbulence production mechanism in this region.

The correlation coefficients in Fig. 8(*b*) indicate that the incoming turbulence near the midspan is uncorrelated, as would be expected for random turbulence. In the flow approaching the vane along the endwall, the correlation coefficient, R_{uw} has peak magnitudes lower than those occurring for a turbulent boundary layer with low free-stream turbulence, which would typically be a value of $R_{uw} = -0.4$. These lower values (-0.1) agree with those previously reported for a turbulent boundary layer subjected to high free-stream turbulence levels [21] and are a result of uncorrelated free-stream turbulence penetrating into the boundary layer. Moving toward the vane, the turbulence becomes more correlated, as indicated by the high negative values. The negative values are a result of the streamwise velocity moving away from the vane ($-U$) and upward away from the wall ($+W$) thereby giving negatively correlated turbulence. Next to the vane surface along the endwall, positive values occur as higher speed streamwise fluid ($+U$) being brought down toward the endwall where the W component is larger than the fluid transported there giving a ($+W$) and a positive correlation coefficient. Moving along the turbine vane span toward the endwall, the magnitude of the W component increases, resulting in a change in the sign of the correlation coefficient.

To verify the unsteadiness of the horseshoe vortex, velocity probability density functions were recorded for the low and high free-stream turbulence cases. Figures 9(*a*, *b*) and 10(*a*, *b*) illustrate the probability density functions of the streamwise and spanwise velocities. The measurements shown in these figures were at different locations relative to the endwall (Z/S) for a given axial position. The axial position was chosen to be slightly upstream of the center of the vortex for each of the respective flow cases. The probability density functions are reported for both the normalized

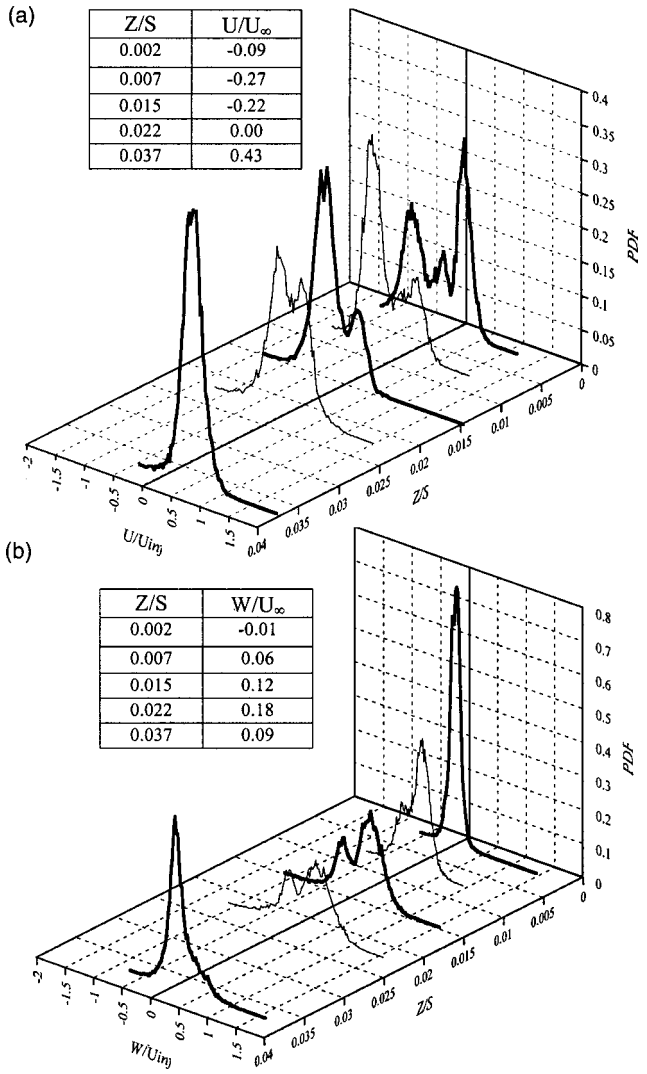

Fig. 9 Probability density functions of: (*a*) streamwise, and (*b*) spanwise velocity components in the leading edge horseshoe vortex at a turbulence level of 0.6 percent

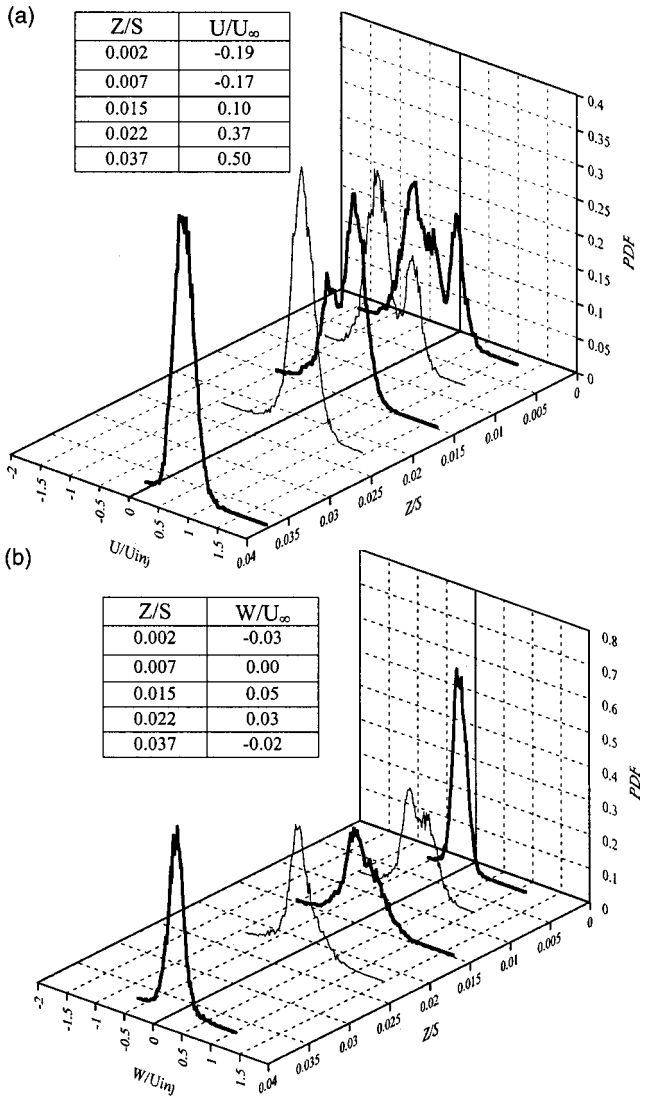

Fig. 10 Probability density functions of: (*a*) streamwise, and (*b*) spanwise velocity components in the leading edge horseshoe vortex at a turbulence level of 19.5 percent

streamwise (U/U_∞) and spanwise (W/U_∞) velocity components. The probability density functions are defined by the following [22]:

$$\text{PDF} = \frac{N_i}{N}\left(\frac{k}{b-a}\right) \tag{1}$$

where N_i is the number of times a particular velocity occurs in a certain bin size; N is the total number of data points; k is the width of the bins; and a and b are the minimum and maximum range of velocities considered.

For the low free-stream turbulence case, shown in Fig. 9(*a*), the PDF for the streamwise velocities indicate that at a position farthest from the endwall ($Z/S=0.037$) there is a Gaussian distribution of the measured mean velocities. This Gaussian distribution is what one would expect for a random turbulent flow. Closer toward the endwall, particularly in the vortex center, the PDF curves indicate that there are two distinct peaks with a shift in the relative heights of the peaks. These two peaks indicate that the flow is oscillating, or rather unsteady, in the vortex region. The PDF curves for the spanwise velocity components also show two distinct peaks for $Z/S=0.022$, 0.015, and 0.007, but return to just a single peak at the position closest to the wall, $Z/S=0.002$. The spanwise component is distinctly different from the streamwise velocity because of the suppression near the wall. This suppression is also evident in the lower rms levels in the spanwise velocity near the wall.

Figures 10(*a*) and 10(*b*) show PDF curves at the same vertical positions but at an axial position closer to the vane, which corresponds to just upstream of the vortex center for the high free-stream turbulence case. For the streamwise velocities, there are still two peaks evident, indicating an unsteady vortex. The spread between the two peaks, however, is much closer for the high free-stream turbulence case, as compared with the low free-stream turbulence case. This reduction in the spread between the two peaks is due to the highly turbulent flow that is transported into the vortex. The PDF curves for the spanwise velocity components do not show strong evidence of bimodal flow. This may be expected because, as was shown for the low free-stream turbulence case, the bimodal peaks were much closer together for the spanwise velocity as compared with the streamwise velocity. The high free-stream turbulence, which is Gaussian in nature, is transported into the vortex region through the downward flow, causing the PDF to appear less bimodal.

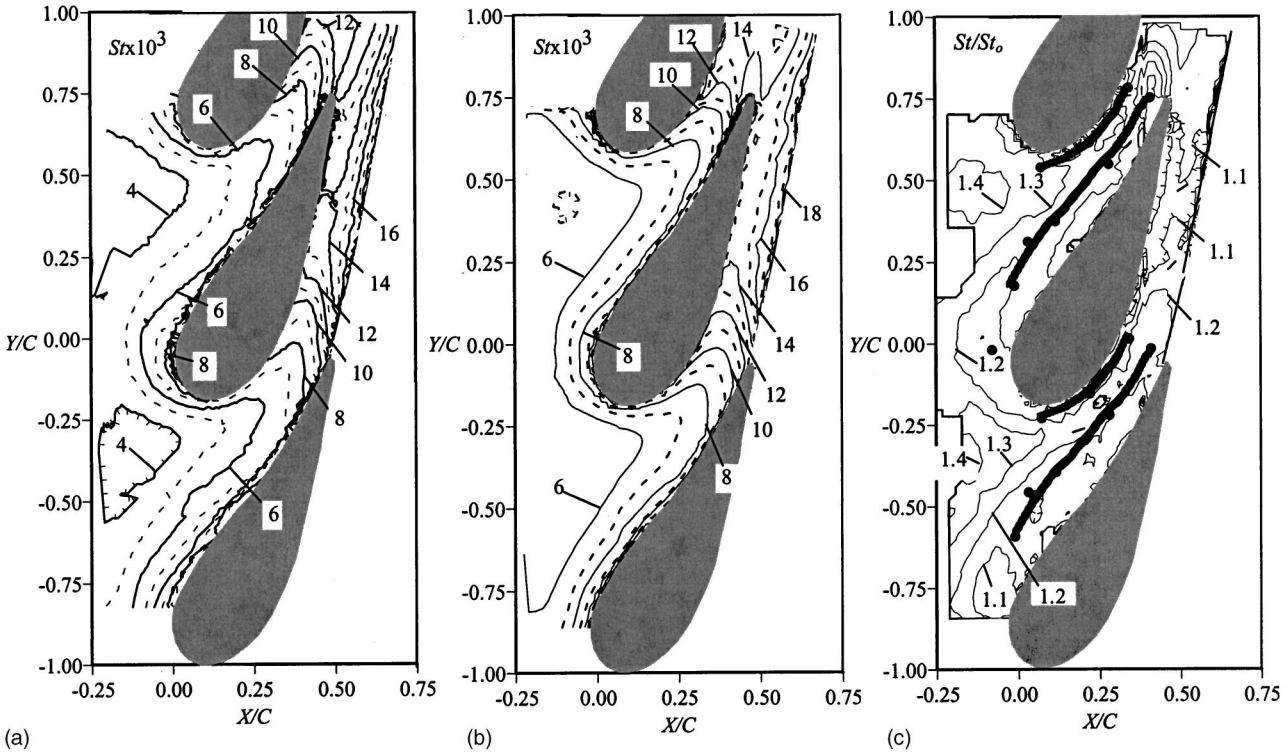

Fig. 11 Contours of Stanton number ($St\times10^5$) on the vane endwall at: (*a*) $Tu=0.6$ percent [10], and (*b*) $Tu=19.5$ percent; (*c*) contours of Stanton number augmentation (St/St_0) as a result of free-stream turbulence at 19.5 percent

Endwall Heat Transfer Measurements at High Turbulence Levels

Endwall surface heat transfer measurements were performed at the high free-stream turbulence level of 20 percent. These heat transfer measurements were made for the flow characteristics listed in Table 3 for the high and low turbulence cases, allowing direct comparisons to determine the effects of high free-stream turbulence on endwall heat transfer. As stated previously, the difference in momentum thickness Reynolds numbers between the two cases should result in a 9.5 percent augmentation between the low and high turbulence cases.

The heat transfer results plotted in terms of a Stanton number, where Stanton number is based on the inlet velocity approaching the test section, are given in Figs. 11(*a*) and 11(*b*). Many similarities exist between the low and high free-stream turbulence cases. A region of high heat transfer is observed in front of the vane stagnation point as a result of the formation of the horseshoe vortex. The strong downward flow, previously shown in the flowfield measurements, causes high heat transfer levels very near the vane endwall juncture. Moving into the passage, the heat transfer contours show that the peak Stanton number contours are being swept near the suction surface. Farther into the vane passage, the Stanton number contours become aligned parallel to the direction of flow. High Stanton number contours are observed near the flexible wall as a result of the passage vortex impinging on the endwall surface. Lower Stanton number values are observed near the suction surface of the stator vane where the passage vortex is lifting the flow away from the endwall. As a result of the higher turbulence levels, higher values for the Stanton number are observed throughout the vane endwall. Near the trailing edge of the stator vane, however, the Stanton number levels are very similar, with only slightly higher values being seen for the higher turbulence level. This would suggest that in this region, the heat transfer is being dominated by the secondary flow effects rather than high free-stream turbulence effects.

Figure 11(*c*) indicates the augmentation of the heat transfer due to high free-stream turbulence. The augmentation is defined as the Stanton number occurring at high free-stream turbulence (St) conditions divided by the Stanton number at low free-stream turbulence (St_0) conditions. The augmentation was calculated by defining a small region, averaging the Stanton number in that area for both the low and high turbulence cases at a given location, and then dividing the two quantities. The defined region was that of a circle with a radius equal to the averaging area of the infrared camera.

Superimposed on the contours shown in Fig. 11(*c*) is the trajectory of the center of the passage and leading edge vortices based on the flowfield measurements reported by Kang and Thole [7] for the low free-stream turbulence case. Given the fact that the leading edge horseshoe vortex mean flowfield was close to the same for both the low and high free-stream turbulence cases, it is reasonable to presume that the path of the passage vortex is much the same for the two cases. Figure 11(*c*) indicates the highest augmentation occurs in the midpitch region at the start of the passage. Moving into the passage the augmentation decreases with values around unity near the suction side surface indicating essentially no augmentation due to high free-stream turbulence. Along the pressure side, higher augmentation values occur in heat transfer. These augmentations are consistent with the fact that the highest augmentations due to high free-stream turbulence generally occur along the pressure side of the airfoil itself. In comparing the path of the vortex with the augmentation footprint, it is clear that for a given axial location, the lowest augmentations occur in the regions with the most intense vortex action. These low contour levels can be tracked coming off the leading edge as the leading edge horseshoe vortex develops into the passage vortex. The passage vortex then sweeps from the pressure side to the suction side, which also coincides with much lower augmentation levels. Clearly, these results indicate that the heat transfer in the

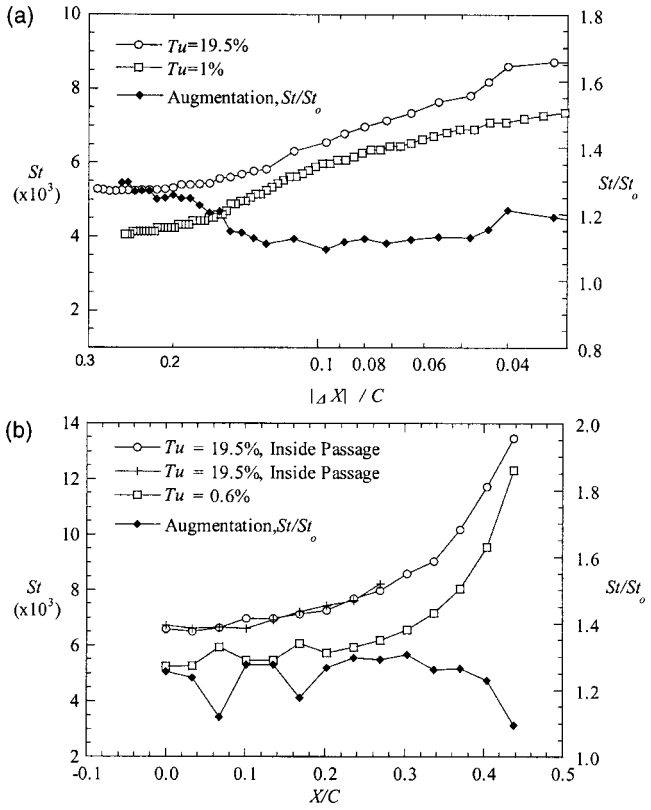

Fig. 12 Comparison of $Tu=0.6$ and 19.5 percent for: (*a*) Stanton numbers approaching the vane stagnation point, and (*b*) Stanton numbers that have been pitchwise averaged at a given axial location

region of the vortices (leading edge and passage) is dictated by the vortices rather than the elevated turbulence level augmentation.

Figure 12(*a*) presents the Stanton numbers and augmentation values approaching the stagnation location along a line parallel to the incoming velocity vector (along the endwall for the stagnation flowfield measurements presented in this paper). For the high free-stream turbulence levels, the Stanton numbers are relatively constant at the inlet to the test section. For a turbulent boundary layer on a flat plate subjected to 20 percent turbulence levels and a dissipation length scale that is 25 percent of the vane pitch, one would expect from flat plate correlations that there would be an augmentation in Stanton number of 0.26 for a TLR parameter [23] of 0.033 [24]. This is in close agreement with the augmentation indicated in Fig. 12(*a*).

Figure 12(*a*) indicates an increase in Stanton number is observed starting at $|\Delta x|/C=0.2$. At this location the flowfield is decelerating in front of the horseshoe vortex that has formed near the endwall. The Stanton number continues to increase until $|\Delta x|/C=0.05$ where it begins to level off. This location is very close to the location of the center of the horseshoe vortex. Comparisons of the Stanton number distribution at the lower turbulence level shows lower heat transfer levels well upstream of the vane stagnation point. Closer to the vane surface, the Stanton numbers for the low and high turbulence cases are closer. This is seen in the augmentation data, showing high augmentation levels at 1.3 farthest from the vane, which then decrease to a minimum of 1.1 closer to the vane. This decrease again suggests that the heat transfer in this region is more a function of the horseshoe vortex, which is similar for that of both high and low turbulence levels, rather than the high levels of free-stream turbulence.

Figure 12(*b*) compares the heat transfer coefficients averaged over the pitch for a range of axial position. In addition, Fig. 12(*b*) illustrates good agreement between data taken in both passages surrounding the central airfoil for the high free-stream turbulence case. For most of the axial distance, the augmentation is relatively constant at 25 percent above the low free-stream turbulence case. Only near the end of the vane where the passage vortex dominates, beyond X/C of 0.38, is there a decrease in the augmentation.

Conclusions

Flowfield results indicated a downstream shift of the leading edge vortex for the high free-stream turbulence case relative to the low free-stream turbulence case. This effect can be attributed to the differences in the approaching boundary layers. The rms levels of the velocity fluctuations increase with the added free-stream turbulence. High turbulence levels in the leading edge vortex can result from wall-generated turbulence, momentum transport of the free-stream turbulence into the vortex region, and an unsteadiness of the horseshoe vortex. As with previously reported literature, the rms of the velocity fluctuations are much higher than those that occur for wall-generated turbulence alone. Supporting the fact that the high fluctuations occur as a result of an unsteadiness of the vortex were probability density functions of the streamwise and spanwise velocity components. The streamwise velocity component was bimodal in nature for both low and high free-stream turbulence cases rather than the typical Gaussian distribution that occurs for wall-generated turbulence. Although these bimodal distributions occur for both the low and high free-stream turbulence cases, indicating an important unsteady contribution to the rms levels, there was still a further increase in the rms levels for the high free-stream turbulence case. This increase for the high free-stream turbulence case is believed to be due to the momentum transport of the highly turbulent free-stream into the vortex region.

The endwall surface measurements revealed that there was an increase in the endwall heat transfer due to high free-stream turbulence. The relative difference in augmentations on the endwall between the suction and pressure sides of the airfoil are consistent with those reported along on the airfoil itself. The augmentations due to free-stream turbulence, however, were either small or nonexistent in the leading edge region where the horseshoe vortex has a dominating effect and near the suction side of the airfoil where the passage vortex has a dominating effect.

Acknowledgments

The authors would like to acknowledge the Department of Energy Advanced Gas Turbine Systems Research Program with thanks going to Larry Golan for serving as the contract monitor. Partial support for this work also came from Pratt & Whitney with William Kvasnak and Fred Soechting serving as contract monitors.

Nomenclature

b = bar width
C = true chord of stator vane
H = shape factors δ^*/θ
k = turbulent kinetic energy $=1/2(u_{\text{rms}}^2+v_{\text{rms}}^2+w_{\text{rms}}^2)$
Ma = Mach number $=U_\infty/\sqrt{\kappa RT}$
P = vane pitch
R = gas constant
R_{uw} = correlation coefficient $=\overline{u'w'}/u_{\text{rms}}w_{\text{rms}}$
Re_{in} = Reynolds number $=CU_\infty/\nu$
Re_θ = Reynolds number $=U_\infty\theta/\nu$
s = surface distance along vane measured from flow stagnation
S = span of stator vane
St = Stanton number $=h/\rho CpU_\infty$
U_∞ = incident upstream velocity
U, V, W = mean velocity in the X, Y, Z directions

$\overline{u'w'}$ = Reynolds shear stress
X, Y, Z = global coordinates defined from stagnation location
δ_{99} = boundary layer thickness
δ^* = displacement thickness
θ = momentum thickness
κ = ratio of specific heats
Λ_x = integral length scale
ν = viscosity
ρ = density
τ_w = wall shear stress

Subscripts

avg = average
in = inlet
rms = root mean square

Superscripts

$+$ = normalization using friction velocity, defined as $\sqrt{\tau_w/\rho}$

References

[1] Goldstein, R. J., Lau, K. Y., and Leung, C. C., 1983, ''Velocity and Turbulence Measurements in Combustion Systems,'' Exp. Fluids, **1**, pp. 93–99.
[2] Kuotmos, P., and McGuirk, J. J., 1989, ''Isothermal Flow in a Gas Turbine Combustor—A Benchmark Experimental Study,'' Exp. Fluids, **7**, pp. 344–354.
[3] Goebel, S. G., Abuaf, N., Lovett, J. A., and Lee, C. P., 1993, ''Measurements of Combustor Velocity and Turbulence Profiles,'' ASME Paper No. 93-GT-228.
[4] Moss, R. W., 1992, ''The Effects of Turbulence Length Scale on Heat Transfer,'' University of Oxford, Department of Engineering Science, Report No. OUEL 1924, Ph.D. dissertation.
[5] Radomsky, Roger W., and Thole, Karen A., 2000, ''Flowfield Measurements for a Highly Turbulent Flow in a Stator Vane Passage,'' ASME J. Turbomach., **122**, pp. 255–262.
[6] Gaugler, R. E., and Russell, L. M., 1984, ''Comparison of Visualized Turbine Endwall Secondary Flows and Measured Heat Transfer Patterns,'' ASME J. Eng. Gas Turbines Power, **106**, pp. 168–172.
[7] Kang, Moon Kyoo Brian, and Thole, Karen A., 2000, ''Flowfield Measurements in the Endwall Region of a Stator Vane,'' ASME J. Turbomach., **122**, pp. 458–466.
[8] Graziani, R. A., Blair, M. F., Taylor, J. R., and Mayle, R. E., 1980, ''An Experimental Study of Endwall and Airfoil Surface Heat Transfer in a Large Scale Turbine Blade Cascade,'' ASME J. Eng. Power, **102**, pp. 257–267.
[9] Boyle, R. J., and Russell, L. M., 1990, ''Experimental Determination of Stator Endwall Heat Transfer,'' ASME J. Turbomach., **112**, pp. 547–558.
[10] Kang, M. B., Kohli, A., and Thole, K. A., 1999, ''Heat Transfer and Flowfield Measurements in the Leading Edge Region of a Stator Vane Endwall,'' ASME J. Turbomach., **121**, No. 3, pp. 558–568.
[11] Gregory-Smith, D. G., and Cleak, J. G. E., 1992, ''Secondary Flow Measurements in a Turbine Cascade With High Inlet Turbulence,'' ASME J. Turbomach., **110**, pp. 1–8.
[12] Spencer, M. C., Jones, T. V., and Lock, G. D., 1996, ''Endwall Heat Transfer Measurements in an Annular Cascade of Nozzle Guide Vanes at Engine Representative Reynolds and Mach Numbers,'' Int. J. Heat Fluid Flow, **17**, pp. 139–147.
[13] Giel, P. W., Thurman, D. R., Van Fossen, G. J., Hippensteele, S. A., and Boyle, R. J., 1998, ''Endwall Heat Transfer Measurements in a Transonic Turbine Cascade,'' ASME J. Turbomach., **120**, pp. 305–313.
[14] Khalatov, A. A., Shevtsov, S. V., and Syred, N., 1999, ''Heat Transfer Over Non-Porous and Porous Smooth End Wall of Linear Guide Vane in the Presence of Freestream Turbulence,'' ASME Paper No. 99-GT-329.
[15] Moore, J., Schaffer, D. M., and Moore, J. G., 1987, ''Reynolds Stresses and Dissipation Mechanisms Downstream of a Turbine Cascade,'' ASME J. Turbomach., **109**, pp. 258–267.
[16] Gregory-Smith, D. G., Graves, C. P., and Walsh, J. A., 1988, ''Growth of Secondary Losses and Vorticity in an Axial Turbine Cascade,'' ASME J. Turbomach., **114**, pp. 173–183.
[17] Devenport, W. J., and Simpson, R. L., 1990, ''Time-Dependent and Time-Averaged Turbulence Structure Near the Nose of a Wing-Body Junction,'' J. Fluid Mech., **210**, pp. 23–55.
[18] Praisner, T. J., Seal, C. V., Takmaz, L., and Smith, C. R., 1997, ''Spatial-Temporal Turbulent Flow-Field and Heat Transfer Behavior in End-Wall Junctions,'' Int. J. Heat Fluid Flow, **18**, pp. 142–151.
[19] Moffat, R. J., 1988, ''Describing the Uncertainties in Experimental Results,'' Exp. Therm. Fluid Sci., **1**, pp. 3–17.
[20] FLUENT/UNS User's Guide, 1998, Release 5.0, Fluent, Inc., Lebanon, NH.
[21] Thole, K. A., and Bogard, D. G., 1996, ''High Freestream Turbulence Effects on Turbulent Boundary Layers,'' ASME J. Fluids Eng., **118**, No. 2, pp. 276–284.
[22] Bendat, J. S., and Piersol, A. G., 1985, *Random Data Analysis and Measurement Procedures*, 2nd ed., Wiley, New York.
[23] Ames, F. E., and Moffat, R. J., 1990, ''Heat Transfer With High Intensity, Large Scale Turbulence: The Flat Plate Turbulent Boundary Layer and the Cylindrical Stagnation Point,'' Stanford University, Report HMT-44.
[24] Thole, K. A., and Bogard, D. G., 1995, ''Enhanced Heat Transfer and Skin Friction Due to High Free-Stream Turbulence,'' ASME J. Turbomach., **117**, pp. 418–424.

Influence of Surface Roughness on Heat Transfer and Effectiveness for a Fully Film Cooled Nozzle Guide Vane Measured by Wide Band Liquid Crystals and Direct Heat Flux Gages

S. M. Guo
C. C. Lai
T. V. Jones
M. L. G. Oldfield

Department of Engineering Science,
University of Oxford,
Oxford, England

G. D. Lock
Department of Mechanical Engineering,
University of Bath,
Bath, England

A. J. Rawlinson
Rolls-Royce plc,
Derby, England

The influence of surface roughness on heat transfer coefficient and cooling effectiveness for a fully film cooled three-dimensional nozzle guide vane (NGV) has been measured in a transonic annular cascade using wide band liquid crystal and direct heat flux gages (DHFGs). The liquid crystal methods were used for rough surface measurements and the DHFGs were used for the smooth surfaces. The measurements have been made at engine representative Mach and Reynolds numbers and inlet free-stream turbulence intensity. The aerodynamic and thermodynamic characteristics of the coolant flow have been modeled to represent engine conditions by using a heavy ''foreign gas'' (30.2 percent SF_6 and 69.8 percent Ar by weight). Two cooling geometries (cylindrical and fan-shaped holes) have been tested. The strategies of obtaining accurate heat transfer data using a variety of transient heat transfer measurement techniques under the extreme conditions of transonic flow and high heat transfer coefficient are presented. The surfaces of interest are coated with wide-band thermochromic liquid crystals, which cover the range of NGV surface temperature variation encountered in the test. The liquid crystal has a natural peak-to-peak roughness height of 25 μm creating a transitionally rough surface on the NGV. The time variation of color is processed to give distributions of both heat transfer coefficient and film cooling effectiveness over the NGV surface. The NGV was first instrumented with the DHFGs and smooth surface tests preformed. Subsequently the surface was coated with liquid crystals for the rough surface tests. The DHFGs were then employed as the means of calibrating the liquid crystal layer. The roughness of 25 μm, which is the typical order of roughness for the in-service turbine blades and vanes, increases the heat transfer coefficient by up to 50 percent over the smooth surface level. The film cooling effectiveness is influenced less by the roughness.
[S0889-504X(00)00804-7]

1 Introduction

The specific power output and level of efficiency of gas turbine engines improves with increased turbine entry temperatures. In the modern aeroengine, such temperatures can exceed the metallurgical limit of blade materials. To achieve acceptable durability, both temperature levels and temperature gradients can be controlled in the engine components exposed to the hot gas stream by using coolant that has been diverted, at a cost, from the engine compressor. An efficient cooling system uses a minimum amount of coolant, and the optimization of such a system is one of the primary goals of the engine designer.

There is a vast quantity of experimental and computational work on the topic of gas turbine film cooling, dating back to the 1940s [1–3]. The main quantities of interest in film cooling experiments are the convective heat transfer coefficient (h) based on local adiabatic wall temperature and the film effectiveness (η). The definition of cooling effectiveness used by the authors is:

$$\eta = \frac{T_{aw} - T_r}{T_{oc} - T_{om}} \tag{1}$$

where T_{aw} corresponds to the temperature of an isothermal wall that is adiabatic at the local point of interest and T_{om} (the total temperature of the mainstream) is used in the denominator instead of the more common recovery temperature, T_r [4]. The heat transfer coefficient is then defined by $h = q/(T_s - T_{aw})$.

The cooling effectiveness and heat transfer coefficients are primarily a function of the following: cooling geometry (the angles of inclination and orientation, the relative spacing of the coolant holes, the hole shape); the state of the oncoming boundary layer; the free-stream turbulence intensity; the surface curvature; and the ratios of the coolant-to-mainstream density, mass and momentum fluxes, specific heats, and the surface roughness. It is well known that the surfaces of the in-service vanes and blades are generally not hydraulically smooth. Thermal barrier coating surfaces may have a peak-to-peak roughness of about 55 μm, depending on the method of deposition. This is reduced to 17 μm when polished [5]. The corrosion of the vanes and blades and deposition of dust, sand, or other particulates in general adversely affects the profile loss of gas turbine vanes and rotor blades [6–8]. Taylor [9] mea-

Contributed by the International Gas Turbine Institute and presented at the 45th International Gas Turbine and Aeroengine Congress and Exhibition, Munich, Germany, May 8–11, 2000. Manuscript received by the International Gas Turbine Institute February 2000. Paper No. 2000-GT-204. Review Chair: D. Ballal.

sured a surface roughness of 10 μm on a number of first-stage turbine blades from TF-39 and F-100 aero-engines. Abuaf and Bunker [10] reported that a roughness of 2.33 μm could increase the heat transfer on the suction surface by 25 percent.

The nondimensional roughness Reynolds number is more important than the actual roughness height. There are several text books, e.g., [11], describing the nondimensional roughness Reynolds number:

$$\mathrm{Re}_k = \frac{\rho U_\tau d}{\mu} \tag{2}$$

where U_τ is shear velocity, which can be calculated using

$$U_\tau = \sqrt{\frac{\tau_0}{\rho}} = \sqrt{\frac{C_f U_\infty^2}{2}} \tag{3}$$

Three regimes can be identified from experimental data in terms of roughness Reynolds number, Re_k: for $\mathrm{Re}_k \leqslant 5$ the surface can be considered to be hydraulically smooth; for $5 \leqslant \mathrm{Re}_k \leqslant 70$ the surface is transitionally rough; and for $\mathrm{Re}_k \geqslant 70$ the surface is considered to be fully rough.

In basic terms, the three main influences of surface roughness are as follows: (*i*) the point of onset of laminar–turbulent transition advances upstream with increasing roughness; (*ii*) the turbulent boundary layer skin friction increases with increasing roughness; and (*iii*) the turbulent mean heat transfer increases with increasing roughness. Hence surface roughness can have a detrimental effect on the aerodynamics and thermal characteristics of turbine blades and vanes. The performance of film cooling is also affected by the surface roughness. Most studies concerning the influence of surface roughness on film cooling have been conducted using a flat-plate geometry [12,13] for one or two rows of film cooling holes simulating only the low-speed region of vanes or blades. To the authors' knowledge there are no published studies on rough surface NGVs in a film cooled engine representative environment.

This paper will demonstrate the strategies of applying a variety of techniques to measure accurately the influence of surface roughness on NGV heat transfer coefficient and film cooling effectiveness in a short-duration transonic annular cascade, which creates engine-representative conditions. Both perspex and aluminum NGVs have been used. The aluminum NGV was employed for the heat transfer coefficient measurements using combined DHFG and liquid crystal; the perspex model was mainly used for the measurement of adiabatic wall effectiveness.

The surface roughness was created by spraying the NGV with liquid crystals. Unpolished crystals have a maximum peak-to-peak roughness element size, measured using a *tally-surf* machine, of 25 μm [14]. This corresponds to about 17 μm at engine scale. Only the two extremes of roughness were employed in the experiments reported here: the surfaces sprayed with liquid crystals to create a roughened surface ($l = 25\ \mu$m); or the surfaces covered with Direct Heat Flux Gages [15] or the thin film gages [16] to create hydraulically smooth ($l < 1\ \mu$m) surfaces.

The roughness Reynolds number used here is based on the peak-to-peak roughness height of 25 μm, not the length dimension used by Nikuradse [17], and was calculated using Eqs. (2) and (3). The roughness Reynolds number over the NGV surface at the engine design condition is plotted in Fig. 1. The local shear velocity was predicted by a boundary layer code without film cooling. The only purpose in showing the figure here is to show the trend of the nondimensional roughness height variation along the NGV. Figure 1 clearly indicates that the most of the NGV is in the transitionally rough regime and that Re_k increases from the leading edge toward the trailing edge. The roughness Reynolds number with film cooling may differ from the non-film cooling case because the cooling jets will alter the boundary layer, but they are expected to be of similar order.

2 Experimental Apparatus

The measurements were conducted in the Oxford University Cold Heat Transfer Tunnel (CHTT) in which the mainstream is running at ambient temperature and the test section is preheated to an elevated temperature. The test section of the tunnel is an annular cascade of 36 engine-representative NGVs at 1.4 times larger than engine scale. The test duration is typically 3 to 5 seconds and a detailed description of this tunnel can be found in Martinez-Botas et al. [18]. The instrumented NGV and its four immediate neighbors are preheated *in situ* before the test begins inside a heat transfer cassette [16]. A unique shutter system in the cassette creates the boundary conditions for a ''step-change'' in gas temperature during the test. During operation, with flow through the cascade, the shutter opens in less than 100 ms.

The cooling configuration of the NGV under investigation consists of 14 rows with a total of 340 cooling holes. The holes are fed from two internal cavities, as illustrated in Fig. 2(*a*). These cavities are independently supplied with coolant so as to maintain the engine coolant-to-mainstream total pressure ratio. The forward cavity supplies 12 of the 14 rows, a total of almost 300 cooling holes, positioned around the leading edge, the early regions of the pressure surface and suction surface. The rear cavity feeds two rows, a total of approximately 40 cooling holes, nearest the trailing edge on the pressure surface. Two film cooling geometries have been tested. The first was with all holes cylindrically shaped. The second was with rows 1–4 and 11–14 fanned (Fig. 2(*a*, *b*)) having holes with a cylindrical entry and a fan-shaped exit [19].

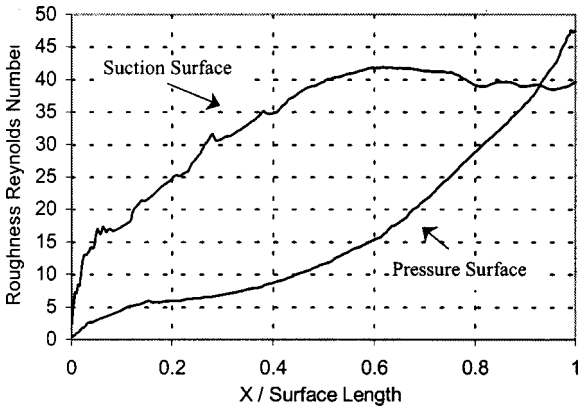

Fig. 1 Roughness Reynolds number along NGV midspan

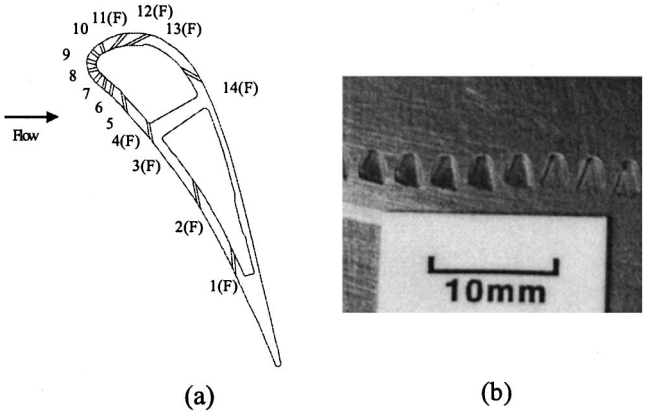

Fig. 2 (*a*) Midspan cross section of a CHTT NGV and film cooling geometry, illustrating row positions and two-cavity construction. Holes marked (F) are fan-shaped in the fan-shaped geometry. (*b*) Close-up view of the fan-shaped holes.

Table 1 Engine/tunnel comparison

Parameter	Engine	Tunnel
Inlet Total Pressure	32 bar	2 bar
Coolant/Main Stream Total Pressure Ratio	1.02	1.02
Coolant/ Main Stream Total Density Ratio	1.77	1.54
Coolant Temperature	1000K	333K
Turbine Inlet Temperature	1750-1800 K	290 K
•Exit Reynolds Number	2.02×10^6	2.02×10^6
Exit Mach Number	0.96	0.96
Mass Flow Rate	120 kg/s	38 kg/s

*Based on axial chord and downstream flow conditions

The experiments were designed to model the engine situation where the coolant is at a lower temperature, and hence more dense, than the mainstream flow. It has been demonstrated [20,21] that this density ratio can be simulated using a heavy, foreign gas. A mixture of SF_6 (30.2 percent by weight) and Ar (69.8 percent by weight) is used here, which has the same ratio of specific heats ($\gamma=1.4$) but is 1.77 times more dense than air. By matching the total pressure ratio of coolant to mainstream, the velocity ratio and density ratio can be made to correspond to engine conditions. Thus mass flux ratio and momentum flux ratio are also identical. The coolant flow passes through the NGV cooling holes with the shutters closed. Because the external heat transfer is the subject of the study, the coolant temperature was set equal to the initial temperature of the NGV to minimize internal heat transfer within the film cooling holes. The surface temperature is monitored to ensure uniformity prior to the opening of the shutter. Table 1 compares operating conditions between the CHTT and engine.

3 Transient Heat Transfer Measurement Techniques

Transient methods have been used to determine the heat transfer coefficient and effectiveness by measuring the transient response of surface temperature to a change in fluid temperature. Four different measurement techniques have been employed to obtain data of the best possible accuracy.

3.1 Smooth Surface Cooling Effectiveness and HTC Measurement Using TFG on Perspex. Thin film gages (TFGs), working on an effectively semi-infinite substrate [16], have been instrumented onto perspex NGVs. The TFGs are platinum temperature sensors with a physical thickness less than 0.1 μm. The details of the TFGs, the data analysis methods, and the cooling effectiveness and heat transfer coefficient data along midspan of the NGV have been presented in [16]. The heat transfer experiments presented in [16] were conducted with a hydraulically smooth surface. These data are compared with the data collected here on a rough surface, and using new experimental techniques.

3.2 Smooth Surface HTC Measurement Using DHFG on Aluminum. The newly developed Direct Heat Flux Gage (DHFG) [15] was employed to measure heat flux. The gage is shown in Fig. 3(*a*). A thin platinum film was sputtered on a flexible polyimide sheet (Upilex), which was attached by adhesive to the aluminum NGV. A thermocouple was mounted in the surface of the aluminum. The gages were 1 mm wide in the flow direction and 10 mm long in the spanwise direction and hence averaged over ~3 hole pitches, the same size as used in [16]. The thermocouple was located as near as possible to the metal NGV surface. The high thermal conductivity of aluminum provides temperature uniformity in the NGV. A total of eight DHFGs were instrumented onto the NGV surfaces along the midspan streamline. The DHFGs were on separate pieces of Upilex and infill pieces were also installed to create a surface completely covered with Upilex, thus giving an aerodynamically smooth surface. Holes were drilled through the Upilex to produce the film cooling geometries. Great care was taken to make certain the film cooling holes were clear after the drilling was complete.

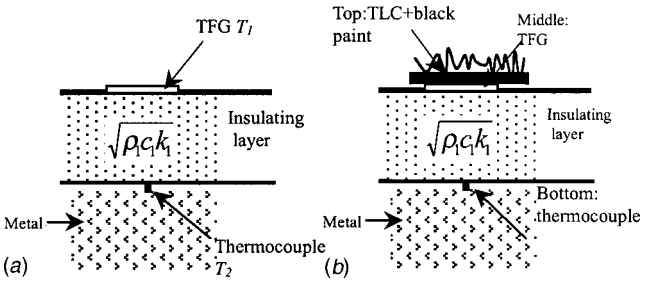

Fig. 3 (*a*) Schematic diagram of DHFG; (*b*) combined TLC and DHFG

The thermal properties and dimensions for this type of DHFG are presented by [15]. The advantages of the DHFG include high accuracy, high frequency response, and, most significantly, no requirement of the knowledge for the structure of the substrate, which is essential if the heat flux is to be deduced from the measured top surface temperature alone in a transient heat transfer test.

The thin film gage and the thermocouple of the DHFG give measurements of surface temperature on both sides of the Upilex plus glue layer. The combined Upilex plus glue layer is treated as one homogeneous layer because the thermal properties are similar [15]. The governing one-dimensional heat conduction equation

$$\frac{\partial^2 T}{\partial x^2}=\frac{1}{\alpha}\frac{\partial T}{\partial t} \tag{4}$$

may be solved for the heat flux at the surface. Here T is the temperature at a distance x from the surface at the time t; α is the diffusivity of the layer material defined in terms of the thermal conductivity, k, the density, ρ, and the specific heat, c, $\alpha=k/(\rho c)$.

The assumed initial condition was a uniform temperature throughout the NGV before the transient experiment began. The method described in [15] was used to obtain a solution (Eq. (5)) for the surface heat transfer rate under the assumption that the top surface temperature history was of the form $A_1 t^{0.5}$ and the bottom surface temperature history was of the form $A_2 t^{0.5}$:

$$q_s=\sqrt{\rho c k}\,\Gamma(1.5)\left[\begin{array}{l} A_1\left(1+2\left(\operatorname{erfc}\left(\frac{2l}{2\sqrt{\alpha t}}\right)+\operatorname{erfc}\left(\frac{4l}{2\sqrt{\alpha t}}\right)+\operatorname{erfc}\left(\frac{6l}{2\sqrt{\alpha t}}\right)+\ldots\right)\right) \\ -2A_2\left(\operatorname{erfc}\left(\frac{l}{2\sqrt{\alpha t}}\right)+\operatorname{erfc}\left(\frac{3l}{2\sqrt{\alpha t}}\right)+\operatorname{erfc}\left(\frac{5l}{2\sqrt{\alpha t}}\right)+\ldots\right)\end{array}\right] \tag{5}$$

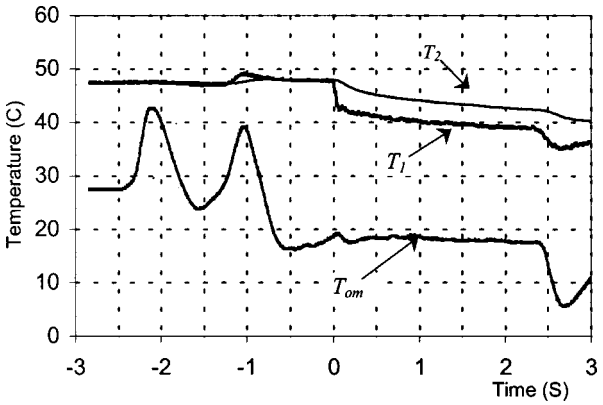

Fig. 4 Temperature history of DHFG and mainstream

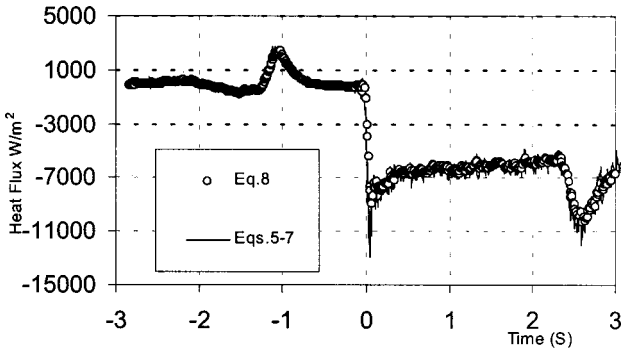

Fig. 5 Heat flux calculated using accurate (Eqs. (5)–(7)) and approximate (Eq. (8)) methods

where A_1 and A_2 are constants and erfc and Γ are the complementary error and gamma function, respectively.

Any other type of top and bottom surface temperature histories may be written as the summation of a series of parabolic functions:

$$T=\sum_n H(t-t_n)b_n(t-t_n)^{0.5} \tag{6}$$

In Eq. (6), b_n is the slope of the nth parabolic function and H is the Heaviside step function. H equals 1 for $t>t_n$ and equals 0 for $t<t_n$.

Each b_n in Eq. (6) gives q_{ns}. The surface heat transfer rate will be the sum of a series of q_{ns} calculated using Eq. (5) but with a time shift. The surface heat flux is obtained by summation:

$$q_s=\sum H(t-t_n)q_{ns} \tag{7}$$

Oldfield and Jones [22] present a more advanced method named Impulse Response Heat Transfer Signal Processing. The Oldfield and Jones [22] method gives the same results as Eq. (7). Their impulse response technique has the advantage that impulse response based filters have only to be designed once (a slower process) but once designed can be used repeatedly. This method can efficiently and quickly process the digitized temperature signals from the DHFG, and has advantages over using Eq. (7). This technique was used for later data analysis.

A typical temperature history measurement from a DHFG is shown in Fig. 4 together with the total temperature of the mainstream. The tunnel begins operation at -2.5 s, the coolant is introduced at -1.2 s, the shutters open at 0 s, and the test ends at 2.3 s. The temperature on the NGV surface (T_2), up to the point where the shutters are opened, is seen to remain constant at its initial value near 47°C and is not influenced significantly by the heated coolant or cold mainstream air passing through the 32 passages outside the cassette. The total temperature of the mainstream (T_{om}) has two initial peaks associated with compression heating of the gas upstream of the test section. The shutters are opened once this mainstream temperature has stabilized, and over the 2.3 second course of the experiment this total temperature decreases by less than 1°C. The DHFG top surface temperature (T_1) is observed to experience a rapid drop once the shutters have opened and then to fall more gradually. The DHFG bottom surface temperature (T_2) shows a much smoother trend. It is observed that the difference between the two temperatures is almost constant after less than 0.5 seconds after the shutters have opened. These temperature traces are typical of a layered substrate with a low thermal product (ρck) material (Upilex plus glue) at the top and a high thermal product material (aluminum) underneath. Because of the high thermal product of the metal, the aluminum surface temperature changes slowly. This generates a high heat flux through the DHFG and makes the signal easily measurable. The surface heat flux was calculated using Eq. (5)–(7) or using the impulse response technique [22]. These calculations give the heat flux value immediately from the start of the flow over the NGVs. A much simpler method,

$$q=k\frac{(T_2-T_1)}{l} \tag{8}$$

where l is the DHFG thickness, can be employed to give a good approximate DC signal after less than 0.5 s from the shutter opening. The heat fluxes calculated using both methods are shown in Fig. 5. The approximation provides good agreement after the heat has penetrated through the Upilex/glue layer, whose physical thickness is 100 μm.

3.3 Rough Surface Cooling Effectiveness Measurement Using TLC on Perspex. The application of thermochromic liquid crystals (TLC) to heat transfer experiments is described in detail by Ireland et al. [23]. TLC can be bought commercially in micro-encapsulated form and in the work reported here are spray-painted onto the NGV, which has previously been spray-painted black to create a contrasting background for the TLC color changes. The crystals display color from blue to green to red as the surface temperature cools from a temperature above the high threshold level (or in reverse if the surface is heated from below the lower threshold temperature.) Above this upper threshold and below the lower threshold level, the TLC is clear. The thermal response of TLC has been measured to be of the order of 3 ms [24]. The TLC method has a great advantage over thin film gages as it provides such temperature histories on the entire wetted surface visible to the camera. TLC is sprayed onto a perspex NGV and the semi-infinite thermal boundary condition is assumed for analysis purposes.

The classical solution of the one-dimensional conduction equation (Eq. (4)) is as follows [25]:

$$\beta=\frac{h\sqrt{t}}{\sqrt{\rho ck}},\quad \frac{T_s-T_i}{T_{aw}-T_i}=1-e^{\beta^2}\,\mathrm{erfc}(\beta) \tag{9}$$

To observe the TLC color changes during the experiment, three miniature CCD cameras were placed inside the tunnel. Two were located upstream to view the NGV pressure surface and leading edge, and a third was located downstream and observed the suction surface via a mirror mounted on a sting designed to minimize aerodynamic disturbances. The head diameter of the cameras was 17.4 mm and each body was 60 mm long. The upstream cameras were positioned to avoid shedding a wake into the passage under study. The lighting for the enclosure comes from inside the cascade employing a series of 50 W miniature Halogen lamps.

A PC based frame-grabber card system was used and was capable of recording images at 25 frames per second for 5 seconds.

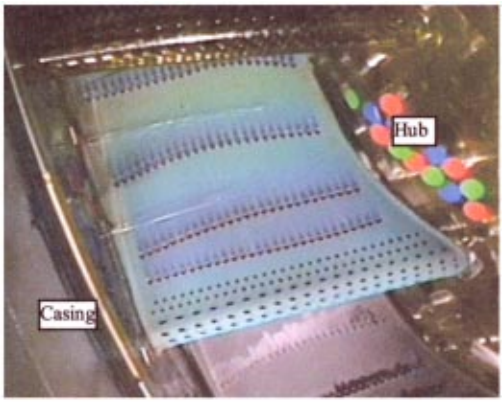

Fig. 6 Pressure surface TLC image

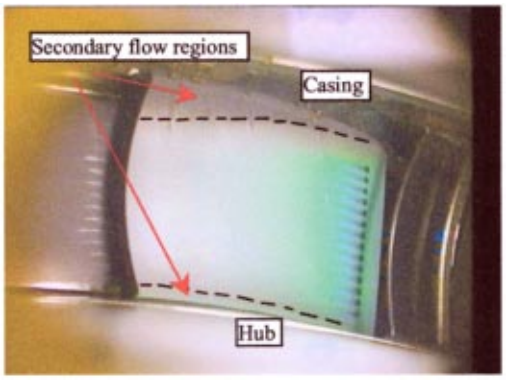

Fig. 8 Suction surface TLC image

The color histories at any pixel location within view can then be extracted. The data were archived onto CD-ROMs.

Typical images of the NGV pressure surface, leading edge, and suction surface, recorded with this system during an experiment, are shown in Figs. 6–8. These are single-frame images taken during the transient experiment recorded at 25 frames per second. The outer casing and inner hub have been identified in these figures. Figure 6 shows the pressure surface although the trailing edge of the NGV is not visible in this view. The cooling footprints downstream of many of the film cooling holes are clearly visible. Close inspection of an enhanced image identifies areas where the cooling jets have separated from the surface and reattached further downstream. The view from the camera monitoring the leading edge (Fig. 7) gives more detail in the shower-head region. Close-up lenses are available to gain more detail when required. The TLC color patterns on the suction surface are shown in Fig. 8 from the downstream camera. The coolant trajectories are clearly visible and can be seen to be swept both downstream and towards the hub due to the radial pressure gradient in the annular cascade. Also visible in Fig. 8 are regions of low effectiveness (shown as a darker shade, the edges of which are marked by dashed lines) near the casing and hub endwalls. These are regions that are influenced by the secondary flows (distinct from the coolant flow) within the turbine passage which originate from the inlet boundary layer [26] and have been identified in the CHTT using oil and dye flow visualization [27]. The radial pressure gradient also influences the secondary flow and the extent of the region is greater at the casing than at the hub.

The thermal response of the color signals from wide-band crystals are sensitive to both the lighting and camera viewing angles, which vary over the NGV surfaces. An accurate calibration was only possible if it was conducted *in situ* and under identical lighting conditions to those which would occur during the experiment. Such a calibration was performed by heating the NGV within the heat transfer cassette enclosure to a uniform temperature, monitored by thermocouples around the surface. The shutters were then opened and the NGV surface cooled slowly. Images were recorded and the liquid crystal color matched carefully to these temperatures. As the TLC response is sensitive to viewing angle, each pixel (or area of pixels) requires its own individual calibration for the camera used. A calibration is performed before each experiment to eliminate any degradation of color response as the crystals age. A typical calibration of T_s versus hue is shown in Fig. 9.

Difficulties were experienced in acquiring a complete temperature trace from the wide-band TLC under the high heat transfer coefficients ($\sim$1000 W/m^{2}k) during the transient test for a number of reasons. The most significant is that the available image acquisition system is limited to a sample rate of 25 frames per second. With a sample rate of 25 Hz, it is impossible to capture a clear liquid crystal image during the starting process when a large step change of heat transfer is encountered. The images captured in that short period (typically 0.5s) were unclear due to the rapid color changes caused by the rapid change of temperature.

Without the complete surface temperature history, the traditional method of calculating heat flux and plotting heat flux versus surface temperature to obtain the adiabatic temperature and the heat transfer coefficient [28] cannot be used. The data were analyzed by fitting an analytical solution through the incomplete surface history. In this case the analytic solution of a step change in gas temperature was used [25]. The semi-infinite assumption is valid because the test time (in the order of 3–5 seconds) is short compared with the time taken for the transient thermal response to penetrate through the thickness of the perspex model. Under a

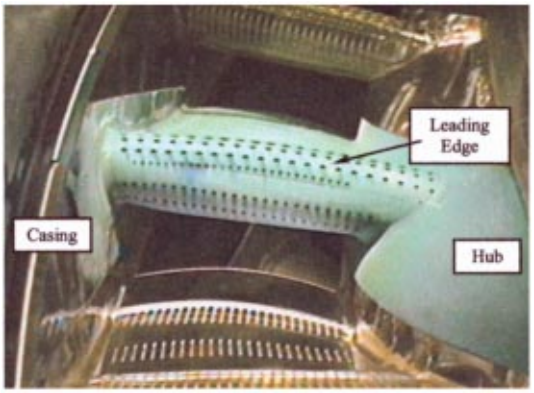

Fig. 7 Leading edge TLC image

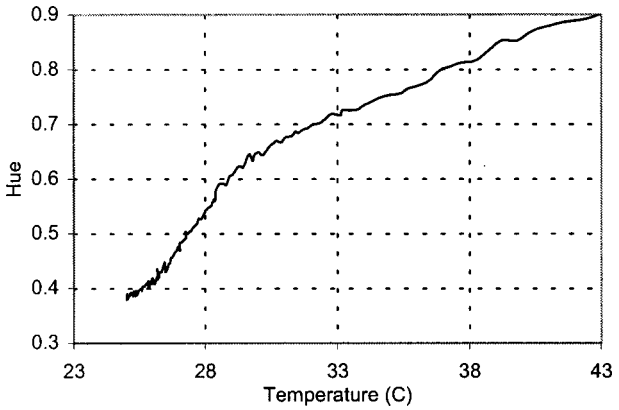

Fig. 9 Calibration of wide band TLC

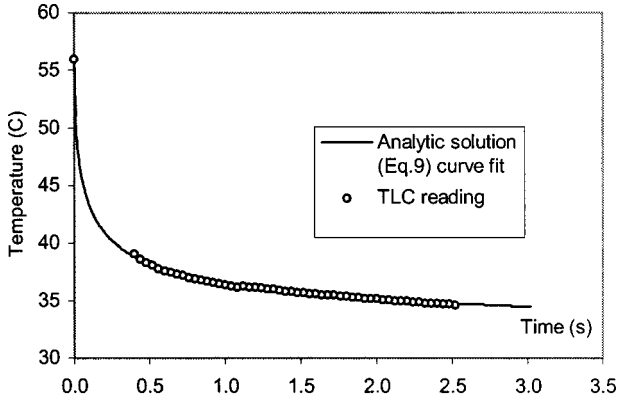

Fig. 10 Temperature history from TLC and curve fit

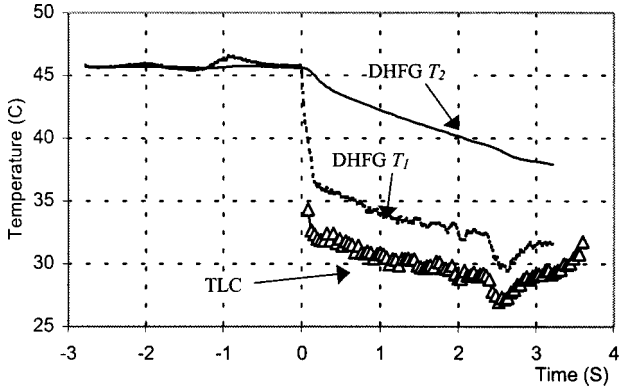

Fig. 12 Temperatures of TLC and DHFG during a test

step change of gas temperature, Eq. (9) describes the surface temperature response. The wide-band TLC yields the temperature history and a regression analysis method is used to fit a curve of the form of Eq. (9) to the measured data. The heat transfer coefficient and adiabatic wall temperature and hence the film cooling effectiveness are then obtained. A typical temperature history obtained using the TLC on a perspex NGV is shown in Fig. 10. The initial temperature is accurately known but the first short segment of the data is missing for the reason explained before. The curve fit appropriate to a step-change response matched the data well.

The accuracy of the results was dominated by the quality of the step change during the test. This has been assessed using the DHFGs described in section 3.2. The heat transfer coefficients measured by the DHFGs for the worst area of step change is shown in Fig. 11. With film cooling of the surface, most of the NGV needed less than 0.1 seconds to reach a step change in heat transfer, as demonstrated by the level portion of the heat transfer coefficient curve. But a small region on the pressure surface experienced a significant peak in heat transfer during the starting processes; see Fig. 11. This peak is believed to be caused by an unsteady interaction process between coolant and mainstream flow. The authors have realized that the uncertainty can be large in certain regions of the NGV where the poor quality step change was present. A set of numerical data was generated to simulate an imperfect step change. These data featured an initial square peak of 150 percent in HTC lasting for 0.2 s in a 5 s test. This overestimates the error because the initial peak in the actual test was not a square step. The authors found the heat transfer coefficients were five times more sensitive to this initial peak than the effectiveness. The authors thus only attempted to obtain the adiabatic wall temperature using the curve-fitting method, which is mainly determined by the later portion of the surface temperature trace and hence not sensitive to the initial portion of data. The heat transfer coefficients were instead obtained using the newly developed combined liquid crystal and DHFG method.

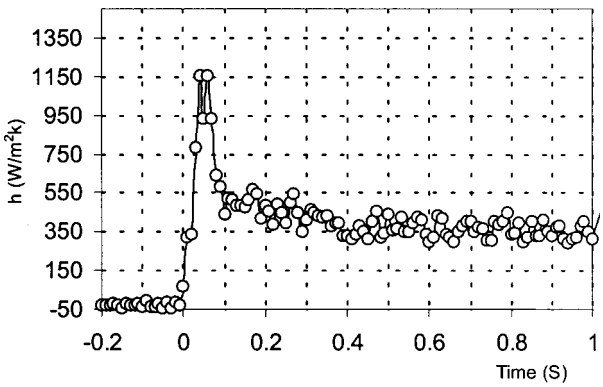

Fig. 11 Heat transfer coefficient from a DHFG

3.4 Rough Surface HTC Measurement Using Combined TLC and DHFG on Aluminum. The measurements of heat transfer coefficient were obtained using an aluminum NGV with the combined use of liquid crystal and DHFGs. The DHFGs were instrumented onto the aluminum NGV prior to spraying the black paint and the liquid crystal layer (Fig. 3(*b*)). The DHFGs were used as temperature sensors to calibrate the liquid crystal in situ for the characterized curve of color versus temperature in a low heat transfer (natural convection) procedure. The heat fluxes were calculated using the approximate method of Eq. (8) taking the temperature difference between liquid crystal and the thermocouple from the latter portion of data where this difference is about constant. Heat transfer coefficients were subsequently calculated from the heat flux, the measured cooling effectiveness, and the surface liquid crystal temperature.

To calculate the heat flux for all surfaces coated with liquid crystal, the only remaining parameter needed is the ratio of thermal conductivity over thickness for the combined liquid crystal and DHFG layer. This was determined by equating the heat flux measured by the DHFGs and the value of heat flux obtained from the temperature difference between the thermocouples and the liquid crystal. There is a total of eight DHFGs on the surfaces of the NGV and they each yields very similar ratio of l/k for the liquid crystal layer. The average equivalent thickness for the black paint plus liquid crystal layer was found to be 35 μm by assuming the thermal conductivity of the combined black paint and liquid crystal layer to be 0.155 W/mK.

A typical temperature history obtained using the TLC on top of a DHFG is shown in Fig. 12 together with the temperatures measured by the DHFG on the aluminum NGV. These temperature traces are essentially parallel to each other, as expected, and the temperature difference between the surface (measured by liquid crystal) and the aluminum substrate (measured by the thermocouples) is easily obtained. The heat flux is then calculated using Eq. (8).

4 Experimental Results and Discussion

The film cooling effectiveness for cylindrical and fan-shaped cooling configurations is plotted against the fraction of surface distance along the midspan streamline in Figs. 13 and 14 for both smooth and rough surfaces. The smooth surface data are taken from [16] and have been double-checked using DHFGs. The DHFGs confirmed the data reported by [16], with the exception of two measurement points on the pressure surface for the cylindrical cooling geometry. It is thought these two thin film gages were damaged during testing and that the true calibration factor differed to the calibration factor measured prior the test. The rough cooling

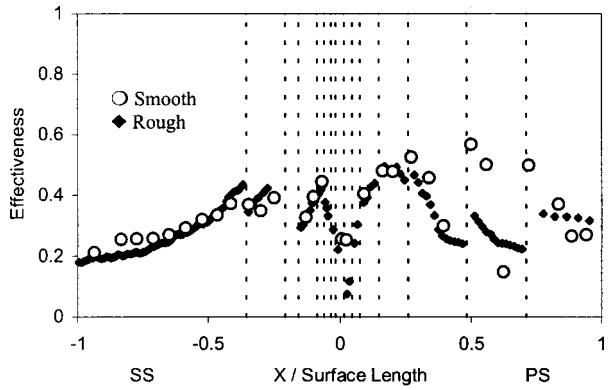

Fig. 13 Influence of roughness on midspan film cooling effectiveness: cylindrical cooling holes

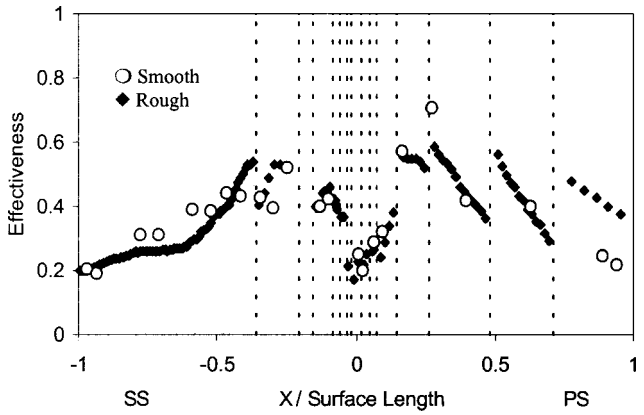

Fig. 14 Influence of roughness on midspan film cooling effectiveness: fan-shaped cooling holes

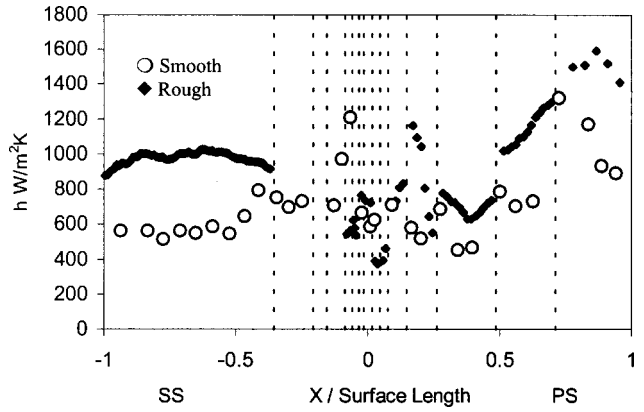

Fig. 15 Influence of roughness on midspan heat transfer coefficient: cylindrical cooling holes

effectiveness data were measured using liquid crystal on a perspex NGV. The liquid crystal measurements have been averaged over areas that cover the width between adjacent film cooling holes and thus give a spanwise average effectiveness in order to compare with the smooth surface data taken by TFGs. The vertical lines in these figures (and in the figures following) indicate the positions of the film cooling holes. The effectiveness is seen to reach local peaks immediately downstream of many of the film cooling rows.

Generally, the roughness does not greatly influence the measured film cooling effectiveness. The exception is the rear of the pressure surface where the roughened effectiveness levels are not

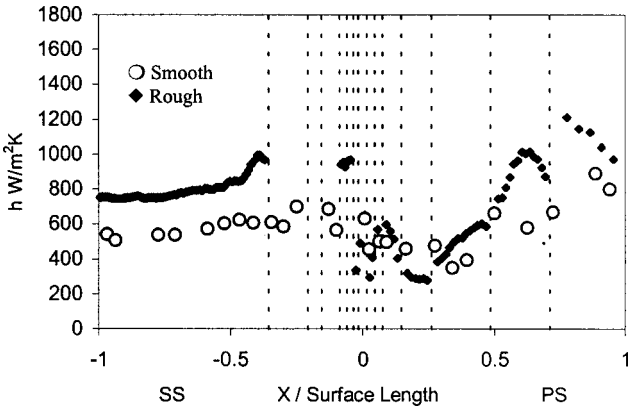

Fig. 16 Influence of roughness on midspan heat transfer coefficient: fan-shaped cooling holes

observed to reach the peaks exhibited by the data from the smooth surface. The smooth surface features high values of effectiveness immediately downstream of the cooling hole exits, but the effectiveness subsequently decreases steeply further downstream. This indicates that the surface roughness helps to distribute the cooling flow retained in the boundary layer as it emerges from the cooling holes. The low ejection angle and the curvature of the pressure surface prevent the coolant from ''blowing off'' into the mainstream. The better distributed coolant at the exit region of the hole remains in a near-wall layer and travels downstream to generate the more level pattern of cooling effectiveness. Downstream of the last film cooling row on the suction surface, the effectiveness is seen to decrease toward the trailing edge.

The effect of surface roughness on heat transfer coefficients around the midspan is shown in Figs. 15 and 16 for the cylindrical and fan-shaped cooling geometries. The ejection of coolant into the turbulent boundary layer generally increases the heat transfer coefficient relative to the case with no film cooling [16]. Some significant local increases in HTC in regions downstream of the cooling rows are observed as would be expected. On the early pressure surface, because the velocity is small, the peak-to-peak roughness height of 25 μm is still in the hydraulically smooth region and the roughness is not expected to influence the heat transfer. At the rear of the pressure surface and on the suction surface, the high shear velocity pushes the 25 μm peak-to-peak roughness into the transitionally rough regime (see Fig. 1). The heat transfer level in these regions is significantly higher for the roughened surface. The increase in heat transfer due to roughness is more pronounced in the cylindrical hole geometry. This is because the fanned hole acts as a diffuser and lowers the near wall velocity, thus lowering the shear velocity. Although the peak-to-peak roughness height is the same for both cylindrical and fan-shaped cooling hole NGVs, the nondimensional roughness height based on the shear velocity is greater for the cylindrical holes. Consequently there is greater increase in heat transfer coefficient for the cylindrical geometry compared with the smooth surface value.

These data have been collected in an environment that closely models the engine, and benefits both the CFD code validation and the engine designer.

5 Conclusions

Strategies have been developed to obtain accurate heat transfer data to turbine nozzle guide vanes with roughened surfaces, using a variety of transient measurement techniques. These techniques include thin film gages on flexible plastic substrates, direct heat flux gages and wide-band thermochromic liquid crystals. The techniques have been combined to obtain data of the best accuracy.

The cooling effectiveness is best achieved using wide-band thermochromic liquid crystals applied to models made of low thermal product material (such as perspex), under a step-change in fluid temperature. The use of liquid crystal has the advantage that information is available everywhere in view of the camera. The liquid crystal was combined with direct heat flux gages to obtain the most accurate measurements of heat transfer coefficient. The calibration and method of analysis for the liquid crystals and gages have been described.

These techniques have been used to measure heat transfer coefficient and film cooling effectiveness in a transient blowdown tunnel under extreme conditions of transonic flow and high heat transfer coefficient ($400 < h < 1600\ \mathrm{W/m^2\,K}$). The test blade models form an annular cascade of fully film cooled nozzle guide vanes from an in-service aeroengine. Both cylindrical and fan-shaped film-cooling geometries have been tested. Engine environment is simulated using representative levels of Mach and Reynolds numbers, and a heavy foreign gas as coolant. The liquid crystals feature a peak-to-peak surface roughness of 25 μm, which is typical of in-service turbines. Measurements have been conducted for both rough and hydraulically smooth surfaces.

The roughness is shown to increase the heat transfer coefficient significantly, particularly in regions near the rear of the pressure and suction surfaces where the nondimensional roughness Reynolds number reaches value as high as 40. The film cooling effectiveness is influenced less by the surface roughness. The differences in heat transfer to the rough and smooth surfaces point to a requirement to conduct further research, including the effect of roughness shape, height, and pattern.

Acknowledgments

This work was funded by Rolls Royce plc, the Defense Research Agency, MoD and DTI. The authors are grateful for the assistance of Trevor Godfrey.

Nomenclature

A = constant
c = specific heat at constant pressure
c_f = local friction coefficient
d = roughness height
h = heat transfer coefficient
k = thermal conductivity
l = thickness of DHFG
Re_k = roughness Reynolds number
t = time
T = temperature
U_τ = shear velocity
U_∞ = mainstream velocity
x = perpendicular distance into the substrate
X = surface distance from leading edge
α = thermal diffusivity
β = dimensionless time
γ = ratio of specific heats
η = film cooling effectiveness
μ = viscosity
ρ = density

Subscripts

aw = adiabatic wall
c = coolant
I = initial
m = mainstream
o = total
r = recovery
s = surface
2 = bottom surface
1 = top surface

Abbreviations

CHTT = cold heat transfer tunnel
DHFG = direct heat flux gage
HTC = heat transfer coefficient
NGV = nozzle guide vane
TFG = thin film gage
TLC = thermochromic liquid crystal

References

[1] Kercher, D. M., 1996, ''Film Cooling Bibliography 1946–1996,'' GE Aircraft publication.
[2] Goldstein, R. J., Eckert, E. R. G., Chiang, H. D., and Elovic, E., 1985, ''Effect of Surface-Roughness on Film Cooling Performance,'' ASME J. Eng. Gas Turbines Power, **107**, pp. 111–116.
[3] Hartnett, J. P., 1985, ''Mass Transfer Cooling,'' *Handbook of Heat Transfer Applications*, Chap. 1, McGraw-Hill, New York.
[4] Jones, T. V., 1991, ''Definition of Heat Transfer Coefficients in the Turbine Situation,'' in: *Turbomachinery: Latest Developments in a Changing Scene*, IMechE 1991-3, C423/046, pp. 201–206.
[5] Watt, R. M., Jones, T. V., Allen, J. L., Baines, N. C., and George, M., 1989, ''A Further Study of the Effects of Thermal-Barrier-Coating Surface Roughness on Gas Turbine Boundary Layers,'' presented at ASME Cogen Turbo, Nice.
[6] Schlichting, H., 1979, *Boundary Layer Theory*, McGraw-Hill, New York.
[7] Tabakoff, W., 1984, ''Review: Turbomachinery Performance Deterioration Exposed to Solid Particulates Environment,'' ASME J. Fluids Eng., **106**, pp. 125–134.
[8] Turner, A. B., Tarada, F. H. A., and Bailey, F. J., 1985, ''Effects of Surface Roughness on Heat Transfer to Gas Turbine Blades,'' AGARD CP-390.
[9] Taylor, R. P., 1990, ''Surface Roughness Measurements on Gas Turbine Blades,'' ASME J. Turbomach., **112**, pp. 175–180.
[10] Abuaf, N., and Bunker, R. S., 1998, ''Effects of Surface Roughness on Heat Transfer and Aerodynamic Performance of Turbine Airfoils,'' ASME J. Turbomach., **120**, pp. 552–529.
[11] Kays, W. M., and Crawford, M. E., 1993, *Convective Heat and Mass Transfer*, McGraw-Hill, New York.
[12] Goldstein, R. J., 1971, ''Film Cooling,'' Adv. Heat Transfer, **7**, pp. 321–370.
[13] Barlow, D. N., and Kim, Y. W., 1995, ''Effect of Surface Roughness on Local Heat Transfer and Film Cooling Effectiveness,'' ASME Paper No. 95-GT-14.
[14] Guo, S. M., Jones, T. V., Lock, G. D., and Dancer, S. N., 1998, ''Computational Prediction of Heat Transfer for Gas Turbine Nozzle Guide Vanes,'' ASME J. Turbomach., **120**, pp. 343–350.
[15] Piccini, E., Guo, S. M., and Jones, T. V., 2000, ''The Development of a New Heat Transfer Gauge for Heat Transfer Facilities,'' Meas. Sci. Technol., **11**, pp. 342–349.
[16] Guo, S. M., Lai, C. C., Jones, T. V., Oldfield, M. L. G., Lock, G. D., and Rawlinson, A. J., 1998, ''Heat Transfer and Effectiveness Measurements for a Fully Film Cooled Nozzle Guide Vane at Engine Simulated Conditions,'' Int. J. Heat Fluid Flow, **19**, No. 6, pp. 594–600.
[17] Nikuradse, J., 1933, Forsch. Arb. Ing.-Wes., No. 361.
[18] Martinez-Botas, R. F., Main, A. J., Lock, G. D., and Jones, T. V., 1993, ''Cold Heat Transfer Tunnel for Gas Turbine Research on an Annular Cascade,'' ASME Paper No. 93-GT-248.
[19] Rowbury, D. A., Oldfield, M. L. G., Lock, G. D., and Dancer, S. N., 1998, ''Scaling of Film Cooling Discharge Coefficient Measurements to Engine Conditions,'' ASME Paper No. 98-GT-79.
[20] Teekaram, H. J. A., Forth, C. J. P., and Jones, T. V., 1989, ''The Use of Foreign Gas to Simulate the Effects of Density in Film Cooling,'' ASME J. Turbomach., **111**, pp. 57–62.
[21] Jones, T. V., 1999, ''Theory for the Use of Foreign Gas in Simulating Film Cooling,'' Int. J. Heat Fluid Flow, **20**, pp. 349–354.
[22] Oldfield, M. L. G., 2000, ''Matlab Processing for Thin Film Heat Transfer Transducers,'' private communication.
[23] Ireland, P. T., Wang, Z. W., and Jones, T., V., 1993, ''Liquid Crystal Heat Transfer Measurements,'' von Karman Institute for Fluid Dynamics 1992–1993 Lecture Series.
[24] Ireland, P. T., and Jones, T. V., 1987, ''The Response Time of a Surface Thermometer Employing Encapsulated Thermochromic Liquid Crystals,'' J. Phys. E, **20**, pp. 1195–1199.
[25] Schultz, D. L., and Jones, T. V., 1973, ''Heat Transfer Measurements in Short-Duration Hypersonic Facilities,'' AGARD AG-165.
[26] Sieverding, C. H., 1985, ''Recent Progress in the Understanding of Basic Aspects of Secondary Flows in Turbine Blade Passages,'' ASME J. Eng. Gas Turbines Power, **107**, pp. 248–257.
[27] Martinez-Botas, R. F., Lock, G. D., and Jones, T. V., 1995, ''Heat Transfer Measurements in an Annular Cascade of Transonic Gas Turbine Blades Using the Transient Liquid Crystal Technique,'' ASME J. Turbomach., **117**, pp. 425–431.
[28] Oldfield, M. L. G., Jones, T. V., and Schultz, D. L., 1978, ''On-Line Computer for Transient Turbine Cascade Instrumentation,'' IEEE Trans. Aerosp. Electron. Syst., **AES-14**, p. 5.

Heat Transfer and Pressure Distributions on a Gas Turbine Blade Tip

Gm. S. Azad

Je-Chin Han

Shuye Teng

Turbine Heat Transfer Laboratory,
Department of Mechanical Engineering,
Texas A&M University,
College Station, TX 77843-3123

Robert J. Boyle
NASA Glenn Research Center,
Cleveland, OH 44135

Heat transfer coefficient and static pressure distributions are experimentally investigated on a gas turbine blade tip in a five-bladed stationary linear cascade. The blade is a two-dimensional model of a first-stage gas turbine rotor blade with a blade tip profile of a GE-E^3 aircraft gas turbine engine rotor blade. The flow condition in the test cascade corresponds to an overall pressure ratio of 1.32 and exit Reynolds number based on axial chord of 1.1×10^6. The middle 3-blade has a variable tip gap clearance. All measurements are made at three different tip gap clearances of about 1, 1.5, and 2.5 percent of the blade span. Heat transfer measurements are also made at two different turbulence intensity levels of 6.1 and 9.7 percent at the cascade inlet. Static pressure measurements are made in the midspan and the near-tip regions as well as on the shroud surface, opposite the blade tip surface. Detailed heat transfer coefficient distributions on the plane tip surface are measured using a transient liquid crystal technique. Results show various regions of high and low heat transfer coefficient on the tip surface. Tip clearance has a significant influence on local tip heat transfer coefficient distribution. Heat transfer coefficient also increases about 15–20 percent along the leakage flow path at higher turbulence intensity level of 9.7 over 6.1 percent. [S0889-504X(00)00404-9]

Introduction

A recent trend in modern gas turbine engines is to increase the combustor outlet temperature to achieve higher thermal efficiency and higher power output. This increase in temperature is detrimental to the downstream first-stage turbine blades. Therefore, a proper combination of aerodynamics, heat transfer, and material capabilities is required to design a high-efficiency gas turbine engine. Many research efforts have been dedicated to developing efficient aerodynamics and cooling techniques for turbine airfoils. However, some critical regions still remain that require more frequent inspection and repair due to frequent breakdowns. Blade tip and near-tip regions fall into this category. Blade tip and near-tip regions are typically difficult to cool, and are subjected to potential damage due to high thermal loads. Blade tips at high temperatures may also wear out due to hard rubs against the shroud. Unshrouded blades have a gap between the blade tip and the shroud surface, which is known as tip gap. Blade tip failure is primarily caused by hot leakage flow through the tip gap. The leakage flow accelerates due to a pressure difference between both the pressure and suction sides of the blade, causing thin boundary layers and high heat transfer rates. This tip leakage flow is undesirable because it chips away the pressure side tip corner from midchord to trailing edge. As the blade tip is chipped away, the tip gap width increases, allowing more leakage flow through the tip gap and accelerating blade tip failure. It has been recognized that the blade tip geometry and subsequent tip leakage flows have a significant effect on the aerodynamic efficiency of turbines. The influence of blade tip clearance on turbine efficiency is so significant that designers have a strong desire to improve efficiency by decreasing tip-to-shroud operating clearances, or by implementing more effective tip leakage sealing mechanisms. Whatever the design choice selected for a particular turbine blade tip, accurate and detailed knowledge of the flow field and heat transfer on the tip and the near-tip region is important for an efficient balanced airfoil design. Reliable experimental data are also important to develop and validate computational codes to predict blade metal temperatures, and an efficient cooling system design.

The existing literature contains many experimental and numerical investigations on flow field in and around turbine blade tip models. Studies by Bindon and Morphus [1] and Bindon [2] have contributed to the general understanding of tip leakage flow patterns. Bindon concluded that the growth of a vortex, which forms as the flow separates on the pressure side wall and exits through the tip gap causing an increase in the secondary flow, results in large aerodynamic losses. Moore et al. [3] also contributed to the understanding of the flow field through tip gaps. Yaras and Sjolander [4] studied the effect of simulated rotation on tip leakage and found a significant reduction in the gap mass flow rate due to rotation. Sjolander and Cao [5] studied the flow field in an idealized turbine tip gap. They concluded that the flow separates from the pressure side tip corner and forms a well-organized chordwise vortex above the blade tip. The separation vortex induces a flow back toward the pressure corner, resulting in the formation of a secondary counterrotating vortex. Thus, the unexpected region of attached flow near the pressure corner may have a reasonably high convective heat transfer coefficient, in addition to the high wall shear stress. Kaiser and Bindon [6] investigated a quantitative analysis of the effects of tip clearance, tip geometry, and multiple stages on turbine stage efficiency in a rotating turbine rig environment. Many other works studied the effect of tip clearances on leakage and efficiency loss prediction.

Turbine blade tip heat transfer is an important aspect that has drawn considerable attention from researchers in the past several years. The earliest study on blade tip heat transfer was done by Mayle and Metzger [7]. They studied heat transfer in a simulated two-dimensional rectangular tip with and without a rotating shroud. They concluded that the effect of blade rotation could be neglected to assess blade tip heat transfer. The pressure-driven flow through the tip gap (tip leakage) mainly influences the heat transfer. Metzger et al. [8] and Chyu et al. [9] studied heat transfer for both flat and grooved rectangular tip models. They incorporated the effect of relative motion by introducing a moving shroud surface over the grooved tip model. They affirmed that relative motion had little effect on the average tip heat transfer, though some local effects were observed.

Contributed by the International Gas Turbine Institute and presented at the 45th International Gas Turbine and Aeroengine Congress and Exhibition, Munich, Germany, May 8–11, 2000. Manuscript received by the International Gas Turbine Institute February 2000. Paper No. 2000-GT-194. Review Chair: D. Ballal.

Experimental data on blade tip heat transfer in a cascade environment are limited in the open literature. Yang and Diller [10] reported local heat transfer coefficient on a turbine blade tip model with a recessed cavity in a stationary linear cascade. Based on a single heat flux sensor, they found the convection coefficients insensitive of tip gap height. Metzger et al. [11] used several heat flux sensors and measured local tip heat fluxes on the flat tips at two different tip gaps in a rotating turbine rig. Their study was primarily confined to the blade forward region. The most recent study on turbine blade tip heat transfer and flow in a linear cascade was carried out by Bunker et al. [12]. Their experimental study investigated the detailed distribution of convective heat transfer coefficients on the first-stage blade tip surface for a geometry typical of a large power generation turbine. This study provided a nearly full surface information on heat transfer coefficients in a nonrotating cascade environment with appropriate pressure distribution on the blade tip and shroud model. They used a three-blade cascade; however, only the center blade (test blade) had a variable tip gap clearance. The test airfoil was modeled after the aerodynamic tip section of a large power generation turbine. They used a hue detection-based liquid crystal technique to obtain detailed heat transfer coefficient distributions on the blade tip surface for flat, smooth tip surfaces, with both sharp and rounded edges.

With the development of efficient numerical codes, some researchers carried out numerical investigations to predict blade tip heat transfer and flow field. Metzger et al. [11] provided a numerical model to estimate tip and shroud heat transfer. Ameri and Steinthorsson [13,14] predicted rotor blade tip and shroud heat transfer for a SSME (Space Shuttle Main Engine) turbine. Ameri et al. [15] also predicted flow and heat transfer on the tip of a full rotating GE-E^3 first-stage rotor blade for both a smooth tip and recessed tip. They found a separation vortex generated by the incoming flow separating off the inner edge of the pressure side rim and exiting near the trailing edge of the blade. For the heat transfer contours on the blade tip, they found a sharp entrance effect on the pressure side of the tip surface, where the heat transfer rate reached a maximum due to flow reattachment. The heat transfer contours on the flat tip also showed that a low heat transfer region existed near the leading edge suction side. The heat transfer rate near the trailing edge was lower, and the suction side had a lower heat transfer rate than the pressure side. Ameri et al. [16] also predicted the effects of tip clearance and casing recess on heat transfer and stage efficiency for several squealer blade-tip geometries. Most recently, Ameri and Bunker [17] performed a computational study to investigate detailed heat transfer distributions on blade tip surfaces for a large power generation turbine. They compared and validated their model with the experimental data of Bunker et al. [12] obtained for the same geometry. However, there are very few experimental data available in the open literature to compare and validate numerical models. Without reliable experimental data, the numerical models could not be properly employed in the design and analysis of blade tip heat transfer and flow field.

This study will fulfill the need for additional heat transfer data on a gas turbine blade tip. The test section used for this study is a five-bladed linear cascade, with the three middle blades having a variable tip gap. The tip profile used here represents a first stage rotor blade tip of a modern aircraft gas turbine engine (GE-E^3). Systematic pressure measurements in the near-tip region and on the shroud surface, and heat transfer measurements on the blade-tip surface are done for a tip gap clearance of 1, 1.5, and 2.5 percent of the blade span. Two inlet free-stream turbulence intensity levels are also considered. The effect of unsteady wakes, shock waves, and blade rotation, which may be important in real operating condition, is not considered in this study. This study provides a complete experimental pressure and heat transfer data on a gas turbine blade tip profile (GE-E^3), whose profile geometry is open to the public domain. These data are presented in a standard format with standardized boundary conditions that could also be used by numerical people in the gas turbine community.

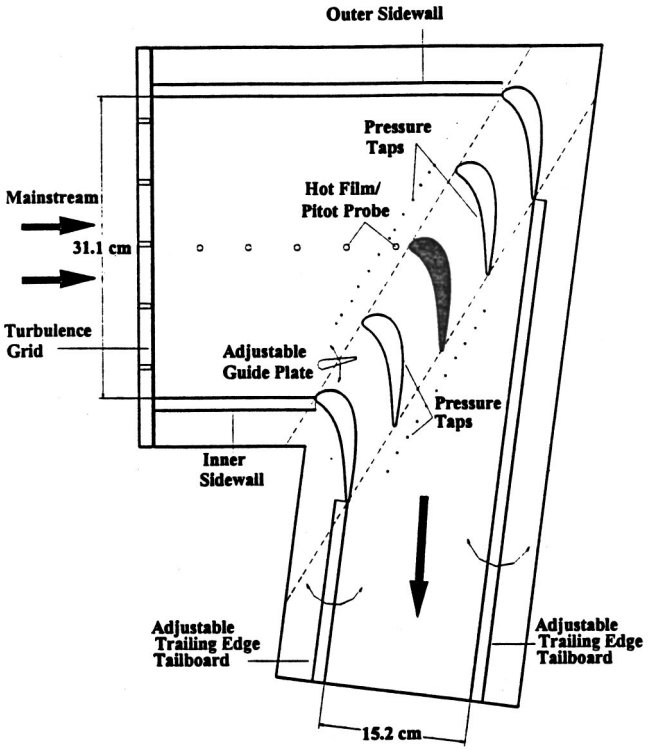

Fig. 1 Test section with five-bladed cascade

Experimental Setup

The experimental setup is a stationary blow down facility with a five-bladed linear cascade. Air from a compressor enters a storage tank at about 280 psig. Then the air enters a high flow pneumatic control valve through a pneumatic ball valve. A controller, regulating the flow rate in downstream of the control valve, is set manually for the desired pressure. The controller gets feedback of the downstream pressure through a pressure line connected to the controller. The controller is capable of maintaining a steady downstream velocity within ± 3 percent of the desired set value. Downstream from the control valve, the test loop consists of a 5-m-long circular duct with a 10.16 cm inside diameter and a 3.1 m long rectangular duct of 31.1×12.2 cm. A symmetric tapered section connects the two ducts. A bypass flow path containing a rupture disk is also connected to the main flow circular duct to safeguard the test section against over-pressure.

The blade cascade is connected at the end of the rectangular duct. A small gap is maintained at the junction of the blade cascade and the rectangular duct to trip the boundary layer. This location for the boundary layer trip is 26.7 cm away from the center blade leading edge. A turbulence-generating grid of 57 percent porosity is also placed at this location to generate high turbulence for the test cases. The turbulence grid is composed of 12.25-mm-wide square bars with 33.02×27.94 mm opening between bars. Hot-film anemometry measurements, using a TSI IFA-100 unit, show that the free-stream turbulence intensity level at a distance of 6 cm upstream from the test-blade leading edge is 6.1 percent without the turbulence grid and 9.7 percent with the turbulence grid. The turbulence length scale was estimated to be 1.5 cm for the 9.7 percent turbulence case, which is slightly larger than the grid size.

The test section is a five-bladed linear cascade with 4-flow passages as shown in Fig. 1. The two far-end blades work as guide vanes, and the outside wall and the center blade work as a test

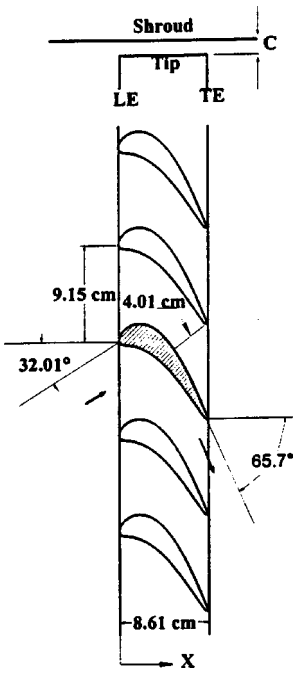

Fig. 2 Blade tip and shroud definition

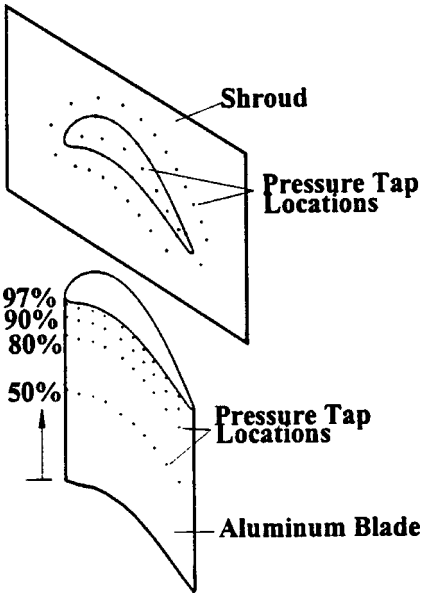

Fig. 3 Pressure tap locations on blade and shroud

blade. The cascade inlet dimensions are 31.1 cm wide and 12.2 cm high (span). Each blade has a 12.2 cm span and a 8.61 cm axial chord length. This dimension is three times (3×) the dimensions of a GE-E^3 blade profile. The blades are made of aluminum and are EDM machine finished. The test section's top, bottom, and sides are made of 1.27-cm-thick clear Polycarbonate (Lexan); however, a 1.2-cm-thick clear acrylic replaces the top cover plate (shroud) for heat transfer tests, to facilitate the best optical access to the test blade (center blade). Two separate but identical blades are used for both the pressure and heat transfer measurements.

Figure 2 represents the blade tip configuration in the cascade. Each blade has a constant cross section for the entire span and represents the tip section of an aerodynamic turbine blade. The blade leading edge pitch is 9.15 cm and the axial chord length is 8.61 cm. The throat diameter at the point of minimum distance between two blades is 4.01 cm, which, with a span of 12.2 cm, gives a throat aspect ratio of about 3. The inlet flow angle to the test blade is 32.01 deg and the exit angle is 65.7 deg, giving a total turning of 97.71 deg. A variable tip gap (C) is maintained between both the tip and shroud surfaces as shown in Fig. 2. The tip gaps used for this study are 1.31 mm, 1.97 mm, and 3.29 mm, which correspond to about 1, 1.5, and 2.5 percent of the blade span (12.2 cm). Hard rubber gaskets of desired thickness are placed on top of the sidewalls, the trailing edge tailboards, and the two outer guide blades to create tip gaps of desired height.

Figure 3 shows the pressure tap blade configuration, which is made of aluminum with a set of pressure taps. Each pressure tap tubing has an outer and inner diameter of 1.65 mm and 1.35 mm, respectively. The tap holes are located in the midspan (50 percent of blade height) of the blade, at a height of 80, 90, and 97 percent of the span as measured from the base of the blade. The pressure taps are placed on both the pressure and suction surfaces. Pressure taps are also placed on the shroud surface, as shown in Fig. 3, to measure the pressure distribution on the shroud surface, which is a representative of the tip surface pressure. A total of 52 pressure taps measure the shroud surface pressure. One set of pressure taps is located around the tip perimeter and along the mean camber line, and a second set of taps is located 12.52 mm outside the tip edge. All these pressure taps are located on the shroud surface opposite the tip surface. No pressure taps are placed on the tip surface. These pressure distributions are useful in estimating the tip leakage flow.

The heat transfer blade, as shown in Fig. 4, is designed with a specific feature. The lower portion of the blade is made of aluminum for structural rigidity against the aerodynamic forces present during the tests. The upper portion of the blade has an inner aluminum core and an outer shell made of black polycarbonate with a low value of thermal conductivity for transient liquid crystal test. The base thickness of the polycarbonate shell is 6.35 mm and the wall thickness is 3.175 mm. It is closely fitted with the inner aluminum core. The shell is also glued to the inner core through the rim contact surface for better rigidity. Three cartridge heaters are embedded into the inner core. The cartridge heater provides heating to the aluminum core, which in turn, heats the outer polycarbonate shell. The blade is fastened to the bottom endwall with screws.

The usual operating condition for this cascade is set at an inlet total pressure of 143 kPa, an exit average static pressure of 108.3 kPa, which gives an overall blade pressure ratio of 1.32. The mass flow rate (up to 60 s) through the cascade is about 5.9 kg/s. During the blow-down test, the inlet air velocity is kept at about 85

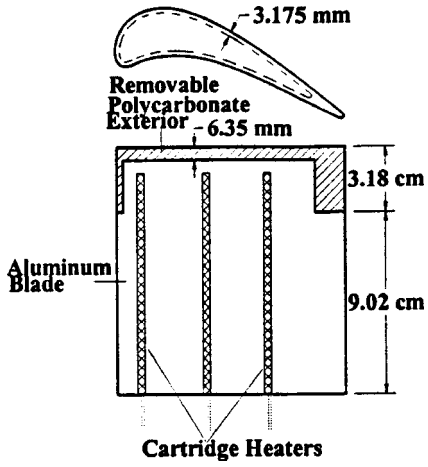

Fig. 4 Heat transfer blade

m/s; the exit air velocity at 199 m/s, and the corresponding Reynolds number of 1.1×10^6 based on axial chord length and exit flow velocity. The corresponding Mach numbers at the inlet and exit are 0.25 and 0.59, respectively.

Flow Condition in the Cascade and Pressure Measurement

To check the flow condition in the cascade, the blades next to the suction and pressure sides of the center (test) blade are instrumented with pressure taps with static pressure holes at midspan of the blades (as shown in Fig. 1). The suction surface of the inner-side blade has six pressure taps and the pressure surface of the outer-side blade has five pressure taps, each at 50 percent height of blade span. Pressure taps are also instrumented at 13 locations at the inlet and 11 locations at the exit plane, as shown in Fig. 1. These inlet and exit plane taps are located at a distance of 25 percent of the blade span upstream from the blade leading edge, and downstream from the blade trailing edge, respectively. The cascade has adjustable trailing edge tailboards. A thinner, adjustable guide plate is also placed near the inlet between the passage of the two interior blades in the shorter flow passage side, as shown in Fig. 1. This guide plate and the adjustable tailboards help provide an identical flow through the pressure and suction side passages of the test blade. With no adjustment, a substantially greater percentage of the total flow would go through the shorter flow passage. The guide plate is rounded on the leading side and tapered and rounded on the trailing side to minimize flow disturbances. A final position for both the adjustable guide plate and trailing edge tailboards is selected after many variations have been tried.

The inlet and exit flow pattern is represented by the coefficient of pressure (C_p). The coefficient of pressure is defined as:

$$C_p=\frac{P_t-P}{P_t-P_{\text{avg}}}$$

Here, P_{avg} is the average static pressure as measured by the inlet (or exit) plane pressure taps, P_t is the total inlet pressure, and P is the local static pressures as measured by the inlet (or exit) pressure taps. This C_p actually represents a nondimensional velocity field, which is important when quickly reviewing the velocity field pattern. Figure 5(*a*) represents the C_p at the cascade inlet and the exit plane. The axial distance is measured from the outermost tap location toward the innermost tap (cascade outer and inner sidewalls are labeled in Fig. 1). Figure 5(*b*) shows pressure distributions at a 50 percent height of the blade span on the center blade and the two nearby blades. The local axial positions are normalized by the axial chord length. The multiple data points represent the variation in repeated tests. The result shows that the flow patterns in the two passages are almost identical.

Static pressure measurements are also made at 80, 90, and 97 percent height of the blade span on both the P/S and S/S, and also on the shroud surface opposite the blade tip surface. A total of 52 pressure taps measured the shroud surface pressure. One set of pressure taps is located around the tip perimeter and along the mean camber line, while a second set of taps is located 12.52 mm outside the tip edge. All these pressure taps are located on the shroud surface opposite the tip surface. Pressures are recorded with a 48-channel Scanivalve System coupled with LabView 5.0 software. LabView discarded all data that fell outside the initial mean ±1.5 standard deviation. It then recorded the mean value of the screened data. The computer steps through each tap and measures the local static pressure on the blade suction and pressure surfaces, and the shroud. Every pressure measurement is repeated at least three times to reduce operating uncertainty and to verify the repeatability of the data. The blow-down facility is capable of giving a required flow for about one minute. The control valve and controller are capable of providing a steady flow condition (the velocity variation is within ±3 percent) in this one minute time period. Figure 6 shows the ratio of the total to local static pressure distributions on the P/S and the S/S at different blade span heights for 1.97 mm (1.5 percent of the span) tip gap and inlet Tu=6.1 percent only. The ratio of pressure distribution (P_t/P) is presented as a function of normalized axial distance (X/C_x). A higher value of P_t/P corresponds to a lower static pressure, while a lower value corresponds to a higher static pres-

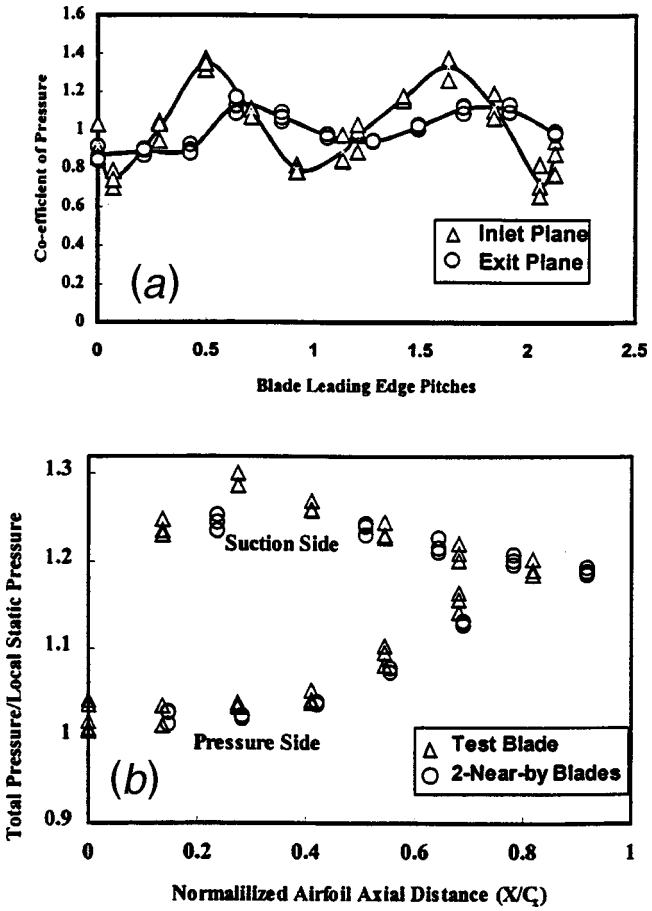

Fig. 5 (*a*) Coefficient of pressure at inlet and exit plane; (*b*) pressure distribution at midspan on test blade and two nearby blades

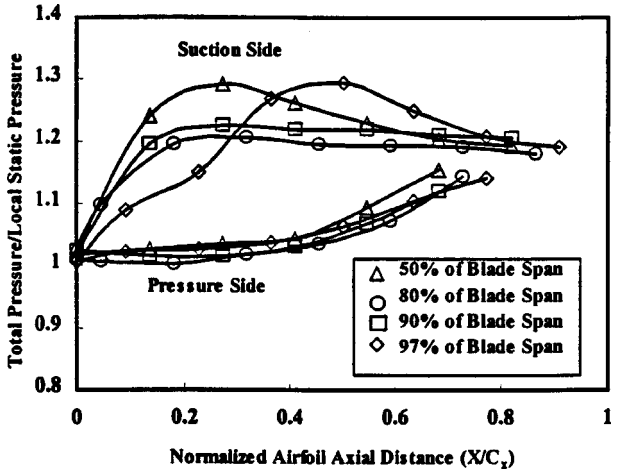

Fig. 6 Pressure distributions from midspan to near-tip locations for 1.5 percent tip gap at Tu=6.1 percent

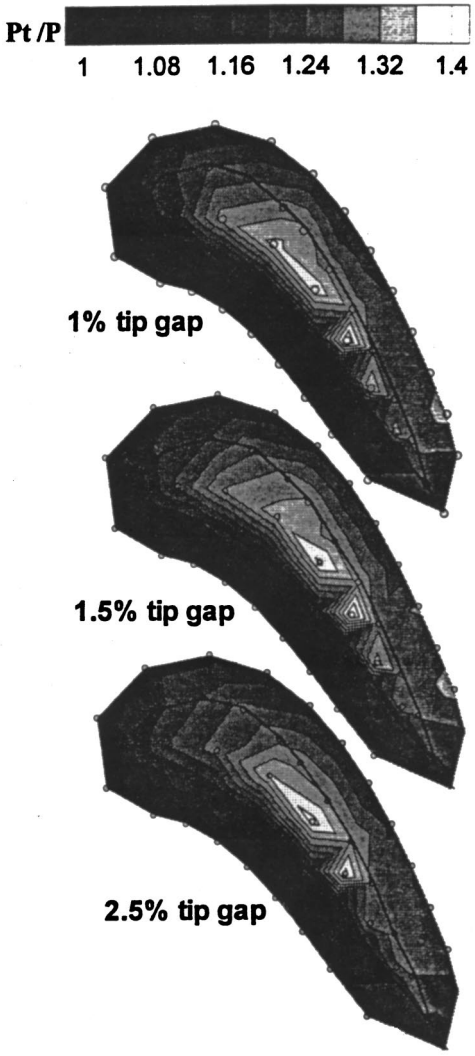

Fig. 7 Pressure ratio distribution (P_t/P) on shroud surface

sure. The static pressure difference between the P/S and the S/S is the main driving force for the leakage flow. Figure 6 clearly shows that the maximum static pressure difference occurs at a distance of 20–30 percent of the axial chord from the leading edge at 50 percent of the blade span. This location of maximum pressure difference has shifted toward the TE at 97 percent of the blade span, and the maximum static pressure difference occurs at about 50 percent of the axial chord from the LE. This shift is due to the leakage flow through the tip gap.

Figure 7 shows the total pressure to local static pressure ratio (P_t/P) contours on the shroud surface for three different tip gaps at Tu = 6.1 percent. This contour plot helps explain the heat transfer results on the tip surface. The small circles on the contour plots represent the pressure tap locations relative to the tip, while the bold line indicates the tip dimension. A smaller P_t/P value means higher static pressure, while a larger value means a lower static pressure. This pressure ratio distribution clearly demonstrates the tip leakage flow path. The lower P_t/P value on the P/S LE indicates that the leakage flow enters the tip gap at this location, while the higher P_t/P value on the S/S indicates that the leakage flow exits the tip through this location. In this flow path, a separation vortex generates as the incoming flow separates off the inner edge of the P/S rim and exits near the S/S TE of the blade. Sjolander and Cao [5] observed this separation vortex and Ameri et al. [15] also predicted this phenomenon. Due to this separation vortex, the heat transfer rate increases in this region as seen in the heat transfer results.

Figure 7 also shows that as the tip gap decreases, the P_t/P ratio increases slightly toward the LE S/S, resulting in a change in the leakage flow path direction. This means that the tip leakage flow path direction is shifting towards the LE S/S at a lower tip gap. This happens because, at lower tip gap, the leakage flow has a smaller gap to flow through, over the boundary layer that develops at the P/S and grows toward the S/S. Thus, the leakage flow has to overcome higher resistance compared to a higher tip gap situation. As a result, it shifts the flow direction toward a shorter path. This effect is reflected in the heat transfer results. Pressure measurements are not made on the blade tip surface. However, Bunker et al. [12] showed that the pressure distribution trends are very similar at both the blade tip and shroud surfaces.

Heat Transfer Measurement and Results

Heat transfer measurement is made at a preset flow condition at which the pressure measurement is done. A threshold intensity method of transient liquid crystal technique is used. The liquid crystals in this study are wide band 30 to 35°C crystals made by Hallcrest (R30C5W). The blade tip surface is initially coated with a thin layer of thermochromic liquid crystals, and the blade is fastened in the test cascade. The cartridge heaters are turned on for three hours. The cartridge heaters heat the inner aluminum core of the test blade and the aluminum core, in turn, heats the polycarbonate shell to a desired steady initial temperature of about 60°C. The initial tip surface temperature is measured using 22 thermocouples placed on the blade tip surface at different discrete locations. Two thermocouples are also placed on the suction and pressure side near-tip region toward the trailing edge. These two thermocouples work as a reference to check the initial tip surface temperature during the heat transfer test. This process of heating the blade and measuring the initial temperature is repeated several times before the final heat transfer test to ensure repeatability of the recorded initial temperature. The initial temperature is very uniform (within 2°C) throughout the tip surface, except near the trailing edge region. These temperatures are then interpolated to get an initial temperature map on the whole surface.

The thermocouples from the tip surface are removed, the blade is then washed and re-sprayed with liquid crystals. The blade is put back in the cascade and the cartridge heaters are turned on for three hours. A region of interest (ROI) is selected and the blow-down test is then carried out. This region of interest (ROI) is the data collection region. The image processing system captures the liquid crystal color change time from green to the onset of red during the blow down test. The image system requires a background intensity correction based upon the lighting conditions on the ROI. This is called threshold, which ensures that all the points in the ROI are at a lower intensity than the real green-to-red transition intensity caused by liquid crystal color change. The system is ready for the blow-down test once the lighting, threshold, and initial temperature are set. Only one test is done per day in a controlled environment (test cell doors are closed and the room temperature is controlled). The reference thermocouples check the initial surface temperature during a heat transfer test. Precise coordination of the image processing system and the flow is critical, since the heat transfer experiments are performed at transient conditions. Thermocouples placed at the cascade inlet provide the free-stream temperature, which is about 24°C. The blade surface color change is monitored using an image processing system. The image processing system consists of a high-resolution RGB color CCD camera, a high-speed PC with a 24-bit true color frame grabber board (from Imaging Technology), and a Color Video Monitor with RGB inputs. The camera captures real-time images through Optimas 3.0, an image processing software. The same software translates the captured image into a data file. The test duration is small enough (~10–30 s) to consider a semi-infinite

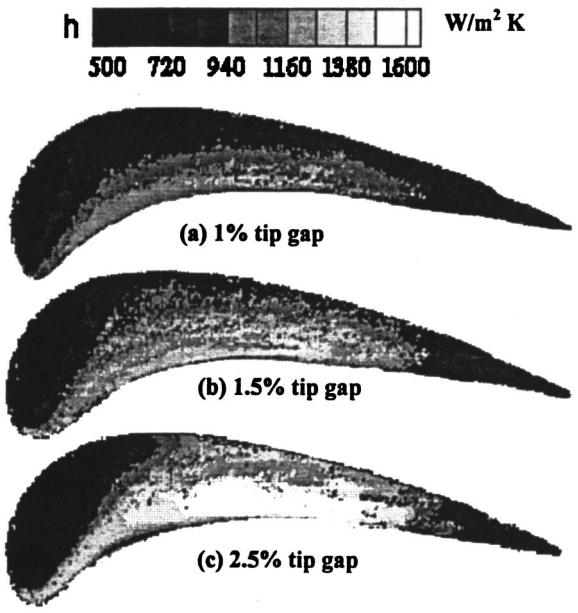

Fig. 8 Heat transfer coefficient at $Tu=6.1$ percent

solid assumption. The local heat transfer coefficient on the blade tip surface is then calculated, assuming a one-dimensional transient conduction into a semi-infinite solid surface with a convective boundary condition using the following equation:

$$\frac{T_w-T_i}{T_\infty-T_i}=1-\exp\left(\frac{h^2\alpha t}{k^2}\right)\mathrm{erfc}\left(\frac{h\sqrt{\alpha t}}{k}\right).$$

Here, T_w (30°C), T_i (60°C), T_∞ (24°C), t (~10–30 s), k (0.18 W/m K), and α are known. The local heat transfer coefficient at any location can then be calculated from the equation given above. The experimental uncertainty is measured using the methods of Kline and McClintock [18]. The uncertainty of the local heat transfer coefficient measured by this method is estimated to be ±7.9 percent or less. The uncertainty estimation does not include the effect of two-dimensionality near the edges. Note that the acrylic blade material (polycarbonate) has a very low thermal conductivity of 0.18 W/m K. The liquid crystal color change transition occurs at the surface, which is kept at a uniform initial temperature. Test duration is also smaller (~10–30 s) than the time required for the temperature to penetrate the full thickness of the insulating acrylic material. Thus, a one-dimensional transient, semi-infinite solid assumption is valid throughout the surface, except near the tip edges. Due to this one-dimensional assumption, the results at the tip edges are less reliable, and may suffer more uncertainty than the reported value because of the existing two-dimensional conduction effect.

The heat transfer coefficient measurements are done for the three cases of tip gaps and at the two different turbulence intensity levels. Figure 8(*b*) shows the tip local heat transfer contour plots for a tip clearance gap of 1.97 mm (1.5 percent of the blade span) and an inlet free-stream turbulence intensity level of 6.1 percent. This is a typical heat transfer coefficient distribution contour plot for each case tested here. The distribution clearly shows various regions of low and high heat transfer coefficient on the tip surface. The magnitude of the heat transfer coefficient varies from 500 to 1700 W/m^2 K on the tip surface. A surprisingly important finding is the development of a low heat transfer region near the LE and toward the S/S.

The pressure ratio (P_t/P) distributions on the shroud surface (Fig. 7) show that this low heat transfer region corresponds to the lowest convective velocity due to a lower static pressure difference (ΔP) between the pressure and the suction sides. A gradual increase in the heat transfer coefficient is observed surrounding the low heat transfer region. The tip leakage flow originates from the pressure side near the leading edge and exits through the suction side, away from the leading edge, as seen in Fig. 7. This region of maximum tip leakage flow corresponds to a high heat transfer coefficient, as seen in Fig. 8(*b*). This means that the higher heat transfer coefficient is observed along the tip leakage flow path. The heat transfer coefficient along this tip leakage flow path is higher toward the pressure side than the suction side. This happens because of the flow entrance effect. The leakage flow enters through the pressure side and exits through the suction side. A separation vortex generates at the pressure side as the incoming flow separates off the inner edge of the pressure side rim and exits near the trailing edge of the blade. Sjolander and Cao [5] observed this separation vortex and they mentioned about the possibility of a high heat transfer rate on the pressure side. The lower heat transfer coefficient toward the suction side may be the result of a boundary layer that develops at the pressure side edge and grows toward the suction side. Figure 8(*b*) also shows a lower heat transfer coefficient near the trailing edge region. This region corresponds to a lower tip leakage flow (lower ΔP) as seen in Fig. 7, thus resulting in a lower heat transfer coefficient.

Bunker et al. [12] found a similar trend of low and high heat transfer region on the tip surface. They termed the low heat transfer region as the ''sweet spot.'' They found that the low heat transfer region originates from the airfoil pressure side at about 20 to 30 percent axial chord location, while we found this location near the LE S/S. This spatial difference may be due to a difference in the tip model geometric profile, and orientation of the blade with respect to the flow path. They used a tip model geometry of a large power generation turbine, while ours is an E^3 profile of an aircraft gas turbine engine. Note that the level of the local heat transfer coefficient on our E^3 blade and on their power generation turbine is of the same order of magnitude. Ameri et al. [15] predicted heat transfer rate on the tip of a full rotating E^3 blade. The trend of their predicted result is very similar to our experimental data. They also predicted a low heat transfer region near the leading edge suction side, while the heat transfer rate is higher on the pressure side and lower near the trailing edge as seen in our case.

Figures 8(*a*) and 8(*c*) show the tip heat transfer coefficient distribution for 1.31 mm (1 percent of the span) and 3.29 mm (2.5 percent of the span) tip gaps, respectively at a same inlet turbulence intensity level of 6.1 percent. These figures clearly show that the tip gap has a significant effect on the local heat transfer coefficient. A larger tip gap results in an overall higher heat transfer coefficient, while a smaller tip gap results in a lower heat transfer coefficient. This is because a larger tip gap increases the amount of tip leakage flow, while a smaller tip gap decreases it. However, the local heat transfer coefficient changes according to a change in the leakage flow path direction. Figure 8 shows that a decrease in the tip gap from 1.5 to 1 percent decreases the tip local heat transfer coefficient distribution by about 10 percent at high heat transfer region along the flow path, while slightly increasing the local heat transfer coefficient in the low heat transfer region. Similarly, an increase in the tip gap from 1.5 to 2.5 percent increases the local heat transfer coefficient by about 20 percent in the high heat transfer region, while slightly decreasing it in the low heat transfer region. It happens, because the tip leakage flow path changes its direction slightly depending on the gap size. At a larger tip gap, the leakage flow can easily pass toward the trailing edge suction side, overcoming the boundary layer thickness. Whereas, at a smaller tip gap, the leakage flow encounters more resistance to the flow toward the trailing edge suction side due to a smaller passage over the boundary layer thickness. Thus, the flow shifts its direction toward a shorter passage in the leading edge suction side, which results in a higher heat transfer coefficient in this region. The shroud pressure distribution in Fig. 7 supports this phenomenon.

Figures 9(*a*, *b*, and *c*) show the heat transfer coefficient distri-

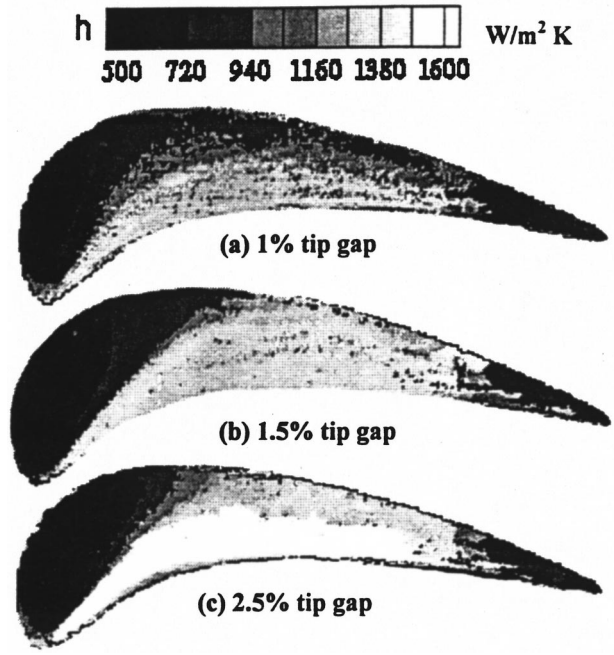

Fig. 9 Heat transfer coefficient at $Tu=9.7$ percent

butions for 1.31 mm (1 percent), 1.97 mm (1.5 percent), and 3.29 mm (2.5 percent), respectively, at a higher inlet turbulence intensity level of 9.7 percent. The heat transfer distribution trend is the same as that of Figs. 8(*a*, *b*, and *c*) at a lower turbulence level of 6.1 percent. However, the magnitude of the overall heat transfer coefficient is about 15–20 percent higher over the low turbulence case of 6.1 percent intensity level. The increase in heat transfer coefficient is more prominent along the leakage flow path, because turbulence does not increase the magnitude of the tip leakage flow; however, it increases flow fluctuations.

The averaged tip heat transfer coefficients for the three different tip gaps and for both the low and high turbulence cases are presented in Fig. 10. The result shows that, for each case of the tip gap, the heat transfer coefficient initially decreases along the axial chord length. It then increases and becomes a maximum at about 70 percent location of the axial chord, and again decreases toward the trailing edge. Smaller tip gaps produce a lower averaged tip heat transfer coefficient. Similar effect of the tip gap is observed at both the lower and higher turbulence levels of 6.1 and 9.7 percent, while the magnitude of heat transfer coefficient is higher at higher turbulence case of 9.7 percent, compared to the low turbulence case of 6.1 percent.

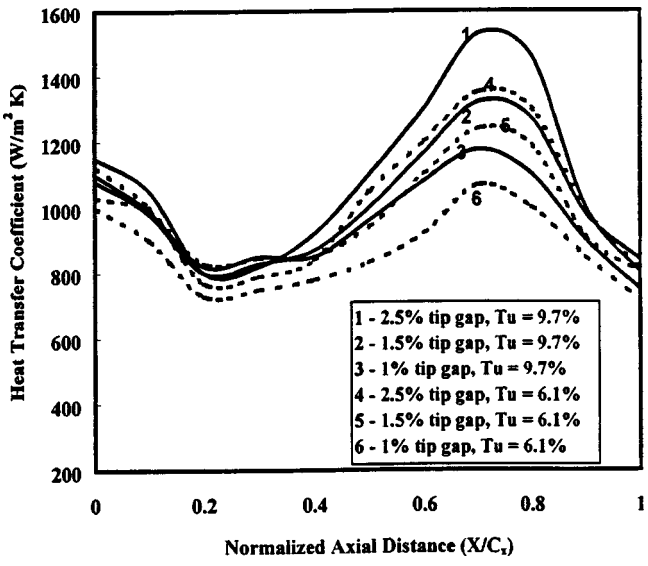

Fig. 10 Averaged heat transfer coefficient

Conclusions

This study investigated the effect of tip gap and inlet turbulence intensity on detailed local heat transfer coefficient distribution on the plane tip surface of a gas turbine blade. The blade tip model is a two-dimensional profile of an E^3 blade of an aircraft gas turbine engine. A transient liquid crystal technique is used for detailed heat transfer measurements. Pressure distributions in the near-tip region and on the shroud surface provide complementary information explaining the local heat transfer behavior on the tip surface in a five-bladed stationary linear cascade. A typical operating condition having a Reynolds number based on airfoil axial chord and an exit velocity of 1.1×10^6 and an overall pressure ratio of 1.32 is used to measure the pressure and heat transfer coefficients. The major findings are:

1 Detailed measurements provide a better understanding of the local heat transfer behavior on the blade tip surface.

2 The pressure measurements in the near tip and on the shroud surface provide complementary information of the tip leakage flow pattern. This pressure data provides a basis for determining the tip leakage flow and also explains the heat transfer results. This detailed pressure and heat transfer measurement also provides a reference for further experimental or computational study.

3 Different heat transfer regions exist on the tip surface. The leading edge side contains a low heat transfer region near the suction side, while a high heat transfer region exists along the leakage flow path.

4 A higher heat transfer coefficient exists on the tip surface toward the pressure side because of the entrance effect.

5 Generally, a larger tip gap results in a higher overall heat transfer coefficient, while a smaller tip gap results in a lower overall heat transfer coefficient. This is because a larger tip gap increases the magnitude of the tip leakage flow, while smaller tip gap decreases it.

6 An increase in the inlet turbulence intensity level from 6.1 to 9.7 percent increases the heat transfer coefficient by about 15–20 percent, along the leakage flow path.

Acknowledgments

This work is prepared with support of the NASA Glenn Research Center under grant No. NAG3-2002. The NASA technical team is Mr. Robert Boyle and Dr. Raymond Gaugler. Their support is greatly appreciated. Technical discussions with Dr. C. Pang Lee of GE Aircraft Engines, Dr. Ron Bunker of GE R&D Center, and Dr. Srinath Ekkad of Louisiana State University were helpful and are acknowledged. Dr. C. Pang Lee also provided us with the E^3 profile for the plane and squealer tips. His help is also appreciated.

Nomenclature

C = tip clearance gap
C_p = coefficient of pressure
C_x = axial chord length of the blades = 8.61 cm
h = local convective heat transfer coefficient, W/m^2 K
k = thermal conductivity of blade tip material = 0.18 W/m K
LE = leading edge of the blade
P = local static pressure
P_{avg} = averaged static pressure
P_t = total pressure at the inlet
P/S = pressure side of the blade

S/S = suction side of the blade
t = transition time for liquid crystal color change
TE = trailing edge of the blade
T_i = initial temperature of the blade tip surface
T_∞ = mainstream temperature of the flow
T_w = color change temperature of the liquid crystal, green-to-red
Tu = turbulence intensity level at the inlet
X = axial distance, cm
α = thermal diffusivity of tip material $=1.25\times10^{-7}\ m^2/s$

References

[1] Bindon, J. P., and Morphus, G., 1988, ''The Effect of Relative Motion, Blade Edge Radius and Gap Size on the Blade Tip Pressure Distribution in an Annular Turbine Cascade With Clearance,'' ASME Paper No. 88-GT-256.

[2] Bindon, J. P., 1989, ''The Measurement and Formation of Tip Clearance Loss,'' ASME J. Turbomach., **111**, pp. 258–263.

[3] Moore, J., Moore, J. G., Henry, G. S., and Chaudhury, U., 1989, ''Flow and Heat Transfer in Turbine Tip Gaps,'' ASME J. Turbomach., **111**, pp. 301–309.

[4] Yaras, M. I., Sjolander, S. A., and Kind, R. J., 1992, ''Effects of Simulated Rotation on Tip Leakage in a Planar Cascade of Turbine Blades: Part I—Tip Gap Flow,'' ASME J. Turbomach., **114**, pp. 652–659.

[5] Sjolander, S. A., and Cao, D., 1995, ''Measurements of the Flow in an Idealized Turbine Tip Gap,'' ASME J. Turbomach., **117**, pp. 578–584.

[6] Kaiser, I., and Bindon, J. P., 1997, ''The Effect of Tip Clearance on the Development of Loss Behind a Rotor and a Subsequent Nozzle,'' ASME Paper No. 97-GT-53.

[7] Mayle, R. E., and Metzger D. E., 1982, ''Heat Transfer at the Tip of an Unshrouded Turbine Blade,'' *Proc. Seventh Int. Heat Transfer Conf.*, Hemisphere Pub., pp. 87–92.

[8] Metzger, D. E., Bunker, R. S., and Chyu, M. K., 1989, ''Cavity Heat Transfer on a Transverse Grooved Wall in a Narrow Flow Channel,'' ASME J. Heat Transfer, **111**, pp. 73–79.

[9] Chyu, M. K., Moon, H. K., and Metzger, D. E., 1989, ''Heat Transfer in the Tip Region of Grooved Turbine Blades,'' ASME J. Turbomach., **111**, pp. 131–138.

[10] Yang, T. T., and Diller, T. E., 1995, ''Heat Transfer and Flow for a Grooved Turbine Blade Tip in a Transonic Cascade,'' ASME Paper No. 95-WA/HT-29.

[11] Metzger, D. E., Dunn, M. G., and Hah, C., 1991, ''Turbine Tip and Shroud Heat Transfer,'' ASME J. Turbomach., **113**, pp. 502–507.

[12] Bunker, Ronald S., Bailey, J. C., and Ameri, A. A., 2000, ''Heat Transfer and Flow on the First Stage Blade Tip of a Power Generation Gas Turbine: Part I—Experimental Results,'' ASME J. Turbomach., **122**, pp. 263–271.

[13] Ameri, A. A., and Steinthorsson, E., 1995, ''Prediction of Unshrouded Rotor Blade Tip Heat Transfer,'' ASME Paper No. 95-GT-142.

[14] Ameri, A. A., and Steinthorsson, E., 1996, ''Analysis of Gas Turbine Rotor Blade Tip and Shroud Heat Transfer,'' ASME Paper No. 96-GT-189.

[15] Ameri, A. A., Rigby, D. L., and Steinthorsson, E., 1998, ''Effect of Squealer Tip on Rotor Heat Transfer and Efficiency,'' ASME J. Turbomach., **120**, pp. 753–759.

[16] Ameri, A. A., Steinthorsson, E., and Rigby, D. L., 1999, ''Effects of Tip Clearance and Casing Recess on Heat Transfer and Stage Efficiency in Axial Turbines,'' ASME J. Turbomach., **121**, pp. 683–693.

[17] Ameri, A. A., and Bunker, R. S., 2000, ''Heat Transfer and Flow on the First Stage Blade Tip of a Power Generation Gas Turbine: Part 2—Simulation Results,'' ASME J. Turbomach., **122**, pp. 272–277.

[18] Kline, S. J., and McClintock, F. A., 1953, ''Describing Uncertainties in Single Sample Experiments,'' Mech. Eng., **75**, Jan, pp. 3–8.

Heat Transfer and Flow on the Squealer Tip of a Gas Turbine Blade

Gm. S. Azad

Je-Chin Han

Turbine Heat Transfer Laboratory,
Department of Mechanical Engineering,
Texas A&M University,
College Station, TX 77843-3123

Robert J. Boyle
NASA Glenn Research Center,
Cleveland, OH 44135

Experimental investigations are performed to measure the detailed heat transfer coefficient and static pressure distributions on the squealer tip of a gas turbine blade in a five-bladed stationary linear cascade. The blade is a two-dimensional model of a modern first-stage gas turbine rotor blade with a blade tip profile of a GE-E^3 aircraft gas turbine engine rotor blade. A squealer (recessed) tip with a 3.77 percent recess is considered here. The data on the squealer tip are also compared with a flat tip case. All measurements are made at three different tip gap clearances of about 1, 1.5, and 2.5 percent of the blade span. Two different turbulence intensities of 6.1 and 9.7 percent at the cascade inlet are also considered for heat transfer measurements. Static pressure measurements are made in the midspan and near-tip regions, as well as on the shroud surface opposite to the blade tip surface. The flow condition in the test cascade corresponds to an overall pressure ratio of 1.32 and an exit Reynolds number based on the axial chord of 1.1 $\times 10^6$. A transient liquid crystal technique is used to measure the heat transfer coefficients. Results show that the heat transfer coefficient on the cavity surface and rim increases with an increase in tip clearance. The heat transfer coefficient on the rim is higher than the cavity surface. The cavity surface has a higher heat transfer coefficient near the leading edge region than the trailing edge region. The heat transfer coefficient on the pressure side rim and trailing edge region is higher at a higher turbulence intensity level of 9.7 over 6.1 percent case. However, no significant difference in local heat transfer coefficient is observed inside the cavity and the suction side rim for the two turbulence intensities. The squealer tip blade provides a lower overall heat transfer coefficient when compared to the flat tip blade. [S0889-504X(00)00504-3]

Introduction

To achieve higher thermal efficiency and thrust, modern gas turbine engines operate at high combustor outlet temperatures of 1300–1500°C. Turbine blades are exposed to these high-temperature gases and undergo severe thermal stress and fatigue. Blade tips are one of the most susceptible regions, because they are difficult to cool and are subject to potential damage due to the large thermal load. The hot gases flowing through the gap between the blade tip and the shroud cause this large thermal load on the blade tip. This flow, sometimes called tip leakage flow, accelerates due to the pressure difference between the pressure and suction sides of the blade, which causes thin boundary layers and high heat transfer rates. This tip leakage flow is undesirable because it chips away the pressure side tip corner from the midchord to the trailing edge. As the blade tip is chipped away, the tip gap width increases, allowing more leakage flow through the tip gap and accelerating blade tip failure. Thus, it increases the losses in the flow.

It is recognized that the blade tip geometry and subsequent tip leakage flows significantly affect the aerodynamic efficiency of turbines. The influence of tip gap on turbine efficiency is so significant that designers have a strong desire to improve the efficiency by decreasing the tip-to-shroud operating gaps, or by implementing more effective tip clearance controls. However, it is difficult to seal the hot leakage flow through the tip gap completely. A common technique to reduce the tip leakage flow is to use a recessed tip, which is known as a squealer tip. A squealer tip allows a smaller tip clearance, without the risk of a catastrophic failure, in case the tip rubs against the shroud during turbine operation. The smaller tip gap reduces the flow rate through the tip gap, resulting in smaller losses and lower heat transfer. It is also believed that the groove (tip recess) acts as a labyrinth seal to increase flow resistance. Thus, it is important to know both the flow field and heat transfer behavior on the squealer tip of a gas turbine blade. Reliable experimental data are also important to develop and validate computational codes to predict flow and heat transfer distributions on turbine blades.

Limited information on the flow field and heat transfer on a squealer blade tip is available in the existing literature. Metzger et al. [1] and Chyu et al. [2] studied heat transfer on rectangular grooved tip models. They performed experiments using cavities of varying depth-to-width (width of the cavity) and tip gap-to-width (width of the cavity) ratios, and incorporated the effect of relative motion by introducing a moving shroud surface over the grooved tip model. They reported that the local heat transfer coefficient in the upstream end of the cavity is greatly reduced when compared with a rectangular flat tip, while in the downstream end of the cavity, the heat transfer coefficient is higher due to flow reattachment inside the cavity. They concluded that for a given pressure difference across the gap, there is an optimum value of depth-to-width ratio beyond which no further flow reduction will occur. They recommended shallow cavities if overall heat transfer reduction on the cavity wall is desired.

The above-cited experimental studies provide insight into the nature of the flow field and heat transfer around the cavity in a rectangular tip model case. Heyes et al. [3] studied tip leakage on plane and squealer tips in a linear cascade environment. They reported leakage flow data on plane tip, suction side squealers, and pressure side squealers. No heat transfer data was reported. They concluded that the use of squealers, particularly, suction side squealers are more beneficial than the flat tip. Yang and Diller [4] reported local heat transfer coefficient on a turbine blade tip model with a recessed cavity (squealer tip) in a stationary linear

Contributed by the International Gas Turbine Institute and presented at the 45th International Gas Turbine and Aeroengine Congress and Exhibition, Munich, Germany, May 8–11, 2000. Manuscript received by the International Gas Turbine Institute February 2000. Paper No. 2000-GT-195. Review Chair: D. Ballal.

cascade environment. Based on the measurement at a single point on the cavity floor, they reported that the convection coefficients are insensitive of tip gap height. Ameri et al. [5] numerically investigated the flow and heat transfer on the squealer tip of a GE-E^3 first-stage gas turbine blade. They considered a smooth tip, 2 percent recess, and 3 percent recess with a 1 percent tip clearance for all cases. They observed higher heat transfer on the bottom of the cavity when compared with the plane tip. The heat transfer on the pressure side rim is comparable to the plane case but higher on the suction side rim. They concluded that large heat transfer on the bottom of the cavity is due to flow impingement containing hot gas.

No other experimental or numerical studies on squealer tip flow and heat transfer are available in the current literature. The existing literature, however, contains many experimental and numerical investigations on the flow field in and around turbine blade plane-tip models. Studies by Bindon and Morphus [6] and Bindon [7] have contributed to the general understanding of tip leakage flow patterns. Moore et al. [8] also contributed to the understanding of the flow field through tip gaps. Yaras and Sjolander [9] studied the effect of simulated rotation on tip leakage and found that rotation causes a significant reduction in the gap mass flow rate. Sjolander and Cao [10] studied the flow field in an idealized turbine tip gap. Kaiser and Bindon [11] investigated a quantitative analysis of the effects of tip clearance, tip geometry, and multiple stages on turbine stage efficiency in a rotating turbine rig environment. Other works studied the effect of tip clearances on leakage and efficiency loss prediction. Several heat transfer studies are available on turbine blade plane-tip models. Mayle and Metzger [12] did the earliest study on rectangular plane-tip model heat transfer. Metzger et al. [13] used several heat flux sensors to measure local tip heat fluxes on the flat tips at two different tip gaps in a rotating turbine rig. They also provided a numerical model to estimate tip and shroud heat transfer. Ameri and Steinthorsson [14,15] predicted rotor blade tip and shroud heat transfer for a SSME (Space Shuttle Main Engine) turbine. Ameri et al. [16] also predicted the effects of tip clearance and casing recess on heat transfer and stage efficiency for several squealer blade-tip geometries. Most recently, Ameri and Bunker [17] performed a computational study to investigate detailed heat transfer distributions on the blade tip surfaces of a large power generation turbine. Bunker et al. [18] studied the flow and heat transfer on the plane-tip in a three-blade linear cascade. Azad et al. [19] also studied flow and heat transfer on the plane tip in a five-blade linear cascade. The plane-tip heat transfer results from Azad et al. [19] are compared with the squealer tip results in this study.

With the development of supercomputers, numerical investigations are playing an increasingly important role in the study and design of turbine blade tip flow and heat transfer. Without reliable experimental data, however, the numerical models could not be validated and properly employed in the design and analysis of blade tip heat transfer and flow field. This study will fulfill the need for experimental heat transfer data on a gas turbine squealer blade tip. These will be the first experimental data available in the open literature with complete information on the pressure and heat transfer on the squealer tip of a gas turbine blade tip profile (GE-E^3) whose profile geometry is open to the public domain. The test section used for this study is a five-blade linear cascade, with the three middle blades having a variable tip gap, and the center blade having a squealer tip. The tip profile used here represents a first-stage rotor blade tip of a modern aircraft gas turbine engine (GE-E^3). Systematic pressure measurements in the near-tip region and on the shroud surface, and heat transfer measurements on the blade-tip surface, are done for a 3.77 percent tip recess and a tip gap clearance of 1, 1.5, and 2.5 percent of the blade span. Two inlet free-stream turbulence intensity levels are also considered. The effect of unsteady wakes, shock waves, and blade rotation, which may be important in real operating condition, is not considered here. However, it provides a basic information of heat transfer and pressure distribution on a gas turbine squealer blade tip. These data are presented in a standard format with standardized boundary conditions that could also be used by numerical people in the gas turbine community.

Experimental Setup

Measurements are done in a stationary blow down facility with a five-bladed linear cascade. A detailed description of the facility is given in Azad et al. [19]. The facility is capable of maintaining a steady flow at the cascade inlet (velocity variation within ± 3 percent) for one-minute period. A small gap is maintained at the junction of the blade cascade and the inlet flow loop to trip the boundary layer. This location for the boundary layer trip is 26.7 cm upstream from the center blade leading edge. A turbulence-generating grid of 57 percent porosity is also placed at this location for high turbulence tests. The turbulence grid is composed of 12.25-mm-wide square bars with 33.02×27.94 mm opening between bars. Hot-film anemometry measurements, using a TSI IFA-100 unit, show that the free-stream turbulence intensity at a distance of 6 cm upstream from the blade leading edge is 6.1 percent without the turbulence grid and 9.7 percent with the turbulence grid. Turbulence length scale is estimated to be 1.5 cm for 9.7 percent turbulence case, which is slightly larger than the turbulence grid size.

The five-bladed linear cascade has 4-flow passages. The two far-end blades work as guide vanes and the outside wall, and the center blade work as a test blade. Figure 1 shows the test cascade model. The cascade inlet dimensions are 31.1 cm wide and 12.2 cm high (span). Each blade has a 12.2 cm span and a 8.61 cm axial chord length. This dimension is three times (3X) the dimensions of a GE-E^3 blade profile. The blades are made of aluminum and are EDM machine finished. The test section's top, bottom, and sides are made of 1.27-cm-thick clear Polycarbonate (Lexan); however, a 1.2-cm-thick clear acrylic replaces the top cover plate (shroud) for heat transfer tests, to facilitate the best optical access to the test blade (center blade). Two separate but identical blades are used for both the pressure and heat transfer measurements.

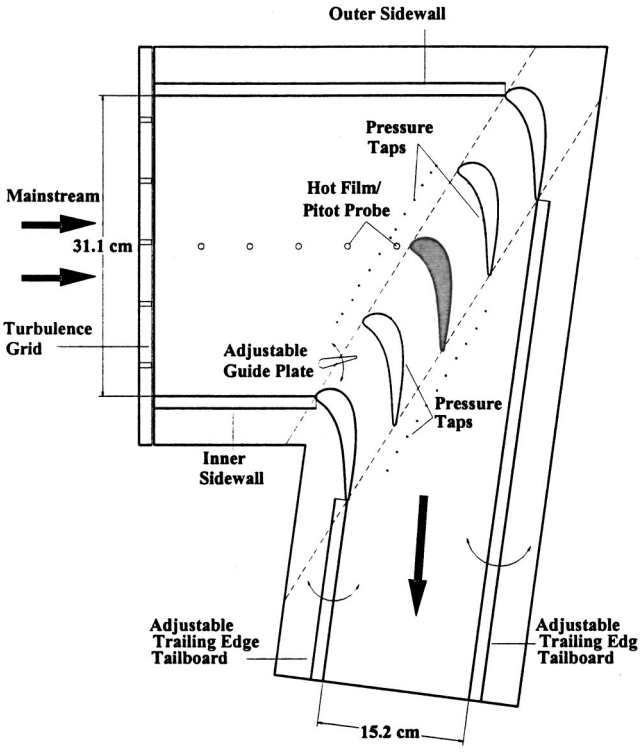

Fig. 1 Test section with five-bladed cascade

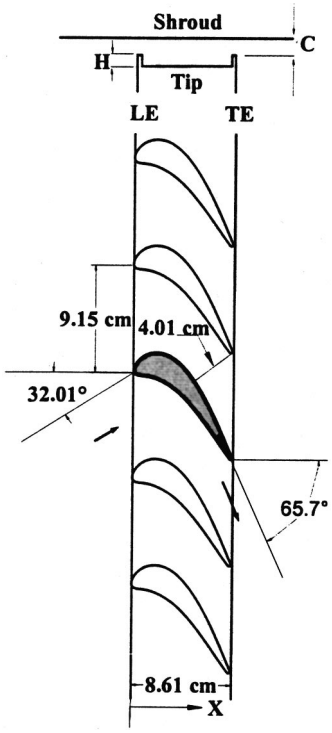

Fig. 2 Blade tip and shroud definition

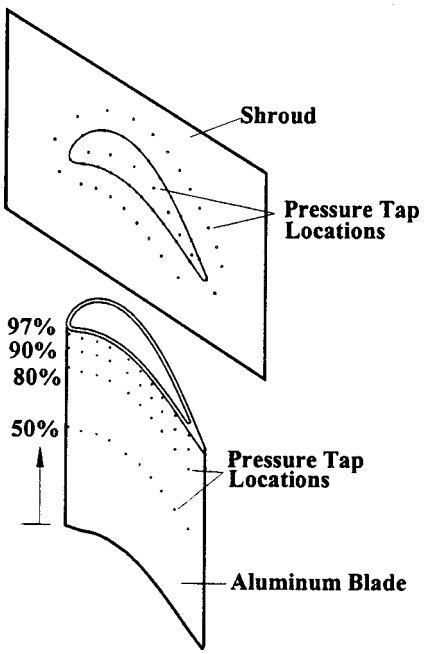

Fig. 3 Pressure tap locations on blade and shroud

Each blade has a constant cross section for the entire span and represents the tip section of an aerodynamic turbine blade. Figure 2 represents the blade tip configuration in the cascade. The blade leading edge pitch (p) is 9.15 cm and the axial chord length is 8.61 cm. The throat diameter at the point of minimum distance between two blades is 4.01 cm, which, with a span of 12.2 cm, gives a throat aspect ratio of about 3. The inlet flow angle to the test blade is 32.01 deg and the exit angle is 65.7 deg, giving a total turning of 97.71 deg. The center blade has a 4.6 mm recess (depth of the cavity, H), which is 3.77 percent of the blade span (12.2 cm). A tip gap (C) is maintained between the tip and shroud surfaces as shown in Fig. 2. The tip gaps used for this study are 1.31 mm, 1.97 mm, and 3.29 mm, which correspond to about 1, 1.5, and 2.5 percent of the blade span (12.2 cm). Hard rubber gaskets of desired thickness are placed on top of the sidewalls, the trailing edge tailboards, and the two outer guide blades to create tip gaps of desired height.

The pressure tap blade is made of aluminum with several sets of pressure taps as shown in Fig. 3. The pressure taps are placed on both the pressure and suction surfaces. Pressure taps are also placed on the shroud surface opposite the blade tip surface to measure the pressure distribution on the shroud surface. Each pressure tap tubing has an outer and inner diameter of 1.65 mm and 1.35 mm, respectively. The tap holes (1.35 mm diameter) are located in the midspan (50 percent of blade height) of the blade, at a height of 80, 90, and 97 percent of the span as measured from the base of the blade. A total of 52 pressure taps measure the shroud surface pressure. One set of pressure taps is located around the tip perimeter and along the mean camber line, and a second set of taps is located 12.52 mm outside the tip edge. No pressure taps are placed on the tip surface. These pressure distributions are useful in estimating the tip leakage flow.

Figure 4 represents the heat transfer blade. The lower portion of the blade is made of aluminum for structural rigidity against the aerodynamic forces present during the tests. The upper portion of the blade has an inner aluminum core and an outer shell made of black polycarbonate with a low value of thermal conductivity for transient liquid crystal test. The polycarbonate tip has a 4.6-mm-deep cavity and a 2.3-mm-thick rim. The base thickness of the polycarbonate shell underneath the cavity is 6.35 mm and the wall that surrounds the inner aluminum core has a thickness of 3.175 mm. The polycarbonate shell is closely fitted with the inner aluminum core. The shell is also glued to the inner core through the rim contact surface for better rigidity. Three cartridge heaters are embedded into the inner core. The cartridge heaters provide heating to the aluminum core, which in turn heats the outer polycarbonate shell. The blade is fastened to the bottom endwall with screws.

The usual operating condition for this cascade is set at an inlet total pressure of 143 kPa, an exit average static pressure of 108.3 kPa, which gives an overall blade pressure ratio of 1.32. The mass flow rate through the cascade is about 5.9 kg/s. During the blowdown test, the inlet air velocity is kept at about 85 m/s; the exit air velocity at 199 m/s, and the corresponding Reynolds number of

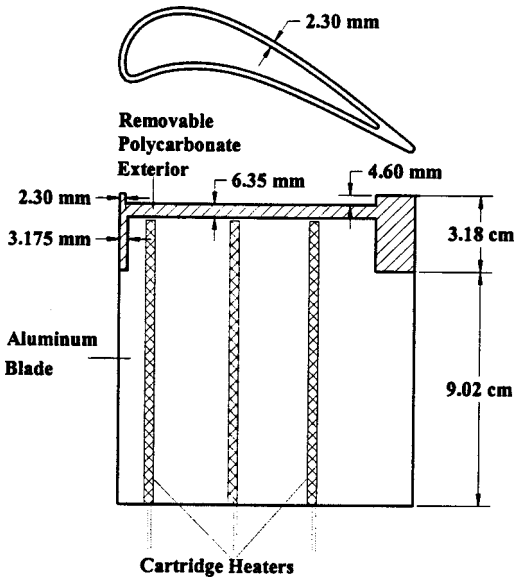

Fig. 4 Heat transfer blade

1.1×10^6 based on axial chord length and exit flow velocity. The corresponding Mach numbers at the inlet and exit are 0.25 and 0.59, respectively.

Flow Condition in the Cascade and Pressure Measurement

The flow patterns at the cascade inlet and exit plane, and through the suction and pressure side passages of the test blade are measured. The detailed measurement is described in Azad et al. [19]. The inlet and exit flow pattern is represented by the coefficient of pressure (C_p). The coefficient of pressure is defined as:

$$C_p=\frac{P_t-P}{P_t-P_{\text{avg}}}$$

Here, P_{avg} is the average static pressure as measured by the inlet (or exit) plane pressure taps, P_t is the total inlet pressure, and P is the local static pressures as measured by the inlet (or exit) pressure taps. This C_p actually represents a nondimensional velocity field, which is important for a quick review of the velocity field pattern. Figure 5(*a*) represents the C_p at the cascade inlet and the exit plane. The measurement planes are selected upstream from the leading edge and downstream from the trailing edge at a distance of 25 percent of the blade span. The axial distance is measured from the outermost tap location toward the innermost tap (cascade outer and inner sidewalls are labeled in Fig. 1). Figure 5(*b*) shows pressure distributions at a 50 percent height of the blade span on the center blade and the two nearby blades. For Fig. 5(*b*), the local axial position is normalized by the axial chord length. The multiple data points in Fig. 5(*a*) and 5(*b*) represent the variation in repeated tests. The result shows that the flow patterns in the two passages are almost identical.

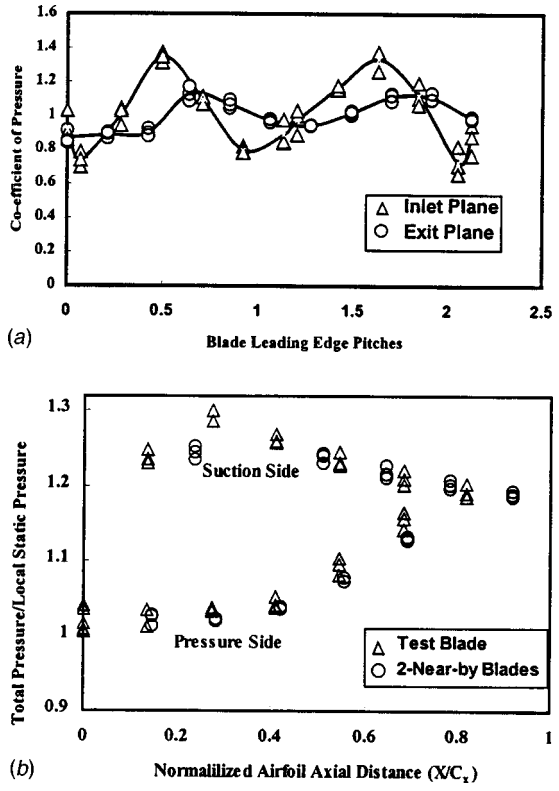

Fig. 5 (*a*) Coefficient of pressure at inlet and exit plane; (*b*) pressure distribution at midspan on the test blade and two nearby blades

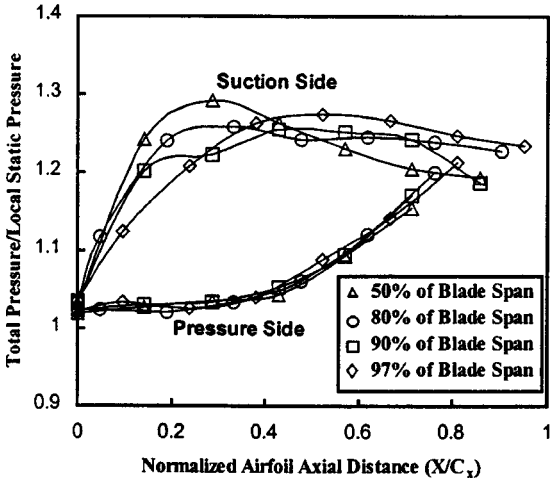

Fig. 6 Pressure distributions from midspan to near-tip locations for *C*=1.5 percent and Tu=6.1 percent

Static pressures are also measured at 80, 90, and 97 percent height of the blade span on both the P/S and S/S, and also on the shroud surface. Pressures are recorded with a 48-channel Scanivalve System coupled with LabView 5.0 software. LabView discarded all data that fell outside the initial mean ±1.5 standard deviation. It then recorded the mean value of the screened data. Every pressure measurement is repeated at least three times to reduce operating uncertainty and to verify the repeatability of the data. The blow-down facility is capable of giving a steady flow (the velocity variation is within ±3 percent) for about one minute. The scanivalve can step through all 48 channels in this one minute to capture the pressure data. Figure 6 shows the ratio of the total to local static pressure distributions on the P/S and the S/S at different height of blade span for 1.97 mm (1.5 percent of the span) tip gap and inlet Tu=6.1 percent only. The ratio of pressure distribution (P_t/P) is presented as a function of normalized axial distance (X/C_x). A higher value of P_t/P corresponds to a lower static pressure, while a lower value corresponds to a higher static pressure. The static pressure difference between the P/S and the S/S is the main driving force for the leakage flow. Figure 6 clearly shows that the maximum static pressure-difference occurs at a distance of 20–30 percent of the axial chord from the leading edge at 50 percent of the blade span. This location of maximum pressure difference has shifted toward the TE at 97 percent of the blade span, and the maximum static pressure difference occurs at about 40–50 percent of the axial chord from the LE. This shift is because of the leakage flow through the tip gap.

Figures 7(*a*), (*b*), (*c*), and (*d*) show the ratio of total to local static pressures (P_t/P) contours on the shroud surface for three different tip gaps at Tu=6.1 percent. Figures 7(*a*), (*b*), and (*c*) are for the squealer tip at 1, 1.5, and 2.5 percent tip gap, while 7(*d*) is for the flat tip at 1.5 percent tip gap. This contour plot helps explain the heat transfer results on the tip surface. The small circles on the contour plots represent the pressure tap locations relative to the tip. The pressure taps along the tip perimeter are connected by a line to indicate the tip dimension. A smaller P_t/P value means higher static pressure, while a larger value means a lower static pressure. This pressure ratio distribution clearly demonstrates the tip leakage flow path. The lower P_t/P value on the P/S indicates that the leakage flow enters the tip gap at this location, while the higher P_t/P value on the S/S indicates that the leakage flow exits the tip through this location. The flow situation in the squealer tip case represents a flow field inside a cavity. In the flow path through the tip gap, a separation vortex generates as the flow separates at the pressure side rim. The flow reattaches inside the cavity and separates again when it exits through the suction side rim. Ameri et al. [5] also predicted this phenomenon.

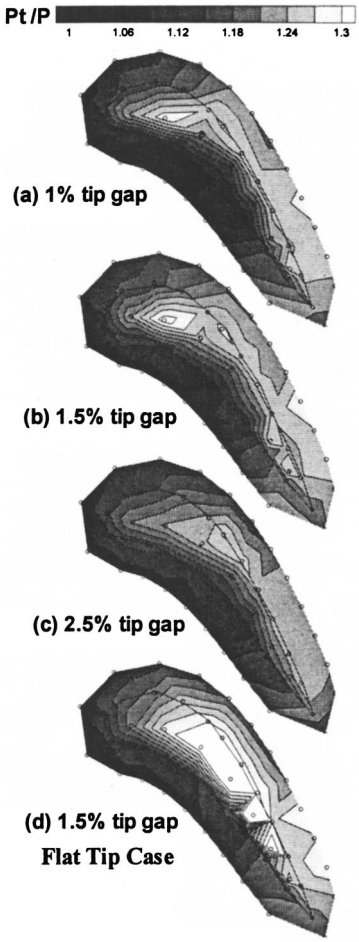

Fig. 7 Pressure ratio distribution on the shroud surface

The flat tip case in Fig. 7(*d*) shows a higher value of P_t/P near the midsuction side, which indicates a very low static pressure in this region. For the same tip gap, the squealer tip in Fig. 7(*b*) shows a much higher static pressure. This means that the leakage flow rate through the flat tip gap is higher than the squealer tip for the same tip gap. The flat tip case also shows that the lower static pressure extends toward the trailing edge through the camber line, thus leading the flow toward the trailing edge. However, the lower static pressure occurs toward the suction side near the leading edge in the squealer tip. Thus, the leakage-flow direction shifts toward the leading edge. This may result in a higher heat transfer coefficient in the cavity toward the leading edge than the flat tip case. There is not much apparent difference between the pressure, distributions at the 1 and 1.5 percent tip gaps as shown in Figs. 7(*a*) and 7(*b*). However, an appreciable difference is observed between 1 and 2.5 percent tip gaps.

Heat Transfer Measurement and Results

A threshold intensity method of transient liquid crystal technique is used. The liquid crystals used in this study are wide band 30 to 35°C crystals made by Hallcrest (R30C5W). The blade tip surface is initially coated with a thin layer of thermochromic liquid crystals, and the blade is fastened in the test cascade with the top acrylic cover in place. The cartridge heaters are turned on for three hours. The cartridge heaters heat the inner aluminum core of the test blade, and the aluminum core, in turn, heats the polycarbonate shell to a desired steady initial temperature of about 60°C. The tip cavity and rim surface initial temperatures are measured by thermocouples placed at 25 discrete locations. Two thermocouples are also placed on the suction and pressure side near-tip region toward the trailing edge. These two thermocouples work as a reference to check the initial tip surface temperature during the heat transfer test. This process of heating the blade and measuring the initial temperature is repeated several times before the final heat transfer test to ensure repeatability of the recorded initial temperature. The initial temperature is very uniform (within 2°C) throughout the tip cavity surface, except near the trailing edge region and the rim. These temperatures are then interpolated to get an initial temperature map on the whole surface. For heat transfer test, the thermocouples from the tip surface are removed. The blade is then washed and resprayed with liquid crystals. The blade is put back in the cascade and the cartridge heaters are turned on for three hours as before. A region of interest (ROI) is selected and a background light intensity is corrected based upon the lighting conditions on the ROI. This region of interest (ROI) is the data collection region. The system is ready for the blow-down test once the lighting, threshold, and initial temperature are set. One test is done per day in a controlled environment (test cell doors are closed and the room temperature is controlled). The reference thermocouples check the initial surface temperature during a heat transfer test. Each heat transfer test is done at a present flow condition at which the pressure measurement is made. Precise coordination of the image processing system and the flow is critical, since the heat transfer experiments are performed at transient conditions. Thermocouples placed at the cascade inlet provide the free-stream temperature, which is about 24°C. The blade surface color change is monitored using an image processing system. The camera captures the color change transition time from green to the onset of red through Optimas 3.0, an image processing software. The same software translates the captured image into a data file. The test duration is small enough (~10–30 s) to consider a semi-infinite solid assumption. The local heat transfer coefficient on the blade tip surface is then calculated, assuming a one-dimensional transient conduction into a semi-infinite solid surface with a convective boundary condition using the following equation:

$$\frac{T_w - T_i}{T_\infty - T_i} = 1 - \exp\left(\frac{h^2 \alpha t}{k^2}\right) \operatorname{erfc}\left(\frac{h\sqrt{\alpha t}}{k}\right)$$

Here, T_w (30°C), T_i (60°C), T_∞ (24°C), t (~10–30 s), k (0.18 W/m K), and α are known. The experimental uncertainty is measured using the methods of Kline and McClintock [20]. The uncertainty of the local heat transfer coefficient measured by this method is estimated to be ±7.9 percent or less. This uncertainty estimation does not include the effect of two-dimensionality near the edges. Note that the acrylic blade material (polycarbonate) has a very low thermal conductivity of 0.18 W/m K. The liquid crystal color change transition occurs at the surface, which is kept at a uniform initial temperature. The test duration is also smaller (~10–30 s) than the time required for the temperature to penetrate the full thickness of the insulating acrylic material. Thus, a one-dimensional transient, semi-infinite solid assumption is valid throughout the surface, except near the edges. Due to this one-dimensional, assumption, the results at the tip edges are less reliable, and may suffer more uncertainty than the reported value because of the existing two-dimensional conduction effect.

The heat transfer coefficient measurements are done for the three cases of tip gaps and at two different turbulence intensities. The local heat transfer coefficient distributions for the squealer tip are presented in Figs. 8(*a*)–(*c*). For comparison, the result from Azad et al. [19] for the flat tip case at 1.5 percent tip gap is also presented in Fig. 8(*d*). The distribution clearly shows various regions of low and high heat transfer coefficients on the tip cavity and rim surface. The magnitude of the heat transfer coefficient varies from 350 to 1150 W/m^2 K inside the cavity and on the trailing edge portion downstream of the cavity. However, the heat transfer coefficient on the rim is much higher at about 1100 to 1700 W/m^2 K. We present the plots in the range of 400–1100 W/m^2 K to clearly distinguish different lower and higher heat transfer zones inside the cavity. The average heat transfer coeffi-

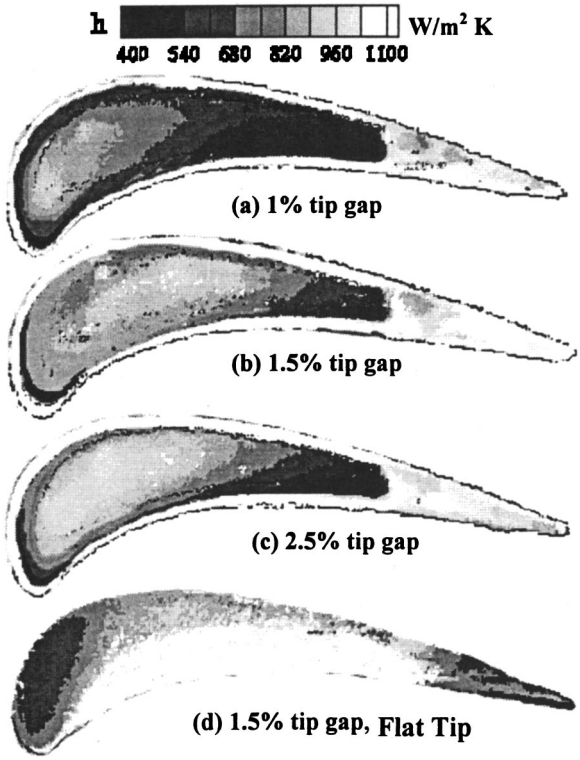

Fig. 8 Heat transfer coefficient at Tu=6.1 percent

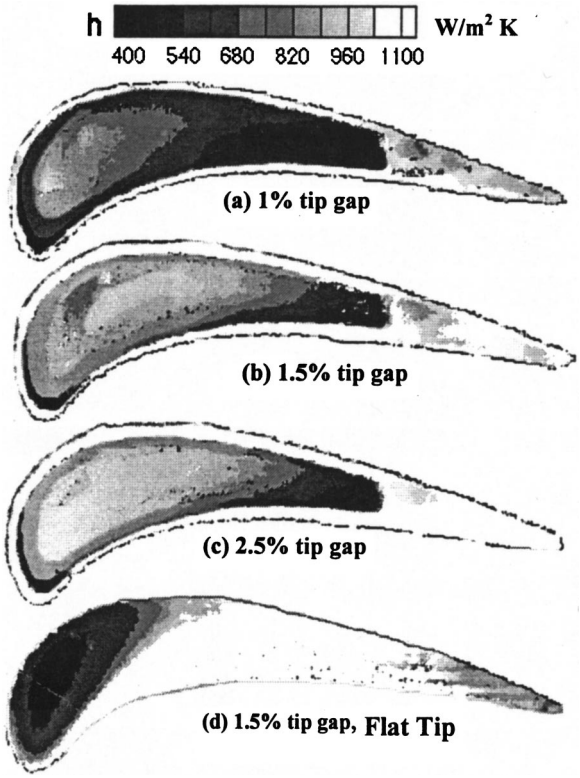

Fig. 9 Heat transfer coefficient at Tu=9.7 percent

cient values on the rim are presented separately in a line plot to show the magnitude of the heat transfer coefficient on the rim. The flat tip result in Fig. 8(*d*) shows that a very low heat transfer coefficient region exists near the leading edge suction side. In the midchord region, the heat transfer coefficient is higher toward the pressure side than the suction side, while the trailing edge has a lower heat transfer coefficient. Upon comparison of the flat tip result of Fig. 8(*d*) with the squealer tip result in Fig. 8(*b*) for the same tip gap, a higher local heat transfer coefficient is observed on the bottom of the cavity toward the leading edge. The local heat transfer coefficient in the trailing edge region is also higher than the flat tip case. The heat transfer coefficient on the pressure side rim is comparable to the flat tip case, while the suction side rim shows a higher heat transfer coefficient than the flat tip case. On the cavity bottom, the heat transfer coefficient is higher in the upstream-central region; however, it is much lower in the midchord region toward the pressure side and downstream-end of the cavity toward the trailing edge. A recirculating dead-flow zone is observed far downstream at the end of the cavity surface. Leakage flow may be entrapped in this narrow region, which causes the heat transfer coefficient to be the lowest in this region. The leakage flow may have an impingement effect on the cavity surface. It separates on the pressure side rim and may reattach inside the cavity surface. Thus, a higher heat transfer coefficient is observed on the central upstream region of the cavity bottom. The high heat transfer on the rim may be due to the flow entrance and exit effect. The leakage spills out of the cavity and exits through the suction side rim and the trailing edge. This may cause more mixing, resulting in a higher heat transfer coefficient in the suction side rim and the trailing edge than the flat tip case.

The effect of tip gap from 1.5 to 1 and 2.5 percent is reflected in Figs. 8(*a*) and (*c*). This figure clearly shows that the tip gap has a significant effect on the local heat transfer coefficient. A larger tip gap results in an overall higher heat transfer coefficient, while a smaller tip gap results in a lower heat transfer coefficient. This is because a larger tip gap increases the amount of tip leakage flow, while a smaller tip gap decreases it.

The effect of inlet turbulence intensity from 6.1 to 9.7 percent is shown in Figs. 9(*a*)–(*d*). The flat tip result in Fig. 9(*d*) at 9.7 percent turbulence intensity shows a similar trend but a higher magnitude of heat transfer coefficient than the 6.1 percent turbulence case, as shown in Fig. 8(*d*). The squealer-tip results in Figs. 9(*a*)–(*c*) at 9.7 percent turbulence intensity show a similar heat transfer distribution trend as that in Figs. 8(*a*)–(*c*) at the low turbulence level of 6.1 percent. The magnitude of the heat transfer coefficient at the cavity bottom is almost the same as in the low turbulence case of 6.1 percent. The cavity rim and the trailing edge region, however, show a higher value. A higher turbulence does not increase the magnitude of the tip leakage; however, it increases the flow fluctuations. The tip gap from 1.5 to 1 percent and 2.5 percent has an effect similar to that in the low turbulence case. However, the turbulence effect is more prominent at the larger tip gap of 2.5 percent.

No experimental data are available in the literature to compare with this result, except for rectangular tip model cavity heat transfer data of Metzger et al. [1]. Metzger et al. [1] found very high heat transfer coefficient on the rim of the upstream (pressure side) and downstream wall (suction side), and these have the same magnitude as in the rectangular flat tip surface. They reported a low heat transfer coefficient on the bottom of the cavity compared to the rectangular flat tip case. The cavity midfloor showed higher heat transfer coefficient than the upstream and downstream end of the cavity. Ameri et al. [15] presented a numerical heat transfer result on the squealer tip of a full rotating GE-E^3 blade for a 2 and 3 percent cavity recess with a 1 percent tip gap case. They observed that the heat transfer on the bottom of the cavity is higher than the flat (smooth) tip case. The pressure side rim showed a similar level, but the suction side rim showed a higher level of heat transfer when compared with the flat tip case. The trend of our experimental data agrees well with results predicted by [5]. It also agrees somewhat with data of [1]. We observed that at the bottom of the cavity, toward the central upstream region, the heat transfer coefficient is higher compared to the flat tip case, while it

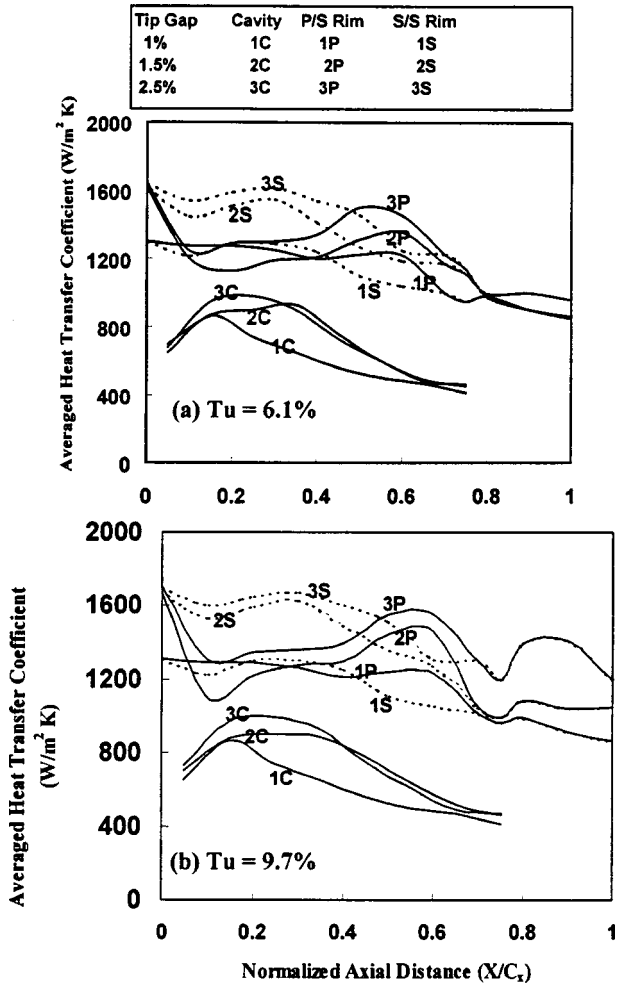

Fig. 10 Averaged heat transfer coefficient at: (*a*) Tu=6.1 percent; (*b*) Tu=9.7 percent

is much lower toward the downstream region and pressure side of the cavity bottom. The pressure side of the cavity rim shows a similar level of heat transfer coefficient compared with the flat tip case, while the suction side rim and the blade trailing edge region show higher heat transfer coefficients when compared with the flat tip case. The heat transfer coefficient in the front-central portion of the cavity is higher than the surrounding area and the trailing side of the cavity.

The averaged heat transfer coefficients are presented in Figs. 10(*a*) and (*b*) for the three different tip gaps and at 6.1 and 9.7 percent turbulence intensities, respectively. The averaged heat transfer coefficient is calculated and plotted as a function of normalized axial distance from the leading edge. The result shows that the heat transfer coefficient inside the cavity and on the rim increases with tip clearance. For each tip gap case, the heat transfer coefficient inside the cavity initially increases slightly along the axial chord, then levels off and decreases toward the downstream edge. The highest heat transfer coefficient is observed on the rim at the leading edge. The heat transfer coefficient on the suction side rim is higher up to the midchord than the pressure side rim, the pressure side rim then shows a higher heat transfer coefficient than the suction side rim. Turbulence has a greater effect on the pressure side rim and the trailing edge than the cavity. As seen in Fig. 10(*b*), this effect is prominent at larger tip clearances.

Conclusions

This study investigated the effect of tip gap and inlet turbulence intensity on detailed local heat transfer coefficient on the squealer tip surface of a gas turbine blade. The result is also compared with the flat tip case. The blade tip model is a two-dimensional profile of an E^3 blade of an aircraft gas turbine engine with a 3.77 percent cavity recess. A transient liquid crystal technique is used to detail heat transfer measurements. Pressure distributions in the near-tip region and on the shroud surface provide complementary information explaining the local heat transfer behavior on the tip surface in a five-blade stationary linear cascade. A typical operating condition having a Reynolds number based on airfoil axial chord and an exit velocity of 1.1×10^6 and an overall pressure ratio of 1.32 is used to measure the pressure and heat transfer coefficients. The major findings are:

1 Detailed measurements provide a better understanding of the local heat transfer behavior on the blade tip surface.

2 The pressure measurements in the near tip and on the shroud surface provide complementary information of the tip leakage flow pattern. These pressure data provide a basis for determining the tip leakage flow, and they also explain the heat transfer results. This detailed pressure and heat transfer measurement also provides a reference for further experimental or computational study.

3 Different heat transfer regions exist on the cavity surface. The front-central portion of the cavity surface contains a high heat transfer region, while a low heat transfer region exists around this region and toward the downstream of the cavity.

4 A higher heat transfer coefficient exists on the rim surface because of the entrance and exit effect. The trailing edge region also contains a high heat transfer coefficient.

5 A larger tip gap results in a higher heat transfer coefficient, while a smaller tip gap results in a lower heat transfer coefficient. This is because a larger tip gap increases the magnitude of the tip leakage flow, while a smaller tip gap decreases it.

6 An increase in the inlet turbulence intensity level from 6.1 percent to 9.7 percent slightly increases the heat transfer coefficient along the pressure side rim and the trailing edge region.

7 The heat transfer coefficient in a squealer tip is higher near the central upstream end of the cavity and the trailing edge region, while it is much lower in the midchord toward the pressure side and downstream end of the cavity when compared to the flat tip case. The squealer tip cavity rim has the same level of heat transfer coefficient on the pressure side but a higher heat transfer coefficient on the suction side when compared to the flat tip case. However, the squealer tip provides an overall lower heat transfer coefficient when compared to the flat tip case.

Acknowledgments

This work is prepared with the support of the NASA Glenn Research Center under grant number NAG3-2002. The NASA technical team is Mr. Robert Boyle and Dr. Raymond Gaugler. Their support is greatly appreciated. Technical discussions with Dr. C. Pang Lee of GE Aircraft Engines, Dr. Ron Bunker of GE R&D Center, and Dr. Srinath Ekkad of Louisiana State University were helpful and are acknowledged. Dr. C. Pang Lee also provided us the E^3 profile for the plane and squealer tips. His help is also appreciated.

Nomenclature

C = tip clearance gap
C_p = coefficient of pressure
C_x = axial chord length of the blade=8.61 cm
h = local convective heat transfer coefficient, $W/m^2 K$
H = cavity depth (recess), mm
k = thermal conductivity of blade tip material=0.18 W/m K
LE = leading edge of the blade
P = local static pressure

P_{avg} = averaged static pressure
P_t = total pressure at the inlet
P/S = pressure side of the blade
S/S = suction side of the blade
t = transition time for liquid crystal color change
T = thickness of the rim, mm
TE = trailing edge of the blade
T_i = initial temperature of the blade tip surface
T_∞ = mainstream temperature of the flow
T_w = color change temperature of the liquid crystal, green-to-red
Tu = turbulence intensity level at the inlet
X = axial distance, cm
α = thermal diffusivity of tip material $= 1.25 \times 10^{-7}$ m^2/s

References

[1] Metzger, D. E., Bunker, R. S., and Chyu, M. K., 1989, ''Cavity Heat Transfer on a Transverse Grooved Wall in a Narrow Flow Channel,'' ASME J. Heat Transfer, **111**, pp. 73–79.

[2] Chyu, M. K., Moon, H. K., and Metzger, D. E., 1989, ''Heat Transfer in the Tip Region of Grooved Turbine Blades,'' ASME J. Turbomach., **111**, pp. 131–138.

[3] Heyes, F. J. G., Hodson, H. P., and Dailey, G. M., 1992, ''The Effect of Blade Tip Geometry on the Tip Leakage Flow in Axial Turbine Cascades,'' ASME J. Turbomach., **114**, pp. 643–651.

[4] Yang, T. T., and Diller, T. E., 1995, ''Heat Transfer and Flow for a Grooved Turbine Blade Tip in a Transonic Cascade,'' ASME Paper No. 95-WA/HT-29.

[5] Ameri, A., Rigby, D. L., and Steinthorsson, E., 1998, ''Effects of Squealer Tip on Rotor Heat Transfer and Efficiency,'' ASME J. Turbomach., **120**, pp. 753–759.

[6] Bindon, J. P., and Morphus, G., 1988, ''The Effect of Relative Motion, Blade Edge Radius and Gap Size on the Blade Tip Pressure Distribution in an Annular Turbine Cascade With Clearance,'' ASME Paper No. 88-GT-256.

[7] Bindon, J. P., 1989, ''The Measurement and Formation of Tip Clearance Loss,'' ASME J. Turbomach., **111**, pp. 258–263.

[8] Moore, J., Moore, J. G., Henry, G. S., and Chaudhury, U., 1989, ''Flow and Heat Transfer in Turbine Tip Gaps,'' ASME J. Turbomach., **111**, pp. 301–309.

[9] Yaras, M. I., and Sjolander, S. A., 1992, ''Effects of Simulated Rotation on Tip Leakage in a Planar Cascade of Turbine Blades: Part I—Tip Gap Flow,'' ASME J. Turbomach., **114**, pp. 652–659.

[10] Sjolander, S. A., and Cao, D., 1995, ''Measurements of the Flow in an Idealized Turbine Tip Gap,'' ASME J. Turbomach., **117**, pp. 578–584.

[11] Kaiser, I., and Bindon, J. P., 1997, ''The Effect of Tip Clearance on the Development of Loss Behind a Rotor and a Subsequent Nozzle,'' ASME Paper No. 97-GT-53.

[12] Mayle, R. E., and Metzger, D. E., 1982, ''Heat Transfer at the Tip of an Unshrouded Turbine Blade,'' *Proc. Seventh Int. Heat Transfer Conf.*, Hemisphere Pub., pp. 87–92.

[13] Metzger, D. E., Dunn, M. G., and Hah, C., 1991, ''Turbine Tip and Shroud Heat Transfer,'' ASME J. Turbomach., **113**, pp. 502–507.

[14] Ameri, A. A., and Steinthorsson, E., 1995, ''Prediction of Unshrouded Rotor Blade Tip Heat Transfer,'' ASME Paper No. 95-GT-142.

[15] Ameri, A. A., and Steinthorsson, E., 1996, ''Analysis of Gas Turbine Rotor Blade Tip and Shroud Heat Transfer,'' ASME Paper No. 96-GT-189.

[16] Ameri, A. A., Steinthorsson, E., and Rigby, D. L., 1999, ''Effects of Tip Clearance and Casing Recess on Heat Transfer and Stage Efficiency in Axial Turbines,'' ASME J. Turbomach., **121**, pp. 683–693.

[17] Ameri, Ali A., and Bunker, R. S., 2000, ''Heat Transfer and Flow on the First Stage Blade Tip of a Power Generation Gas Turbine: Part 2—Simulation Results,'' ASME J. Turbomach., **122**, pp. 272–277.

[18] Bunker, Ronald S., Bailey, J. C., and Ameri, A. A., 2000, ''Heat Transfer and Flow on the First Stage Blade Tip of a Power Generation Gas Turbine: Part I—Experimental Results,'' ASME J. Turbomach., **122**, pp. 263–271.

[19] Azad, Gm S., Han, Je-Chin, Teng, Shuye, and Boyle, Robert J., 2000, ''Heat Transfer and Pressure Distributions on a Gas Turbine Blade Tip,'' ASME J. Turbomach., **122**, this issue, pp. 717–724.

[20] Kline, S. J., and McClintock, F. A., 1953, ''Describing Uncertainties in Single Sample Experiments,'' Mech. Eng. (Am. Soc. Mech. Eng.), **75**, Jan., pp. 3–8.

Recommendations for Achieving Accurate Numerical Simulation of Tip Clearance Flows in Transonic Compressor Rotors

Dale E. Van Zante
Anthony J. Strazisar
Jerry R. Wood
NASA Lewis Research Center,
Cleveland, OH 44135

Michael D. Hathaway
US Army Vehicle Technology Center,
Cleveland, OH 44135

Theodore H. Okiishi
Iowa State University,
Ames, IA 50011

The tip clearance flows of transonic compressor rotors are important because they have a significant impact on rotor and stage performance. A wall-bounded shear layer formed by the relative motion between the overtip leakage flow and the shroud wall is found to have a major influence on the development of the tip clearance flow field. This shear layer, which has not been recognized by earlier investigators, impacts the stable operating range of the rotor. Simulation accuracy is dependent on the ability of the numerical code to resolve this layer. While numerical simulations of these flows are quite sophisticated, they are seldom verified through rigorous comparisons of numerical and measured data because these kinds of measurements are rare in the detail necessary to be useful in high-speed machines. In this paper we compare measured tip-clearance flow details (e.g., trajectory and radial extent) with corresponding data obtained from a numerical simulation. Laser-Doppler Velocimeter (LDV) measurements acquired in a transonic compressor rotor, NASA Rotor 35, are used. The tip clearance flow field of this transonic rotor is simulated using a Navier–Stokes turbomachinery solver that incorporates an advanced $k-\varepsilon$ turbulence model derived for flows that are not in local equilibrium. A simple method is presented for determining when the wall-bounded shear layer is an important component of the tip clearance flow field. [S0889-504X(00)02504-6]

Introduction

Tip clearance flows are of great engineering importance when designing modern axial fans and compressors because of their large impact on pressure rise, efficiency, and stability [1–3]. In recent years Navier–Stokes (NS) codes have become a common component of most modern design systems and attention has turned toward obtaining accurate clearance flow simulations using these codes. Detailed measurements obtained in 1994 on NASA Rotor 37 provided the turbomachine flow simulation community with the data necessary for CFD code assessment in the blade tip region of transonic compressors. These measurements have been used in code assessment efforts organized by ASME [4] and AGARD [5,6]. Suder and Celestina [7], Chima [8], Gerolymos and Vallet [9], and others have also used these measurements specifically to assess the accuracy of rotor tip clearance flow predictions.

A general recommendation coming from these exercises is that turbulent transport models result in more accurate clearance flow simulations than algebraic mixing length turbulence models because of the multiple length scales that exist in the clearance flow region. However, no clear recommendations about the grid topology or grid resolution required for accurate simulation of the tip clearance flow have yet emerged.

Whether or not accurate clearance flow simulations require gridding of the tip clearance gap at all, and if so how much gridding, is still an open issue. Currently there are three general methods for treating the tip clearance gap: (*i*) assuming flow periodicity across a nongridded region above the blade tip [10]; (*ii*) rounding the blade tip by distorting an H-type grid to fill the gap over the blade [11]; (*iii*) fully gridding the gap with a separate grid block. The ability to obtain accurate simulations with minimal or no gridding is desirable because gridding the gap requires increased computational resources due to the added complexity of multiple grid blocks and also increases the total number of grid points (30,000 additional grid points by Chima and 270,000 by Gerolymos and Vallet).

The objectives of the present effort are as follows:

- Determine the grid topology and density that result in an accurate simulation of the tip clearance flow.
- Assess the impact of grid topology on rotor operating range and performance predictions.

These objectives are met using a three-dimensional Navier–Stokes solver that incorporates an advanced $k-\varepsilon$ turbulence model derived for flows that are not in local equilibrium. Predictions are compared to laser anemometer data acquired at several axial locations within the blade passage of a transonic compressor. The laser data used in the present investigation provide a more complete view of clearance flow development than possible with the NASA Rotor 37 data used by previous investigators.

Experiment

LDV measurements were acquired in the NASA Lewis single-stage axial-flow compressor facility using NASA Rotor 35 operating in a rotor-only (no stator) configuration. The rotor has 36 blades, a hub–tip radius ratio of 0.70, an aspect ratio of 1.19, a tip solidity of 1.3, and an axial chord of 4.12 cm at the hub. The design and blade coordinates are found in [12]. Data were acquired at a tip speed of 363 m/s (80 percent design speed) at the near-peak efficiency operating condition. The total pressure ratio and efficiency at this operating condition are 1.44 and 92 percent, respectively. This operating condition was dictated by requirements for rotor/stator matching in a follow-on stage investigation as reported by Van Zante et al. [13].

The nominal tip clearance as measured with touch probes was 0.74 mm, which corresponds to 1.3 percent of rotor tip chord and 1 percent of rotor leading edge span. The touch probes only mea-

Contributed by the International Gas Turbine Institute and presented at the 44th International Gas Turbine and Aeroengine Congress and Exhibition, Indianapolis, Indiana, June 7–10, 1999. Manuscript received by the International Gas Turbine Institute February 1999. Paper No. 99-GT-390. Review chair: D. S. Wisler.

sure the ''tallest'' blade and provide no information about how similar the tallest blade is to the majority of blades or about the magnitude of variations in blade height. Blade heights for Rotor 37 were measured at the completion of testing as part of the ASME test case geometry documentation. In the present investigation, blade height uniformity is most important at the rotor leading edge, since this is the region that most influences the clearance flow. For Rotor 37, 21 of the 36 blade heights were within 0.051 mm (7 percent nominal gap height) of each other at the leading edge, which indicates good blade-to-blade uniformity. The difference in height between the tallest blade and the average of the group of 21 was 0.076 mm (10 percent nominal gap height). This indicates that the clearance value determined from the tallest blade is representative of that for the majority of blades for Rotor 37. Since Rotors 37 and 35 were designed and manufactured at the same time, the results of the Rotor 37 blade height measurements are considered representative for Rotor 35. In addition, detailed analysis of LDV measurements from individual blade passages (which is not presented herein) indicates no strong passage-to-passage flow field variations near the blade tip. The results presented herein, which are based on measurements and predictions for an ''average'' blade passage, are therefore considered to be representative of individual blade passages as well.

The compressor rotor massflow was measured using a calibrated orifice plate located far upstream of the compressor. Performance measurements were acquired using conventional static pressure and total pressure/temperature probes located upstream and downstream of the rotor. Overall performance was calculated by mass-averaging total temperature and energy-averaging total pressure across the annulus [12,13]. Measurement uncertainties are: massflow ± 0.3 kg/s, flow angle ± 0.5 deg, total pressure ± 100 Pa, total temperature ± 0.6 K.

A large window, which conformed to the three-dimensional shroud contour, provided optical access to the flowfield from one rotor chord upstream of the rotor to two rotor chords downstream. LDV measurements were made in detail in the outer 20 percent of span; see Fig. 1. Streamsurface surveys (+ symbols) were acquired at 73, 83, and 92 percent span. Cross-channel surveys (diamond symbols) were acquired near the leading edge, and at 33, 53, 72, and 92 percent rotor chord. Although the stator was not installed, measurements were also acquired at the axial locations corresponding to mid-rotor/stator gap and to the stator leading edge to assess what the tip flow field would be at these locations in the stage environment. The uncertainty in the LDV measurements is approximately ± 1.0 m/s for absolute velocity and ± 0.5 deg in absolute flow angle.

The LDV was configured as a two-channel laser system that acquired axial and tangential velocities simultaneously. For each velocity measurement the rotor position was determined from a shaft angle encoder and the data placed into the window corresponding to that shaft angle position. There were 184 windows across one rotor blade pitch. Typically 40,000 to 60,000 individual velocity measurements were acquired for each survey point. Since the measurements were not evenly distributed over all of the windows, the total number of measurements was chosen so as to insure that there was a minimum of 30 measurements in any window. The LDV data were ensemble averaged using one rotor blade pitch as the length scale. See Strazisar et al. [14] for more detail on the LDV data acquisition and reduction technique.

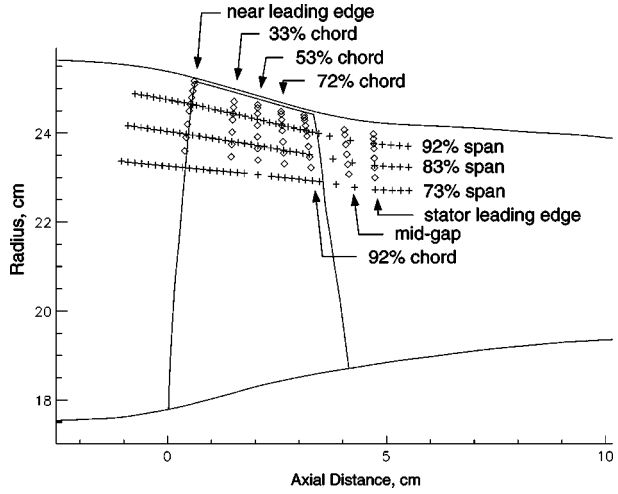

Fig. 1 LDV measurement locations for Rotor 35

LDV Data

Figure 2 shows contours of axial velocity for the 92 percent span streamsurface, which illustrate the lower extent of the flowfield region impacted by the tip clearance flow. Axial velocity is chosen here since the footprint of the clearance flow shows most clearly as gradients in axial velocity on this streamsurface. The projection of the clearance flow trajectory as determined from a detailed analysis of the measurements acquired across the blade pitch at different axial locations is superimposed on the contours as a dashed line. A passage shock can clearly be seen in the figure. Although the rotor is operating near peak efficiency, the shock is spilled forward of the leading edge because the rotor is operating at a part-speed condition.

Cross-channel contour plots of the absolute tangential velocity over the outer 20 percent of the blade span, Fig. 3, provide a more quantitative view of the trajectory and radial extent of the clearance flow. The clearance flow appears as a region of high absolute tangential velocity.

The clearance flow pattern immediately downstream of the clearance flow/shock interaction that occurs near midpitch is shown on the cross-channel plane at 33 percent rotor chord. The tip clearance flow extends radially to 92 percent span. This radial extent remains relatively constant as the clearance flow convects downstream. Farther downstream the clearance flow migrates toward the pressure surface of the adjacent blade, but does not accumulate on the pressure surface, as shown by the data at 92 percent chord. The tip clearance flow then merges with the rotor wake downstream of the rotor as shown by the data acquired at the mid-rotor/stator gap location in Fig. 3 (note the color scale change).

Also visible at 92 percent chord is a second region of elevated tangential velocity adjacent to the suction surface of the blade at the tip. This region is formed when clearance flow fluid from the adjacent passage leaks across the blade tip. We will refer to this feature as the secondary clearance flow to distinguish it from the primary clearance flow that accumulates in the pressure-surface/shroud corner of the passage. The secondary clearance flow is also visible at the mid-rotor/stator gap axial location and has migrated toward the pressure side of the adjacent blade passage. The secondary clearance flow was first identified by Suder and Celestina [7] in measurements and simulations of part-speed operating conditions in NASA Rotor 37. They attributed its presence to the entrainment of radially migrating suction surface boundary layer fluid by the overtip leakage flow in the rear of the blade passage. This secondary clearance flow is also present in the Rotor 37 design-speed simulation of Gerolymos and Vallet [9], who also predicted suction surface boundary layer migration near the tip of the blade. However, blade boundary layer migration is not predicted by any of our simulations. The secondary clearance flow therefore appears to be generic, is due to overtip leakage flow in the rear portion of the blade passage, and is not dependent on migration of suction surface boundary layer fluid.

Navier–Stokes Simulations

Three-dimensional time-averaged Navier–Stokes simulations of the flow through the compressor rotor were generated using the

Average Passage code (APNASA Version 1.11) developed by Adamczyk [15]. The turbulence model used in the simulations was developed by the Center for Modeling of Turbulence and Transition (CMOTT) at NASA Lewis and is a refinement of the standard $k-\varepsilon$ model. This refined model overcomes some of the deficiencies of the standard $k-\varepsilon$ model for flows that are not in local equilibrium. Details of the model and its implementation in the Average Passage code are discussed in [16].

A NASTRAN analysis of the rotor was performed for the 80 percent speed peak efficiency operating condition at which the LDV data were acquired so that the cold blade coordinates could be corrected for pressure, temperature, and centrifugal load deflections. This corrected ''as running'' geometry was used for all the Navier–Stokes simulations.

Shabbir et al. [17] showed that leakage flow from an axial gap between the rotor disk and the nonrotating hub flowpath upstream of the rotor can impact the axisymmetric flow over the entire span of this rotor. This effect arises from pumping of the blind cavity beneath this gap and is present even for zero net leakage flow through the gap. This effect was therefore modeled in the present work using Shabbir's scheme with the assumption of a net leakage of 0.25 percent of the throughflow, which Shabbir found to give the best agreement between simulated and measured performance at 80 percent speed.

While several grid methodologies are explored in this work, the overall character of the grids is similar for each method with variations between grids confined to the tip clearance region. A sheared H-grid topology is used. The blade-to-blade grid, shown in Fig. 4, is aligned with the blade camber angle near the leading edge and slowly turns to axial far upstream of the blade. This grid approximately follows the blade camber angle downstream of the blade. The grid has 71 nodes along the blade chord, which includes 10 nodes each on leading and trailing edge circles, 67–75

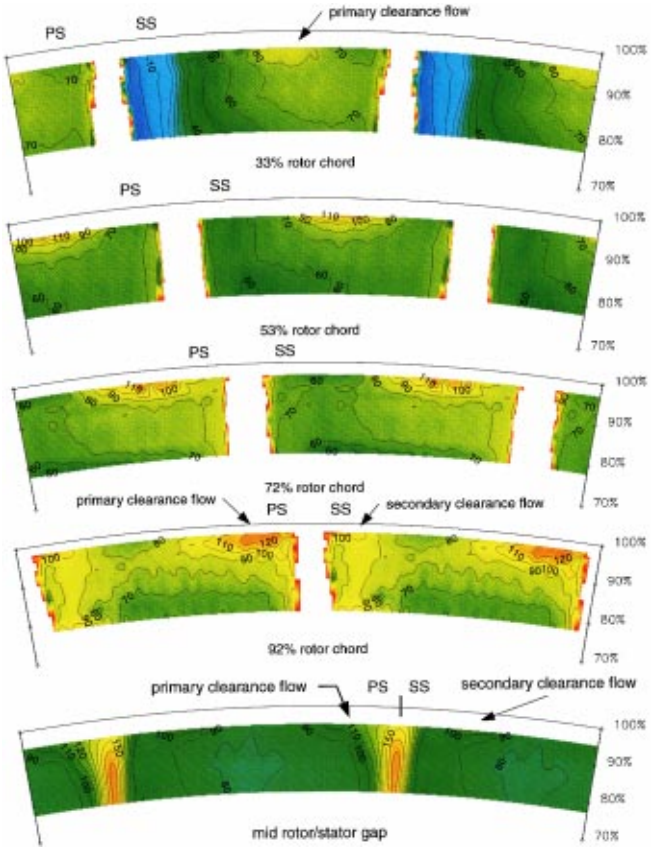

Fig. 3 Contours of tangential velocity (m/s) at 33, 53, 72, and 92 percent rotor chord and midgap from the LDV measurements

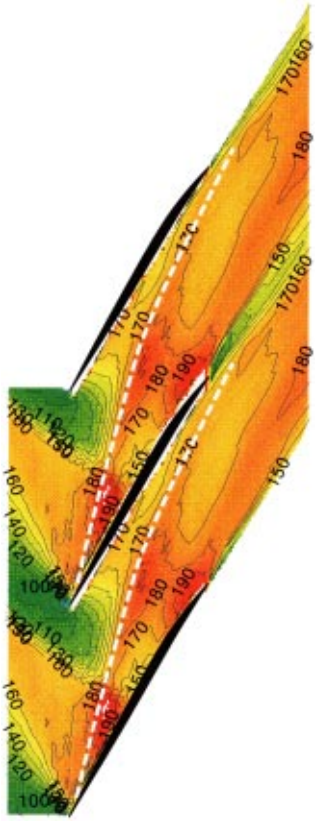

Fig. 2 Contours of axial velocity (m/s) on the 92 percent span streamsurface from the LDV measurements. The clearance flow trajectory is marked by the dashed line.

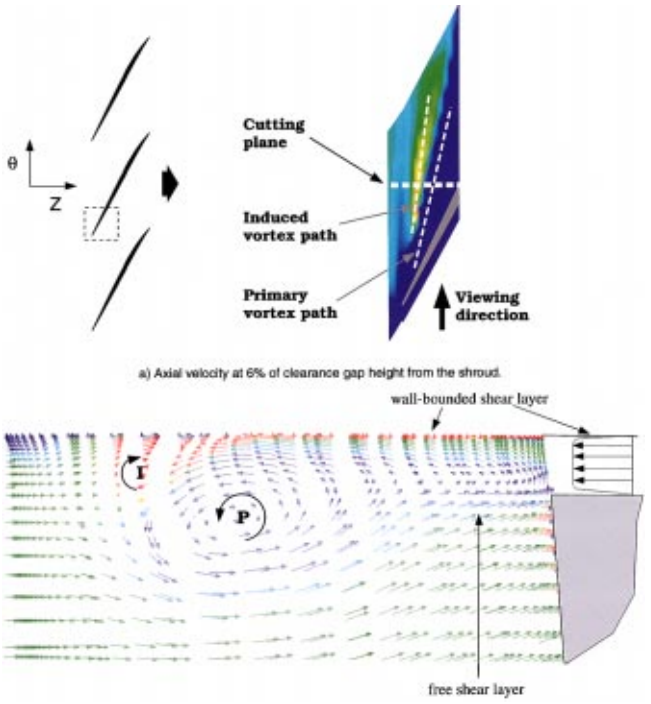

Fig. 8 Visualization of primary and induced clearance vortices

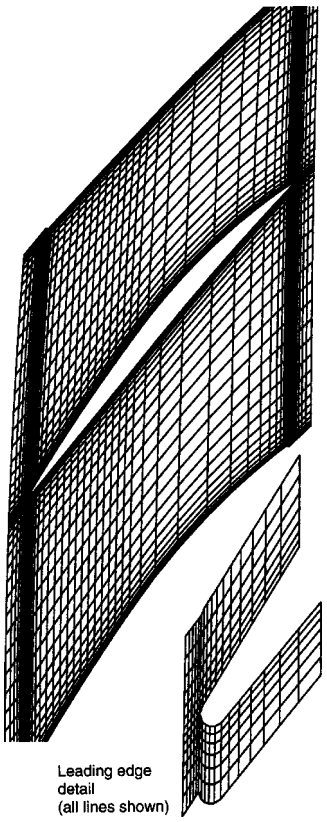

Fig. 4 Detail of rotor mesh at 50 percent span (every other grid line is shown)

nodes radially from the hub to the blade tip, and 51 nodes pitchwise. The axial grid density is doubled in the first 50 percent of rotor chord (to an average node spacing of 1.32 percent chord) to define the passage shock better.

Tip Grid Topology

Simulations were generated using several different grids in the clearance gap region to determine the most accurate simulation methodology. The grids and variations are summarized in Table 1 and Fig. 5. A uniform clearance of 1.3 percent chord is used for all grids. These grids were designed to help resolve the following issues:

- the effect of modeling versus gridding the tip clearance gap
- the effect of the near-shroud grid cell size in the radial direction

The baseline tip gridding scheme used in the present work is that proposed by Kirtley et al. [10]. A view of this type of tip grid, used in Configurations 1 and 3 (see Table 1), is shown in Fig. 5(*a*). This efficient scheme uses a periodic boundary across a non-

Table 1 Summary of clearance gap and grid topology variations investigated

Configuration	Number of cells in gap	Gap gridded or modeled	Radial grid spacing in the clearance gap
1	8	modeled	Constant cell size
2	8	gridded	Same as Configuration 1
3	12	modeled	Clustered at the shroud
4	12	gridded	Same as Configuration 3

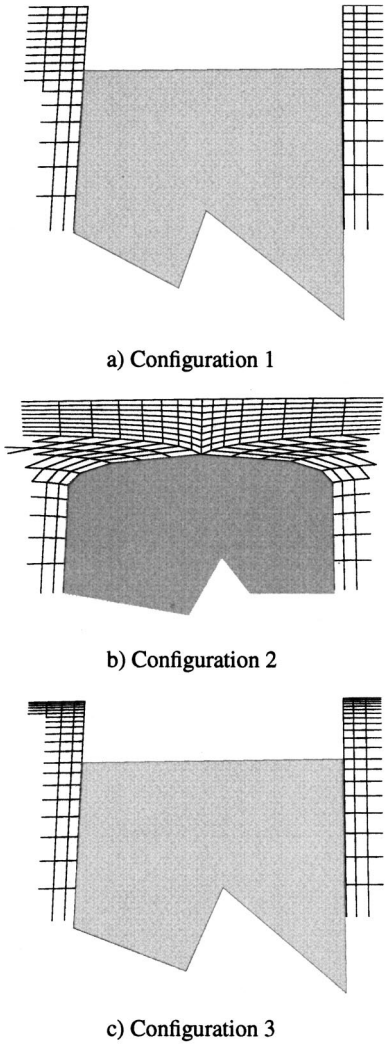

Fig. 5 Detail of mesh in the blade tip region

gridded region over the top of the blade tip to treat the clearance flow as an orifice flow with no change in mass, momentum, or energy across the blade tip. The region from the blade tip to the shroud is constructed by extending the grid from below the blade tip to the shroud while maintaining the tangential thickness of the blade. A benefit of this method is that it is simple to implement, since it does not require a multiblock grid topology or solver. Drawbacks include that the blade tip is implicitly assumed to be square edged, the overtip leakage flow direction is assumed normal to the blade pressure surface (no chordwise movement of clearance flow is allowed), and a discharge coefficient must be chosen to account for any vena contracta in the overtip leakage flow.

Tip grid Configuration 2, shown in Fig. 5(*b*), was generated to investigate differences between a fully gridded tip gap and the modeled gap treatment. This grid employs the same radial spacing in the clearance gap as that used for Configuration 1. The blade corners are rounded in this grid to avoid using a multiblock topology. The blade corner radius used was approximately 0.1 mm. This radius was measured on NASA Rotor 37 [6], which has the same aspect ratio, blade chord, tip speed, and flowpath as Rotor 35. Since Rotors 35 and 37 are so similar in design, they can be expected to exhibit the same blade tip erosion characteristics. The Rotor 37 blade corner radius is therefore considered to be a good approximation to the Rotor 35 corner radius.

To investigate the effect of the near-shroud grid density, a third

grid (Configuration 3) was generated with 12 grid cells nonuniformly spaced in the tip gap. This grid is shown in Fig. 5(*c*). Grid cells in the tip gap are clustered at the shroud and stretched toward the blade tip to maintain nearly the same number of cells on the blade span without violating standard grid stretching rules. This results in a cell size in the radial direction at the shroud which is only one-fourth of that used in Configuration 1 and a smooth stretching ratio variation from the tip gap to the blade. The pitchwise and chordwise grid spacings remained identical to those used previously. A fourth grid configuration (not shown) was generated using the gap-grid topology of Configuration 2 with the 12 cell nonuniform spacing of Configuration 3.

Chima [8] compared a fully gridded simulation of the tip gap to a modeled simulation for Rotor 37 at design speed. The fully gridded simulation indicated an expansion of the overtip leakage flow around the pressure surface/blade tip corner which caused the leakage flow to entirely fill the clearance gap. Gerolymos and Vallet [9] found a similar result. Based on these studies, we assume that a vena contracta does not exist in the overtip leakage flow. A discharge coefficient of 1.0 is therefore used for all simulations in which the gap is modeled.

Results

Near-Wall Grid Spacing Effects. Simulations generated with tip grid Configurations 1 and 3 were compared to assess the impact of the near-shroud grid spacing on simulation fidelity. Solutions for these two cases were converged to the same operating condition near peak efficiency. The predicted tip clearance flow trajectory and penetration are shown in Figs. 6 and 7, respectively. The trajectory of the clearance flow is illustrated in Fig. 6 using contour plots of the axial velocity on the grid plane corresponding to the blade tip. The clearance flow is indicated by two areas of low axial velocity: The shaded region denotes where the axial velocity is less than zero in the primary clearance flow, while the secondary clearance flow is identified as a locus of low axial velocity near the blade trailing edge. Comparison between Figs. 6(*a*) and 6(*b*) indicates that the clearance flow trajectory is more inclined in the streamwise direction when the near-shroud grid spacing is reduced. The clearance flow no longer impacts the pressure surface of the blade near midchord, but rather turns to be more parallel to the pressure surface, which is in closer agreement with the measured result shown in Fig. 2. This change in trajectory is explained in a later section.

The radial penetration of the clearance flow is shown in Fig. 7. Fluid from the primary clearance flow appears as a region of high tangential velocity near the corner formed by the shroud and the pressure surface in the rear of the rotor blade passage. Fluid from the secondary clearance flow can also be seen in the suction surface shroud corner. For Configuration 1 (Fig. 7(*a*)), the primary

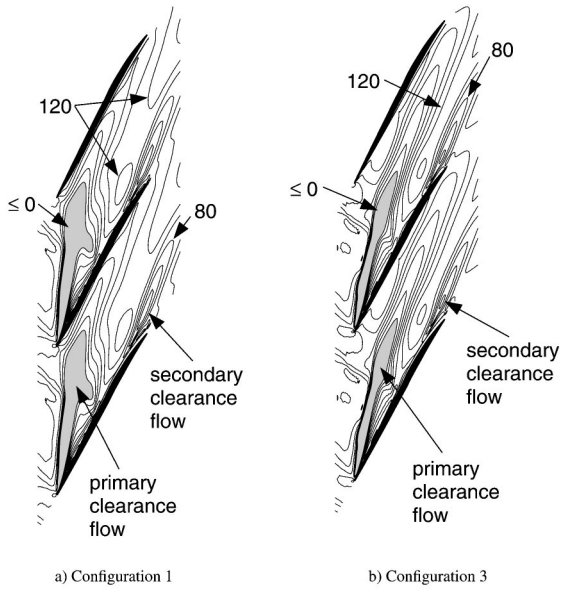

Fig. 6 Axial velocity contours (starting at 0 m/s with 20 m/s intervals) for the blade tip grid plane for configurations 1 and 3

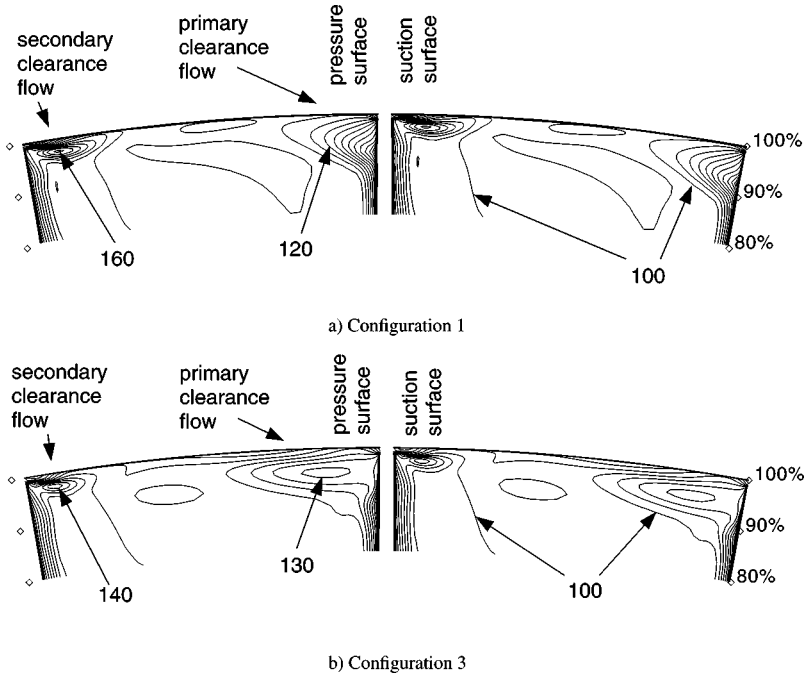

Fig. 7 Tangential velocity contours (10 m/s interval) for the outer 20 percent of span on the cross-channel surface at 92 percent rotor chord for configurations 1 and 3

clearance flow fluid appears closer to the blade pressure surface and has penetrated to lower immersions than shown by the measurements in Fig. 3. Predicted results downstream of the rotor (which are not shown here) indicate that the clearance flow merges with the pressure side of the blade wake for Configuration 1 and mixes quite slowly downstream of the rotor. This behavior does not agree with that observed in the measurements since the data shown in Fig. 3 at the mid-rotor/stator gap location show little indication of a well-defined clearance flow region.

Comparison between the simulations shown in Fig. 7 and the measurements shown at 92 percent chord in Fig. 3 indicates that a reduction in near-shroud grid spacing brings the simulation closer to the data. This is consistent with the conclusion drawn from Fig. 6 for the blade-to-blade plane at the blade tip.

Modeled Versus Gridded Clearance Gap. The solutions generated with tip grid Configurations 2 and 4 were used to assess the accuracy of the modeling methodology proposed by Kirtley et al. [10] and also the impact of rounded blade corners on the amount of overtip leakage flow. Calculation of the mass flow through the clearance gap indicates that the gridded gap cases allowed 30 percent more flow through the gap than the modeled cases. However, the trajectory and radial penetration of the clearance flow for Configurations 1 and 2 were not significantly different. The same was true when results from Configurations 3 and 4 were compared. We therefore conclude that rounding the blade tip and gridding the tip gap are not primary influences on solution fidelity.

Clearance Flow Development. The results presented above indicate that the increase in near-shroud grid resolution between Configurations 1 and 3 significantly alters the predicted trajectory of the clearance flow. Furthermore, the simulation generated with Configuration 3 agrees much more closely with the LDV data than that generated with Configuration 1. The increased resolution of Configuration 3 places four grid cells across the same distance from the wall as covered by the first grid cell in Configuration 1 while leaving the grid cell size at the blade tip virtually unchanged. A case with higher near-shroud grid resolution than Configuration 3 was also run but showed no further change in the clearance flow trajectory, indicating that the grid resolution of Configuration 3 is sufficient to achieve a grid-independent solution. The incoming boundary layer on the shroud and the computed wall shear stress are nearly identical in the Configuration 1 and 3 solutions, indicating that changes in the clearance flow trajectory are not due to different inlet conditions. The solutions were examined closely for any indication of numerical problems in the tip clearance region. No evidence of odd–even decoupling or inconsistencies in the wall shear stress calculated by the turbulence model was found. To understand why the increased spatial resolution of Configuration 3 has such a marked impact on the clearance flow trajectory, we therefore need to consider the fluid mechanic processes at work in the early development of the clearance flow.

Dean [18], Storer and Cumpsty [19], Chen et al. [20], and others have proposed that the formation of the clearance flow jet is predominantly an inviscid phenomenon driven by the pressure difference across the blade tip, wherein the overtip leakage jet and its associated free shear layer roll up into the main clearance vortex. While this is a good approximation in most cases, it neglects the fact that the tip leakage flow consists of two shear layers: (*i*) the free shear layer formed between the overtip leakage jet and the main through flow; (*ii*) a wall-bounded shear layer (WBSL) formed between the leakage jet and the shroud. The wall-bounded shear layer will be present whenever there is a velocity difference between the overtip leakage jet and the shroud in the relative frame of reference. Chima [8] alluded to the presence of the wall-bounded shear layer based on the trajectory of flow tracers he released at midheight in the clearance gap, but did not investigate the interaction between this shear layer and the free shear layer at the blade tip.

The role played by the wall-bounded shear layer in determining the trajectory of the main clearance vortex is illustrated in Fig. 8 using results generated with tip grid Configuration 3. The axial velocity distribution in a blade-to-blade plane that is two grid cells from the shroud is shown in the upper half of Fig. 8. This plane is located just 6 percent of the clearance gap height from the shroud (99.95 percent of the annulus height). Blue regions denote areas in which fluid is moving upstream (negative axial velocity). This fluid is the overtip leakage flow and its upstream motion has been well-documented by previous investigators. The red region denotes an area in which fluid is moving downstream with an axial velocity that is appreciably higher than that in the incoming boundary layer at this immersion. The origin of this high positive axial velocity can be understood by viewing the flow field on a $z-r$ cutting plane denoted by the white line. The projection of the relative velocity vectors onto this plane is shown in the lower half of Fig. 8 as viewed in the positive θ direction. The blade suction surface appears on the right edge of the plot. The velocity vectors are colored by their θ-component of vorticity. The overtip leakage jet forms a vortex centered at the point *P*. The sign of the θ-component of vorticity is negative (rotation in the counterclockwise direction in Fig. 8(*b*)). The wall bounded shear layer appears as the color red in Fig. 8(*b*). In the present case the sign of the vorticity in this shear layer is positive (clockwise rotation in Fig. 8(*b*)). This shear layer initially occupies only about 20 percent of the clearance height, but is then pulled away from the shroud by the vortex centered at *P* and forms a vortex centered at point *I*, which we will call the ''induced vortex.'' The paths of the primary clearance vortex (centered at *P*) and the induced vortex (centered at *I*) are shown in the blade-to-blade view in the upper half of Fig. 8.

The Configuration 1 solution (not shown here) indicates that the wall-bounded shear layer is not adequately resolved by the near-shroud grid spacing used in Configuration 1, while the results shown in Fig. 8 indicate that it is adequately resolved by that used in Configuration 3. Simulations were also done using the standard $k-\varepsilon$ turbulence model with Configuration 1 and 3 grids. The tip clearance flow trajectory in these solutions showed the same dependence on the near wall grid resolution. The standard $k-\varepsilon$ model responded differently than the CMOTT model to the large pressure gradients in the endwall region, which resulted in differences in the fine details of the flow field. However, the WBSL did not roll up into an induced vortex but instead created a stagnation point at the clearance jet/incoming flow interface. The clearance flow trajectory was still accurately predicted. Therefore, for both turbulence models, the WBSL is the most important feature to capture. Whether the WBSL rolls up into an induced vortex is of secondary importance.

One might ask, ''Does the WBSL-induced vortex *cause* a change in the clearance flow trajectory or is it merely an *effect* of the increased grid resolution?'' This issue was addressed by performing a numerical experiment using tip grid Configuration 3 in which the induced vortex was removed without making any other changes to the flow field. This was accomplished by removing the no-slip boundary condition at the shroud over the small region in which the induced vortex forms. This region is located from 2.5–18.5 percent chord and from 0–50 percent of the blade pitch from the suction surface. The wall-bounded shear layer that feeds the induced vortex cannot form without the no-slip boundary condition in this region. The results from this simulation are shown in Fig. 9 along with the region over which the no-slip boundary condition was altered. A detailed examination of the solution indicated that the incoming shroud boundary layer and the formation of the primary clearance flow were unchanged in these two simulations; only the WBSL was altered. With the WBSL removed the primary clearance flow moves forward in the blade

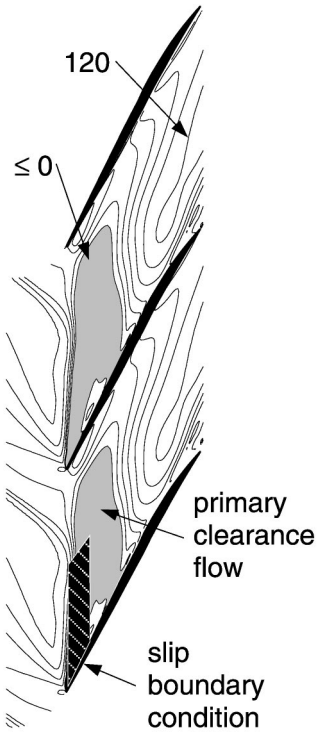

Fig. 9 Axial velocity contours (starting at 0 m/s with 20 m/s intervals) for the blade tip grid plane for configuration 3 with a slip boundary condition applied over the region shown

passage, clearly demonstrating that the WBSL is responsible for altering the tip clearance flow trajectory. Furthermore, a comparison of Figs. 9 and 6(*a*) suggests that the vortex trajectory predicted with tip grid Configuration 1 results from the fact that the wall-bounded shear layer is not adequately captured by the near-wall grid spacing used in Configuration 1. Inspection of cross-channel vector plots similar to Fig. 8 confirm that the induced vortex is not present in the Configuration 1 simulation.

If we consider the vorticity in the WBSL to be concentrated into the induced vortex, then the following kinematic argument can be used to understand why a change in the strength of the WBSL alters the trajectory of the main clearance flow. Both the primary and induced vortices require an image vortex in the shroud to satisfy the condition of zero normal velocity at the shroud. The mutual interaction between the primary vortex and its image acts to move the primary vortex axially upstream and away from the blade suction surface (to the left in the lower half of Fig. 8). Conversely, the mutual interaction between the induced vortex and its image acts to move the induced vortex axially downstream toward the blade suction surface. The circulation in each vortex will determine the equilibrium position of the primary and induced vortices. The circulation for each vortex was calculated for the solutions generated using Configuration 1 and 3 tip grids and for the solution with the slip boundary condition. The vortex strengths (in arbitrary units) are:

Configuration	1	3 (no-slip b.c.)	3 (slip b.c.)
Primary vortex circulation, P	199,200	223,800	238,400
Induced vortex circulation, I	14,200	77,300	0.0
Ratio, I/P	7 percent	35 percent	0 percent

The circulation of the primary vortex increases by about 10 percent in Configuration 3 relative to Configuration 1. Taken by itself, this change would act to move the primary vortex farther

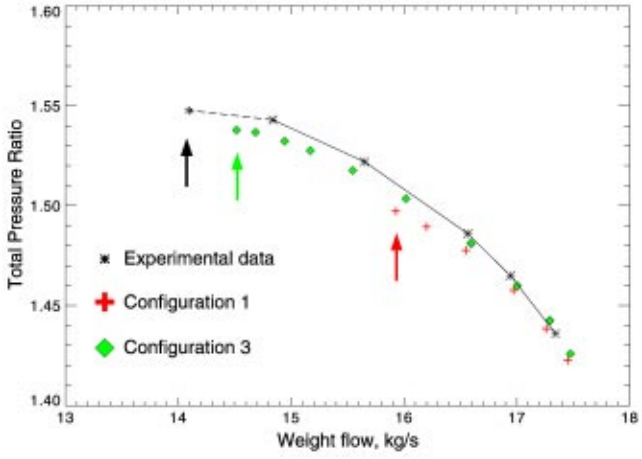

Fig. 10 Comparison of computed and measured operating range for Rotor 35 at 80 percent speed

upstream, away from the suction surface. However, this change is more than offset by the increased strength of the induced vortex in Configuration 3. The net effect of the changes in vortex strength between Configurations 1 and 3 is therefore a movement of the primary/induced vortex pair downstream toward the suction surface, which alters the trajectory of the primary clearance flow.

Operating Range Predictions. Hoying et al. [3] and Adamczyk et al. [2] suggest that rotor stall occurs when the tip clearance vortex spills forward of the leading edge, thereby linking the clearance vortex path to rotor stability. Since our tip grid topology impacts the clearance trajectory, this also implies a link between our grid topology and the predicted stability. Figure 10 shows the 80 percent speed line for Rotor 35 calculated with configuration 1 and 3 grids. The stall point for both simulations and the experiment are marked with arrows. The results confirm a large effect on predicted operating range with configuration 3 showing a much better match to experiment.

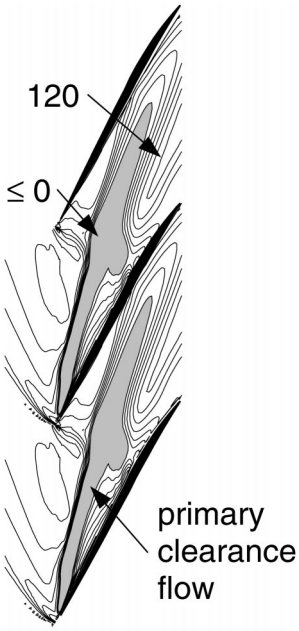

Fig. 11 Axial velocity contours (starting at 0 m/s with 20 m/s intervals) for the blade tip plane for design speed with a grid similar to configuration 3

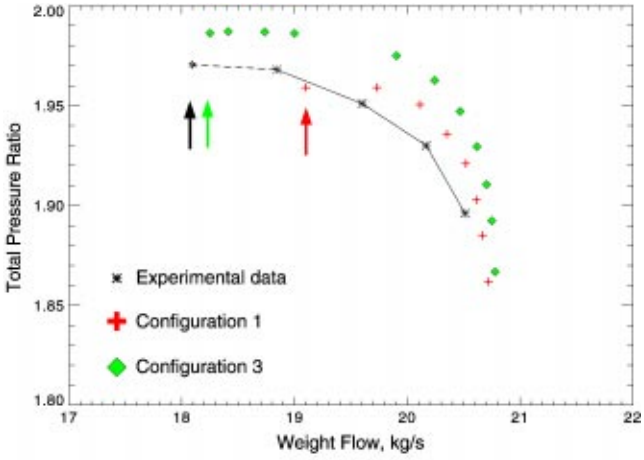

Fig. 12 Comparison of computed and measured operating range for Rotor 35 at design speed

Simulations of Rotor 35 at design speed also show a sensitivity to grid spacing near the wall. Figure 11 shows the clearance flow trajectory for a calculation done with a mesh similar to Configuration 3. Note that the clearance flow does not reach the pressure surface of the adjacent blade until near the exit of the blade passage. This trajectory is a good match to LDV data [21]. In simulations with a mesh similar to configuration 1, the clearance flow moves quickly across the passage (similar to Fig. 6(*a*)) indicating that the presence of a wall bounded shear layer is still important at design speed.

As at part speed, the position of the clearance flow has an influence on the calculated stable operating range. Figure 12 shows the 100 percent speed line which confirms the effect of the clearance flow trajectory on operating range.

The simulation results in Figs. 10 and 12 indicate that the induced vortex has a strong impact on the rotor stability. This indicates that rotor stability can be enhanced by increasing the strength of the induced vortex. As discussed in the next section, the strength of the induced vortex is directly proportional to the speed of the overtip leakage jet.

Velocity Difference Parameter. It is instructive to consider under what conditions the wall-bounded shear layer plays a determining role in the development of the tip clearance flow. The relationship between the leakage jet velocity and the shroud velocity in the relative frame is shown in Fig. 13. The velocity vector lengths and leakage flow angle are drawn to scale, using the blade tip speed and the leakage velocity at midheight in the clearance gap from the Configuration 3 simulation. Let us define a normalized velocity difference between the shroud and leakage jet by the parameter:

$$VD = (V\text{jet} - V\text{wall} \cdot \cos\gamma)/(V\text{wall}) \tag{1}$$

where Vwall is the blade tip speed and γ is the difference between the relative flow angle of the leakage jet and the tangential direction. Evaluating this parameter for Rotor 35 at the 80 percent speed, peak efficiency operating condition simulated herein we find $VD = 0.40$. The sign of this velocity difference determines the sign of the vorticity in the wall-bounded shear layer. When the velocity difference is greater than zero, as in the present case, the θ-component of vorticity is positive and is of opposite sense to that in the free shear layer and the incoming shroud boundary layer. When the velocity difference is less than zero, the θ-component of vorticity in the wall shear layer will be of the same sense as that in the free shear layer. When this velocity difference is small, the wall-bounded shear layer will be weak and will not exert a strong influence on the primary leakage flow. In such cases an inviscid approximation can be used for the leakage jet and a computational grid with relatively few points in the clearance gap will yield an accurate leakage flow simulation.

To check the generality of the criteria set forth above, two additional compressor rotors were simulated. In each case solutions were generated with near-shroud grid spacings representative of those used in Configurations 1 and 3 of the present work, and the results were analyzed for both the presence of the induced vortex and for changes in the primary clearance flow trajectory as near-shroud grid resolution was increased. The first additional case is Rotor 35 at the design speed, near the peak efficiency operating condition. The total pressure ratio, efficiency, and tip speed for this case are 1.90, 86 percent, and 454 m/s, respectively. The velocity difference parameter for this case is $VD = 0.2$ and the solutions show the presence of an induced vortex, which alters the clearance flow trajectory when adequate near-shroud grid resolution is used. Simulations performed close to stall further indicate that the induced vortex impacts the predicted stall point at design speed to nearly the same degree as at 80 percent speed as shown in Figs. 10 and 12. The second additional case is the rotor in the NASA-Lewis LowSpeed Axial Compressor (LSAC), which is a low-speed four-stage model of the General Electric Energy Efficient Engine compressor rear stages [22]. The total pressure ratio and tip speed for this case are 1.042 and 61 m/s, respectively. The velocity difference parameter for the LSAC is $VD = 0.05$, and refining the grid in the tip gap had no significant impact on the clearance flow. Based on these limited cases, values of the velocity difference parameter on the order of 0.2 or higher indicate the presence of a wall-bounded shear layer of sufficient strength to impact the primary clearance flow trajectory. A wider range of rotors needs to be investigated before a more general conclusion can be reached.

In the preceding discussion, the velocity difference parameter, VD, was evaluated using information obtained from the CFD solution itself. When starting the analysis of a new rotor, it would be useful to have an a priori estimate of VD to serve as guidance in selecting the proper near-shroud grid resolution. Such an estimate can be obtained using the leakage jet velocity approximation provided by Khalsa [23]. Based on the formula of Khalsa written in the relative reference frame, the leakage flow angle relative to the blade stagger angle for incompressible flow is:

$$\alpha = \tan^{-1}\left(\frac{Vl}{Vsw}\right) = \tan^{-1}\left(\sqrt{\frac{(P_{T\,\text{rel}} - P_{SS})}{(P_{T\,\text{rel}} - P_{PS})}}\right) \tag{2}$$

where

Vl = leakage velocity normal to blade surface
Vsw = leakage velocity tangent to blade surface
$P_{t\,\text{rel}}$ = relative total pressure on pressure surface
P_{SS} = static pressure on suction surface
P_{PS} = static pressure on pressure surface

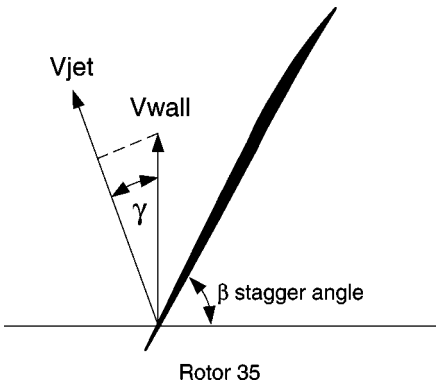

Fig. 13 Relation of the clearance jet velocity and the shroud-wall velocity in the relative reference frame

Noting that *V*jet and *V*wall in Eq. (1) are equal to $Vl/\sin\alpha$ and *U*tip (the blade speed) respectively, one can obtain the following expression for *VD* involving only blade geometry and surface loading parameters:

$$VD=(Vl-U\text{tip}\sin(\beta+\alpha)\sin\alpha)/(U\text{tip}\sin\alpha) \tag{3}$$

where β is the stagger angle. For incompressible flow the leakage velocity can be computed as (ρ is density):

$$Vl=\sqrt{(2(P_{T\,\text{rel}}-P_{SS}))/\rho_{SS}} \tag{4}$$

Equations (2)–(4) can be evaluated with information obtained from the blade design process so that the value of the velocity difference parameter is known prior to grid generation for a Navier–Stokes simulation.

Conclusions

The tip clearance flow field of NASA Rotor 35 was simulated using a Navier–Stokes turbomachinery solver to determine the impact of grid topology and tip gap treatment on solution fidelity. Detailed laser anemometer measurements of the rotor tip clearance flow field were used as a basis for comparison between the measured and predicted clearance flow trajectory and radial extent. The following conclusions are drawn from these comparisons:

- Gridding the tip gap does not yield any significant advantages in solution accuracy compared to using a simple tip clearance model. Accurate clearance flow predictions can be generated without gridding the gap and we recommend that the computationally efficient tip clearance model of Kirtley et al. [10] be used for thin blades typical of most compressors.
- When the relative velocity difference between the leakage jet and shroud is large, a wall-bounded shear layer is an important component of the tip clearance flow. Because this shear layer impacts the trajectory of the primary clearance flow, adequate resolution of the wall- bounded shear layer is critical to achieving accurate clearance flow predictions.
- The wall-bounded shear layer can have a major impact on the rotor stability depending on its strength. Therefore, accurate prediction of stable operating range requires careful attention to grid resolution near the casing. Increasing the relative velocity difference between the leakage jet and shroud strengthens the shear layer and increases the stable operating range. Rotor designs that enhance this velocity difference should demonstrate increased stability.

Appendix: Total Temperature Distributions in the Tip Region

CFD simulations of tip clearance flow generated during the ASME and AGARD CFD assessment exercises on NASA Rotor 37 display a temperature excess in the blade tip region compared to temperatures measured downstream of the rotor with thermocouple probes, as summarized by Dunham and Meauze [5], AGARD [6], and Denton [4]. This overshoot has been attributed to an inability to model the tip clearance flow correctly and results in a significant underestimation of the efficiency in the outer 10–20 percent of blade span. It is therefore important to determine whether the predicted temperature excess is ''real'' or represents a deficiency in the CFD modeling. The Rotor 37 temperature measurements were acquired far downstream (almost two chords) of the blade trailing edge. While thermocouple measurements of temperature can be acquired closer to the rotor trailing edge, conventional instrumentation often yields questionable results within one chord of the rotor due to the highly unsteady flowfield. Additionally any measurement made downstream of the rotor will be impacted by mixing, which is difficult to accurately predict with CFD.

The LDV data acquired within the rotor during this investigation provide more detailed measurements in the tip clearance flow region then were available for Rotor 37 and thus provide a unique opportunity to assess the accuracy of CFD predictions of temperature rise in the rotor tip region. To address this issue, the tangential velocity measured by the LDV system is used to calculate the total temperature within the tip clearance flow field using the Euler turbine equation. This derived fluid temperature is then used to provide a more accurate assessment of the simulation fidelity than is possible using temperature measured far downstream.

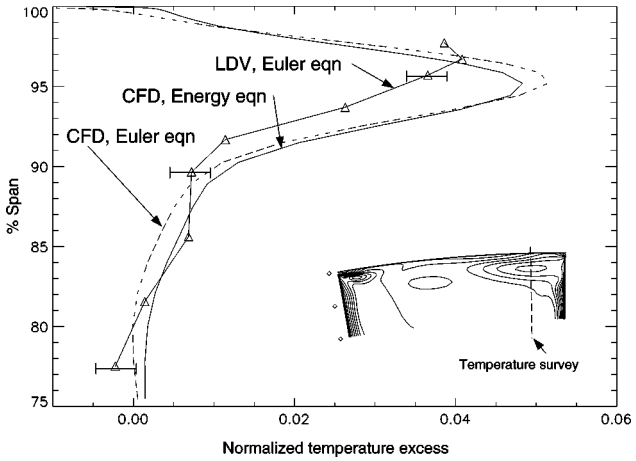

Fig. 14 Total temperature excess of the clearance flow at 92 percent rotor chord along the survey line shown

One normally obtains the temperature predicted by a CFD simulation from the energy equation. However, in order to provide a back-to-back comparison with the derived fluid temperature as measured by the LDV system, we will obtain the CFD-predicted temperature using the predicted tangential velocity and the Euler turbine equation. This Euler-derived temperature will be slightly different near the shroud than that obtained from the energy equation. This is due to the fact that the Euler turbine equation assumes that rothalpy is conserved, an assumption that is not valid near the wall because of the shear work done on the fluid by the moving shroud wall in the relative frame of reference.

A quantitative comparison between the measured and predicted total temperature is obtained by displaying the results along a radial line that cuts through the center of the primary clearance flow at 92 percent blade chord. The Euler-derived measured temperature distribution is compared to the predicted (Configuration 3) temperature distribution in Fig. 14. Predicted temperatures obtained from the energy equation and derived through the Euler equation are both shown. The survey line for these results is shown in the inset of Fig. 14. The local levels of the measured and predicted temperatures are somewhat different over the outer 20 percent of the blade span. All temperatures are therefore shifted such that the Euler-derived measured and predicted temperatures match at 80 percent span. The abscissa in Fig. 14 is therefore the normalized temperature excess:

$$(T(r)-T_{80})/T_{\text{std}} \tag{5}$$

where $T(r)$ is the temperature at radius r along the survey line, T_{80} is the temperature at 80 percent span along the survey line, and $T_{\text{std}}=288.2$ K.

The comparison shown in Fig. 14 confirms for the first time that a CFD simulation accurately predicts the local temperature excess associated with the increased turning in the clearance flow. The radial penetration of the clearance flow is also reasonably predicted. Other comparisons to simulations with nonuniform tip clearance are shown in Van Zante [21]. The overall temperature rise of the rotor is 12 percent of the inlet total temperature for the operating condition considered here. The temperature excess within the clearance flow is therefore significant since its magni-

tude corresponds to 25–35 percent of the overall temperature rise. The results shown here suggest that temperature measurements derived from velocities measured within the rotor may provide the most reliable data for future assessments of CFD simulation accuracy.

The results presented indicate that the choice of near-wall grid spacing has a significant impact on accurate prediction of the nonuniform temperature distribution that exists in the rotor as a result of the clearance flow. When the WBSL is not adequately resolved, the primary clearance flow accumulates on the adjacent blade pressure surface before reaching the rear of the blade passage, as shown in Fig. 6(*a*). The low axial momentum fluid of the clearance flow is then worked on by the adjacent rotor blade, further increasing its total temperature. This results in overprediction of the temperature rise in the tip region. Additionally, when the primary clearance flow accumulates on the adjacent blade pressure surface, the clearance flow merges with the pressure side of the blade wake and the total temperature excess in the clearance flow mixes very slowly downstream of the rotor. For axial blade spacings representative of those in modern multistage compressors, this results in a temperature excess entering the stator. These errors result from an inaccurate prediction of the primary clearance flow trajectory and will contribute to an underprediction of rotor efficiency. In a multistage environment these errors can build in successive stages possibly resulting in a large overprediction of temperature at the blade tip and casing at the exit of the compressor.

Acknowledgments

The authors wish to thank Tim Beach for his assistance with grid generation, John Adamczyk for much assistance in interpreting the solutions, Aamir Shabbir for assistance with the LSAC and design speed Rotor 35 solutions, Mark Celestina for guidance in running APNASA, and Nick Cumpsty for useful discussions. The first author thanks the National Research Council for their sponsorship during the execution of this research.

References

[1] Wisler, D. C., 1985, ''Loss Reduction in Axial Flow Compressors Through Low-Speed Model Testing,'' ASME J. Turbomach., **107**, pp. 354–363.
[2] Adamczyk, J. J., Celestina, M. L., and Greitzer, E. M., 1993, ''The Role of Tip Clearance in High-Speed Fan Stall,'' ASME J. Turbomach., **115**, pp. 28–38.
[3] Hoying, D. A., Tan, C. S., Vo, H. D., and Greitzer, E. M., 1999, ''Role of Blade Passage Flow Structures in Axial Compressor Rotating Stall Inception,'' ASME J. Turbomach., **121**, pp. 735–742.
[4] Denton, J. D., 1996, ''Lessons Learned From Rotor 37,'' presented at the 3rd International Symposium on Experimental and Computational Aerothermodynamics of International Flows (ISAIF), Beijing, China, Sept. 1–6.
[5] Dunham, J., and Meauze, G., 1998, ''An AGARD Working Group Study of 3D Navier–Stokes Codes Applied to Single Turbomachinery Blade Rows,'' ASME Paper No. 98-GT-50.
[6] AGARD, 1998, ''CFD Validation for Propulsion System Components,'' J. Dunham, ed., AGARD-AR-355.
[7] Suder, K. L., and Celestina, M. L., 1996, ''Experimental and Computational Investigation of the Tip Clearance Flow in a Transonic Axial Compressor Rotor,'' ASME J. Turbomach., **118**, pp. 218–229.
[8] Chima, R. V., 1998, ''Calculation of Tip Clearance Effects in a Transonic Compressor Rotor,'' ASME J. Turbomach., **120**, pp. 131–140.
[9] Gerolymos, G. A., and Vallet, I., 1999, ''Tip-Clearance and Secondary Flows in a Transonic Compressor Rotor,'' ASME J. Turbomach., **121**, pp. 751–762.
[10] Kirtley, K. R., Beach, T. A., and Adamczyk, J. J., 1990, ''Numerical Analysis of Secondary Flow in a Two-Stage Turbine,'' Paper No. AIAA-90-2356.
[11] Dawes, W. N., 1987, ''A Numerical Analysis of the Three-Dimensional Viscous Flow in a Transonic Compressor Rotor and Comparison With Experiment,'' ASME J. Turbomach., **109**, pp. 83–90.
[12] Reid, L, and Moore, R. D., 1978, ''Performance of Single-Stage Axial-Flow Transonic Compressor With Rotor and Stator Aspect Ratios of 1.19 and 1.26, Respectively, and With Design Pressure Ratio of 1.82,'' NASA TP 1338.
[13] Van Zante, D. E., Adamczyk, J. A., Strazisar, A. J., and Okiishi, T. H., 1997, ''Wake Recovery Benefit in a High-Speed Axial Compressor,'' ASME Paper No. 97-GT-535.
[14] Strazisar, A. J., Wood, J. R., Hathaway, M. D., and Suder, K. L., 1989, ''Laser Anemometer Measurements in a Transonic Axial-Flow Fan Rotor,'' NASA TP 2879.
[15] Adamczyk, J. J., Celestina, M. L., Beach, T. A., and Barnett, M., 1990, ''Simulation of Three-Dimensional Viscous Flow Within a Multistage Turbine,'' ASME J. Turbomach., **112**, pp. 370–376.
[16] Shabbir, A., Zhu, J., and Celestina, M. L., 1996, ''Assessment of Three Turbulence Models in a Compressor Rotor,'' ASME Paper No. 96-GT-198.
[17] Shabbir, A., Celestina, M. L., Adamczyk, J. J., and Strazisar, A. J., 1997, ''The Effect of Hub Leakage Flow on Two High Speed Axial Compressor Rotors,'' ASME Paper No. 97-GT-346.
[18] Dean, R. C., Jr., 1954, ''The Influence of Tip Clearance on Boundary-Layer Flow in a Rectilinear Cascade,'' MIT Gas Turbine Laboratory Report No. 27-3.
[19] Storer, J. A., and Cumpsty, N. A., 1991, ''Tip Leakage Flow in Axial Compressors,'' ASME J. Turbomach., **113**, pp. 252–259.
[20] Chen, G. T., Greitzer, E. M., Tan, C. S., and Marble, F. E., 1991, ''Similarity Analysis of Compressor Tip Clearance Flow Structure,'' ASME J. Turbomach., **113**, pp. 260–271.
[21] Van Zante, Dale E., Strazisar, Anthony J., Wood, Jerry R., Hathaway, Michael D., and Okiishi, Theodore H., 2000, ''Recommendations for Achieving Accurate Numerical Simulation of Tip Clearance Flows in Transonic Compressor Rotors,'' NASA TM 210347.
[22] Barankiewicz, W. S., and Hathaway, M. D., 1998, ''Impact of Variable-Geometry Stator Hub Leakage in a Low Speed Axial Compressor,'' ASME Paper No. 98-GT-194.
[23] Khalsa, A. S., 1996, ''Endwall Blockage in Axial Compressors,'' PhD. Dissertation, Massachusetts Institute of Technology, June.

Experimental Investigation of the Blade-to-Blade Flow in a Compressor Rotor by Digital Particle Image Velocimetry

N. Balzani

F. Scarano

M. L. Riethmuller

F. A. E. Breugelmans

Von Karman Institute for Fluid Dynamics, Rhode-St.-Genèse, Belgium

The purpose of this study is to investigate the blade-to-blade flow in an axial compressor, providing a detailed description of the entire flow-field on multiple layers through the use of Particle Image Velocimetry (PIV). Typical problems that relate to flow seeding, light-sheet generation, and camera-laser timing control are successfully dealt with, bringing additional knowledge in the domain. An extensive data set is analyzed to obtain statistical flow information (mean and fluctuating quantities). Spatial data reconstruction procedures allow the complete planar flow distributions to be determined. The multiplanar mean velocity field constitutes the final result of a three-dimensional reconstruction of the domain geometry and the proper introduction of the available planar measurements. [S0889-504X(00)00304-4]

Introduction

Rotor performance depends strongly on the blade-to-blade flow behavior, which in turn is strictly connected with the efficiency of a turbomachine. A better understanding of this flow is required to improve design and analysis computations. The requirement for experimental data in rotational flow increases with the development of advanced tools for numerical investigations.

Currently the range of flow measurement techniques, which can be used for turbomachinery, can be classified as intrusive, partially intrusive, and completely nonintrusive [1]. PIV works with seeding, which is an intrusive component: The application of this measurement technique in the study of rotating components of a turbomachine is very attractive because of all the difficulties encountered in these environments (centrifugal force acting on measurement probes, complex data acquisition and transmission) [2].

Currently stereo viewing optical configurations and holography present difficult implementations and constraints not suitable for turbomachinery environments.

Since the flow in the rotor of an axial compressor is mostly axisymmetric and defining axisymmetric streamsurfaces, it can be investigated through the use of a two-dimensional technique, such as PIV.

Particle Image Velocimetry is a nonintrusive measurement technique, which provides the simultaneous measurement of the velocity distribution over a planar domain. Small tracer particles are added to the flow and illuminated twice by a light-sheet produced by a laser. The orientation of the light-sheet plane is such that it contains the dominant flow direction. The light scattered from the particles is collected at 90 deg and recorded either on a single frame or on two different frames. After processing the double-exposed image or the two single-exposed images recorded, the displacement of particles is determined. From the time interval between the two exposures the magnitude of the velocity vector can be computed.

Since this technique measures the velocity of the tracers added to the flow, it is essential to achieve a uniform flow seeding with an optimum concentration. This difficulty becomes even more critical in a rotating environment. The main consequence of a nonuniform seeding is the spatial loss of data and consequently a low confidence level in the whole instantaneous measurement, losing one of the most important advantages provided by the technique.

The technique is not yet routinely applied in turbomachinery. Major reasons include difficult setup installations and the flexibility needed for the environment encountered.

The purpose of this work is to apply this technique for measurement on multiple layers, from the hub to the tip, in order to get the flow distribution in the three-dimensional geometry defined by the blade-to-blade channel. It is therefore of fundamental importance for this work to have a flexible setup, which provides improved performance of the PIV technique.

The high velocities encountered in rotating parts of a turbomachine and the request of highest spatial resolution image measurements has led in recent years to the use of the photographic technique as fully optical PIV or opto-digital PIV configuration. The consequence is very difficult and long image processing [3], not suitable for extensive measurement sessions. Recent technology developments have led to modern cross-correlation video cameras that allow the use of a frame straddling technique. This technique allows the time interval between single exposures to be decreased, increasing the range of velocity that can be analyzed. This opens an interesting possibility of applying electronic image acquisition systems to fast flow phenomena with an acceptable resolution and with an improved robustness for whole-field velocimetry in turbomachinery. Wernet [4] applied a complete digital system successfully in a transonic compressor. This work proposes and tests a setup developed in order to make possible the acquisition of data on multiple layers and fast image processing.

Measurements have been carried out in the axial compressor facility (R2) at von Karman Institute for Fluid Dynamics (VKI). The measurement planes investigated extend from the hub to tip every 10 mm at a rotational speed of 4000 rpm. For each plane the periodic blade-to-blade flow is deduced from the recorded set of PIV pictures of different blade passages with a random blade position. The optical periscope probe, proposed by Tisserant and Breugelmans [2] and already applied by Bryanston-Cross et al. [5] and Wernet [4], is successfully applied in the current investigation to generate and introduce the light sheet at different heights. A specific solution is proposed for the seeding supply system in order to meet the uniformity constraint. A description of the experimental setup and of the results obtained is presented.

Contributed by the International Gas Turbine Institute and presented at the 45th International Gas Turbine and Aeroengine Congress and Exhibition, Munich, Germany, May 8–11, 2000. Manuscript received by the International Gas Turbine Institute February 2000. Paper No. 2000-GT-55. Review Chair: D. Ballal.

Experimental Setup

The compressor facility R2 at VKI is a semi-closed-loop system for the testing of different axial-flow rotors. This experimental work is performed in a single-stage configuration and it concerns a single stage axial-flow rotor characterized by a tip diameter of 400 mm and a hub diameter of 200 mm. It consists of 24 subsonic blades of the NACA 65 family. The tip chord is 49 mm while the hub chord is 40 mm. The inlet provides an almost axial flow, while a stator mounted behind the rotor turns the exit flow axial and allows increasing the pressure rise in the compressor. The total–total compressor ratio is 1.1. The facility is characterized by a flat optical access window of 40 mm×40 mm installed in the casing. Its axis is inclined at 45 deg with respect to the horizontal plane, as shown in the sketch in Fig. 1 representing the cross section of the rotor.

The light sheet is introduced upstream of the optical access using the periscope probe, shown in Fig. 2. The advantage of this probe is the possibility to change and control the height of the light-sheet plane independently of the laser optics placement. The laser beam is deflected by two prisms, P, and meanwhile goes through a cylindrical negative lens (focal length of −19 mm) that generates the diverging light sheet from the incident beam.

Prism supports are manufactured with nylon. Recessed holes have been made to avoid local accumulation of energy in glass during the laser impact. One part is fixed on the casing; a nut allows the translating of the part containing the lens and the second prism with respect to the second part. As shown in Fig. 2, the outer prism remains always at the same height from the casing, while it is the inner one that goes up and down. Hence, there is no constraint affecting the location of the laser device: Moving the laser sheet at different locations in the blade channel, the laser device does not need to be moved. The periscope probe is inserted through the compressor casing upstream the measurement location. In Fig. 3 it can be noticed that the insert location of the probe

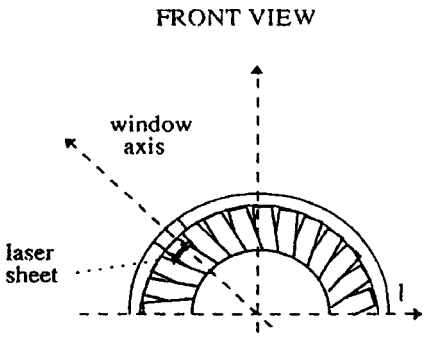

Fig. 1 Cut section of rotor

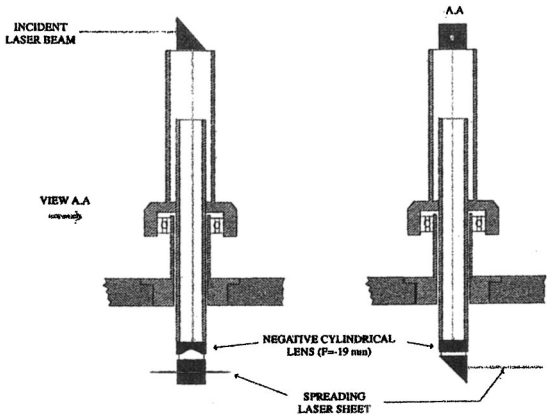

Fig. 2 Light-sheet forming probe

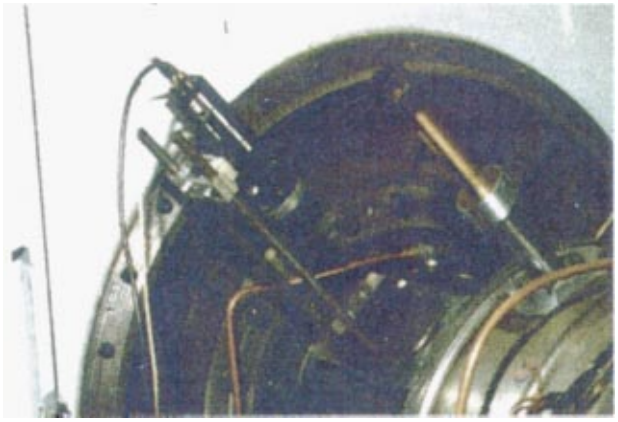

Fig. 3 Optical port and insert location of the periscope probe

is moved in the longitudinal direction along the casing with respect to the optical access port: This ensures that the probe wake does not interfere with the flow in the measurement plane.

From Fig. 2 it is also clear that with this kind of probe it is not possible to control the light-sheet thickness. To overcome this problem, a collimator is inserted in the optical path between the laser outlet and the inlet prism of the probe. This collimator is characterized by a convergent lens (focal length 200 mm) and a divergent one (focal length −100 mm) as shown in Fig. 4. The resulting light sheet is 40 mm wide×2 mm thick. The laser beam converges toward the focal point F_1 of the first convergent lens. Placing a divergent lens on the optical path just before F_1, it is possible to have a straight beam of a smaller diameter. The second divergent lens has to be placed upstream of the focal point F_1 at a distance from F_1 equal to the focal length f_2 of the second lens. The laser used is a double cavity Nd:Yag laser. It produces short duration (10 ns) high-energy (200 mJ) pulses of green coherent light (532 nm). The pulses are fired at 10 Hz. Using the PIV technique, a critical parameter for an accurate velocity measurement is the flow seeding. A uniform concentration is the optimal condition in order to achieve a high confidence level. Nevertheless, instantaneous and local loss of seeding can bring undesired loss of data (intermittence). Within a rotating environment, it is particularly difficult to achieve a uniform seeding with an optimal concentration.

In the present experiment, glycerine oil vapor mixed with air is used. The seed injection tube is located several tube diameters upstream of the measurement plane and externally to the inlet, adding a negligible disturbance to the test section. A smoke supply system (sketched in Fig. 5) provides particles that are injected into the flow through a diffuser placed on the front left side with respect to the compressor inlet, in such a way the seeded flow goes into the test section following inlet streamlines. The outflow from the smoke generator is first mixed with air before entering the diffuser. This solution allows the control of the smoke mass flow to be maintained and a better condensation of the smoke particles into droplets is observed. Since the seeded flow is not visible at the outlet of the diffuser (due to the low concentration for optimal PIV images), the correct placement of the smoke sup-

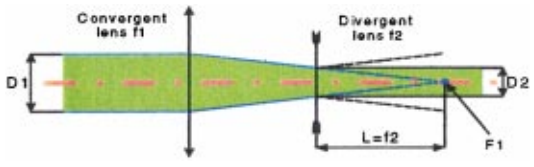

Fig. 4 Convergent–divergent lens system

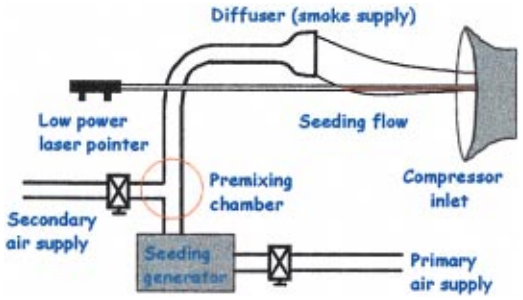

Fig. 5 Seeding system and laser pointer

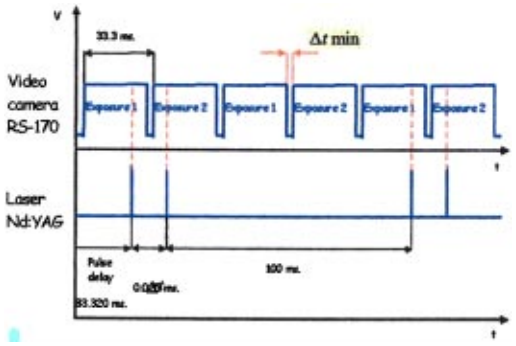

Fig. 6 Frame straddling approach

ply is particularly difficult. Thus a low power laser pointer is used to visualize the smoke stream ensuring the exact location of the seeded flow.

Moreover, the large contraction ratio of the facility induces a significant reduction of the seeded stream tube, meaning that the smoke outlet extent and the outlet concentration is not the same as in the measurement section. This makes the setting of particle concentration very difficult, underlying the necessity of working with an ''on-line'' technique. This last consideration introduces the choice of the recording device. It can be either a photographic or a video camera. The photographic film offers the highest spatial resolution for image measurements, although one has to keep in mind that the real particle image size does not correspond to the recorded one, due to the diffraction-limited imaging and to the optics between the recording device and the measurement location. Considering this effect and the resolution of modern video cameras, it is possible to obtain very similar performance with both devices [6].

In addition, the use of a video camera brings many other advantages compared with photographic film: namely, the immediate access to the recorded picture; this gives a real-time feedback of the flow seeding conditions and, more generally, of the measurement quality (exposure, focusing). Indeed, the photographic film needs to be developed, rinsed, and dried. Only after this may the film negatives be analyzed. Also, the analysis process (autocorrelation) is quite long (Young's fringes approach) unless one transfers the film into a digital form and processes it by autocorrelation, introducing a further step before obtaining the velocity field. The video mode directly provides an image in digital form, ready for immediate processing. The video method also has a very high sensitivity; usually it allows less laser energy to be used than with the photographic one.

Another very important factor should definitively influence the choice of a video camera. Indeed, while a photographic camera only allows the recording of multiple exposed pictures, a video camera allows single exposures to be recorded. The first advantage of this method of recording is that it enables a cross-correlation of successive corresponding interrogation cells to be carried out. Using cross-correlation algorithms, unlike autocorrelation ones, the evaluation yields the direction of the tracer displacements. It is also possible to cover a larger range of velocities, since there is no longer the limitation for the tracers to move sufficiently between two exposures in such a way that they do not overlap. Moreover, the signal-to-noise ratio obtained is usually higher than that obtained with autocorrelation algorithms.

At this point only one further question needs to be discussed. The usual working frequency of video cameras is 30 Hz. If the laser was pulsed once at the start of each video frame, the time between pulses would be 33 ms. High-speed flows cannot be measured on the basis of this time interval, which should be of the order of μs.

The architecture and the read-out electronics of modern cross-correlation cameras [7] give peculiar characteristics that make them useful for fast sequential acquisitions. At the end of the first exposure, all the pixel charges are moved to a buffer array simultaneously in the camera (shift register). The time for complete transfer of the charge is between 100 ns to some μs. Since the camera is always light sensitive and the charge representing the image is transferred shortly after the exposure, it is possible to obtain two separate frames illuminated in quick succession by exposing the camera a second time after the charge transfer is completed and during the read-out process. This can be achieved through the use of the so-called ''frame straddling'' approach (Fig. 6).

After the start of a video frame, the first laser pulse is delayed until just before the end of the frame exposure time. The second laser pulse happens just after the next frame exposure has started. When the time interval decreases to values comparable with the charge transfer time, the synchronization process becomes much more critical and a very accurate synchronizer is required. In this work the RS-170 cross-correlation camera is used. It is a camera having a CCD captor of 640×480 pixels. This camera has been equipped with a focusing lens (Micro Nikkor) having a focal length equal to 55 mm. The F-number is adjusted to 3.5. The time interval is fixed to 25 μs. This choice is imposed by the synchronizer.

To facilitate the camera positioning, it is mounted on a rigid rail support fixed on the viewing port and centered on the window axis. Since the camera belongs to a fixed reference frame, the measured velocity is the absolute one.

At 4000 rpm the smoke particles condense on the window of the optical access degrading it. To avoid this problem the shutter system designed by Tisserant and Breugelmans [8] is used (Fig. 7).

Data Processing and Averaging Velocity Vector Maps

The maximum expected velocity is evaluated around 95 m/s; these data are deduced from pressure measurements and confirmed by previous measurements done in the same facility con-

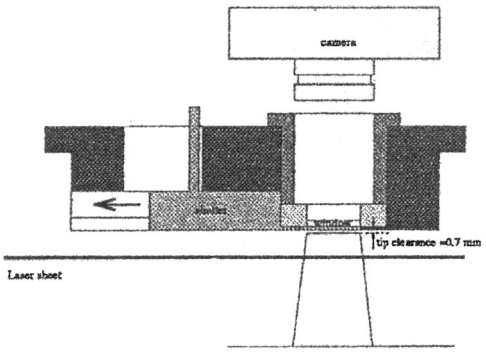

Fig. 7 Shutter system

figuration by Tisserant and Breugelmans [2]. The inter-frame time and the maximum expected velocity would not respect the ''one-quarter rule'' needed to apply cross-correlation successfully [9].

WIDIM (window displacement iterative multigrid) is used to process each image. It is a PIV evaluation method developed at VKI by Scarano and Riethmuller [10]. This software performs the cross-correlation analysis of PIV pictures by means of an improved cross-correlation method that allows de-coupling space-resolution and accuracy. It computes the two-dimensional and two-component velocity field distribution from pairs of pictures appropriately stored in digital form. At the current state of development, the program allows the cross-correlation technique to be applied to a pair of images by the window displacement and window distortion technique. Using this program, all recorded images have been processed successfully using interrogation areas of 32 $\times$32 pixels with 75 percent overlap.

The check for the validity of measured vectors is made evaluating the signal-to-noise ratio (highest correlation peak versus second highest peak) for each correlation map. Additionally, a local median operator is applied [11]; the deviation of the velocity from the local median is compared with the local rms; if their ratio exceeds the user threshold, the vector is considered erroneous [12].

The application of PIV, with an electronic image acquisition system, results in an extensive amount of data acquired for each radial station of interest. About 50 pairs of pictures are acquired for each station. The optical access does not allow the complete picture of the blade channel to be obtained: It is then necessary to superimpose all the different images acquired to obtain it. Moreover, some information is lost in instantaneous pictures due to seeding intermittence. The periodicity and steady flow conditions are the underlying hypotheses to superimpose different images at a given height.

Since the blade position is different from picture to picture, and considering the large number of instantaneous pictures acquired for each height, a fully automatic algorithm is needed to get the average flow. The algorithm developed for this application uses the flare light from the blade suction surface to calculate the offset between images recorded at the same height. Let us suppose that we are calculating the offset between the two images, recorded at different times, reported in Figs. 8(*a*) and 8(*b*). Plotting the light intensity profile along a vertical line at the same X_1 location for both images, one obtains the profiles on the right sides of Figs. 8(*a*) and 8(*b*). The peaks are in correspondence with the light impingement on the blade suction surface. Then the offset can be simply found as:

$$\text{Offset} = YP_5 - YP_3$$

where YP_5 and YP_6 are corresponding light impingement points on the blade suction surface, respectively, in Figs. 8(*a*) and 8(*b*). This offset detection procedure has been automated and it enables the superposition of all measured grids and computation of the average of data points located in the same position.

Results

From inlet pressure measurements (two chords before the leading edge) it is possible to evaluate the Reynolds number based on the chord and the inlet relative velocity. It is 1.66×10^5 at the hub and 2.43×10^5 at the tip for the rotational speed 4000 rpm.

The camera is fixed on the carriage support in such a way that the field of view covers most of the blade passage in the circumferential direction for all the measurement planes. An example of a single exposed picture is shown in Fig. 9. In the following pictures the flow direction is from right to left and the rotational speed is from bottom to top. In Figs. 10 and 11 a processed instantaneous velocity vector map at 50 mm from the hub is shown. Absolute velocity vectors are directed toward the blade suction surface.

Adding the rotor speed, the relative velocity field is obtained (Fig. 11) and the relative velocity magnitude is color coded. Vectors are represented with different spacing between Figs. 10 and 11 for a clear display. In particular, Fig. 11 shows the final grid spacing achieved with WIDIM.

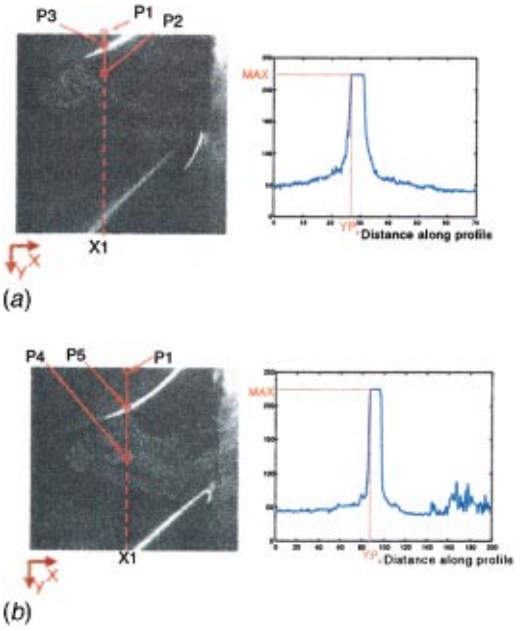

Fig. 8 (*a*) Image taken at time t_1; (*b*) image taken at time t_2

Fig. 9 Single exposed recorded plate

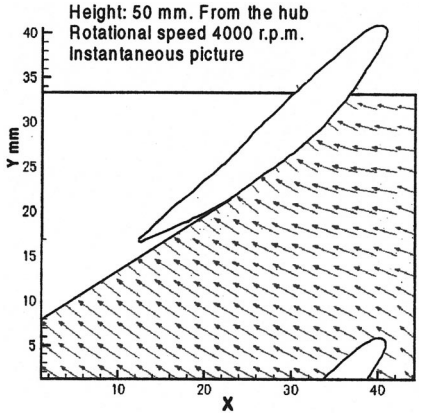

Fig. 10 Instantaneous absolute velocity field

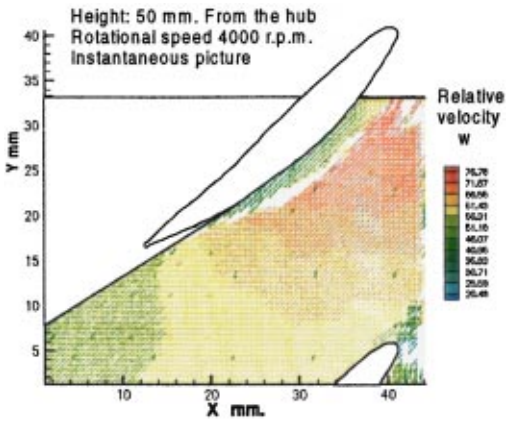

Fig. 11 Instantaneous velocity field

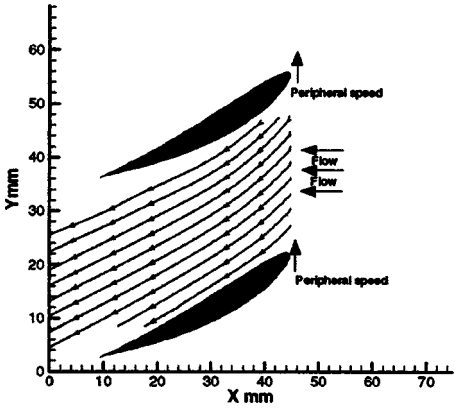

Fig. 14 Relative velocity field at 30 mm from the hub, averaging 65 pair images

The average velocity contour map (Fig. 12) and the average relative flow angle contour (Fig. 13) are obtained averaging the sets of the instantaneous velocity fields. The relative velocity field streamlines in the blade-to-blade channel visualizes the turning flow (Fig. 14). The following analysis is done at a height of 30 mm from the hub, performing the statistics over 65 field samples. Analogous considerations can be deduced for other heights.

It can be noticed from Figs. 12 and 13 that the periodicity condition is satisfied. The information found in neighbors' channels is obtained with the relative offset between pictures in the data reduction procedure. The mean velocity magnitude distribution is shown in Fig. 12, while the corresponding flow angle distribution is given in Fig. 13. The flow distribution exhibits a clear diffusion occurring in the channel. In the region just after the leading edge on the suction side, the flow reaches the maximum velocity and from there on it starts decelerating (Fig. 12). A higher flow turning on the suction surface is observed, as shown by the flow angle spatial distribution.

It is possible to analyze in detail the blade-to-blade channel flow, plotting the evolution of the relative Mach number and of the relative flow angle along two streamlines (one nearer to the blade suction surface and the other nearer to the blade pressure surface) (Figs. 15 and 16). Information along two vertical lines, crossing the channel behind the leading edge and behind the trailing edge respectively, is shown in Figs. 17 and 18.

The Mach number distribution versus the percentage of chord (Fig. 15) highlights a strong acceleration located at about 15 percent of the blade profile and a subsequent deceleration. This corresponds to a higher turning on the suction surface than on the pressure surface, shown in the relative flow angle distribution versus the percentage of chord (Fig. 16). A smaller relative flow angle is observed on the suction surface than on the pressure surface where the blade suction surface starts to be tilted. This explains the crossing point between the two profiles in Fig. 16.

The relative Mach number and relative flow angle evolution is confirmed by profiles plotted along vertical lines crossing the channel (Figs. 17 and 18). Here the parameter is plotted versus the percentage of the pitch. At the location measured behind the trailing edge, 20 percent chord from the trailing edge, it can be noticed that the flow is not completely mixed.

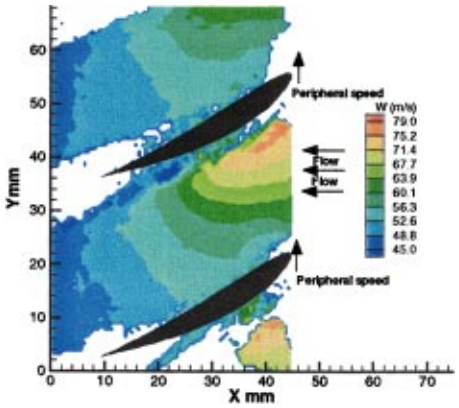

Fig. 12 Relative velocity contours at 30 mm from the hub, averaging 65 pair images

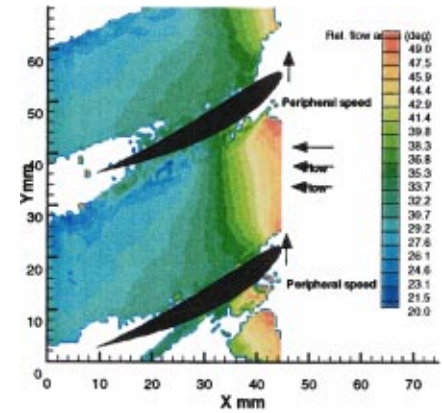

Fig. 13 Relative flow angle contours at 30 mm from the hub, averaging 65 pair images

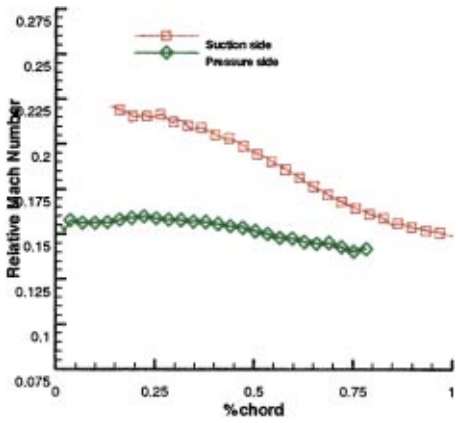

Fig. 15 Relative Mach number distribution from Fig. 12 (suction/pressure side)

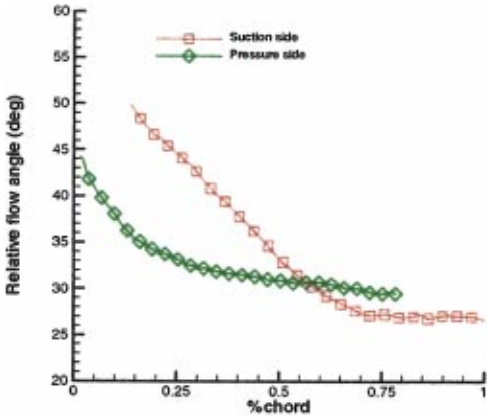

Fig. 16 Relative flow angle distribution from Fig. 13 (suction/pressure side)

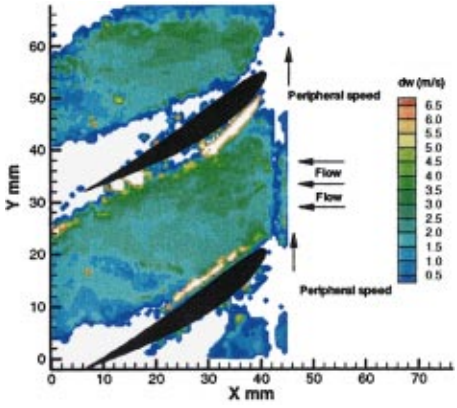

Fig. 19 Uncertainty evaluation of the relative velocity at 30 mm from the hub

The uncertainty of the presented results is evaluated taking into account the most important errors affecting the measurement. These errors arise mainly from the uncertainty related to the rotational speed (10 rpm), to the light-sheet positioning (1 mm) and to the camera field of view calibration. The statistical analysis is performed introducing these uncertainties directly into the averaging procedure. The standard deviation found also contains the effect of flow turbulence, estimated from hot-wire measurements at around 1 percent, and the error related to the data shift-and-average.

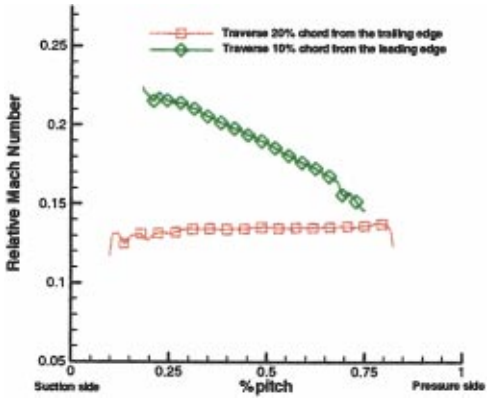

Fig. 17 Relative Mach number distribution from Fig. 12 (traverses crossing the channel)

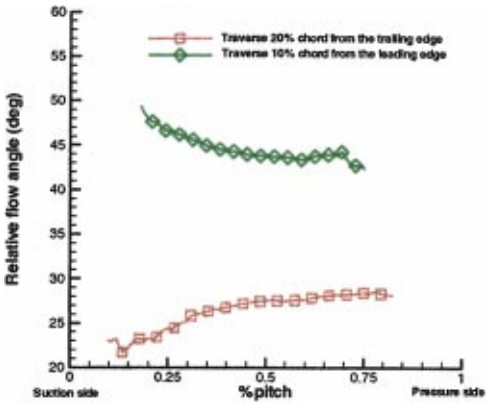

Fig. 18 Relative flow angle distribution from Fig. 13 (traverses crossing the channel)

With a 95 percent confidence interval, the uncertainty affecting the relative velocity measurement is less than 5 percent in most of the measurement domain. This result is obtained also in other measurement planes. However, an uncertainty increase near the blade suction side and from tip to hub is observed. This trend is caused mainly by light reflection phenomena and is larger on the blade suction surface than on the hub. As an example is presented in Fig. 19, the uncertainty affecting the measurement at 30 mm from the hub as a two-dimensional distribution.

Errors due to the three-dimensional flow motion (radial shift affecting streamlines and noncoincidence between the illumination plane and the stream surface) [2] and due to the image processing (0.1 pixel) [10] are found to be negligible with respect to the previous ones. Finally, there is an additional error from the averaging procedure that calculates the relative offset between two blades. The relative displacement is considered to lie on a plane. In reality, blades move in the circumferential direction. This error increases going from the tip to the hub; however, it is negligible with respect to the main errors.

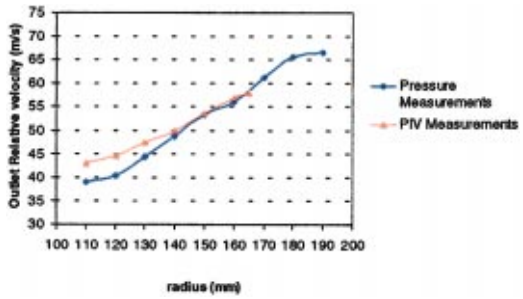

Fig. 20 Outlet relative velocity magnitude

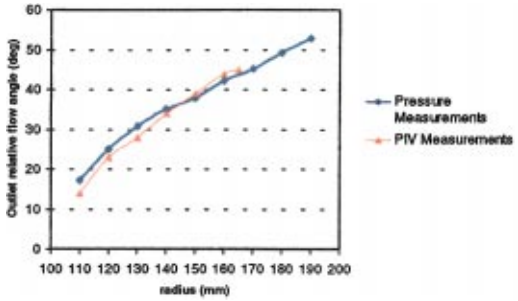

Fig. 21 Outlet relative flow angle magnitude

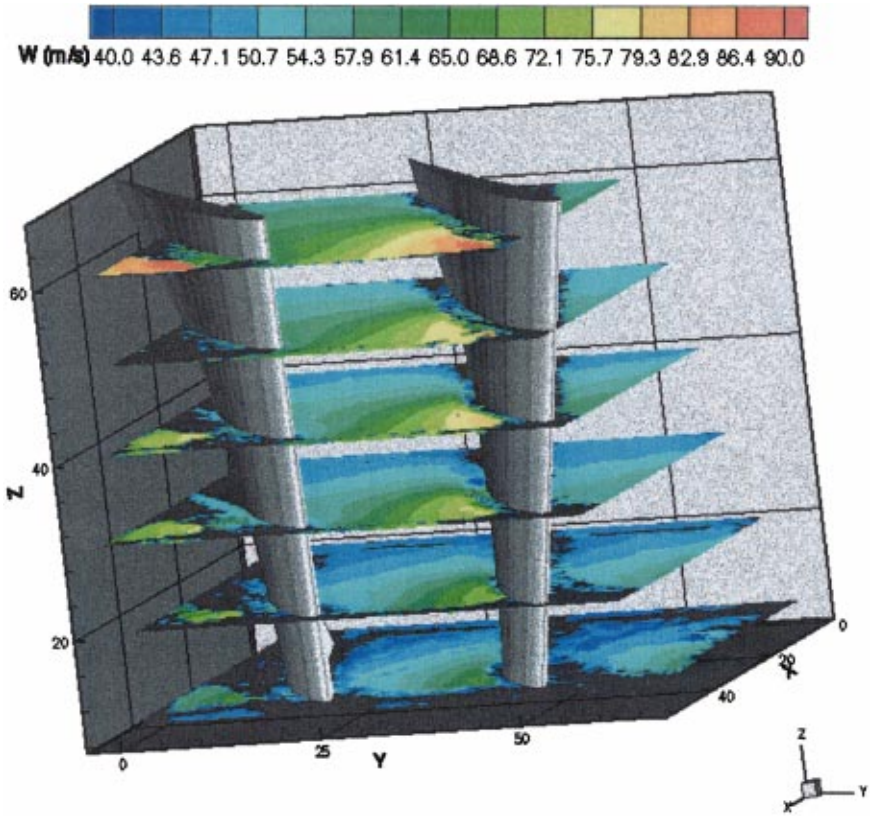

Fig. 22 Multiplanar picture; planes from 10 to 60 mm from the hub

The comparison between PIV measurements and pressure measurements is done behind the trailing edge. Outlet relative velocity profile and outlet relative flow angle measured by means of PIV (averaged values) and by means of conventional pressure measurements are compared (Figs. 20 and 21). The parameters are plotted versus the distance from the hub. Good agreement between the two techniques is observed. The little difference is justified by the fact that the outlet probe is located at about one chord downstream the leading edge, while PIV measurements are taken at a distance equal to 20 percent chord from the trailing edge, where incomplete flow-mixing is observed. Applying the whole processing procedure for the measurement planes investigated at different heights and defining the three-dimensional domain geometry, each measurement plane can be placed correctly in the three-dimensional geometry. This allows the multiplanar flow distribution of the blade-to-blade channel to be obtained. In Fig. 22 the relative velocity contours in the three-dimensional geometry are presented. Measurement planes from 10 mm to 60 mm far from the hub are shown.

The relative velocity magnitude increases going from hub to tip. The maximum relative velocity is reached in the region after the leading edge between 15–20 percent of the blade chord. It extends from 65 m/s up to 90 m/s, meaning that the flow increases its relative velocity by about 20 percent with respect to inlet relative velocity (detected by pressure measurements).

Conclusion

The blade-to-blade flow in an axial compressor is investigated on multiple layers through the use of a digital PIV.

This measurement technique shows its adequacy for this kind of investigation due to the ''on-line'' aspect that allows high flexibility and fast user feedback. Moreover, the electronic image recording allowed the use of an advanced image-processing algorithm yielding a significant improvement with respect to the predecessor photographic-optical PIV technique.

The periscope probe has been demonstrated to be a suitable tool for such applications, making the setup implementation easy and flexible. The main problem of controlling the light sheet thickness, related to the use of the available periscope probe, is solved by adding a light beam collimator, consisting of a convergent and a divergent lens, in the optical path.

As far as the seeding uniformity and concentration is concerned, the premixing chamber added to the smoke generator, the use of a laser pointer, and the ''on-line'' technique make it possible to achieve favorable seeding conditions.

An extensive data set has been analyzed obtaining statistical flow information (mean and fluctuating quantities). Spatial data reconstruction procedures allow complete planar flow distributions to be obtained. The multiplanar mean velocity field constitutes the final result of a three-dimensional reconstruction of the domain geometry and the proper introduction of the available planar measurements.

These experiments have demonstrated that digital PIV is well suited for turbomachinery applications; improvements expected in the hardware domain will allow even better synchronization of the laser, camera, and rotor. Moreover, the possibility of reducing the time interval between laser pulses will make it possible to analyze the flow field at higher speeds.

References

[1] Bryanston-Cross, P. J., Chana K. S., and Healey N., 1997, ''Particle Image Velocimetry Measurements From the Stator–Rotor Interaction Region of a High Pressure Transonic Turbine Stage at the DERA Isentropic Light Piston Facility,'' AGARD PEP Symposium on ''Advanced Non-Intrusive Instrumentation for Propulsion Engines.''

[2] Tisserant, D., and Breugelmans, F. A. E., 1997, ''Rotor Blade-to-Blade Mea-

surements Using Particle Image Velocimetry,'' ASME J. Turbomach., **119**, pp. 176–181.
[3] Westerweel J., 1993, ''Digital Particle Image Velocimetry—Theory and Application,'' Ph.D. Dissertation, Delft University Press, Delft.
[4] Wernet, M., 1997, ''Demonstration of PIV in a Transonic Compressor,'' AGARD PEP Symposium on ''Advanced Non-Intrusive Instrumentation for Propulsion Engines.''
[5] Bryanston-Cross, P. J., Towers, C. E., Judge, T. R., Towers, D. P., Harasgama, S. P., and Hopwood, S. T., 1992, ''The Application of Particle Image Velocimetry (PIV) in a Short-Duration Transonic Annular Turbine Cascade,'' ASME J. Turbomach., **114**, pp. 504–509.
[6] Willert, C. E., and Gharib, M., 1991, ''Digital Particle Image Velocimetry,'' Exp. Fluids, **10**, pp. 181–193.
[7] Raffael, M., Willert, C. E., and Kompenhans, J., 1998, *Particle Image Velocimetry, a Practical Guide*, Springer.
[8] Tisserant, D., and Breugelmans, F. A. E., 1995, ''Study of the Blade-to-Blade Flow in a Compressor Rotor Using PIV,'' presented at the SABE Conference, Melbourne, Australia.
[9] Keane, R. D., and Adrian, R. J., 1992, ''Theory of Cross-correlation Analysis of PIV Images,'' Appl. Sci. Res., **49**, pp. 191–215.
[10] Scarano, F., and Riethmuller, M. L., 1998, ''Turbulence Analysis on the BFS With Iterative Multigrid PIV Image Processing,'' *Proc. Ninth International Symposium on the Applications of Laser Techniques to Fluid Mechanics*, Lisbon, Portugal, pp. 22.5.1–22.5.8.
[11] Westerweel, J., 1994, ''Efficient Detection of Spurious Vectors in Particle Image Velocimetry-data,'' Exp. Fluids, **16**, pp. 236–247.
[12] Scarano, F., and Riethmuller, M. L., 1999, ''Iterative Multigrid Approach in PIV Image Processing With Discrete Window Offset,'' Exp. Fluids, **26**, No. 6, pp. 513–523.

Nonuniform Flow in a Compressor Due to Asymmetric Tip Clearance

Seung Jin Song
e-mail: sjsong@snu.ac.kr

Seung Ho Cho

School of Mechanical and Aerospace Engineering,
Seoul National University,
Seoul 151-742, Korea

This paper presents an analytical study of flow redistribution in a compressor stage due to asymmetric tip clearance distribution. The entire stage is modeled as an actuator disk and it is assumed that upstream and downstream flow fields are determined by the local tip clearance. The flow is assumed to be inviscid and incompressible. First, an axisymmetric flow model is used to connect upstream and downstream flows. Second, a linear perturbation approximation is used for nonaxisymmetric analysis in which each flow variable is assumed to consist of a mean (axisymmetric value) plus a small perturbation (asymmetric value). Thus, the perturbations in velocity and pressure induced by the tip clearance asymmetry are predicted. Furthermore, rotordynamic effects of such flow nonuniformity are examined as well. [S0889-504X(00)01404-5]

1 Introduction

Nonaxisymmetric tip clearance degrades both aerodynamic and structural performance of turbomachinery, and the tip clearance asymmetry can have many causes, such as rotor shaft bending, whirling, casing asymmetry, and deformation of components. The effects of rotor tip clearance asymmetry on turbine rotors were initially suggested by Thomas [1] and Alford [2]. They suggested that the variation in efficiency with local clearance would lead to a destabilizing forward whirl-inducing force. This suggestion was experimentally verified by Urlichs [3], Wohlrab [4], and Martinez-Sanchez et al. [5]. Martinez-Sanchez et al. also identified nonaxisymmetric pressure acting radially on the turbine hub as a second source of forcing mechanism in addition to the nonaxisymmetric torque initially hypothesized by Thomas and Alford. Analytically, Song and Martinez-Sanchez [6,7] developed an actuator disk model that could accurately predict both nonaxisymmetric torque and pressure effects in turbines.

To examine the effects of compressor tip clearance asymmetry, Horlock and Greitzer [8] and Colding-Jorgensen [9] formulated actuator disk models. Also, Ehrich [10] and Graf et al. [11] developed parallel compressor models. All of these models require compressor performance data as inputs. Therefore, Park [12] developed an analytical model to predict the effects of nonaxisymmetric rotor tip clearance in a single-stage compressor without empiricism. All the models predict a backward whirl-inducing force due to torque asymmetry at the design point. In addition, Park [12] predicts a forward whirl-inducing cross force due to pressure asymmetry.

Until now, attention has been focused only on the effects of rotor tip clearance asymmetry. However, real machines operate with tip clearances in both rotors and stators. Furthermore, the results from a recent experiment conducted in the Low Speed Research Compressor (LSRC) at GE [13] strongly suggest contributions from the stator tip clearance asymmetry.

Therefore, this investigation aims to understand the flow fields and rotordynamic effects in compressors caused by nonaxisymmetry in both rotor and stator tip clearances. The scope of current investigation is limited to the effects of static tip clearance asymmetry in a single stage compressor. An analytical actuator disk approach is used in this investigation.

2 Analytical Model

The modeling approach is similar to the approach of Song and Martinez-Sanchez [6,7]. A two-step process is used to solve for the flow through a compressor stage. First step is an axisymmetric, two-dimensional, meridional plane analysis, or the blade scale analysis. This analysis examines radial redistribution of flow due to axisymmetric rotor and stator tip clearances. The top part of Fig. 1 shows the blade scale view of the stage. Due to tip clearance flows, the radially uniform upstream flow is assumed to split into three streams–''*a*,'' ''*b*,'' and ''*c*''–upon going through the inlet guide vane (IGV), rotor, and stator. Streams ''*a*'' and ''*c*'' are associated with the rotor and stator tip clearances, respectively. Stream ''*b*'' is the rest of the passage flow, which has passed through the bladed part of both rotor and stator rows.

The second step is a nonaxisymmetric, two-dimensional, radial plane analysis. The tip clearance asymmetry is a nonuniformity with a length scale on the order of the compressor radius. Therefore, this latter analysis is referred to as the radius scale analysis. It examines the flow redistribution in the azimuthal direction caused by nonaxisymmetric tip clearance distribution. This view is shown schematically in the bottom part of Fig. 1. This analysis is a small perturbation (tip clearance asymmetry) analysis about the mean (axisymmetric) solution provided by the blade scale analysis. Therefore, the results from the blade scale analysis are perturbed to provide connecting conditions across the actuator disk.

The actuator disk in this study consists of an inlet guide vane (IGV) row, a rotor blade row, and a stator blade row. The IGV has full-span blades while rotor and stator have partial span blades. Axial, tangential, and radial directions are denoted by x, y, and z, respectively. On the blade scale, $-\infty$ refers to a location far upstream of the IGV. Near upstream of the IGV is referred to as Station 0. Inlet to the rotor is referred to as Station 1, and the rotor exit is called Station 2. Downstream of the stator row is called Station 3. Far downstream is referred to as $+\infty$. On the radius scale $x=0-$ and $x=0+$ are equivalent to $-\infty$ and $+\infty$ at the blade scale, respectively. The compressor's rotational speed, absolute velocity, and relative velocity are U, C, and W, respectively. α is the absolute flow angle, and β is the relative flow angle.

The model assumes an inviscid, incompressible flow. The compressor geometry is assumed to be two dimensional at the mean radius values. Also, the flow is assumed to follow the blades perfectly. Thus, effects such as blockage and deviation are not accounted for in this model.

2.1 Tip Scale Analysis. Martinez-Sanchez [14] developed an inviscid tip clearance flow model (Fig. 2) whose predictions agreed with the theory and data of Chen [15]. The tip clearance flow (''jet'' in Fig. 2) is modeled as a jet driven by the pressure difference between the pressure and suction sides. This jet then collides with an equal amount of passage (''pass'' in Fig. 2) flow

Contributed by the International Gas Turbine Institute and presented at the 45th International Gas Turbine and Aeroengine Congress and Exhibition, Munich, Germany, May 8–11, 2000. Manuscript received by the International Gas Turbine Institute February 2000. Paper No. 2000-GT-416. Review Chair: D. Ballal.

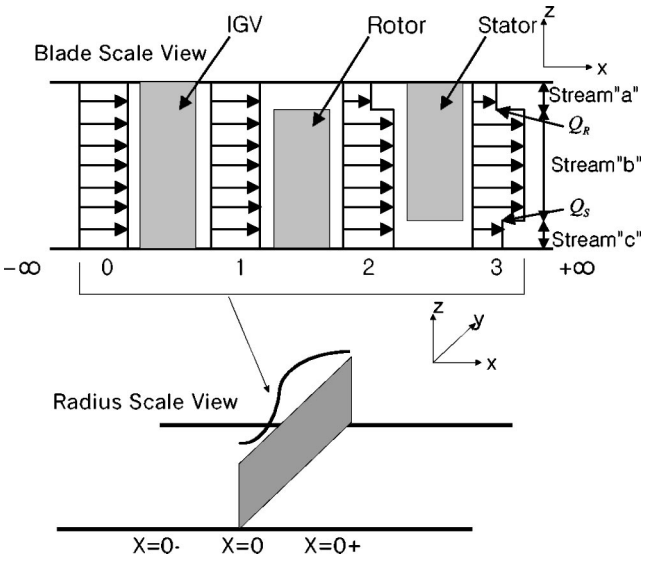

Fig. 1 Blade and radius scale views of a compressor stage

before rolling up into a vortex. Finally, this tip vortex forms a layer that is underturned relative to the passage flow. For example, at the rotor exit, Stream ''*b*'' is the passage flow and Stream ''*a*'' is the underturned flow due to the rotor tip clearance.

The turbine tip clearance flow model has been modified for compressors [16], and the compressor tip clearance flow model is shown schematically in Fig. 3. The flow velocities on suction and pressure sides are obtained from the Bernoulli equation

$$W_{ps}=\sqrt{W_1^2-2\frac{p_{ps}-p_1}{\rho}} \tag{1}$$

$$W_{ss}=\sqrt{W_1^2-2\frac{p_{ss}-p_1}{\rho}} \tag{2}$$

where the subscript 1 refers to the rotor inlet condition. Also,

$$W_G=\sqrt{2\frac{p_{ps}-p_{ss}}{\rho}} \tag{3}$$

Since the flow is assumed to be inviscid, the two streams (''jet'' and ''ss'' in Fig. 3) that collide have same total pressure, temperature, and also equal static pressures along their contact line. Therefore, these two streams must have equal velocity magnitudes, and the line OP bisects the angle made by $\vec{W}_{jet}$ and $\vec{W}_{ss}$ (Fig. 3). Then

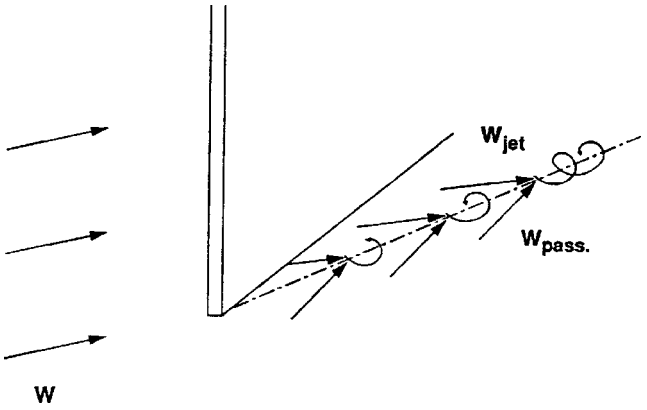

Fig. 2 Schematic of the tip clearance flow model of Martinez-Sanchez [14]

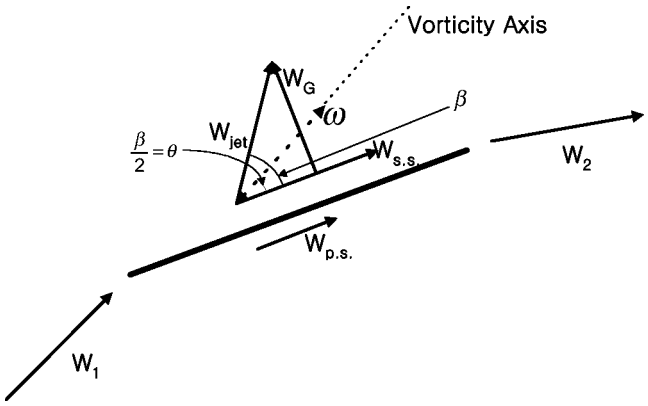

Fig. 3 Geometry of compressor tip vortex roll up

$$\tan 2\theta=\frac{W_G}{W_{ps}}=\sqrt{\frac{C_{p_{ps}}-C_{p_{ss}}}{1-C_{p_{ps}}}} \tag{4}$$

where $C_p=(p-p_1)/(\rho W_1^2/2)$. Notice that $C_l'=C_{p_{ps}}-C_{p_{ss}}$, and it can be shown that the degree of underturning of the vortex relative to the passage flow can be obtained as

$$\theta=\cos^{-1}\sqrt{\frac{4}{4+C_l'}} \tag{5}$$

where

$$C_l'=ZW\left(\frac{\cos\beta_1}{\cos\beta_2}\right)^2 \tag{6}$$

and *ZW* refers to the Zweifel coefficient

$$ZW=2\frac{(s/c)}{(H/c)}\cos^2\beta_2(\tan\beta_1-\tan\beta_2) \tag{7}$$

2.2 Blade Scale Analysis. The azimuthal momentum equation for the flow is

$$\vec{C}_\perp\cdot\nabla C_y=0 \tag{8}$$

where $\vec{C}_\perp=\vec{i}C_x+\vec{k}C_z$ is the meridional velocity decoupled from the azimuthal velocity. The azimuthal component of vorticity $\omega_y=(\partial C_x/\partial z)-(\partial C_z/\partial x)$ can be described in terms of the stream function Ψ as

$$\omega_y(\Psi)=\nabla_\perp^2\Psi\left(\nabla_\perp^2=\frac{\partial^2}{\partial x^2}+\frac{\partial^2}{\partial z^2}\right) \tag{9}$$

The upstream flow is irrotational ($\omega_y=0$). Therefore, Ψ obeys the Laplace equation. Downstream, ω_y is concentrated at the interfaces between Streams ''*a*,'' ''*b*,'' and ''*c*'' (Q_R and Q_S in Fig. 1).

Defining the Bernoulli constant as $B_\perp=P/\rho+(1/2)C_\perp^2$,

$$\omega_y=\frac{dB_\perp}{d\Psi} \tag{10}$$

From the definition of $B_\perp$, with the continuity constraint and the assumption of spanwise uniform blading,

$$B_{\perp 3}-B_{\perp 1}=\frac{P_3-P_1}{\rho} \tag{11}$$

Upstream of the stage, $dB_{\perp 1}/d\Psi=0$ due to the flow's irrotationality. Then, Eq. (10) becomes

$$\omega_{y3}=\frac{dB_{\perp 3}}{d\Psi}=\frac{d(B_{\perp 3}-B_{\perp 1})}{d\Psi}=\frac{d}{d\Psi}\left(\frac{P_3-P_1}{\rho}\right) \tag{12}$$

and ω_y can be determined from the static enthalpy addition $(P_3 - P_1)/\rho$ by the compressor. From Euler's equation, the static enthalpy rise is given by

$$\left(\frac{P_3-P_1}{\rho}\right)=U(C_{y2}-C_{y1})-\frac{1}{2}(C_3^2-C_1^2) \tag{13}$$

At the IGV exit, tangential velocity is given as

$$C_{y1}=C_{x1}\tan\alpha_1 \tag{14}$$

At the rotor exit, the flow has split into two streams. For the bladed stream (Stream ''*b*''), the tangential velocities at the rotor exit (2) and stator exit (3) are

$$C_{y2}^b=U-C_{x2}^b\tan\beta_2 \tag{15}$$

$$C_{y3}^b=C_{x3}^b\tan\alpha_3 \tag{16}$$

Thus, the pressure rise for Stream ''*b*'' is

$$\left(\frac{P_3-P_1}{\rho}\right)^b=U(C_{y2}^b-C_{y1})-\frac{1}{2}[C_{x3}^{b2}+C_{y3}^{b2}-(C_{x1}^2+C_{y1}^2)] \tag{17}$$

For Stream ''*a*,'' the tip scale analysis predicts its rotor exit azimuthal velocity to be

$$C_{y2}^a=U-C_{x2}^a\frac{\cos(\theta_R)\sin(\beta_m+\theta_R)}{\cos(\beta_m)} \tag{18}$$

where β_m is the mean flow angle through the rotor and θ_R is the underturning of the Stream ''*a*'' relative to the Stream ''*b*.'' Also at the stator exit,

$$C_{y3}^a=C_{x3}^a\tan\alpha_3 \tag{19}$$

Similarly, for Stream ''*c*,'' the tangential velocities at the rotor exit (2) and stator exit (3) are given as

$$C_{y2}^c=C_{y2}^b \tag{20}$$

$$C_{y3}^c=C_{x3}^c\frac{\cos\theta_s\sin(\alpha_m+\theta_s)}{\cos\alpha_m} \tag{21}$$

Thus, the pressure rises for Streams ''*a*'' and ''*c*'' are

$$\left(\frac{P_3-P_1}{\rho}\right)^a=U(C_{y2}^a-C_{y1})-\frac{1}{2}(C_{x3}^{a2}+C_{y3}^{a2})-\left(C_{x2}^a\frac{\sin(\theta_R)}{\cos(\beta_m)}\right)^2+(C_{x1}^2+C_{y1}^2) \tag{22}$$

and

$$\left(\frac{P_3-P_1}{\rho}\right)^c=U(C_{y2}^b-C_{y1})-\frac{1}{2}(C_{x3}^{c2}+C_{y3}^{c2})-\left(C_{x3}^c\frac{\sin(\theta_S)}{\cos(\alpha_m)}\right)^2+(C_{x1}^2+C_{y1}^2) \tag{23}$$

The third terms on the right-hand side of Eqs. (22) and (23) are the kinetic energy dissipated when the leakage through the tip gaps collides with the passage flow before rolling up into vortices.

To focus on the tip clearance effects, the coordinate system is transformed to the streamline coordinate from the z coordinate. Then, the equation for Ψ becomes

$$\text{Upstream}\,(x<0)\quad \nabla_\perp^2\Psi=0 \tag{24}$$

$$\text{Downstream}(x>0)$$

$$\nabla_\perp^2\Psi=Q_R\delta(\Psi-\Psi_{\text{rotortip}})+Q_s\delta(\Psi-\Psi_{\text{statortip}}) \tag{25}$$

where $Q=\int_i^j\omega_y d\Psi=B_{\perp 3}^j-B_{\perp 3}^i$ is the strength of the ω_y between streams i and j, and δ is Dirac's delta function.

The boundary conditions are

$$\Psi(x,0)=0\quad \Psi(x,H)=C_{x0}H$$

$$\Psi(x=0-,z)=C_{x0}z\quad \frac{\partial\Psi}{\partial x}(x=0+,z)=0 \tag{26}$$

$$\Psi_1(z)=\Psi_3(z)\quad \frac{\partial\Psi_1(z)}{\partial z}=\frac{\partial\Psi_3(z)}{\partial z}$$

From the definition of $B_\perp$ and Eqs. (17), (22), and (23), the strengths of vorticity, Q_R and Q_S, in the shear layers (Fig. 1) are

$$Q_R=U(C_{y2}^a-C_{y1})-U(C_{y2}^b-C_{y1})-\frac{1}{2}\left(C_{y3}^{a2}+\left(C_{x2}^a\frac{\sin(\theta_R)}{\cos(\beta_m)}\right)^2-C_{y3}^{b2}\right) \tag{27}$$

$$Q_S=U(C_{y2}^b-C_{y1})-U(C_{y2}^c-C_{y1})-\frac{1}{2}\left(C_{y3}^{b2}-\left(C_{x3}^c\frac{\sin(\theta_S)}{\cos(\alpha_m)}\right)^2-C_{y3}^{c2}\right) \tag{28}$$

Subsequently, the velocities at various axial locations can be determined. At the rotor exit, axial velocities for Streams ''*a*'' and ''*b*'' are

$$C_{x2}^a=C_{x1}\left(1+\frac{q_R}{2}(1-\lambda_R)\right) \tag{29}$$

$$C_{x2}^b=C_{x1}\left(1-\frac{q_R}{2}\lambda_R\right) \tag{30}$$

where $q_R=Q_R/C_{x1}^2$ and λ_R is the nondimentional mass fraction of Stream ''*a*.'' Tangential velocities are given in Eqs. (15) and (18).

At the stator exit, the axial velocities are

$$C_{x3}^a=C_{x1}\left(1+\frac{q_R}{2}(1-\lambda_R)+\frac{q_S}{2}\lambda_S\right) \tag{31}$$

$$C_{x3}^b=C_{x1}\left(1-\frac{q_R}{2}\lambda_R+\frac{q_S}{2}\lambda_S\right) \tag{32}$$

$$C_{x3}^c=C_{x1}\left(1-\frac{q_s}{2}(1-\lambda_S)-\frac{q_R}{2}\lambda_R\right) \tag{33}$$

and tangential velocities are given in Eqs. (16), (19), and (21).

Far downstream of the stator, the axial velocities are

$$C_{x+\infty}^a=C_{x1}(1+q_R(1-\lambda_R)+q_S\lambda_S) \tag{34}$$

$$C_{x+\infty}^b=C_{x1}(1-q_R\lambda_R+q_s\lambda_s) \tag{35}$$

$$C_{x+\infty}^c=C_{x1}(1-q_s(1-\lambda_s)-q_R\lambda_R) \tag{36}$$

and tangential velocities are equivalent to those at the stator exit given in Eqs. (16), (19), and (21).

Substituting for velocities in Eqs. (27) and (28) yields two quadratic equations for Q_R and Q_S as functions of blade geometry and mass fractions of Streams ''*a*'' and ''*c*,'' λ_R and λ_S.

$$[(1-2\lambda_R)\tan^2\alpha_3]\left(\frac{q_R}{2}\right)^2+2\left[2+\tan^2\alpha_3\left(1+\frac{\lambda_s q_s}{2}\right)\right]\left(\frac{q_R}{2}\right)+\left[\left(1+\frac{q_R}{2}(1-\lambda_R)\right)^2\left(\frac{\sin\theta_R}{\cos\beta_m}\right)^2+\frac{2}{\Phi}\left(1+\frac{q_R}{2}(1-\lambda_R)\right)T-\frac{2}{\Phi}\left(1-\frac{q_R\lambda_R}{2}\right)\tan\beta_2\right]=0 \tag{37}$$

where $T=[\cos(\theta_R)\sin(\beta_m+\theta_R)]/\cos(\beta_m)$

and for the stator

$$[\lambda_S^2(\tan^2\alpha_3 - G_S) - (1-2\lambda_s)G_S]\left(\frac{q_S}{2}\right)^2 + 2\left[2+\left(1-\frac{q_R\lambda_R}{2}\right)\{\lambda_S(\tan^2\alpha_3 - G_S)+G_S\}\right]\left(\frac{q_S}{2}\right) + \left(1-\frac{q_R\lambda_R}{2}\right)^2(\tan^2\alpha_3 - G_S) = 0 \quad (38)$$

where $G_S = \left(\frac{\sin(\theta_s)}{\cos(\alpha_m)}\right)^2 + \left(\frac{\cos(\theta_S)\sin(\alpha_m+\theta_S)}{\cos(\alpha_m)}\right)^2$.

Next, the mass fractions, λ_R and λ_S, can be determined from the given tip clearances as

$$\lambda_R = \frac{4(t_R/H)}{\left(1-\frac{q_R}{2}-\frac{q_S}{2}\frac{\lambda_S}{2}\right)+\sqrt{\left(1-\frac{q_R}{2}-\frac{q_S}{2}\frac{\lambda_S}{2}\right)^2-4\frac{q_R}{2}\frac{t_R}{H}}} \quad (39)$$

and

$$\lambda_S = \frac{4(t_S/H)}{\left(1+\frac{q_S}{2}+\frac{q_R}{2}\frac{\lambda_R}{2}\right)+\sqrt{\left(1+\frac{q_S}{2}+\frac{q_R}{2}\frac{\lambda_R}{2}\right)^2-4\frac{q_S}{2}\frac{t_S}{H}}} \quad (40)$$

Thus, from the prescribed tip clearances t_R/H and t_S/H, Eqs. (37)–(40) can be solved for Q_R, Q_S, λ_R, and λ_S.

Far downstream, after the completion of flow readjustment, the thicknesses of Streams ''*a*'' and ''*c*'' can be determined as

$$\frac{\Delta_R}{H} = \lambda_R\left[1-\frac{q_R}{2}\left(1-\frac{\lambda_R}{2}\right)-\frac{q_S}{2}\frac{\lambda_S}{2}\right]\frac{1+\frac{q_R}{2}(1-\lambda_R)+\frac{q_S}{2}\lambda_S}{1+q_R(1-\lambda_R)+q_S\lambda_S} \quad (41)$$

$$\frac{\Delta_S}{H} = \lambda_S\left[1+\frac{q_S}{2}\left(1-\frac{\lambda_S}{2}\right)+\frac{q_R}{2}\frac{\lambda_R}{2}\right]\frac{1-\frac{q_s}{2}(1-\lambda_S)-\frac{q_R}{2}\lambda_R}{1-q_s(1-\lambda_s)-q_R\lambda_R} \quad (42)$$

Also, the pressure rise across the compressor stage can be determined as

$$\frac{P_{-\infty}-P_{+\infty}}{\rho} = U(C_{y1}-C_{y2}^b)+\frac{1}{2}C_{x+\infty}^{b\,2}-\frac{1}{2}C_{x-\infty}{}^2+\frac{1}{2}C_{y3}^{b\,2} \quad (43)$$

2.3 Radius Scale Analysis. The rotor offset, e, is assumed to be much smaller than the blade span. Therefore, the tip clearance distribution is given by

$$t = \overline{t} + \mathrm{Re}[\hat{e}e^{i(y/R)}] \quad (44)$$

where $\overline{t}$ is the mean rotor tip gap, and y is the distance from the maximum tip gap in the azimuthal direction (Fig. 4).

2.3.1 Upstream Flow. The irrotational upstream flow is given by

$$\nabla^2\phi = 0 \quad (45)$$

where ϕ is the velocity potential. Far upstream, $C_x(-\infty) = \overline{C}_{x-\infty}$. Near upstream of the stage at $x = 0-$, the axial and tangential velocities are

$$C_x(0-,y,t) = \mathrm{Re}[\overline{C}_{x-\infty} + \hat{K}_0 e^{i(y/R)}] \quad (46)$$

$$C_y(x,y,t) = \mathrm{Re}[i\hat{K}_0 e^{x/R+i(y/R)}] \quad (47)$$

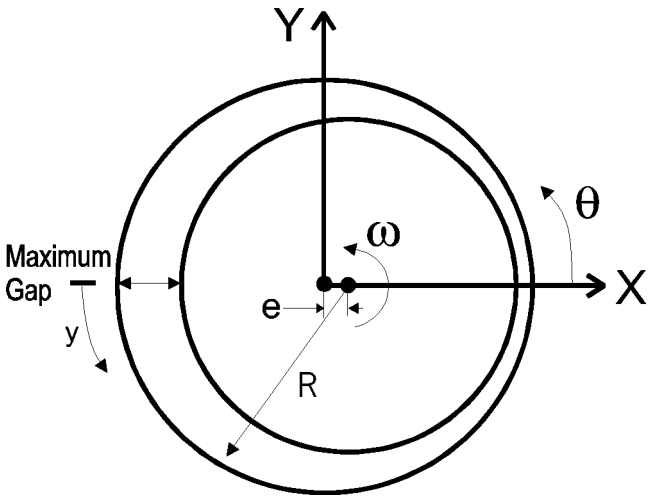

Fig. 4 Coordinate system for the model

where $\hat{K}_0$ is the complex amplitude of axial velocity perturbation as the flow approaches the disk. Therefore, the upstream pressure is given by

$$P(x,y,t) = P(-\infty) - \mathrm{Re}[\rho(\overline{C}_{x-\infty})\hat{K}_0 e^{x/R+i(y/R)}] \quad (48)$$

2.3.2 Downstream Flow. Downstream of the stage, the flow consists of three regions: Streams ''*a*,'' ''*b*,'' and ''*c*.'' The continuity equation for each stream can be written as

$$\frac{\partial\Delta_R}{\partial t}+\frac{\partial(C_x^a\Delta_R)}{\partial x}+\frac{\partial(C_y^a\Delta_R)}{\partial y} = 0 \quad (49)$$

$$\frac{\partial\Delta_S}{\partial t}+\frac{\partial(C_x^c\Delta_S)}{\partial x}+\frac{\partial(C_y^c\Delta_S)}{\partial y} = 0 \quad (50)$$

$$\frac{\partial(H-\Delta_R-\Delta_S)}{\partial t}+\frac{\partial(C_x^c(H-\Delta_R-\Delta_S))}{\partial x}+\frac{\partial(C_y^c(H-\Delta_R-\Delta_S))}{\partial y} = 0 \quad (51)$$

where H is annulus height and Δ_R and Δ_S are given by Eqs. (41) and (42). The momentum equations for the three streams can be written as

$$\frac{\partial\vec{C}^{a,b,c}}{\partial t}+(\vec{C}^{a,b,c}\cdot\nabla)\vec{C}^{a,b,c}+\frac{1}{\rho}\nabla P = 0 \quad (52)$$

where $\vec{C}$ is a two-dimensional velocity with axial and tangential components. Now, each flow parameter can be expressed as

$$C = \overline{C} + C' \quad (53)$$

and

$$C' = \mathrm{Re}[\hat{C}e^{\alpha x+i(y/R)}] \quad (54)$$

is a small perturbation about the mean. A homogeneous set of equations for eigenvalues is obtained by substituting for each flow variable and linearizing.

$$\begin{bmatrix} \alpha\overline{\Delta}_R & i\overline{\Delta}_R/R & 0 & 0 & 0 & 0 & A & 0 & 0 \\ 0 & 0 & \alpha\overline{\Delta}_S & i\overline{\Delta}_S/R & 0 & 0 & 0 & C & 0 \\ 0 & 0 & 0 & 0 & D & E & -B & -B & 0 \\ A & 0 & 0 & 0 & 0 & 0 & 0 & 0 & \alpha \\ 0 & A & 0 & 0 & 0 & 0 & 0 & 0 & i/R \\ 0 & 0 & C & 0 & 0 & 0 & 0 & 0 & \alpha \\ 0 & 0 & 0 & C & 0 & 0 & 0 & 0 & i/R \\ 0 & 0 & 0 & 0 & B & 0 & 0 & 0 & \alpha \\ 0 & 0 & 0 & 0 & 0 & B & 0 & 0 & i/R \end{bmatrix} \begin{bmatrix} \hat{C}_x^a \\ \hat{C}_y^a \\ \hat{C}_x^c \\ \hat{C}_y^c \\ \hat{C}_x^b \\ \hat{C}_y^b \\ \hat{\Delta}_R \\ \hat{\Delta}_S \\ \hat{P}/\rho \end{bmatrix} = 0 \tag{55}$$

where $A=\alpha\overline{C}_x^a+i(\overline{C}_y^a/R)$, $B=\alpha\overline{C}_x^b+i(\overline{C}_y^b/R)$, $C=\alpha\overline{C}_x^c+i(\overline{C}_y^c/R)$, $D=\alpha(H-\overline{\Delta}_R-\overline{\Delta}_S)$, $E=i(H-\overline{\Delta}_R-\overline{\Delta}_S)/R$.

Then, the nontrivial homogeneous solution is

$$\left(\hat{C}_x^a,\hat{C}_y^a,\hat{C}_x^b,\hat{C}_y^b,\hat{C}_x^c,\hat{C}_y^c,\hat{\Delta}_R,\hat{\Delta}_S,\frac{\hat{P}}{\rho}\right)=\sum_{i=1}^{8}\hat{K}_iE_i \tag{56}$$

where E_i's are eigenvectors, and the complex constants $\hat{K}_i$'s are to be determined from matching.

2.3.3 The Upstream–Downstream Coupling. To connect upstream and downstream flows, the results from the blade scale analysis are used. According to the blade scale analysis, the flow variables depend on the local nondimensional tip clearances, t_R/H & t_S/H, and flow coefficient, Φ. For example,

$$\frac{C_{x4}^a}{U}=\frac{C_{x4}^a}{U}\left(\frac{t_R}{H},\frac{t_S}{H},\Phi\right) \tag{57}$$

The downstream and upstream perturbation quantities are determined from the blade scale results as shown below. The axisymmetric blade scale results on the right-hand side of Eq. (58) are perturbed to account for the given geometric nonaxisymmetry. The perturbation solutions then become nonaxisymmetric radius scale results on the left-hand side of Eq. (58). The local flow coefficient, Φ, is also determined from matching upstream and downstream flows.

Radius Scale / Blade Scale / Perturbation

$$\begin{pmatrix} \hat{C}_x^a \\ \hat{C}_x^b \\ \hat{C}_x^c \\ \hat{C}_y^a \\ \hat{C}_y^b \\ \hat{C}_y^c \\ \hat{\Delta}_R \\ \hat{\Delta}_S \\ \hat{P}/\rho \end{pmatrix}_{x=0+} = \left[\hat{\Phi}\frac{\partial}{\partial\Phi}+\left(\frac{e}{H}\right)_R\frac{\partial}{\partial\left(\frac{t_R}{H}\right)}+\left(\frac{e}{H}\right)_S\frac{\partial}{\partial\left(\frac{t_S}{H}\right)}\right]\begin{pmatrix} C_x^a \\ C_x^b \\ C_x^c \\ C_y^a \\ C_y^b \\ C_y^c \\ \Delta_R \\ \Delta_S \\ P/\rho \end{pmatrix}=\sum_{i=1}^{8}K_i\{E_i\} \tag{58}$$

2.4 Calculation of Rotordynamic Coefficients. From the perturbations in flow variables, rotordynamic excitation forces can be predicted. The tangential force exerted on the compressor by the fluid per azimuthal length is defined as

$$f_y=\lambda_R q(C_{y1}-C_{y2}^b)+(1-\lambda_R)q(C_{y1}-C_{y2}^b) \tag{59}$$

where q is the local mass flux. The mean and the perturbation of f_y are, respectively

$$\overline{f_y}=\overline{\lambda}_R\overline{q}(\overline{C}_{y1}-\overline{C}_{y2}^a)+(1-\overline{\lambda}_R)\overline{q}(\overline{C}_{y1}-\overline{C}_{y2}^b) \tag{60}$$

$$f_y'=\overline{\lambda}_R\overline{q}(\overline{C}_{y1}-\overline{C}_{y2}^a)\left[\frac{\lambda_R'}{\overline{\lambda}_R}+\frac{q'}{\overline{q}}+\frac{C_{y1}'-C_{y2}^{a\prime}}{\overline{C}_{y1}-\overline{C}_{y2}^a}\right]$$
$$+(1-\overline{\lambda}_R)\overline{q}(\overline{C}_{y1}-\overline{C}_{y2}^b)\left[\frac{-\lambda_R'}{1-\overline{\lambda}_R}+\frac{q'}{\overline{q}}+\frac{C_{y1}'-C_{y2}^{b\prime}}{\overline{C}_{y1}-\overline{C}_{y2}^b}\right] \tag{61}$$

The perturbation in f_y is almost like the torque variation envisioned by Thomas and Alford. However, they assumed that the flow remains axisymmetric upstream and downstream of the compressor, and, thus, ignored the effects of mass flux perturbation, $q'/\overline{q}$. However, as Eq. (48) shows, rotor and stator tip clearances do indeed induce azimuthal flow redistribution, and this flow redistribution results in a nonaxisymmetric pressure distribution.

The pressure acting on the rotor hub is approximated as the average of pressures at the inlet and the exit of the rotor, $\langle P \rangle$.

$$\langle P \rangle = \frac{P_1 + P_2}{2} = P_1 - \frac{P_1 - P_2}{2}$$

$$= P_1 - \frac{1}{2}\frac{\rho}{2}[(C_{x2}^b)^2 \tan^2 \beta_2 - (U - C_{y1})^2] \tag{62}$$

$$\langle P \rangle' = P_1' - \frac{\rho}{2}[\overline{C}_{x2}^b C_{x2}'^b \tan^2 \beta_2 + (U - \overline{C}_{y1}) C_{y1}'] \tag{63}$$

Nonuniform tangential force and nonuniform pressure can thus be obtained from Eqs. (61) and (63). Upon projection onto the *X*, *Y* axes, the total excitation force coefficients, or the rotordynamic stiffness coefficients, are

$$(\alpha_Y + i\alpha_X)_{(\text{total})} = \frac{-\hat{f}_y + iL\langle \hat{P} \rangle}{|\overline{f}_y(e/H)|} \tag{64}$$

The total coefficients $\alpha_{(\text{total})}$, are composed of contributions from tangential force asymmetry $\alpha_{(wd)}$, and pressure asymmetry $\alpha_{(p)}$. Forces along the rotor offset are called direct forces and are denoted with a subscript *X*. Forces perpendicular to the rotor offset are called cross forces and are denoted with a subscript *Y*.

3 Model Predictions

This section presents the model predictions for the selected baseline compressor and other compressors. Initially, the ''baseline'' compressor chosen for this study is explained, and the predictions for this compressor are given in the following order. First, the radial flow redistribution induced by axisymmetric rotor and stator tip clearances is presented. Second, the azimuthal flow redistribution due to nonaxisymmetric tip clearances is shown. For both, differences and similarities between the predictions of the new model with rotor and stator clearances (RSC model) and those of the model with only the rotor clearance (RC model) [12] are brought out. Third, rotordynamic coefficients at the design point and off-design points are discussed. Finally, the effects of various compressor designs on rotordynamic stiffness coefficients are presented

The characteristics of the ''baseline'' compressor are given in Table 1. The design flow coefficient, reaction, and work coefficient have all been set to 0.5 because they are representative of modern compressors. The tip clearance values of 2 percent of the annulus height have been selected because such value is common in research experiments.

3.1 Blade Scale Predictions. Figure 5 shows the radial profiles of axial velocity, absolute tangential velocity, and relative flow angle at the rotor exit after the flow has split into two streams. The hub and endwall are at $z/H=0.0$ and $z/H=1.0$, respectively. Stream ''*a*'' is retarded in the axial direction and underturned in the tangential direction relative to Stream ''*b*.'' Figure 6 shows the absolute velocity and flow angle profiles at the stator exit. Now, the flow has split into three streams. Relative to Stream ''*b*,'' which goes through both rotor and stator blades, Stream ''*c*'' shows characteristics similar to those of Stream ''*a*.'' Such results agree with the corresponding predictions from the RC model of Park [12] shown in Figs. 7 and 8. Underturning is due to the effects of the tip leakage flow. The axial momentum defect is caused by flow migration away from the tip clearance where the pressure rise across the compressor stage is sensed more. Such effects increase with increasing tip clearance, and this

Table 1 Baseline compressor specifications at the design point

Parameter	Value
Φ_D	0.50
Ψ_D	0.50
R_D	0.50
t_R/H	0.02
t_S/H	0.02

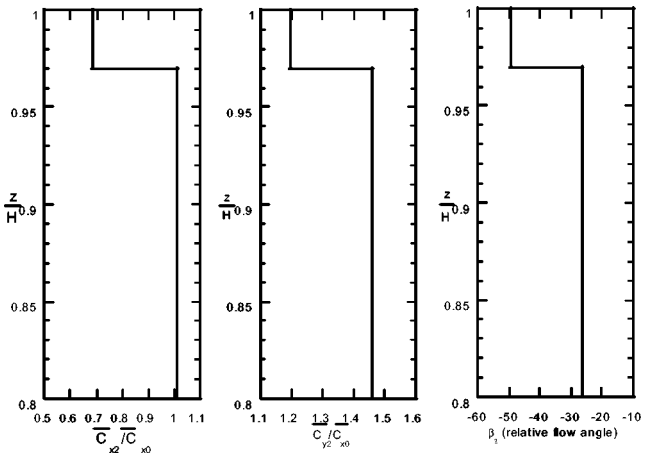

Fig. 5 Radial distributions of axial velocity, absolute tangential velocity, and relative flow angle at rotor exit predicted by the new RSC model

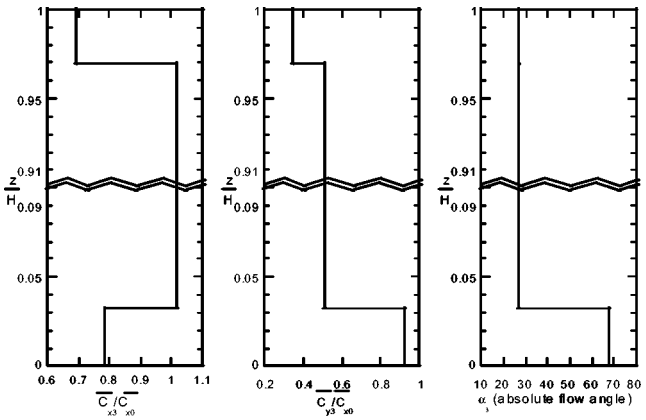

Fig. 6 Radial distributions of axial velocity, absolute tangential velocity, and absolute flow angle at stator exit predicted by the new RSC model

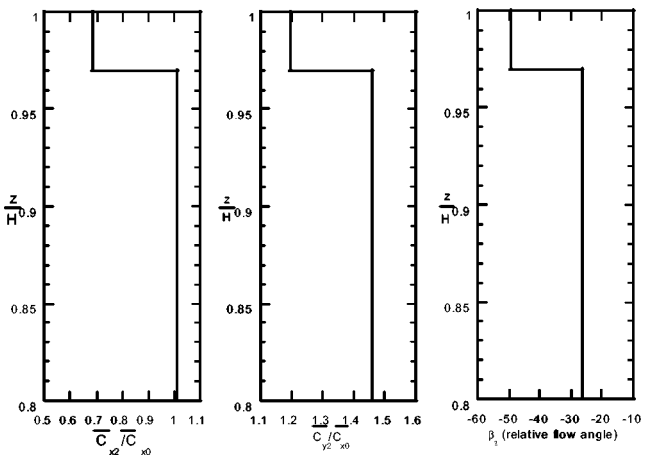

Fig. 7 Radial distributions of axial velocity, absolute tangential velocity, and relative flow angle at rotor exit predicted by the RC model of Park [12]

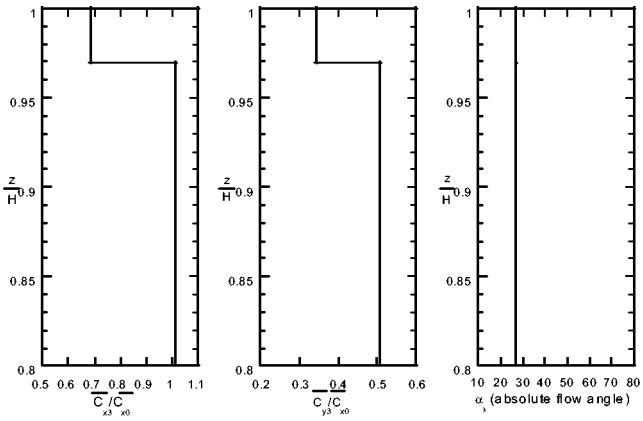

Fig. 8 Radial distributions of axial velocity, absolute tangential velocity, and absolute flow angle at stator exit predicted by the RC model of Park [12]

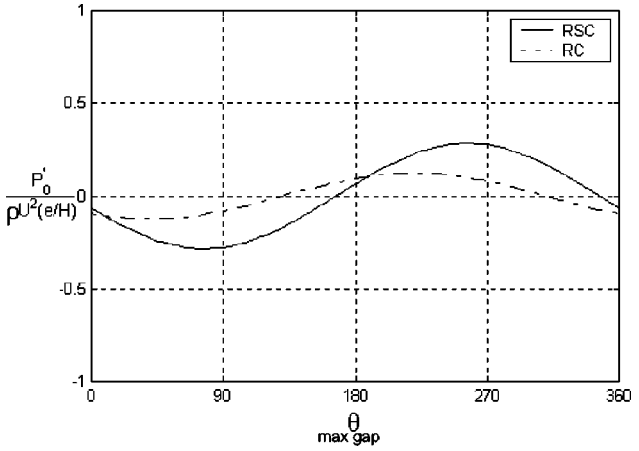

Fig. 10 Upstream pressure perturbation versus azimuthal angle

trend agrees with the experimental findings of Hunter and Cumpsty [17].

Comparing Figs. 6 and 8, the obvious difference between the new RSC model and the RC model is Stream ''*c*,'' which does not exist in Fig. 8. Thus, the new model can incorporate the effects of stator gap on the flow field. Focusing on Stream ''*a*,'' the stream's mass fraction, degree of axial momentum defect, and underturning in Figs. 6 and 8 are virtually identical. This is because the downstream stator tip clearance effect occurs over a length scale on the order of the tip clearance. However, the axial blade spacing is on the order of the blade chord, which is at least a couple of orders of magnitude larger than the tip clearance. Thus, Streams ''*a*'' and ''*c*'' are practically decoupled from each other.

3.2 Radius Scale Predictions

3.2.1 Azimuthal Flow Redistribution. First, the upstream azimuthal flow redistribution induced by tip clearance asymmetry is discussed. Nondimensional velocity and pressure perturbations upstream of the compressor predicted by the RC model and the new RSC model are plotted versus azimuthal location θ in Figs. 9 and 10, respectively. The minimum gap is at $\theta=0$ deg and maximum gap is at $\theta=180$ deg. Roughly, the mass flux is higher near the minimum gap in both cases. Again, the higher downstream pressure is ''felt'' more near the maximum gap ($\theta=180$ deg). The result is a tangential flow migration away from the larger gap toward the smaller gap. Then from the Bernoulli relation, the pressure decreases as flow accelerates. The magnitudes of both perturbations increase significantly when the stator clearance is introduced. As Eq. (58) shows, the clearance asymmetry acts as the forcing term, which induces azimuthal flow redistribution. Therefore, imposing stator tip clearance asymmetry in addition to the rotor tip clearance asymmetry strengthens the forcing effect. Thus, the flow becomes more nonuniform with rotor and stator tip clearances.

Next, the rotordynamic consequences of such flow redistribution are presented. Tangential force perturbation (also referred to as the torque asymmetry or blade loading variation) is plotted versus θ in Fig. 11. Since the force on the compressor by the fluid acts in a direction opposite to the direction of rotation, the mean value of tangential force, $\bar{f}_y/\dot{m}U$, is negative. Therefore, according to Fig. 11, the compressor rotor blade is loaded less near the maximum gap. The unloading near the maximum gap occurs mainly because the tip leakage flow rate is higher there. Such prediction has been verified by the experimental data from the GE LSRC [18]. Also, introducing stator clearance asymmetry hardly changes the perturbation in blade loading because the rotor tip leakage flow is practically decoupled from the stator tip clearance.

The perturbation in the rotor region static pressure is plotted versus θ in Fig. 12. The pressure has its maximum near the maximum gap ($\theta=180$ deg). Although a similar trend is suggested by the GE's LSRC data, the corresponding experimental data do not exist yet to confirm this effect in compressors. Unlike the blade loading perturbation, the pressure perturbation is more sensitive to

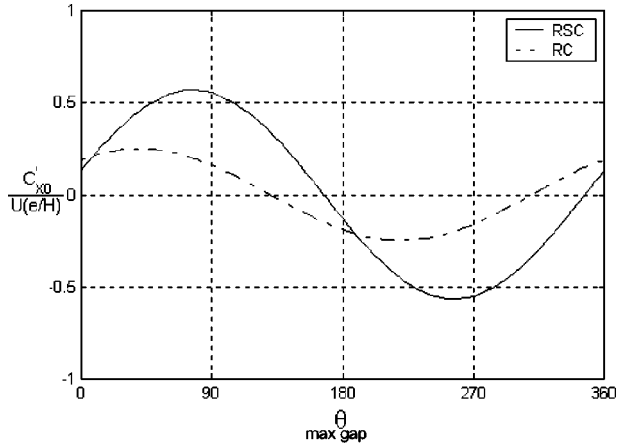

Fig. 9 Upstream axial velocity perturbation versus azimuthal angle

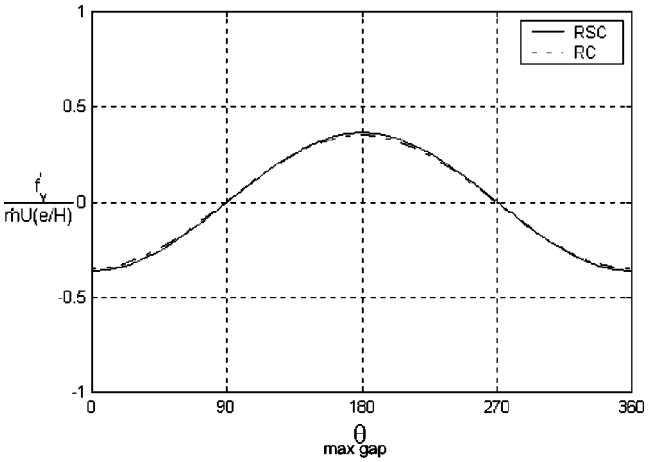

Fig. 11 Rotor blade loading perturbation versus azimuthal angle

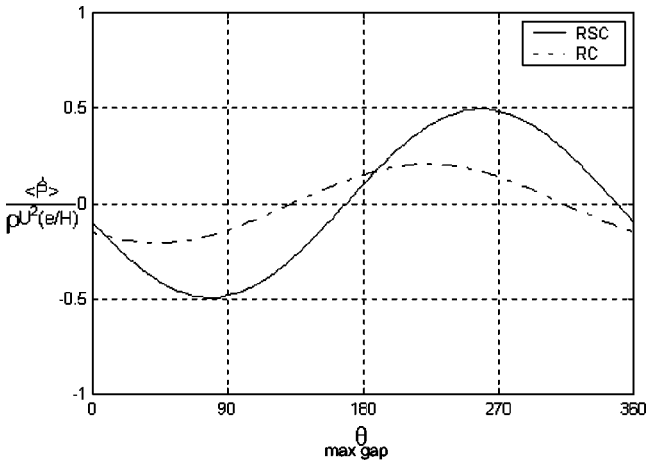

Fig. 12 Perturbation in the average pressure on rotor hub versus azimuthal angle

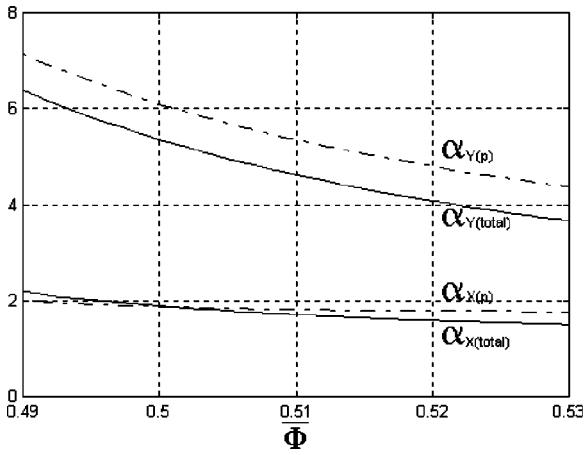

Fig. 13 Predicted total and pressure rotordynamic coefficients versus operating flow coefficient

the addition of stator clearance asymmetry (Fig. 10). In turbines, the pressure asymmetry, predicted by a similar actuator disk model, matched well with experimental data [7].

3.2.2 Design Point Rotordynamic Coefficients. The predicted excitation coefficients from the new RSC model are listed in Table 2 and those from the RC model are given in Table 3. The coefficients due to blade loading variation are $\alpha_{(wd)}$'s and those due to pressure variation are $\alpha_{(p)}$'s. Both models predict the following: The blade loading variation induces a negative cross force, which promotes a backward whirl, and a negligible direct force. The pressure effect leads to a positive cross force, which induces a forward whirl, and a positive direct force. However, the models predict different total coefficients. The new model predicts that the $\alpha_{Y(\text{total})}$, is positive because $\alpha_{Y(p)}$ is bigger than $\alpha_{Y(wd)}$. Thus, a net positive cross force is predicted. However, the RC model predicts a negligible cross force because the blade loading and pressure effects cancel each other out in Y direction. Both models predict a positive $\alpha_{X(\text{total})}$ between 0.4 and 0.6.

In comparison, the parallel compressor model of Ehrich [10] can predict only $\alpha_{Y(wd)}$. The model uses the difference between compressor characteristics at different axisymmetric tip clearances to predict torque asymmetry, which is assumed to be in phase with the clearance distribution. However, no pressure information is available for the parallel compressor model to predict pressure asymmetry. Nevertheless, like the new RSC model, the parallel compressor model predicts a negative cross force due torque asymmetry.

Table 2 Excitation force coefficients for the baseline compressor (Φ_D=0.50, Ψ_D=0.50, R_D=0.50) predicted from the new model (RSC)

Direction	$\alpha_{(wd)}$	$\alpha_{(p)}$	α_{total}
X	0	+0.4	+0.4
Y	−0.7	+2.1	+1.4

Table 3 Excitation force coefficients for the baseline compressor (Φ_D=0.50, Ψ_D=0.50, R_D=0.50) predicted from the rotor clearance-only (RC) model of Park [12]

Direction	$\alpha_{(wd)}$	$\alpha_{(p)}$	$\alpha_{(\text{total})}$
X	0	+0.6	+0.6
Y	−0.7	+0.6	−0.1

3.2.3 Off-Design Point Rotordynamic Coefficients. Figure 13 shows a graph of excitation force coefficients versus the operating flow coefficient. In this case, to model an embedded stage, the IGV has been replaced with a stator row. If a compressor operates below its design flow coefficient, excitation force coefficients increase in magnitude because the amplitudes of flow perturbations are magnified at low $\bar{\Phi}$. These trends are similar to those predicted and measured in turbines [7]. Figure 14 shows a graph of the cross force excitation coefficient due to blade loading variation, $\alpha_{Y(wd)}$, plotted versus $\bar{\Phi}$. $\alpha_{Y(wd)}$ remains negative but decreases slightly in magnitude as $\bar{\Phi}$ increases. This trend has been verified experimentally in the LSRC at General Electric [18].

3.3 Parametric Analysis Predictions. This section presents the predicted effects of compressor design parameters on the excitation force coefficients. The selected parameters are the design flow coefficient, Φ_D, the design work coefficient, ψ_D, and the design reaction, R_D. They determine compressor blade angles as shown below.

$$R_D = \frac{1}{2} - \left(\frac{\tan\alpha_1 - \tan\beta_2}{2}\right)\Phi_D \tag{65}$$

$$\psi_D = 1 - \Phi_D(\tan\alpha_1 + \tan\beta_2) \tag{66}$$

Thus, a change in the value of one of the parameters changes both rotor and stator blade shapes (i.e., angles), and the effects of vari-

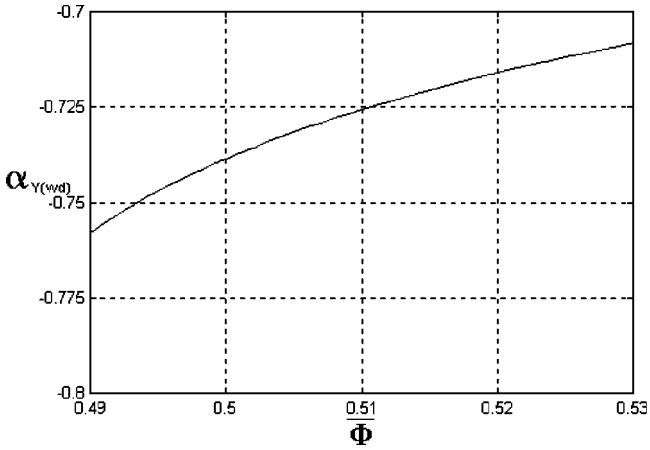

Fig. 14 Predicted cross rotordynamic coefficients due to blade loading perturbation versus operating flow coefficient

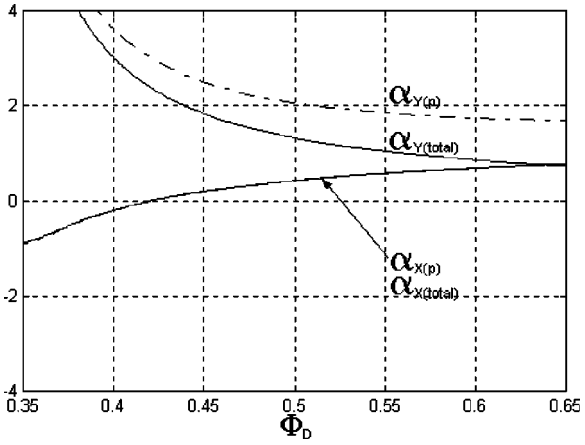

Fig. 15 Predicted total and pressure rotordynamic coefficients versus design flow coefficient

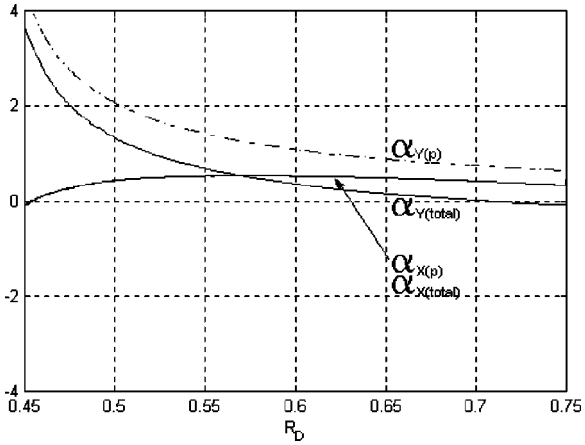

Fig. 17 Predicted total and pressure rotordynamic coefficients versus design reaction

ous compressor designs can be examined. For parametric analysis, one of the three variables is changed while the other two are held constant at the ''baseline'' values.

Figure 15 shows variation of $\alpha_{(\text{total})}$ and $\alpha_{(p)}$ as the design flow coefficient is increased. $\alpha_{(wd)}$ is the difference between $\alpha_{(\text{total})}$ and $\alpha_{(p)}$. For the cross force, $\alpha_{Y(\text{total})}$ decreases with increasing Φ_D primarily because $\alpha_{Y(p)}$ decreases as the magnitude of azimuthal flow nonuniformity is decreased. Also, $\alpha_{Y(wd)}$ remains negative and its magnitude increases with Φ_D. For the direct force, $\alpha_{X(p)}$ dominates over $\alpha_{X(wd)}$ and changes sign as the phase of pressure non-uniformity relative to tip clearance distribution shifts. These trends are similar to those predicted for turbines in Song and Martinez-Sanchez [7].

Figure 16 shows variation of excitation force coefficients as the design work coefficient is increased. In the Y direction, $\alpha_{Y(\text{total})}$ increases primarily because $\alpha_{Y(p)}$ increases in magnitude. In the X direction, $\alpha_{X(\text{total})}$ does not change much while $\alpha_{X(wd)}$ increases. Overall, increasing the work coefficient is equivalent to strengthening the intensity of discontinuity across the actuator disk. Thus, for a given imposed tip clearance asymmetry, the perturbations in the flow field increase. In addition, the phases of the flow perturbations relative to the clearance distribution also shift.

Figure 17 shows the variation of excitation force coefficients versus the design reaction. As R_D increases, $\alpha_{X(p)}$ does not change much, but $\alpha_{Y(p)}$ is reduced significantly. This change is due to the decrease in the magnitude of azimuthal flow nonaxisymmetry. $\alpha_{(wd)}$ is relatively insensitive to R_D. Thus, at low design reactions, $\alpha_{Y(\text{total})}$ is increased.

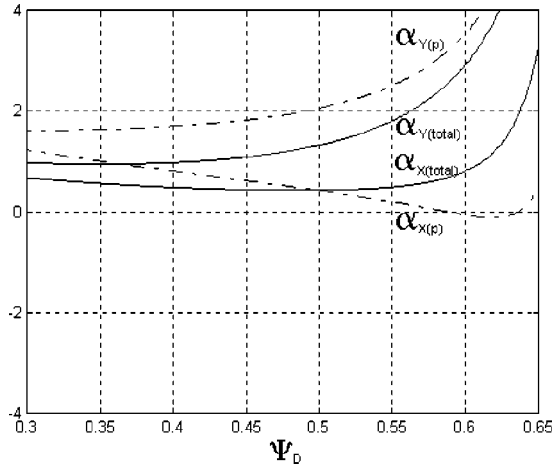

Fig. 16 Predicted total and pressure rotordynamic coefficients versus design work coefficient

4 Conclusions

The new conclusions of this study can be summarized as follows:

1 A new analytical model has been developed to examine the effects of nonaxisymmetry in rotor and stator tip clearances on the compressor flow field.

2 The new model has reconfirmed the following previously found trends: (*a*) radial flow migration away from the tip clearance; (*b*) azimuthal flow migration towards smaller gap area; and (*c*) direction of rotordynamic forces that arise due to pressure and torque (i.e., blade loading) asymmetry.

In addition, for the baseline compressor, the following conclusions can be drawn.

3 Direct force is mostly due to the pressure asymmetry and is positive.

4 Torque asymmetry results in a negative cross force that, without damping, would promote a backward whirl. However, pressure asymmetry results in a positive cross force, which would promote a forward whirl. The net result is a positive cross force.

5 The dominance of pressure asymmetry effects over those of blade loading asymmetry is due to the introduction of stator clearance asymmetry.

6 The flow associated with the rotor tip clearance is hardly affected by the existence of the downstream stator tip clearance.

7 The pressure asymmetry induced by azimuthal flow redistribution increases significantly in magnitude with the addition of stator tip clearance asymmetry.

8 Operating at below the design flow coefficient increases the magnitude of excitation force coefficients.

Finally, from the results of parametric variation about the baseline compressor, the following conclusions can be drawn.

9 High design flow coefficient and high design reaction decrease the magnitudes of excitation force coefficients.

10 High design work coefficient increase the excitation force coefficients' magnitudes.

Acknowledgments

The financial support for this study has been provided by the Seoul National University Research Fund and the Institute of Advanced Machinery and Design. Also, the authors have benefitted from constructive discussions with Professor Martinez-Sanchez of MIT.

Nomenclature

B = Bernoulli constant, m^2/s^2
C = absolute flow velocity, m/s
c = axial blade chord, m
C_l' = lift coefficient per unit span
C_p = pressure coefficient
e = magnitude of rotor offset, m
E_i = eigenvector for downstream perturbations
F_X = lateral force in the direction of the offset, N
F_Y = lateral force perpendicular to the direction of the offset, N
H = annulus height, m
H_b = rotor blade span, m
$\hat{K}_j$ = complex amplitude of flow perturbations
L = axial rotor hub thickness, m
$\dot{m}$ = mass flux, kg/s
P = pressure, Pa
Q = strength of shear layer, m^2/s^2
q = nondimensional vorticity strength; local mass flux
R = mean compressor radius, m
s = blade pitch, m
t = radial tip clearance, m
U = ωR = compressor rotational speed at the mean radius, m/s
W = relative velocity, m/s
X = direction along the rotor offset
x = axial direction
Y = direction perpendicular to rotor offset
y = tangential direction
z = radial direction
ZW = Zweifel coefficient
α = absolute flow angle, deg; eigenvalue
α_X = direct excitation force coefficient
α_Y = cross excitation force coefficient
β = relative flow angle, deg
Δ = thickness of underturned layer downstream of actuator disk, m
ϕ = upstream velocity potential
Φ = C_x/U = flow coefficient
λ = nondimensional mass fraction of underturned flow
θ = azimuthal angle measured in the direction of rotation from the minimum gap location, deg; angle of underturning relative to passage flow, deg
ρ = density, kg/m^3
ω = angular velocity of rotor shaft rotation, s^{-1}
ψ = meridional stream function; work coefficient

Subscripts

D = design value
G = gap
m = mean
p = indicates effect due to nonuniform pressure
ps = pressure side
R = rotor
S = stator
ss = suction side
t = stagnation condition
wd = indicates effect due to variation of torque or tangential force
$0-$ = near upstream of the actuator disk on the radius scale
$0+$ = near downstream of the actuator disk on the radius scale
$-\infty$ = far upstream on the blade scale
0 = IGV inlet on the blade scale
1 = rotor inlet on the blade scale
2 = stator inlet on the blade scale
3 = stator outlet on the blade scale
$+\infty$ = far downstream on the blade scale
$\perp$ = meridional component

Superscripts

a = the part of downstream flow associated with the rotor tip gap
b = the part of downstream flow that has crossed the bladed part of compressor
c = the part of downstream flow associated with the stator tip gap
$'$ = nonaxisymmetric perturbation
$-$ = azimuthal mean, or axisymmetric value
$\wedge$ = complex amplitude

References

[1] Thomas, H. J., 1958, ''Unstable Natural Vibration of Turbine Rotors Induced by the Clearance Flow in Glands and Blading,'' Bull. de I'A.I.M., **71**, No. 11/12, pp. 1039–1063.
[2] Alford, J., 1965, ''Protecting Turbomachinery From Self-Excited Rotor Whirl,'' ASME J. Eng. Power, **87**, pp. 333–334.
[3] Urlichs, K., 1983, ''Clearance Flow Generated Transverse Forces at the Rotors of Thermal Turbomachines,'' NASA TM-77292.
[4] Wohlrab, R., 1983, ''Experimental Determination of Gap-Flow Conditioned Forces at Turbine Stages, and Their Effect on the Running Stability of Simple Rotors,'' NASA TM-77293.
[5] Martinez-Sanchez, M., Jaroux, B., Song, S. J., and Yoo, S., 1995, ''Measurement of Turbine Blade-Tip Rotordynamic Excitation Forces,'' ASME J. Turbomach., **117**, pp. 384–393.
[6] Song, S. J., and Martinez-Sanchez, M., 1997, ''Rotordynamic Forces Due to Turbine Tip Leakage: Part 1–Blade Scale Effects,'' ASME J. Turobmach., **119**, pp. 695–703.
[7] Song, S. J., and Martinez-Sanchez, M., 1997, ''Rotordynamic Forces Due to Turbine Tip Leakage: Part 2—Radius Scale Effects and Experimental Verification,'' ASME J. Turbomach., **119**, pp. 704–713.
[8] Horlock, J. H., and Greitzer, E. M., 1983, ''Non-Uniform Flows in Axial Compressors Due to tip Clearance Variation,'' Proc. Inst. Mech. Eng., **197C**, pp. 173–178.
[9] Colding-Jorgensen, J., 1992, ''Prediction of Rotordynamic Destabilizing Forces in Axial Flow Compressors,'' ASME J. Fluids Eng., **114**, pp. 621–625.
[10] Ehrich, F. F., 1993, ''Rotor Whirl Forces Induced by the Tip Clearance Effect in Axial Flow Compressor,'' ASME J. Vibr. Acoust., **115**, pp. 509–515.
[11] Graf, M. B., Wong, T. S., Greitzer, E. M., Marble, F. E., Tan, E. S., Shin, H. W., Wisler, D. C., 1998, ''Effects of Nonaxisymmetric Tip Clearance on Axial Compressor Performance and Stability,'' ASME J. Turbomach., **120**, pp. 648–661.
[12] Park, K. Y., 1998, ''Non-uniform Compressor Flow Fields Induced by Nonaxisymmetric Tip Clearance,'' M.S. Thesis, Department of Aerospace Engineering, Inha Univ. Korea.
[13] Storace, A., et al., 2000, ''Unsteady Flow and Whirl-Inducing Forces in Axial-Flow Compressors; Part 1—Experiment,'' ASME Paper No. 2000-GT-565.
[14] Martinez-Sanchez, M., and Gauthier, R. P., 1990, ''Blade Scale Effects of Tip Leakage,'' Gas Turbine Laboratory Report #202, M.I.T.
[15] Chen, G. T., 1991, ''Vortical Structures in Turbomachinery Tip Clearance Flows,'' Ph.D. thesis, Department of Aeronautics and Astronautics, M.I.T.
[16] Roh, H. Y., 1997, ''Blade Scale Effects of Tip Leakage Flow in Axial Compressors,'' B.S. Thesis, Department of Aerospace Engineering, Inha Univ., Korea.
[17] Hunter, I. H., and Cumpsty, N. A., 1982, ''Casing Wall Boundary-Layer Development Through an Isolated Compressor Rotor,'' ASME J. Eng. Power, **104**, pp. 805–818.
[18] Ehrich, F. F., et al., 2000, ''Unsteady Flow and Whirl-Inducing Forces in Axial-Flow Compressors; Part 2—Analysis,'' ASME Paper No. 2000-GT-566.

Analysis of Aerodynamically Induced Whirling Forces in Axial Flow Compressors

Z. S. Spakovszky
Gas Turbine Laboratory,
Department of Aeronautics and Astronautics,
Massachusetts Institute of Technology,
Cambridge, MA 02139

A new analytical model to predict the aerodynamic forces in axial flow compressors due to asymmetric tip-clearance is introduced. The model captures the effects of tip-clearance induced distortion (i.e., forced shaft whirl), unsteady momentum-induced tangential blade forces, and pressure-induced forces on the spool. Pressure forces are shown to lag the tip-clearance asymmetry, resulting in a tangential (i.e., whirl-inducing) force due to spool pressure. This force can be of comparable magnitude to the classical Alford force. Prediction and elucidation of the Alford force is also presented. In particular, a new parameter denoted as the blade loading indicator is deduced. This parameter depends only on stage geometry and mean flow and determines the direction of whirl tendency due to tangential blade loading forces in both compressors and turbines. All findings are suitable for incorporation into an overall dynamic system analysis and integration into existing engine design tools. [S0889-504X(00)01604-4]

1 Introduction

Nonuniform engine tip-clearance distributions, due for example to a compressor shaft offset from its casing centerline or whirling in its bearing journal, can induce destabilizing rotordynamic forces. These forces stem from the strong influence of the tip-clearance on the local performance of the compressor. As first reported by Smith [1], reduced compressor tip-clearance yields increased compressor pressure rise. In the case of an offset compressor shaft, the blades passing through regions of small tip-clearance will experience higher blade loading and generate more lift than the blades operating in the large tip-clearance region. This results in a net tangential force acting perpendicular to the direction of the shaft offset and is referred to as the aerodynamically induced cross-coupled force.

Early studies conducted by Thomas [2] and Alford [3] on axial flow turbines with statically deflected rotors resulted in the postulation of a purely tangential destabilizing reaction force. The so-called Alford or Thomas force model is based on a cross-coupled stiffness coefficient $K_{r\theta}$ (tangential force F_θ induced on the rotor per unit radial deflection $\Delta\epsilon$) of the form

$$K_{r\theta}=\frac{F_\theta}{\Delta\epsilon}=\frac{\beta T}{Dl}, \tag{1}$$

where T denotes the stage torque, D the mean wheel diameter and l the blade span. The Alford β parameter was originally conceived as the change in thermodynamic efficiency per unit change in normalized clearance. In practice β has become an empirical factor to match computational predictions to experimental data. If β is positive, the net tangential force on the rotor F_θ is in the direction of shaft rotation inducing forward whirl. Similarly, a negative β indicates backward whirl tendency. It is recognized that axial flow turbines tend to generate forward rotor whirl. The early analysis for turbines set the foundation for new research and created an important empirical factor that is considered in the design of modern jet engines and gas turbines.

Several modeling efforts have been undertaken by many researchers [4–7] to address the issues of whirl-inducing forces in both compressors and turbines. The disparity between the findings and the lack of definitive measurements of cross-coupled excitation forces in axial compressors have led to an experimental and analytical program in the GE Aircraft Engines Low-Speed Research Compressor [8,9]. Two important effects, which could not be evaluated in the experimental program and have not yet been modeled in compressors, motivated the work presented here. In the actual case of a whirling shaft (only static shaft deflections could be simulated in the experiment), the unstable rotor would be whirling at the offset radius at the natural frequency of the system. It has been suggested that this whirling might have some significant effect on the value of the Alford β coefficients. Second, nonaxisymmetric pressure distributions on the rotor spool were identified as a separate forcing source in turbines and its effects were analyzed by Song and Martinez-Sanchez [7]. It is important to assess the nature and magnitude of nonaxisymmetric pressure effects in compressors as well. More specifically, the following research questions are of interest and are addressed in this paper:

- What level of modeling detail is needed to capture the experimental observations in axial flow compressors?
- How are compressors different from turbines regarding rotor whirl tendency?
- Can one construct a simple analytical model from first principles to determine the whirl tendency in compressors *and* in turbines?
- What drives the destabilizing spool pressure loading and how important is this effect compared to the Alford force?
- How does rotor whirl frequency affect the aerodynamically induced destabilizing forces?

The new model presented here was developed under these thrusts and applied in the GE Aircraft Engines LSRC test program [9]. In addition a simple, analytical model from first principles is presented, which predicts the cross-coupled whirl tendency in compressors and turbines.

2 Model Derivation

The new approach consists of two parts: a modified version of an existing two-dimensional, incompressible tip-clearance compressor stability model reported by Gordon [10] and an aerodynamically induced force model.

2.1 Unsteady Compressor Tip-Clearance Model. Hynes and Greitzer [11] present a compressor stability model to assess the effect of inlet flow distortion. Based on this conceptual framework Graf et al. [12] extended this model to account for steady

Contributed by the International Gas Turbine Institute and presented at the 45th International Gas Turbine and Aeroengine Congress and Exhibition, Munich, Germany, May 8–11, 2000. Manuscript received by the International Gas Turbine Institute February 2000. Paper No. 2000-GT-418. Review Chair: D. Ballal.

nonaxisymmetric tip-clearances. Gordon [10] further modified this approach to investigate the effect of rotating (unsteady) clearance asymmetries on compressor performance and stability. The unsteady reduced order force model presented in this paper uses a modified version of Gordon's model. The derivation of the compressor model equations is omitted here and a short description of the modified model is given instead.

The overall analysis consists of models of the inlet and exit ducts, the blade rows, the downstream plenum and throttle. The hub-to-tip ratio is assumed high enough to neglect radial variations of the flow quantities. Thus the model is two-dimensional with axial and circumferential unsteady flow field variations. Effects of viscosity and heat transfer outside of the blade rows are also neglected. The rotor and stator blade rows are modeled as semi-actuator disks with unsteady inertia and loss terms. Unsteady deviation effects are not modeled and the relevant Mach numbers are assumed to be low enough that compressibility effects can be neglected.

The inputs to the model are the compressor geometry, an axisymmetric compressor characteristic, and its sensitivity to changes in axisymmetric rotor tip-clearance. Assuming linear sensitivity, a family of compressor characteristics can be generated that is bounded by the maximum and minimum rotor tip clearance characteristics. In addition, any steady or unsteady tip-clearance distribution can be prescribed, e.g., shaft offsets, whirling shafts, etc. The compressor operating point is set by the throttle area.

The model assumes that the background flow is steady in the reference frame locked to the (rotating) tip-clearance asymmetry. Hence the steady, nonlinear flow field equations are solved in the asymmetry frame (see Fig. 3) to obtain the nonuniform background flow. The model outputs the two-dimensional, nonuniform distribution of flow coefficient, which is steady in the reference frame locked to the tip-clearance asymmetry. In the modified version of the model the entire distorted flow field (axial and tangential velocity and static pressure distributions through the compression system) is reconstructed and transformed back to the absolute frame. This flow field (now unsteady) will be used to determine the aerodynamically induced forces on the rotor.

In this paper, the model will be demonstrated using data [5] from a low-speed compressor with four repeating stages. Figure 1 depicts the experimentally measured axisymmetric compressor characteristics for $\epsilon = 1.4$ and 2.8 percent, along with the characteristics used as inputs to the model (solid). It also shows the computed mean operating point (+) and the corresponding locus of local operating points around the circumference (lightly dashed) for a steady shaft offset of $\Delta\epsilon = 0.7$ percent. The measurement of mean operating points for a steady shaft offset in the same compressor and comparison to the tip-clearance model predictions is reported in Ehrich et al. [9].

2.2 Aerodynamically Induced Force Model. Once the unsteady, two-dimensional flow field has been computed as described above, the aerodynamically induced forces can be computed. These forces consist of a spool pressure loading and a tangential force due to asymmetric turning. Simplified expressions for these quantities are derived here, and integrated to get the net forces acting on the rotor.

The spool pressure loading in the rotor frame is readily obtained from the flow field solution. Since the compressor blade rows have been modeled as semi-actuator disks, only the static pressure distribution between the blade rows can be directly computed. The unsteady spool pressure loading $p_{\text{spool}}(\theta',t)$ (where $\theta' = (\theta - \Omega t)$ is the tangential coordinate in the rotor frame) is estimated by averaging the static pressures upstream and downstream of the rotor:

$$p_{\text{spool}}(\theta',t) = \frac{p_1(\theta',t) + p_2(\theta',t)}{2}. \tag{2}$$

This approach assumes that the blade pitch is much smaller than the wavelength of the circumferential pressure distribution and makes use of the high hub-to-tip ratio assumption.

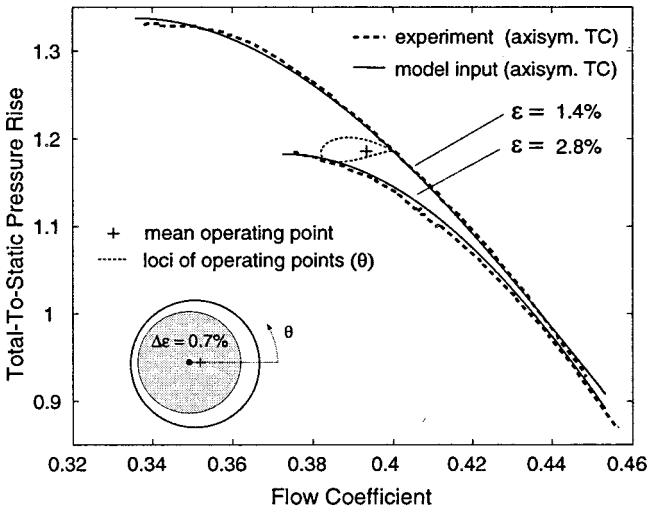

Fig. 1 Compressor performance prediction for a steady shaft offset of $\Delta\epsilon = 0.7$ percent in the four repeating stage compressor reported in [5]

To determine the local, unsteady tangential blade loading $f_\theta(\theta',t)$, an *unsteady* control volume analysis is conducted locally in the rotor frame. The advantage of this approach is that any unsteady flow regime (whirling shaft, rotating stall, etc.) can be considered. A control volume is defined in the rotor frame bounding one blade along the steady streamlines as sketched in Fig. 2, where the relative velocity vectors are labeled with **w**. The blade pitch, blade span, blade chord, mean wheel radius and the stagger angle are denoted by s, l, c, R, and γ, respectively. Generally the vector momentum equation in integral form is written for inviscid flows as

$$\frac{\partial}{\partial t}\oint_V \rho\mathbf{v}\,dV + \oint_{\partial V}(\rho\mathbf{v}\cdot\mathbf{n}\,dS)\mathbf{v} = -\oint_{\partial V} p\mathbf{n}\,dS + \oint_V \rho\mathbf{f}_b\,dV, \tag{3}$$

where **v** is the velocity field vector, p the static pressure field, and $\mathbf{f}_b$ the elemental body force vector per unit mass. Assuming incompressible flow through a constant height annulus, applying Eq. (3) to the control volume in Fig. 2 in the tangential direction, and replacing the body force integral by the *total* blade loading $F_{l\theta}$ of opposite sign (the body force acting on the fluid is equal to the negative of the fluid force on the body: $\mathbf{f}_b = -\mathbf{F}_{l\theta}$) yields

$$-\rho s l\cos\gamma c\frac{\partial}{\partial t}\overline{w_{\theta 12}} + \rho s l\cdot w_x\cdot(w_{\theta 1} - w_{\theta 2}) + \Delta \mathfrak{f}_{ss} = \Delta \mathfrak{p}_{ss} + F_{l\theta}. \tag{4}$$

The contributions of the net momentum flux and net pressure force across the streamwise surface boundaries are denoted by $\Delta\mathfrak{f}_{ss}$ and $\Delta\mathfrak{p}_{ss}$, respectively. Note that the only pressure terms arise from the streamwise surface boundaries since the pitchwise surface normal **n** is perpendicular to the tangential direction θ'. It is assumed for the unsteady term that the velocity inside the control volume is equal to the average of the velocities at stations 1 and 2.[1] The projection of this average velocity in the θ direction is denoted by $\overline{w_{\theta 12}}$.

The expression obtained is fairly complicated and needs to be simplified. Intuitively one can argue that if the wavelength of the flow nonuniformity is large compared to the blade pitch s, then $\Delta\mathfrak{f}_{ss}$ and $\Delta\mathfrak{p}_{ss}$ across the streamwise surfaces should vanish in

[1]Using this particular tip-clearance compressor model the flow field *inside* the blade rows cannot be reconstructed (actuator disk approach).

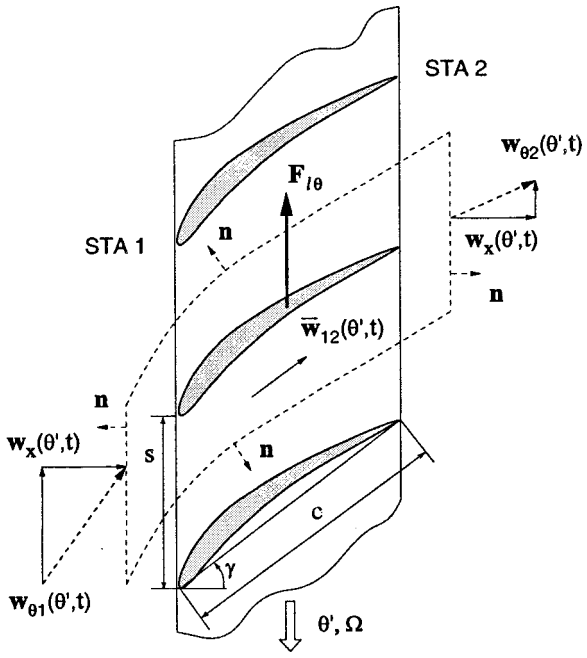

Fig. 2 Unsteady momentum control volume analysis locked to rotor frame

magnitude compared to the unsteady and tangential momentum flux terms. In fact, if the control volume width set by blade pitch s is taken to the limit $R \cdot d\theta$, it can be shown that the streamwise surface terms are negligible to first order. The *local* (per unit circumferential angle), unsteady, tangential blade loading f_θ can then be written as

$$f_\theta(\theta',t) = \rho R l \cdot w_x \cdot (w_{\theta 1} - w_{\theta 2}) - \frac{\rho R l \cos\gamma c}{2} \frac{\partial}{\partial t}\{w_{\theta 1} + w_{\theta 2}\}. \tag{5}$$

The next step is to integrate the spool pressure loading and tangential blade loading distributions defined in Eqs. (2) and (5) around the circumference. This is done in the rotor reference frame (x',y') shown in Fig. 3 to obtain the unsteady forces on the rotor:

$$\begin{aligned} f^s_{x'}(t) &= -\int_0^{2\pi} p_{\text{spool}}(\theta',t) \cdot \cos(\theta') \cdot c_{\text{sp}} R \cdot d\theta' \\ f^s_{y'}(t) &= -\int_0^{2\pi} p_{\text{spool}}(\theta',t) \cdot \sin(\theta') \cdot c_{\text{sp}} R \cdot d\theta' \\ f^b_{x'}(t) &= +\int_0^{2\pi} f_\theta(\theta',t) \cdot \sin(\theta') \cdot d\theta' \\ f^b_{y'}(t) &= -\int_0^{2\pi} f_\theta(\theta',t) \cdot \cos(\theta') \cdot d\theta' \end{aligned} \tag{6}$$

where the superscripts s and b denote *spool* loading and *blade* loading, respectively. The spool pressure load acts on the spool surface of axial length c_{sp}, which includes the interblade row gaps upstream and downstream of the rotor. Finally, these unsteady forces are transformed back to the reference frame locked to the tip-clearance asymmetry using the transformation given in Eq. (7) to get the aerodynamically induced forces F^s_x, F^s_y, F^b_x and F^b_y:

$$\begin{bmatrix} F_x \\ F_y \end{bmatrix} = \begin{bmatrix} \cos((\Omega-\omega)t) & -\sin((\Omega-\omega)t) \\ \sin((\Omega-\omega)t) & \cos((\Omega-\omega)t) \end{bmatrix} \cdot \begin{bmatrix} f_{x'}(t) \\ f_{y'}(t) \end{bmatrix}. \tag{7}$$

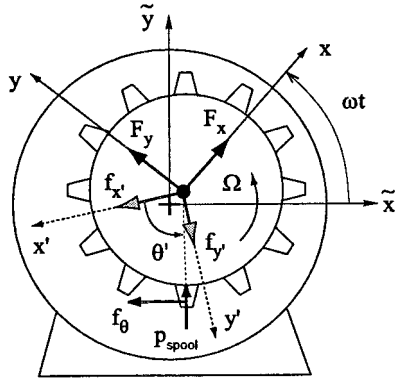

Fig. 3 Definition of reference frames: rotor frame (x',y'), rotating asymmetry frame (x,y), and absolute frame $(\tilde{x},\tilde{y})$

Note that, since the model assumed steady flow in the reference frame of rotating tip-clearances, the aerodynamically induced forces are steady in the asymmetry frame.

The magnitude and direction of the four aerodynamically induced rotor forces F^s_x, F^s_y, F^b_x and F^b_y are discussed next. The main focus will be on the sign of F^b_y, F^s_y, and their sum, since they determine the tendency of shaft whirl. Two parameters will be used in the analysis, the Alford β parameter (nondimensional F^b_y) and a new parameter denoted as the spool loading parameter β_{spool} (nondimensional F^s_y).

3 Analysis and Modeling Results

The model is implemented in a sample analysis for the second stage of the four repeating stage axial compressor reported in Ehrich [5].

3.1 Importance of the Alford β Parameter. In the case of a steady shaft offset, the tip-clearance asymmetry frame is identical to the absolute frame. The aerodynamic force model is implemented for the example compressor with a shaft offset of $\Delta\epsilon = 0.7$ percent. To analyze the destabilizing effect of a net tangential blade loading, only F^b_y is considered here. The Alford β parameter (Eq. (1)) is computed using the same mean stage torque T as in Ehrich [5] in order to compare the model predictions to the experimentally driven results of Ehrich. The direction of whirl depends on the direction of the net tangential force F^b_y with respect to shaft rotation. If F^b_y is positive (in the direction of rotation) β is positive and the rotor will tend to forward whirl. Similarly, a negative β indicates backward whirl tendency. The Alford β parameter is plotted for different flow coefficients in Fig. 4 (solid line). The magnitude of the Alford β parameter and the dependence of the whirl direction on the flow coefficient agrees well with the experimentally based predictions by Ehrich [5] (dashed line). For low flow coefficients a strong backward whirl tendency is predicted whereas forward whirl is induced for high flow coefficients. It should be mentioned that three-dimensional phenomena such as stator hub clearance and seal leakage effects can alter the Alford β parameter and are not accounted for in the two-dimensional approach. A comparison of the modeling results to experimental blade force data obtained in the GE Aircraft Engines LSRC facility and a discussion of the stator clearance and seal leakage effects are given in Ehrich et al. [9].

The two-dimensional unsteady modeling approach seems to capture the observed compressor phenomena well. The following questions arise from the result given above: What determines the direction of whirl tendency in compressors and how do compressors differ from turbines in this regard?

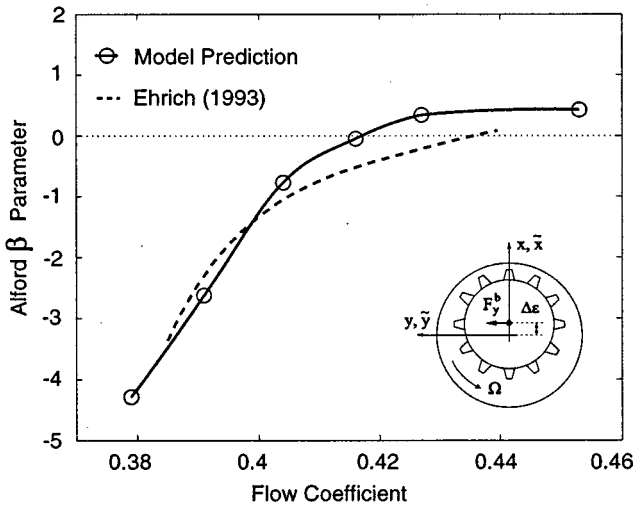

Fig. 4 Alford β parameter for four stage compressor reported in [5] and model prediction

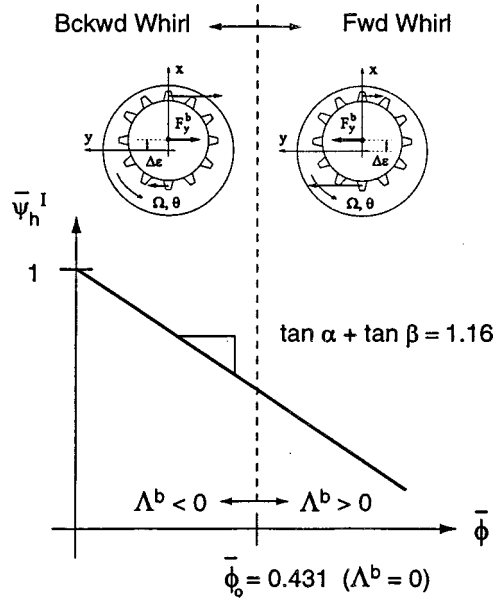

Fig. 6 Simplified whirl analysis of four-stage compressor

3.2 Blade Loading Indicator Parameter. In order to assess the difference between the whirl tendency in compressors and the whirl tendency in turbines, one would like to construct a general, simple analytical model from first principles. Simplifying Eq. (5) by neglecting unsteady effects and again assuming constant axial velocity through the stage, the tangential momentum balance can be written for both compressors and turbines as shown in Figs. 5(*a*, *b*), where f_θ^{comp} and f_θ^{turb} denote compressor and turbine tangential blade loading, ϕ is the flow coefficient, and $W=w/U$ is the nondimensional relative velocity. Using kinematic relations and the velocity triangles the tangential blade loading can be written in general as

$$f_\theta \sim \phi \cdot [1-(\tan\alpha+\tan\beta)\cdot\phi] = \phi\cdot\psi_h^I. \tag{8}$$

Note that f_θ points in the negative θ direction in Fig. 5. This expression holds for both compressors and turbines where ψ_h^I is the ideal static enthalpy rise for compressors or the ideal static enthalpy drop for turbines, α is the absolute inlet swirl angle and β denotes the relative exit swirl angle. Since only variations in tangential blade loading distribution contribute to the net tangential rotor force F_y^b, Eq. (8) can be expanded to first order and written as

$$\delta f_\theta \sim -[2(\tan\alpha+\tan\beta)\cdot\bar{\phi}-1]\cdot\delta\phi. \tag{9}$$

Let the bracketed expression be denoted as the *blade loading indicator* Λ^b, which only depends on the stage geometry and the mean value of the flow coefficient $\bar{\phi}$. If the tip-clearance is increased the blockage increases and yields a decrease in flow coefficient ($\delta\epsilon \sim -\delta\phi$). Combining this with Eq. (9), the following simple relation holds between the tip-clearance distribution and the distribution of the local tangential blade loading:

$$\delta f_\theta \sim \Lambda^b\cdot\delta\epsilon. \tag{10}$$

Let us assume that the variation in flow coefficient is purely sinusoidal and flow inertia effects are neglected. If Λ^b is positive, δf_θ is in phase with the tip-clearance distribution, and integration around the annulus yields a positive net tangential blade loading F_y^b (in the direction of rotation). The opposite holds for a negative blade loading indicator inducing F_y^b in the negative direction as sketched in Fig. 6 at the top. Hence the blade loading indicator is conjectured to determine the whirl direction for compressors and turbines.[2]

This simple model is applied to the four-stage compressor reported in Ehrich [5]. The inlet and exit swirl angles are known at midspan and assumed to be constant over the compressor operating range, yielding $\tan\alpha+\tan\beta=1.16$. Setting the blade loading indicator Λ^b to zero one can solve for the mean flow coefficient $\bar{\phi}$ for which the net tangential force should vanish. For this particular compressor if $\bar{\phi}=0.431$ the net tangential rotor force is zero, if $\bar{\phi}>0.431$ then Λ^b is positive, inducing forward whirl, and if $\bar{\phi}<0.431$ the compressor tends to backward whirl due to a negative blade loading indicator Λ^b. This situation is sketched in Fig. 6 together with the ideal compressor characteristic $\bar{\psi}_h^I$. Comparison of this result to the experimentally based Alford β predictions by Ehrich [5] in Fig. 4 shows that the β curve crosses zero at a flow coefficient of 0.435. This agrees well with the simple model result of $\bar{\phi}=0.431$ and the predictions of whirl direction tendency. In order to give more generality to the assessment, two other compressors reported in Ehrich [5] are analyzed. The predictions by the simple, first principles approach and experimentally based results by Ehrich [5] are summarized for all three compressors in Table 1.

The simple model can also be applied to turbines. Turbines inherently exhibit much higher flow turning than compressors, especially if they are of impulse type with a degree of reaction close to zero. Hence, the absolute inlet and relative exit swirl angles will be much higher than in a compressor rotor. Therefore,

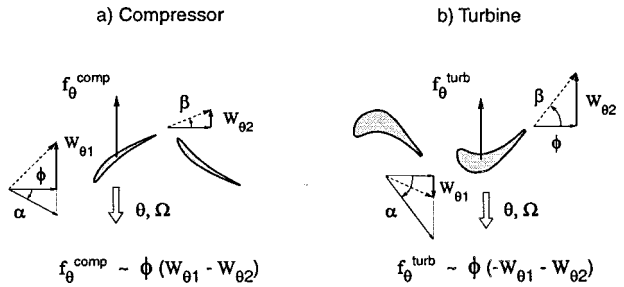

Fig. 5 Simplified blade loading analysis for compressors and turbines

[2]This analysis is limited to the sign of the Alford β only and does not include the effect of spool pressure loading.

Table 1 Experimentally based predictions [5] and Λ^b approach for three axial flow compressors reported in [5]: backward whirl tendency for $\bar{\phi}<\bar{\phi}_0$, forward whirl tendency for $\bar{\phi}>\bar{\phi}_0$

Method	Compressor 1	Compressor 2	Compressor 3
$\Lambda^b=0$	$\bar{\phi}_o=0.464$	$\bar{\phi}_o=0.506$	$\bar{\phi}_o=0.431$
Ehrich	$\bar{\phi}_o=0.457$	$\bar{\phi}_o=0.490$	$\bar{\phi}_o=0.435$

the blade loading indicator Λ^b is always positive and its sign is independent of the mean flow coefficient, unless $\bar{\phi}$ is very small or the degree of reaction is relatively high (less turning). This leads to the conjecture that, in turbines, the net tangential blade loading induces forward whirl over the entire operating range. This is in agreement with Alford's hypothesis and observations reported in literature.

3.3 Effects of Spool Pressure Loading. Nonaxisymmetric pressure distributions on the rotor spool were identified as a separate forcing source in turbines, and its effects were analyzed by Song and Martinez-Sanchez [7]. It is suggested that this effect is also important in compressors and its nature and magnitude are assessed in this section.

To quantify the destabilizing effect of spool pressure loading, a parameter similar to the Alford β coefficient is defined:

$$\beta_{\text{spool}}=\frac{F_y^s Dl}{T\Delta\epsilon}. \tag{11}$$

The β_{spool} parameter is computed for different flow coefficients and plotted in Fig. 7. Forward whirl ($\beta_{\text{spool}}>0$) is induced, with a maximum value of β_{spool} near compressor stall. This is mostly due to the fact that the flow field is more distorted for flow coefficients less than 0.41 (the family of compressor characteristics are further apart at low flows in Fig. 1). The magnitude of β_{spool} is about half the magnitude of the Alford β parameter for low-flow coefficients. Note that the forward whirl induced by spool pressure loading mitigates the backward whirl tendency due to the net tangential blade loading (Fig. 4). The nature of the forward whirl tendency due to spool pressure effects is discussed next.

First let us consider a family of axisymmetric tip-clearance compressor characteristics with no curvature and neglect unsteady losses and flow inertia effects in the blade rows and ducts. In this case the flow instantaneously responds to the distortion induced by the asymmetric tip-clearance. Regions with tight tip-clearance yield high total-to-static pressure rise, less blockage, and therefore a higher flow coefficient. Conserving total pressure in the upstream duct (potential flow) and matching the uniform pressure distribution at the compressor exit yields a lower spool pressure in the tight tip-clearance region. The opposite holds for regions of large tip-clearance. The variation in total-to-static pressure rise $\delta\psi_{ts}$, the variation in flow coefficient $\delta\phi$, and the variation in non-dimensional spool pressure $\delta p_{\text{spool}}/\rho U^2$ are plotted in Fig. 8 as dashed lines for the given shaft offset (the tip-clearance distribution is shown as the dotted line in the top plot). Evaluation of the first two integrals in Eq. (6) and transformation to the frame of the shaft offset using Eq. (7) yields $F_x^s>0$ and $F_y^s=0$ for this sinusoidal spool pressure distribution. In other words, the aerodynamically induced rotor force due to spool loading is a purely radial destabilizing force, as sketched in Fig. 9(*a*). The purely sinusoidal spool pressure loading distribution does not induce whirl since the aerodynamic rotor force has no tangential component ($F_y^s=0$).

Now let us consider the family of compressor characteristics shown in Fig. 1 and assume that unsteady losses and unsteady flow inertia effects are present. The total-to-static pressure rise distribution $\delta\psi_{ts}$ is now distorted due to the curvature of the compressor characteristics as depicted in the top plot of Fig. 8 (solid line). A part of the compressor pressure rise is now devoted to acceleration of the fluid in the blade row passages. Assuming quasi-steady flow and no exit swirl, it can be shown that the following pressure balance across the compressor must hold:

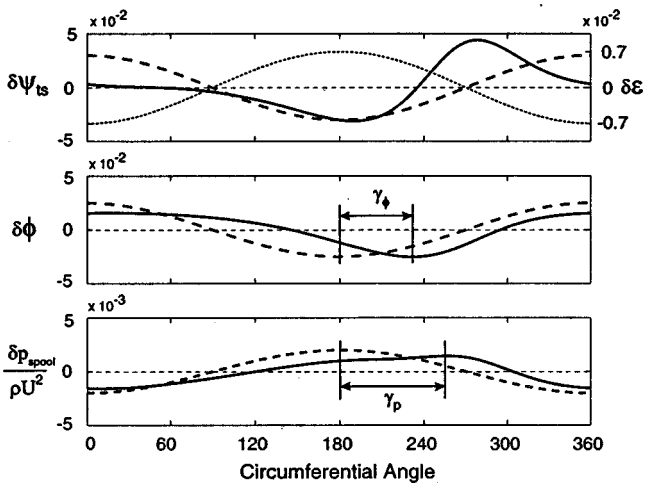

Fig. 8 Compressor flow field with inertia effects included (solid) and inertia effects neglected (dashed) for a given tip-clearance distribution $\delta\varepsilon$ (dotted)

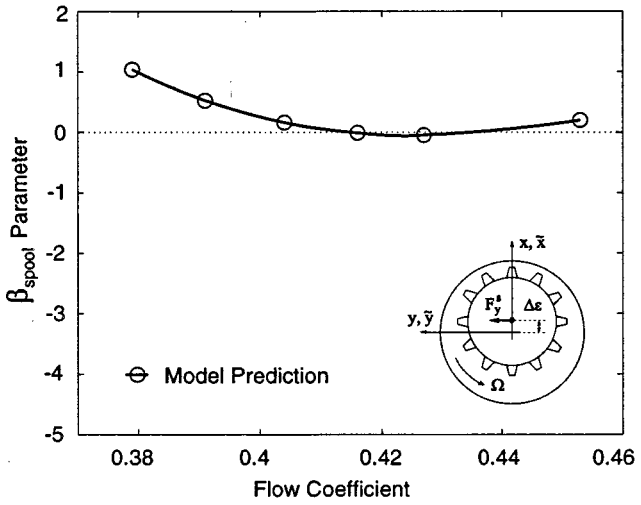

Fig. 7 Spool loading parameter β_{spool} for four repeating stage compressor reported in [5]

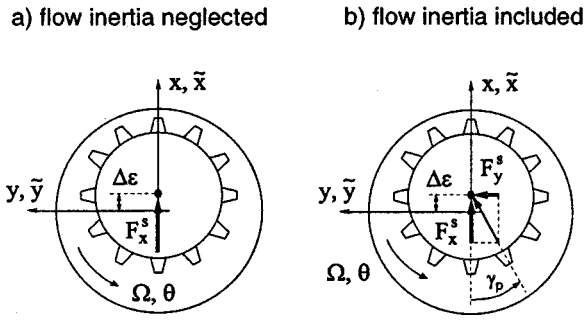

Fig. 9 Effect of flow inertia on rotor forces due to spool pressure loading

$$\frac{p^{\mathrm{dn}}-p_t^{\mathrm{up}}}{\rho U^2}=\psi_{ts}-\lambda\cdot\frac{\partial\phi}{\partial\theta}, \tag{12}$$

where λ denotes the nondimensional fluid inertia in the rotor blade rows [13]

$$\lambda=\sum_{\text{rotors}}\frac{c_x/R}{\cos^2\gamma}. \tag{13}$$

In steady flow, the compressor upstream total pressure p_t^{up} and compressor downstream static pressure p^{dn} are uniform, so circumferential variations in ψ_{ts} must be directly balanced by variations in the gradient of flow coefficient

$$0=\delta\psi_{ts}-\lambda\cdot\frac{\partial\delta\phi}{\partial\theta}. \tag{14}$$

This explains why the flow coefficient variation lags the clearance distribution in Fig. 8. Including flow inertia in the compressor model results in a relative phase shift in the flow coefficient and spool pressure distributions, denoted γ_ϕ and γ_{p} in Fig. 8. Due to this positive phase shift, the spool pressure loading now also yields a force component in the tangential direction F_y^s and induces forward whirl as shown in Fig. 9(*b*).

3.4 Effects of Forced Shaft Whirl. In the case of a whirling shaft, the rotor would be whirling at the offset radius at the natural frequency of the system. It is therefore important to assess the effects of this whirling on the β parameters.

The following parameter study is conducted to assess the effects of forced shaft whirl on the destabilizing rotor forces. The whirl frequency ω is varied from synchronous backward whirl ($\omega=-\Omega$) to synchronous forward whirl ($\omega=\Omega$) for a shaft offset of $\Delta\epsilon=0.7$ percent. The aerodynamically induced forces acting in the rotating asymmetry frame are computed using Eqs. (6) and (7). In order to examine the whirl tendency due to unbalanced blade and spool loading effects, the Alford β parameter and the spool loading parameter β_{spool} are determined. Figure 10 depicts the β parameters for different flow coefficients and nondimensional whirl frequencies ω/Ω. The tip-clearance compressor model can also be used to determine compressor stability. Due to the flow distortion, which is affected by the shaft whirl, the rotating stall frequency varies slightly with the forced whirl frequency. For the four-stage compressor discussed here, rotating stall is predicted to occur between 22 and 46 percent of rotor frequency. This rotating stall frequency range is indicated by Ω_{RS}.

Notice that for low flow coefficients, the Alford β parameter is amplified and the spool loading β_{spool} changes sign close to zero forced whirl frequency. A detailed analysis of the flow field shows that the rotating tip-clearance asymmetry induces an enhanced distortion of the flow near rotating stall. Consider an observer sitting on the rotating asymmetry frame at the location of the smallest tip-clearance. The observer will then perceive a steady, nonuniform flow field, which will have a certain orientation relative to the observer's location. The phase and the magnitude of the fundamental wave form (a single lobed sinusoid indicated by subscript 1) of the flow coefficient and the nondimensional spool pressure are analyzed for different forced whirl frequencies. The results for a compressor operating point close to stall are shown in Fig. 11 and the rotating stall frequency range is again indicated by Ω_{RS}.

If shaft motion occurs at negative whirl frequencies, the flow field lags the clearance asymmetry and the relative phase between the clearance asymmetry and the spool pressure distribution γ_p is positive. This translates to a spool loading induced forward whirl, as described in Fig. 9. The opposite holds for positive whirl frequencies higher than 0.1 and yields backward whirling forces, as shown in the bottom plot of Fig. 10. Similar arguments hold for the blade loading distribution since the relative phase between the net tangential blade loading F_y^b and the rotating clearance asymmetry can be related to the phase of the flow coefficient (see Eq. (5)). Notice that γ_ϕ never exceeds ± 90 deg so that F_y^b does not change sign. This yields a whirl frequency independence of the sign of the Alford β parameter as shown in the top plot of Fig. 10. The enhanced flow field distortion and the zero phase γ_ϕ near the

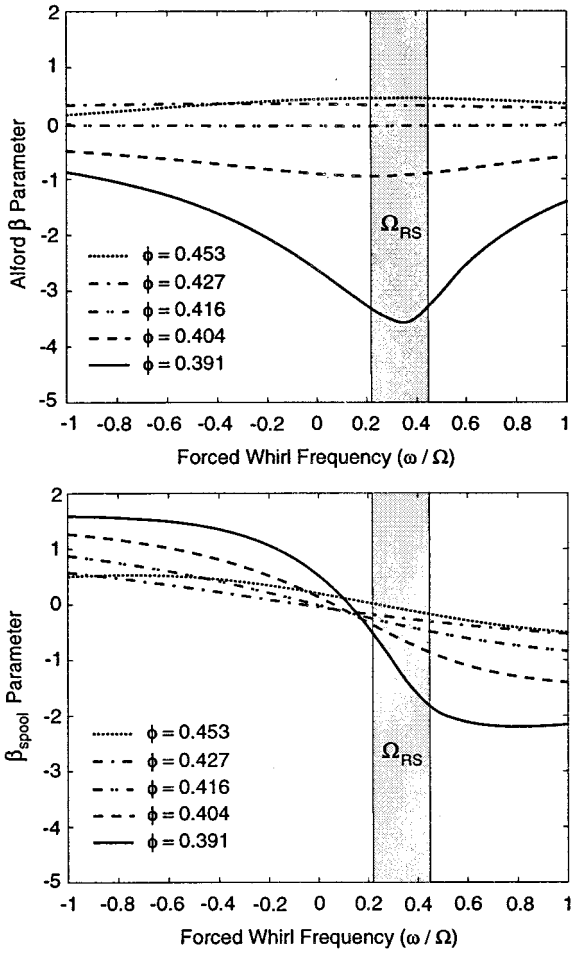

Fig. 10 Alford β parameter and spool loading parameter β_{spool} for forced rotor whirl

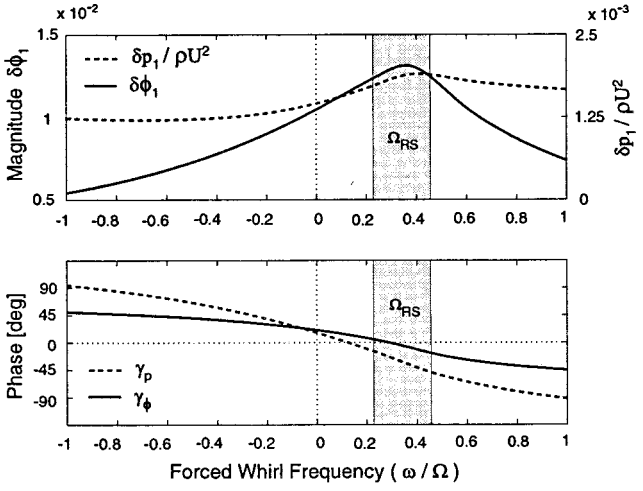

Fig. 11 Magnitude and phase of fundamental wave form of flow coefficient (solid) and nondimensional spool pressure (dashed) for $\phi=0.391$

rotating stall frequency (see Fig. 11) are felt in the net tangential blade loading and reflected in an amplification of β near Ω_{RS}.

It is important to note the following results from Fig. 10: (1) The spool loading parameter β_{spool} acts in the direction against whirl for both large positive and negative forced whirl frequencies. (2) β_{spool} is of comparable magnitude to the Alford β. (3) β_{spool} opposes the effects of the Alford β for two cases: for negative whirl frequencies and low flow coefficients and for positive whirl frequencies and high flow coefficients. (4) The net effect of β_{spool} and the Alford β yields backward whirl for forced whirl frequencies ranging from -0.5 to $+1$. To the author's knowledge no rotor whirl experiment has been reported in literature in order to compare the modeling results to data. Spakovszky et al. [14] report a feasibility study of a magnetic bearing servo-actuator for a high-speed compressor stall control experiment. The described experiment could be used to whirl and precess the compressor shaft actively to investigate rotordynamic–aerodynamic coupling effects.

Note also that the frequency coincidence between enhanced whirl tendency and rotating stall leads to the conjecture that in an engine, where the rotordynamics and compressor aerodynamics form one dynamic system, shaft whirl can interact and resonate with flow instability patterns such as rotating stall. The current uncoupled modeling results are an important piece of an overall dynamic system analysis since they separate the basic effects of whirl inducing forces. A nonlinear, coupled system analysis is suggested to investigate the dynamic behavior of the compressor–rotor system. Current research on rotordynamic–aerodynamic interaction in axial compression systems is reported by Al-Nahwi [15].

4 Conclusions and Summary

This paper reports a new unsteady low-order model to predict aerodynamically induced whirling forces in axial flow compressors. The model consists of two parts: a tip-clearance induced distortion model and an aerodynamically induced force model. The distortion model predicts the flow response to given (rotating) tip-clearance asymmetries. The force model then uses this distorted unsteady flow field to deduce the forces on the rotor. The force model is not limited to this particular compressor model; any prediction of the compressor flow field can be used (i.e., CFD, experimental data, etc.). The model computes destabilizing rotor forces due to nonuniform tangential blade loading and nonuniform spool pressure loading effects for steadily deflected and whirling shafts.

The model is implemented in a sample analysis for the four repeating stage axial compressor reported in Ehrich [5]. A steady shaft offset of $\Delta\epsilon = 0.7$ percent tip-clearance over span is considered first and the computed Alford β parameter is in good agreement with the results reported in Ehrich [15].

In addition, a simple model from first principles is presented. This analytical approach introduces a simple parameter denoted as the *blade loading indicator*. The blade loading indicator depends only on the stage geometry and the mean flow coefficient and determines the direction of whirl tendency due to tangential blade loading forces in both compressors and turbines.

A spool loading parameter β_{spool}, analogous to the Alford β parameter, is introduced and predicts forward whirl for steady shaft offsets. The effect of flow inertia on the spool pressure loading is investigated and the modeling results show that the flow field lags the clearance distribution due to the fluid inertia. This phase shift induces destabilizing rotor forces, due to spool pressure loading effects, which add to the forces predicted by Alford.

Forced shaft whirl is simulated to assess the effects of shaft motion on the destabilizing rotor forces. The β_{spool} parameter acts in the direction against whirl and is of comparable magnitude to the Alford β. It opposes the effects of the Alford β for negative whirl frequencies and low flow coefficients and for positive whirl frequencies and high flow coefficients. Also, the frequency coincidence between shaft whirl and rotating stall suggests nonlinear coupling effects between the aerodynamics and the rotordynamics.

An important element in the design of rotordynamically stable jet engines is the accurate prediction of the aerodynamically induced forces. The reported results are compared to experimental blade force data obtained from the GE Aircraft Engines LSRC test facility in Ehrich et al. [9]. The presented aerodynamically induced force model forms an important basis for an overall dynamic system analysis and is suggested as an integral part of engine design tools.

Acknowledgments

The author would like to thank A. Al-Nahwi and Dr. F. Ehrich for the very useful comments and insightful discussions. This research was conducted under NASA grant No. NAG3-2052.

Nomenclature

α = absolute inlet swirl angle
β = relative exit swirl angle, Alford parameter
c = chord
D = mean wheel diameter
$f, F, \mathfrak{f}$ = loading, force, momentum flux
ϕ = flow coefficient
$\epsilon, \Delta\epsilon$ = tip-clearance/span, shaft offset/span
γ = stagger angle, phase angle
$K_{r\theta}$ = cross-coupled stiffness coefficient
l = blade span
λ = rotor blade row inertia
Λ^b = blade loading indicator
$\mathbf{n}$ = surface normal
$p, \mathfrak{p}$ = static pressure, pressure force
ψ, ψ_h = pressure rise, enthalpy rise
R, ρ = mean wheel radius, density
s = blade pitch
t, T = time, stage torque
θ, θ' = circumferential angle (absolute and rotor frame)
U = mean wheel speed
$v, \mathbf{v}$ = absolute velocity (vector)
$w, \mathbf{w}$ = relative velocity (vector)
ω, Ω = whirl frequency, rotor frequency
x, y = coordinates in asymmetry frame
x', y' = coordinates in rotor frame
$\tilde{x}, \tilde{y}$ = coordinates in absolute frame

References

[1] Smith, L., 1958, ''The Effect of Tip Clearance on the Peak Pressure Rise of Axial-Flow Fans and Compressors,'' *Proc. ASME Symposium on Stall*, pp. 149–152.
[2] Thomas, H., 1958, ''Unstable Natural Vibration of Turbine Rotors Induced by the Clearance Flow in Glands and Blading,'' Bull. de l'A.I.M, **71**, No. 11/12, pp. 1039–1063.
[3] Alford, J., 1965, ''Protecting Turbomachinery From Self-Excited Rotor Whirl,'' ASME J. Eng. Power, **87**, pp. 333–344.
[4] Colding-Jorgensen, J., 1992, ''Prediction of Rotor Dynamic Destabilizing Forces in Axial Flow Compressors,'' ASME J. Fluids Eng., **114**, pp. 621–625.
[5] Ehrich, F., 1993, ''Rotor Whirl Forces Induced by the Tip Clearance Effect in Axial Flow Compressors,'' ASME J. Vibr. Acoust., **115**, pp. 509–515.
[6] Yan, L., Hong, J., Li, Q., Zhu, Z., and Zhao, F., 1995, ''Blade Tip Destabilizing Force and Instability Analysis for Axial Rotors of Compressors,'' Beijing University of Aeronautics and Astronautics Report.
[7] Song, S., and Martinez-Sanchez, M., 1997, ''Rotordynamic Forces Due to Turbine Tip Leakage: Part I—Blade Scale Effects,'' ASME J. Turbomach., **119**, pp. 695–703.
[8] Storace, A., Wisler, D., Shin, H. W., Beacher, B., Ehrich, F., Spakovszky, Z., Martinez-Sanchez, M., and Song, S., 2000, ''Unsteady Flow and Whirl Inducing Forces in Axial-Flow Compressors; Part I—Experiment,'' ASME Paper No. 2000-GT-565.
[9] Ehrich, F., Spakovszky, Z., Martinez-Sanchez, M., Song, S., Wisler, D., Storace, A., Shin H. W., and Beacher, B., 2000, ''Unsteady Flow and Whirl Inducing Forces in Axial-Flow Compressors; Part II—Analysis,'' ASME Paper No. 2000-GT-566.

[10] Gordon, K., 1999, ''Three-Dimensional Rotating Stall Inception and Effects of Rotating Tip Clearance Asymmetry in Axial Compressors,'' Ph.D. thesis, Department of Aeronautics and Astronautics, MIT.
[11] Hynes, T., and Greitzer, E., 1987, ''A Method for Assessing Effects of Circumferential Flow Distortion on Compressor Stability,'' ASME J. Turbomach., **109**, pp. 371–379.
[12] Graf, M., Wong, T., Greitzer, E., Marble, F., Tan, C., Shin, H. W., and Wisler, D., 1998, ''Effects of Nonaxisymmetric Tip Clearance on Axial Compressor Performance and Stability,'' ASME J. Turbomach., **120**, pp. 648–661.
[13] Moore, F., and Greitzer, E., 1986, ''A Theory of Post-Stall Transients in Axial Compressors: Part I—Development of the Equations,'' ASME J. Eng. Gas Turbines Power, **108**, pp. 68–76.
[14] Spakovszky, Z., Paduano, J., Larsonneur, R., Traxler, A., and Bright, M., 2000, ''Tip-Clearance Actuation with Magnetic Bearings for High-Speed Compressor Stall Control,'' ASME Paper No. 2000-GT-528.
[15] Al-Nahwi, A., 2000, ''Aerodynamic-Rotordynamic Interaction in Axial Compression Systems,'' Ph.D. thesis, Dept. of Mechanical Engineering, MIT.

A Navier–Stokes Analysis of the Stall Flutter Characteristics of the Buffum Cascade

Stefan Weber
Post-Doctoral Research Associate,
Deutsche Forschungsgemeinschaft,

Max F. Platzer
Professor,
Fellow ASME

Department of Aeronautics and Astronautics,
Naval Postgraduate School,
Monterey, CA 93943-5000

Numerical stall flutter prediction methods are much needed, as modern jet engines require blade designs close to the stability boundaries of the performance map. A Quasi-3D Navier–Stokes code is used to analyze the flow over the oscillating cascade designed and manufactured by Pratt & Whitney, and studied at the NASA Glenn Research Center by Buffum et al. The numerical method solves for the governing equations with a fully implicit time-marching technique in a single passage by making use of a direct-store, periodic boundary condition. For turbulence modeling, the Baldwin–Lomax model is used. To account for transition, the criterion to predict the onset location suggested by Baldwin and Lomax is incorporated. Buffum et al. investigated two incidence cases for three different Mach numbers. The low-incidence case at a Mach number of 0.5 exhibited the formation of small separation bubbles at reduced oscillation frequencies of 0.8 and 1.2. For this case the present approach yielded good agreement with the steady and oscillatory measurements. At high incidence at the same Mach number of 0.5 the measured steady-state pressure distribution and the separation bubble on the upper surface was also found in good agreement with the experiment. But computations for oscillations at high incidence failed to predict the negative damping contribution caused by the leading edge separation. [S0889-504X(00)01304-0]

Introduction

A review of aeroelastic prediction methods for axial-flow turbomachinery [1] showed that the commonly used unsteady flow models were limited to two-dimensional linearized methods. During the past twelve years, tremendous advances in CFD have made it possible to replace some of these models by nonlinear three-dimensional flow models. However, the simulation of strong viscous flow effects is still fraught with many uncertainties, making it difficult to predict some important aeroelastic phenomena. One of these phenomena is stall flutter, where the currently used empirical correlations for the stall flutter boundary prediction of compressor and fan blades have yet to be replaced by ''rational'' computational methods based on the solution of the Navier–Stokes equations. These uncertainties are caused by the well-recognized difficulties to model laminar-to-turbulent flow transition and turbulent flow in the presence of strong flow oscillations. Furthermore, it is likely that stall flutter cannot be modeled by purely two-dimensional methods because separated flows tend to be three-dimensional. This situation is complicated even further for the case of high subsonic/transonic stall flutter due to the formation of shock waves.

In this situation the computational fluid dynamicist has no choice but to proceed to increasingly more demanding flow modeling and to evaluate the validity of the model against well-controlled experiments. Most investigators are agreed that the modeling has to be based on the Navier–Stokes equations. However, great savings in CPU times can be achieved if the flow is decomposed into a steady nonlinear flow upon which small harmonic perturbations are superimposed. The most recent example for this type of approach was presented by Clark and Hall [2] following the work of Hall and Crawley [3], Kahl and Klose [4], and Montgomery and Verdon [5]. On the other hand, time linearization imposes limits on the oscillation amplitudes and hence it is prudent to evaluate time-linearized results against solutions of the nonlinearized unsteady Navier–Stokes equations. Furthermore, recent steady and dynamic stall computations for single airfoils have yielded markedly improved agreement with measured hysteresis loops if the Baldwin and Lomax [6] algebraic turbulence model was replaced by the one-equation Baldwin and Barth [7] and Spalart and Allmaras [8] models and the laminar-to-turbulent transition onset and length was incorporated into computations, as shown by Ekaterinaris and Platzer [9], Sanz and Platzer [10], Weber and Platzer [11], Weber et al. [12], and Eulitz [13].

The approach presented in this paper is based on the reasoning given above. Although three-dimensional flutter computations are presently being developed, for example by Bakhle [14] and Chew et al. [15], we believe that such an approach is still premature for the analysis of stall flutter. Therefore, the present analysis is based on the Quasi-3D Navier–Stokes equations without any further linearization assumptions. Such an approach was also adopted by He [16], Eguchi and Wiedermann [17], Abhari and Giles [18], Grüber and Carstens [19], Weber et al. [20,21], Kato et al. [22], Tuncer et al. [23], Carstens and Schmitt [24], Fourmaux [25], and Lin and Murthy [26]. The turbulence modeling still relies on the simple algebraic Baldwin–Lomax model, but the transition onset criterion introduced by Baldwin–Lomax is incorporated. The results are evaluated by comparison with the oscillating cascade measurements of Buffum et al. [27] which appear to be the most reliable data for such a comparison at the present time.

Mathematical Model

The present algorithm solves the nondimensinalized time-dependent Quasi-3D Navier–Stokes equations. The equations are derived for an m, φ-coordinate system with m in axial and φ in circumferential direction. It represents S1-stream surfaces of revolution at a radius r with a variable stream surface thickness B to account for three-dimensional flow effects. Following Benetschik [28], the Favre-averaged governing equations in strong conservation law-form transformed to curvilinear coordinates (ξ, η) can be given in a rotating frame of reference as follows:

$$\partial_t \hat{\mathbf{U}} + \partial_\xi \left(\hat{\mathbf{E}} - \frac{1}{\mathrm{Re}} \hat{\mathbf{E}}_v \right) + \partial_\eta \left(\hat{\mathbf{F}} - \frac{1}{\mathrm{Re}} \hat{\mathbf{F}}_v \right) = \hat{\mathbf{Q}} \qquad (1)$$

Contributed by the International Gas Turbine Institute and presented at the 45th International Gas Turbine and Aeroengine Congress and Exhibition, Munich, Germany, May 8–11, 2000. Manuscript received by the International Gas Turbine Institute February 2000. Paper No. 2000-GT-385. Review Chair: D. Ballal.

in which $J=\partial(m,\varphi)/\partial(\xi,\eta)$ is the Jacobian matrix of transformation, and where $\hat{\mathbf{U}}$ is the vector of conservative variables

$$\hat{\mathbf{U}}=JrB\begin{Bmatrix}\rho\\ \rho v_m\\ \rho r v_\varphi\\ \theta_{\mathrm{rot}}\end{Bmatrix}, \tag{2}$$

$\hat{\mathbf{E}}$ and $\hat{\mathbf{F}}$ are the Euler fluxes

$$\hat{\mathbf{E}}=JB\begin{Bmatrix}\rho W^\xi\\ \rho v_m W^\xi+rp\xi_m\\ \rho r v_\varphi W^\xi+rp\xi_\varphi\\ e_{\mathrm{rot}}W^\xi+pw^\xi\end{Bmatrix}, \tag{3}$$

$$\hat{\mathbf{F}}=JB\begin{Bmatrix}\rho W^\eta\\ \rho v_m W^\eta+rp\eta_m\\ \rho r v_\varphi W^\eta+rp\eta_\varphi\\ e_{\mathrm{rot}}W^\eta+pw^\eta\end{Bmatrix}, \tag{4}$$

and $\hat{\mathbf{E}}_v$ and $\hat{\mathbf{F}}_v$ the viscous fluxes

$$\hat{\mathbf{E}}_v=J\begin{Bmatrix}0\\ r\rho\tau_{mm}\xi_{mm}+\tau_{m\varphi}\xi_\varphi\\ r(r\rho\tau_{m\varphi}\xi_{mm}+\tau_{\varphi\varphi}\xi_\varphi)\\ rE_{ev}\xi_m+F_{ev}\xi_\varphi\end{Bmatrix}, \tag{5}$$

$$\hat{\mathbf{F}}_v=J\begin{Bmatrix}0\\ r\rho\tau_{mm}\eta_{mm}+\tau_{m\varphi}\eta_\varphi\\ r(r\rho\tau_{m\varphi}\eta_{mm}+\tau_{\varphi\varphi}\eta_\varphi)\\ rE_{ev}\eta_m+F_{ev}\eta_\varphi\end{Bmatrix}, \tag{6}$$

where

$$E_{ev}=w_m\tau_{mm}+w_\varphi\tau_{m\varphi}+q_m, \tag{7}$$

$$F_{ev}=w_m\tau_{m\varphi}+w_\varphi\tau_{\varphi\varphi}+q_\varphi, \tag{8}$$

and the source vector $\hat{\mathbf{Q}}$ due to the coordinate transformation for the S1-system

$$\hat{\mathbf{Q}}_v=JrB\begin{Bmatrix}0\\ \rho v_\varphi^2\dfrac{1}{r}\dfrac{\partial r}{\partial m}+\dfrac{p}{rB}\dfrac{\partial rB}{\partial m}\\ 0\\ 0\end{Bmatrix}. \tag{9}$$

The transformed components of the heat flux q and the stress tensor τ are given in more detail in Weber et al. [20]. In these equations ρ denotes the density and p the pressure. The absolute and relative velocity components are v_m, v_φ, and w_m, w_φ, respectively. The contravariant velocities W^ξ and W^η are given by:

$$W^\xi=r\xi_m(w_m-c_{\xi m})+\xi_\varphi(w_\varphi-c_{\xi\varphi}) \tag{10}$$

and

$$W^\eta=r\eta_m(w_m-c_{\eta m})+\eta_\varphi(w_\varphi-c_{\eta\varphi}) \tag{11}$$

with the components of the contravariant cell face velocities c^ξ, c^η which have to be introduced due to the time-dependent deformation of the grid. The volume specific total energy e_{rot} and the rothalpy H_{rot} assuming perfect gas are defined as:

$$e_{\mathrm{rot}}=\frac{p}{\kappa-1}+\frac{\rho}{2}(v_m^2+v_\varphi^2)-\Omega r\rho v_\varphi \tag{12}$$

and

$$H_{\mathrm{rot}}=\frac{e_{\mathrm{rot}}+p}{\rho} \tag{13}$$

with κ the ratio of the specific heats, and Ω in case of a rotor flow as the angular velocity. To model the turbulent stresses, a turbulent eddy viscosity is computed following the turbulence model of Baldwin and Lomax [6]. The laminar viscosity is predicted by Sutherland's law. The onset of laminar/turbulent transition is found with the criterion suggested by Baldwin and Lomax [6] using C_{mutm} of 14. Furthermore, an effective thermal transport coefficient is introduced, using a laminar and a turbulent Prandtl number.

Equation (1) is nondimensionalized referring to the free-stream total density, the free-stream total velocity of sound, the free-stream total viscosity, and the chord length.

Numerical Method

A finite volume technique is applied for the numerical solution of Eq. (1), which is discretized in a node-centered form. Central and antisymmetric differences are used to compute the viscous fluxes. The inviscid fluxes are computed with an upwind FDS scheme by Roe [29]. At each volume cell face it solves for an approximative Riemann problem by computing a numerical flux function. For example in the ξ direction, the definition of the flux function for a cell face located at $(i+1/2,j)$ is:

$$\hat{\mathbf{E}}(\hat{\mathbf{U}})_{i+1/2,j}=\frac{1}{2}[\hat{\mathbf{E}}(\hat{\mathbf{U}}_L)_{i+1/2}+\hat{\mathbf{E}}(\hat{\mathbf{U}}_R)_{i+1/2} -(\hat{\mathbf{R}}^\xi|\hat{\mathbf{\Lambda}}^\xi|\hat{\mathbf{L}}^\xi(\hat{\mathbf{U}}_R-\hat{\mathbf{U}}_L))_{i+1/2}] \tag{14}$$

with the initial state vectors $\hat{\mathbf{U}}_L$ at the left and $\hat{\mathbf{U}}_R$ at the right side of the cell face, $\hat{\mathbf{L}}^\xi$ the left and $\hat{\mathbf{R}}^\xi$ the right matrices of the left and the right eigenvectors, respectively and $\hat{\mathbf{\Lambda}}^\xi$ the diagonal matrix of eigenvalues with respect to $\hat{\mathbf{E}}$. The components of the matrices are obtained using the Roe average.

With Eq. (14), a characteristic wave decomposition is achieved, resulting in two acoustic waves, one shear, and one entropy wave. Herein the eigenvalues describe the characteristic speed and the direction of the waves. Consistent with the characteristic compatibility relations, the change of the characteristic variable across the cell face can be computed due to the particular eigenvalue formulation.

To assure a minimum amount of artificial viscosity in the whole computational domain, a method suggested by Harten [30] is implemented, as well as a correction of the eigenvalues to overcome a nonphysical negative entropy change across expansion fans. The spatial discretization of the inviscid fluxes is extended to third-order accuracy by applying the MUSCL technique [31] together with the TVD scheme by Harten [30] and the van Albada limiter function to avoid stability problems.

The fully implicit time-integration of Eq. (1) is performed second-order accurate in time following the scheme of Rai and Chakravarthy [32]. Time accuracy is improved by using Newton subiterations to minimize linearization errors at each time step while the system of equations itself is solved iteratively by a Gauss–Seidel relaxation method. For unsteady computations best performance in terms of accuracy and convergence was found by using three Newton subiterations at each time step.

Boundary Conditions and Unsteady Grid Generation. The numerical treatment of the far field boundary conditions follows a method of characteristics proposed by Chakravarthy [33]. For the up- and downstream boundaries, the number of physical boundary conditions depends on the number of characteristics entering the computational domain neglecting all viscous terms. At the inflow boundary the total pressure, the total temperature, and the inflow angle are imposed. At the outflow boundary only the exit pressure is prescribed. For viscous flows Stokes' nonslip condition is applied on the surface of the blade, assuming an adiabatic wall and a vanishing normal pressure gradient. The assumption of a zero normal pressure gradient for unsteady flows is still correct if the reduced frequency of the blade oscillation is small.

At the periodic boundary use is made of the direct store method introduced by Erdos et al. [34]. This boundary condition allows the simulation of harmonically oscillating blades for any interblade phase angle with only one passage. Convergence is achieved if the difference between the flow quantities compared with the flow quantities of the previous cycle are below a certain limit. To avoid large storage requirements, the flow variables at the periodic boundaries are not stored at each time step, making use of a technique introduced by Peitsch et al. [35].

The simulation of the blade motion requires an unsteady regeneration of the C- or O-type grid. Therefore, the grid is divided into three zones. The first zone includes the blade surface and the grid lines inside the boundary layer preserving the orthogonality of the grid on the surface. This zone moves as a solid body according to the chosen mode of oscillation. Wrapped around the first zone is the second zone, which is surrounded by a stationary nondeforming third zone. The second zone is deformed at each time step and the grid is regenerated by solving the Laplace equation. Experience shows that it is not necessary to run the grid regeneration at each time step. Instead, it is sufficient to use a linear interpolation between newly regenerated grids. The third zone is kept fixed to save the orthogonality of the grid at the outer boundaries.

The Navier–Stokes code has been tested extensively for a variety of steady and unsteady subsonic and transonic test cases, such as [20,21,28].

Computational Results and Discussion

Computations were performed to investigate the flutter characteristics of the Buffum cascade. This cascade was developed to improve the understanding of the unsteady flow phenomena which cause stall flutter. The measurements were taken in the wind tunnel of the NASA Glenn Research Center, where this linear nine-blade cascade was installed. A series of steady and oscillatory measurements were taken for free-stream Mach numbers of 0.2, 0.5, and 0.8 at low and high incidence. In the experiment all blades were executing a harmonic pitching motion around the midchord point with an amplitude $\hat{\alpha}$ of 1.2 deg at an interblade phase angle Φ of 180 deg. The reduced frequency $k=2\pi fc/U_\infty$ was varied between 0.4 and 1.2. The stagger angle γ of the low-aspect-ratio fan blade tip section was 60 deg, the chord length c was 0.0889 m, and the solidity c/s was 1.52.

In this paper we analyze only the steady and oscillatory data for a free-stream Mach number of 0.5 and a Reynolds number Re of 0.9×10^6. The corresponding experimental results as well as the details of the test facility were discussed and given in detail by Buffum et al. [27].

All steady-state and unsteady computations for the Buffum cascade were performed on an O-type 241×61 point Navier–Stokes grid. Several grids were tested and the initial wall spacing decreased until the solution became independent of the grid for $y^+<1.5$. The grid is shown in Fig. 1, including a magnification of the leading edge (top left) and the trailing edge (bottom right).

Steady-State Low-Incidence Flow. Before running an unsteady computation, a steady-state solution was computed. In Buffum et al. [27], the in-flow angle α corresponding to low incidence was given to be 60 deg at a pressure ratio p_{exit}/p_∞ of 0.93. In order to obtain good agreement with the experimental data, the pressure ratio for the numerical simulation had to be changed to 0.936, resulting in an averaged inflow angle of 61.1 deg. The computed data were compared with the measured chordwise pressure coefficient distributions with a definition of the steady pressure coefficient as follows:

$$Cp\left(\frac{x}{c}\right)=\frac{p\left(\frac{x}{c}\right)-p_\infty}{\rho_\infty U_\infty^2}. \tag{15}$$

Two steady-state computations, one fully turbulent and one including transition, were performed. In Fig. 2 the predicted pressures are seen to compare well with the experimental data.

Figure 2 also includes experimental data on the neighboring blades to indicate the degree of periodicity in the test cascade. The difference between the development of the boundary layer without and with transition is seen to be small. A re-laminarization was predicted at the trailing edge while the strongest influence of transition could be seen close to the leading edge. In Fig. 3 the pressure distribution at the leading edge is given in more detail. Both computations predicted the stagnation point slightly on the lower surface, reaching a Cp of 0.5. Starting from the stagnation point, the flow was accelerated on both surfaces of the blade, as can be seen from the two suction peaks. The higher acceleration was

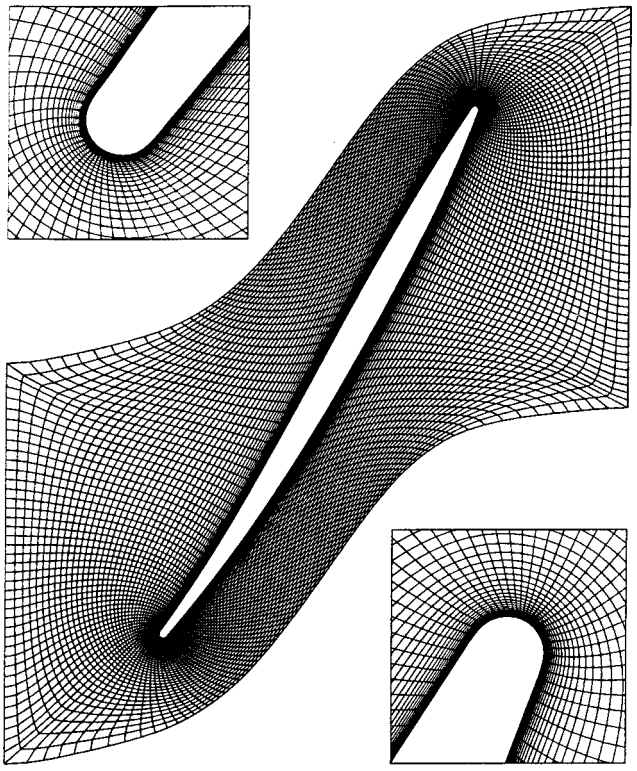

Fig. 1 O-type 241×61 point grid for the Buffum cascade

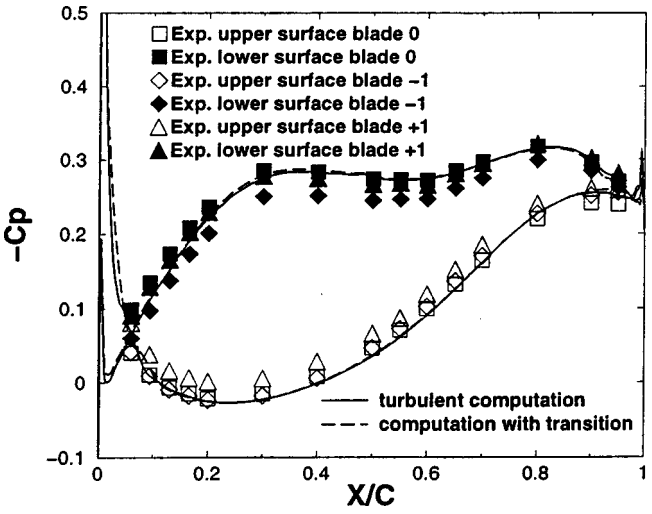

Fig. 2 Steady-state pressure distribution, $M=0.5$, $\alpha=61.1$ deg, $\text{Re}=0.9\times10^6$

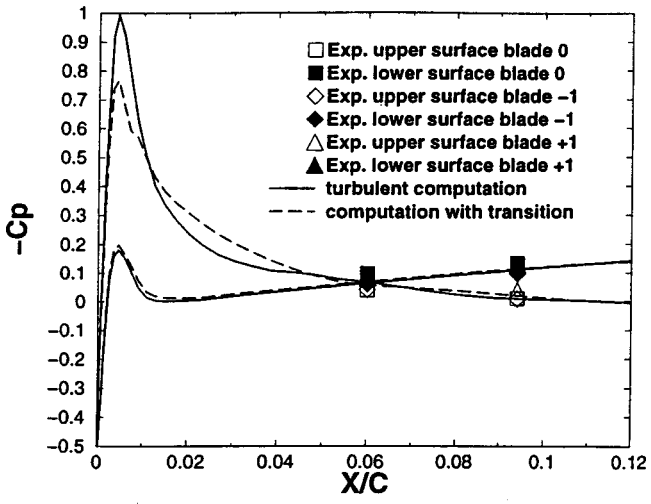

Fig. 3 Steady-state pressure distribution at leading edge, $M=0.5$, $\alpha=61.1$ deg, Re$=0.9\times10^6$

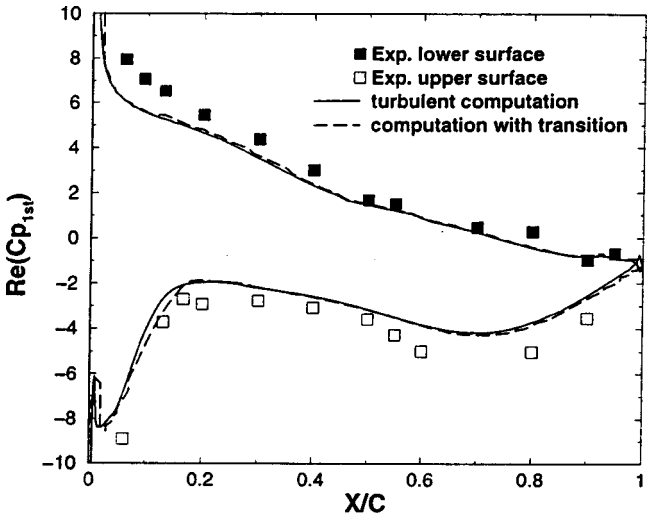

Fig. 5 Real part of unsteady pressure distribution at low incidence, $k=1.2$, $\Phi=180$ deg, $M=0.5$, Re$=0.9\times10^6$

found on the upper surface, e.g., the fully turbulent flow prediction reached a Cp of -1 (Fig. 3). The transition criterion of Baldwin–Lomax predicted a laminar region for 11 percent chord length on the lower surface. On the upper surface the turbulent flow started at 1 percent chord length. Furthermore, a separation bubble was found on the upper surface. The bubble length was approximately 5.5 percent of chord length independent of transition, while the bubble size was bigger for the computation, including transition. The predicted steady-state velocity vector distribution including transition is given in Fig. 4. One can see that the separation occurs on the upper surface of the blade at the point where the curvature of the blade surface changes sign.

Flutter at Low Incidence. At low incidence oscillatory measurements were taken for reduced frequencies of 0.4, 0.8, and 1.2. However, for $k=0.4$, the measured data have not been published because the passage-to-passage periodicity was too poor. For analysis of the unsteady data a first harmonic unsteady pressure coefficient is defined as follows:

$$Cp_{1st}\left(\frac{x}{c}\right)=\frac{p_{1st}\left(\frac{x}{c}\right)}{\hat{\alpha}\rho_\infty U_\infty^2}. \tag{16}$$

In Figs. 5 and 6 the real or in-phase part Re( ) and the imaginary or out-of-phase part Im( ) of the first harmonic unsteady pressure coefficient are compared with the experimental data for a reduced frequency of 1.2.

The real part is seen to agree well with the measured data. Again, the fully turbulent computation differed only slightly from the computation, including transition. The biggest difference was found on the upper surface of the blade between the leading edge and 16 percent chord length. Although the trend of the measured out-of-phase part of the unsteady pressure is predicted well, the quantitative agreement is worse than for the in-phase part. The influence of transition is again strongest on the upper surface between the leading edge and 16 percent chord length. Similar re-

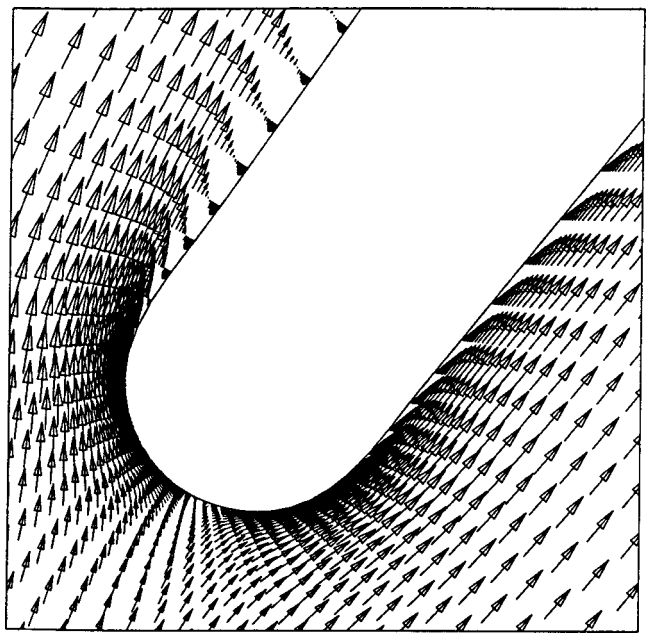

Fig. 4 Steady-state velocity vectors at leading edge, $M=0.5$, $\alpha=61.1$ deg, Re$=0.9\times10^6$

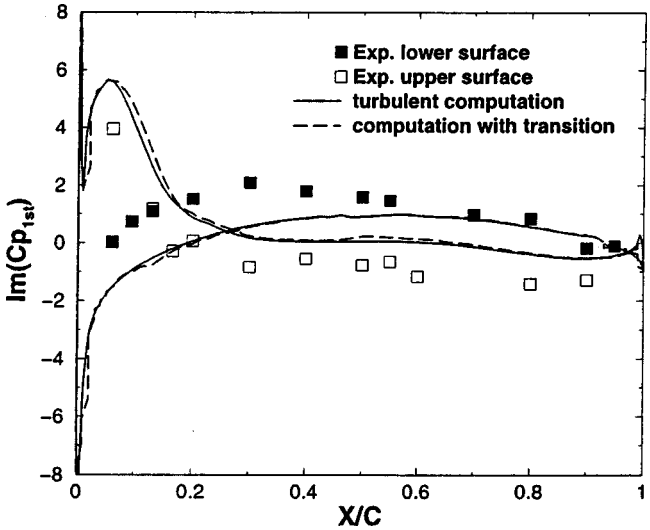

Fig. 6 Imaginary part of unsteady pressure distribution at low incidence, $k=1.2$, $\Phi=180$ deg, $M=0.5$, Re$=0.9\times10^6$

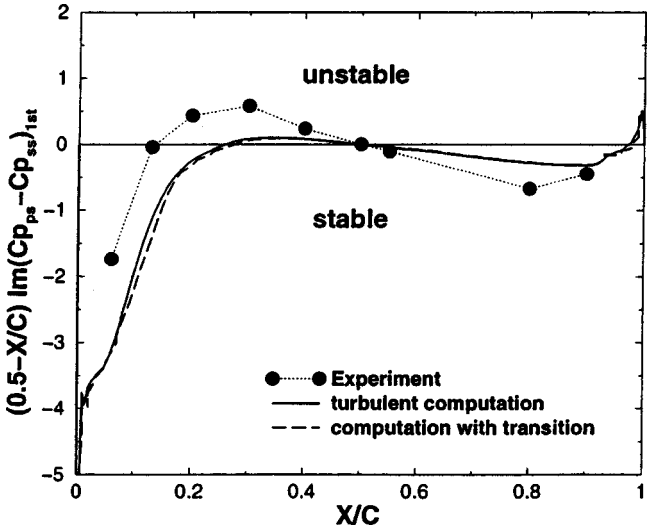

Fig. 7 Local stability analysis at low incidence, $k=1.2$, $\Phi=180$ deg, $M=0.5$, $\mathrm{Re}=0.9\times10^6$

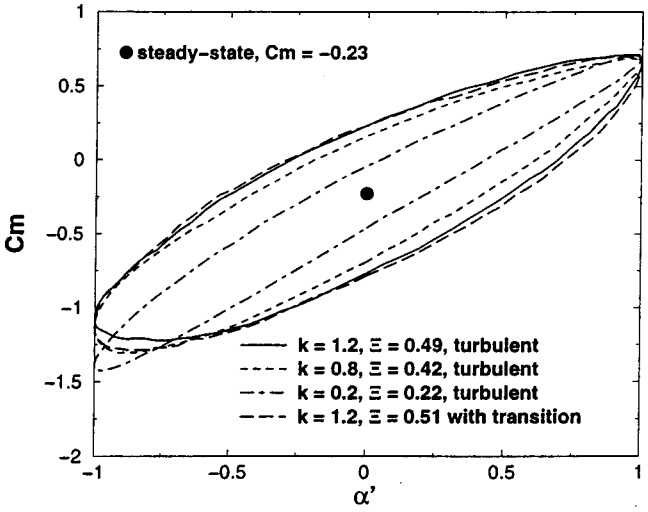

Fig. 9 Predicted pitching moment coefficient at low incidence, $\Phi=180$ deg, $M=0.5$, $\mathrm{Re}=0.9\times10^6$

sults were found for a reduced frequency of 0.8. Since the out-of-phase part of the unsteady pressure determines the damping or excitation of the blade motion, it is convenient to define the aerodynamic damping parameter $\Xi=-\mathrm{Im}(Cm)$ with Cm as the time-dependent moment coefficient:

$$Cm(t)=\frac{-\int\frac{\vec{r}}{c}\times\left[p\left(\frac{x}{c},t\right)\frac{dx}{c}\vec{e}_n\right]}{\hat{\alpha}\rho_\infty U_\infty^2} \tag{17}$$

with $\vec{r}$ the vector pointing from the pivot location to an arbitrary point on the surface and $\vec{e}_n$ the unit vector normal to the blade surface. A positive value corresponds to a damped oscillation.

Buffum et al. presented a local stability analysis by plotting $(0.5-x/c)\mathrm{Im}(Cp_{ps}-Cp_{ss})_{1st}$. The numerically predicted local stability in comparison with the experimental data is given in Figs. 7 and 8 for reduced frequencies of 1.2 and 0.8, respectively. For both reduced frequencies the computed local stability was greater than the measured stability between 0 and 40 percent chord length and smaller thereafter. The incorporation of transition for a reduced frequency of 1.2 slightly increased the stability.

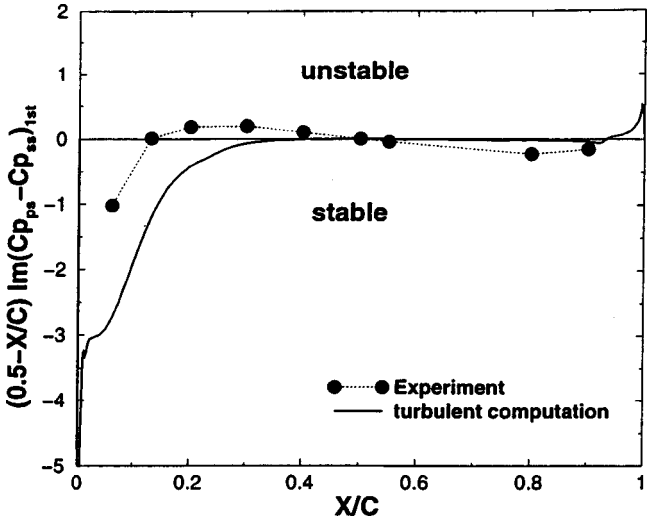

Fig. 8 Local stability analysis at low incidence, $k=0.8$, $\Phi=180$ deg, $M=0.5$, $\mathrm{Re}=0.9\times10^6$

Figure 9 shows a counterclockwise variation of the pitching moment during one oscillation cycle thus indicating positive damping. As expected, the aerodynamic damping increased with increased reduced frequency. In this figure the time-dependent development of the moment coefficient is plotted versus the non-dimensional pitching angle $\alpha'=[\alpha(t)-\gamma]/\hat{\alpha}$. As already seen from Fig. 7, including transition slightly increased the damping.

It is of special interest to study the behavior of the separation bubble as a function of the oscillation frequency. Therefore, computations for a reduced frequency of $k=0.2$ were also performed. The bubble length during the blade oscillation was almost 22 percent of chord length, independent of the reduced frequency. For a reduced frequency of 0.2, the largest bubble size occurred shortly after reaching the highest pitching angle. For the reduced frequencies of 0.8 and 1.2 the maximum was reached almost a quarter cycle later. Furthermore, a separation bubble of a maximum size of 3 percent chord length was predicted on the lower surface. The bubble occurred shortly before reaching the lowest pitching angle and vanished completely a quarter cycle later. As expected, a further decrease of the reduced frequency decreased the damping parameter even more. It is also interesting to note that the blade is subjected to a pitching moment fluctuating between positive and negative values for all reduced frequencies.

At low-incidence convergence of the unsteady computations was reached after 6 to 8 cycles using 1000 time steps per cycle and three Newton subiterations for each time step.

Steady-State High-Incidence Flow. Contrary to the experimentally determined inflow angle of 70 deg at a pressure ratio of 1.03, the best agreement between the measured and computed pressure distribution was obtained for a pressure ratio of 0.97 resulting in an inflow angle of 67.2 deg; see Fig. 10.

At this angle, the predicted pressure distribution on the lower surface agreed well with the measured data up to 70 percent chord length and was slightly too high thereafter. On the upper surface good agreement was found between the leading edge and 20 percent chord length. Starting at 20 percent chord length the predicted pressure was slightly higher until 45 percent chord length and again between 75 percent chord length and the trailing edge.

A study of the influence of three-dimensional effects due to the formation of corner vortices was performed by varying the $S1$-stream surface thickness of the grid shown in Fig. 1. The two-dimensional numerical results with and without transition shown in Fig. 10 could not be improved by this Quasi-3D computation. Transition onset was found at 0.6 percent chord length on the upper surface while laminar flow to 13 percent chord

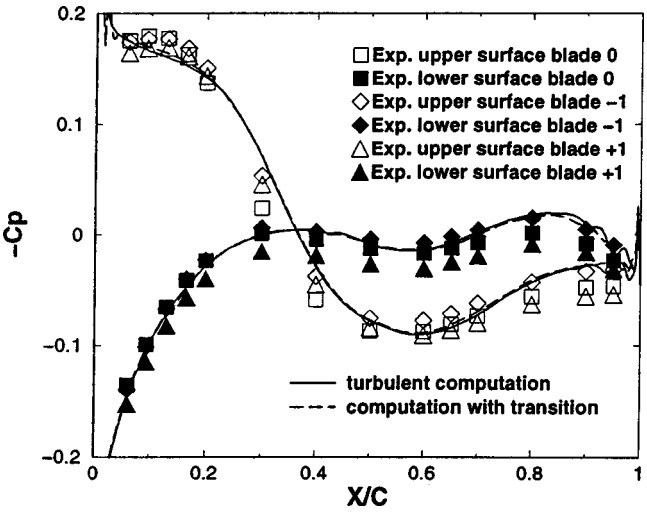

Fig. 10 Steady-state pressure distribution, $M=0.5$, $\alpha=67.2$ deg, $Re=0.9\times10^6$

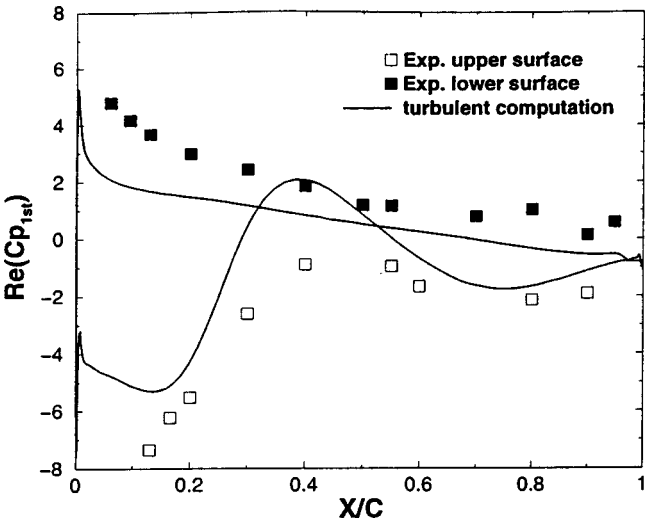

Fig. 12 Real part of unsteady pressure distribution at high incidence, $k=1.2$, $\Phi=180$ deg, $M=0.5$, $Re=0.9\times10^6$

length was predicted on the lower surface. The turbulent boundary layer was re-laminarized at the trailing edge. Including transition improved the predicted pressure distribution on the upper surface between the leading edge and 20 percent chord length. In Fig. 11 the steady-state Mach number contours show the separated flow region on the upper surface. A bubble of almost 50 percent chord length was found that was 10 percent longer than the measured bubble.

Flutter at High Incidence. Measurements for reduced frequencies of 0.4, 0.8, and 1.2 were taken at high incidence. In Figs. 12 and 13 the computed real and imaginary parts of the first harmonic unsteady pressure coefficient at a reduced frequency of 1.2 are compared with the experimental results. Although the measured trend of the real part, especially on the upper surface, was predicted by the computation, the agreement is less accurate than for the low incidence case; see Fig. 5. However, in contrast to the unsteady low incidence computations, the predicted imaginary part at high incidence is in better agreement with the experimental results than the real part. A similar behavior was found for the reduced frequencies of 0.4 and 0.8. The overall agreement became slightly worse with decreasing reduced frequency. The opposite behavior was found for the low-incidence computations.

In Fig. 14 snapshots of the unsteady Mach number contours at a reduced frequency of 1.2 are shown. The snapshots were taken at four different times during one cycle *T*. Here the development of the separation bubble from a small bubble to a bubble extending to 64 percent chord length can be seen.

A comparison of the low- and high-incidence measurements of the local stability, Figs. 7, 8, 15, 16, 17, shows that the leading edge region makes a decisive contribution to the total stability. In the low-incidence case the leading edge contributes positive damping, whereas in the high-incidence case the flow separation near the leading edge on the upper surface causes a destabilizing pitching moment. As seen in Figs. 15, 16, 17, the computations fail to capture this destabilizing leading edge moment, but the local moment contribution from about 15 percent chord to the

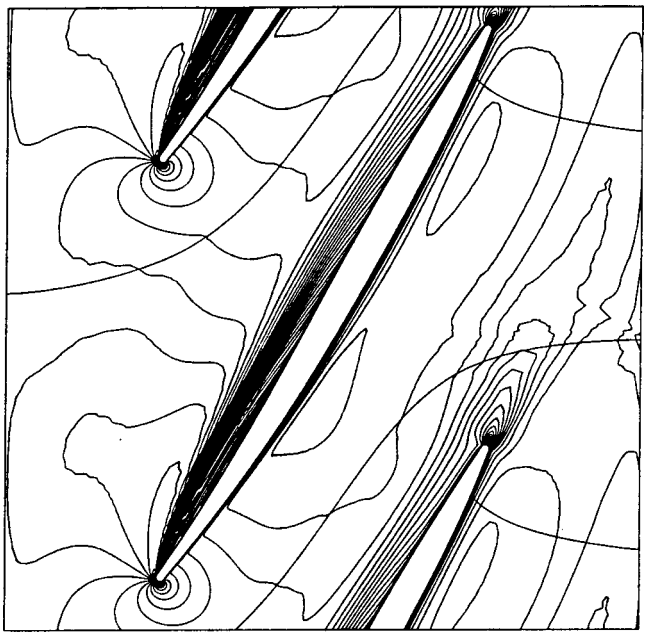

Fig. 11 Steady-state Mach number contours, $M=0.5$, $\alpha=67.2$ deg, $Re=0.9\times10^6$

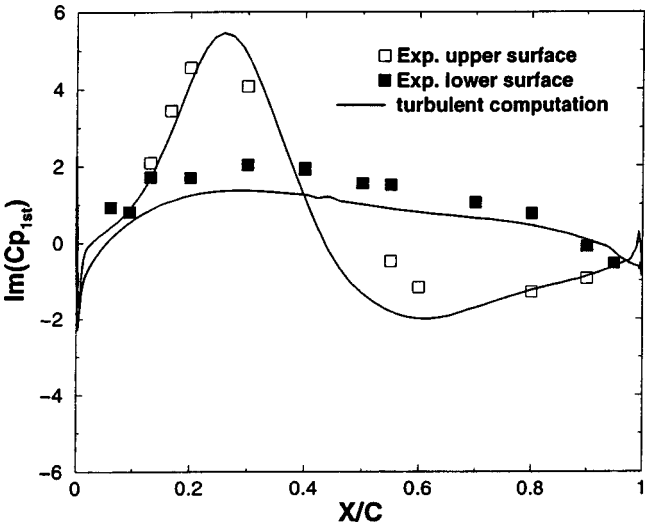

Fig. 13 Imaginary part of unsteady pressure distribution at high incidence, $k=1.2$, $\Phi=180$ deg, $M=0.5$, $Re=0.9\times10^6$

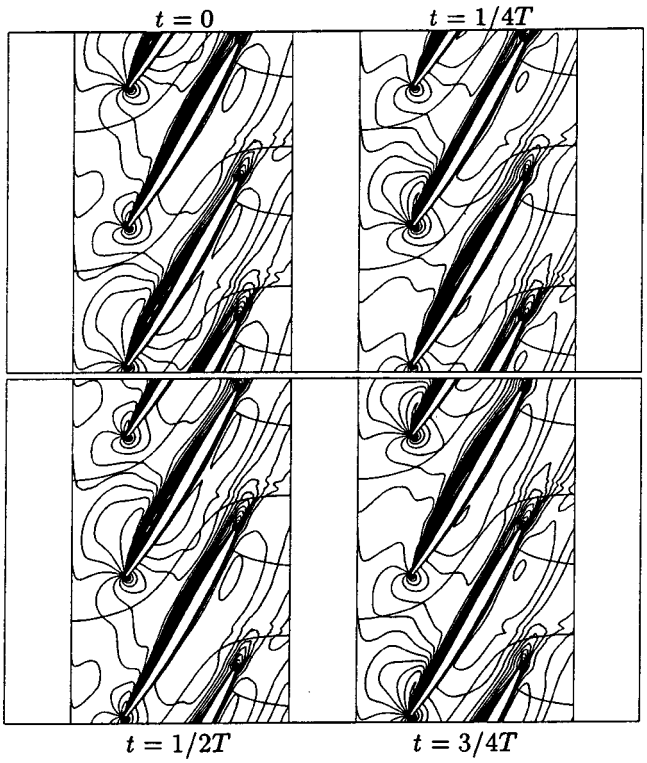

Fig. 14 Predicted unsteady Mach number contours at high incidence, $k=1.2$, $\Phi=180$ deg, $M=0.5$, Re$=0.9\times10^6$

trailing edge are predicted quite well for $k=1.2$, while significant differences are apparent up to midchord for the $k=0.8$ and $k=0.4$ cases. A separation bubble is found to exist on the upper surface during the complete oscillation cycle. At $t=0.14T$ the bubble reaches its smallest length of 34 percent chord length, which is 16 percent less than in the steady-state solution. The largest bubble is seen at $t=0.9T$, where it reaches a length of 65 percent chord. On the lower surface the flow remained attached during the complete oscillation cycle.

The pitching moment hysteresis loops and the damping parameter in dependency of the reduced frequency are given in Fig. 18.

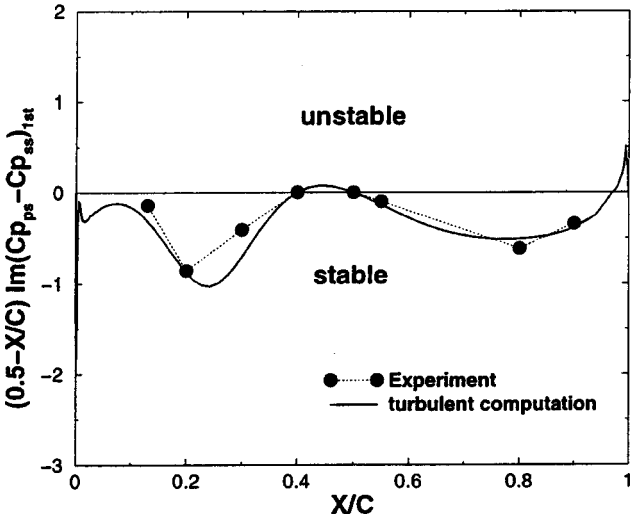

Fig. 15 Local stability analysis at high incidence, $k=1.2$, $\Phi=180$ deg, $M=0.5$, Re$=0.9\times10^6$

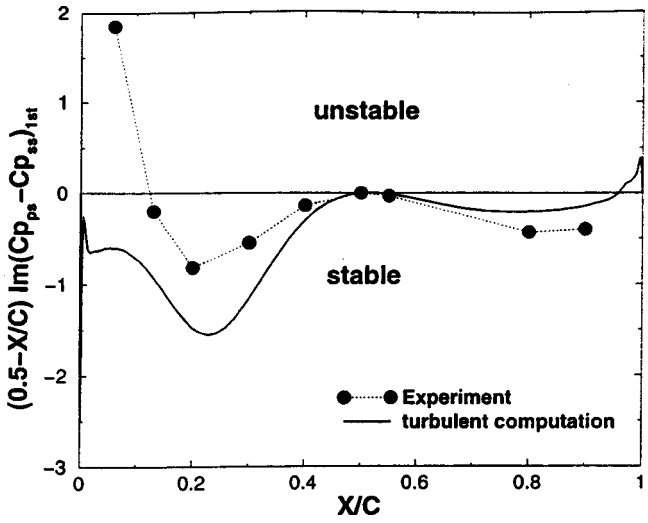

Fig. 16 Local stability analysis at high incidence, $k=0.8$, $\Phi=180$ deg, $M=0.5$, Re$=0.9\times10^6$

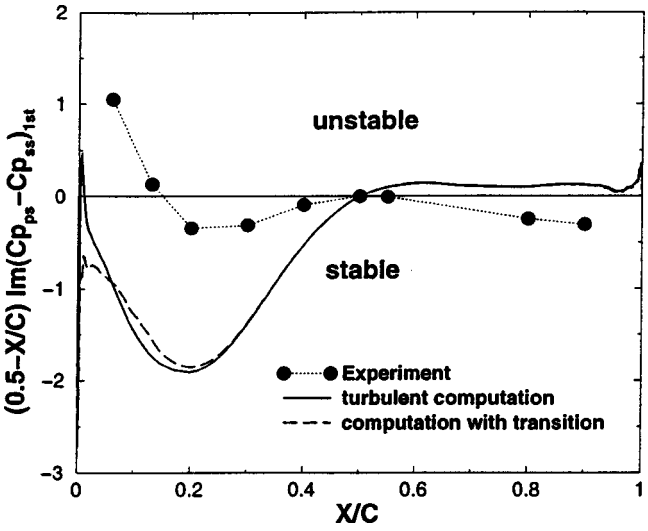

Fig. 17 Local stability analysis at high incidence, $k=0.4$, $\Phi=180$ deg, $M=0.5$, Re$=0.9\times10^6$

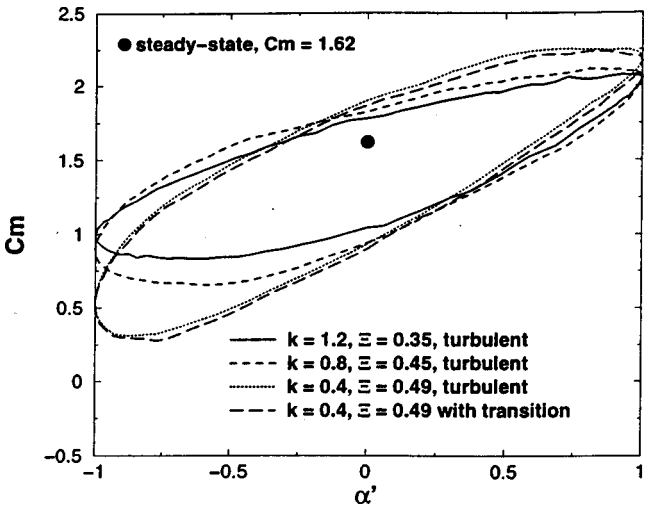

Fig. 18 Predicted unsteady aerodynamic moment coefficient at high incidence, $\Phi=180$ deg, $M=0.5$, Re$=0.9\times10^6$

The almost elliptical shape of the hysteresis loops indicate a linear response of the flow field to the prescribed motion. Furthermore, in contrast to the low-incidence case, the pitching moment is seen to be positive for all reduced frequencies.

Convergence of the computations for the different high-incidence cases was obtained after 8 to 12 cycles. As for the low-incidence case, 1000 time steps per cycle in combination with three Newton subiterations for each time step were used. All computations were performed on SGI Octane 250 MHz, R10000 workstations, and Pentium II-400 Linux PCs.

Concluding Remarks

At low incidence the steady and oscillatory flow cases showed encouraging agreement with the experiment. As expected, the computed aerodynamic damping increased with increasing oscillation frequency. These results are consistent with the time-linearized Navier–Stokes computations of Clark and Hall [2].

On the other hand, at high incidence the numerical model failed to predict the negative damping close to the leading edge although the steady-state solution was in good agreement with the measured data.

This failure suggests to explore the use of more sophisticated transition and turbulence modeling. Such models were already incorporated for the prediction of dynamic stall on single airfoils and led to significantly improved agreement with the available experimental data, as summarized by Ekaterinaris and Platzer [9]. Therefore, it is planned to apply these models in the next series of computations for the Buffum cascade.

Acknowledgments

The first author gratefully acknowledges the support of the Deutsche Forschungsgemeinschaft (DFG) and the Naval Postgraduate School.

References

[1] AGARDograh No. 298, 1987, AGARD Manual on Aeroelasticity in Axial-Flow Turbomachines.
[2] Clark, W. S., and Hall, K. C., 2000, ''A Time-Linearized Navier–Stokes Analysis of Stall Flutter,'' ASME J. Turbomach., **122**, pp. 467–476.
[3] Hall, K. C., and Crawley, E. F., 1993, ''Calculation of Unsteady Flows in Turbomachinery Using the Linearized Euler Equations,'' AIAA J., **27**, pp. 777–787.
[4] Kahl, G., and Klose, A., 1993, ''Computation of Time Linearized Transonic Flow in Oscillating Cascades,'' ASME Paper No. 93-GT-269.
[5] Montgomery, M. D., and Verdon, J. M., 1995, ''A Linearized Unsteady Euler Analysis for Turbomachinery Blade Rows Using an Implicit Wave-Split Scheme,'' *Proc. 7th Int. Symp. on Unsteady Aerodynamics and Aeroelasticity of Turbomachines*, Elsevier Science b.v. Amsterdam.
[6] Baldwin, B. S., and Lomax, H., 1978, ''Thin Layer Approximation and Algebraic Model for Separated Turbulent Flow,'' AIAA Paper No. 78–257.
[7] Baldwin, B. S., and Barth, T. J., 1990, ''A One-Equation Turbulence Transport Model for High Reynolds Number Wall-Bounded Flows,'' NASA TM 102847.
[8] Spalart, P. R., and Allmaras, S. R., 1992, ''A One-Equation Turbulence Model for Aerodynamic Flows,'' AIAA Paper No. 92-0439.
[9] Ekaterinaris, J. A., and Platzer, M. F., 1997, ''Computational Prediction of the Airfoil Dynamic Stall,'' Prog. Aerosp. Sci., **33**, pp. 759–846.
[10] Sanz, W., and Platzer, M. F., 1998, ''On the Navier–Stokes Calculation of Separation Bubbles With a New Transition Model,'' ASME J. Turbomach., **120**, pp. 36–42.
[11] Weber, S., and Platzer M. F., 1999, ''Steady and Dynamic Stall Analysis of the NLR 7301 Airfoil,'' ASME Paper No. 99-GT-21.
[12] Weber, S., Jones, K. D., Ekaterinaris, J. A., and Platzer, M. F., 1999, ''Transonic Flutter Computations for a 2D Supercritical Wing,'' AIAA Paper No. 99-0798.
[13] Eulitz, F., 1999, ''Unsteady Turbomachinery: Numerical Simulation and Modelling,'' *Proc. ODAS 99*, ONERA-DLR Aerospace Symposium.
[14] Bakhle, M. A., Srivastava, R., Stefko, G. L., and Janus, J. M., 1996, ''Development of an Aeroelastic Code Based on an Euler/Navier–Stokes-Aerodynamic Solver,'' ASME Paper No. 96-GT-311.
[15] Chew, J. W., Marshall, J. G., Vahdati, M., and Imegrum, M., 1998, ''Part-Speed Flutter Analysis of a Wide-Chord Fan Blade,'' *Proc. 8th Int. Symp. on Unsteady Aerodynamics and Aeroelasticity of Turbomachines*, Stockholm, Kluwer Academic Publishers.
[16] He, L., 1993, ''New Two Grid Acceleration Method for Unsteady Navier–Stokes Calculations,'' J. Propul. Power, **9**, pp. 272.
[17] Eguchi, T., and Wiedermann, A., 1995, ''Numerical Analysis of Unstalled and Stalled Flutter Using a Navier–Stokes-Code with Deforming Meshes,'' *Proc. 7th Int. Symp. on Unsteady Aerodynamics and Aeroelasticity of Turbomachines*, Elsevier Science b.v. Amsterdam.
[18] Abhari, R. S., and Giles, M., 1997, ''A Navier–Stokes Analysis of Airfoils in Oscillating Transonic Cascades for the Prediction of Aerodynamic Damping,'' ASME J. Turbomach., **119**, pp. 77–84.
[19] Grüber, B., and Carstens, V., 1998, ''Computation of the Unsteady Transonic Flow in Harmonically Oscillating Turbine Cascades Taking Into Account Viscous Effects,'' ASME J. Turbomach., **120**, pp. 104–111.
[20] Weber, S., Benetschik, H., Peitsch, D., and Gallus, H. E., 1997, ''A Numerical Approach to Unstalled and Stalled Flutter Phenomena in Turbomachinery Cascades,'' ASME Paper No. 97-GT-102.
[21] Weber, S., Gallus, H. E., and Peitsch, D., 1998, ''Numerical Solution of the Navier–Stokes Equations for Unsteady Unstalled and Stalled Flow in Turbomachinery Cascades With Oscillating Blades,'' *Proc. 8th Int. Symp. on Unsteady Aerodynamics and Aeroelasticity of Turbomachines*, Stockholm, Kluwer Academic Publishers.
[22] Kato, D., Outa, E., and Chiba, K., 1998, ''On Sub-Cell Structure of Deep Rotating Stall in an Axial Compressor,'' *Proc. 8th Int. Symp. on Unsteady Aerodynamics and Aeroelasticity of Turbomachines*, Stockholm, Kluwer Academic Publishers.
[23] Tuncer, I. H., Weber, S., and Sanz, W., 1999, ''Investigation of Periodic Boundary Conditions in Multipassage Cascade Flows Using Overset Grids,'' ASME J. Turbomach., **121**, pp. 341–347.
[24] Carstens, V., and Schmitt, S., 1999, ''Comparison of Theoretical and Experimental Data for an Oscillating Transonic Compressor Cascade,'' ASME Paper No. 99-GT-408.
[25] Fourmaux, A., 1999, ''Blade-Row Interaction in a Transonic Turbine,'' *Proc. ODAS 99*, ONERA-DLR Aerospace Symposium.
[26] Lin, J.-S., and Murthy, D. V., 1999, ''Unsteady Aerodynamic Analysis of an Oscillating Cascade at Large Incidence,'' ASME Paper No. 99-GT-22.
[27] Buffum, D. H., Capece, V. R., and El-Aini, Y. M., 1998, ''Oscillating Cascade Aerodynamics at Large Mean Incidence,'' ASME J. Turbomach., **120**, pp. 122–130.
[28] Benetschik, H., 1991, ''Numerische Berechnung der Trans- und Überschall-Strömung in Turbomaschinen mit Hilfe eines impliziten Relaxationsverfahrens,'' Doctorthesis, RWTH Aachen, Germany.
[29] Roe, P. L., 1981, ''Approximative Riemann Solvers, Parameter Vectors and Difference Schemes,'' J. Comput. Phys., **43**, pp. 357–372.
[30] Harten, A., 1983, ''High Resolution Schemes for Hyperbolic Systems of Conservation Laws,'' J. Comput. Phys., **49**, pp. 357–393.
[31] van Leer, B., 1979, ''Towards the Ultimative Conservative Difference Scheme V, A Second Order Sequel to Godunov's Method,'' J. Propul. Power, **32**, pp. 101–136.
[32] Rai, M. M., and Chakravarthy, S. R., 1986, ''An Implicit Form of the Osher Upwind Scheme,'' AIAA J., **24**, No. 5, pp. 735–743.
[33] Chakravarthy, S. R., 1983, ''Euler Equations—Implicit Schemes and Boundary Conditions,'' AIAA J., **21**, No. 5, pp. 699–705.
[34] Erdos, J. I., Alzner, E., and McNally, W., 1977, ''Numerical Solution of Periodic Transonic Flow Through a Fan Stage,'' AIAA J., **15**, pp. 1559–1568.
[35] Peitsch, D., Gallus, H. E., and Weber, S., 1995, ''Computation of Unsteady Transonic 3D-Flow in Turbomachine Bladings,'' *Proc. 7th Int. Symp. on Unsteady Aerodynamics and Aeroelasticity of Turbomachines*, Elsevier Science b.v. Amsterdam.

Impeller–Diffuser Interaction in a Centrifugal Compressor

Y. K. P. Shum

C. S. Tan

Gas Turbine Laboratory,
Massachusetts Institute of Technology,
Cambridge, MA 02139

N. A. Cumpsty
Whittle Laboratory,
University of Cambridge,
Cambridge, England CB3 0DY

A study has been conducted, using an unsteady three-dimensional Reynolds-averaged Navier–Stokes simulation, to define the effect of impeller–diffuser interaction on the performance of a centrifugal compressor stage. The principal finding from the study was that the most influential aspect of this unsteady interaction was the effect on impeller tip leakage flow. In particular, the unsteadiness due to the upstream potential effect of the diffuser vanes led to larger viscous losses associated with the impeller tip leakage flow. The consequent changes at the impeller exit with increasing interaction were identified as reduced slip, reduced blockage, and increased loss. The first two were beneficial to pressure rise, while the third was detrimental. The magnitudes of the effects were examined using different impeller–diffuser spacings and it was shown that there was an optimal radial gap size for maximum impeller pressure rise. The physical mechanism was also determined: When the diffuser was placed closer to the impeller than the optimum, increased loss overcame the benefits of reduced slip and blockage. The findings provide a rigorous explanation for experimental observations made on centrifugal compressors. The success of a simple flow model in capturing the pressure rise trend indicated that although the changes in loss, blockage, and slip were due largely to unsteadiness, the consequent impacts on performance were mainly one-dimensional. The influence of flow unsteadiness on diffuser performance was found to be less important than the upstream effect, by a factor of seven in terms of stage pressure rise in the present geometry. It is thus concluded that the beneficial effects of impeller–diffuser interaction on overall stage performance come mainly from the reduced blockage and reduced slip associated with the unsteady tip leakage flow in the impeller. [S0889-504X(00)01704-9]

1 Introduction

The interaction between impeller and vaned diffuser is far more difficult to model than configurations with vaneless diffuser [1,2]. Matching a vaned diffuser to an impeller is a nontrivial task due to the complicated flow mechanics involved and the absence of quantitative understanding. Satisfactory performance in an individual component does not guarantee that the integrated design will also have satisfactory flow range and overall stage efficiency. In fact, Cumpsty [3] states that mismatching is far more common as a cause of poor performance with high pressure ratio machines than details of impeller or diffuser vane shape.

So far most of the attention to impeller–diffuser interaction has been focused on understanding the effect of upstream conditions on the diffuser performance. Results reported by Filipenco et al. [4] and Deniz et al. [5] showed that the time-averaged flow alignment with the diffuser vanes, i.e., incidence, expressed as the momentum averaged swirl angle, was the single most important parameter in setting diffuser performance. Computations by Phillips [6] also showed that diffuser pressure recovery is largely independent of diffuser inlet flow axial distortions. The only remaining question is whether unsteadiness at the diffuser inlet, induced by interaction, can affect diffuser performance.

No attempt has been made to understand the effect of downstream conditions on the impeller flow field with the exception of the work reported by Kirtley and Beach [7]. They investigated the influence of impeller–diffuser interaction on upstream flow by applying CFD to a configuration with tip Mach number of about 0.5. Body force modeling and deterministic stresses were used to avoid the then very expensive time-accurate calculation. By comparing the divergence of deterministic stress to that of Reynolds stress, they came to a conclusion that vane-induced unsteadiness was more important than turbulence in affecting the flow field upstream of the diffuser vanes. They also found that the impeller flow field in the stage calculation had less shroud separation compared to the isolated impeller flow field.

Recently, Dawes [8] and Domercq and Thomas [9] reported results from time-accurate simulation of unsteady flow in an impeller–diffuser stage. Their computed results indicated that upstream influence of the vaned diffuser on the impeller flow can be significant. All these previous efforts have not however explained the cause(s) for an interaction-related phenomenon: The existence of an optimum radius ratio between the diffuser vane leading edge and the impeller blade trailing edge ($r_{2'}/r_2$) for the maximum stage total-to-static pressure ratio. The existence has been confirmed experimentally by various workers including Rodgers [10] and Clements and Artt [11], and their results strongly indicate that optimal radial gap size is geometry-dependent.

This paper will describe the implementation of time-accurate simulations of flow fields in an impeller–diffuser stage, an isolated impeller, and an isolated diffuser. The computed results will establish an understanding of the impact of unsteady impeller–diffuser interaction on the performance of a centrifugal compressor stage. The key objectives for the investigation are: (1) to assess the importance of interaction on the impeller and diffuser flow field (in terms of time-averaged pressure rise capability, loss, blockage, etc.), and its consequence on the stage performance; (2) to determine the flow mechanisms by which interaction influences these figures of merit for performance, especially the optimum gap size for total pressure rise as observed by Rodgers [10] and Clements and Artt [11]; (3) to develop a simple low-order flow model that describes the observed phenomenon for preliminary design evaluation.

To accomplish these objectives, the following three fluid dynamic questions need to be addressed: (1) How do downstream conditions, in the form of an unsteady pressure field, affect the impeller performance? (2) How do upstream conditions, characterized by the rotating jet-and-wake structure, affect the diffuser performance? (3) With all the factors considered, can flow cou-

Contributed by the International Gas Turbine Institute and presented at the 45th International Gas Turbine and Aeroengine Congress and Exhibition, Munich, Germany, May 8–11, 2000. Manuscript received by the International Gas Turbine Institute February 2000. Paper No. 2000-GT-428. Review Chair: D. Ballal.

pling between the impeller and the diffuser benefit stage performance, and under what conditions can this occur?

This paper is arranged as follows: The technical approach is first described; the influence of interaction on impeller flow and the influence of interaction on diffuser flow are then delineated. They are followed by a synthesis of computed results. Finally, the main conclusions are stated.

2 Technical Approach

2.1 The Stage Geometry. The centrifugal compressor stage selected for this investigation is representative of current industry design. It was designed for a stage total-to-static pressure ratio of 5.4. The impeller is backswept with an outlet angle of 52 deg. At design speed $U_2/\sqrt{C_{p0}T_{01}}=1.13$, the diffuser inlet angle is 68 deg.

2.2 The Solution Algorithm and Grid. The code developed by Dawes [8] is used in the present investigation. It simulates the real impeller motion by using a sliding plane to transfer axial and circumferential distortions between impeller and diffuser flow field at each time step, thus preserving the flow details in the interaction region. A volume weighted interpolation procedure is adopted to ensure conservation.

The equations being solved are the five fully three-dimensional, unsteady, compressible, Reynolds-averaged Navier–Stokes equations expressed in strong conservation form, coupled to two additional equations for the $k-\varepsilon$ turbulence model. The seven equations are discretized in finite volume form on each of the tetrahedral control volumes with vertex variable storage, and time-marched to convergence using a four-step Runge–Kutta residual smoothing procedure.

At the inflow boundaries the total pressure (p_{01}), total temperature (T_{01}), turbulent kinetic energy (k_1), turbulent dissipation rate (ε_1), and the two flow angles are prescribed, while at the outflow boundaries the static pressure (p_3) is specified. Thus, the time-averaged mass flow of the stage is actually computed, instead of being specified. Wall function is employed to avoid the need of simulating the laminar sublayer, allowing coarser grid at the viscous surface.

With a resolution of about 70,000 nodes, the unstructured mesh generated for the present numerical simulation is shown in Fig. 1. The stage modeled has 17 full blades and 17 splitters in the impeller, together with 19 vanes and 19 splitters in the diffuser. For the numerical simulation, the blade-to-vane ratio has been adjusted to 1:1 to avoid the necessity of modeling the entire annulus. In the process, the thickness of the impeller blade is reduced to preserve the original solidity of the passage. It has also been verified that the impeller flow is not choked, so the small modification should have little influence on the flow.

For tip region modeling, Storer and Cumpsty [12] have shown that the tip-leakage flow is controlled by primarily inviscid mechanism, thus even with relatively coarse mesh the static pressure field and the magnitude of leakage flow rate can be predicted satisfactorily. Recently Van Zante et al. [13] have pointed out that a substantially finer grid can be required to resolve the important details of the wall-bounded shear layer, which impacts the trajectory of the primary clearance flow, and was shown to be important for quantifying the stall inception point. The focus of the present investigation, however, is on understanding how the blockage associated with leakage flow reacts to downstream unsteadiness at an operating point well away from stall. The use of three grid points in the tip clearance gap is deemed adequate.

2.3 The Numerical Experiments. As the main goal is to quantify the stage performance change with different degree of impeller–diffuser interaction, it is necessary to use a control experiment environment to isolate the underlying factors and mechanisms. To assess the effect of downstream vanes on the impeller performance, an identical impeller is coupled to three different diffuser configurations to simulate different degrees of interaction.

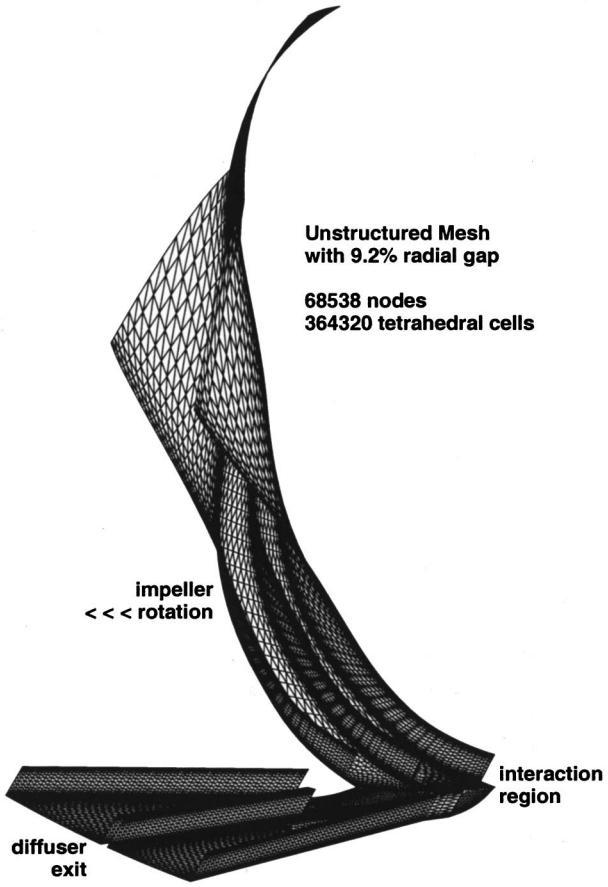

Fig. 1 Unstructured mesh used for the $r_{2'}/r_2=1.092$ configuration with the casings of both impeller and diffuser removed

The major difference between these three configurations is the size of the radial gap, expressed as the radius ratio of diffuser leading-edge to impeller trailing-edge ($r_{2'}/r_2$).

Calculation 1 is for a vaneless diffuser with $r_{2'}/r_2=\infty$, corresponding to the absence of impeller–diffuser interaction. Calculation 2 is for a vaned diffuser with $r_{2'}/r_2=1.092$. Calculation 3 is for a vaned diffuser with $r_{2'}/r_2=1.054$, intended to give the strongest interaction in the three configurations. Other than $r_{2'}/r_2$, all geometric parameters, such as the vane stagger angle and the channel area distribution $A(r)$, are kept the same for all three diffusers. The performances, from these three configurations are generated using the same impeller speed U_2 and are compared at the same time-averaged mass flow $\dot{m}$. Some iterations on the prescribed value of p_3, the diffuser exit pressure, are necessary before the computed mass flow can match the same target mass flow for each of the three configurations.

To save computational time, the stage is calculated over a wide range of flow rates only for the $r_{2'}/r_2=1.092$ configuration (Calculation 2), and it is treated as the reference case. Calculation 4 is then performed for the diffuser with steady inlet flow prescribed at the interaction plane location. The steady inlet conditions ($p_{02+}, T_{02+}, \alpha_{2+}$) are the time-average of the results from Calculation 2. They retain both the axial distortions (from hub to shroud) and the circumferential variations due to the downstream diffuser vanes.

Attempts at prescribing uniform boundary conditions at the original diffuser inlet boundary (interaction plane) failed because the distance between the inlet boundary and the vane entrance is too close for the flow to align with the vanes, resulting in unreasonably high loss. Some of the flow adjustment in response to the downstream vanes in fact takes place inside the impeller. Thus,

Table 1 Comparison of boundary conditions at the diffuser grid inlet for Calculations 2, 4, and 5, with vane leading edge located at $r_{2'}/r_2=1.092$

No.	2	4	5
Location	Interaction plane	Same as no. 2	Moved upstream
Unsteadiness	Present	Absent	Absent
Axial non-uniformity	Present	Present	Absent
Circumferential non-uniformity from upstream	Present	Absent	Absent
Circumferential non-uniformity from downstream	Present	Present	Present (negligible)

the inlet boundary for Calculation 5 was moved upstream by about one pitch where a set of uniform boundary conditions (p_0, T_0, α) could be applied. Some iteration on the inlet boundary conditions was required to match the integrated quantities (mass flow, angular momentum, and impulse) to the time-average of those of Calculation 2 at the original inlet boundary. Once these integrated quantities are matched, the resulting flow field of Calculation 5 resembles that of Calculation 2 except that both unsteadiness and inlet axial nonuniformity are absent. Table 1 outlines the difference between the three calculations in terms of inlet diffuser boundary location.

As designed, the difference between Calculations 2 and 4 isolates out the effect of unsteadiness, while the difference between Calculations 4 and 5 isolates out the effect of axial distortion. It should be emphasized that both factors are representative of those from a typical impeller exit flow, as they are derived directly from the results of Calculation 2. Moreover, all three calculations allow the presence of downstream-induced circumferential nonuniformity in the interaction region.

3 Influence of Interaction on Impeller Flow

This section presents qualitative and quantitative descriptions of the flow in the impeller with different degree of impeller–diffuser interaction. Calculations 1, 2, and 3 are obtained by varying the radius ratio $r_{2'}/r_2$, the only control variable in this numerical experiment. The same approach has been taken experimentally by Rodgers [10] and by Clements and Artt [11], both of whom show that stage total-to-static pressure ratio peaks for an impeller–diffuser radius ratio greater than unity.

3.1 Overall Impeller Performance. The impeller pressure ratio p_{02}/p_{01} from Calculations 1, 2, and 3 are plotted versus mass flow rate in Fig. 2. The characteristic line is determined by applying least-squares best-fit to the computed pressure ratios at various flow rate in Calculation 2 for the $r_{2'}/r_2=1.092$ configuration. The values of $\dot{m}$ in Calculations 1, 2, and 3 vary by about 1 percent of the reference value, reflecting the difficulty and time involved in achieving a desired mass flow rate by back pressure adjustment. The difference in $\dot{m}$ is small enough that the associated changes in performance may be neglected. The pressure ratios for both the vaneless build and the $r_{2'}/r_2=1.054$ configuration are well away from the $r_{,2}/r_2=1.092$ characteristic,

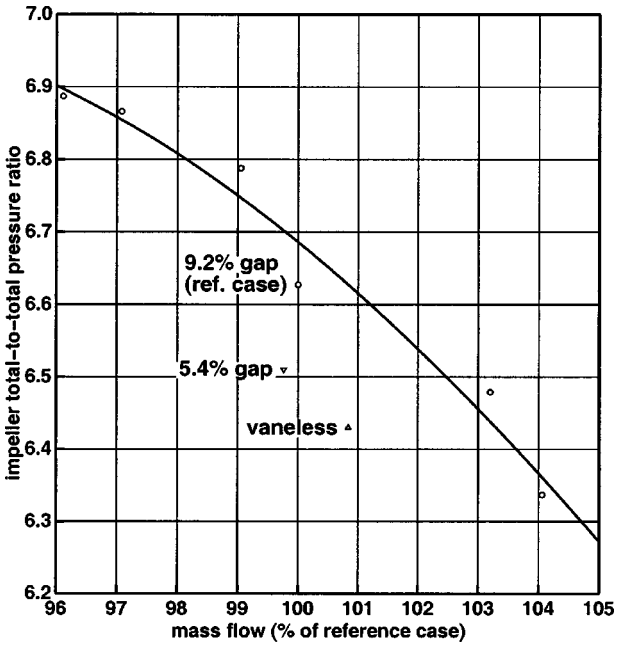

Fig. 2 Impeller total-to-total pressure ratio for the three different radial gap sizes, with the compete characteristic of $r_{2'}/r_2=1.092$ case shown

confirming that the radial gap size can indeed influence the impeller total pressure ratio. Thus, the degree of impeller–diffuser interaction is identified as a major contributor to the performance change, with the moderate radius ratio configuration ($r_{2'}/r_2=1.092$ in the current investigation) giving larger pressure ratios than the vaneless or small gap configurations.

The performance parameters from the three calculations are tabulated in Table 2 for comparison. Both the total-to-total and total-to-static pressure ratios are highest for $r_{2'}/r_2=1.092$. The polytropic efficiency η_{poly}, evaluated using

$$\frac{p_{02}}{p_{01}}=\left[1+\frac{V_{t2}U_2}{C_{p0}T_{01}}\right]^{\eta_{\text{poly}}\gamma/\gamma-1} \tag{1}$$

Table 2 Comparison of computed impeller performance parameters from different radial gap size

Interaction	no	medium	strong
radius ratio $r_{2'}/r_2$	∞	1.092	1.054
mass flow $\dot{m}$ (% of reference value)	100.8	100.0	99.8
impeller total-to-total pressure ratio p_{02}/p_{01}	6.43	6.63	6.51
impeller total-to-static pressure ratio p_2/p_{01}	3.49	3.54	3.46
tangential velocity V_{t2}/U_2	0.618	0.629	0.628
polytropic efficiency η_{poly} (in %)	90.6	90.9	90.2

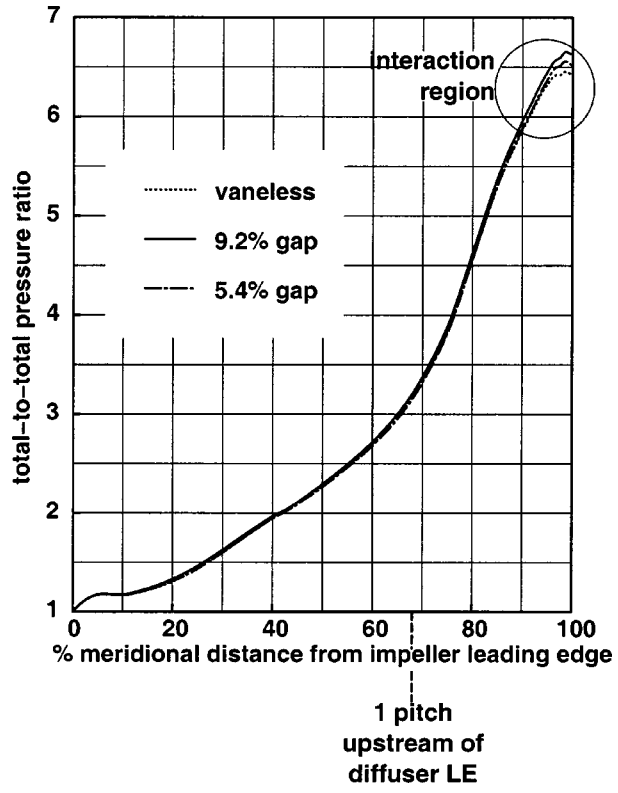

Fig. 3 Mass and time-averaged total pressure distribution along the impeller passage for the three different radial gas sizes

also shows a small peak with moderate strength of interaction. V_{t2} is the mass and time-averaged tangential velocity at the impeller exit flow.

3.2 The Origin of Performance Changes. Figure 3 shows the variation in total pressure p_0/p_{01} in the flow direction for the three calculations. The quantity p_0/p_{01} has been mass and time-averaged at each meridional station. It is only in the last 10 percent of the impeller passage, near the blade trailing edge, that significant difference arises. This region is within a one pitch distance upstream of the diffuser vane leading edge, and is expected to be under significant influence of the potential field posed by the diffuser vanes.

3.2.1 One-dimensional Model on Impeller Pressure Ratio. To explain why impeller total pressure ratio p_{02}/p_{01} changes with the addition of diffuser vanes downstream, it is more convenient from here on to express the average pressure ratio and loss relationship in terms of entropy s. Equation (1) is thus rewritten as,

$$\frac{p_{02}}{p_{01}}=\left[1+\frac{V_{t2}U_2}{C_{p0}T_{01}}\right]^{\gamma/\gamma-1}e^{-(s_2-s_1)/R} \tag{2}$$

The advantage of Eq. (2) is that entropy s_2 is an extensive property, which can be mass-averaged and obtained directly from the computed flow data. V_{t2} is the mass and time-average of the absolute whirl velocity at the impeller exit.

Linearization of Eq. (2) thus gives an expression for the incremental change in impeller total pressure ratio due to the presence of downstream vanes, with respect to that of the vaneless configuration,

$$\frac{\Delta p_{02}}{p_{02}}=\left[\left(\frac{\gamma}{\gamma-1}\right)\left(\frac{V_{t2}U_2}{C_{p0}T_{01}+V_{t2}U_2}\right)\right]\frac{\Delta V_{t2}}{V_{t2}}-\left[\frac{\gamma}{\gamma-1}\right]\frac{\Delta s_2}{C_{p0}} \tag{3}$$

However, V_{t2} is not the most fundamentally independent variable for this consideration because it in turn depends on W_2, the exit velocity in the relative frame. W_2 itself also depends on the channel effective area and density (thus on pressure and entropy).

The actual tangential velocity V_{t2} lags behind the ideal counterpart V_{t2i}, by a slip velocity, which depends largely on the circumferential spacing of the impeller blades and is predominantly a result of inviscid effect. Since the impeller geometry has not been changed in this numerical experiment, any change in the slip velocity can only be attributed to the presence of the downstream vanes. It is, however, simpler to express V_{t2} in terms of W_2 and θ, the angle between the radial direction and the average exit flow direction in the relative frame:

$$V_{t2}=U_2-W_2\sin\theta \tag{4}$$

where θ is related to the slip velocity. Equation (4) can then be linearized as

$$\frac{\Delta V_{t2}}{V_{t2}}=\left[\frac{-(U_2-V_{t2})}{V_{t2}}\right]\frac{\Delta W_2}{W_2}+\left[\frac{1}{\tan\alpha}\right](-\Delta\theta) \tag{5}$$

The negative sign preceding θ in Eq. (5) implies that a smaller θ implies reduced slip, which increases absolute whirl velocity V_{t2}.

The response of W_2 to changes in the local flow condition can be derived following Shapiro [14], by using one-dimensional flow conservation equations expressed in incremental form. The resulting relationship is as follows:

$$\frac{\Delta W_2}{W_2}=\left[\frac{-1}{1-\mathrm{M}_{\mathrm{rel},2}^2}\right]\frac{\Delta A_{\mathrm{eff}}}{A_{\mathrm{eff}}}+\left[\left(\frac{\gamma}{\gamma-1}\right)\left(\frac{1}{1-\mathrm{M}_{\mathrm{rel},2}^2}\right)\right]\frac{\Delta s_2}{C_{p0}} \tag{6}$$

where $\mathrm{M}_{\mathrm{rel},2}$ is the relative Mach number of impeller passage flow evaluated in the frame of the impeller, and A_{eff} is the effective flow passage area, which is the geometric passage area minus the flow blockage. The nondimensional blockage term is defined by

$$1-B=\frac{A_{\mathrm{eff}}}{A_{\mathrm{actual}}} \tag{7}$$

The step-by-step procedures to evaluate blockage using streamwise velocity distribution can be found in Khalid et al. [15].

With some algebraic manipulation, Eqs. (3), (5), and (6) can be consolidated into a single expression to eliminate the dependence on ΔW_2 and ΔV_{t2}, and establish the relationship between the perturbed impeller total pressure ratio and the three independent incremental changes, $\Delta A_{\mathrm{eff}}, \Delta s_2, -\Delta\theta$. These three changes completely represent the influence of impeller-diffuser interaction. The expressions for this relationship are:

$$\frac{\Delta p_{02}}{p_{02}}=C_A\left(\frac{\Delta A_{\mathrm{eff}}}{A_{\mathrm{eff}}}\right)+C_s\left(\frac{\Delta s_2}{C_{p0}}\right)+C_\theta(-\Delta\theta) \tag{8}$$

where C_A, C_s, and C_θ are the influence coefficients of the three independent incremental changes. The area coefficient is given by

$$C_A=\left[\frac{\gamma(U_2-V_{t2})}{(\gamma-1)V_{t2}}\right]\left(\frac{1}{1-\mathrm{M}_{\mathrm{rel},2}^2}\right)\left(\frac{V_{t2}U_2}{C_{p0}T_{01}+V_{t2}U_2}\right)>0, \tag{9}$$

the entropy coefficient is given by

$$C_s=-(1+C_A)\left(\frac{\gamma}{\gamma-1}\right)<0, \tag{10}$$

and the relative swirl angle coefficient is given by

$$C_\theta=\left(\frac{1}{\tan\alpha}\right)\left(\frac{\gamma}{\gamma-1}\right)\left(\frac{V_{t2}U_2}{C_{p0}T_{01}+V_{t2}U_2}\right)>0. \tag{11}$$

The sign convention of the influence coefficients in Eqs. (9)–(11) is determined by assuming both quantities (U_2-V_{t2}) and θ are positive, which is true for any impeller with backsweep. After substituting Eqs. (9)–(11) into Eq. (8), it can be seen that a positive influence coefficient (C_A, C_θ) implies contribution to impel-

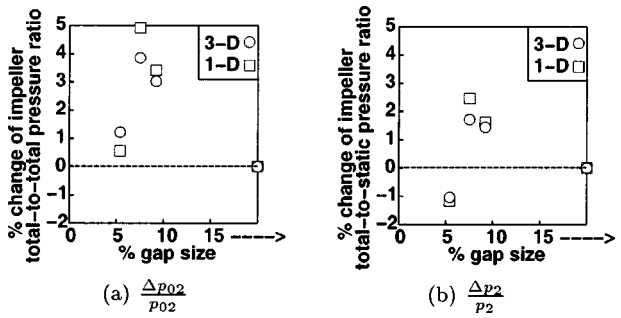

Fig. 4 Effect of radial gap size on impeller total pressure ratio and static pressure ratio, expressed in incremental change from vaneless configuration

ler pressure ratio, while the negative coefficient (C_s) implies the opposite. In summary, higher impeller total-to-total pressure ratio can be achieved by any of the following:

1 reduced blockage
2 reduced loss
3 reduced slip.

The comparison between this one-dimensional estimate (Eq. (8)) and the computed value of $\Delta p_{02}/p_{02}$, obtained directly from the three-dimensional unsteady flow data after mass and time averaging, is shown in Fig. 4(*a*). It can be seen that the agreement between the one-dimensional estimate and the three-dimensional results is good, and the trend for the total pressure ratio with reducing radial gap size is captured.

Evaluated using Eq. (8), the individual contribution to impeller total pressure ratio p_{02}/p_{01} due to blockage, loss and slip are summarized in Table 3. The results show that reduction in p_{02}/p_{01} as the radius ratio is decreased to 1.054 is caused by the pronounced effect of the increase in loss, which surpasses the effect of reduced blockage and slip.

Similar to the development for Δp_{02}, the perturbed impeller static pressure rise Δp_2 due to the interaction-induced incremental changes can also be evaluated using the one-dimensional approach of Shapiro. As static pressure is a frame-independent thermodynamic variable, the resulting relationship can be obtained by selecting the corresponding terms in Shapiro's influence coefficient table. The complete expression is

$$\frac{\Delta p_2}{p_2} = C_{\tilde{A}}\left(\frac{\Delta A_{\text{eff}}}{A_{\text{eff}}}\right) + C_{\tilde{s}}\left(\frac{\Delta s_2}{C_{p0}}\right) \tag{12}$$

where $C_{\tilde{A}}$ and $C_{\tilde{s}}$ are the influence coefficients defined as

Table 3 Relative importance of independent factors for impeller total pressure ratio

radius ratio $r_{2'}/r_2$	1.092	1.054
reduced blockage	+1.80%	+2.21%
increased loss	+0.53%	-3.32%
reduced slip	+1.08%	+1.67%
Σ	+3.41%	+0.56%

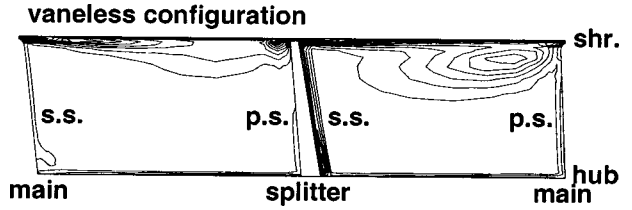

Fig. 5 Contours of entropy production $\rho Ds/Dt$ at impeller exit for the vaneless configuration

$$C_{\tilde{A}} = \frac{\gamma M_{\text{rel},2}^2}{1 - M_{\text{rel},2}^2} > 0 \tag{13}$$

$$C_{\tilde{s}} = -(1 + C_{\tilde{A}})\left(\frac{\gamma}{\gamma - 1}\right) < 0 \tag{14}$$

The sign convention in Eqs. (13) and (14) assumes the impeller passage is subsonic at exit ($M_{\text{rel}} < 1$).

The comparison between the one-dimensional estimate (Eq. (12)) and the computed value of $\Delta p_2/p_2$ is shown in Fig. 4(*b*). Again, the trend of the static pressure ratio with reducing radial gap size is in agreement with the one-dimensional model.

Figures 4(*a*) and 4(*b*) also show extra data points generated from a $r_{2'}/r_2 = 1.075$ configuration. Although both static and total pressure ratios are marginally higher than those from the reference configuration with $r_{2'}/r_2 = 1.092$, it is apparent that both pressure ratios are leveling off at this particular range of radial gap size. The results are in accord with the suggestion of Clements and Artt [11], based on experiments, that the optimum values for the vaneless space radius ratio is in the range $r_{2'}/r_2 = 1.06$ to 1.10.

In summary, the one-dimensional model for estimating Δp_{02} and Δp_2 helps identify the effect of interaction-induced change in three independent factors (blockage, loss, and slip) on the impeller pressure ratio. The simple model is in agreement with the computed and measured trend of impeller pressure ratio when radial gap size is varied.

3.2.2 Computed Impeller Flow Field. This section investigates why impeller–diffuser interaction can cause the observed change in blockage, loss, and slip by examining the computed unsteady three-dimensional flow field. The first quantity being looked at is the local volumetric entropy production rate $\rho Ds/Dt$ (unit: J/K.s.m^3), which provides immediate identification of the high loss generation region. The $\rho Ds/Dt$ contours on the transverse plane at the impeller trailing edge for the vaneless configuration are shown in Fig. 5; it clearly shows that high entropy is being generated near the shroud, especially at the tip leakage exit region. Figure 6 shows four $\rho Ds/Dt$ contour snapshots at the impeller exit (as in Fig. 5) for the $r_{2'}/r_2 = 1.092$ configuration. Each of the results in Fig. 6 is obtained at an instant with equal time interval of one-fourth of a blade passing ($\Delta t = 1/4T$). Besides showing that loss again originates mostly in the tip leakage flow region, this set of results also demonstrate the unsteady nature of the loss generation.

A more important practical question is whether this unsteady phenomenon can cause a change in the time-averaged loss at the impeller exit and this can be answered by examining the incremental change of entropy production from the vaneless configuration. $\Delta(\rho Ds/Dt)$, for the $r_{2'}/r_2 = 1.054$ and 1.092 configurations. In Fig. 7, the $\Delta(\rho Ds/Dt)$ contours have been nondimensionalized against the entropy production in the vaneless configuration, a spatially invariant constant, to quantify the effect of downstream vanes. It shows that significantly higher incremental loss, more than 100 times greater than elsewhere, is generated at the exit of the tip leakage flow when comparing the two vaned cases to the vaneless configuration. In addition, the smaller the

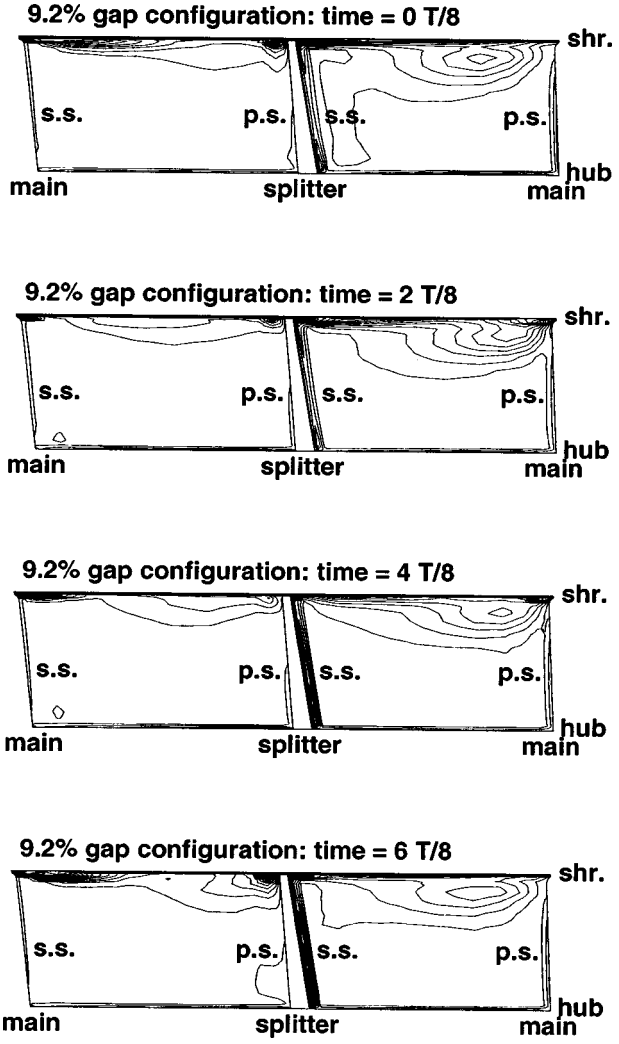

Fig. 6 Contours of instantaneous entropy production $\rho Ds/Dt$ at impeller exit collected at 0.25T time interval for the $r_{2'}/r_2 = 1.092$ configuration

radial gap size, the higher the loss is, implying that the loss generation at the tip leakage exit is related to impeller–diffuser interaction.

The tip leakage mass flux, ρW_{tip}, is a measure of the velocity gradients of the clearance flow, which in turn determines the local viscous dissipation. Figure 8 compares the tip leakage mass flux, which has been nondimensionalized by the quantity $\overline{\rho_2} U_2$, for the main blade clearance of the three different radial gap sizes at 90, 95, and 99 percent meridional stations. At the 90 percent meridional station, only minor unsteadiness can be observed for the vaned cases, but the periodicity of the tip leakage has become very apparent by the time the flow reaches the 95 percent meridional station. Farther downstream at the 99 percent meridional station, the tip leakage mass flux for the vaned cases is so unsteady that its peak-to-peak amplitude of the mass flux is roughly equal to its time-averaged value. The behavior of the splitter tip leakage flow is very similar to that of the main blade. All the qualitative description on main blade tip leakage can be applied to that of the splitter, except that the peak and trough are shifted by half a blade passing.

It is expected that a closer radial gap introduces more unsteadiness to the flow field near the impeller exit, and the tip leakage flow is no exception. As seen in Fig. 8, at the 99 percent meridional station the $r_{2'}/r_2 = 1.054$ configuration has a peak-to-peak variation of 0.247 for the quantity $\rho W_{\text{tip}}/\overline{\rho_2} U_2$, while that of the

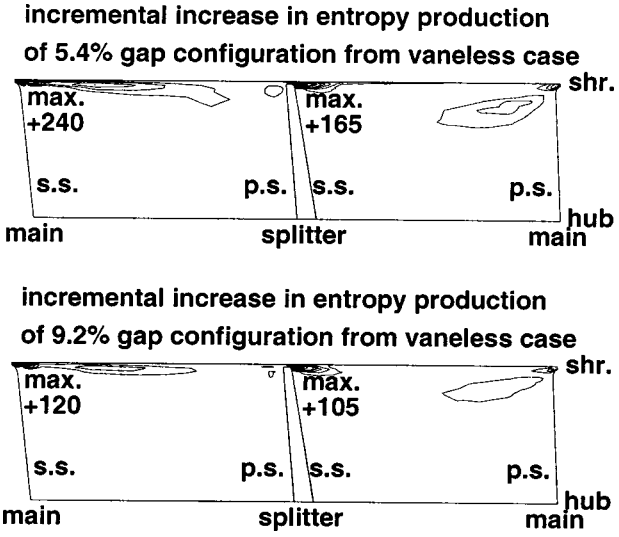

Fig. 7 Incremental entropy production $\Delta(\rho Ds/Dt)$ for the two vaned configurations when compared to the vaneless configuration

$r_{2'}/r_2 = 1.092$ configuration is 0.198. The time-averaged value of $\rho W_{\text{tip}}/\overline{\rho_2} U_2$ at this location ranges from 0.231 to 0.244 for all three cases.

For both the vaneless (Fig. 5) and the vaned (Fig. 6) configurations, the high viscous dissipation observed near the shroud region is caused by high-velocity gradients associated with the crossflow between tip leakage flow and the main stream flow. For the unsteady vaned cases, the time variation in tip leakage mass flux ρW_{tip} comes mostly from the variation in jet velocity W_{tip} because the tip leakage flow can be considered as almost incompressible since the corresponding Mach number is about 0.5.

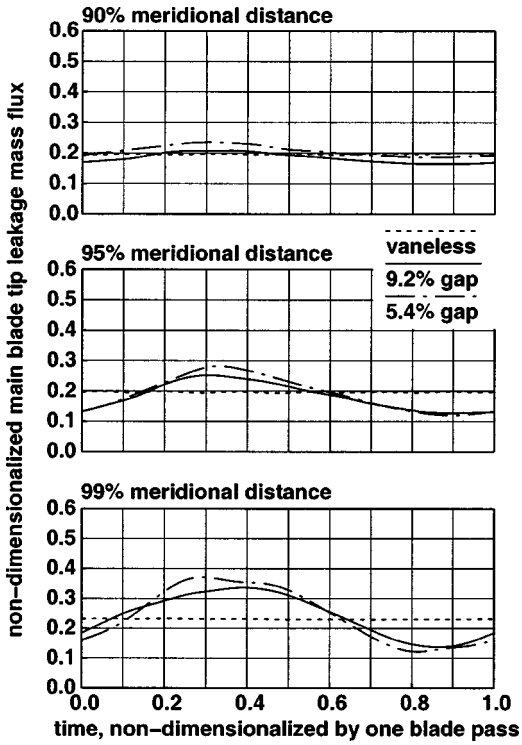

Fig. 8 Comparison of main blade clearance periodic tip leakage mass flux at 90, 95, and 99 percent meridional stations

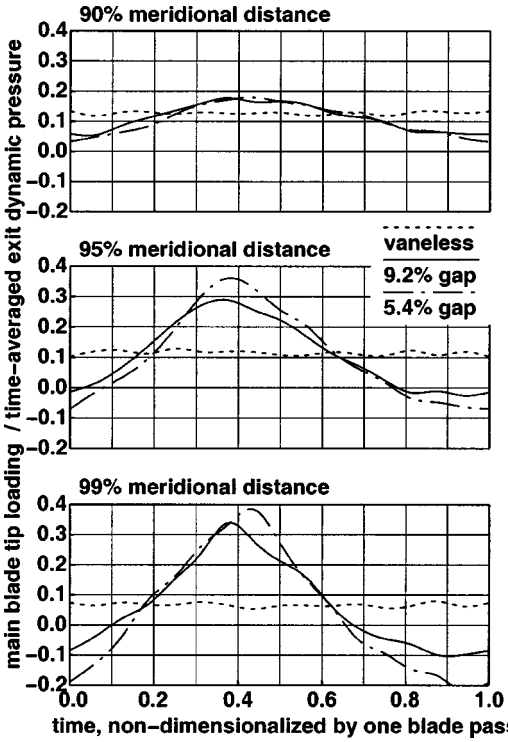

Fig. 9 Comparison of periodic main blade tip loading $(p_{ps}-p_{ss})/(\overline{p_{02}}-\overline{p_2})$ at 90, 95, and 99 percent meridional stations

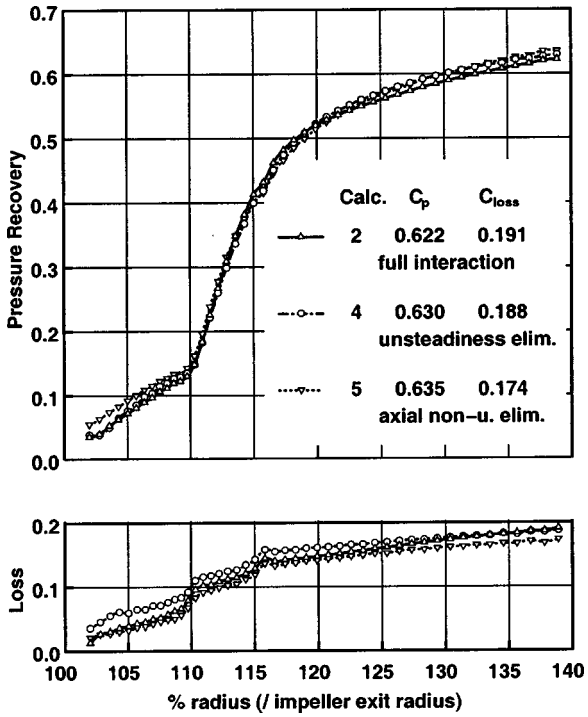

Fig. 10 Comparisons of pressure recovery C_p and loss C_{loss} for calculations 2, 4, and 5

Therefore, the substantial unsteadiness in ρW_{tip} seen in Fig. 8 should lead to an additional instantaneous tangential velocity gradient at the tip leakage region. The result is an increased rate of viscous dissipation, evident as the increased entropy production rate shown in Fig. 7.

The blade loading, expressed as the static pressure difference across the tip $(p_{ps}-p_{ss})/(\overline{p_{02}}-\overline{p_2})$, is plotted for the main blade in Fig. 9. The comparison of the three configurations (vaneless, $r_{2'}/r_2=1.092$ and 1.054) are conducted at the same meridional stations as above (90, 95, 99 percent). It can be seen that the tip leakage mass flux in Fig. 8 are synchronized with the corresponding blade tip loading in terms of the occurrence of the peak and trough. As expected, the closer the vanes are placed to the impeller trailing edge, the more unsteady the flow field is. The agreement between the loading and the mass flux confirms that the unsteady pressure gradient set up by the downstream vanes is the driving force of the unsteady variation in tip leakage flow.

Besides increasing loss, the higher viscous dissipation in the vaned cases can reduce flow blockage, as seen in Table 3. McDougall and Dawes [16] have demonstrated, by using both numerical and experimental approaches, that the presence of tip leakage jet can counteract separation and thus reduce blockage. It is likely that the same unsteady mechanism that increases the entropy production in the tip region is also responsible for the reduction of blockage. The following summarizes the cause and effect of the increased viscous dissipation for a reduction in radius ratio $r_{2'}/r_2$:

- Increased loading unsteadiness
- Increased instantaneous pressure gradient across tip clearance
- Increased tip leakage mass flux unsteadiness
- Increased instantaneous velocity gradient
- Increased time-averaged viscous dissipation
- Increased time-averaged loss
- Decreased time-averaged flow blockage

With the effect of unsteadiness on loss (Δs_2) and blockage (ΔA_{eff}) addressed, the only remaining factor is slip, which is expressed in terms of the swirl angle incremental change $(\Delta\theta)$. It is recognized that flow separation can also significantly change the impeller exit flow angle; however, the mass flux contours for all three configurations indicate that little separation occurs near the shroud at the impeller exit, thus leaving the inviscid effect from the vanes as the primary factor for the incremental change in slip $(\Delta\theta)$.

4 Influence of Interaction on Diffuser Flow

4.1 Background and Numerical Results. This section presents qualitative and quantitative descriptions of the flow in the diffuser with different combination of upstream parameters prescribed at the interaction plane. The main objective is to investigate the role of inlet unsteadiness on the diffuser performance; or more specifically, to quantify its importance compared to the other two upstream factors: (1) axial, hub-to-shroud distortion: and (2) momentum-averaged inlet swirl angle [4]. The influence of the axial distortion has been investigated by Phillips [6], who concluded that its effect on diffuser pressure recovery $C_p=(p-p_2)/(p_{02}-p_2)$ is minimal compared to that from the inlet swirl angle, which has been identified by Filipenco and Deniz et al. [5] as the single most important parameter in determining C_p.

It is recognized that interaction can change the impeller outflow angle, but a designer can always match the diffuser geometry to the time mean impeller outflow angle by adjusting the diffuser vane alignment. Unsteadiness thus remains a factor that cannot be designed out.

Again, the approach is to set up three numerical experiments, so that the two inlet factors stated above can be isolated out as the only difference. The time-accurate calculation for the $r_{2'}/r_2=1.092$ configuration is chosen as the reference case, which also provides the boundary conditions for the two subsequent diffuser-alone steady calculations (Table 1). The effects of unsteadiness and axial distortion so determined are representative of those found in the impeller exit flow as they are all derived from the full unsteady calculation of the stage.

The results of the three calculations are summarized in Fig. 10 in terms of the development of pressure recovery C_p and loss C_{loss}

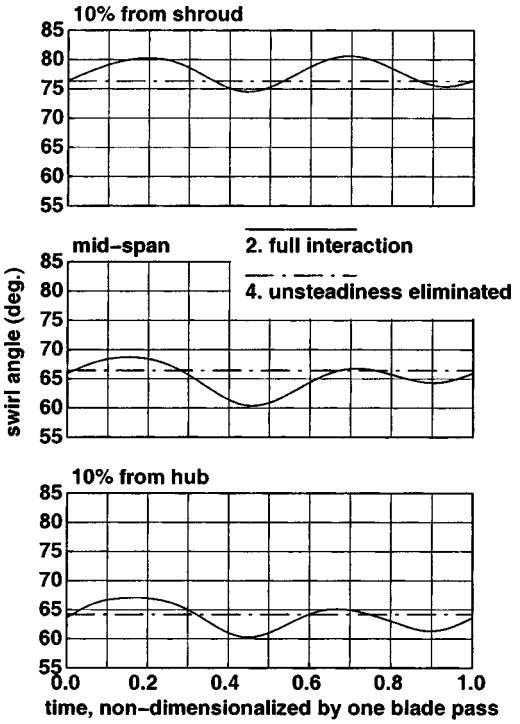

Fig. 11 Effect of unsteadiness on the swirl angle at midpitch of the diffuser inlet plane

along the diffuser channel. It can be seen that the radial distribution of the pressure recovery is virtually the same for all three cases. More than half of the pressure recovery is obtained in the throat region, which extends from $r/r_2=1.092$ (leading edge) to $r/r_2=1.18$, demonstrating the capability of the vaned diffuser in reducing the angular momentum of the incoming flow.

Elimination of upstream unsteadiness (difference between Calculations 2 and 4) only increases C_{p3} at diffuser exit by 0.008 while further elimination of upstream axial distortion (difference between Calculations 4 and 5) increases exit C_{p3} by another 0.005. The 0.008 reduction in C_{p3} due to unsteadiness is equivalent to mismatching the vane orientation by a mere 0.3 deg, as demonstrated in the experiments of Deniz et al. [5] experiments with straight-vaned diffusers. Such change is an order of magnitude smaller than the operating range (from choke to stall) of those diffusers, confirming again that the flow angle alignment with the diffuser vane is the single most important factor that determines diffuser performance.

4.2 Effect of Interaction on Diffuser Performance. The time variation of swirl angle at midpitch at the leading edge radius is shown in Fig. 11. These are given at 10 percent from shroud, midspan, and 10 percent from hub from the full interaction calculation. Also shown for comparison is the swirl angle at the same locations for the steady calculation (No. 4) with upstream unsteadiness eliminated. The data at locations away from both surfaces are selected to ensure that the observation is not marred by the boundary layer development on the surfaces. For the steady case, it can be seen that variation of swirl angle $\alpha_{2',mp}(x)$ from hub to shroud is more than 12 deg. The unsteadiness adds another 8 deg from the periodic peak-to-peak angle fluctuation, so the total variation comes to about 20 deg. Deniz et al. have shown experimentally that a typical straight-vaned diffuser has its C_{p3} reduced by about 0.1 for every 4 deg change in $\alpha_{2'}$ from the stall point, so on this reasoning a 20 deg variation should have removed the diffuser pressure rise.

It is found that the flow can enter the diffuser channel without triggering massive separation when the angle misalignment is only over part of the span (e.g., near hub or shroud). This is because the flow is subject to some predominantly two-dimensional pressure gradient (after time-averaging), whose establishment depends on the average flow incidence, based on momentum-averaged inlet swirl angle. The evidence here suggests that nonuniformity due to unsteadiness from the upstream rotor is largely irrelevant to the pressure recovery in the diffuser, but this may not be true for all ratios of impeller blades to vane numbers. Also, the diffuser is operating at design condition in Calculations 2, 4, 5, and upstream unsteadiness may have a larger influence on performance if the diffuser is operating at near-stall condition.

5 Effect of Interaction on Overall Stage Pressure Ratio

So far the discussion on the two aspects of interaction remains separate, the effect of downstream flow field on impeller performance and the effect of upstream flow field on diffuser performance. To establish a quantitative description of interaction effect on the stage total-to-static pressure ratio, it is necessary to resort to the definition of diffuser pressure recovery, which has been rearranged as,

$$\frac{p_3}{p_{01}}=C_{p3}\frac{p_{02}}{p_{01}}+(1-C_{p3})\frac{p_2}{p_{01}} \tag{15}$$

Of the three independent variables, p_{02} and p_2 are the contribution from the impeller, while C_{p3} is the contribution from the diffuser.

The relative importance of each of the factors can be studied by linearizing Eq. (15) into the following:

$$\frac{\Delta' p_3}{p_3}=K_{p02}\left(\frac{\Delta' p_{02}}{p_{02}}\right)+K_{p2}\left(\frac{\Delta' p_2}{p_2}\right)+K_{C_p}\left(\frac{\Delta' C_{p3}}{C_{p3}}\right) \tag{16}$$

where Δ' signifies the change due to the reduction of $r_{2'}/r_2$ and K_{p02}, K_{p2}, and K_{C_p} are the corresponding influence coefficients. Their definitions are

$$K_{p02}=\frac{C_{p3}p_{02}}{p_3}>0 \tag{17}$$

$$K_{p2}=\frac{(1-C_{p3})p_2}{p_3}>0 \tag{18}$$

$$K_{C_p}=\frac{(p_{02}-p_2)C_{p3}}{p_3}>0 \tag{19}$$

The performance changes associated with the reduction of radial gap size from $r_{2'}/r_2=1.092$ (Calculation 2) to $r_{2'}/r_2=1.054$ (Calculation 3) can then be substituted into Eq. (16) for evaluation of their effect on the stage total-to-total pressure ratio p_3/p_{01}. The changes are summarized in Table 4.

As seen in Table 4, the gap size reduction (increased interaction) has more influence on the impeller performance, for which both p_{02}/p_{01} and p_2/p_{01} have roughly a 2 percent reduction. In comparison, the diffuser performance is relatively insensitive to the gap size reduction, as C_p increases by less than 1 percent. Substituting these changes into Eq. (16), $\Delta' p_3/p_3$ is found to be -1.65 percent. Of this -1.65 percent change, -1.32 percent is due to the $\Delta' p_{02}$ term and 0.60 percent is due to the $\Delta' p_2$ term, while only $+0.27$ percent is due to the diffuser term $\Delta' C_p$. As discussed above, the unsteadiness associated with the tip-leakage flow is responsible for the change in blockage and loss in the impeller exit flow. Both factors are major contributors to both impeller pressure ratios p_{02}/p_{01} and p_2/p_{01} (Table 3). In other words, impeller performance is more susceptible to interaction influence because of tip-leakage flow.

6 Discussion: Implications of Computed Results

It is found that diffuser performance depends primarily on the alignment of the diffuser vanes with the spatially averaged and

Table 4 Change of stage total-to-total pressure ratio and other performance parameters due to a reduction of radial gap size r_2'/r_2 from 1.092 to 1.054

Interaction	medium	strong	Δ'
$r_{2'}/r_2$	1.092	1.054	
impeller influence			
p_{02}/p_{01}	3.542	3.456	-2.44%
p_2/p_{01}	6.625	6.509	-1.75%
diffuser influence			
C_p	0.622	0.627	+0.77%
α_2	67.4°	66.9°	
Σ: stage performance (from Equation 16)			
p_3/p_{01}	5.461	5.371	-1.65%

time-averaged impeller exit flow angle. The implication is that reasonably accurate prediction of diffuser performance (in terms of C_p and C_{loss}) can be obtained from quasi-steady calculation because the upstream impeller merely determines the mean inlet flow. However, to improve further the prediction accuracy of diffuser pressure recovery and loss, modeling of upstream unsteadiness is necessary.

However, simulating impeller performance with a calculation based on the replacement of the downstream diffuser vanes with asymmetric boundary conditions will have substantially more adverse effect on prediction accuracy because of tip leakage flow. As seen above, the unsteadiness in the tip leakage flow substantially alters the blockage and loss associated with tip leakage, which in turn causes a significant change in impeller performance.

Since stage performance depends on both impeller performance and diffuser performance, and impeller performance can be significantly affected by interaction, the time-accurate calculation for stage performance prediction is desirable, provided computational resources are available. However, design engineers can still find guidance of the one-dimensional model developed in the current investigation, because it clearly shows the trade-off between loss, blockage, and slip which leads to an optimum $r_{2'}/r_2$ value between 1.05 and 1.09. Thus, this model provides an effective platform to present flow data (whether they are from CFD or experiment) for engineers to evaluate and make design decisions.

7 Summary and Conclusions

A computational investigation has been undertaken to elucidate the effects of impeller–diffuser interaction on the performance of a centrifugal compressor stage, especially on stage total-to-static pressure ratio. The following conclusions were deduced from computed results:

1 Impeller–diffuser interaction has a pronounced effect on impeller tip leakage flow and a consequent impact on loss, blockage, slip and, ultimately. on stage pressure rise.

2 The effect of impeller outlet unsteadiness on diffuser pressure recovery and loss is similar in magnitude to that from diffuser inlet axial distortion. Both have little influence when compared to the dominant factor: incidence of the spatially averaged and time-averaged flow onto the diffuser vanes.

3 The optimum radial gap size to achieve the highest total pressure ratio in an impeller occurs because the penalty of increased loss overtakes the benefits from reduced blockage and slip when diffuser vanes are moved very close to the impeller blades. The computed results agree both qualitatively and quantitatively with measurements of some stages with varied tip gap radius ratio.

4 Most of the interaction effects on impeller pressure rise could be captured with a one-dimensional model, although the factors involved (loss, blockage, and slip) had to be obtained here from time-accurate calculation.

Acknowledgments

The work presented in this paper has been partially supported by Ishikawajima-Harima Heavy Industries (IHI) Co., Ltd., at Toyosu, Honeywell Engines, and NASA Glenn Research Center. Mr. Hiroshi Yamaguchi and Mr. Hideaki Tamaki of IHI, Dr. A. Sehra (formerly) of Honeywell Engines, Dr. D. Reddy and Dr. K. Suder of NASA Glenn Research Center acted as technical monitors. Additional computational resources have been provided by the NASA Lewis LACE computer cluster. The CFD code used was provided by Prof. W. Dawes of Cambridge University while the compressor design was obtained from Honeywell Engines. The authors have benefited from discussions with Prof. E. Greitzer of MIT, Prof. W. Dawes of Cambridge University, and Prof. F. Marble of Caltech. All support is gratefully acknowledged.

Nomenclature

A = actual channel geometric area
A_{eff} = effective passage area at impeller exit
B = blockage
C_A, C_s, C_θ = influence coefficients for impeller total pressure
C_A^-, C_s^- = influence coefficients for impeller static pressure
C_{loss} = diffuser loss coefficient
C_p = diffuser pressure recovery coefficient
C_{p0} = specific heat capacity at constant pressure
K_{p02}, K_{p2}, K_{C_p} = influence coefficients for stage pressure ratio
k = turbulent kinetic energy
M = Mach number
$\dot{m}$ = mass flow
p, p_0 = static, total pressure
R = gas constant
r = radial coordinate
s = entropy
T, T_0 = static, total temperature
T = period, blade passing
t = time
U = impeller speed
V = absolute velocity
W = relative velocity
x = axial coordinate (from diffuser hub to shroud)
α = absolute swirl angle referenced to the meridional direction
γ = specific heat ratio
Δ = incremental change from vaneless configuration
Δ' = incremental change due to reduction of radial gap size
ε = turbulent dissipation rate

η_{poly} = impeller polytropic efficiency
θ = relative flow angle
ρ = density

Subscripts and Superscripts

1 = at impeller inlet
2 = at impeller exit or same as vaneless space inlet
2+ = interaction plane location where impeller grid and diffuser grid meets
2′ = at diffuser inlet or same as vaneless space exit
3 = at diffuser exit
i = ideal
mp = midpitch, midway between the diffuser leading edges
ps = pressure side
rel = in relative (impeller) frame
ss = suction side
t = tangential
tip = tip leakage
( ) = time-averaged quantities, for expression with both time-averaged and instantaneous quantities present

References

[1] Dean, R., and Senoo, Y., 1960, ''Rotating Wakes in Vaneless Diffusers,'' ASME J. Basic Eng., **82**, pp. 563–574.
[2] Johnston, R., and Dean, R., 1966, ''Losses in Vaneless Diffusers of Centrifugal Compressors and Pumps,'' ASME J. Basic Eng., **88**, pp. 49–60.
[3] Cumpsty, N., 1989, *Compressor Aerodynamics*, Longman Scientific and Technical, Essex, England.
[4] Filipenco, V., Deniz, S., Johnston, J., Greitzer, E., and Cumpsty, N., 2000, ''Effects of Inlet Flow Field Conditions on the Performance of Centrifugal Compressor Diffusers: Part 1—Discrete-Passage Diffuser,'' ASME J. Turbomach., **122**, pp. 1–10.
[5] Deniz, S., Greitzer, E., and Cumpsty, N., 2000, ''Effects of Inlet Flow Field Conditions on the Performance of Centrifugal Compressor Diffusers: Part 2—Straight-Channel Diffuser,'' ASME J. Turbomach., **122**, pp. 11–21.
[6] Phillips, M., 1997, ''Role of Flow Alignment and Inlet Blockage on Vaned Diffuser Performance,'' Report No. 229, Gas Turbine Laboratory, Massachusetts Institute of Technology.
[7] Kirtley, K., and Beach, T., 1992, ''Deterministic Blade Row Interactions in a Centrifugal Compressor Stage,'' ASME J. Turbomach., **114**, pp. 304–311.
[8] Dawes, W., 1995, ''A Simulation of the Unsteady Interaction of a Centrifugal Impeller with its Vaned Diffuser: Flows Analysis,'' ASME J. Turbomach., **117**, pp. 213–222.
[9] Domercq, O., and Thomas, R., 1997, ''Unsteady Flow Investigation in a Transonic Centrifugal Compressor Stage,'' AIAA Paper No. 97-2877.
[10] Rodgers, C., 1982, ''The Performance of Centrifugal Compressor Channel Diffusers,'' ASME Paper No. 82-GT-10.
[11] Clements, W., and Artt, D., 1989, ''The Influence of Diffuser Vane Leading Edge Geometry on the Performance of a Centrifugal Compressor,'' ASME Paper No. 89-GT-163.
[12] Storer, J., and Cumpsty, N., 1991, ''Tip Leakage Flow in Axial Compressors,'' ASME J. Turbomach., **113**, pp. 252–259.
[13] Van Zante, D., Strazisar, A., Wood, J., Hathaway, M., and Okiishi, T., 2000, ''Recommendations for Achieving Accurate Numerical Simulation of Tip Clearance Flows in Transonic Compressor Rotors,'' ASME J. Turbomach., **122**, this issue, pp. 733–742.
[14] Shapiro, A., 1953, *The Dynamics and Thermodynamics of Compressible Fluid Flow*, The Ronald Press Company, New York.
[15] Khalid, S. A., Khalsa, A., Waitz, I., Tan, C., Greitzer, E., Cumpsty, N., Adamczyk, J., and Marble, F., 1999, ''Endwall Blockage in Axial Compressors,'' ASME J. Turbomach., **121**, pp. 499–509.
[16] McDougall, N., and Dawes, W., 1987, ''Numerical Simulation of the Strong Interaction Between a Compressor Blade Clearance Jet and Stalled Passage Flow,'' presented at Seventh GAMM Conference on Numerical Methods in Fluid Mechanics, Louvain, Belgium.